CLRC

COUNCIL FOR THE CENTRAL LABORATORY
OF THE RESEARCH COUNCILS

Central Laser Facility

Rutherford Appleton Laboratory

Annual Report 1999-2000

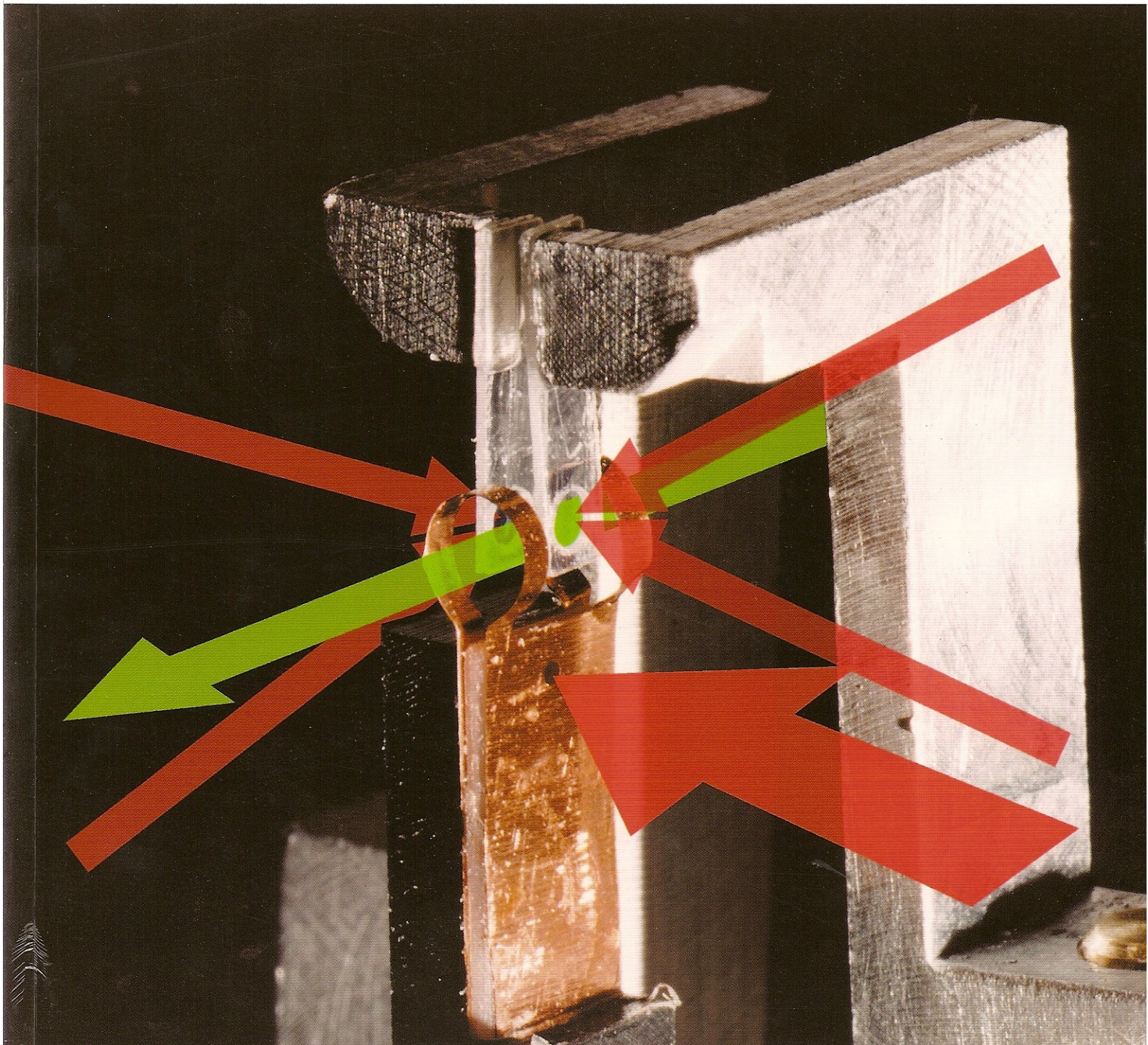

Enquiries about copyright, reproduction and requests for
additional copies of this report should be addressed to:

The Central Laboratory of the Research Councils
Library and Information Services
Rutherford Appleton Laboratory
Chilton
Didcot
Oxfordshire
OX11 0QX
Tel: 01235 445384 Fax: 01235 446403
E-mail: library@rl.ac.uk

ISSN 1358-6254

Central Laser Facility

Rutherford Appleton Laboratory

Annual Report 1999/2000

Central Laser Facility
Rutherford Appleton Laboratory
Chilton, Didcot
Oxfordshire OX11 0QX
Tel. 44 (0) 1235 445655
Fax. 44 (0) 1235 445888
E-mail. clf@rl.ac.uk
Web site. http://www.clf.rl.ac.uk

RAL Report No. RAL-TR-2000-034

The front cover shows an innovative integrated target consisting of two thin foils positioned at the centre of a millimetre scale Helmholtz coil. Also shown are the laser beams which drive the Helmholtz coil and explode the foils and the green laser beam which probes the plasma. (Photograph courtesy of Robert Grundy).

ISBN 0902376012

Acknowledgements

The production team for this Annual Report was as follows:

Editor	Brian Wyborn
Overall Co-ordination	Alison Brown
Production	Dave Burgess
Chapter Editors	David Neely, Steven Rose, Andrew Langley, Tony Parker, Colin Danson, Graeme Hirst
Section Editors	Ric Allott, Margaret Notley, David Neely, Pavel Matousek, Stanley Botchway, Waseem Shaikh, Colin Danson, Andrew Langley, Mike Towrie, Rob Clarke, Ian Ross
Technical Support	Chris Reason, RAL CLEO Support.

This report is available on the CLF's Web Page Ref. http://www.clf.rl.ac.uk/.

The document has been reproduced by the RAL Reprographics Section.

Thanks to all the above for their contribution towards producing this report and of course to all the authors for their submissions.

Contents

Long Pulse Plasmas Physics and X-Ray Laser Physics

Theory and Computation

Biology

Physics

Facility Development

Vulcan

Contents

Long Pulse Plasmas Physics and X-Ray Laser Physics

Theory and Computation

Biology

Physics

Facility Development

Vulcan

Foreword

M H R Hutchinson

Central Laser Facility, CLRC Rutherford Appleton Laboratory, Chilton, Didcot, Oxon, OX11 0QX

This report contains scientific accounts of the work which has been carried out at the Central Laser Facility (CLF) of the Rutherford Appleton Laboratory (RAL) both by university users and facility staff during the financial year 1999/2000. The year has again been highly productive with important developments both in Vulcan, Astra and the Lasers *for* Science Facility (LSF).

One of the most conspicuous developments in the CLF during the year has been the progress towards the construction of the Petawatt upgrade of Vulcan. This is a major project which, when complete in 2002, will enable the users of the facility to study the interaction of light with matter at the highest intensities available world-wide.

The Vulcan laser has continued to provide the focus of the very strong, international research programme in laser-plasma interactions. Experiments using intensities of up to $5x10^{19}$ W/cm^2 have shown that laser-produced plasmas can be an efficient source of very energetic electrons, gamma rays and ions. The first experiments on point projection imaging radiography of solids and plasmas with protons from laser-produced plasmas have been carried out. In other experiments, heavy ion fusion of ions produced at high energy has been developed as a diagnostic for high-intensity laser-solid interactions and the acceleration of electrons up to 10 MeV by self-modulated laser wakefield processes has been studied using photo-nuclear activation for electron diagnostics. In the first demonstration experiment, it was shown that potential difficulties in the Fast Ignition concept for Inertial Fusion Energy (IFE) may be overcome using alternative target geometries. Using longer pulses, novel studies of x-ray laser schemes have been carried out.

The Astra laser has been further upgraded to produce higher intensities. New studies of the ionisation and dissociation of molecular systems have been performed and methods for analysing environmentally-sensitive gases and solid phase materials have been developed. At higher intensities, the generation of protons from a compact, table-top system has been demonstrated in preliminary experiments.

Over the past years the LSF has developed high repetition rate picosecond/femtosecond optical parametric amplifier (OPA) systems for investigating ultrafast dynamics of molecules in condensed phase. During the year, EPSRC awarded funding to build the PIRATE (Picosecond IR Absoption and Transient Excitation) facility which extends the current OPA capabilities to provide high brightness spectral coverage in the Mid IR. This facility will be used for a programme of research in transient absorption and TR^3 spectroscopy. A wide-ranging programme in physics, chemistry and biology has been carried out using a variety of specialist laser systems.

The science being carried out within the CLF by university colleagues from both within the UK and elsewhere in Europe continues to be of the highest quality. This was recognised in the independent report on “International Perceptions of UK Research in Physics and Astonomy” which noted that “due to the availability of the Vulcan laser at RAL several outstanding experiments on laser-plasma interactions have recently been carried out by productive university groups” and recognised the laser facility as “the most outstanding facility world-wide for performing high intensity laser experiments.” I believe we can look forward to further successes, both in the development of world-class facilities at RAL and the excellence of the science being carried out.

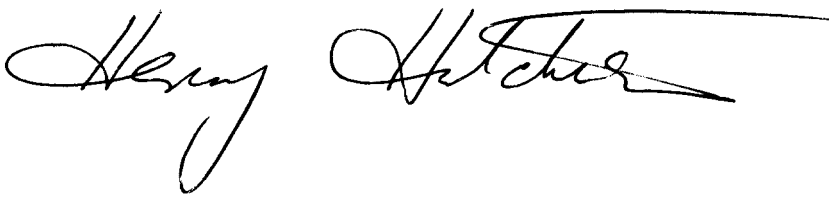

Overview of the Central Laser Facility

C B Edwards

Central Laser Facility, CLRC Rutherford Appleton Laboratory, Chilton, Didcot, Oxon, OX11 0QX

Main contact email address: *c.b.edwards@rl.ac.uk*

Laser Facilities for Users

The Central Laser Facility (CLF) is a world leading centre for research using lasers. Facilities available to users include the Vulcan Nd: glass laser which delivers multi- TW beams to two target areas, the Astra ultra- short pulse interaction facility based on titanium sapphire laser technology, a range of state of the art table top laser systems and specialised diagnostic instruments within the Lasers *for* Science Facility and the Laser Loan Pool.

Vulcan

Vulcan is a highly versatile large scale Nd: glass laser installation which delivers a maximum of 2.5 kJ of energy in its six 10 cm and two 15 cm beamlines to two target areas, each of which is equipped with frequency conversion optics to enable both 1 μm and 0.5 μm operation of all beams. A range of pulse durations are available from 100 ps to 20 ns in various geometries.

A short pulse (700 fs) high irradiance (~5x10 ^{19} Wcm $^{-2}$) chirped pulse amplification (CPA) capability is available, with vacuum propagation to target and reflective beam focusing optics. Additional low energy beams, including sub- picosecond CPA probes, are provided for diagnostics with high temporal resolution. The system is fully characterised and equipped with advanced diagnostics.

A 3 year development of Vulcan began in April 1999. The project, which will upgrade the short pulse beamline to the Petawatt level, involves the addition of an additional stage of disc amplifiers, the construction of a large aperture vacuum beam compressor and a new target chamber within a new target area building. The new amplifiers will be installed in the area formerly known as TA2, the two beam target area, which was closed to users in March 2000 after 20 years of highly productive operation.

Lasers *for* Science Facility (LSF)

The LSF operates a suite of state of the art table-top laser systems and associated instrumentation giving users access to highly tuneable (vuv - ir) and variable pulse width (ns to fs) laser radiation. This includes lasers for ns and ps time- resolved resonance Raman spectroscopy (TR^3), a unique dual wavelength multi- khz femtosecond synchronised pump- probe apparatus based on optical parametric amplification (OPA) technology, a femtosecond laboratory, a high average power laser plasma x- ray source and a fast gated (100 ps) confocal microscopy laboratory.

This year saw the commissioning of the new PIRATE facility (Picosecond Infrared Absorption and Transient Excitation). The high brightness PIRATE laser, which is tunable down to 1000 cm $^{-1}$, came on line to users in 2000 for experiments in chemistry, physics, biological and material sciences.

Commercial laser systems are available from the Laser Loan Pool for periods of up to 6 months at the user's home laboratory.

Astra

The Astra laser facility delivers high power laser radiation to target at 10 Hz. The facility has been upgraded substantially during the year with the addition of an additional stage of amplification and a new vacuum pulse compression system and target chamber in a new target area.

Target Area I provides pulses of 50 fs duration with an energy of 10 mJ, producing irradiance on target in excess of 10^{16} Wcm $^{-2}$. The Target Area II currently delivers 250 mJ in 50 fs with target irradiance in the 10 ^{18} Wcm^{-2} regime. This performance is presently limited by the availability of titanium sapphire crystals of the required quality but the laser hardware is in place to increase the energy output and increase the irradiance to approximately 10 ^{19} Wcm^{-2}.

Engineering Services

Mechanical, electrical and software engineering support is provided for the operation of the laser facilities at the CLF, for the experimental programmes on these facilities and for the CLF's research and development activities. Access to mechanical and electrical computer aided design (CAD) tools and workshop facilities enable a rapid response to be provided to users.

Access to Facilities

The primary funding sources of the Central Laser Facility are the UK Research Councils, who make beam time available for UK University researchers and their overseas collaborators through the responsive mode grant mechanism. A small proportion of access is available for "Direct Access", to enable rapid access for urgent, topical and proof of principle experiments.

Bids for Direct Access beamtime are peer reviewed by an expert panel who advise the Director of the CLF on scientific priority, etc. Calls for Direct Access are publicised in scientific journals and on the CLF Web site. Further information is available from the Director of the CLF.

Arrangements for funding of beamtime for experiments within the remit of the BBSRC programme differs from the EPSRC model and potential applicants working in these areas should contact the Director of the CLF in the first instance for further information.

In the current year, the EC provided beam time for European researchers through a Large Scale Facility Access contract under the TMR programme. This activity will be continued in the Fifth Framework Programme under the new theme of Improving Human Potential (IHP). Calls for Proposals are publicised in Physics Today and on the CLF Web site. For information on forthcoming calls for proposals, eligibility criteria, etc. please contact Dr Ric Allott (r. allott@ rl. ac. uk).

The Laser Loan Pool is funded directly by an EPSRC rolling programme. These facilities are available to all UK researchers performing work falling within the EPSRC science programme. For information on calls for proposals, eligibility criteria, etc. please contact Dr Mike Towrie (M.Towrie@ rl. ac. uk).

Hiring of the facilities and access to CLF expertise is also available on a commercial basis for industrial research and development.

CLF Web site

Further information on the CLF, its facilities, and the scientific programmes is available on the CLF Web site at http:// www. clf. rl. ac. uk/.

Science – High Power Laser Programme

1) Short Pulse Plasma Physics

2) Long Pulse Plasma Physics and X-Ray Laser Physics

3) Theory and Computation

Investigation of ultra-intense laser interaction with overdense preformed plasma

D H Campbell, A Schiavi, O Willi

Blackett Laboratory, Imperial College of Science, Technology and Medicine, London, SW7 2BZ, UK

M Borghesi

Department of Pure and Applied Physics, The Queen's University, Belfast, UK

A J Mackinnon

Lawrence Livermore National Laboratory, Livermore, CA, USA

M Galimberti, L A Gizzi

IFAM-CNR, 56100 Pisa, Italy

W Nazarov

Chemistry Department, University of Dundee, UK

Main contact email address: *duncan.campbell@ic.ac.uk*

Introduction

The interaction of ultra-high intensity laser pulses with overdense plasmas is of particular relevance to the Fast Ignitor scheme[1)] for Inertial Confinement Fusion. This scheme requires the deposition of energy of an ultra-intense laser pulse as close as possible to the core of a compressed fuel pellet. It is necessary for the pulse to propagate and channel through a long scale-length plasma which reaches densities many times critical. Investigation of propagation in well characterised overdense plasmas has thus far been limited to computational modeling [2)] and interaction with thin solid targets [3,4)].

Here we present results of experimental investigations of the interaction of an ultra-intense laser pulse with overdense preformed plasmas. The plasmas were preformed using soft x-ray preheating of low-density foam targets of various thicknesses. Simulations indicate interaction with an overdense region 50-200 μm in length. X-ray pinhole camera images reveal emitting filaments along the laser path extending through the plasma. Localised expanding plasma was observed on the rear of the target, in line with the laser direction. In addition, observations suggest possible marginal transmission of laser energy through shorter plasmas.

Experimental Set-up

The experiment was performed using the Vulcan laser operating in the Chirped Pulse Amplification (CPA) mode. The experimental arrangement is shown in Figure 1.

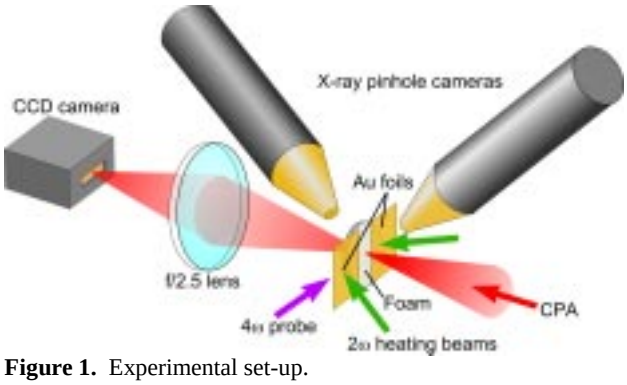

Figure 1. Experimental set-up.

Triacrylate and CH foams of different densities and lengths were used as targets. The triacrylate foams were 50 μm thick with density 10 or 20 mg/cc and were mounted in washers with a parylene backing. The CH foams were free-standing and had density 30 or 50 mg/cc and lengths from 100 to 250 μm. Two gold burn-through foils (700 Å of Au on 1 μm formvar) were positioned 50 μm in front of the foam, 200 μm apart. Two 600 ps beams were used to preheat the target. These were frequency doubled to 527 nm using KDP crystals. The two heating beams were focused onto the gold foils using f/10 lenses. This produced intensity of the order of 2×10^{14} Wcm^{-2} at the foils. The x-rays emitted by the foils [5)] were used to heat and ionise the foam target [6)] to produce the required plasma conditions. The CPA beam, operating at 1054 nm with a pulse length of 1 ps FWHM, was focused onto the preheated foam plasma with a f/3.5 off-axis parabola producing an intensity on target in excess of 10^{19} Wcm^{-2}. The delay between the plasma preforming pulses and the CPA pulse was between 800 and 1500 ps to allow the radiation wave to propagate through the foam.

Several diagnostics were used during each shot to provide information on the plasma formation and laser interaction. X-ray pinhole cameras with 25 μm pinholes were placed in front of and behind the target (Figure 1). The cameras were loaded with Kodak Industrex x-ray film. A 25 μm Be foil was used as a filter, transmitting radiation above 1 keV. Transmitted laser light was collected with an f/2.5 lens behind the target. The lens imaged the focal plane of the parabola onto an optical CCD camera to record transmission of the main laser pulse.

A 4ω pulse, 1 ps FWHM was used as a transverse optical probe. Delay relative to the main pulse was controlled to within a few picoseconds. An UV f/4 objective was used to image the target onto photographic film.

Experimental Results

Figure 2 presents a typical CCD image of the rear of one of the thinner targets showing transmitted radiation. This is observed only through foams 50 μm thick with density of 20 or 10 mg/cc.

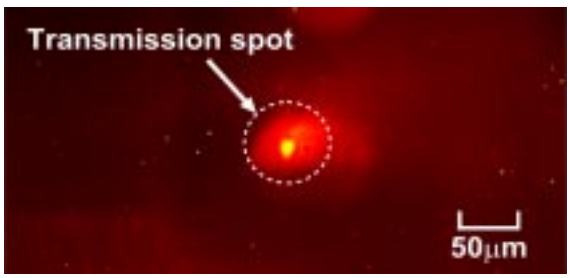

Figure 2. CCD image of target rear, transmission observed through a 20 mg/cc, 50 μm long foam target.

A bright spot is seen corresponding to the size, shape and position of the laser focal spot, suggesting that the energy transmission takes place during the CPA interaction.

The optical CCD was calibrated with a low energy shot (0.1 J). From this it is estimated that less than 10^{-5} of the initial laser energy was transmitted.

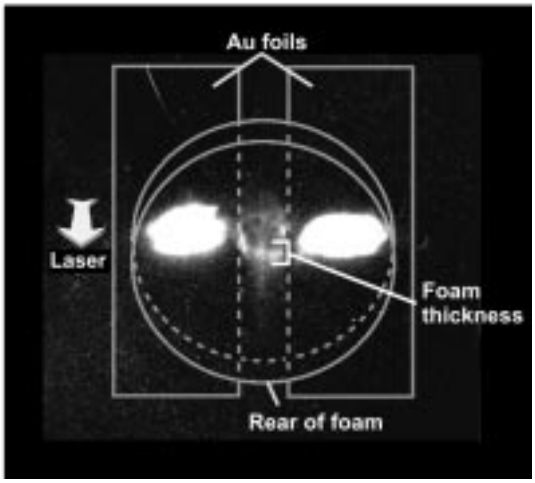

Figure 3. Soft x-ray image from rear pinhole camera with overlay showing the position of the surfaces of the foam and the gold foils.

X-ray images from the rear pinhole camera (Figure 3) show bright filaments extending through the foam and some distance beyond. The film shows the bright spots of the heating beams on the foils with a vertical filament in the centre. Such filaments are observed on several shots for different foam densities and lengths. In rare cases, breaking up of the filaments at the rear of the foam was observed.

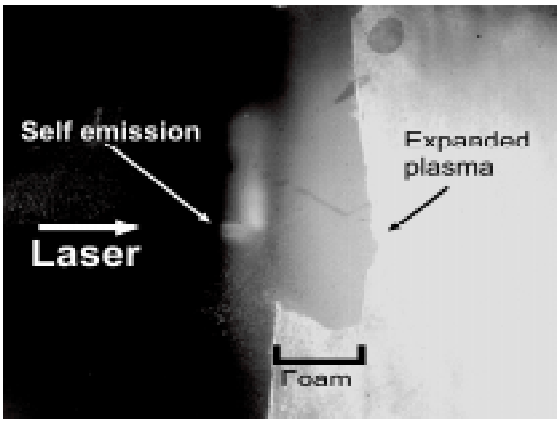

Figure 4. Shadowgram of a 150 μm freestanding foam showing expansion of the rear side.

Figure 4 presents a shadowgram produced by transverse optical probing. The image displays a profile of the target 50 ps after the CPA pulse. A localised region of expanding plasma is visible on the rear of the foam which lines up with the self-emission from the CPA interaction at the front. This localised expansion implies a collimated transport of energy through the foam.

Modelling and discussion

Plasma simulations have been carried out using the 1D Lagrangian hydrocode MEDUSA to determine the electron density of the plasma at the time of laser interaction. Simulated CH and triacrylate foams were heated with x-rays with temperature 60 or 120 eV (corresponding to one or two heating beams). Typical results (Figure 5) show a uniform ionisation with an electron density profile peaking for all target types at around $8n_c$. The electron density remains above critical density for length similar to the unexploded foam length. PIC simulations are planned to discriminate between the various mechanisms that could be responsible for the observed results.

The x-ray filaments within the plasma could be produced by heating of the plasma by the laser as it propagates through the overdense plasma. This is possible in the high intensity regime due to either induced transparency[7] caused by relativistic modification of critical density or hole boring[8] due to the ponderomotive pressure. Alternatively, the filaments could be produced by a stream of fast electrons, accelerated by the laser. As a matter of fact, localized expansion at the rear of the target has been attributed, in the past [9], to fast electrons emerging from the target. The set of results seems to indicate that overdense laser propagation takes place, but in order to confirm this, further observations, analysis and modelling are required.

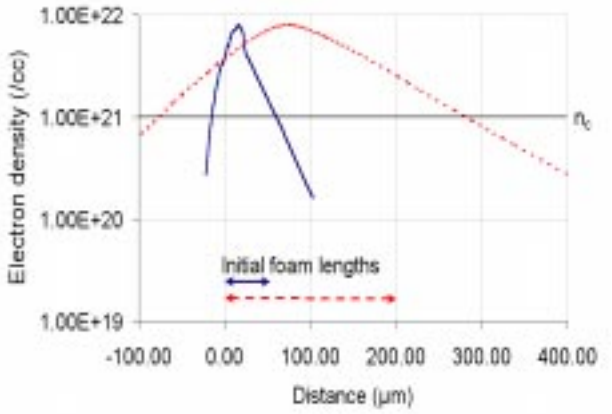

Figure 5. Simulated electron density profiles for 20 mg/cc, 50 μm long (solid line) and 30 mg/cc, 200 μm long (dashed line) foams at the time of CPA interaction.

Acknowledgements

Our thanks go to the staff of the Central Laser Facility for their assistance and support throughout the experiment. The experiment was funded by an EPSRC grant.

References

1. M. Tabak *et al*, Phys. Plasmas. 1**,** 1626, (1994)
2. A. Pukhov & J. Meyer-ter-Vehn, Phys. Rev. Lett. 79, 2686 (1997)
3. J. Fuchs *et al*, Phys. Rev. Lett. 80, 2326 (1998)
4. M. Zepf *et al*, Phys. Plasmas 3, 3242 (1996)
5. D. R. Kania *et al*, Phys. Rev. A 46, 7853 (1992)
6. T. Afshar-rad *et al*, Phys. Rev. Lett. 73, 74 (1994)
7. P. Kaw & J. Dawson, Phys Fluids 13, 472 (1970)
8. S. C. Wilks *et al*, Phys. Rev. Lett. 69, 1383 (1992)
9. M. Tatarakis *et al*, Phys. Rev. Lett. 81, 999 (1998)

Propagation of 50 TW, picosecond pulses through preformed plasma channels

M Borghesi

Department of Pure and Applied Physics, The Queen's University, Belfast, Northern Ireland BT7 1NN, UK

A Schiavi, H Campbell, O Willi

Blackett Laboratory, Imperial College of Science, Technology and Medicine, London SW7 2BZ, UK

M Galimberti, L A Gizzi

IFAM-CNR, 56100 Pisa, Italy

Main contact email address: *m.borghesi@qub.ac.uk*

Introduction

The Fast Ignitor (FI) approach[1] to Inertial Confinement Fusion motivates much of the present interest in ultra-intense laser-plasma interaction studies. In fact, as the scheme relies on the energy of an extremely intense laser pulse to start ignition in a compressed capsule, the study of the propagation of ultra-intense laser pulses through dense plasmas is of great relevance to the success of this scheme. Nonetheless, this type of studies is of great topical interest even due to the novel and complex physics involved. This paper presents results obtained in an experimental campaign recently carried out at the Vulcan laser facility, Rutherford Appleton Laboratory (UK). In the Chirped Pulse Amplification (CPA) mode the Vulcan laser provides up to 75 J in 1 ps pulses at a wavelength of 1.054 µm. The propagation of relativistically intense pulses through preformed plasmas was investigated in the experiments. The analysis and the interpretation of the data are currently in progress. In the following sections, the aims of the experiments, the techniques employed and the main results obtained will be briefly described.

Experimental arrangement

The plasmas were produced by exploding thin plastic foils (0.1, 0.3 or 0.5 µm thick) with two 1 ns, 0.527 µm laser pulses at a total irradiance of about 5 x 10^{14} W/cm^2 as shown in Figure 1. After a suitable delay (typically of the order of 1 ns) the CPA pulse was focused into the plasma.

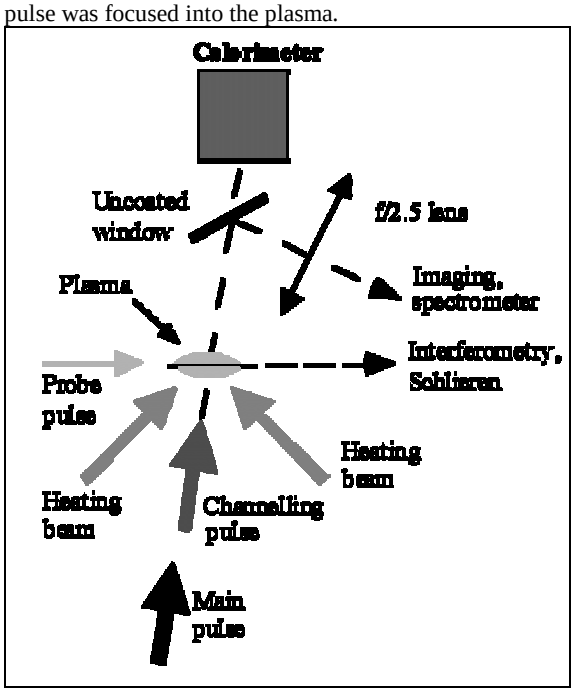

Figure 1. Experimental arrangement.

At this time the peak density of the plasma was below $n_c/10$ and its longitudinal extension was of the order of 1-2 mm. With f/3.5 focusing optics the CPA vacuum irradiance was up to 5 x 10^{19} W/cm^2 (about 50 J on target, with up to 50 % of the energy in a 10-15 µm focal spot). A fraction of the energy of the main CPA pulse was used to provide a prepulse, collinear with the main pulse. The prepulse could be focused into the plasma ahead of the main pulse and used to open a density channel. A further small fraction of the CPA pulse was frequency quadrupled and used as a transverse optical probe. Interferometry was performed along this line using a modified Nomarsky interferometer[2]. Other diagnostics included calorimetry of the energy transmitted through the plasma, imaging of the transmitted laser spot, forward and back-scatter spectroscopy, γ-ray measurements.

Experimental results

The propagation of the main CPA pulse through the plasma was first studied without a preformed plasma channel. The energy transmission through the plasma in this case was very low, as seen in Figure 2. The peak densities were estimated using the London and Rosen model[3]. Even when using 0.1 µm targets, which gave a plasma with a peak density of a few times $n_c/100$, the energy transmitted was limited to a few per cent of the laser energy incident on target. This is consistent with numerical simulations[4] and previous experiments[5], which have reported anomalously high laser absorption even in very underdense plasmas for relativistically intense laser pulses.

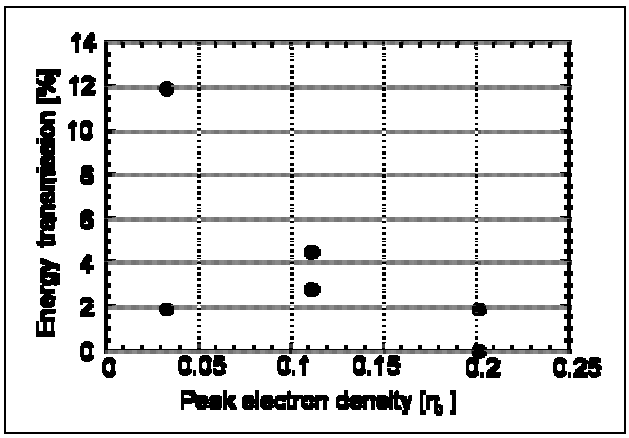

Figure 2. Transmission of CPA pulse energy versus peak density in long-scale, underdense plasmas.

Reduction in energy transmission may also be related to the onset of relativistic filamentation[5] rather than whole-beam self-focusing [6]. Relativistic filamentation can cause spreading of the beam energy at angles much larger than the focusing angle and has been correlated with more efficient energy transfer into hot electrons. Filamentation and beam spreading was indeed observed in the experiment, as seen for example in Figure 3(a), showing an interferogram taken 5 ps after the interaction of a 50 TW pulse with the plasma. The dashed white line indicates the angle of the cone defined by the focusing optics (f/3.5). Some of the filaments appear to diverge at angles larger than the collection angle (about f/3.5) of the calorimeter. The filamentation is even more evident in Figure 3(b), showing the

second image of the interaction region in the same interferogram of Figure 3(a). As the fringes on this second image were coarser, the image can be interpreted as a shadowgram of the interaction region. Filaments breaking into other filaments can be seen. It should be noted that such a behaviour was not observed in previous experiments performed at lower laser power (20 TW), in which a single self-focused filament was observed[7,8]. This, together with observations at varying intensities carried out in the present experiment, suggests a transition between two different regimes of interaction (whole beam self-channelling to relativistic filamentation) taking place in the 20-50 TW range.

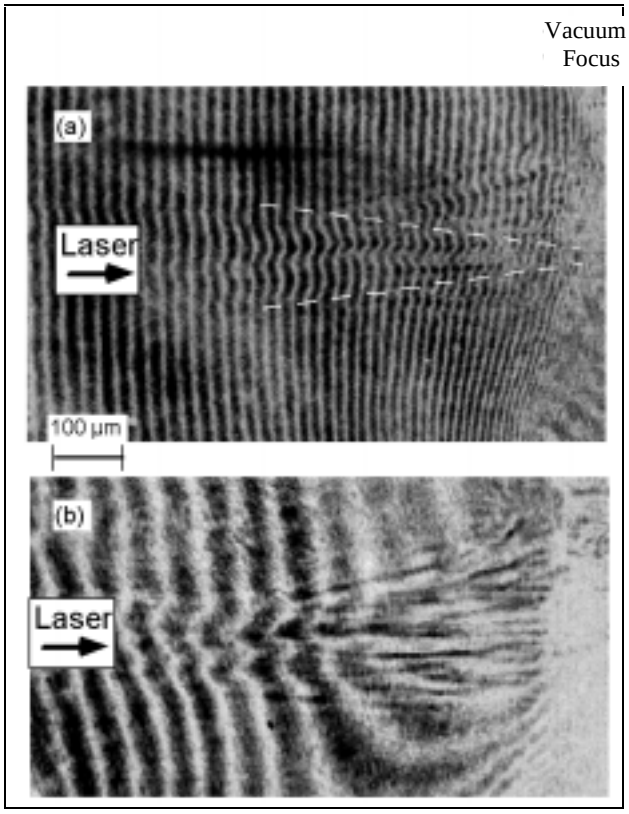

Figure 3. Details of an interferogram taken 5 ps after the propagation of a 50 TW pulse through a laser beam. The two images (a) and (b) (from the same interferogram) both show the interaction region. Laser-break-up and formation of filaments are clearly visible.

The effect of the presence of a preformed channel on the propagation of the main pulse was investigated. The channel was formed by focusing into the plasma the prepulse, with a prepulse-to-main ratio of 1:2. The intensity of the prepulse was also above 10^{19} W/cm^2, and a rapidly expanding channel was formed via ponderomotive expulsion of the electrons and subsequent Coulomb explosion, as observed in a previous experiment[7,8]. The interaction of the 25 TW pulse with the plasma appeared to be less affected by filamentation than in the 50 TW pulse case. An interferogram showing the channel 45 ps after its formation can be seen in Figure 4.

The main CPA pulse was focused into the channel at various stages of the channel expansion, and the CPA main pulse transmittance was measured, for various plasma conditions, as a function of the delay between the main and the channeling pulse.

A clear increase in energy transmission was observed, as visible for example in the graph shown in Figure 5. In the figure the energy transmission is plotted for the case of plasmas produced from 0.1 µm targets.

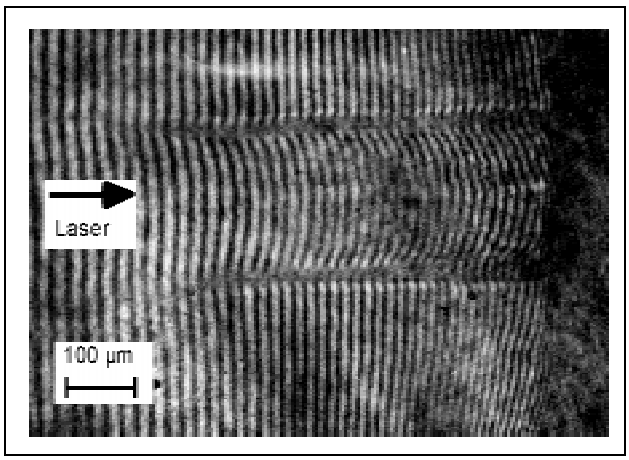

Figure 4. Interferogram of the channel taken 45 ps after its formation.

The energy transmitted through the plasma grows from the few per cent transmittance measured in absence of preformed channel to almost 100 % transmission when the channelling-to-main delay is of the order of 100 ps.

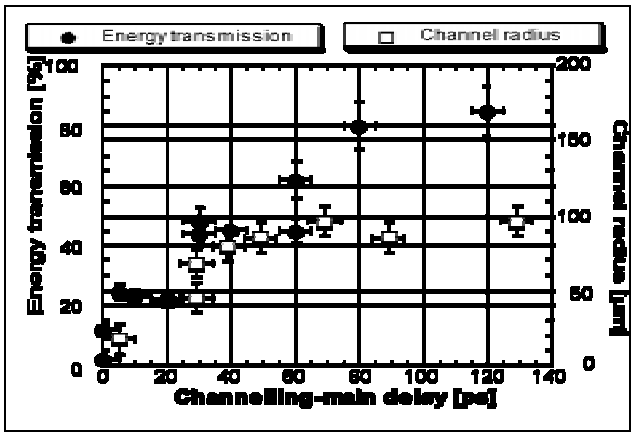

Figure 5. Energy transmission through an underdense plasma (peak density ≈ 0.03 n_c, length ≈ 1-2 mm, obtained from explosion of 0.1 µm targets) in presence of a preformed channel. The transmission is plotted versus the delay between the channel formation and the propagation of the main pulse. The temporal evolution of the channel radius is also plotted.

Although a detailed analysis of the data has still to be done, a number of preliminary considerations can be made. First, one has to take into account the energy distribution in the focal plane of the laser. Typically, only 30-40% of the energy is contained in the small size central spot (10-20 µm diameter), and this determines an intensity exceeding 10^{19} W/cm^2 in this spot. The rest of the energy is distributed throughout lower intensity wings extending around the central spot (a systematic characterization of the focal spot may be required, as previously done [9]). Efficient propagation of the energy contained in the high intensity spot is achieved even after 10-20 ps , with more than half of the energy transmitted through the plasma. The factors leading to increased transmission are substantially two:

1) the fact that the density profile across the channel acts as a positive lens on the main pulse propagating through it, limiting the diffraction of the beam.

2) the fact that the density inside the channel is significantly lower than the background plasma. This leads to decreased absorption and also reduces the effect of relativistic filamentation (as the threshold for relativistic self-focusing $P \propto n_c/n_e$ is increased).

The transmitted energy increase when the channelling-to-main delay is increased may be explained by the fact that, as the

channel expands, the low intensity, larger diameter wings of the focal spot are encompassed by the channel walls. The internal dynamics of the channel (e.g. the temporal evolution of the density inside the channel) will also play a role. Detailed modeling and data analysis are required to determine the relative importance of the different factors.

A similar trend for the transmission has been observed through denser plasmas, obtained by exploding 0.3 µm targets. The overall transmission is lower, and this may be due to less efficient channel formation over the whole plasma length as a consequence of the higher density of the plasma. Even in this case the transmission appears to grow with the delay, but a transmission peak is observed at a delay of 40 ps, where conditions for more efficient guiding may have been achieved due to channel density dynamics. Experimental measurements carried out in plasmas obtained from 0.5 µm foils also indicate higher transmission at delays of the order of 30-40 ps. This data set shows a considerable scatter probably due to variation in the plasma conditions. Careful analysis of the interferogram is required in order to discriminate between the various measurements and isolate the data referring to similar plasma conditions.

It is interesting to note that the high transmission observed in the data sets at delays of the order of 20-40 ps seems to correlate with γ-rays measurements performed during the same experiment, which are discussed elsewhere in this Annual Report [11].

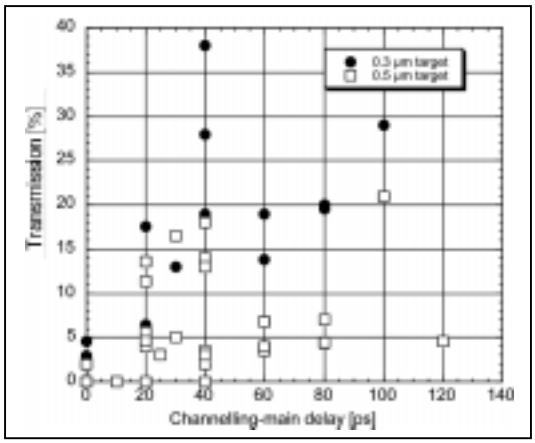

Figure 6. Transmission through plasmas obtained from explosion of 0.3 and 0.5 µm thick CH foils.

Conclusions

The propagation and transmission of relativistically intense picosecond pulses through underdense plasmas have been studied for different plasma conditions. Low transmission was observed even through very underdense plasmas, in correspondence with observation of filamentary laser break-up. The transmission was greatly improved when a channel was preformed ahead of the main laser pulse, using a fraction of the energy of the pulse itself. Under the right conditions up to 90% of the laser energy on target could be propagated through the plasma.

These measurements have obvious relevance to Fast Ignition. In particular, the measurements stress the importance of the presence of a preformed density channel in order to achieve efficient energy propagation through the plasma at ultrahigh intensity. In fact, in absence of a preformed channel the mm-sized coronal plasma surrounding the compressed core of the imploded capsule would be able to absorb most of the energy transported by the pulse.

Acknowledgements

We would like to acknowledge the important contribution to the experiment given by all members of staff of the Central Laser Facility at the Rutherford Appleton Laboratory.

References

1. M. Tabak, J. Hammer, M. E. Glinsky, W. L. Kruer, S. C. Wilks, J. Woodworth, E. M. Campbell, M. D.Perry and R. J. Mason, Phys. Plasmas, 1 1626 (1994)
2. R. Benattar, C.Popovics and R.Siegel Rev.Sci.Instrum. 50 1583 (1979)
3. R.A.London and M.D.Rosen Phys. Fluids 29 3813 (1986)
4. P. Chessa, O. Mora and T. M. Antonsen Jr Phys. Plasmas, 5 3451 (1998)
5. J. A. Cobble, R. P. Johnson and R. J. Mason Phys. Plasmas, 4 3006 (1997)
6. P. E. Young and P. R. Bolton Phys. Rev. Lett, 77 4556 (1996)
7. X.Wang, M. Krishnan, N.Saleh, H. Wang and D. Umstadter, Phys. Rev. Lett, 84 5324 (2000)
8. M.Borghesi, A.J. MacKinnon, L. Barringer, R. Gaillard, L.A. Gizzi, C. Meyer, O. Willi, A. Pukhov, J. Meyer-ter-Vehn, Phys. Rev. Lett., 78, 879 (1997)
9. M.Borghesi, A.J. MacKinnon, R. Gaillard, O. Willi, A. Pukhov, J. Meyer-ter-Vehn Phys. Rev. Lett., 80 5137 (1998)
10. C.N.Danson et al. J. Mod. Opt., 45 1653 (1998)
11. L.A.Gizzi *et al*, Central Laser Facility Annual Report 1999/2000, p21

Radiography of dense matter with laser-produced protons: preliminary tests

M Borghesi

Department of Pure and Applied Physics, The Queen's University, Belfast, Northern Ireland BT7 1NN, UK

A J Mackinnon*

Lawrence Livermore National Laboratory, California, USA

A Schiavi, H Campbell, O Willi

Blackett Laboratory, Imperial College of Science, Technology and Medicine, London SW7 2BZ, UK

Main contact email address: *m.borghesi@qub.ac.uk*

Introduction

During the interaction of ultra-intense laser pulses with plasmas and solid targets, a considerable fraction of the laser energy is deposited into highly energetic charged particles. In particular, great attention has recently been devoted to the generation of highly energetic proton beams. In a number of experiments, performed with different laser systems and different interaction conditions, protons with energies up to tens of MeV have been detected behind targets irradiated with high intensity pulses [1-4]. The particular properties of these beams (small source size, high degree of collimation, short duration, energy and directionality dependence on the target characteristics) make them of particular interest in view of possible applications.

Among these, their use as the ignition trigger in Fast Ignition has been proposed[5]. The characteristics of the proton beam make it very suitable for applications as a probe in high-density matter investigations. The use of protons as a radiographic source is an idea that has circulated for many years[6]. Protons can be used to probe the interior structure of systems that are either static or evolving with time. Biomedical applications of this technique have been proposed, particularly as a diagnostic tool in tumor treatment[7]. Also, a radiography facility to image imploding or exploding objects is presently being developed at LANL (US)[8], with the aim of using proton radiography in hydro-testing of nuclear-weapons primaries. Linear or cyclotron accelerators are usually used to obtain the proton energies required for these applications. Laser produced proton beams may represent a feasible alternative more suited to applications in which a very high spatial/temporal resolution is required. Since it consists of charged particles, a further diagnostic application of the proton beam is the detection of electric and magnetic fields generated during the interaction of intense laser pulses with high density plasmas.

In order to evaluate the effective promise of this application, some preliminary experimental tests of the propagation of the laser produced proton beams through plasmas and solid targets have been carried out.

Experimental set-up

The Vulcan Nd:glass laser operating in the Chirped Pulse Amplification mode (CPA) was used in the experiment. The main targets (used for the production of the proton beams) were Al foils, 1 mm wide and about 1 cm long and 25 µm thick. The 1.054 µm CPA interaction pulse, 1 ps in duration, with an energy of about 50 J was focused by an F/3.5 off-axis parabola (OAP) onto the centre of the main target. The incidence was about 15° off normal. The focal spot was between 8 and 10 µm in diameter at full width at half maximum (FWHM), containing 30-40 % of the energy, giving intensities up to 5×10^{19} W/cm^2. The protons were detected by using several layers of radiochromic film positioned at variable distance behind the target. Radiochromic films consist of two layers of plastic material containing a layer of organic dye, which reacts to ionizing radiation. The equivalent dose of energetic protons stopped in the film can be measured from the changes in optical density undergone by the film, yielding information on the number and energy of the protons. Al filters were placed in front of the first layer of film giving a minimum, detectable proton energy of 3.5 MeV.

Experimental results

The energy spectrum of the proton beam produced by the interaction is discussed elsewhere in this Annual Report [4]. At maximum laser intensity, protons with energies up to 20 MeV were observed. The beam was directed along the normal to the back surface of the Al foil, and was semi-collimated (with a typical aperture of about 15°). The size of the proton source was determined by using a penumbral image method. The edge of a 125 µm thick Ta foil was inserted on the proton beam. The foil was positioned at a distance of 2 mm from the main target, parallel to it, and covered approximately one half of the proton beam. A shadow of the object was observed in the proton beam, and by analysis of the optical density profile across the beam in the edge region, the size of the proton source could be estimated. In particular it was observed that the size of the source decreased for increasing energies, yielding for example 45 µm FWHM for 5 MeV protons, and 15-20 µm FWHM for 10 MeV protons. The shadow observed for 10 MeV protons is shown in Figure 1. For our intended applications, the source can be regarded as a point source, and used for point projection imaging of proton-absorbing objects placed between the source and the detector. Schematics of the set-up for the different parts of the experiment will be shown in the following sections.

Imaging of solid obstacles

When thick solid obstacles were placed in the beam a shadow of the object was observed in the proton beam, due to absorption of the proton energy in the target, as visible in Figure 1.

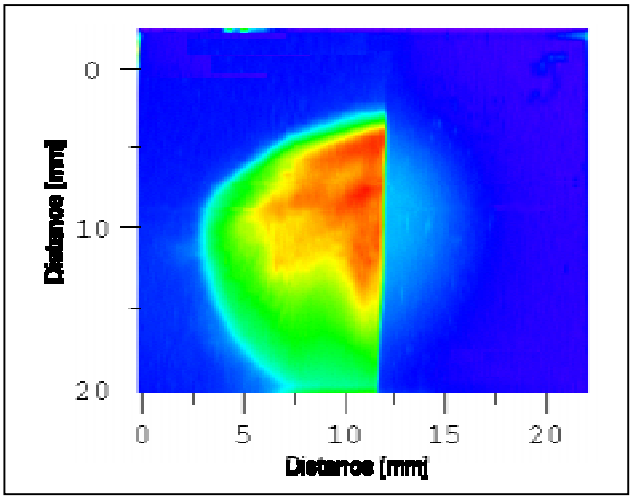

Figure 1. Shadow of a 125 µm thick Ta foil. The Ta foil covered the right half of the proton beam.

However a shadow was observed even when objects with a thickness much smaller than the proton penetration depth were used. For example a mesh formed by 10 µm Cu wires with 25 µm spacing was used. The set-up for this particular test is depicted in Figure 2. The mesh was parallel to the main target,

i.e. perpendicular to the proton beam. The distance between the proton source and the mesh was 500 µm, while the first of the radiochromic film layers was positioned at about 16 mm from the source.

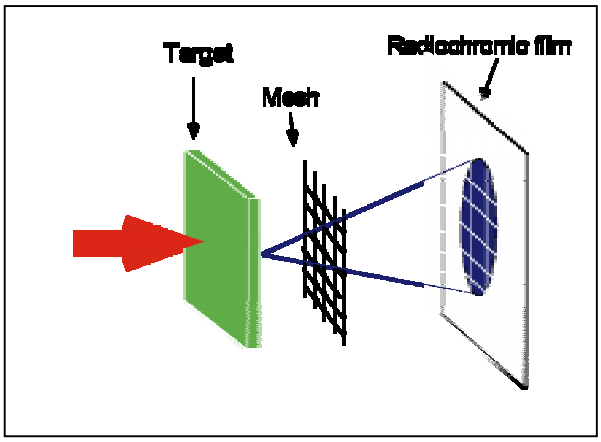

Figure 2. Set up for proton imaging of a mesh.

An image of the mesh was observed on the radiochromic film, as shown in Figure 3. The image shown in the picture has been obtained with protons with an energy of 10 MeV. The shadow of the wires can be observed quite clearly, the contrast of the picture being quite sharp.

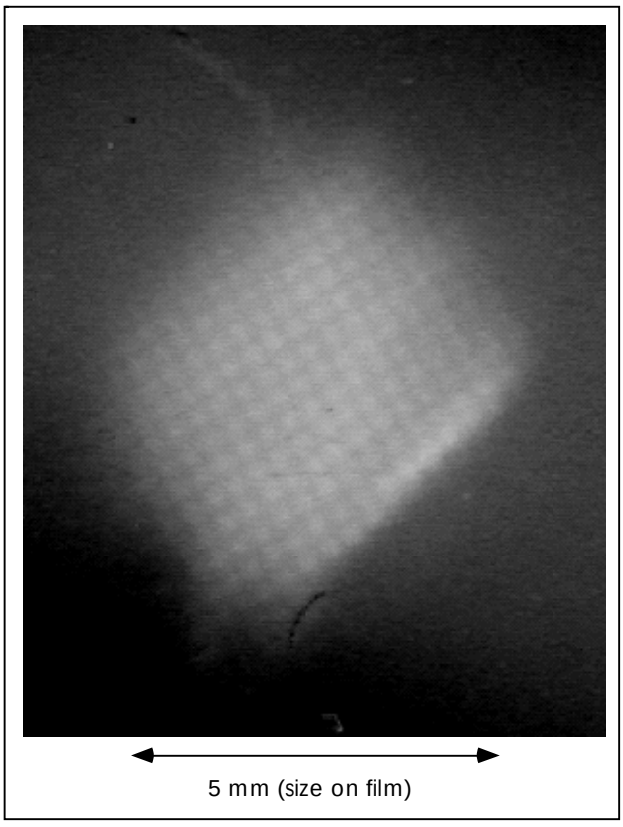

Figure 3. Shadow of a grid obtained on the radiochromic film with 10 MeV protons.

The interpretation of the data is currently in progress. Since the thickness of the wires is sensibly smaller than the stopping range for 10 MeV protons in Cu (which is about 250 µm), the protons passing through the wires of the mesh would suffer an energy loss of only about 0.1 MeV. This may determine a small contrast variation across the beam. However, one of the hypotheses under consideration is that the mesh charges up due, for example, to hot electron precursors, and that the deflection of the protons due to the electric field in the proximity of the wires contributes to produce a shadow of the mesh.

Proton imaging of plasmas

Preliminary observations of the interaction of the proton beam with a preformed plasma created on a secondary target were also carried out. The experimental set-up for this part of the experiment is shown in Figure 4. The proton beam was produced as usual from a 25 µm Al foil. A 125 µm Ta foil was inserted as shown in Figure 4. In some shots a plasma was preformed on the side of the Ta foil using a 600 ps, 0.5 µm pulse at an irradiance of 5 x 10^{14} W/cm^2.

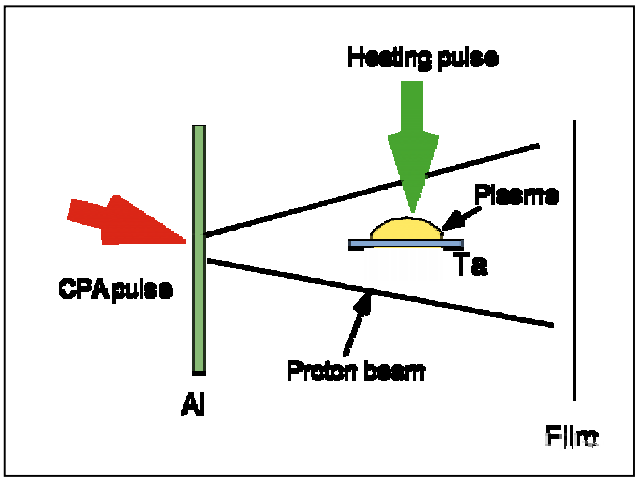

Figure 4. Set-up for proton imaging of a Ta plasma (top view).

When no preformed plasma was produced onto the Ta foil a shadow of the target was observed on the radiochromic film. When the foil was laser-heated the situation changed, and the presence of the plasma perturbed significantly the proton beam, as can be seen in Figure 5.

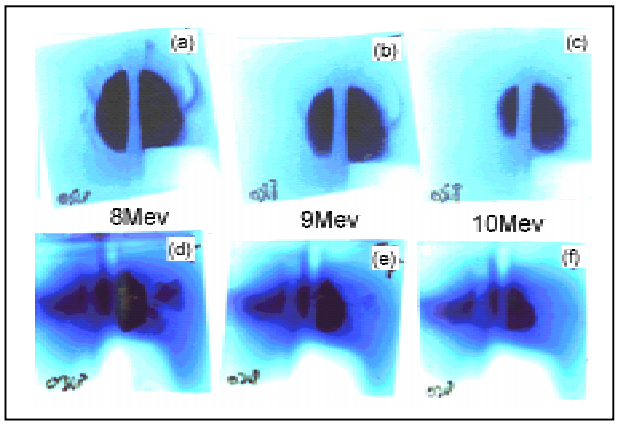

Figure 5. Proton radiographs after transmission through an unheated 125 µm Ta (a),(b),(c) and through a laser-produced Ta plasma (d),(e),(f). The proton energies corresponding to the various layers are indicated in the figure. The heating pulse (used to produce the plasma) was incident on the left of the target.

The plasma was formed on the Ta foil 1 ns before the CPA interaction with the Al foil. The distance between the main target and the axis of the preformed plasma was approximately 2 mm, while the distance between the main target and the first layer of the radiochromic films was about 13 mm. In Figure 5 the signal obtained on film with 8 MeV, 9 MeV and 10 MeV protons (i.e. on three consecutive layers of radiochromic film) is shown for the case of unheated target and for the case of preformed plasma. It can be seen that, while the proton signal

on the unheated target side stays relatively unperturbed, it is significantly distorted on the plasma side. As a matter of fact, the proton beam appears elongated and strongly modulated.

In a separate test, described in more detail elsewhere in this Annual Report [4], a second 25 µm Al foil was placed between the main target and the radiochromic film, and aligned parallel to the main target. A plasma was pre-formed on the back of the second target, before the interaction of the CPA beam with the main target. In this way, the proton beam propagated along the symmetry axis of the second target. It is interesting to observe that in this case the beam was substantially unperturbed by the presence of the plasma.

Various effects will have to be considered in the interpretation of the data, which is underway, and in modeling the propagation of the protons through the heated target. Collisional energy losses, scattering, and deflection by electric and magnetic fields inside the plasma can all contribute to the production of the patterns observed in the proton signal.

Conclusions

Preliminary experimental tests have been carried out in view of radiographic applications of laser-produced proton beams. The small size of the proton source allows its use in point-projection imaging radiography. Shadows of solid objects, including a fine mesh, have been obtained. Patterns resulting from the interaction of the proton beam with preformed plasmas show complex features, and their interpretation is underway.

Acknowledgements

The authors thank all the CLF staff for the assistance in preparing and carrying out the experiment. The work was funded by an ESPRC grant.

***** Work performed under the auspices of the U.S. Department of Energy by Lawrence Livermore National Laboratory under contract No. W-7405-ENG-48.

References

1. E. L. Clark *et al*
Phys. Rev. Lett, 84, 670 (2000)

2. A. Maksimchuk, S. Gu, K. Flippo, D. Umstadter and V. Yu. Bychenkov
Phys. Rev. Lett, 84 ,4108 (2000)

3. S. P. Hatchett *et al*.
Phys. Plasmas, 7 , 2076 (2000)

4. A.J.MacKinnon *et al.*
Central Laser Facility Annual Report 1999/2000, p37

5. P. Fews *et al*
Phys. Rev. Lett., 73 , 1801 (1994)

6. M.Roth *et al*.
Book of Abstract, XXVI Eclim, 101 (2000)

7. A.M.Koehler , Science, 160 , 303 (1968), D.West, A.C. Sherwood , Nature, 239 , 157 (1972), J.A. Cookson Naturwissenschaften, 61 , 184 (1974)

8. U.Schneider, E.Pedroni
Medical Phys., 22, 353 (1995), P. Pemler *et al*,
Nucl. Instr. Methods Phys. Res. A, 432, 483 (1999)

9. N.S.P.King *et al*,
Nucl. Instr. Methods Phys. Res. A, 424, 84 (1999)

10. W.L.C. McLaughlin *et al*,
Nucl. Instr. Methods Phys. Res. A, 302, 165 (1991)

Gamma-ray measurements in relativistic interactions with underdense plasmas

M Galimberti, A Giulietti, D Giulietti, L A Gizzi

Intense Laser Irradiation Laboratory - IFAM, Area della Ricerca - CNR, Pisa (Italy)

M Borghesi

The Queen's University, Belfast BT7 1NN, UK

H D Campbell, A Schiavi, O Willi

Blackett Laboratory, Imperial College of Science, Technology and Medicine, SW7 2BZ, London, UK.

Main contact email address: *leo@ifam.pi.cnr.it*

Introduction

Fast electrons generated in laser-plasma interactions at relativistic intensities can be studied directly by using electron spectrometers, or indirectly by detecting the gamma-ray bremmsstrahlung radiation generated by the interaction of these electrons with matter[1]. The gamma-ray detection technique is particularly suitable when the energy of these electrons is very high (>>10 MeV) and traditional spectroscopy would require dedicated, large scale equipment. Here we report on a recent investigation in which this technique was employed to study the effect of a precursor channelling pulse on the electron generation during the interaction of a relativistic laser pulse with an underdense plasma.

Experimental set-up

The 75 J, 1 ps Chirped Pulse Amplified (CPA) Vulcan laser pulse was focused with an f/3.5 optics in a preformed plasma. The preformed plasma was generated by laser explosion of a thin CH foil irradiated at intensities exceeding 10^{14} W/cm^2. Fourth harmonic, picosecond Nomarski interferometry was used to characterise the temporal evolution of the electron density along the axis perpendicular to main CPA pulse. (See elsewhere in this Annual Report [2] for a detailed description of interferometry measurements). We report on gamma-ray measurements performed using gamma-ray detectors based on NaI(Tl) scintillator coupled to photomultipliers[3]. A set of detectors with the thickness of the scintillating crystal ranging from 12.5 to 50.1 mm was placed along the direction of the incident CPA pulse. Other detectors were placed at 45º and 90º. All scintillators were shielded from scattered radiation by a 50 mm lead case.

Experimental results and discussion

A preliminary survey of the data indicates that a large number of very high energy electrons are generated, mostly in the forward direction. Numerical simulations were performed using the code GEANT4[4]. Assuming a given direction of the primary electrons (i.e. the direction of CPA), the comparison of simulation with the experimental data obtained from the scintillators allows a correlation to be established between the number of electrons and their energy. This calculation, combined with the condition set by the energy conservation principle indicates that the minimum electron energy must be around 10 MeV. In this case up to 10^{13} electrons are accelerated. On the other hand our data are also compatible with a flux of 10^7 electrons. Further analysis is in progress to clarify this point.

The gamma-ray emission yield was measured in different preformed channel conditions. Figure 1 shows the dependence of the gamma-ray yield as a function of the delay between the channel forming pulse and the main CPA pulse for three different values of the thickness of the scintillating crystal. In this plot the "zero" delay corresponds to the interaction of the main CPA pulse with the unperturbed preformed plasma (no channel-forming pulse). According to this plot the signal has a minimum around 20 ps and then increases over the entire range of delays explored.

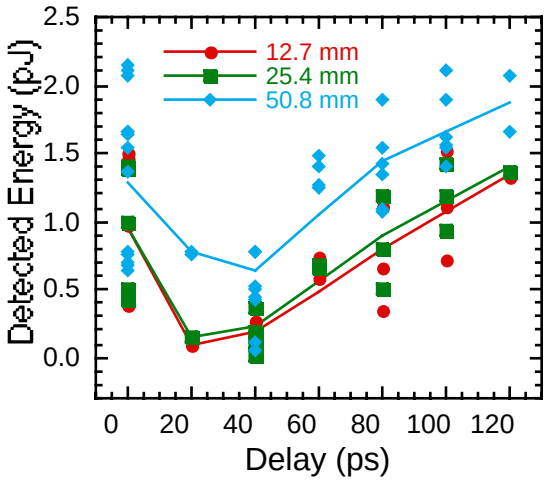

Figure 1. Energy released by the gamma-ray photons in the detector scintillating crystal as a function of the delay between the channel forming pulse and the main CPA pulse. Results are shown for three different thicknesses of the crystal.

Interferometric measurements show that when the main CPA pulse interacts with the unperturbed preformed plasma, it breaks into many filaments. In this case a substantial fraction of electrons can be accelerated in the filaments where the effective laser intensity may be higher than the incident one. This effect may explain the relatively high gamma-ray yield found in this condition as already observed [5]. The interaction changes completely when the channel preforming pulse is present. For small delays the gamma-ray signal drops rapidly and increases again for delays larger than 20 ps. Simultaneous interfermometric measurements confirm that the presence of a channelling pulse, regardless of its timing, prevents filamentation of the main pulse. On the other hand, for delays greater than 20 ps a long channel develops and the main pulse propagates in this channel. Moreover, the radius of this channel saturates at approximately 100 µm for delays greater than 40 ps.

Although the analysis is still in progress, this preliminary survey shows that the dynamics of plasma channels plays a fundamental role in electron acceleration processes and may be the key to achieving efficient production of energetic electrons from laser-plasmas.

References

1. A.Giulietti et al., ECLIM 2000, Prague 12-16 June, 2000.
2. M. Borghesi et al., Central Laser Facility Annual Report 1999/2000, p15.
3. L.A.Gizzi et al., TMR Network SILASI report 1998.
4. GEANT4: LCB Status Report/RD44, CERN/LHCC-98-44, 1998
5. X. Wang et al, Phys. Rev. Lett., 84, 5324 (2000).

Nonlinear absorption of ultra-intense laser pulses in glass

A Schiavi, D H Campbell, O Willi

Blackett Laboratory, Imperial College of Science,Technology and Medicine, London, UK

M Borghesi

Department of Pure and Applied Physics, The Queen's University of Belfast, Belfast, UK

Main contact email address: *a.schiavi@ic.ac.uk*

Introduction

This paper reports about measurements of nonlinear absorption of short laser pulses in fused silica. The intensities produced in the experiment were in the region immediately below the breakdown threshold for fused silica with 1 ps pulses (~7 x 10^{12} W cm^{-2}) [1]. The beginning of a nonlinear absorption regime was observed. This is of great importance for the design of experiments involving ultra-intense laser pulses.

Experimental set-up

The experimental set-up is depicted in Figure 1. The CPA beam of the Vulcan laser was focussed in vacuum with an F3.5 off-axis parabola. The expanded beam went through a SiO_2 window plate positioned at 20 cm from the focal plane. The plate was tilted at an angle to avoid back-reflections along the beam line. The beam cone emerging from the plate was collected by a calorimeter, which measured the energy transmitted through the glass.

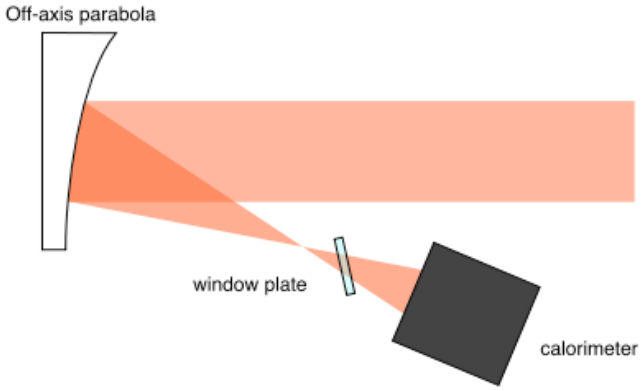

Figure 1. Experimental arrangement.

The laser pulse had a gaussian profile with a FWHM duration of 1 ps. The laser wavelength was λ =1.053 µm. Different intensities on the window plate were produced by changing the total energy delivered during the shot.

Discussion and results

When a low-intensity light beam passes through a window, only a negligible fraction of the beam energy is deposited as heat in the window material. However, in high intensity regimes, nonlinear absorption mechanisms dependent on the laser irradiance are activated. These processes increase significantly the density of free electrons, which eventually reaches the critical value for avalanche ionization of the material. Above this critical value, breakdown occurs in the material, and permanent deformations or even rupture of the window are induced. Among the absorption mechanisms at high-intensity, one major process is multi-photon absorption. This mechanism corresponds to the simultaneous absorption of two or more laser photons by a single bound electron, promoting it into the conduction band of the crystal[2]. The cross section for this absorption mechanism is a function of the photon density, and therefore of the laser irradiance.

The transition from total transmittance to the nonlinear absorption regime was observed in the intensity range (below the breakdown threshold) spanned in the experiment.

Figure 2 shows the total energy detected by the calorimeter with and without the window plate inserted on the beam line, plotted as a function of the incident energy. A deviation from linearity as the energy increases is clearly visible. Figure 3 shows the transmission of the plate as a function of the incident intensity.

Conclusions

Direct observation of intensity dependent absorption in fused silica was obtained in the experiment. The intensities produced were below the breakdown threshold for $Si0_2$, so that permanent damage to the glass due to plasma formation was avoided. A significant decrease in the transmitted energy was observed for increasing intensity. The intensity threshold for nonlinear absorption in fused silica for 1 µm laser irradiation was estimated to be in the order of 1-3 x 10^{11} W cm^{-2}.

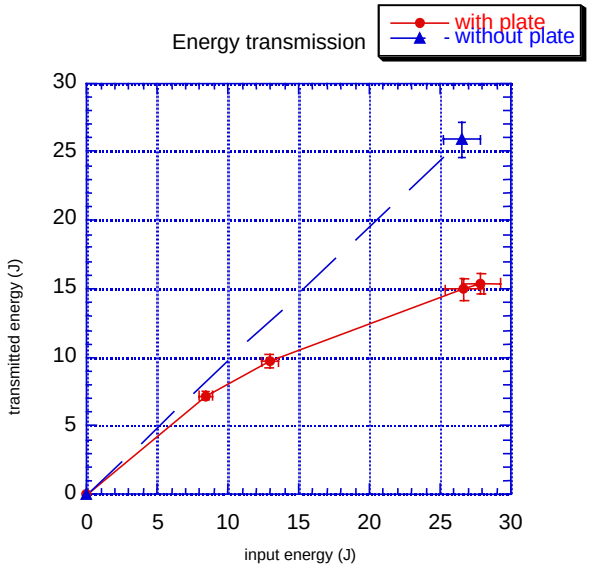

Figure 2. Transmitted energy with and without window plate.

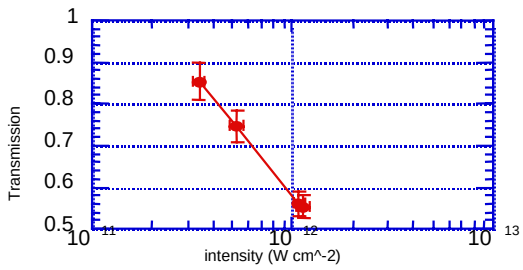

Figure 3. Intensity dependence of the energy transmission.

References

1. D.Du, X.Liu et al., Appl.Phys.Lett. 64, 3071 (1994)
2. E.W. Van Stryland et al., in Laser-Induced Damage in Optical Materials: 1993, Proceedings of SPIE, 2114 (1994)

Proton induced nuclear reactions from intense laser-plasma interactions

M I K Santala, M Zepf, F N Beg, E L Clark, A E Dangor, K Krushelnick, M Tatarakis, I Watts

Blackett Laboratory, Imperial College of Science, Technology and Medicine, London SW7 2BZ, UK

K W D Ledingham, T McCanny, I Spencer

Department of Physics and Astronomy, University of Glasgow, Glasgow G12 8QQ, UK

R Allott, R J Clarke, P A Norreys

Central Laser Facility, CLRC Rutherford Appleton Laboratory, Chilton, Didcot, Oxon, OX11 0QX, UK

AC Machacek

Department of Physics , University of Oxford, Oxford, OX1 3PU, UK

Main contact email address: *msantala@ic.ac.uk*

Introduction

High intensity laser solid interactions at intensities greater than 10^{19} W/cm^2 have recently enabled the exploration of new regimes in plasma physics. Such interactions can produce fast electrons of greater than 100 MeV[1], gamma rays of tens of MeV [2] and energetic ions with up to several hundred MeV in energy[3,4] . There are clearly many potential applications for these energetic particles such as compact particle accelerators and as diagnostic probe beams of high density plasmas. The results of these experiments are particularly interesting for technological applications since such sources should be easily scalable to "table-top" sizes. The development of energetic proton beams from laser-produced plasmas also suggests that there may be further important applications of this technology for the efficient production of radioactive isotopes for medical applications such as positron emission tomography[5].

In this work, we discuss experiments to examine the properties of energetic ions produced during the high power laser-plasma interaction by measuring the nuclear activation induced in different materials exposed to fast ions emitted from the plasma. The nuclides observed include ^{63}Zn, ^{13}N and ^{11}C. These are positron emitting nuclides with half-lives of the order of tens of minutes, which makes the measurement of induced activity practical. The ion-induced production reactions have reaction thresholds of approximately 4 MeV[46]. The primary mechanism for the production of these energetic ions is expansion of the hot plasma where ion accelerating space-charge fields are created by the hot electron population which escape the target.[7]

Previously, nuclear activation has been observed in laser-solid interactions from γ ray -induced reactions [2,8]. It should be noted that (p,n) reaction thresholds are typically only a fraction of the (γ,n) reaction thresholds, especially for light elements, and the cross-sections may be nearly an order of magnitude larger. However, the range of energetic ions in matter is very short compared to that of γ-rays. Consequently, in these experiments, activation samples for (p,n) reactions are usually thin foils while large pieces of solid matter have been used for (γ,n) studies[8] . This is beneficial since the significance of target self-absorption in the measurement of the induced activity can be reduced.

These experiments were carried out using the CPA (chirped pulse amplification) beam of the Vulcan Nd:glass laser system [9]. The laser wavelength was 1.054 μm, the pulse length was 0.9 – 1.2 ps and the energy incident on target was 20-50 J. The laser beam (111 mm x 200 mm) was focused onto the target surface using a 225 mm focal length on-axis parabolic mirror (Figure 1). The laser beam was *p*-polarised and was incident at an angle of 45^o. The peak intensity was measured to be about 2 x 10^{19} W/cm^2. The targets were 0.5 - 1.5 mm thick slabs of BK-7 glass, some of which were coated with a 2-3 μm layer of polyethylene as well as thin foils of aluminum and titanium. The target and all of the optics for the beam after pulse compression were placed in a vacuum chamber which was evacuated to less than 10^{-4} mbar pressure.

Figure 1. Schematic experimental lay-out. Laser beam entering from right is focused by an on-axis parabola (left) to target surface (middle). Blow-off plasma hits activation sample (top) in the target normal direction.

The sample materials for this diagnostic were placed in front of the target in the direction of the target normal 15 cm away from the target. The sample materials used were Cu-foil, Pyrex glass (which contains boron) and PVC-foil. The activated samples were removed from the target chamber as soon as possible after each shot and taken for radioactivity measurements. This typically causes a delay of 10 minutes before the activity can be measured. The principal reaction products studied are nearly 100% positron emitters so the activity can thus be measured by counting 511 keV positron annihilation gamma rays in coincidence. This results in very high sensitivity and low background even with minimal detector shielding. A detection system with two 3" x 3" NaI(Tl) scintillators shielded with 2 cm of lead was used for measuring the positrons. The set-up has about 10 % positron detection efficiency, and a background count rate of less than 0.01 cps.

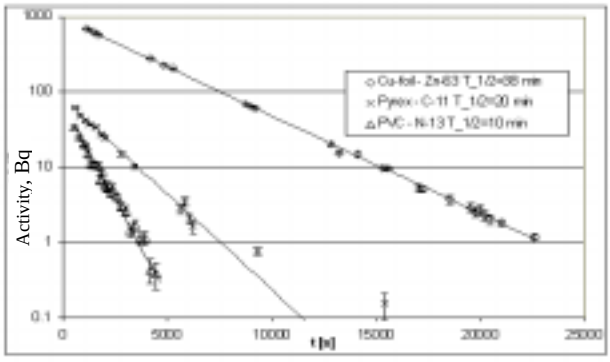

Figure 2. The observed activity vs. time of a copper foil, Pyrex glass and PVC foil targets. Decays matching the suggested reaction products are clearly observed. The background level corresponds to less than 0.1 Bq, and has not been subtracted.

The average initial activity of the copper foils was 600 Bq, corresponding to 2 x 10^6 ^{63}Zn nuclei produced in a single shot. The size of Cu foils was typically 25 mm by 25 mm,

100-250 μm thick, and they were 15 cm from the target. Results from the half-life measurements are shown in Figure 2.

Very pure exponential decays are observed, indicating that only one nuclide is present. The solid lines display least-squares fit to the measured activities. The best-fit half-lives are 38.7, 19.9, and 10.0 min for Cu-foil, Pyrex-glass and PVC foil, respectively. This would indicate that ^{63}Zn, ^{11}C, and ^{13}N are produced in these target materials. The literature values for their half-lives are 38.47, 20.38, and 9.96 min. Likely production reactions for the first two are ^{63}Cu(p,n)^{63}Zn, ^{11}B(p,n)^{11}C. There are two reaction candidates for the production of ^{13}N: ^{16}O(p,α)^{13}N and ^{13}C(p,n)^{13}N, both of which are likely to contribute. ^{13}N and ^{11}C are particularly interesting for medical applications as is ^{18}F which has a similar cross-section as ^{13}N and ^{11}C and hence should also be easily created in such experiments.

By stacking several thin (12 μm) Cu foils, information about the incident spectrum of protons can be deduced by utilising the classical stopping ranges of ions in solid matter. A response matrix method was then used to unfold the proton spectrum from measurements of the activation of individual copper foils (see Figure 3). These results indicate that, the spectrum can be described approximately by an exponential distribution with a temperature parameter varying on shot-to-shot basis in the range of 1-2 MeV. The results suggest that the total number of protons is greater than 10^{12}/sr and greater than 10^{11}/sr above 5 MeV. Fine-scale modulations in the ion energy spectrum which are observed when using a Thomson parabola ion spectrometer do not appear in the activation measurements. This is likely to be due to the large degree of smoothing caused by the broad activation cross-section in copper. However, activation measurements are the only low background method for determining the entire high energy spectrum of energetic ions. The shot-to-shot fluctuations in the measured spectra for interactions at a similar intensity are not unexpected since these very energetic ions are produced by highly non-linear processes in the laser produced plasma.

In conclusion, we have shown that nuclear activation caused by ion-induced reactions can be a useful diagnostic for high-intensity laser-solid interactions. Compared to conventional ion spectrometer diagnostics it has a much larger sensitive solid angle and a measurement of the total conversion efficiency is much easier to obtain. The results are thus more likely to reflect the large-scale properties of the emitted ions. Angularly resolved measurements are possible by exposing several spatially independent samples to the blow-off plasma. One of the main advantages of this ion diagnostic is its complete insensitivity to other particles or to lower-energy processes. It is also immune to electrical noise generated by the laser-plasma interaction as counting is carried out off-line. This diagnostic can also have a very large dynamic range, although, at low proton numbers counting statistics can be poor – with a corresponding increase in the uncertainty.

Ion-induced activation by high-intensity lasers may prove to be an attractive source of short-lived radionuclides. The total activation could be increased by an order of magnitude through the use of samples that span a larger solid angle. If the energy spectrum of ions depends only on the incident intensity and number of ions scales with laser pulse energy, small high-repetition rate lasers with similar focused intensity to Vulcan could produce similar samples in a few seconds. Integrating activity over minutes to hours samples with activities in the 10^6 Bq range may be produced – which could begin to be applicable as isotope sources. The use of a high repetition rate system will average the proton spectrum (and the shot-to-shot fluctuations) making this a more consistent source for such applications. As well, further improvement could almost certainly be achieved by optimising the laser prepulse, the target material and surface treatment.

We would like to acknowledge the technical assistance of the Vulcan operations team and the support of the UK Engineering and Physical Sciences Research

References

1. A. Modena *et al.*, Nature 377, 606 (1995).
2. M. H. Key *et al.*, Phys. Plasmas 5, 1966 (1998).
3. E. L. Clark et al. Phys. Rev. Lett. (to be published, July 2000).
4. A. P. Fews *et al.*, Phys. Rev. Lett. 73, 1801 (1994); F. N. Beg *et al.*, Phys. Plasmas 4 , 447, (1997).
5. M. Yamagiwa and J. Koga, J. Phys. D: Appl. Phys. 32 2526 (1999).
6. EXFOR database on-line at http://www-nds.iaea.org
7. S. J. Gitomer *et al.*, Phys. Fluids. 29, 2679 (1984).
8. M. I. K. Santala et. *al*., Phys. Rev Lett 84, 1459 (2000); P. A. Norreys et *al*., Phys. Plasmas 6, 2150, (1999).
9. C. N. Danson *et al*., J of Mod. Opt. 45, 1653 (1998).

Observations of heavy ion fusion during high intensity laser plasma interactions using nuclear activation techniques

M I K Santala, M Zepf, F N Beg, E L Clark, A E Dangor, K Krushelnick, M Tatarakis, I Watts

Blackett Laboratory,Imperial College of Science, Technology and Medicine, London SW7 2BZ, UK

K W D Ledingham, T McCanny, I Spencer

Department of Physics and Astronomy, University of Glasgow, Glasgow G12 8QQ UK

R Allott, R J Clarke, P A Norreys

Central Laser Facility, CLRC Rutherford Appleton Laboratory, Chilton, Didcot, Oxon, OX11 0QX, UK

AC Machacek

Department of Physics , University of Oxford, Oxford, OX1 3PU, UK

Main contact email address: *msantala@ic.ac.uk*

Recent experimental work studying high intensity laser plasma interactions at intensities greater than 10^{19} W/cm^2 has shown that such plasmas can potentially be an efficient source of very energetic electrons, gamma rays and ions [1-21]. At such energies one of the most promising methods for diagnosis of these high energy particles is through the use of nuclear activation techniques. Previous work has shown that much of the important physics of the production of electron beams and proton beams can be uncovered using (γ,n) and (p,n) reactions. There are clearly many potential applications for these energetic particles such as compact accelerators and as diagnostic probe beams of high density plasmas. The results of these experiments are particularly interesting for technological applications since such sources should be easily scalable to "table-top" sizes.

In this paper, we examine the generation of energetic heavy ions through similar nuclear activation techniques. We show that heavy ion fusion reactions can be measured – a technique which may prove useful as a low background diagnostic of these ions.

These experiments were carried out using the CPA beam of the Vulcan Nd:glass laser system [22]. The laser wavelength was 1.054 μm, pulselength 0.9 – 1.2 ps and energy incident on target was 20-50 J. The laser beam (111 mm x 200 mm) was focused on to the target surface using a *f.l.*=225 mm on-axis parabolic mirror. The laser beam was *p*-polarised and was incident at an angle of 45^o. The peak intensity was measured to be about 2 x 10^{19} W/cm^2. The targets were typically thin foils of aluminum and mylar (carbon and hydrogen). The target and all of the optics for the beam after compression were placed in a vacuum chamber evacuated to less than 10^{-4} mbar pressure.

Nuclear activation caused by ion-induced reactions can be an useful diagnostic for high-intensity laser-solid interactions since compared to ion spectrometer diagnostics it has a much larger sensitive solid angle. The results are thus more likely to reflect better the large-scale properties of the emitted ions. One of the main advantages of the ion diagnostic is the complete insensitivity to other particles or lower-energy processes. It is also immune to electrical noise generated by the laser-plasma interaction as counting is carried out off-line. This diagnostic can have a very large dynamic range, however, at low proton numbers counting statistics can be poor.

To measure the heavy ions produced in these experiments, aluminium foils were exposed to the ion blow-off. After the interaction these foils were examined with the Germanium detector gamma ray detector to measure the characteristic x-rays produced by any radioactive isotopes produced during the experiment. In several samples the characteristic emission lines of ^{34m}Cl (146, 1177, 2127, and 3304 keV) and of ^{38}K (2167 keV) were found (Figure 1). In addition, positron emission was also detected. Decay of these lines was found to be consistent with the half-lives of these nuclides (32 min and 7.6 min).

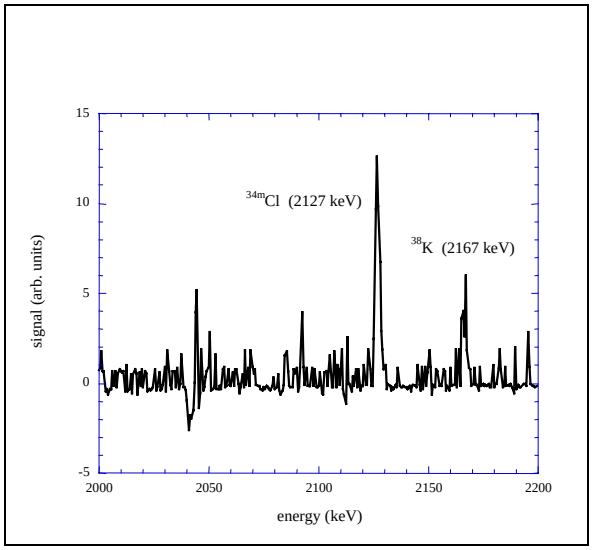

Figure 1. Characteristic emission lines observed from activated Al foils.

These observations prove conclusively that ^{34m}Cl and ^{38}K are produced in the Al foil. This can be explained by fusion of fast ^{12}C ions in the blow-off with ^{27}Al in the foil. This forms highly excited ^{39}K, and subsequently several lighter nuclides through nucleon evaporation. ^{34m}Cl and ^{38}K are the only ones with long enough half-lives (~10 min) to be seen in the off-line counting.

The initial activities can be found to be 15-20 Bq for ^{34m}Cl and 20-30 Bq for ^{38}K using the measured line intensities. This corresponds to production of about $5x10^4$ ^{34m}Cl nuclei and $2x10^4$ ^{38}K nuclei. The reaction thresholds are approximately 40 MeVand the typical reaction cross-sections are ~300 mb. The stopping power of ~50 MeV ^{12}C ions is about 0.6 MeV/μm, so they exceed the reaction threshold for about 15 μm. $2x10^9$ ^{12}C ions are then needed to produce the observed activation. This is consistent with measurements of the heavy ion spectrum using Thomson parabola ion spectrometers.

In these experiments thin aluminium foils were placed on both the front and the rear of thin solid targets. These measurements indicated that, although there was significant proton emission in both directions, energetic carbon ions were only measurable at the front of the target. This is because either: (a) the source of both the energetic carbon ions and protons is the front surface and carbon ions are stopped before they can pass through the target or (b) the mechanism for accelerating ions on the rear surface is not as efficient for accelerating carbon ions as it is for protons. Further research is clearly necessary to address these questions.

We would like to acknowledge the technical assistance of the Vulcan operations team.

References

1. G. Malka *et al.,* Phys. Rev. Lett. 77, 75 (1996).
2. K. B. Wharton *et al.*, Phys. Rev. *Lett.* 81, 822 (1998).
3. M. H. Key *et al.*, Phys. Plasmas 5, 1966 (1998)
4. P. Norreys *et al.* Phys. Plasma 6, 2150 (1999).
5. A. P. Fews *et al.*, Phys. Rev. Lett. 73, 1801 (1994); F. N. Beg *et al.*, Phys. Plasmas 4 , 447, (1997).
6. M. Key *et al.* Paper presented at IFSA'99 conference
7. A. Modena *et al.*, Nature 377, 606 (1995).
8. E. L. Clark *et al.*, Phys. Rev. Lett. 84, 670 (2000).
9. M. Borghesi *et al.*, Phys. Rev. Lett. 81, 112 (1998).
10. L. Gremillet *et al.*, Phys. Rev. Lett. 83, 5015 (1999).
11. M. Tabak *et al.*, Phys. Plasmas 1, 1626, (1994).
12. D. W. Forslund *et al.*, Phys. Rev. Lett. 48, 1614 (1982).
13. R. L. Carlson *et al.*, IEEE J. Quantum Electron. 17, 1662 (1981).
14. S. J. Gitomer *et al.*, Phys. Fluids. 29, 2679 (1984).
15. F. Beg *et al.*, Phys. Fluids, 25, 1675 (1982); T. Tan *et al.*, Phys. Fluids 27, 296 (1984); A. H. Ehler *et al.*, J. Appl. Phys. 46, 2464 (1975).
16. K. W. D. Ledingham *et al*., Phys. Rev. Lett. 84, (2000)
17. K. W. D. Ledingham and P. A. Norreys, Contemporary Physics, December 1999.
18. K. Krushelnick *et al.*, Phys. Rev. Lett. 83, 737 (1999).
19. Y. Kishimoto *et al.*, Phys. Fluids 26, 2308 (1983).
20. L. M. Wickens *et al.*, Phys. Rev. Lett. 41, 243 (1978).
21. M. I. K. Santala et. *al*., Phys. Rev Lett 84, 1459 (2000); P. A. Norreys et *al*., Phys. Plasmas 6, 2150, (1999).
22. C. N. Danson *et al.*, J of Mod. Opt. 45, 1653 (1998).

The dependence of self focusing on the observation of Raman Side Scatter in high intensity laser interaction with under-dense plasmas

Z Najmudin, K Krushelnick, E L Clark, M I K Santala, M Tatarakis, A E Dangor

Blackett Laboratory, Imperial College of Science, Technology, and Medicine, London SW7 2BZ, UK

V Malka, J Faure

Laboratoire pour l'Utilisation des Lasers Intenses (LULI) Unité mixte n°7605 CNRS - CEA - École Polytechnique - Université Pierre et Marie Curie, France

D Neely, R J Clarke

Central Laser Facility, CLRC Rutherford Appleton Laboratory, Chilton, Didcot, Oxon, OX11 0QX, UK

Main contact email address: *zn1@ic.ac.uk*

Introduction

Much work has been focused recently on the interaction of extremely high-power short pulse length lasers with underdense plasmas, not least because of the relevance for particle accelerators[1,2] and in fast ignitor type experiments[3]. Propagation of a laser pulse under such conditions is of great interest because of the non-linearity of the interaction, which can lead to such effects as relativistic self-focusing [4].

In this paper we present measurements made for the interaction of a 50 TW, 800 fs laser pulse with plasma densities in the range 3 x 10^{18} to 1 x 10^{20} cm^{-3}. The laser is an Nd:Glass CPA system centred at 1.054 µm, which through the use of correction optics can be focused down to a spot smaller than 10 µm. Thus in vacuum the laser can be focused to intensities greater than 2 x 10^{19} Wcm^{-2} [5]. The plasma is formed by optical field ionisation of a supersonic helium gas jet [6] by the intense laser beam. The propagation is primarily observed with two diagnostics; shadowgraphy and spectrally resolved self-scattered images. For the shadowgraphy a second frequency doubled probe beam, was passed unfocused through the interaction region. The probe was derived from the same source as the main beam to ensure jitter free timing. Gradients of density within the plasma deflect the probe, so that on reimaging areas of highest density gradients are delineated.

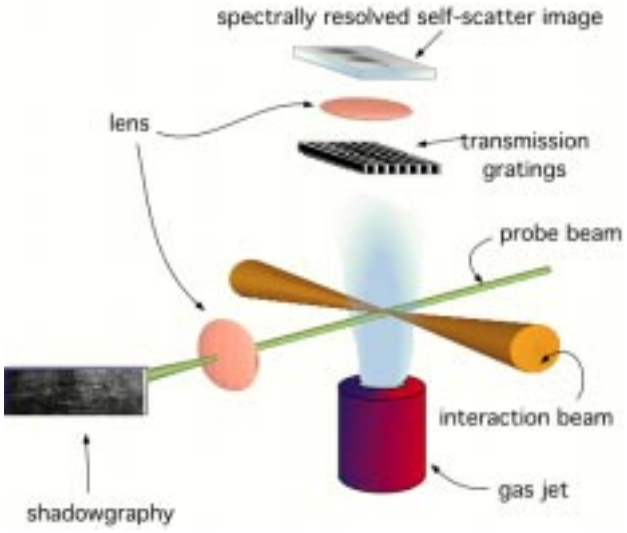

Figure 1. Experimental Set-up.

For the scattering images, a fully reflecting (telescope based) imaging system is used to capture and reimage the self-scattered light of the interaction emitted at 90˚. In front of the imaging telescope is placed a transmission grating with its rulings parallel to the direction of propagation. Thus one not only forms an image of the scattered light at all wavelengths (at the zero order of the grating) but one also obtains spectra of these images, correlated to the spectrally integrated images in space. A schematic of the experiment is shown in Figure 1.

Results (Images)

A typical set of shadowgrams and self-scattered images is shown for a variety of densities in Figure 2. The density measured from plasma frequency measurements from forward Raman scattering on the same shots, is given along with the images. The self scatter image of the corresponding shot as the shadowgram is shown directly below the shadowgram with the same scale and same relative horizontal position for easy comparison between the two. The pressure shown is the corresponding backing pressure for the gas jet required to obtain the measured plasma density.

The lowest density at which signature of the propagation can be observed is around 3×10^{18} cm^{-3} (Figure 2a). On all of these shots the laser has been focused right on the edge of the supersonic gas jet to ensure the interaction is at the highest intensities possible. The shadowgram shows the 'fan' shaped plasma expected to be created by a defocusing laser beam of cone angle $\approx f4$. However the self-scattered image below it is surprisingly different. It is narrower and shows two brighter features originating from the same point but curving towards one another. Directly below the self-scattered image, on the same picture, is the same image spectrally dispersed by the transmission grating. Since both first order (off the grating) and zeroth order image are identical and of the right displacement for the fundamental wavelength (1.054 µm), one can discern that all the scattered light is at that wavelength. Previously this 'forked' image was thought to be indicative of multiple filaments [7]. However the curved nature of the light, which consistently shows the curved shape, appears to contradict that. It is possible that what is observed is an increase in scattering due to extra plasma density at these points, due perhaps to ponderomotive blow out, or perhaps the sharp plasma gradient from a region of doubly to singly ionised helium.

Doubling the plasma density (Figure 2b) does not change the shadowgram greatly. However there is a marked difference in the self-scattered image. Now the 'forked' image gives way to a single long line of emission. From the spectrally dispersed image, one can see that most of the scattered light early in the propagation is at the fundamental frequency or up-shifted due to ionisation blueshifting. (Note also that the CCD used for this observation is more sensitive to the blue side of the laser frequency.) However at about a millimetre into the propagation ($x \approx 1.5$ mm on the scale), the emission gets brighter, and one is able to observe clearly a bright satellite towards the red side of the fundamental (i.e. at longer wavelength). The spacing between the satellite and the fundamental wavelength λ_0 is the plasma frequency ω_p and hence is a signature of Raman Side Scatter. This is an instability where the main laser beam (frequency ω_0) couples to a plasmon (of frequency ω_p) to give electromagnetic radiation of frequency $\omega_0 \pm \omega_p$. The corresponding satellite(s) to the blue side can also be observed but is(are) weaker. This is as expected since laser light can be downshifted directly by the interaction of only three waves (the

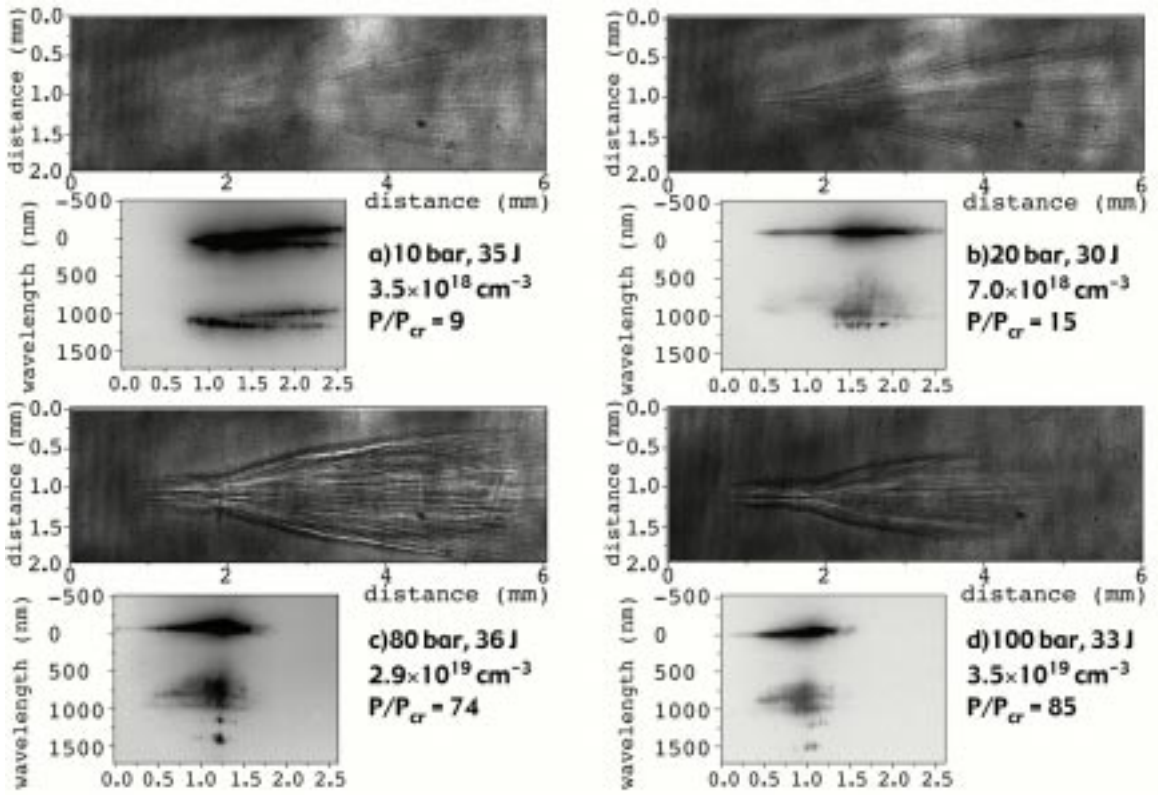

Figure 2. Typical shadowgrams (above) and self-scattered images (below) for a variety of plasma densities (parameters given in figure). The self scattered images are also spectrally dispersed directly below the image.

incident, the plasmon and the scattered wave). However creation of the blue satellite is energetically unfavourable and so requires a 4 wave process (involving also the generation of the other downshifted satellite too). Interestingly the red (Stokes) satellite has a very erratic nature, showing up only in bursts.

In the shadowgram of Figure 2b, one can see striations within the cone of the created plasma. It seems that the laser intensity is anything but uniform on the outward going cone, leading to slight variations in plasma density, again due to different rates of plasma creation, compounded by ponderomotive and thermal expansion of the plasma. Close to the start of the propagation, there is one darker striation, which corresponds to a greater drop of density due to ponderomotive blow out. This is likely the 'blow-out' channel generated by ponderomotive / relativistic self-focusing of the laser beam. The length of this deepest channel is close to the length of the less intense scattering before the side scatter is initiated. This suggests that a deep self-focusing channel can inhibit side scatter, even at such large angles. This would have consequences for modulation of the beam, which side-scatter is purported to stimulate. Note that the self-scatter image is over 2 mm in length, well over five Rayleigh lengths away from focus. Even longer images, have been observed in similar configurations. Importantly, under the same conditions, ion and plasma wave scattering (probed Thomson scattering) diagnostics have shown that the intensity within this central filament is greater than 10^{18} Wcm^{-2} for greater than 10 Rayleigh lengths. The laser beam is therefore clearly relativistically self-focusing.

The self-focusing channel is even clearer in Figure 2c. Indeed initially all the laser light seems to be travelling forward parallel, and the cone shape seen in Figures 2a and 2b is absent. However at this higher density this initial channel is shorter, and appears to end abruptly, after which the laser beam defocuses in the usual fan. This unusual behaviour is replicated in the side scatter image. Initially the scattering is weak, correlating to the length of the deep central channel. This light consists of λ_0 light as well as weak signs of the blue satellites. The corresponding red satellite is probably present but not observed due to the falling sensitivity of Si CCDs at wavelengths above 1.1 µm. However at about x = 1.25 mm, the scattering becomes very intense. In fact one sees not only one Stokes satellite, (despite the supposed insensitivity of the detector at that wavelength,) but the second Stokes too, which is at an even longer wavelength. This implies that the scattering is extremely intense as well as being spatially short. Indeed the fact that the channel end is correlated to this intense scattering is further corroborated by the observation in the shadowgram of ionising filaments at large angles. These filaments originate at the end of the deep channel, and propagate away almost orthogonal to the driver beam. That these bursts of side scatter have sufficient intensity to ionise the helium, suggesting that they have energies of the order of tens of millijoules.

The final pair of images, in Figure 2d, reiterates this behaviour. At this yet higher density, the central channel created in the shadowgram is clearer, but again ends in an intense burst of side scatter. (Note how the wavelength of the side-scatter satellites increases with increasing density, corresponding to an increase in plasma density). After this intense burst the whole beam defocuses naturally but with a greater divergence, than at low densities. Note how all the propagation lengths are shorter, the length of the plasma in the shadowgram, the length of the side-scatter and the length of the side-scatter bursts. This shows that the beam is heavily absorbed. This is not surprising as these same conditions have shown the efficient conversion of a great amount of the laser energy to fast electrons, with the resulting possible application for a source of relativistic electrons [8].

Discussion and conclusions

To précis the above discussion some of the main scalings are presented graphically in Figure 3 and Figure 4. Figure 3 shows some of the characteristic lengths obtained by our diagnostics as a function of plasma frequency ($\propto \sqrt{}$plasma density n_e). As noted before the side-scatter length shows a definite maximum at around $\omega_p/\omega_0 \approx 0.1$, ($n_e \approx 1 \times 10^{19}$ cm^{-3}). Above this density

both the length of this image and the associated Stokes satellite burst become shorter, indicating a rapid decrease in the propagation length due to the side-scattering. However the plasma as seen from shadowgraphy continues to increase in length up until the very highest density. Presumably lower intensity filaments can continue to propagate and would be easier to observe at the highest densities. As said before at the very highest density the length is reduced in the shadowgram (to less than 4 mm), and is presumably due to strong absorption of the laser light.

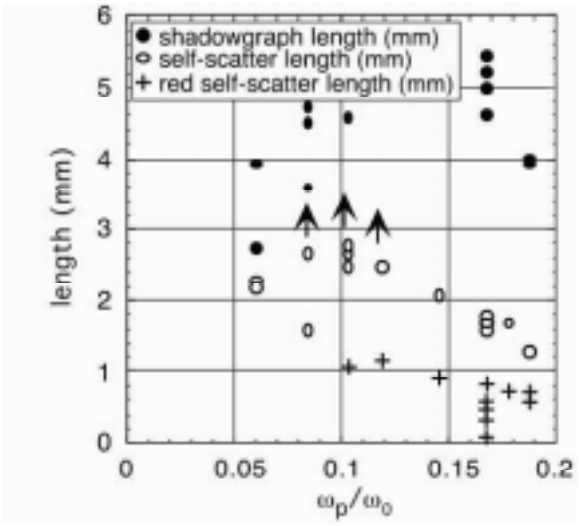

Figure 3. Some characteristic lengths as a function of plasma frequency for shots with on target energies 30-37 J.

Indeed the only time such short plasmas are seen otherwise, is when the laser energy is purposely reduced to less than 10 J on target. Otherwise above 20 J on target, there is sufficient laser energy to fully ionise from one edge of the gas jet to the other. Also with increasing laser energy the side-scatter image length increases mildly, but the burst length of the Stokes satellite decreases gently. This shows that the influence of intensity on the instability growth-rate is not as great as compared to the density effects. This is in part due to the relativistic effect of high intensity on plasma electrons, whose quiver motion approaches the speed of light in the intense laser field. These relativistic electrons exhibit a relativistic mass increase, thus reducing the effective plasma frequency, so compensating for the effect of greater intensity.

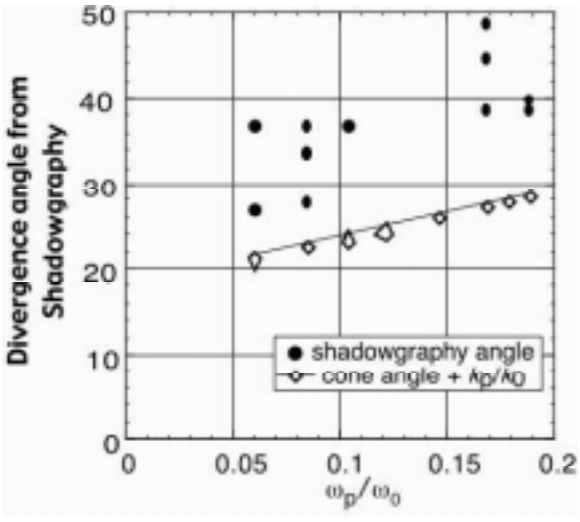

Figure 4. Angle of divergence measured from Shadowgraphy versus ω_p for shots with on target energies 30-37 J.

Figure 4 shows the increasing cone angle of the final expansion of the laser beam as a function of density. It shows as commented before that the divergence angle increases monotonically with density. The open polygons with the line through them show the cone angle with the addition of an angle corresponding to the ratio of the plasma wavenumber k_p to the laser wavenumber, k_0. The filaments observed in the plasma as observed by shadowgraphy, have been seen in simulation by Antonsen et al [9]. In their numerical study, they found that different rates of ionisation due to imperfections in beam quality could cause the generation of filamentation. This ionisation-induced filamentation is supposed to have its greatest growth at an angle corresponding to k_p/k_0. The increase in our observed cone angle of filaments agrees qualitatively with this. However the cone angle is also observed to increase with increasing intensity. It is therefore surmised that there is an added influence due to the presence of relativistic self-focusing. The smaller the minimum beam-waist due to self-focusing, which decreases both with increasing density and intensity, the greater the final divergence of the beam. This is simply due to optical considerations. However the influence of atomic optical non-linearities (i.e. before the plasma is formed), which is an important consideration in the ionisation induced filamentation is still likely to be important. This is because of the formation of many more filaments than the ratio of laser power P to the critical power for relativistic self-focusing P_{cr}. A simple treatment of relativistic self-focusing shows that for a laser beam to self-focus, it must possess a minimum power, $P > P_{cr} = 17\cdot(\omega_p/\omega_0)^2$ GW. Since there are too many filaments for each one to be above this threshold, atomic effects must also be important to enhance the filamentation. The intensity of each filament can easily be great enough ($> 10^{15}$ Wcm^{-2}) for this to be possible.

In conclusion, the effect of Raman side-scatter correlated with observation through plasma probing of channel formation due to relativistic self-focusing, has been observed. In particular despite the importance of side-scatter in many theories on the enhanced self-modulation of intense laser beams [10], very little large angle side-scatter is observed in the initial formation of the propagation. Indeed it almost appears that channel formation can inhibit strong Raman side-scatter, and that it is only with the termination of the strong channelling that one sees the onset of intense Raman side-scatter. In light of these observations the role of these instabilities in the interaction and their order of occurrence needs to be reconsidered.

References

1. E Esarey, P Sprangle, J Krall and A Ting
IEEE Trans. Plas. Sci., 24 252-288, (1996)

2. A Modena, Z Najmudin, A E Dangor, et al.
Nature, 377 606-608, (1995)

3. M Tabak, J Hammer, M E Glinsky, et al.
Physics of Plasmas, 1 1626, (1994)

4. P Sprangle, C M Tang and E Esarey
IEEE Trans. Plas. Sci., 15 145-153, (1987)

5. C N Danson, J Collier, D Neely, et al.
Journal of Modern Optics, 45 1653-1669, (1998)

6. V Malka, C Coulaud, J P Geindre, et al.
Review of Scientific Instruments, 71 2329-33, (2000)

7. C E Clayton, K C Tzeng, D Gordon, et al.
Physical Review Letters, 81 100-3, (1998)

8. M I K Santala, Z Najmudin, E C Clark, et al.
submitted to Physical Review Letters, (2000)

9. T M Antonsen and Z Bian
Physical Review Letters, 82 3617-3620, (1999)

10. C D Decker, W B Mori, K C Tzeng and T Katsouleas
Physics of Plasmas, 3 2047-2056, (1996)

Energetic proton generation and plasma jet formation from ultra-intense laser-plasma interactions with solids

E L Clark[1], M Zepf, F N Beg, M Tatarakis, C Escoda, M Norrefeldt, A E Dangor, K Krushelnick

Blackett Laboratory, Imperial College of Science, Technology and Medicine, London SW7 2BZ, UK

[1]Radiation Physics Department, AWE plc, Aldermaston, Reading, RG7 4PR, UK

R J Clarke, P A Norreys

Central Laser Facility, CLRC Rutherford Appleton Laboratory, Chilton,Didcot, Oxon, OX11 0QX , UK

I Spencer, K W D Ledingham

Department of Physics and Astronomy, University of Glasgow, Glasgow, G12 8QQ, UK

Main contact email address: *eugene.clark@awe.co.uk*

The advances in ultra intense laser-plasma interaction experiments have produced observations of many interesting new phenomena – such as the acceleration of electrons to energies over 100 MeV[1)], the production of intense, directional proton beams[2,3)] and the generation of multi-MegaGauss magnetic fields[2)] . Such developments may one day make it possible to build compact table top accelerators with applications to high energy and medical physics and possible to explore the properties of matter in intense magnetic fields.

This report details measurements of protons produced from the interaction of ultra intense lasers pulses with solid density materials. Energy spectra of protons were recorded with high spatial and spectral resolution and exhibit new features at intensities in excess of 5×10^{19} W/cm^2. In this new regime, the previously observed proton rings are now replaced by diffuse proton discs with proton energies up to 47 MeV. A plasma jet is also observed from the rear surface of the target containing low energy ($\leq$ 1 MeV) electrons and low energy ($\leq$ 4 MeV) protons. The plasma jet is observed as a ring indicating a toroidal plasma formation at the rear of the target. This plasma is likely formed by collimated electron transport inside the target heating the rear surface. Self-generated magnetic fields in the expanding plasma then help form the toroidal plasma in a similar manner to that observed at the front of the target[4)] .

These experiments were carried out at the Rutherford Appleton Laboratory using the CPA beam of the Vulcan laser[5)] which produces pulses having energies of up to 120 Joules at 1.053 µm wavelength and temporal durations of 0.9 – 1.2 ps. The laser beam was p-polarized and was focused onto a thin foil target with a f/4 off-axis parabolic mirror at an incident angle of 45 degrees from the target normal. The maximum intensity on target, up to 10^{20} W/cm^2, was determined from simultaneous measurements of the pulse energy, spot size and pulse duration. The level of pre-plasma at the target surface, caused by the inherent prepulse in the laser, was measured by optical probing and was typically found to be a few microns. Ion emission was measured from the rear of the target. To measure the proton spectrum, a stack of copper and plastic was placed behind the target. The nuclear activation of the copper by the protons enabled the proton spectrum to be determined. In addition, the energy spectrum and spatial distribution of protons emitted from the interaction was determined by placing a stack of several pieces of radiochromic film (which is sensitive to ionising radiation) and CR39 detectors behind the target.

The copper in the activation stack is activated by the reaction ^{63}Cu(p,n)^{63}Zn when high energy protons are incident on it. The resulting zinc decays with a characteristic half life by positron emission. The activity is measured as a function of time after the shot so that the number of zinc atoms created at the time the protons are incident on the copper can be determined. The activity is measured with a coincidence detection unit. Figure 1 shows the response of each layer of copper to incident protons in terms of the number of zinc atoms produced per incident proton as a function of proton energy. The layers of copper towards the rear of the stack are sensitive to the highest energy protons as each layer of copper and plastic in the stack acts as a filter. The final spectrum is derived via an unfolding routine.

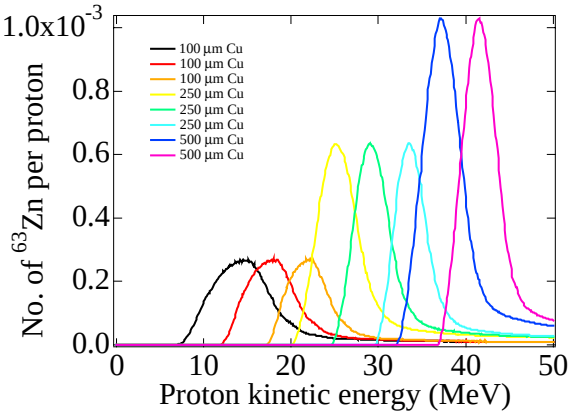

Figure 1. Number of zinc atoms produced per proton as a function of proton energy for each copper layer in the activation stack.

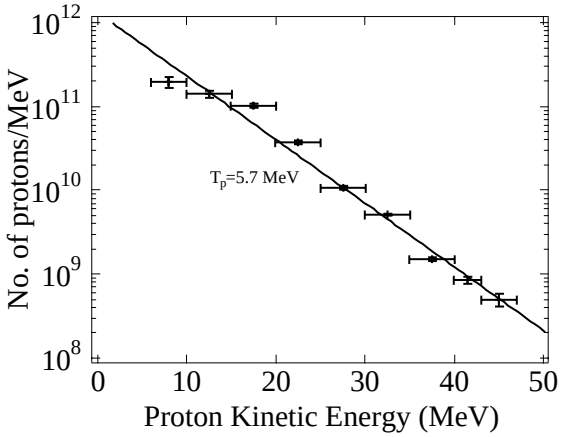

Figure 2. Proton spectrum unfolded from the copper activation stack indicating proton energies up to 47 MeV.

Figure 2 shows a spectrum from the highest intensity shot when the laser was incident on a 10 µm thick aluminium target. A total number of 2×10^{12} protons (≥6 MeV) was measured with energies up to diagnostic limit of 47 MeV. Assuming the proton distribution is of the form ~exp(-E/T), where E is the proton energy (MeV) and T is the proton temperature (MeV), a temperature of 5.7 ± 0.3 MeV can be derived. Fitting a Maxwellian distribution would imply that the total number of protons would be up to 10^{13}. It has been previously shown[2,3)] that the protons are likely to originate from a region near the front surface of the target. Indeed, a monolayer of hydrocarbons

at either the front or the rear of the target, which is the order of the focal spot size is insufficient to act a source for the total number of protons measured. It is therefore more likely that the protons originate from a volume source inside the target and not merely from a monolayer of hydrocarbons. A volume source of contaminants is routinely observed in electron beam interaction experiments with solids[6].

The diagnostic method used to measure the proton spectrum releases up to 10^9 neutrons per shot which have been detected with scintillators coupled to photomultiplier tubes. The maximum neutron energy recorded during these experiments was up to 25 MeV. The use of activation diagnostics, with lower thresholds for activation, could be used to enhance the neutron yield and produce in excess of 10^{10} neutrons per shot.

The spatial and spectral distribution of the ions was measured using a sandwich of radiochromic film (RCF)[7] and CR39 plastic track detectors[8]. RCF is a nylon substrate, coated with an organic dye which increases in optical density when exposed to ionising radiation. At the surface of the different layers of RCF/CR39 in this detector stack, protons having a particular range of energies release most of their energy just as they stop. Consequently, this produces a signal on the RCF/CR39 for only this range of energies. The stopping range of protons in radiochromic film and RCF/CR39 is well known – so, at a particular layer, the energy of protons producing the signal can be easily determined.

The CR39 / radiochromic film detector stack was aligned to the target normal at a distance of 12 cm from the surface so that the centre of the stack coincided with the target normal. Figure 3 shows the data taken when such a stack was placed behind a 175 μm mylar target. Unlike previous observations of the proton spatial distribution, where the protons were distributed into monoenergetic rings which increased in radius as the proton energy decreased, the protons now form discs (Figures 3c to 3h) which decrease in radius as the proton energy increases. This has been seen before with thin targets at lower energy[9] and is likely related to the electron spectral distribution as a function of intensity and the consequent electron penetration into the target. The heating caused by energy deposition in the target will likely modify the target resistivity and change the spatial distributions of magnetic and electric fields found within the target. Simultaneous proton rings and discs have also been observed (Figure 4). In this case, the discs observed at low energy tended to remain constant in radius, whereas at high energy, rings were observed which were 20 degrees away from the target normal and highly distorted.

The first 2 pieces of RC film, which is sensitive to all ionising radiations, are shown in Figures 3a and 3b. The periphery of the observable signal on the film or "halo", which covers a total angle of 45 degrees, clearly correlates with the signal on the CR39 in Figure 3c and agrees with the total number of protons as measured by the copper activation diagnostic. This signal is therefore almost certainly predominantly due to protons. The signal in the centre of the film, which is saturated in Figure 3a and the darkest signal in Figure 3b, is likely due to a plasma jet from the rear of the target. This signal, which covers an angle 15 to 20 degrees, has a ring like structure similar to that which has been measured at the front of the target[4] (Figure 5). This signal is predominantly electrons with energies of up to 1 MeV as no corresponding signal is observed on the CR39 which is only sensitive to protons and ions. Low energy protons with energies up to 4 MeV have been observed in this jet and can be detected in some shots on the CR39 behind the RC film (Figure 4b) in a ring which correlates with the emission on the RC film. The ring like structure in this plasma jet also correlates with the toroidal plasma observed at the rear of the target[11]. The toroidal plasma formation at the rear may be caused by self generated magnetic fields in the expanding plasma which can deflect the plasma into the shape observed. A similar phenomenon occurs at the front of the target. However, when this plasma structure is observed, no protons rings are formed. Such toroidal plasma formation does not result in the formation of high energy proton rings at the front of the target either (Figure 4). The plasma jet has also been seen to move in the vertical direction, relative to the proton signal, as measured on the RC film and by optical probing[12]. The "cross" pattern evident in Figure 3a is likely formed by low energy ions leaving the front of the target and then taking the shortest route around the 5 mm by 5 mm square target to the rear. Similarly, low energy ions from the plasma at the rear of the target will do the same and enhance the characteristic pattern that is observed.

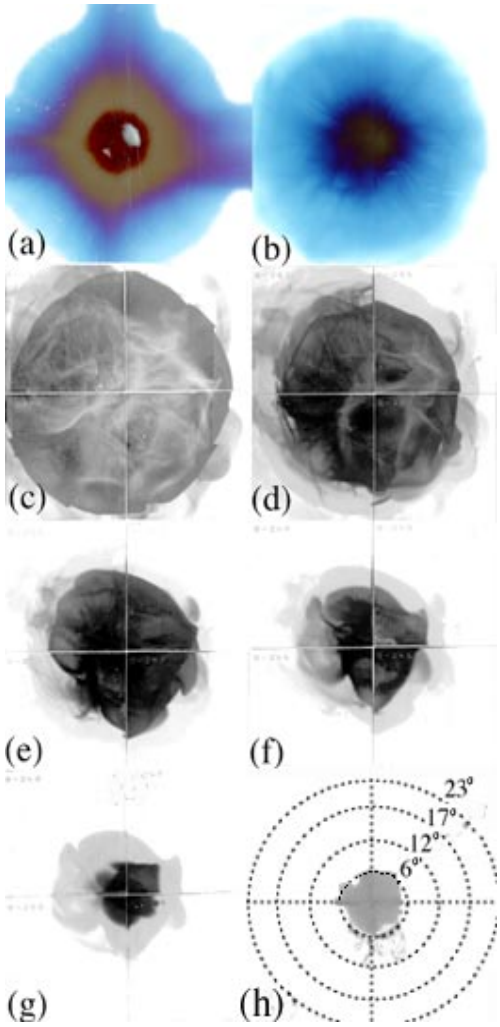

Figure 3. Radiochromic film/CR39 detector package behind the target. a) RCF (Proton Energy (E) < 3 MeV) b) RCF (E < 4 MEV) c) CR39 (E ~4 & 10 MeV) d) CR39 (E~10 & 14 MeV) e) RCF (E~14 & 18 MeV) f) CR39 (E~18 & 22 MeV) g) CR39 (E~22 & 26 MeV) h) CR39 (E~26 MeV). Note: Two energies may be indicated as the CR39 has been scanned and shows signal from both sides simultaneously. Each CR39 layer is made from a composite of four 5 cm by 5 cm, 0.75 mm thick pieces of CR39.

The interpretation of the observations in Figure 3 are in contradiction to similar work[13] undertaken on Vulcan, which attribute the "halo" to electron signal and the intense signal in the centre as being predominantly due to protons. It is obvious care must be taken when interpreting such diagnostics and the conclusions drawn when using detectors (RCF) which are sensitive to electrons, protons and photons and detectors (mylar) used for measuring protons which are only sensitive to bulk radiation damage[14].

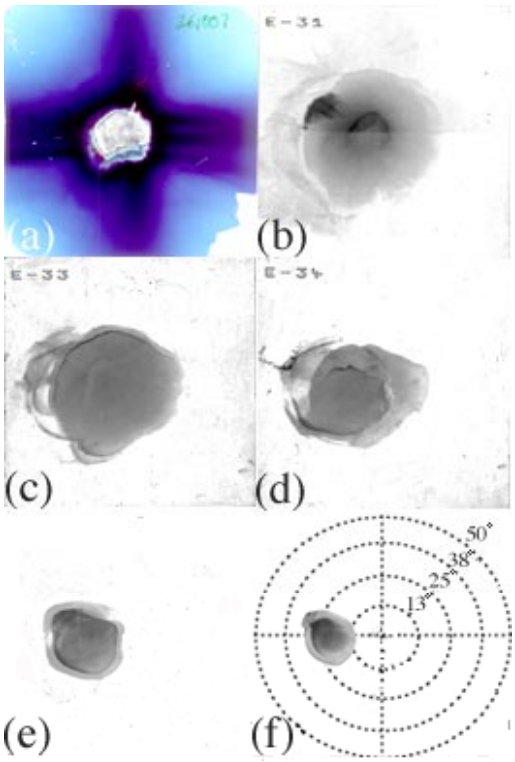

Figure 4. Radiochromic film/CR39 detector package behind a 10 μm aluminium target. a) RCF (Proton Energy (E) < 3 MeV) b) RCF (E ~ 3 MeV & 7 MeV) c) CR39 (E ~10 MeV &11 MeV) d) CR39 (E~16 MeV & 18 MeV) e) CR39 (E~21 MeV & 24 MeV) f) CR39 (E~27 MeV & 29 MeV). Two energies may be indicated as the CR39 has been scanned and shows signal from both sides simultaneously. Each piece of CR39 was 5 cm by 5 cm by 0.5 mm thick and was placed 2.2 cm from the target.

A plot of the maximum ion energy against $I\lambda^2$ ($Wcm^{-2}\mu m^2$) from data taken during these series of experiments is shown in Figure 6 (squares) together with data from Beg et al[15] and Tanet al[15] (circles). Clearly, there are large shot-to-shot variations in the data over the entire range of intensities plotted from 10^{13} to 10^{20} $Wcm^{-2}\mu m^2$. However, least squared fits to the data reveal two regimes. Up to 10^{18} $Wcm^{-2}\mu m^2$, the maximum ion energy scales as $(I\lambda^2)^{0.4}$ but when the oscillatory velocity of the fast electrons becomes relativistic, the maximum ion energy scales as $(I\lambda^2)^{0.5}$. It is likely that this scaling is a transition from classical resonance absorption to the $J \times B$ absorption mechanism at relativistic intensities[16]. The scaling is complex and it varies as the intensity regime changes. The scaling of the maximum ion energy has been related to the hot electron temperature by Gitomer[15] and Kishimoto[17] and it is therfore apparent that the ponderomotive scaling of the electron temperature with intensity cannot simply be inferred from limited data over a small range of intensities[18].

In conclusion, protons with energies up to 47 MeV have been measured with a 100 TW laser, a result only previously achieved with a petawatt laser.

References

1. Modena et al., Nature 377, 606 (1995). M. I. K. Santala, to be published
2. E. L. Clark et al., Phys. Rev. Lett. 84, 670 (2000)
3. Maksimchuk et al., Phys. Rev. Lett. 84, 4108 (2000)

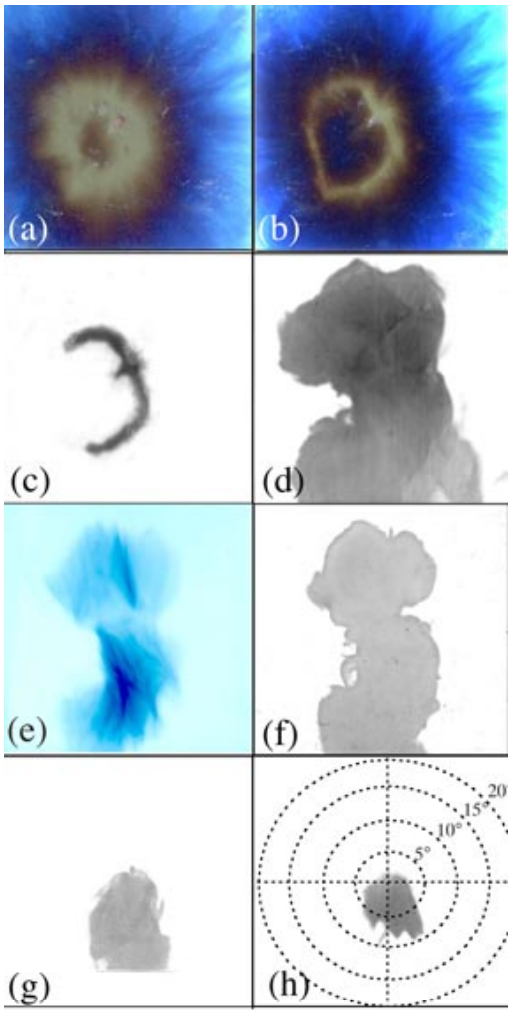

Figure 5. Radiochromic film/CR39 detector package in front of a 125 μm aluminium target. a) RCF (Proton Energy (E) < 3 MeV) b) RCF (E ~ 4 MeV) c) CR39 (E ~4 MeV) d) CR39 (E~11 MeV) e) RCF (E~13 MeV) f) CR39 (E~13 MeV) g) CR39 (E~18 MeV) h) CR39 (E~20 MeV). The horizontal axis in Figure 5(h) is the plane of propagation of the laser. Each piece of CR39 was 5 cm by 5 cm by 1 mm thick and was placed 7 cm from the target.

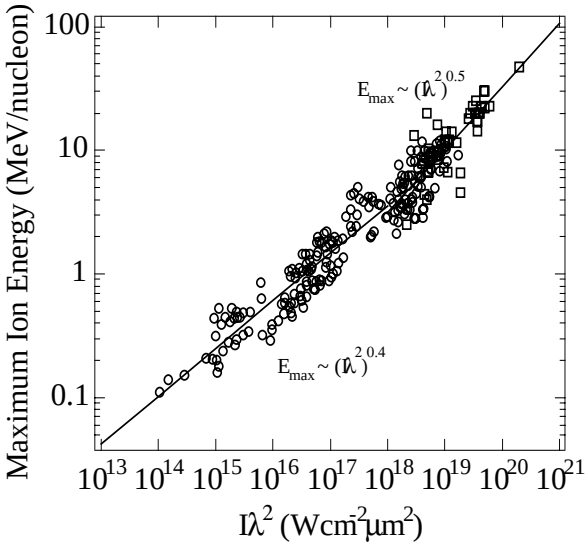

Figure 6. Maximum Ion energy (keV/nucleon) as a function of $I\lambda^2$. Data from Tan and Beg is indicated by circles. Squares denote the most recent data.

4. E. L. Clark et al, Phys. Rev. Lett. 84 (to be published Aug 2000)

5. C. N. Danson et al., Journal of Mod, Opt. 45, 1653 (1998).

6. Vermare et al, IEEE Transactions on Plasma Science, 27, No.5, 1501 (1999)

7. W. L. McLaughlin et al., Nucl. Instrum. Methods Phys. Res., Sect. A 302 165 (1991).

8. P. Fews, Nucl. Instrum. Methods Phys. Res., Sect. B 71, 465 (1992); 72, 91 (1992).

9. K. Krushelnick et al , Proceedings of the 4th International Workshop on the Fast Ignition of Fusion targets, Paris, 2000

10. L. Clark et al, Proceedings of the 26th ECLIM, Prague, 2000

11. M. Tatarakis et al , to be published

12. M. Tatarakis, Proceedings of the 3rd International Workshop on the Fast Ignition of Fusion targets, RAL, 1998

13. O. Willi, M. Borghesi, A. Mackinnon et al, Proceedings of the 4th International Workshop on the Fast Ignition of Fusion targets, Paris, 2000

14. P. Fews, private communication (2000)

15. S. J. Gitomer et al., Phys. Fluids. 29, 2679 (1984);
T. Tan et al., Phys. Fluids 27 296 (1984);
A. P. Fews et al., Phys. Rev. Lett. 73, 1801 (1994);
F. N. Beg et al., Phys. Plasmas 4, 447, (1997).

16. M. I. K. Santala et., Phys Rev Lett 84 1459 (2000);
P. A. Norreys et al., Phys. Plasmas 6, 2150, (1999).

17. Y. Kishimoto et al, Phys. Fluids, 26, 2308 (1983)

18. M. Borghesi et al, Phys. Rev. Lett., 83, 4309 (1999)

Experimental Studies of the Advanced Fast Ignitor Scheme

P A Norreys, R Allott, R J Clarke, J Collier, D Neely, S J Rose

Central Laser Facility, CLRC Rutherford Appleton Laboratory, Chilton, Didcot, Oxon, OX11 0QX, UK

M Zepf, M Santala, A R Bell, K Krushelnick, A E Dangor

Blackett Laboratory, Imperial College of Science, Technology and Medicine, Prince Consort Road, London SW7 2BZ

N C Woolsey, R G Evans

Department of Physics, University of York, Heslington, York, YO1 5DD

H Habara, T Norimatsu, R Kodama

Institute of Laser Engineering, Osaka University, 2-6 Yamada-oka, Suita, Osaka 565, Japan

Main contact email address: *p.norreys@rl.ac.uk*

Introduction

There are many aspects of the fast ignitor scheme for ICF that need detailed study, but one particular problem appears to be the 'hole boring' phase that is required to guide the multi-PWatt laser pulse through the coronal plasma and close to the compressed DT fuel. This phase risks instabilities in both the ablation hydrodynamics and the laser propagation. The ability to produce a channel that remains empty and stable for long enough that the ignitor beam can pass up it has been seriously questioned. This problem is being vigorously addressed experimentally[1,2].

To avoid this difficulty altogether, an *alternative fast ignition scheme* has been suggested that removes the hole-boring phase of the process by requiring that the initial implosion does not take place in spherical geometry. Two possibilities have been considered (although a variety of other geometries suggest themselves once the restriction of a spherical implosion is lifted). These are illustrated in Figure 1. The first (a) requires the implosion of a spherical shell that is almost complete, but involves a gold cone which keeps the channel clear for the short-pulse beam to reach the imploded plasma at stagnation[3] . The second method (b) is much more speculative and requires that the implosion take place down a cone and the ignitor beam interacts with the imploded plasma at the base of the cone[4]. In this case the presence of the fast ignitor relaxes the constraints on ρ and ρR of the compressed fuel and opens up the design space, but with the danger of mixing high Z material into the burn region. In each case these advanced fast ignition concepts have effectively traded a plasma physics problem (the hole boring problem) for a hydrodynamics problem (an implosion in the presence of a cone).

Experiments performed at the Central Laser Facility this year have investigated one of these advanced fast ignition concepts. These experiments, described below, have tested aspects of the physics underlying the scheme using an implosion driven down a cone. We chose the geometry in Figure 1(b) rather than (a) because it is impossible to drive the target in (a) with the long pulse energy available with the Vulcan Nd:glass laser (a few kJ). The attraction of the target in 1(b) for this experiment was that it reduced the long-pulse laser energy required by a factor of about ten, allowing the experiment to be undertaken on Vulcan whilst providing us with experimental information on the hydrodynamic behaviour of shells driven down cones. This is essential for the evaluation of both schemes in Figure 1. Indeed, experiments have been performed recently that have demonstrated that electron beam direction can be precisely controlled with the careful control of the plasma density scale-length. The advanced fast ignition scheme, which is the subject of this paper, provides a much shorter scale length for the interaction of the ignitor pulse with the plasma than in the original fast ignition scheme. It thus offers the opportunity for much more precise control of the energy deposition process, in addition to these other benefits.

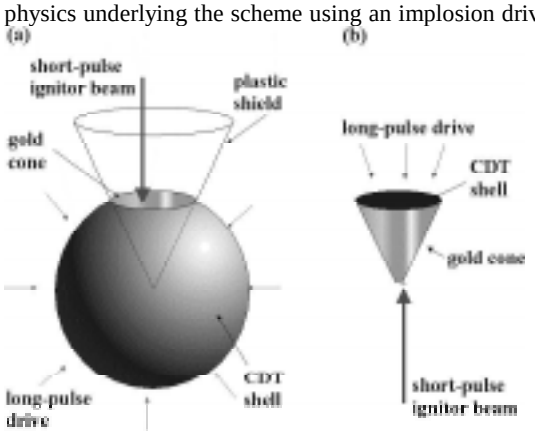

Figure 1. Schematic of advanced fast ignitor schemes.

Laser Configuration

The first question to address in guided compression is the effect of the high Z walls on the stability of the foil during the compression phase. To study this interesting stability problem, an experiment was conducted on the Nd:glass laser Vulcan. The laser was configured such that the output of the broad-bandwidth (16 nm) Tsunami Ti-S oscillator was stretched to 300 ps with additional amplification before being split between the two rod amplifier arms. This eliminated all timing jitter between the different beam lines, and provided broad bandwidth for spectral smoothing in the long pulse drive beams. In the long pulse arm, a beam splitter was used to stack two pulses to provide a 600 ps full width at half maximum (FWHM) duration pulse. The ratio between the two pulses in the beam splitter was adjusted to provide a flat top output pulse; i.e. the effect of gain saturation in the laser amplifier was taken into account on the final pulse shape. This pulse was then amplified in the rod chain and then split between the six 108 mm disk amplifiers. All long pulse beams were frequency doubled to 527 nm. Two beams were stacked to provide a foot pulse of 16 J in 1 ns resulting in an intensity of 5×10^{13} Wcm^{-2} to target. The remaining four beams were displaced in time to provide a flat top main drive pulse to target of 320 J in 2 ns resulting in an intensity of 5×10^{14} Wcm^{-2} on target. Shaped random phase plates, together with f/10 lenses generated a focal spot diameter of 200 μm. The intensity distribution in the focal plane was doughnut shaped and was higher on the edges than in the centre by a factor of 1.2:1.0. The doughnut intensity profile was used in an attempt to shape the flat foil during the implosion (although our simulations have revealed that this was not particularly successful due to thermal smoothing). In the short pulse arm of the Vulcan laser, the beam was amplified to the 60 J level (45 J to target) and compressed using large area diffraction gratings to 15 ps. The beam was focused onto target using a f/3 off-axis parabola and was either used to provide a x-ray backlighter for the radiographic studies (the first 'v-groove'

experiment) or heat the compressed plasma (in the second 'conical' experiment).

'V-groove' experiment

Figure 2 shows the first 'v-groove' experimental layout. The short pulse beam was focused onto an aluminium disk (13 μm thickness, 270 μm diameter) which was coated with 0.5 μm of bismuth. The beam was incident onto target at 30° from the target normal with a peak intensity of 5×10^{15} Wcm^{-2}. The Bi backlighting target was placed 700 μm from the edge of a 2 mm thick copper block which had a v-groove cut into the side. The depth of the groove was 250 μm and the entrance size was 200 μm. On this Cu block was mounted a foil consisting of 12.5 μm thick polyethylene with 2.0 μm of chlorinated paralyene coated on the inner edge. The 2ω drive beams were focused 500 μm from the edge of the Cu block closest to the back-lighter target. The 5 μm diameter pinhole was positioned either at 7 mm or 17 mm from the Bi target. The 16-bit Intaspec x-ray CCD detector (which was filtered by 125 μm Be to all eliminate Cu L-shell emission) was positioned 21 cm from the Cu target, giving a magnification of ×12 for Figure 3(a).

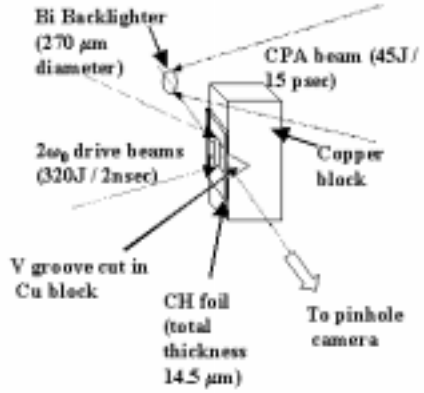

Figure 2. Layout of the "v-groove" experiment.

Figure 3(a) shows an image of the guided plasma taken 1.0 ns from the leading edge of the 2 ns, 5×10^{14} Wcm^{-2} pulse. Since the drive laser beam profile has an intensity profile that falls off from the edge of the focal region, some of the foil at the two free ends of the foil is accelerated into the v-groove to lower velocities than the material in the bulk of the foil. This lower velocity component at the free edges has absorbed most of the back-lighting radiation between the stationary foil and the inner edge. Nevertheless, a close examination of the inner edge of the imploding foil reveals that the inner edge of the foil has moved into the cone. Moreover, the foil is essentially flat over most of its surface and does not yet exhibit the growth of any hydrodynamic instability. However, at the top and bottom of the image, which corresponds to the edges of the guiding v-groove, the foil has obtained some inner curvature and has rolled up on the edge of the v-groove.

There is good agreement between the inner edge observation and that of 2D hydrodynamic simulations of this experiment [see Figure 3 (b)], except the drive intensity had to be reduced to 1×10^{14} Wcm^{-2} in the simulation to match the observed implosion velocity.

Conical Compression Experiment

The good agreement between theory and observation encouraged us to perform a more fully integrated conical compression experiment to determine the efficiency of fast electron heating. In this second experiment, the six 2ω long pulse beams irradiated a 12.5 μm flat polyethylene CH foil, which was covered with a 2.0 μm of deuterated polystyrene CD foil. The difficulty of target manufacture prevented the use of spherical shaped foils in this experiment (although advances in target fabrication technology will allow their deployment in future experiments). A 100 μm diameter, 100 nm thick signature layer of Ti and a 500 nm thick layer of chlorinated paralyene were deposited between the CH and CD foils, with the CD layer facing the apex of the cone. The Au cone was manufactured using micro-machining techniques similar to those used in the fabrication of holhraum targets. The distance from the entrance hole to the apex was 250 μm and the Au cone material was 20 μm thick. A 20 μm hole was machined in the apex of the cone, so that the target could be precisely positioned and the fast electrons transport was through the compressed CH/CD material only. A 12.5 μm thick, 270 μm diameter polyethylene foil was placed over the apex of the cone, in order to control the scale-length of the short pulse interaction process. The p-polarised 45 J, 15 ps, pulse was focused onto this foil in a 20 μm spot, giving a peak intensity on target of 10^{18} Wcm^{-2} and electrons with a temperature of between 200-300 keV.

The diagnostics for this experiment consisted of both time integrated and time resolved crystal spectrometers, a highly sensitive Ag activation counter and a number of current mode time-of-flight neutron detectors. The spatially integrated x-ray emission from the signature layers in the compressed/heated targets was observed using flat crystal spectrometers with a Si 111 crystal for the Cl Lα ($\lambda = 4.185$ Angstroms) and a Si 220 crystal for Ti Heβ ($\lambda = 2.221$ Angstroms) lines. A flat KAP crystal was coupled to a Kentech x-ray streak camera to observe the spatially integrated, but spectrally and temporally resolved x-ray emission.

A highly sensitive Ag activation detector was constructed to measure the d(d,n)^{3}He neutrons from the heated CD layer. The detector consisted of a conical-cylindrical block of HDPE moderator. Embedded in the moderator was a polished $5 \times 5 \times 10$ cm^3 perspex block which was surrounded by a 5 mm thick NE102 plastic scintillator, the outside of which was covered by 0.5 mm Ag foil. The 2.45 MeV neutrons were

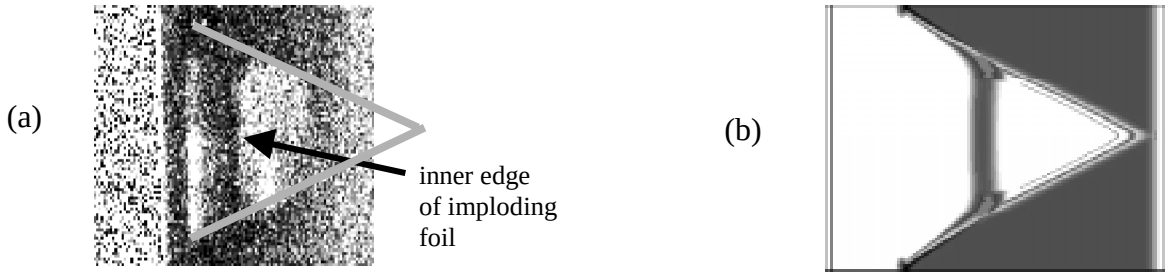

Figure 3. (a) Radiograph of imploding foil taken 1.0 nsec from leading edge of drive pulse (b) POLLUX simulation taken at the same time.

moderated in the plastics in the detector and the slowed-down neutrons then interacted with the Ag via the reactions $^{107}_{47}Ag$ (n, γ) $^{108}_{47}Ag$ and $^{109}_{47}Ag$ (n, γ) $^{110}_{47}Ag$. The $^{108}_{47}Ag$ and $^{110}_{47}Ag$ then β^- decay to $^{108}_{48}Cd$ and $^{110}_{48}Cd$ with a half-lives of 24.6 seconds and 144 seconds respectively. The β^--particles are stopped in the scintillator and produce a light pulse. The perspex block acts as a wave-guide for these photons to the photo-multiplier whose electrical signal was then fed into an amplifier/counting set-up. The instrument was located such that the perspex block was 10.7 cm from the target, resulting in a collection angle which was close to 1 steradian. The instrument was calibrated off-line using a moderated ^{241}Am/Be neutron source.

The time resolved x-ray spectra showed that there was a significant increase in x-ray emission which peaked at 1.7 ns after the beginning of the main pulse when only the main drive beams were fired, suggesting that this increase in x-ray emission corresponded to the onset of stagnation. Both time integrated x-ray spectra for this shot did reveal that some M-band Au emission was present, as well as some Cl Lα emission from the Si 111 crystal spectrometer, suggesting that kinetic energy of the stagnating foil was converted to thermal energy, as expected. The high intensity heating pulse was then employed and moved to coincide with the stagnation time. The Si 220 crystal spectrometer showed no evidence of time integrated Ti Heβ emission when the short pulse beam was fired at 1.7 ns.

Calculations with the atomic physics package FLY[5] suggest that pressure ionisation of the n=3 level only becomes significant with densities above ~30 gcm^{-3}. Since the densities simulated in POLLUX were an order of magnitude lower, this effect is not expected to be important in this experiment. The calculations did show, however, that Ti Heβ emission should have been observed with an electron temperature of 1.0 keV for densities in the range 1-20 gcm^{-3}. Thus, the absence of Ti Heβ line emission in the experiment sets an upper bound to the heated electron temperature of ~700 eV.

Neutrons were observed when the short pulse beam was fired at 1.7 ns. At other times (within ± 100 ps from this point in time) no neutron emission was detected. This implies that if any neutrons were generated at these other times, they were below the threshold of the detector (5×10^3). They tend to rule out (γ,n) and (p,n) neutron generation processes in the target or the surrounding equipment, because then the neutrons would have been generated at all times. The observed β^- decay curve is consistent with a 25 second half life, and a yield of 2 x 10^4 neutrons (the signal to noise is too small to unambiguously count the $^{109}_{47}Ag$ (n, γ) $^{110}_{47}Ag$ reaction). The data strongly suggests that the neutrons are generated as a result of the thermonuclear reaction d(d,n)^{3}He from the heated CD layer.

We can make an estimate of the plasma temperature needed to generate the observed neutron yield. Assume the fast electrons uniformly heat the plasma. The energy obtained from an inertially confined DT plasma is equal to the burn-up fraction multiplied by the total energy available from the fuel. The burn up fraction is given by the expression

$$f_b \approx 5.6\times10^3(\rho R)\exp(-19.9/kT_{keV}^{1/3})/kT_{keV}^{1/3}$$

When CD material is substituted for DT and the ρR of 10 mgcm^{-2} from the simulations is used, then the plasma temperature of the CD layer needed to generate 2×10^4 neutrons is ~500 eV. This means that ~7% of the short pulse laser energy was coupled to the plasma to produce this temperature. While this coupling efficiency appears somewhat low, it may be increased by a more suitable match of the range of the fast electrons, which depends upon $I\lambda^2$, to the achieved ρR . For instance, at 10^{18} Wcm^{-2}, the electron temperature is 200 - 300 keV with a range in plastic of ~140 mgcm^{-2}, somewhat higher than could be achieved in the experiment. An optimisation of the coupling of short pulse energy to the compressed plasma will be the subject of further investigation.

Summary

We have shown that the advanced fast ignitor concepts have effectively traded a plasma physics problem (the hole boring problem) for a hydrodynamics problem (an implosion in the presence of a cone). We have provided the first demonstration, using an open geometry and x-ray backlighting, that the guided foil remains stable during the compression, and that good agreement is obtained with two-dimensional hydrodynamic simulations. An integrated conical compression experiment has confirmed that this approach to fast ignition demands detailed investigation.

References

1. R.Kodama, *et al.* Rev. Sci. Instrum. 70, 543 (1999).
2. A.J.Mackinnon *et al.* Phys. Plasmas 6, 2185 (1999).
3. M.H.Key (*private communication)*
4. S.J.Rose *(private communication).*
5. R.W.Lee and J.T.Larsen J. Quant. Spectrosc. Radiat. Transfer 56, 535 (1996).

Effect of plasma scalelength on multi MeV proton production by ultra short laser pulses

A J Mackinnon, S Hatchett, M H Key, P Patel, R Snavely, S C Wilks

Lawrence Livermore National Laboratory, Livermore CA 94550, USA

M Borghesi

Department of Pure and Applied Physics, The Queen's University, Belfast, Northern Ireland BT7 1NN

A Schiavi, H Campbell, O Willi

Blackett Laboratory, Imperial College of Science, Technology and Medicine, London, SW7 2BZ, UK

Main contact email address: *mackinnon2@llnl.gov*

Introduction

The generation of multi-MeV proton and ion beams from plasmas produced following the interaction of an ultra-short laser pulse is a rapidly growing research area. Early work using long pulse $C0_2$ (wavelength, $\lambda = 10$ μm) lasers at an irradiance of $I\lambda^2 \sim 5 \times 10^{17}$ Wcm^{-2} has been ongoing from the early 70s [1-3]. More recent work at $I\lambda^2 > 5 \times 10^{18}$ Wcm^{-2} has shown proton production up to 5 MeV [4,5]. The production of multi-MeV particles in distinct collimated beams has been observed in a number of very recent experiments. In particular, Clarke et al [6] observed protons with energies up to 20 MeV emitted into a half angle of 30 degrees in the forward direction from a 110 μm thick aluminum foil that was irradiated by a 1 ps, 1 μm laser pulse, at 5×10^{19} Wcm^{-2}. In another experiment at somewhat lower laser irradiance ($I\lambda^2 = 2 \times 10^{18}$ W/cm^2), $\lambda = 0.527$ μm, on 1.5 μm Al and plastic foils, Maksimchuck et al.[7] also observed protons accelerated in the forward direction to a maximum energy of 2 MeV.

The interpretation for both these experiments was that the protons were generated and accelerated from hydrogen impurities present in the plasma at the front of the target. This interpretation contrasts strongly with the results obtained from experiments performed on the petawatt laser at Lawrence Livermore National Lab, which produced forward going protons with energies up to 50 MeV in a collimated beam from 125 μm thick, gold and plastic targets [8]. These experiments provided clear evidence that the proton acceleration of impurity layers occurred through an electrostatic mechanism at the back of the target. In this mechanism protons are accelerated by the energetic electrons, which are created during the laser-plasma interaction, which then penetrate through the target, to its back surface. Modeling has shown that efficient production of high-energy protons depends on a large hot electron temperature and an initially, short ion density scalelength at the back of the target [9,10]. A study of the influence of plasma at the back surface of a thin foil target on the production of MeV protons thus provides a direct test of this theoretical mechanism.

This report describes experimental observations of the interaction of ultra-intense laser pulses with aluminum (Al) and Al coated Mylar (AlCHO) foils with and without preformed plasmas on the back surface of the foil. Particle detectors were used to diagnose the energy characteristics of the ions produced during the interaction. Time - resolved optical probing was used to measure the preformed plasma on both the front and rear of the foils. The proton beam was found to depend strongly on the plasma scalelength at the back of the target. A simple analytic electrostatic ion model was found to account for the observed influence of plasma density scalelength on the peak and mean ion energies. Computational modeling also indicated that this was consistent with electrostatic acceleration occurring predominantly at the back surface of the target.

Experimental set-up

The experiment was performed on the Vulcan Nd:glass laser operating in the Chirped Pulse Amplification mode (CPA). The targets were Al foils, 1 mm wide and about 1 cm long and 25 μm thick (i.e. in the laser propagation direction). The 1.054 μm CPA interaction pulse, 1 ps in duration, with an energy of about 50 J was focused by an F/3.5 off-axis parabola (OAP) at normal incidence onto the centre of the coated side of the target. The focal spot was between 8 and 10 μm in diameter at full width at half maximum (FWHM), containing 30-40 % of the energy giving peak intensity of 5×10^{19} W/cm^2. A fraction of the CPA pulse was compressed with a separate pair of gratings to a duration of 1 ps (FWHM); frequency quadrupled using two KDP crystal and used as a temporally independent probe. The probe, a collimated beam with a diameter of about 3 mm propagated through the target along a direction transverse to the interaction axis. The relative timing of probe and interaction pulse was controlled to within a few picoseconds. A microscope objective, operating at F/4 imaged the target with a magnification of 55 onto UV sensitive photographic film resulting in a spatial resolution of 2-3 μm in the target plane.

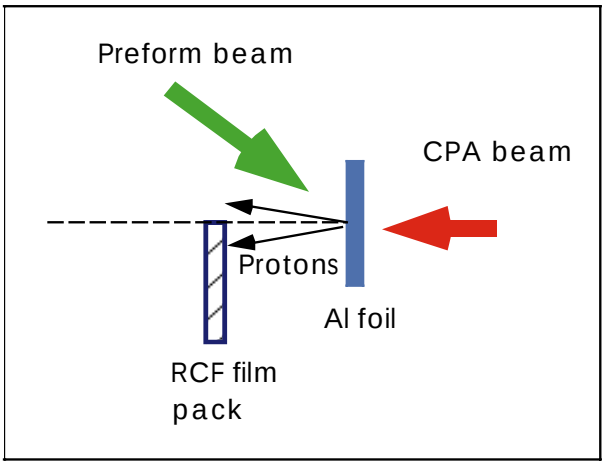

Figure 1. Experimental layout.

Experimental results

The main experimental diagnostic of the proton flux produced during the interactions was radiochromic film (RCF). This consists of an organic dye sandwiched between two or more layers of plastic with a total thickness of 250 μm [8,9]. The dye is sensitive to the total radiation dose (x-rays, ions and electrons) and the optical density is absolutely calibrated to give the absorbed radiation dose in krads (10^{-2} J/g). Typically layers of RCF were placed at a known distance behind the target and aligned so that the face of the film was perpendicular to the back normal of the target. Al filters were placed in front of the first layer of film, giving a minimum detectable proton energy of 3.5 MeV. In some shots each film layer acted as an energy filter for the subsequent layer while in others the RCF were separated by additional layers of Mylar. These intermediate Mylar layers were subsequently etched to reveal particle tracks. This provided a complementary method of measuring the energy deposited by the protons, analogous to the use of CR39 particle detectors [4,6]. In addition to these particle diagnostics,

interferograms of the target were made 5 ps before the incidence of the interaction pulse, thus allowing the preformed plasma scalelength to be measured up to a density of 5 x 10^{20} cm^{-3}. The preformed plasma was created by focusing a 600 ps duration laser pulse at λ = 0.527 μm onto the back surface of the foil with an F/10 lens. The prepulse energy, focal spot and relative timing were all controlled on a shot to shot basis. For most shots the energy on target was 10 J within a focal spot of 300 μm (FWHM), and the prepulse started 250 ps before the interaction pulse, thus giving a mean intensity on target of 3 x 10^{13} Wcm^{-2}. Figure 1 shows a schematic of the experimental arrangement.

Proton production with and without preformed plasma

Data from the second RCF layer of a typical proton beam generated from a 25 μm Al foil with an unperturbed back surface is shown in Figure 2 (a).

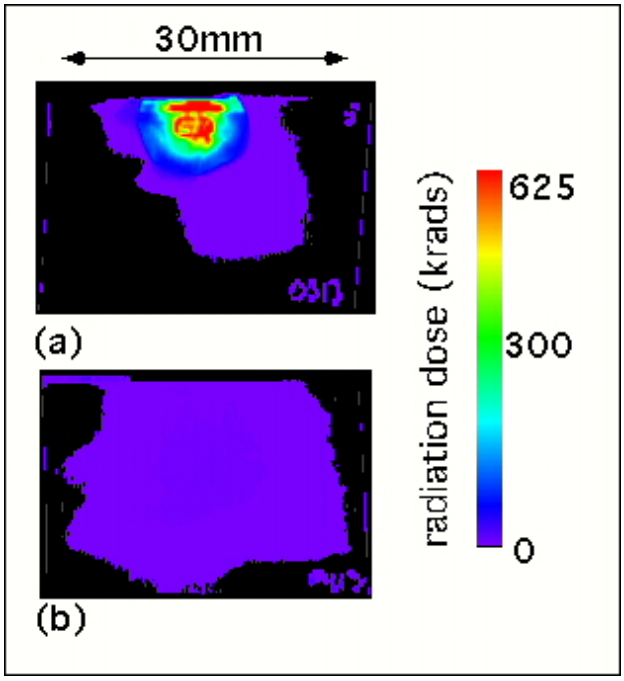

Figure 2. RCF signal for (a) initially unperturbed foil and (b) with 100 μm scalelength plasma on the back of the foil.

The proton beam is the distinct feature at the top edge of the film surrounded by a diffuse background due to energetic electrons. Only half of the proton beam is visible on the RCF because the pre-pulse beam was incident from directly above the film pack and the pack consequently had to be lowered to allow all of the pre-pulse beam to hit the back of the target. The first layer of RCF was protected by a 50 μm Al filter. For protons, only those above 3 MeV could penetrate this filter. The response of each film is determined by the energy deposition of the protons within the active layer, for ions the majority of the energy is deposited towards the end of the stopping range (the Bragg peak) [11]. The response of each RCF layer to high-energy protons has been determined using Monte Carlo modeling of the deposited energy by the particles. Each film responds to ions within an energy band of a few MeV. The data from the second layer shown in Figure 2 (a) represents proton energies between 5 MeV and 7 MeV. For the unperturbed case a strong proton signal was observed out to the fifth RCF layer, which corresponded to proton energy just under 20 MeV. This cut off is in quantitative agreement with the data presented by Clarke et al [6], which were obtained using the same Vulcan laser facility.

The situation was very different when a pre-pulse was incident on the back surface of the foil, 250 ps prior to the arrival of the interaction pulse. The RCF data for this case is shown in Figure 2(b).

It can be seen that there is no evidence of a proton beam on the second RCF layer. In fact there was no evidence of protons or ions after the first RCF layer. This means that there were no protons above an energy of 3.5 MeV. The same effect was also observed on the ALCHO targets, which were arranged with the Al side facing towards the CPA and the CHO side towards the pre-forming beam, and the effect was reproducible (observed three times from 3 shots). Further confirmation that the proton signal was very much reduced in the preformed plasma case was obtained by etching one of the three Mylar layers between the first two RCF layers. There was a one to one correspondence between the track features in the etched Mylar and the RCF data. For the unperturbed case, in each layer the track density within the proton beam was very high and the signal fell off very sharply at the edge region of the spot. In contrast, for the preformed plasma case the track density is high only on the first Mylar layer and it drops off very rapidly to background levels before the 2nd layer of RCF.

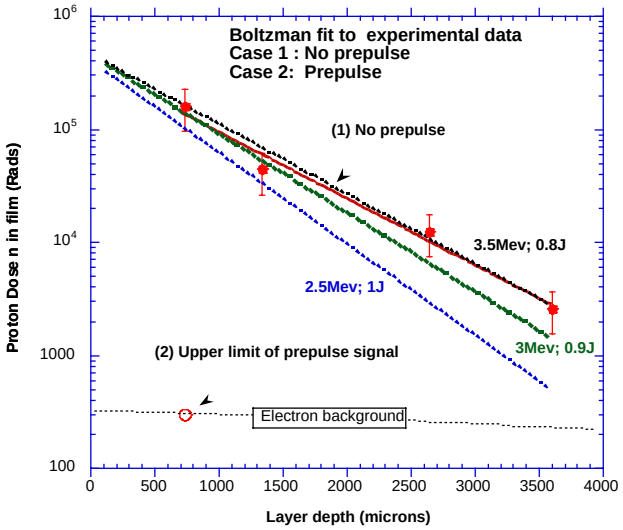

Figure 3. Energy spectrum of protons with and without preformed plasma.

The energy deposited within each film layer can be extracted from the absolutely calibrated film. By doing this for each film layer and fitting an exponential energy spectrum, an estimate of the proton energy spectrum and total energy can be extracted from the film data [8,9].

Figure 3 shows the dose as a function of layer depth for both cases. For the unperturbed foil the dose is plotted for all RCF layers apart from the first. The best fit to the remaining four RCF layers is shown in Figure 3. The mean energy of the exponential is given by kTp = 3 MeV ± 0.3 MeV and a total energy of 0.9 ± 0.2 J in protons above 3.5 MeV. For the preformed plasma case, it was not possible to fit a proton energy spectrum from this method because a signal above background was only detected on the first layer of radiochromic film. The film in this layer was saturated for both the unperturbed and preformed plasma cases so these layers did not provide useful data. One can however, compare the energy deposited in the 2nd RCF layer to the corresponding signal in the unperturbed foil case. As there is no signal visible due to protons on the 2nd RCF layer an upper limit can be placed, if it is assumed that the proton signal is just below the electron background. The background level, shown in Figure 3, is a factor 1000 lower than the corresponding signal produced from the unperturbed foil. For the signal to be this strongly reduced either the mean energy of the proton beam and/or the production efficiency was reduced to sub MeV levels by the preformed plasma on the back surface of the target.

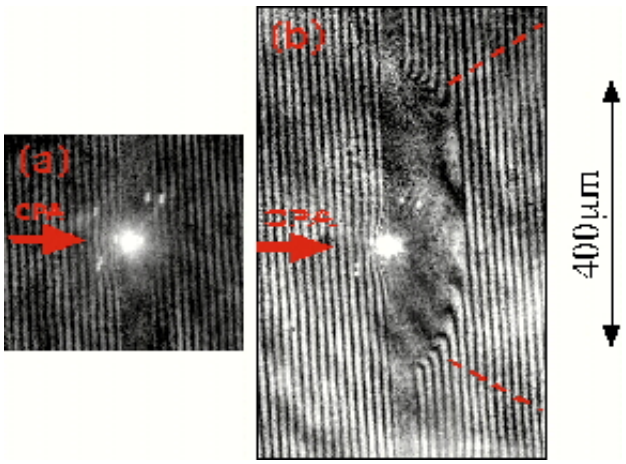

Figure 4. Interferograms corresponding to data in Figure 2, (a) no preformed plasma and (b) with a 100 μm scalelength preformed plasma on the back of the foil.

Interferograms of the preformed plasma immediately before the arrival of the interaction pulse are shown in Figure 4 a, b. In case (b) the plasma is clearly visible on the back of the foil, extending for 100 μm from the original target position, with a diameter of 300 μm, which is much larger than the interaction focal spot, and with a 1/e density scalelength of 100 μm. In both cases a small preformed plasma created by the generic prepulse is visible on the front of the target with a scalelength of a few microns. It is clear from these images that, apart from the generic pre-plasma region, the original target surface at the front is still intact. This is important as it shows the pre-pulse on the back did not change the laser plasma interaction at the front of the target, which was still dominated by the conditions prevailing in the generic preformed plasma.

The possibility that protons from the front surface were somehow stopped by the preformed plasma on the back of the target was tested by performing another experiment using two separate foils. The CPA pulse was focused on the first target, producing a proton beam. This beam passed through the second foil, which had a preformed plasma on its back surface. It was found that protons (above 3 MeV) from the first foil were not strongly affected by the preformed plasma on the back of the subsidiary target. This also confirmed that the main acceleration mechanism of protons >3 MeV occurred at the back of the target[12].

The theory describing electrostatic acceleration in the Debye sheath at the back surface of the target has been described recently in Hatchett et al.[9] following on from earlier ion acceleration models [2,3]. A simplified picture is as follows. When the intense laser pulse hits the front of the target hot electrons flood through the target and drive the acceleration of ions from both the front and back surface of the foil. Assuming the hot electron density follows Boltzmann statistics and solving Poisson's equation, hot electrons will set up a sheath electric field, $E_d \sim kT_h/e*(\max(L_d , L_i))$ where L_d is the hot electron Debye length and L_i the ion density scalelength at the front and/or back of the target [9]. It can be seen that the sheath field depends strongly on the hot electron temperature and inversely on the characteristic length for acceleration. If L_i is increased, then the sheath forms in a region at lower hot electron density where L_d is correspondingly larger. This in turn causes a reduction in hot electron charge density driving the accelerating field, thus leading to lower proton energies. If it is assumed that 40% of the incident laser energy is absorbed into hot electrons with a mean energy of 1.5 MeV and that these electrons fill the majority of the 25 μm thick target (a volume of ~300 x 300 x 25 μm), giving $L_d \sim 1.6$ μm. For a short scalelength $E_d \sim 1.3$ MeV/micron and protons should be accelerated to a maximum energy of 20 MeV by the end of the laser pulse by such a field. If however the scale is set by the 100 μm ion density scalelength of the preformed plasma, then the maximum proton energy will be only in the few MeV range, as observed experimentally. 2D PIC code simulations of this effect, which support this simple analytical model have recently been carried out [10]. In these simulations the influence of short density scalelength on the peak accelerated ions was investigated. For an initial hot electron temperature of 1 MeV and short L_i ($10n_{cr}$ – 0 in 0.05 μm, where n_{cr} is the peak density used in the simulation) present at the back of the target, the peak electric field was 1 MeV/μm and protons were accelerated up to 21 MeV. When L_i was increased from 0.05 to 14 μm the peak ion energy was reduced to 5 MeV. This is in qualitative agreement with the experimental observations where for the longer scalelength of 100 μm, no protons above 3 MeV were observed.

In conclusion the acceleration of energetic protons from thin foil targets has been studied as a function of plasma density scalelength at the back of the target. The maximum energy and efficiency of acceleration was found to depend very strongly on the existence of a short density scalelength on the back surface of the target. The observations were consistent with the modified electrostatic acceleration mechanism [9]. Furthermore these measurements are important because they directly show that manipulation of the back surface of the target can significantly modify the energy and spatial distribution of the protons. Such energy modifications could conceivably be used to concentrate the proton/ion beam locally in a specific spatial region [10]. Such a proton flux enhancement would be beneficial for many potential applications.

The authors would like to acknowledge the excellence of the staff at the Central Laser Facility. This work was funded by ESPRC/MoD grants and also under the auspices of the U.S. Department of Energy by the Lawrence Livermore National Laboratory under contract No. W-7405-ENF-48.

References

1. S.J.Gitomer
Phys. Fluids 29, 2679 (1986)

2. J.E.Crow, P.L. Auer and J.E.Allen,
J. Plasma Physics 14, 65 (1975)

3. Y. Kichimoto, K. Mima, T. Watanabe and K. Nishikawa
Phys. Fluids 26, 2308 (1983)

4. A.P. Fews, et al.,
Phys. Rev. Lett 73, 1801 (1994)

5. F.N. Beg et al.,
Phys. Plasmas 4, 447 (1997).

6. E.L. Clark et al.,
Phys. Rev. Lett 84, 670 (2000)

7. A. Maksimchuk et al.,
Phys. Rev. Lett. 84, 4108 (2000)

8. R.A.Snavely et al.,
Phys. Rev. Lett (2000) (in press)

9. S. P. Hatchett et al.,
Phys. Plasmas 7, 2076 (2000)

10. S.C Wilks et al.,
Accepted for publication in Phys. Plasmas (2000).

11. A. Caruso and V.A. Pais,
Nucl. Fusion 36, 745 (1996).

12. A.Mackinnon et al.,
Submitted to Phys.Rev.Lett.

Photo-nuclear activation in characterising laser-plasma accelerators

M I K Santala[*)], Z Najmudin, M Tatarakis, K Krushelnick, A E Dangor

Blackett Laboratory, Imperial College of Science, Technology and Medicine, London, SW7 2BZ, UK

J Faure, V Malka

LULI, CNRS – CEA, École Polytechnique – Université Pierre et Marie Curie, 91128 Palaiseau Cedex, France

R Allott, R J Clarke

Central Laser Facility, CLRC Rutherford Appleton Laboratory, Chilton, Didcot, Oxon, OX11 0QX, UK

Main contact email address: *Marko.Santala@hut.fi*

[*)] *Present address: Helsinki University of Technology, Po. Box 2200, 02015 HUT, Finland*

Introduction

Plasmas produced by intense (> 10^{19} W/cm^2) sub-picosecond laser pulses are potentially efficient sources of high-energy electrons[1)]. Coupling of transverse laser fields to longitudinal plasma waves can generate electric fields exceeding 100 GV/m[2,3)]. Hence, electrons with energies up to 100 MeV can be observed using sources with dimensions on the order of 1 mm e.g. [4,5)].

One method for producing these plasma waves – the self-modulated laser wakefield accelerator (SM-LWFA) – has recently been the subject of intense investigation. Operating in moderately dense plasmas (10^{19} cm^{-3}) they are capable of producing very large accelerating fields as relativistic plasma-waves are generated through Raman-scattering and self-modulation of the focused laser beam in the plasma [6,7)]. Direct laser acceleration (DLA) is another acceleration mechanism recently identified in 3D particle-in-cell (PIC) simulations[8)] and observed in experiments at a moderate power [9)]. It occurs due to betatron oscillations of electrons in the quasi-static fields generated by the relativistically self-focussed and channelled laser beam in plasma. Simulations (in non-uniform plasmas) suggest that this mechanism can be at least as efficient as the LWFA near the threshold of relativistic self-focusing.

Physics of these acceleration mechanisms is not yet fully understood so actual measurements of the high-energy electrons are very important. For applications (e. g. the Fast Ignitor[10)]) it is necessary to characterise the accelerated electron beams in terms of energy spectrum, electron yield, and beam divergence. In this work we develop the photo-nuclear activation techniques previously used in laser-solid interaction studies[11-13)] for measurement of the electron beam divergence in a high power (50 TW) plasma-accelerator experiment. As the diagnostic is completely insensitive to electron energies below the reaction thresholds (8 – 22 MeV) only electrons with energies exceeding them contribute to our results.

Experiment

The experiment was carried out at Vulcan TAW using the "100 TW beamline". The target was a helium gas-jet produced by a supersonic nozzle (diameter 4 mm). The jet has a very homogeneous density profile and a sharp edge[14)]. The laser beam was focused to the front edge of the jet by an off-axis parabola in *f*/4 geometry resulting in spot size < 10 μm (monitored by an equivalent plane monitor). The linear-polarised beam could be converted to circular-polarisation by inserting a λ/4 plate in the beam. The electron density could be changed in the range (0.5 – 4.5) x 10^{19} cm^{-3} by varying the nozzle backing pressure. The density was measured by forward Raman scattering.

The activation target (Figure 1) consisted of 1 mm of tantalum (Ta) as a bremsstrahlung converter and the main activator made of segmented copper (Cu) pieces 1 cm thick. Additionally, a 3 mm layer of PTFE ($(CF_2)_n$), behind the Cu pieces was used on several shots. Radiochromic film was placed in front of the Ta layer as an additional beam monitor. The high-energy electrons

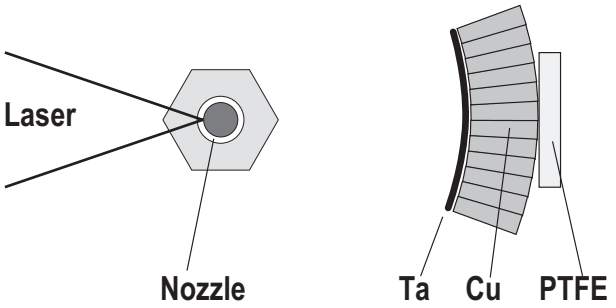

Figure 1. Schematic drawing of the target.

produce bremsstrahlung with good efficiency in the Ta converter, and to some extent also in Cu. Bremsstrahlung is directed in a narrow cone along the direction of the incident electrons, so only the copper pieces in that direction are exposed. A part of the bremsstrahlung photons induce photo-nuclear reactions in the target materials. As the different reactions are sensitive to different energies, spectral information can be deduced by measuring several reactions simultaneously.

Two techniques were used for measuring the induced activity, coincidence counting [12)] was applied for short-lived positron emitting nuclides, and high-resolution gamma-spectroscopy for the others. For spectroscopy, a 25 % efficient N-type germanium detector within a 10 cm thick lead shield was used. The gamma spectra were measured by a PC-based multi-channel analyser.

To deduce the initial number of electrons and their spectrum the slowing-down of the electrons and generation of brems-strahlung in the target materials was modelled numerically. The incident electrons were assumed to have a quasi-thermal energy spectrum $f(E) = f_0\exp(-E/kT)$. This is a reasonable assumption as seen in experiments under various conditions as well as in several PIC simulations[4,9)]. The resulting bremsstrahlung spectrum was folded with photo-nuclear reaction cross-sections[15)] to estimate the activation yield of each reaction at different "effective" temperatures T. Matching the ratio of measured yields of two reactions to these estimates gives T, and f_0 can be found from the absolute yield.

Results

The angular distribution was measured in the horizontal plane at different plasma densities. In this measurement the ^{62}Cu activity (γ,n) in each copper segment was measured and corrected for decay. Two measured and normalised distributions and the observed width (FWHM) as function of plasma density are shown in Figure 2. It is seen that electrons are emitted in a fairly wide cone and the cone angle increases with plasma density until it is similar to that of the laser. The angle is found to be only weakly sensitive to the laser power.

The effective electron temperatures were determined separately from the measured ^{61}Cu/^{62}Cu, ^{11}C/^{18}F, and ^{178}Ta/^{180}Ta activity ratios. These differ in a consistent fashion from shot to shot.

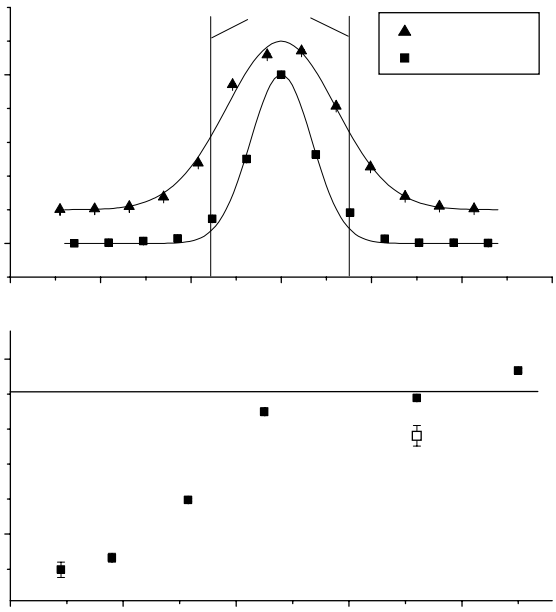

Figure 2. (a) Normalised angular distributions measured with ^{62}Cu activation for a low (squares) and high plasma density (cm^{-3}). The lines indicate Gaussian fit to data. (b) Width (FWHM) of the electron beam as function of plasma density. Energy on target was 25 – 45 J, except a low energy shot (open square) that was 10 J.

The average effective electron temperatures for shots with a large activation yield are 8.2 MeV for Cu, 10.8 MeV for C/F. A much lower value of 4.4 MeV is obtained for Ta. However, this measurement may be skewed by uneven source distribution and self-absorption effects. The major point of interest is that ^{178}Ta, with the reaction *Q*-value 22 MeV and a cross-section peaking at 25–30 MeV, can be observed at all, proving conclusively the presence of large numbers of electrons above this threshold.

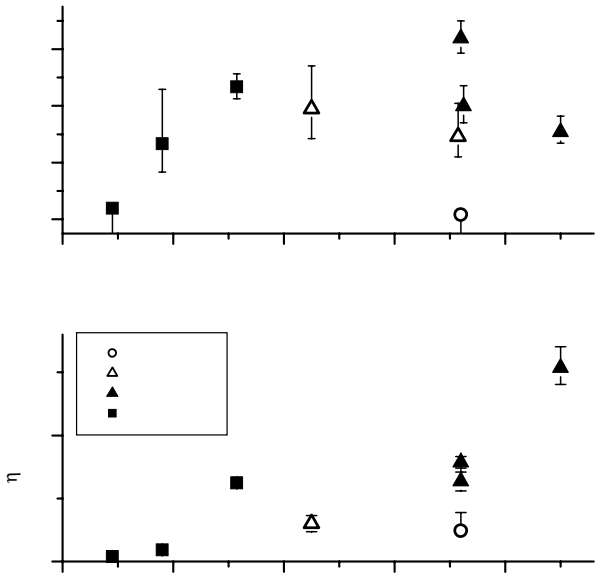

Figure 3. (a) Measured (Cu activation) temperatures at different plasma densities and laser powers. (b) Energy conversion efficiency from laser energy to fast electrons.

There is clear evidence of temperature increase with an increasing laser power at constant density (Figure 3a). The same figure also indicates, that at lower densities the temperature of the electrons increases with density but beyond about 2 x 10^{19} cm^{-3} a slight decrease is observed. The results show an increasing coupling of the laser energy to the plasma, up to a saturation which is consistent with the on-set of wavebreaking[2].

The electron yield (E > 10 MeV) was also estimated using the exponential model. For high-energy, high-density shots the yield was 1.5 – 3.8 x 10^{11} electrons while lowest yields were about 10^{10}. The highest electron yield would correspond to all the electrons in a volume of more than 8000 μm^3. To explain the largest ^{178}Ta activation 10^9 – 10^{10} of the electrons must be at or above 40 MeV. Assuming a 1 ps bunch duration[16], the beam current (E > 10 MeV) is up to 60 kA, a major fraction of the Alfvén limit (350 kA at 10 MeV). The total energy carried by the fast electrons was up to 1 J with peak conversion efficiency up to 2 %. It increases with plasma density (Figure 3b). Laser beam polarisation did not affect the yield.

Discussion

Laser-plasma accelerators could have an application in production of short-lived radioactive sources. In high density shots, the typical total ^{62}Cu activity produced was 10 – 20 kBq. This can be compared to the solid-target experiments, where similar Cu targets result typically only to less than 1 kBq of activity[12]. The more efficient production of activity results from the higher electron temperature in the LWFA resulting in more efficient production of high-energy bremsstrahlung.

In conclusion, we have applied photo-nuclear activation to characterising > 10 MeV electrons in a self-modulated LWFA experiment. We have measured up to 4 x 10^{11} electrons above 10 MeV having a characteristic temperature of about 8 MeV. We have observed that the angular spread of the emitted electron beam increases with plasma density but appears to saturate. The total yield of fast electrons is found to increase with plasma density. The total activity yield is found to be more than an order of magnitude greater than in solid-target experiments with similar laser parameters, which is of interest for potential applications.

References

1. T Tajima and J M Dawson, Phys. Rev. Lett. 43, 267 (1979). E Esarey et al., IEEE Trans. Plasma Sci. 24**,** 252 (1996). T Tajima and P Chen, Nucl. Inst. Meth. A 410, 344 (1998).
2. A Modena et al., Nature 377, 606 (1995).
3. C E Clayton et al., Phys. Rev. Lett. 81, 100 (1998).
4. D Gordon et al., Phys. Rev. Lett. 80, 2133 (1998).
5. S Y Chen et al., Phys. Plasmas 6, 4739 (1999).
6. P Sprangle et al., Phys. Rev. Lett. 69, 2200 (1992). E Esarey, Phys. Fluids B 5, 2690 (1993).
7. A Pukhov et al, Phys. Plasmas 5, 1880 (1998).
8. A. Pukhov et al., Phys. Plasmas 6, 2847 (1999).
9. C Gahn et al. Phys. Rev. Lett. 83, 4772 (1999).
10. M Tabak et al., Phys. Plasmas 1, 1626 (1994).
11. M H Key et al., Phys. Plasmas 5, 1966 (1998).
12. M I K Santala et al., Phys. Rev. Lett. 84**,** 1459 (2000).
13. K W D Ledingham et al., Phys. Rev. Lett. 84, 899 (2000).
14. V Malka et al., Accepted to Rev. Sci. Inst. (2000).
15. EXFOR online-database at http://www-nds.iaea.org
16. A Ting et al., Phys. Rev. Lett. 77, 5377 (1996). S P Le Blanc et al. Phys. Rev. Lett. 77, 5381 (1996).

Preliminary studies of collisionless shocks in the laboratory

N C Woolsey, R A D Grundy, Y Abou-Ali, S J Pestehe

Department of Physics, University of York, Heslington, York, YO10 5DD, UK

P A Norreys, M M Notley, R Steele, S J Rose

Central Laser Facility, CLRC Rutherford Appleton Laboratory, Chilton, Didcot, Oxon, OX11 0QX, UK

P Carolan, N Conway, R O Dendy

Euratom/UKAEA Fusion, Culham, Abingdon, Oxfordshire OX14 3DB, UK

Main contact email address: *n.woolsey@rl.ac.uk*

Introduction

Initial experiments to study the formation of collisionless shocks in magnetised laser produced plasmas were carried out in Target Area East of Vulcan. This article outlines the experimental methods used and a brief summary of some of the results. Our principal objectives were to demonstrate the usefulness of the Vulcan laser system for collisionless shock studies, and the scaling of these shocks to astrophysical phenomena such as supernova remnants. This required the generation of large (tens of tesla) magnetic fields, and collisionless plasmas that could be immersed in this magnetic field. In addition it was essential the experiment be well diagnosed.

Experimental Details

The experimental discussion is divided into three topics. The first topic covers the formation and measurement of a magnetic field. The second and third topics describe collisionless colliding plasmas without and with a magnetic field respectively.

a) *Generating a Magnetic Field.* The magnetic field was generated using a novel mm-scale Helmholtz coil target. This target design offers the advantage of a uniform magnetic field in the region between the Helmholtz coils combined with good laser and diagnostic access. The target consists of a photo-etch 50 µm copper sheet. The copper sheet is bent to form a 2.5 mm diameter coil in the centre with two parallel copper plates as shown in Figure 1.

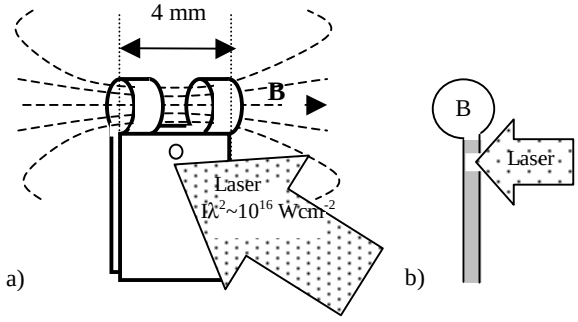

Figure 1. a) Schematic of the Helmholtz target showing the laser irradiating the target through a hole in the front plate and magnetic field B, b) side view of target.

A plastic insulating spacer, typically 500 µm thick separated the copper plates. By altering the spacer thickness, the plate spacing was adjusted between 250 µm and 750 µm. A 1 µm laser with 300 J in a 1 ns laser pulse was focussed to a 100 µm diameter spot on the inner face of the back plate. To allow laser access a hole was cut in the front plate and insulating spacer with diameters of 0.5 mm and 1.2 mm respectively. At peak $I\lambda^2$ of 10^{16} W-µm^2/cm^2 hot electrons, with approximate temperature of 15 keV, stream from the laser spot onto the front copper plate. The resulting potential difference between the back and front plates drives a large current in the Helmholtz coils inducing a strong magnetic field. Similar methods, using a single wire coil, were employed in the mid-1980s using a CO_2 laser, generating magnetic fields of 60 T[1)].

The magnetic fields were diagnosed using 1 mm diameter search coils. The search coils were covered to prevent charged particles entering the coil, cabling was screened from electrical and magnetic noise and connected to a digital 1 GHz oscilloscope. The L/R response time of the search coil is estimated to be 1 ns. Energy resolved X-ray spectroscopy using a single photon counting technique was used to estimate the electron temperature of the plasma. A cooled 16 bit silicon CCD detector with a 5 µm depletion layer was positioned 50 cm from Helmholtz coils. Al filters 500 µm thick ensured X-rays with energies above 8 keV were detected.

In a separate experiment a CH slab was inserted in the Helmholtz coil. Carbon plasmas are produced by illuminating the slab with 80 ps pulses (see below) while the magnetic field was present. This allowed independent measurement of the magnetic field through Zeeman splitting measurements of the C^{4+} 2^3P-2^3S transition at 227 nm. The diagnostic used a polariser constructed from 6 fused silica glass plates placed at the Brewster angle, fused silica imaging optics, and a 1 metre spectrometer with a 3600 lines/mm grating. Data was recorded onto a CCD camera.

b) *Collisionless Plasma Formation*. Collisionless plasmas were formed in the low density rapidly expanding plasma typical of exploding foil targets. The combination of low particle density ($<10^{18}$ cm^{-3}) and high particle velocities result in mean-free-paths exceeding typical scale lengths. We explored the use of such exploding foil plasmas in a counter-streaming configuration as shown in Figure 2. In the experiment, two CH foils 1000 Å thick, mounted on Mylar washers with a 1.2 mm diameter hole, were positioned 1 mm apart. The foils were simultaneously illuminated over a 1 mm diameter spot, by defocusing the laser *or* using phase zone plates (PZP), with 80 ps pulses from Vulcan at 10^{14} W/cm^2.

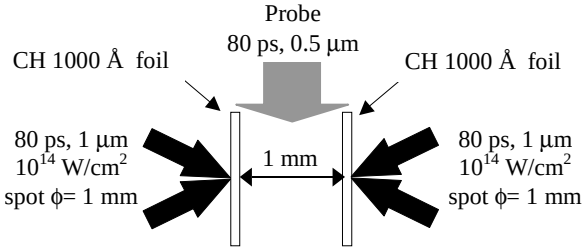

Figure 2. Colliding low density, rapidly expanding exploding plasma are used to form interacting collisonless system.

The main diagnostics for study of the collisionless plasma was an 80 ps duration frequency doubled (wavelength 0.53 µm) probe laser beam, and spatially resolved soft X-ray spectroscopy of the carbon K-shell. The probe beam was directed normal to the plasma flow between the two exploding foils. Simultaneous two dimensional electron density measurements and electron density gradients were obtained by splitting the probe laser to interferometic and Schlieren imaging diagnostics. The probe beam could be delayed using an

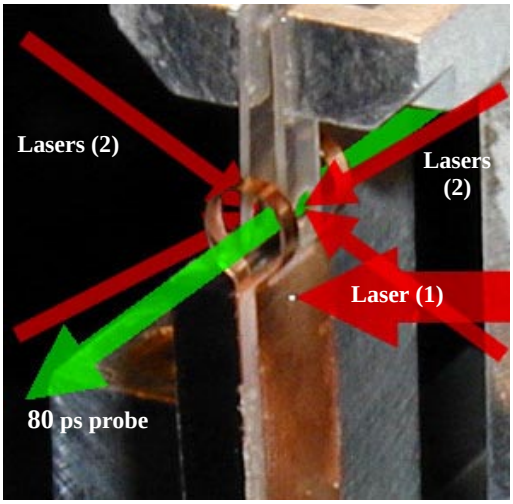

Figure 3. The integrated target showing two exploding foils positioned at the centre of the Helmholtz coil. Laser (1) is a 1 ns, 10^{16} W/cm^2 laser and generates the current in the coil. The 80 ps 10^{14} W/cm^2 lasers (2) explode the two foil targets.

independent timing slide allowing 80 ps snapshots of the plasma to be taken from 0 to 2 ns after the foil targets were irradiated.

The soft X-ray measurements used an imaging flat-field spectrometer with a 1200 lines/mm grating and Ni mirror coupled to a back-thinned 16-bit CCD detector filtered with 4 µm of Al. The spectrometer was configured to image the two exploding foils and the region between them in one dimension and carbon K-shell spectra (between 30 Å and 45 Å) in the second dimension.

c) *Collisionless Shock Experiment*. The magnetic field and the two foils were combined to attempt measurements of counter-streaming collisionless plasma in a magnetic field. A photograph of the target, showing the laser configuration is reproduced in Figure 3. As Figure 3 indicates the exploding foil targets were positioned inside the Helmholtz coil targets, with the centre point between the two foils placed in the centre of the Helmholtz target.

In this experiment the Helmholtz coil target was irradiated between 1 ns and 3 ns prior to the foils being exploded. The exploding plasmas were probed 200 to 600 ps later. The search coils, probe laser (interferometry and Schlieren), hard and soft X-ray spectroscopy were used to diagnose the experiment.

Preliminary Results

Large magnetic fields were recorded by the search coil and Zeeman splitting diagnostics. Magnetic fields of 40 T are estimated from the signal recorded on a search coil probe shown in Figure 4.

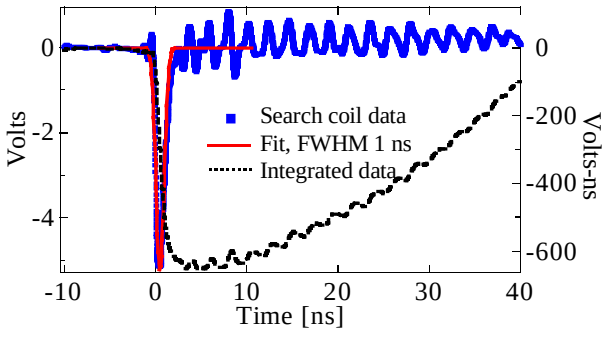

Figure 4. The search coil data (blue) and integrated signal (black). The response (red) of the search coil is consistent with calculations.

The full-width-half-maximum response of the search coil agrees with our estimates, and the integrated signal indicates that the magnetic field decays with a time constant of 30 ns.

This is in rough agreement with an estimated equivalent circuit L/R decay time of 20 ns. Spatially resolved, time-integrated Zeeman splitting of the C^{4+} 2^3P-2^3S transitions was observed. Preliminary analysis of these results indicate magnetic fields of 10 T 5 mm from the Helmholtz coil centre. These are in fair agreement with the search coil results.

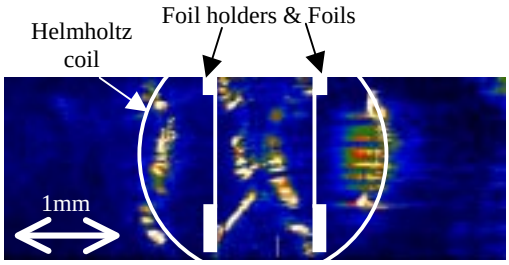

Figure 5. Schlieren image of two exploding foil with *no* magnetic field. The foils are mounted inside a Helmholtz coil, image taken 500 ps after peak of the laser. The positions of the foils and Helmholtz coil are indicated.

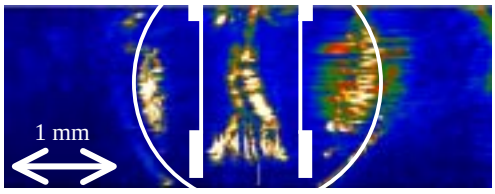

Figure 6. Schlieren image of two exploding foil in a magnetic field. The image is taken 500 ps after the peak of the laser. The positions of the foils and Helmholtz coil are indicated.

A false colour Schlieren image of the counter-streaming exploding foils is shown in Figure 5. The position of the Helmholtz coil target, the two foil holders, and initial position of the foils are shown. This image was taken 500 ps after the peak of the laser pulse with *no* magnetic field. The Schlieren diagnostic is sensitive to electron density gradients. In this image, the two edges of each of the exploding foils are seen to extend to the Helmholtz coil and collide in the centre of the figure. There are pronounced intensity modulations across the foils. This observation is surprising and results from non-uniform electron density across the exploding plasmas. Structure is observed at all times: data was taken with probe delays between 200 ps and 600 ps. In addition, similar structure is observed when the laser is defocused to a 1 mm diameter spot, as in Figure 5, or if PZPs are used.

In Figure 6 Schlieren data for the exploding foils immersed in a magnetic field is shown.

The data was taken 2 ns after the magnetic field was formed and 500 ps after the peak of the lasers driving the exploding foils. We observe consistent differences between the *no* magnetic field case (Figure 5) and magnetic field case (Figure 6). Analysis of the data is in progress.

Conclusion

During the Direct Access experiment, we successfully demonstrated three essential requirements for the laboratory simulations of collisionless shocks. These are:-

1) the generation of a large magnetic field using novel methods that can be synchronised to a laser experiment,
2) the creation of collisionless plasmas inferred from Schlieren data,
3) immersing of the colliding plasma in the magnetic field.

Our results have highlighted areas of considerable interest such as the uniformity of low-density expanding plasmas which we believe to be due to laser imprint[3], and magnetic field penetration into these plasmas. In a related article, we discuss the exciting possibility of scaling these experiments for the laboratory simulation of astrophysical phenomena such as a supernova remnant impacting the interstellar medium[2].

References

1. H Daido, *et al.* , Phys Rev Lett 56, 846(1986)
2. N C Woolsey *et al*, Central Laser Facility Annual Report 1999/2000, pg 59.
3. R Evans and N Woolsey, Central Laser Facility Annual Report 1999/2000, pg 77.

Thomson Scattering from an Aluminium Plasma

J Hawreliak, J S Wark, E Wolfrum

Department of Physics, Clarendon Laboratory, University of Oxford, Parks Road, Oxford, OX1 3PU, UK

S Glenzer

Lawrence Livermore National Laboratory, Livermore, CA 94550, USA

D Chambers

The University of Arizona, Tucson, AZ 85721, USA

R Marjoribanks

University of Toronto, 60 St. George St., Toronto, Ontario, Canada, M5S 1A7

S Topping

Queen's University Belfast, University Road, Belfast, BT7 1NN, UK

M Notley, R Steel

Central Laser Facility, CLRC Rutherford Appleton Laboratory, Chilton, Didcot, Oxon, OX11 0QX, UK

Main contact email address: *j.hawreliak@physics.ox.ac.uk*

Introduction

Thomson Scattering is a very powerful diagnostic, simultaneously giving time-dependent information on the density, temperature, heat flow and velocity of the plasma. With due care the Thomson optical probe beam has little effect on the plasma it is probing.

The experiments described here have the overall aim of determining the time-dependent hydrodynamics of an expanding aluminium plasma, and ultimately relating such data to high-resolution spectra of optically-thick X-ray line radiation that has been radiatively transferred through the plasma. Such detailed information will, we believe, act as a critical test of our understanding of the transfer process. In this particular article we report on our progress in determining the hydrodynamic parameters via Thomson scattering and comparing it with simulation. We first give a quick overview of the theory related to Thomson Scattering, before relating the results of a recent experiment performed on the Vulcan laser.

Outline of Basic Theory

The scattered radiation from the plasma can be determined by looking at the fields radiated by the free electrons under the acceleration of the electric field of the probing laser beam.

The electron will have an initial velocity which will be governed by the micro-fields of the plasma in the vicinity of the electron. This will add a first order effect to the phase of the radiated field.

The electron is assumed to be non-relativistic at all times so we can ignore the Lorentz force from the magnetic field of the radiation. Also the amplitude of the electron oscillation is assumed to be much smaller then the wavelength of emitted light so that the dipole approximation can be used.

The resulting scattering equations[4] are:-

$$I(\vec{k},\omega)d\omega d\Omega = NI_0\sigma(\vec{k},\omega)d\omega d\Omega$$
$$\sigma(\vec{k},\omega) = \sigma_T S(\vec{k},\omega) \qquad (1)$$
$$\sigma_T = \left(\frac{e^2}{mc^2}\right)^2 \sin^2\beta$$

$$S(k,\omega)d\omega =$$
$$\left|\frac{1-G_i(\frac{\omega}{k})}{1-G_e(\frac{\omega}{k})-G_i(\frac{\omega}{k})}\right|^2 F_e(\tfrac{\omega}{k})d\omega + Z\left|\frac{G_e(\frac{\omega}{k})}{1-G_e(\frac{\omega}{k})-G_i(\frac{\omega}{k})}\right|^2 F_i(\tfrac{\omega}{k})d\omega$$

$$G_e = -\alpha^2 W(x_e) \;,\; x_e = \frac{\omega}{kv_e} \;,\; G_i = -Z\frac{T_e}{T_i}\alpha^2 W(x_i) \;,\; x_i = \frac{\omega}{kv_i}$$

$$\alpha = \frac{1}{k\lambda_D}$$

$$W(x) = 1 - 2xe^{-x^2}\int_0^x e^{p^2}dp - i\pi x e^{-x^2}$$

Using Fourier analysis to break the electron motion into a series of waves allows the physical interpretation of a three wave interaction of having the laser wave, $\mathbf{k_0}$, scatter off the plasma waves , $\mathbf{k}$, into the direction of the collected radiation $\mathbf{k_S}$.

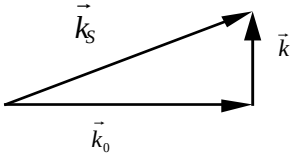

Figure 1. Vector diagram of the scattering of the waves in the plasma.

The scattering spectrum has two very distinct peaks close to the probe frequency. These are known as the ion feature because it is caused by scattering off the ion acoustic wave.

$$\omega^2 = k_{ia}{}^2\frac{\gamma_i T_i}{m_i} + Z^*\frac{k_{ia}{}^2\gamma_e\frac{T_e}{m_i}}{1+\gamma_e k_{ia}{}^2\lambda_e{}^2} \qquad (2)$$

From the spacing of these two peaks and the ion acoustic dispersion relation, equation (2) , it is possible to get a measurement of the electron and the ion temperature. The density is calculated using equation (1) by knowing the scattering volume and the total scattered radiation. The velocity along the scattering direction is determined by the Doppler shift of the scattered spectrum.

Experimental Setup

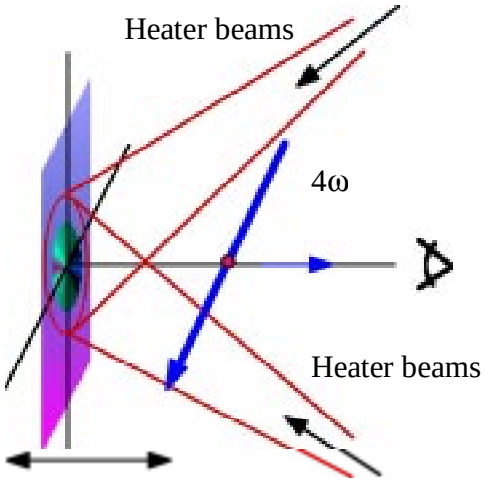

Figure 2. Target surface geometry of the Thomson scattering diagnostic.

The Thomson scattering was used to diagnose a laser-irradiated Al target. The Al target was irradiated with 1053 nm radiation in a pulse length of 1 nsec, with a typical irradiance of 5 x 10^{14} Wcm^{-2}. The geometry of the Thomson scattering beams at the front surface of the target is shown in Figure 2. The probe beam is frequency quadrupled to 263.3 nm, focused down to a 50 µm spot a variable distance in front of the centre of the Aluminium target in the plasma using an f/10 lens. The location of the probe beam can be moved along the axis of the target to probe different locations on subsequent shots. The collecting optic is an f/10 lens looking normal to the target to get the Doppler shifted spectrum along the direction of plasma expansion. The collecting optics image the probe location onto a 200 µm slit of a Spex spectrometer. The output of the spectrometer is directed into an Imacon 500 streak camera with a 100 µm slit in front.

Results

Figure 3 shows a typical streaked Thomson scattered image. Specifically this image was taken 300 µm in front of the target surface. By running a series of post experimental tests the image is calibrated as 6.06 ps/pixel in the vertical direction and 4.967 pm / pixel spectrally in the horizontal direction. The position of λ_0 at 263.3 nm is approximately at pixel 435.

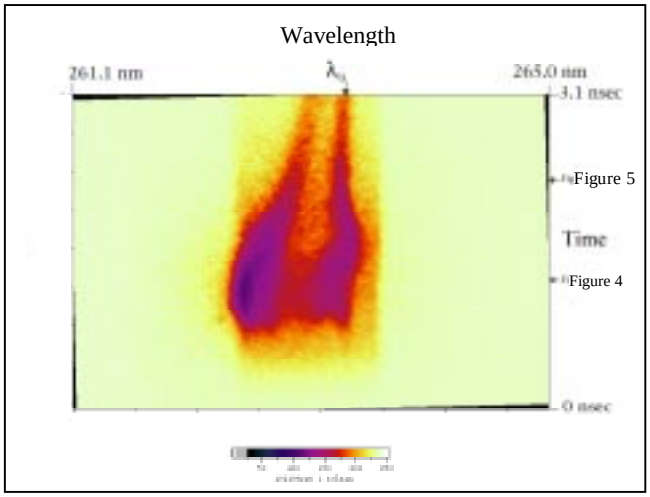

Figure 3. Streaked Thomson scattering image covering 3.1 nsecs of time and wavelengths 261.1 nm to 265.0 nm spectrally.

Owing to the storage scheme for TIFF images the time access is numbered decreasing from pixel 512, so time is increasing vertically on the image even though the numbers are decreasing. The number of counts is also calibrated so it is possible to get an estimate for the density.

Figures 4 and 5 are two line outs taken from the image and plasma parameters fitted to match the scattering spectrum. Figure 4 is from a plasma with T_e = 1.9 keV, T_i= 958 eV, n_e= 1.2 x 10^{26} m^{-3} and plasma velocity of 4.9e5 m/s. Figure 5 which is a lineout 1 ns later is T_e = 756 eV, T_i= 429 eV, n_e= 5.6 x 10^{26} m^{-3} and plasma velocity of 2.5e5 m/s.

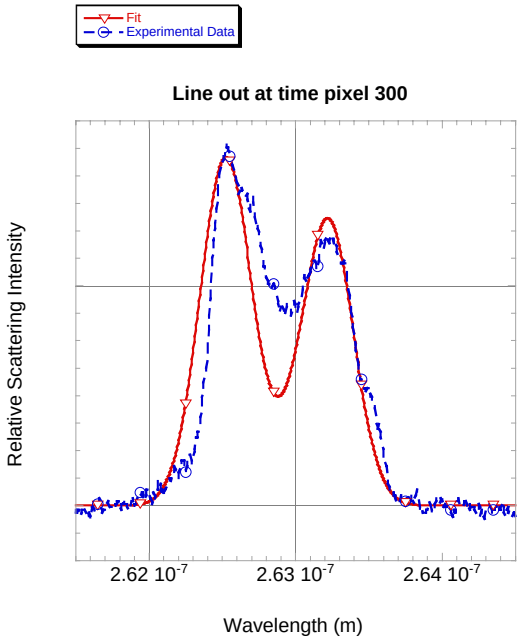

Figure 4. Line out from Thomson streak image.

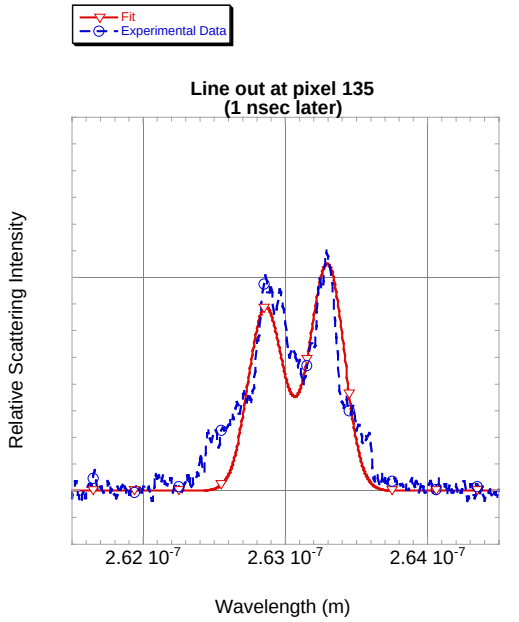

Figure 5. Line out from Thomson streak image 1 nsec after Figure 4.

Overall the Thomson scattered image shows us how temperature decreases by changes in the spacing of the ion acoustic peaks over time, the decreasing velocity by the way the Doppler shift of the spectrum decreases, and the density by how the overall intensity of the signal decreases. The interesting feature in the data is that the asymmetry changes sides over

time. This is caused by the change in the direction of the heat flow in the plasma [6].

Conclusion

Thomson scattering provides an excellent tool for looking at the hydrodynamic parameters in a very small region of the plasma. The processing and analysis of the data is now being automated such that a computer program will be able to read in images captured from the streak camera and output the hydrodynamic parameters of the plasma as a function of time.

References

1. Glenzer *et al*, Physics of Plasmas, 6, 2117 (1999)
2. Glenzer *et al*, Rev. Sci. Instrum. , 68, 668 (1997)
3. Wark *et al*, SPIE , 2015 , 270
4. Evans, Rep. Prog. Phys. 32, 207-271 (1969)
5. Renner *et al*, Rev. Sci. Instrum , 66 (1995)
6. Hawreliak *et al* (ibid).

Investigation into Inner Shell X-ray Laser Transitions

R Keenan, S J Topping, C L S Lewis
School of Mathematics and Physics, The Queen's University of Belfast, Belfast, BT7 1NN, UK

G J Pert, G J Tallents, F Strati
Department of Physics, University of York, York YO1 5DD, UK

A Klisnick, D Ros, J Kuba, R Smith
LSAI, Université Paris-Sud, Bât. 350, 91405 Orsay, France

P V Nickles, K A Janulewicz, F Bortolotto
Max Born Institute, Rudower Chaussee 6, D-12489 Berlin, Germany

A G MacPhee, R J Clarke, R Allott
Central Laser Facility, CLRC Rutherford Appleton Laboratory, Chilton, Didcot, Oxon, OX11 0QX, UK

Main contact email address: *r.keenan@qub.ac.uk*

Introduction

Previous attempts[1)] to observe the inner shell 2p→2s transition of the $1s^2 2s 2p_{1/2}^2 2p_{3/2}^4 3s$ J=0 to $1s^2 2s^2 2p_{1/2}^2 2p_{3/2}^3 3s$ J=1 line in Ne-like Ge, which is predicted to lase at 62 Å, had been unsuccessful. Simulations suggested that this was because the peak gain coefficient was low, <20 cm^{-1}, compared to >100 cm^{-1} for the 'normal' 3p→3s transition when pumped in the transient mode[2)]. In this experiment, we created a longer line focus so targets up to 18 mm could be used, increasing the potential gain-length product, and thereby increasing the chance of producing an observable signal. It was thought going to lower Z ions might also improve the possibility of seeing a measurable signal as they would be easier to pump and gain would probably be improved. Modelling, which to date has been limited mainly to Z=32, gave us the optimum pumping conditions for the Ge inner shell transition to be[3)]:

Long pulse, 300 ps duration, intensity ~ 10^{13} W/cm^2, without a pre-pulse.

CPA pulse of ~1 ps duration, intensity 2 x 10^{15} W/cm^2, incident 100 - 200 ps after the peak of long pulse.

These gave a peak in small signal gain of about 20 cm^{-1}. Ray-tracing this peak SSG for targets up to 15 mm long gives a ray averaged gain on the 62 Å line of ~10 cm^{-1} and an output of ~ 0.5 µJ.

Experiment and Results

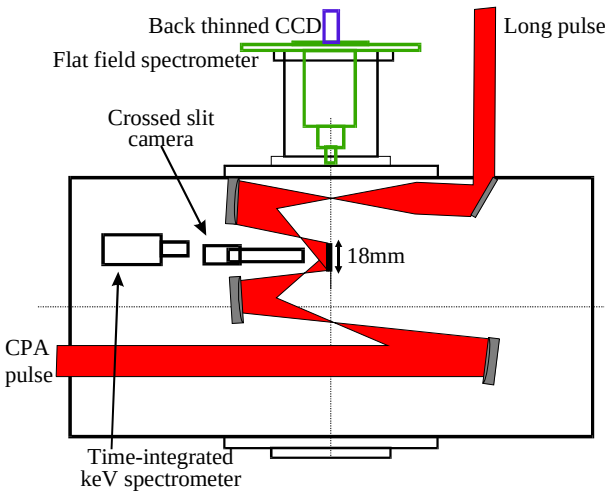

Figure 1. Experimental setup and diagnostics.

The primary diagnostic was a flat-field spectrometer, coupled to a CCD with 13 µm pixels, set up to detect from 20 - 150 Å. The travelling wave velocity on the CPA beam was measured to be c and the pulse duration of 1.7 ps was measured using an autocorrelator. Both long pulse and CPA beams were focussed to a 100 µm wide and ~18 mm long common line focus. Intensities of 2 x 10^{15} W/cm^2 were achieved on the CPA pulse and the long pulse at ~ 10^{13} W/cm^2 could be moved to change the peak-peak delay between the beams. Slab targets 18 mm long were used for Ti, Fe and Ni. For Ge 18 mm long x 100 µm wide stripes coated on glass were irradiated. The wavelengths of the inner shell transitions for the various elements are shown below in Figure 2 with Ne-like Yt (Z=39), lasing at 42 Å, showing how well these transitions scale towards the water window.

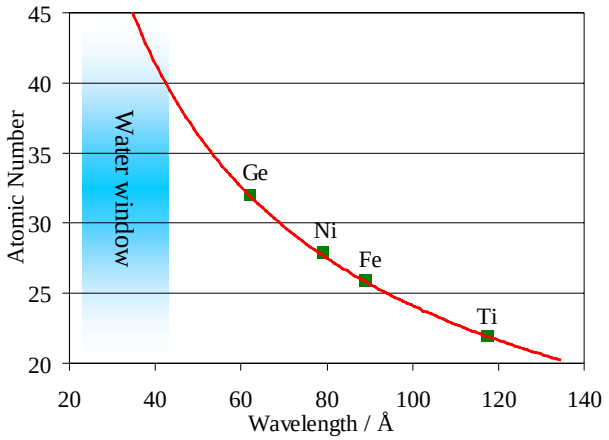

Figure 2. Wavelengths of the 2p→2s inner shell transitions.

The filter used on the flat-field spectrometer was Mo sandwiched between CH. A gold reflection filter was used for the Ni, Fe and Ti shots, cutting off wavelengths below 70 Å (and hence 2nd order signal for detector positions below 140 Å) where its transmission falls to < 0.1.

Two shots were taken on Ti. No lasing signal was detected, although our filtering was least optimised for this case. Shots on Fe targets were taken at different delays and one at lower energy as shown in Table 1. None of these shots showed a lasing line.

Shot No.	Long pulse Intensity / W/cm^2	CPA pulse Intensity / W/cm^2	Peak-peak delay / ps
#032801	7 x 10^{12}	2.0 x 10^{15}	200
#032803	7 x 10^{12}	1.8 x 10^{15}	250
#032805	8 x 10^{12}	1.9 x 10^{15}	300
#032806	8 x 10^{12}	2.1 x 10^{15}	150
#032807	5 x 10^{12}	1.5 x 10^{15}	250

Table 1. Shots taken on Fe.

Shots were taken on Ni, which was closer to the Ge for which simulations had been done, changing delay and intensity as shown in Table 2. Some lines were present but they did not change with intensity or large variation in delay and their angular distribution was not that of an x-ray laser line. Shots were taken on different length targets but no lines exhibited gain.

Shot No.	Long pulse intensity/ W/cm^2	CPA pulse intensity/ W/cm^2	delay / ps	target length/mm
#032810	6 x 10^{12}	1.6 x 10^{15}	250	18
#032812	4 x 10^{12}	1.6 x 10^{15}	250	18
#032814	3 x 10^{12}	0.9 x 10^{15}	250	18
#032815	6 x 10^{12}	1.7 x 10^{15}	250	8
#032817	7 x 10^{12}	1.9 x 10^{15}	250	13
#032901	6 x 10^{12}	1.3 x 10^{15}	-50	18
#032903	7 x 10^{12}	1.7 x 10^{15}	450	18

Table 2. Shots taken on Ni.

Table 3 shows the shots that were taken on Ge stripes, all with long pulse intensities of (1 ± 0.1) x 10^{13} W/cm^2. These failed to show any lasing action at 62 Å. As for the Ni, there was little change for the various shots. The time-integrated spectrum from the flat-field spectrometer is shown in Figure 3 with multiple orders of the plasma emission.

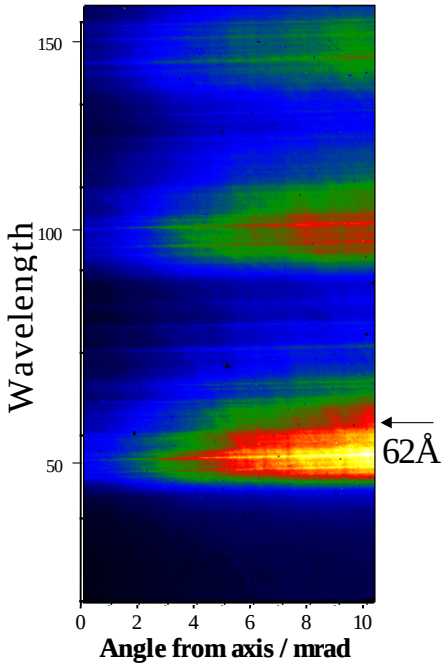

Figure 3. Flat-field spectrometer Ge spectrum.

Shot No.	CPA pulse intensity / W/cm^2	Delay / ps
#032908	1.8 x 10^{15}	250
#032909	1.7 x 10^{15}	250
#032911	1.9 x 10^{15}	250
#032913	1.9 x 10^{15}	150
#033003	2.0 x 10^{15}	50
#033005	2.0 x10^{15}	350
#033006	1.6 x10^{15}	-150
#033008	2.1 x10^{15}	450

Table 3. Shots taken on Ge.

The space-resolving time-integrated crystal spectrometer, which operated for the Ge shots, showed there was reasonably good uniformity along the target, as seen from the lineout across the Ne-like 3d→2p in Figure 4. It also showed the correct ionisation stage had been achieved, with Ne-like lines dominating the spectrum (see Figure 5).

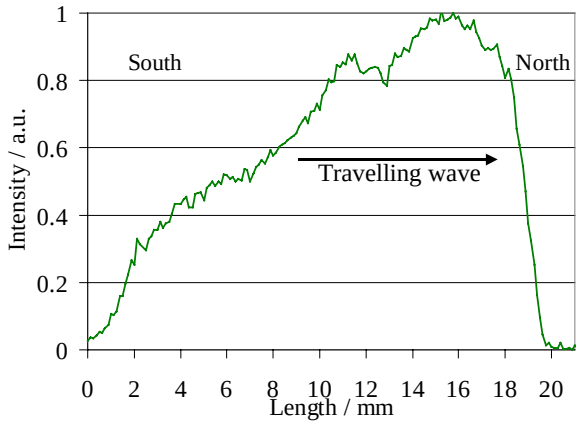

Figure 4. Uniformity along line focus.

Figure 5. Ne-like Ge keV spectrum.

Conclusions

No inner shell lasing line was observed for any of the shots on any target. A large parameter space of delay and intensity was not covered for Ge and more shots are needed. In particular we need to try shots concentrated around 100 - 200 ps delay, only one of which was taken. The large number of shots taken with long delay was due to a systematic error in relative beam timing, discovered only after this set of shots was completed. Also, simulations show that the output power on the inner shell line continues to increase as CPA intensity is raised to 5 x 10^{15} W/cm^2 [4]. The lower Z elements have not been modelled and so the shots taken may not be close to optimum. Improving the spectral resolution of the flat-field spectrometer will improve the signal to noise and increase our chances of detecting a weak signal.

References

1. C L S Lewis et al.
X-ray lasers 1990, Inst. Phys. Conf. Ser. 116, 231, (1990)

2. S B Healy, K A Janulewicz and G J Pert.
Opt Commun. 144, 24, (1997)

3. F Strati.
Private communication (2000).

4. P A Simms, S McCabe, G J Pert.
Opt Commun. 153, 164, (1998)

Temporal resolution of a transient pumping x-ray laser

J Kuba, A Klisnick, D Ros, R Smith, R Schott, G Jamelot

LSAI, Université Paris-Sud, Bât. 350, 91405 Orsay Cedex, France

C Chenais-Popovics

LULI, Ecole Polytechnique, 91123 Palaiseau, France

P Nickles, K A Janulewicz, F Bortolotto

Max Born Institut, Max-Born-Str. 2 A, D-12489 Berlin, Germany

R Keenan, S J Topping, C L S Lewis

Department of Pure & Applied Physics, The Queen's University of Belfast, Belfast BT7 1NN, UK

F Strati, G J Tallents

Department of Physics, York University, Heslington, YO10 5DD, UK

D Neely, R Clarke, J Collier, A G MacPhee

Central Laser Facility, CLRC Rutherford Appleton Laboratory, Chilton, Didcot, Oxon, OX11 0QX, UK

Main contact email address: *Annie.Klisnick@lsai.u-psud.fr*

A preliminary time-resolved study of the output from the Ni-like Ag transient collisional excitation X-ray laser is described. A fast XUV streak camera with a resolution as high as 1.9 ps was used to diagnose the output of the J = 0→1 4d-4p lasing line 139.9 Å. The FWHM duration of the x-ray pulse is measured to be less than 2 ps at optimum conditions of pump laser irradiation, which is about four times shorter than was estimated in previous experiments[1)]. The x-ray laser duration rose significantly when the short (heating) pulse duration was increased, when doubling the peak-to-peak delay of the two irradiation pulses and did not change when the short pulse energy was increased**.**

Introduction

Saturated x-ray laser output in the transient collisional excitation scheme has been observed for a number of atomic materials (Z = 22 - 62) in the wavelength range 326 – 73 Å [1-3)].

In this scheme a long (~300 - 600 ps) pre-pulse generates a plasma with a large population of the desired ion species. The preplasma is allowed to expand and is then strongly heated by a short ~ps pulse. A large transient population inversion is obtained via collisional excitation from free electrons on a time scale before ionisation can occur. Therefore high gains are expected in the period before collisional redistribution of the excited state populations can occur[3)]. The results presented in this paper are the first direct measurements of the temporal profile of the x-ray laser output at a high resolution and give an insight into the mechanisms involved within this scheme.

Experimental Arrangement

Two beamlines from the Nd-Glass Vulcan laser at 1.06 µm were used to irradiate a 10 mm long flat silver slab target in a standard line focus geomery[2)]. A 300 ps prepulse typically delivered 10 J on target into a 21 x 0.12 mm line focus with intensities of ~2 x 10^{12} W/cm^2. This pulse generates a plasma which, after a controlled delay, was strongly heated to optimum lasing conditions by a 1.3 ps CPA pulse in a 19 x 0.08 mm line focus. The CPA pulse was capable of delivering up to 75 J on target yielding maximal intensities of 4 x 10^{15} W/cm^2. The peak-to-peak separation of the two pulses was controlled by varying the optical path length of the long pulse via a timing slide within the target area. For some shots we increased the FWHM of the CPA pulse by varying the grating separation within the stretcher. The extent to which the pulse width was increased and any shot-to-shot variations were monitored off-axis by an autocorrelator[4)].

The motivation for using a larger line focus width for the long pulse was to produce a more uniform plasma in the lateral direction which was expected to reduce the effects of refraction in that direction. The line foci were superimposed to an accuracy within 10% of the focus line width. A CCD x-ray cross-slit camera monitored the line focus plasma uniformity and overlap of the laser pulses. The focal lines were longer than the target length to avoid creation of cold plasma at the target ends. Due to the previously inferred[1)] short gain durations (less than 10 ps) relative to the transit time of the x-ray photons with the gain medium (< 30 ps) it was necessary to implement travelling wave pumping[2)].

A combination of three effects was used to implement an optimum travelling wave (TW) velocity at the speed of light (c) in the direction towards the primary x-ray laser diagnostic:

(i) intrinsic travelling wave introduced by the off-axis focusing geometry,

(ii) an additional 600 lines/mm grating was inserted into the CPA beamline to introduce an extra shear in the energy front of the beam,

(iii) for fine tuning, the technique of slightly tilting the second compressor grating was employed[5)].

Results

In the first part of the experiment we varied several parameters in order to find the conditions that optimised the energy within 139.9 Å lasing line. An on-axis flat field spectrometer (FFS) was used to diagnose the output of the x-ray laser both spectrally and angularly (in the direction normal to the target surface).

It was observed that the x-ray laser emission peaked at ~5 mrad off axis for a range of pumping conditions. Through integration of the signal recorded on the CCD we estimate the optimum pumping conditions to be 4.3 J/cm (1.2 x 10^{12} W/cm^2) in the 300 ps pre-forming pulse and 11.8 J/cm (1.1 x 10^{15} W/cm^2) in the CPA pulse with the temporal peak-to-peak delay of 200 ps between both pulses.

For the time-resolved shots an AXIS-Photonique XUV streak camera[6)] equipped with a KBr photocathode was positioned at the focal plane of the flat field spectrometer to give temporal resolution of the x-ray laser emission. In our set-up the 1 x 15mm photocathode was placed parallel to the direction of spectral dispersion and at an angular position off axis

corresponding to the peak of the x-ray laser output. The streak camera thus gave wavelength resolution at an integrated horizontal angle of 1.1 mrad around the angular peak of the XRL emission. The output from the streak camera was amplified and recorded by the combination of a 50/40 Kentech intensifier butt-coupled to an optical CCD camera. This configuration was estimated to give a temporal resolution of 1.92 ± 0.16 ps.

An optical trigger system including an air compressor and a Ge switch was specifically designed for this experiment to allow a stable triggering of the high voltage Streak ramp, with a jitter better than 10 ps. Paralene-E ($C_{18}H_{20}$) filters were used to attenuate the x-ray laser emission sufficiently to ensure our detection system was not saturated.

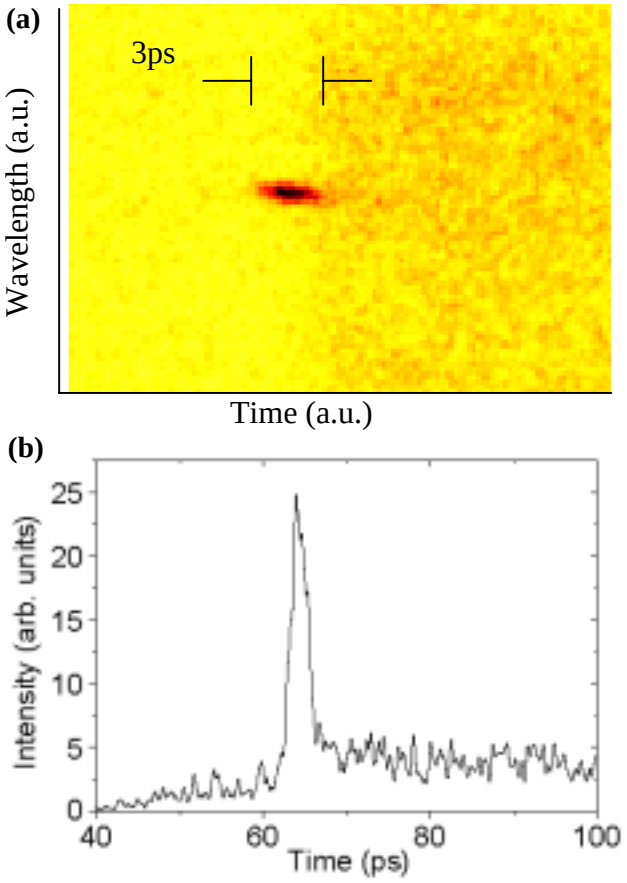

Figure 1. Time resolved spectrum of the Ni-like transient pumping silver x-ray laser at the optimal travelling wave irradiation conditions. The FWHM x-ray laser duration at 139.9 Å was measured to be 1.8 ± 1.0 ps. (a) The CCD image, (b) Intensity versus time plot at the lasing wavelength. The irradiation conditions are: 4.3 J/cm (1.2 x 10^{12} W/cm^2) in the 300 ps pre-forming pulse and 11.8 J/cm (1.1 x 10^{15} W/cm^2) in the 1.3 ps CPA pulse with the temporal peak-to-peak delay of 200 ps between both pump laser pulses.

Figure 1(a) shows the time resolved spectral output from the Ni-like Ag emitted at the optimal irradiation conditions in the travelling wave geometry, as recorded at the output of the streak camera. The cut-off of the x-ray laser output is observed to coincide with the increased continuum emission by free electrons. After the peak of the x-ray laser pulse increased collisional effects are expected to cause over-ionisation and simultaneously quench the population inversion[3]. Figure 1(b) shows the wavelength integrated output of the x-ray laser as a function of time after the continuum emission has been subtracted. The FWHM duration of the x-ray laser was measured to be 1.8 ± 1.0 ps. This value, as well as the other temporal measurements presented, was obtained after de-convolution from the instrumental resolution, using the formula $\tau' = (\tau^2 - T_R^2)^{1/2}$, where T_R is the temporal resolution of the system, τ stands for the measured duration of the signal, and τ' is the actual duration.

To use this temporal measurement to make an estimate of the gain duration experienced by the x-ray photons within the amplifying medium, it is necessary to consider the propagation of the x-ray beam. Using a simple small-signal exponential model with an assumed Gaussian temporal gain profile, we can find that the FWHM of the gain duration corresponds to the product of the x-ray laser duration and a constant, K, which depends on g_0L only. Here g_0 represents the small signal gain and L is the length of the gain medium. In the first approximation we obtain $K \approx (g_0L)^{1/2}$. By taking experimental values[1] of g_0 = 30 cm^{-1} and L = 4 mm (K ˜ 3.5) and for the x-ray laser pulse width of 2 ps, a gain duration of ~ 6-7 ps is expected.

The variation of the x-ray laser duration with main irradiation parameters was investigated. For each case we varied just one parameter from the optimal irradiation conditions (see above). First we lengthened the short pulse duration from 1.3 ps to 2 ps, with a corresponding increase in laser pulse energy to maintain a constant irradiation intensity. The measured x-ray laser duration increased by a factor of three over the optimal case to 5.5 ± 1.5 ps. Secondly we changed the peak-to-peak separation between the two pulses to 400 ps from 200 ps. Once again the duration of the x-ray laser pulse was seen to increase significantly to 5.8 ± 1.5 ps.

Finally the short pulse energy was increased to 20.5 J/cm (2 x 10^{15} W/cm^2) over the optimum pumping conditions of 11.8 J/cm. In this case the x-ray laser duration was measured to be 2.2 ± 1.2 ps which is similar to the optimum duration of 1.8 ± 1.2 ps. The relative temporal delay of the continuum emission and the XRL peak remains the same as in the optimal pump irradiation case. Taking into account the resolution of the streak camera, we interpret these results as the independence of the XRL duration on the heating pulse energy in the energy interval of our measurements.

In conclusion, we measured the FWHM duration of the Ni-like transient pumping Ag x-ray laser at 139.9 Å to be 1.8 ± 1.2 ps at optimal travelling wave irradiation conditions. The duration of the x-ray laser pulse was observed to depend strongly on the peak-to-peak separation of the two pumping pulses and on the duration of the main heating pulse. In contrast, initial results seem to indicate that, within a given energy interval, the output pulse duration is largely insensitive to energy fluctuations within the main heating pulse.

References

1. A. Klisnick et al., in Proceedings of the SPIE Conference on Soft X-Ray Lasers and Application III, SPIE 3776, 282 (1999); J. Kuba et al., Phys. Rev. A, to be published
2. G J Tallents, App. of High Field and Short Wavelength Sources VIII OSA Tech. Digest Series 7, 47 (1997); M.P. Kalachnikov et al., Phys. Rev. A, 57 (6), 4778 (1998); Lewis CLS, SPIE 3776 (1999).
3. J. Nilsen et al., J. Opt. Soc. Am B.17, No. 6 (2000)
4. J. Collier, C. Danson, C. Johnson, and C. Mistry, Rev. of Scientific Instruments 70, 1599 (1999).
5. J.-C. Chanteloup et al., J. Opt. Soc. Am. B 17, 151 (2000); A. Klisnick et al., J. Opt. Soc. Am. B 17, 1093 (2000)
6. Cote et al, Proc. SPIE 2869, p. 956-961, 22nd International Congress on High-Speed Photography and Photonics, Dennis L. Paisley Ed.

Optimization of the Ne-like Ge X-Ray laser at 19.6 nm with CPA irradiation

F Strati, G J Tallents, G J Pert

Department of Physics, The University of York, Heslington, YO10 5DD York, UK.

C L S Lewis, R Keenan, S Topping

School of Mathematics and Physics, Queen's University of Belfast, Belfast, UK.

A Klisnick, D Ros, J Kuba, R Smith

LSAI, Université Paris Sud, Orsay, France.

A G MacPhee, D Neely, R Allott, R Clarke

Central Laser Facility, CLRC Rutherford Appleton Laboratory, Chilton, Didcot, Oxon, OX11 0QX, UK

F Bortolotto, P Nickles, K Janulewicz

Max Born Institute, Berlin, Germany.

Main contact email address: *fs112@york.ac.uk*

Introduction

The "transient" collisional excitation (TCE) scheme[1)] is today a well-established technique for the generation of saturated ASE output of soft x-ray lasers in Ne-like and Ni-like ions. The first transient excitation demonstration was achieved at the Max Born Institute in Berlin[2)] with neon-like ions. The technique has subsequently been successfully developed and extended in a number of experimental investigations at the Rutherford Appleton Laboratory[3,4)] (RAL), at LLNL[5)] and at LULI[6)]. In relatively recent experiments at RAL, saturation has been achieved on the 196 Å Ge neon-like lasing line while appreciable energy output has been observed on both the 139 Å Ag and 73 Å Sm nickel-like transitions using traveling wave irradiation[7)] for the short (CPA) optical pulse. In this paper, we report on experimental and theoretical investigations of the optimum optical pumping pulse configuration for the generation of the 196 Å Ge neon-like soft x-ray laser in the transient collisional scheme.

Experimental Setup and Results

Two sets of experimental results have been obtained under slightly different experimental conditions. In the first experiment (hereafter labeled "Ral Oct 1998"), a plane solid Ge target strip of fixed length of 5 mm was irradiated in a line focus geometry setup of 10 mm length and 100 μm width by a multiple pulse arrangement where two long pulses (280 ps FWHM), of average intensities of 10^{12} W/cm^2 (prepulse) and 10^{13} W/cm^2 (background pulse), separated by a constant 2 ns delay, preceded a 3 ps CPA pulse of ~10^{15} W/cm^2 from the Vulcan Nd:glass amplifier laser chain (all pulses with a wavelength of 1.06 μm). During this first experiment the CPA pulse timing was varied so that the short CPA pulse was incident on target with a delay of 0, +75, +175, +275 ps after the peak of the background pulse. During the second experiment (hereafter labeled "Ral Mar 2000"), a Ge target strip of 5 mm length was irradiated in a line focus geometry setup of 18 mm length and 100 μm width by a similar multiple pulse arrangement where the two long pulses (280 ps FWHM) had average intensities of 10^{12} W/cm^2 (prepulse) and 10^{13} W/cm^2 (background pulse). These two pulses were again separated by a constant 2 ns delay and were used in combination with a 1.7 ps CPA pulse of ~10^{15} W/cm^2 average intensity. The CPA pulse timing was varied so that the pulse was incident on target with a relative delay of -100, -50, 0, +50 and +350 ps with respect to the peak of the background pulse. In both experiments the CPA pumping pulse was incident on target with its pulse front tilted at ~45° with respect to the propagation direction so that the excitation and local gain along the plasma column could match the speed of the traveling x-ray photons.

The experimental results from both experiments are shown in Figure 1 along with theoretical modeling which we will discuss later. The data show a good degree of consistency across the two experimental runs and indicate that the optimum pumping pulses configuration is achieved when the CPA heating pulse is incident on target with a delay ranging from 0 to 75 ps after the peak of the second (background) long pulse.

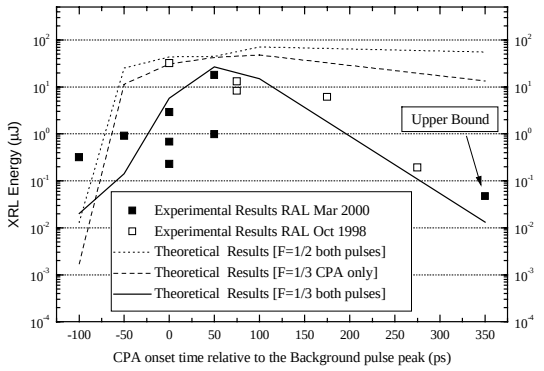

Figure 1. Experimental and theoretical integrated energy outputs of the Ge Ne-like XRL at 19.6 nm from a fixed target length of 5 mm as a function of the relative delay between the CPA pulse and the background long pulse peak time (for the definition of the F parameter see the main text).

Theoretical modeling

We analyzed the experimental results by using the 1.5D EHYBRID hydrodynamic Lagrangian code[8)] to model the interaction of the driving optical laser pulses with the plasma and the 3D geometric RAYTRACE code[9)] to simulate the propagation (including saturation effects) and refraction of the X-ray laser beam through the plasma. Absolute values of the X-ray laser output are obtained in the simulation.

The results of the simulation runs are plotted in Figure 1 together with the experimental results. In order to get agreement with the experimental data an absorption fraction parameter $F \le 1$ is usually introduced to account for the various energy loss mechanisms that are not modeled in EHYBRID (such as Brillouin and Raman backscattering) and the experimental intensities are inputted to the code after scaling with this parameter. In Figure 1 the simulation results for different values of F are shown. The dotted line represents the results for a value of $F = 1/2$ for both long and short (CPA) pulses, the dashed line the results with $F = 1/3$ for the CPA pulse and $F = 1/2$ for both the long pulses and, finally, the solid line the results obtained with $F = 1/3$ for both short (CPA) and long pulses.

The best agreement between experimental results and theoretical predictions is obtained when a value of $F = 1/3$ for

the absorption fraction parameter for both long and short (CPA) pulses is used (solid line in Figure 1). We note that the "accepted" value of the F parameter that has been used in the past to model experiments in the quasi steady-state (QSS) collisional excitation scheme is $F=1/2$. The discrepancy in the F values found in QSS and TCE schemes reflects probably the increasing importance of high intensity laser-plasma interaction phenomena due to the high CPA irradiances (10^{15} W/cm^2) normally used at the fundamental wavelength of 1.06 μm. However, on this basis it is difficult to understand why a smaller F value has to be used to model also the long pulses absorption: further discussion of this issue clearly necessitates a detailed model of the various absorption energy losses to be introduced in the calculations and cannot be pursued here.

In Figure 2 the small signal gain time and spatial evolution for the optimum pumping pulse configuration given by a delay of +50 ps between the background peak and the CPA pulse, as predicted by EHYBRID, is shown.

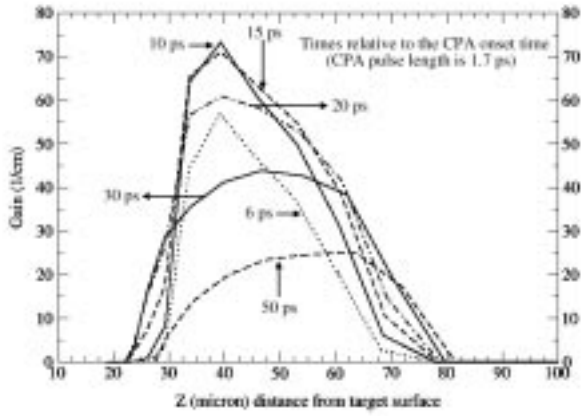

Figure 2. Small signal gain time and spatial evolution as predicted by EHYBRID in the case where the CPA is incident 50 ps after the peak of the background pulse, i.e. close to the optimum pumping pulse configuration.

The small signal gain quickly reaches a maximum value of about 70/cm at 10 ps after the onset of the CPA pulse and maintains this condition for about 5 ps. Later, the gain slowly decreases with an exponential tail with characteristic 1/e time of about 30 ps. The highest gain region is situated in the higher density portion of the plasma column, but as time increases, an almost spatially constant gain occurs extending for about 40 μm in the target normal direction.

Figures 3 and 4 illustrate, respectively, the plasma conditions at the time of the onset of the CPA and at that of the maximum gain (10 ps after) in the optimum condition when the CPA is incident 50 ps after the peak of the background pulse. It is seen that at the onset of the CPA (as determined by the long pulses irradiation alone, Figure 3) the plasma has an average ionization close to the Ne-like stage and long density scale-lengths but a small population inversion on the lasing transition. As the CPA irradiates the plasma (Figure 4) its main effect is to quickly raise the electronic temperature and to drive efficiently the population inversion on the lasing transition.

Conclusions

The optimum pumping conditions for the Ge Ne-like X-Ray laser at 19.6 nm in the TCE scheme have been investigated experimentally. Good agreement between theoretical results and the relative experimental trend has been found although the reproduction of the absolute experimental values necessitates the introduction of a free absorption parameter whose significance is not completely clear.

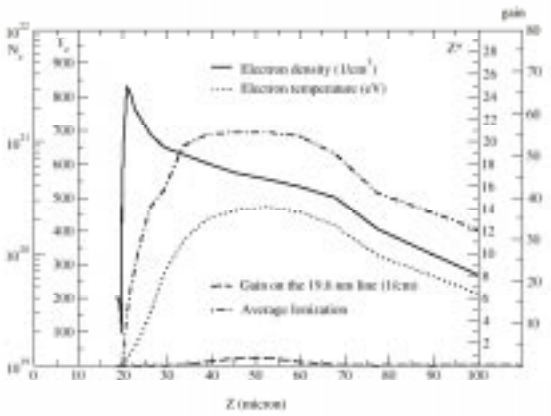

Figure 3. Plasma conditions as predicted by EHYBRID at the onset of CPA when the CPA is incident 50 ps after the peak of the background pulse (optimum pumping pulse configuration).

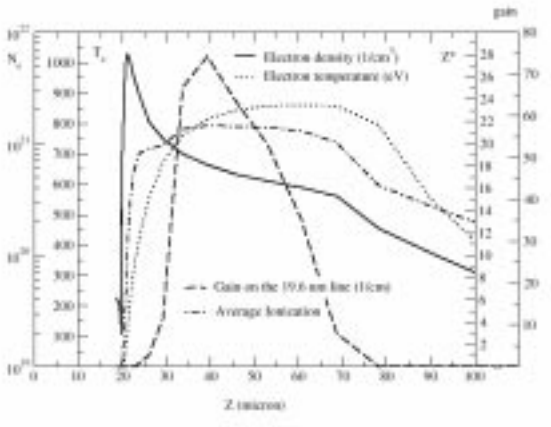

Figure 4. Plasma conditions as predicted by EHYBRID at the time of maximum gain when the CPA is incident 50 ps after the peak of the background pulse (optimum pumping pulse configuration).

References

1. Yu V Afanasyev and V N Shlyaptsev, Sov. J. Quantum Electron., 19 1606, (1989)
2. P V Nickles *et al.*, Phys. Rev. Lett., 78 2748, (1997)
3. M P Kalachnikov *et al.*, Phys. Rev. A, 57 4778, (1998)
4. P J Warwick *et al.*, J. Opt. Soc. Am. B, 15 1808, (1998)
5. J Dunn *et al.*, Phys. Rev. Lett., 80 2825, (1998)
6. A Klisnick *et al.*, in *X-Ray Lasers 1998*, edited Y. Kato and H. Daido, IOPP Conf. Series, 159 107, (1999)
7. C N Danson *et al.*, in *Superstrong Fields in Plasmas*, edited M. Lontano, G. Mourou, F. Pegoraro, E. Sindoni, AIP Conf. Proc., 426 473, (1998)
8. G J Pert, J. Fluid Mech., 131 401, (1983)
9. J A Plowes *et al.*, Opt. Quant. Elect., 28 219, (1996)

Resonance line emission in X-ray laser experiments

S J Pestehe, G J Tallents, G J Pert

Department of Physics, University of York, Heslington, York, YO10 5DD, UK

Main contact email address: *sjp24@york.ac.uk*

Introduction

Resonance line emission from different ion stages has been used to monitor the plasma electron temperature and irradiance uniformity along the plasma length in x-ray laser experiments[1,2]. The resonance lines are usually measured using a crystal spectrometer with a slit to provide spatial resolution along the plasma line. The spectra are recorded using a CCD detector. Simulating crystal spectra requires taking into account the effect of plasma opacity on the radiation escaping the plasma as well as the variation of the emissivity during the plasma lifetime. Doppler shifts of the emission and absorption line profiles complicate the simulations. In this paper, we report simulations of 124 Ne-like and 399 F-like Ge resonance line intensities with different driving laser pulse configurations. We obtain agreement between the simulated and experimental germanium spectra measured during x-ray laser experiments at RAL.

Experimental Set-up

In recent years, two-pulse configurations have been used to produce x-ray lasing at RAL (Figure 1). In the long pulse configuration, three beams of the Vulcan laser with 75 ps duration, in a double pulse irradiation mode, were focused in a 90 μm wide by 18 mm long line. The peak intensity on this line focus was ~5 × 10^{13} W/cm^2. The first pulse intensity was fixed at 10 % of the second pulse with a delay between the pre-pulse and main pulse of 2 ns.

In the short pulse configuration, one beam with 280 ps duration in a double pulse mode and a 2.7 ps CPA beam are focused on a 100 μm by 9 mm target. The delay between the prepulse and main pulse was 2 ns, while the delay between the CPA and peak of the main pulse was 75 ps. The peak intensity in the line focus was ~ 1 × 10^{15} W/cm^2 during CPA irradiation and was ~ 5 × 10^{12} W/cm^2 from the main pulse. The prepulse intensity was 10% of the main pulse intensity.

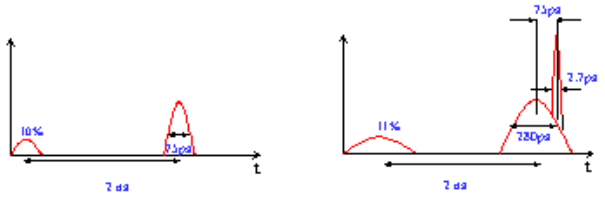

Figure 1. A diagram showing the driving laser pulses configuration for long pulse (a) and short pulse (b) experiments.

Modeling

A post processor to the EHYBRID[3] atomic and fluid code has been used to calculate resonance line intensities. For comparison to measured spectra, the spectral line intensities are integrated spatially with distance from the target surface and in time. The emissivities are calculated from the code values of the quantum level numbers densities using oscillator strengths utilised by the code.

The importance of opacity in observed line emissions has long been recognized in a variety of astrophysical sources and laboratory based plasmas. There are two approaches to deal with opacity: (1) use a comprehensive radiative transfer calculation method (Avertt & Hummer[4] (1965) and Mihalas[5] (1978)), or (2) model the transfer problem in terms of escape probabilities (Hummer & Rybicki[6] (1982), Rybicki[7] (1984), Doyle & McWhirter[8] (1980), Kaastra & Mewe[9] (1995), and Irons[10] (1978)).

To enable fast calculations, we have adopted the escape factor technique to model the opacity effect of photo-excitation in population densities. However, we have endeavored to ensure that the model applies to the condition of our plasma. A new escape factor model has been developed. We assume planar geometry, spatially constant Doppler broadened line profiles, exponentially decreasing emissivity and absorption coefficient with distance with a step rising at a particular point and a linear with distance bulk plasma velocity profile (see Figure 2).

Escape factors have two uses in modeling the radiative transfer of the spectral lines[10,11]. They are correction factors, so called 'net radiative brackets', to the radiative transition probabilities to allow for the radiation trapping photo-excitation on quantum state densities. They can also be used as factors, so called escape probabilities, which multiply the emission expected from an optically thin plasma to allow for the effect of opacity on the emitted lines.

An EHYBRID default net radiative bracket has been used for the present calculations. An optical depth τ is calculated transversely across the plasma width and the net radiative bracket evaluated assuming a stationary plasma. The escape of emitted light along the line-of-sight is modelled using an escape factor approximation[12] incorporating Doppler decoupling via the parameter R = ℓx/d*, where ℓx is the plasma scale-length (see Figure 2) and d* is the Doppler decoupling length. We can write that:-

$$d^* = \frac{c\Delta\lambda}{\frac{dv}{dx}\lambda_o} \qquad (1)$$

where c is the speed of light in vacuum, Δλ is the spectral width of the absorption line profile, λ_o is the wavelength of the radiation and $\frac{dv}{dx}$ is the velocity gradient.

Escape probabilities can be fitted to a simple formula of the form[13]

$$T = \frac{1-\exp\left(-a\tau^b\right)}{a\tau^b} \qquad (2)$$

where a and b are fitting parameters dependent on the ratio R of the plasma scale length to the Doppler decoupling length. We found that for our plasma conditions (as in Figure 2):-

$$a = \frac{1}{1.166+R} \text{ and } b = \frac{0.22}{1+R} \qquad (3)$$

In equations (3) and (4), R and τ vary with θ the angle which the line of sight makes with the normal to the target surface.

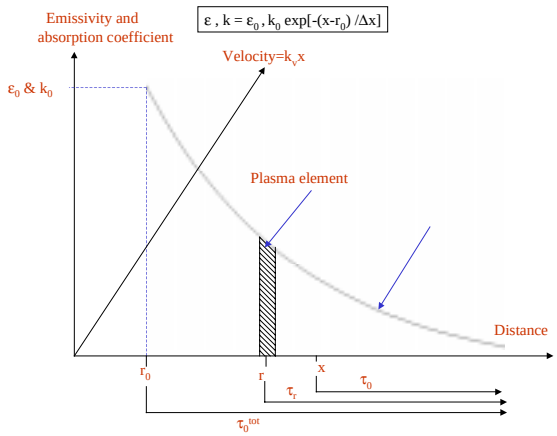

Figure 2. The plasma conditions assumed for our escape factor model.

Taking into account this angular dependence of R and τ and assuming a planar geometry the escape probability can be rewritten as

$$T = \frac{1-\exp\left\{-\sqrt{\pi}\left[\frac{\tau_0^{1+\frac{0.22}{1+Ru}}}{(ru+1.166)u^{1+\frac{0.22}{1+Ru}}}\right]\right\}}{\sqrt{\pi}\left[\frac{\tau_0^{1+\frac{0.22}{1+Ru}}}{(Ru+1.166)u^{1+\frac{0.22}{1+Ru}}}\right]} \qquad (5)$$

where u = cos(θ) and θ is the angle between the line of sight and the normal to the target.

The output of the EHYBRID code has been employed in a post processor code to solve the radiation transfer equation using the escape factor from equation (4) and to simulate the Ge resonance line intensities. Figures 3 and 4 show the simulated spectra superimposed on the experimental spectra.

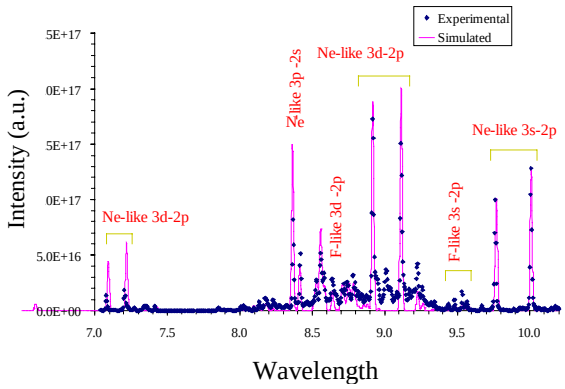

Figure 3. Simulated spectrum for long pulse driver laser configuration (dashed lines) superimposed on the experimental spectrum (solid line).

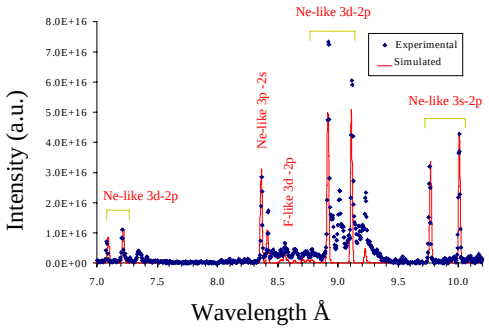

Figure 4. Simulated spectrum for short pulse driver laser configuration (dashed lines) superimposed on the experimental spectrum (solid line).

It can be seen that the F-like lines are less intense in the short pulse configuration, both in the experimental and simulated spectra. With short pulses, there is less over-ionisation which leads to greater efficiency in the pumping of the X-ray lasing.

References

1. Demir, et. al., Phys. Rev. E 55, 1827, (1997)
2. G.F. Cairns et al., Inst. Phys. Conf. Series, 151, 380, (1996)
3. G.J. Pert, J. Fluid Mech., 131, 401, (1983)
4. E.H. Avert, D.G. Hummer, MNRAS, 130, 295, (1965)
5. D. Mihalas , 1978, Stellar Atmospheres, W.H. Freeman Co., San Francisco
6. D.G. Hummer, G.B. Rybicki, APJ, 263, 925, (1982)
7. G.B. Rybicki, 1984, in W. Kalkofen ed., Methods in Radiative Transfer, Cambridge Univ. Press, Cambridge, pp. 21-64 (1989)
8. J.G. Doyle and R.W.P. McWhirter, MNRAS, 193, 947, (1980)
9. J.S. Kaastra and R. Mewe, A & A, 302, L13, (1995)
10. F.E. Irons JQRST 22,1, (1979)
11. F.E. Irons JQRST 45,217, 1991
12. S.J. Pestehe, DPhil Thesis, in preparation.
13. G.J. Tallents, Central Laser Facility Annual Report 1997/98, p 60.
14. F.E. Irons, Mon. Not. R. Astr. Soc., 182, 705, (1978)

A study of Four Wave Sum Difference Frequency Non-Linear effects with XRLs

S J Topping, R Keenan, C L S Lewis, R O'Rourke, A G MacPhee, S Dobosz

School of Mathematics and Physics, Queens University of Belfast, Belfast, BT7 1NN, UK.

G J Tallents

Department of Physics, The University of York, Heslington, York, YO1 5DD, UK

M Notely, D Neely

Central Laser Facility, CLRC Rutherford Appleton Laboratory, Chilton, Didcot, Oxon, OX11 0QX, UK

Main contact email address: *s.j.topping@qub.ac.uk*

Introduction

Preliminary experimental investigations into four wave sum difference mixing began in early January 1999. This was then followed up by a full experiment in target area east of Vulcan in September 1999. The process essentially involves the combination of three input beams to generate an output with a frequency corresponding to the sum difference of the constituent parts. In this case we attempt the combination of two XRL photons at 231.2 Å from Ne-like Ni and one optical photon at 1.054 µm, in a Na-like Ar plasma with the aim of achieving a near frequency doubled output[1].

Experiment

The Ne-like Ni XRL was created using the single sided five beam geometry developed at RAL[2]. The drive beams had a standard 80 ps pulse length with an average energy of 36 J per beam and when distributed across a 100 µm x 35 mm line focus gave an on target intensity of 3 x 10^{13} W/cm^2. A 10% pre-pulse was set 2 ns ahead of the main drive and the beams were positioned and timed along the target length to simulate a travelling wave. A diagram of the experimental chamber is shown in Figure 1.

The main diagnostic for the XRL was an on-axis grazing incidence flat field spectrometer with a 1200 lines/mm aperiodic ruled grating and a back thinned CCD. This was used to optimise the primary XRL beam and was later blocked with an X-ray mirror. The illumination uniformity and the ionisation balance were monitored on a shot-shot basis using a crossed slit camera and Bragg spectrometer respectively. The XRL beam was divided into two beamlets using a Lloyd's mirror and an XRM used to recombine the beamlets in a plane containing a gas jet at x2 the magnification.

The sixth Vulcan beam was used as the optical mixing component in the four wave mixing process. This eliminated timing problems created by jitter with respect to beam 7 (heating beam for the gas jet) which comes from a separate oscillator. The mixing beam was apertured down to a 15 mm (horizontal) and 45 mm (vertical) rectangle and focused into the mixing medium using a 3 m lens. This was done to ensure the horizontal beam dimension was small enough to be captured by a beam block placed at the rear of the target to protect the imaging XRM from damage. The intensity in this beam could be varied up to 8.4 x 10^{13} W/cm^2 although care had to be taken not to cause further ionisation in the gas jet, which would deplete the optimum Na-like content in the plasma[3].

The Gas Jet

The Ar gas jet was ionised using one of the back-lighters focused with cylindrical optics to a line focus of 300 µm x 3 mm. The neutral atom densities had been measured previously using a Nomarski interferometer. Modelling suggested working at a distance of 2 – 3 mm from the nozzle tip to work at the optimum atom/electron density[4]. During spectroscopic analysis of the gas jet emission (using the flat field) the on-target intensity was varied from 1.8 – 7.9 x 10^{13} W/cm^2. The signal from the gas jet was then reflected to the flat field using the beam splitter, which was required to isolate any non-linear signal generated in full mixing shots.

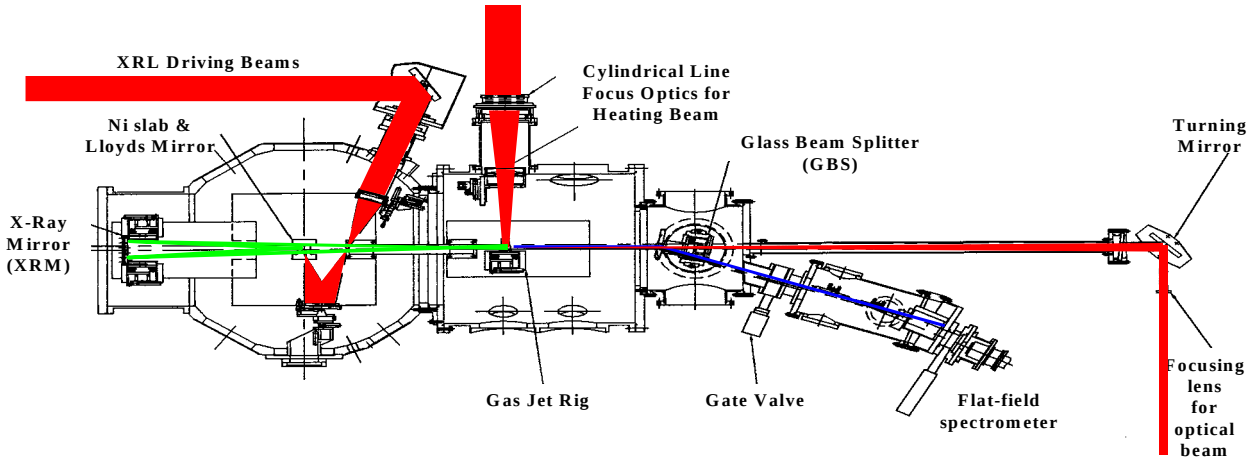

Figure 1. Experimental Scheme (XRM to GBS is ~ 2.5 m).

The beam splitter is estimated to have a reflectivity in excess of 65% when operating at 10^0. A gas jet spectrum taken with an incident 56 J, 80 ps pulse giving an on target irradiance of 6.1 x 10^{13} W/cm^2 is shown in Figure 2. The sodium resonance lines are indicated on the spectrum, as are some identifiable Al, Mg, F, O, C, N and B-like features. Modelling indicates that optimum Na-like densities are generated for on target intensities of 7.2 x 10^{13} W/cm^{-2} and ion densities of 1.1 x 10^{18} cm^{-3}. Further experimental work (including time resolution) is needed to verify this.

The Ne-like Ni XRL

Most of the parameters regarding pumping the XRL were fixed, the area of optimisation being quite well known for Ne-like

XRLs in this region of the periodic table. Figure 3 shows a time integrated axial lasing spectrum taken with a flat field from the south end (the end to which the quasi-travelling wave moves) from a 33 mm target.

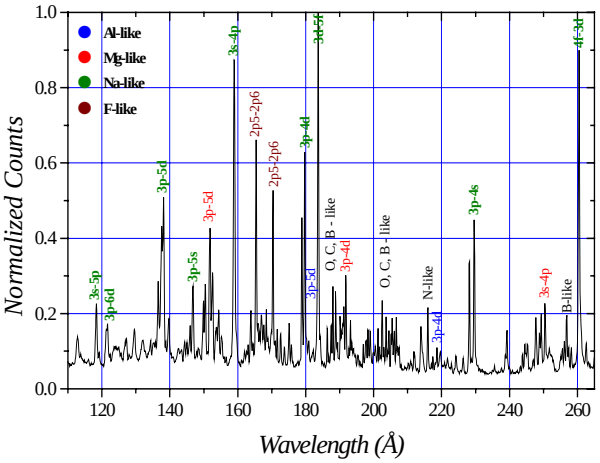

Figure 2. Ionised Ar emission spectrum.

This lineout shows an XRL with a FWHM divergence of 8 mrad and an off-axis refraction angle of 7 mrad. The target length was varied to obtain an estimate of the small signal gain coefficient which was estimated to be 14 cm^{-1}. Both Ni slabs and stripes were used, but it was found that use of the slab targets resulted in a much reduced turn around time and also gave a reliable signal output (although output did vary with the quality of finish).

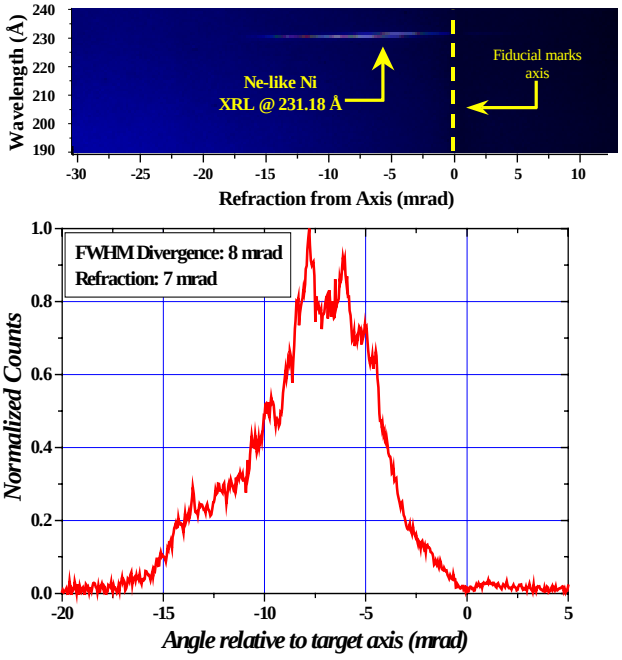

Figure 3. Ne-like Ni axial lasing spectrum (33 mm target).

Creating two XRL beamlets

For the FWSDM shots the XRL was split into two separate beamlets by a Lloyds mirror. This consisted of a thin piece of glass that reflects a portion of the XRL while allowing the remainder to travel directly to the X-ray mirror, see Figure 4. The Lloyds mirror was positioned parallel to the axis and the angle required at the gas jet to compensate for the phase mismatch[4] was secured by using the natural refraction of the XRL coupled with a target tilt to the degree of 11 mrad for most of the FWSDM data shots taken. Allowing for the magnification of the system ~ x2, corresponds to an XRL co-angle at the gas jet of 20 mrad. The positioning of the Lloyds mirror and the degree of target tilt is critical if phase matching is to be achieved.

The two XRL beamlets had a co-angle at the gas jet, which corresponds roughly to the non-collinear phase matching conditions for the estimated electron density in the gas jet. The mirror used to focus the XRL to the gas jet was a 1 m ROC multilayer with a diameter of 50 mm (R ~ 20%). The use of such a large aperture mirror enabled us to eliminate alignment problems arising from using two smaller aperture XRMs. The plane of overlap of the split and direct beams at the Lloyds mirror were then imaged to the gas jet.

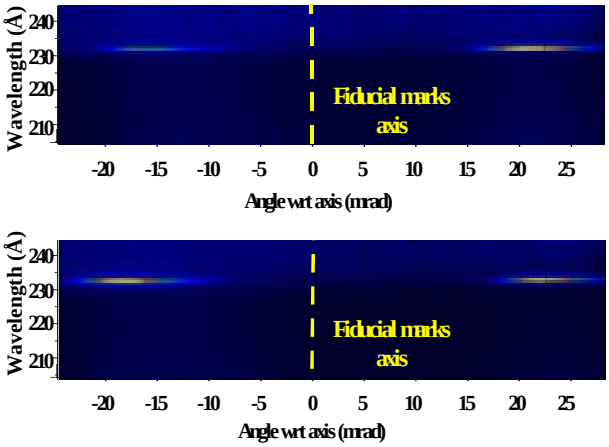

Figure 4. Split XRL with Lloyds mirror at (a) 500 µm (b) 575 µm.

Figure 4 outlines the procedure to achieve an equal split of the XRL with the Lloyds mirror. In Figure 4 (a) the Lloyds mirror has been moved to 500 µm from the XRL axis and the target has been tilted to 11 mrad, in this case the split ratio of reflected to non-reflected beamlets is 0.62:1.00. In Figure 4 (b) the Lloyds mirror has been moved to 575 µm of axis and we can see from the image two beams of almost equal intensity, the split ratio of reflected to non-reflected beams is 0.91:1.00, this mode was used when looking for the FWSDM signal.

Interference measurements and Spatial Coherence

To effectively demonstrate the FWM process the XRL beams must have a certain degree of coherence. With this in mind we carried out interference measurements to help assess the degree of spatial coherence present in the XRL beamlets. The set-up used in acquiring the interference fringes is shown in Figure 5. Alignment into the mixing medium is critical and was simulated using a visible diode laser coupled to an optical fibre, the output of which was placed at the exit plane of the Lloyds mirror. A camera with a microscope lens was mounted on a Sony Magnascale mount and placed at the gas jet plane.

The second imaging mirror could be translated in space to allow investigation of the two beams with a different degree of overlap in the gas jet plane. There was some uncertainty as to whether or not we would be able to reproduce the beam splitting from shot to shot. However it was found that there were clearly identifiable characteristics in each image taken, which could be isolated through blocking one or other of the beams.

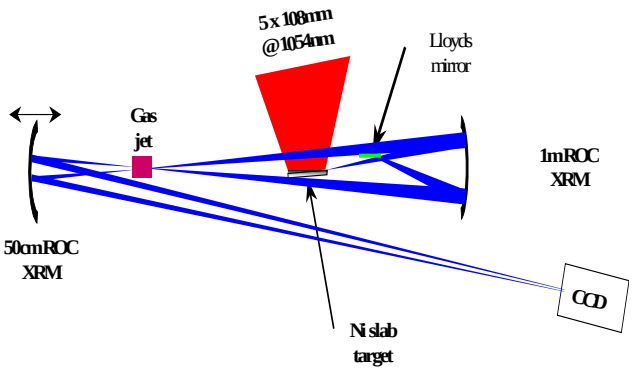

Figure 5. Measurement of Interference Fringes.

Adjusting the target tilt (and therefore the co-angle in the gas jet plane) allowed us to make small variations in the fringe spacing and with a known co-angle to determine the size of the fringes (of the order of ~ 1 µm). Figure 6 shows an image taken with the beams overlapped.

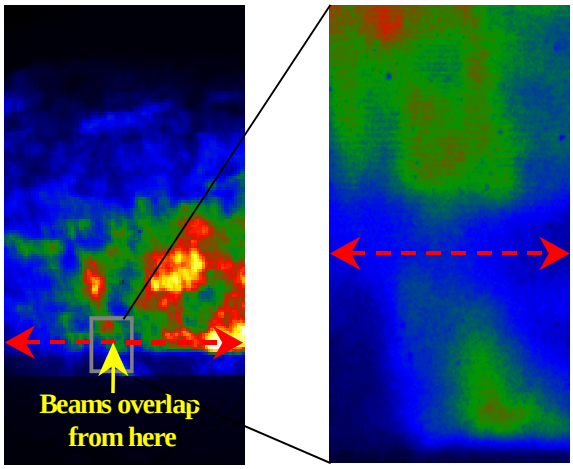

Figure 6. Beams overlapped and interference fringes.

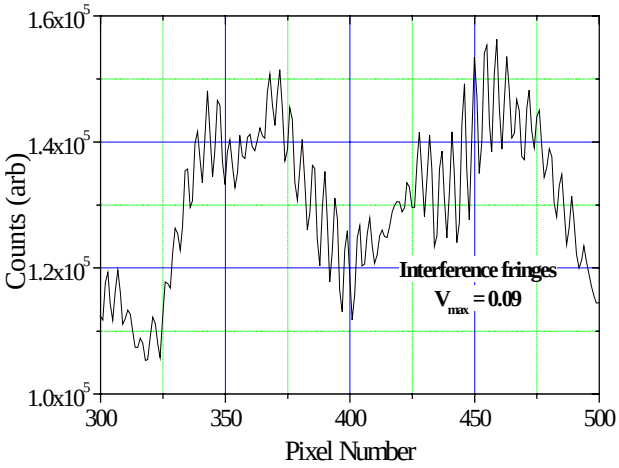

Figure 7. Integrated lineout over region with fringes.

The contribution from both beams can be clearly seen. Figure 7 illustrates this more clearly by taking a vertical bin in the region where fringes are visible across the image. The fringe visibility (V) was ~ 0.06 – 0.09 with a separation between 1 – 2 µm. An estimate of the resolution of the system was obtained from modelling of the fringe visibility. We assume a perfect set of $\cos^2$ fringes (i.e. V = 1) with a spacing of 1 µm which we then convolved with a Gaussian instrument function. The modelling suggests that the resolution of the system is somewhere between 1 – 2 µm, which is comparable to values calculated previously for similar systems.

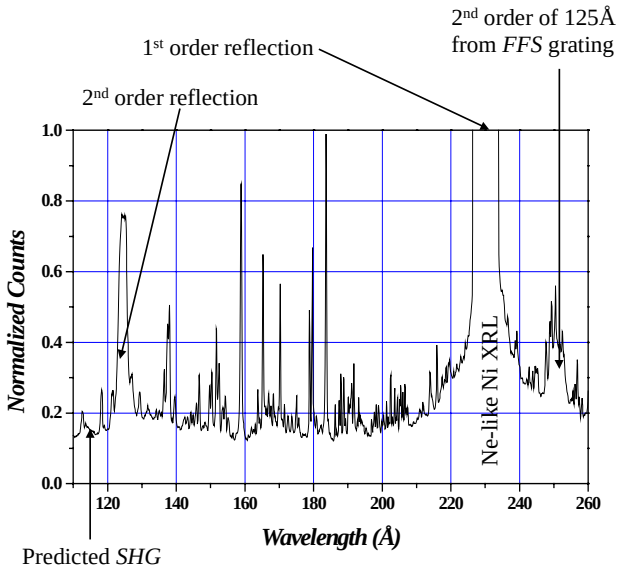

Figure 8. Ionised Ar emission spectrum with XRL.

Conclusions

Attempts were made to demonstrate the FWSDM process and observe the non-linear signal. However only a limited number of shots were tried and no non-linear signal was detected. Figure 8 shows a spectrum with both XRL beamlets and the optical beam fired into the gas jet (c.f. Figure 2 with no XRL). In Figure 8 we note the co-incidence of the XRL line and the 3p–4s ArVIII transition as well as XRL target continuum emission reflected by the XRM in 2nd order.

Factors likely to contribute to the null result include, imperfect spatial coherence between the two beams, the Na-like number density may have been lower than expected or the timing of the interaction between the XRL and the optical mixing beam could be slightly off. For future work and development a more exhaustive parameter scan is necessary. Other possibilities are to investigate other laser/media combinations, to maximize and measure the coherence of the XRL and to investigate the homogeneity of the mixing medium for phase matching.

References

1. M.H. Muendel & P.L. Hagelstein Physical Review A, Vol. 44, Num. 11, 1991.
2. R Keenan *et al*, Central Laser Facility Annual Report, 1998/99, pg 56.
3. R.M.N. O'Rourke *et al*, Central Laser Facility Annual Report, 1998/99.
4. R.M.N. O'Rourke, PhD Thesis, Queens University of Belfast, 1999.

Scaling considerations for supernova remnant simulations on Vulcan

N C Woolsey

Department of Physics, University of York, York, YO10 5DD, UK

R O Dendy, K G McClements

Euratom/UKAEA Fusion, Culham, Abingdon, Oxfordshire OX14 3DB, UK

J G Kirk

Max-Planck-Institut für Kernphysik, Postfach 10 39 80, D-69029 Heidelberg,Germany

P A Norreys, S J Rose

Central Laser Facility, CLRC Rutherford Appleton Laboratory, Chilton, Didcot, Oxon, OX11 0QX, UK

Main contact email address: *n.woolsey@rl.ac.uk*

High-power laser experiments have been used to test models of space and astrophysical interest in the UK, USA and Japan as illustrated in the reviews by Ripin *et al.*[1)], Rose[2)], Remington *et al.*[3)] and Takabe *et al.*[4)]. Experiments have studied both radiative properties[2)] and hydrodynamic properties[1,3-4)] of plasmas. Laser-plasma results have been applied previously to the study of such diverse phenomena as active galactic nuclei[5)], and to experimental investigation of the Earth's bow shock[6)]. By ensuring that the laser-produced plasmas have certain key dimensionless parameters similar to those of space and astrophysical plasmas, experiments may be used for detailed simulation in the laboratory. Aspects of space and astrophysical plasma modelling can be tested directly against experiment. A successful Direct Access experiment was recently completed that attempted to scale a laboratory experiment to a typical supernova remnant (SNR) impacting the interstellar (ISM). Experimental details and preliminary results are discussed in a related article[7)]. We discuss the scaling of this experiment in this report.

The one dimensional laser-plasma model Med103[8)] was used to design the Direct Access experiment. Using Med103 and the scaling considerations described below we explored a number of experimental configurations. The requirement was to produce a collisionless plasma that can be scaled using key dimensionless parameters to an astrophysical environment of interest, in this case the interaction of an SNR with the ISM. Additionally, consideration of Vulcan energy limitations and the need for a planar experiment amenable to detailed measurement is essential.

We considered four key scaling parameters. The system must be collisionless, this is determined by a collisionality parameter ζ, the ratio of an ion mean-free-path (mfp) to a typical scale length which must be greater than unity. The hydrodynamic scaling, determined by Euler number, *Eu*, is based on the work of Ryutov *et al.*[9)], who demonstrated invariance of the fluid equations for systems with equal ratios of characteristic speed to sound speed. The magnetic field is chosen such that the plasma β, the ratio of thermal to magnetic energy, is the same in the object of interest and in the laboratory. Finally, it is necessary to ensure that a shock forms; whether this occurs is determined by using the sonic (M) or Alfvénic Mach (M_A) numbers (depending on whether the plasma is weakly or strongly magnetised).

In Figure 1 we show the results from a Med103 simulation. In Figures 1a) the electron density n_e, 1b) the ion temperature T_i, 1c) the fluid velocity u_p, and 1d) pressure of two exploding plasmas are shown. The targets were two 1000 Å thick CH plastic foils irradiated with a 1 μm wavelength laser at 10^{14} W/cm^2 in a 80 ps duration Gaussian pulse. Initial foil separation is 1 mm as indicated by the dashed lines. The laser approaches from the left of the foil positioned at –0.05 cm and right of the foil positioned at 0.05 cm. The foils explode and stream towards each other, impacting approximately 250 ps after the peak of the laser pulse. After 250 ps a central n_e peak is observed as two shocks form between the interface of the flowing and stagnating plasma. The n_e of the shocked region increases in time as material continues to stagnate. The regions either side of the two shocks is referred to as the 'upstream', and the shocked or stagnated material the 'downstream'. This simulation provides numerical data for comparison with data believed to be typical of SNR 100 years after the supernova

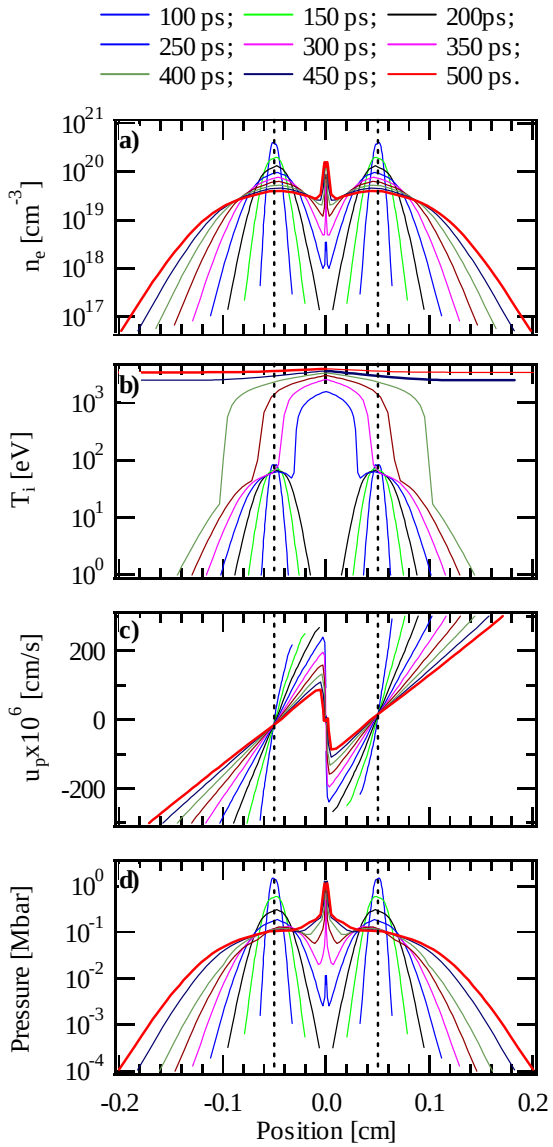

Figure 1. Med103 simulation of the colliding foils experiment. These are fluid calculations and do not model the interpenetration as the plasmas collide at position 0 cm. Dashed lines indicate the foils' initial positions. a) electron density, b) thermal ion temperature, c) velocity, and d) pressure are shown.

explosion. However, Med103 is a fluid model that accurately predicts the hydrodynamic expansion of the exploding foils but *will not* simulate the interpenetration of counter-flowing plasmas. In this case we believe the simulation data for the experiment 'upstream' are accurate whereas the simulation data 'downstream' of the experiment are much more speculative.

In Tables 1 to 4 the collisionality, the hydrodynamic scaling, the magnetic scaling, and the shock characteristics respectively are shown. Typical parameters for a SNR 100 years after the explosion of the supernova are compared to the simulated experiment 500 ps after the peak of the laser pulse. The upstream of the simulated experiment is scaled to the SNR; key parameters for comparison are highlighted bold in the right-hand columns. The upstream and downstream plasmas are labelled Sim U and Sim D respectively. The atomic number and mass used for the CH plasma are 3.5 and 6.5 respectively.

	n_e[cm^{-3}]	T_i [eV]	L [cm]	λ_{ii} [cm]	$\zeta=\lambda_{ii}/L$
SNR	1	10	3 x 10^{18}	8 x 10^{13}	**3 x 10^4**
Sim U	3 x 10^{19}	5 x 10^4	0.05	3.1	**56**
Sim D	1 x 10^{20}	3850	5 x 10^{-3}	5 x 10^{-3}	1

Table 1. Both the SNR and upstream-simulated experiment at 500 ps are collisionless, as indicated by the collisionality parameter ζ, which is greater than unity. Electron densities n_e, ion-ion mfp (λ_{ii}), sizes of the systems, L, as shown. The ion temperatures T_i calculated from the flow velocity are compared.

Typical particle mfp are much larger than the size of a SNR as shown by ζ in Table 1. This cannot be matched in the laboratory. However, as long as the simulated experiment ζ *exceeds* 1 the plasma is collisionless, and in this respect similar to the SNR and ISM. In this experiment we achieve high ζ by ensuring high ion velocities and low n_e. Since the laboratory plasma is collisionless we consider the hydrodynamic scaling as summarised in Table 2.

	v [cm/s]	ρ [g/cc]	p dy/cm^2	t [s]	***Eu***
SNR	2 x 10^2	10^{-24}	10^{-7}	3 x 10^9	**3.1**
Sim U	9 x 10^7	8 x 10^{-5}	1 x 10^{11}	5 x 10^{-10}	**2.8**
Sim D	2 x 10^7	5 x 10^{-4}	1 x 10^{12}	1 x 10^{-10}	1

Table 2. The hydrodynamic equivalence of an SNR and experiment is achieved by matching the Euler number, *Eu.* Typical values of an SNR are matched to the experiment upstream at 500 ps. v is the particle velocity, t characteristic time (i.e. age of system), ρ the density, p the pressure.

The hydrodynamics and magnetic scaling of the SNR and experiment crosses factors of up to 10^{20}. The SNR is described by the parameters (v, ρ, p, t, B) and the experiment by (v_1, ρ_1, p_1, t_1, B_1). The work of Ryutov *et al.*[9] verified that the hydrodynamics of different systems are equivalent if the Euler numbers are the same, i.e. $Eu=v(\rho/p)^{1/2}= v_1(\rho_1/p_1)^{1/2}$. The data shown in Table 2 indicates that the upstream-simulated *Eu* at 500 ps is similar to SNR at 100 years at approximately 3. The magnetic scaling is achieved using the plasma β. In the experiment, the magnetic field is simulated by an external magnetic field imposed on the counter-streaming plasmas. The experimental magnetic field is adjusted such that $p/B^2=p_1/B_1^2=\beta$. We have assumed the external magnetic field will penetrate the plasma, however, it is not clear if this will occur and this is an area of great experimental and theoretical interest. Typical ISM magnetic fields are extremely small, resulting in large β as shown in Table 3. However, the magnetic field is believed to produce collective behaviour and collisionless shock formation. In contrast, to achieve the correct scaling in the laboratory, large magnetic fields of 20 kGauss (20 T) must be generated.

	B [Gauss]	r_i [cm]	r_e [cm]	β
SNR	1 x 10^{-6}	3.2 x 10^8	7.5 x 10^6	**400**
Sim U	2 x 10^5	8.3 x 10^{-2}	3.6 x 10^{-4}	**400**
Sim D	2 x 10^5	2.3 x 10^{-2}	9.2 x 10^{-4}	190

Table 3. Magnetic parameters of the upstream simulation are scaled to values typical of an SNR by adjusting the magnetic field strength, B, to give the same plasma β. Here $r_{i,e}$ are the ion and electron gyro-radii respectively.

Finally, it is essential to form a shock. This is achieved using counter-streaming plasmas. As noted, the Med103 model assumes fluid-like plasma motion and does not include a magnetic field. The simulation values extracted from Figure 1 and used in Table 4 should be viewed with caution. However, comparing the simulated experiment with the SNR is instructive. The SNR Mach and Alfvén Mach numbers exceed 10, which indicate the presence of strong shocks. Matching these Mach numbers in the laboratory is challenging. Upstream of the counter-streaming experiment an intermediate strength sonic shock, and strong magnetic shock may form.

	U_s[cm/s]	C_s[cm/s]	u_A[cm/s]	***M***	***M_A***
SNR	5 x 10^8	4 x 10^6	2 x 10^5	**~100**	**2 x 10^3**
Sim U	1 x 10^8	2 x 10^7	6 x 10^6	**~5**	**80**
Sim D	1 x 10^8	1 x 10^8	3 x 10^6	1	190

Table 4. Values of Mach number, M, and Alfvén Mach number, M_A, ≥10, indicate the SNR and the upstream simulation at 500 ps are in the strong shock regime. Here U_s is the shock speed, C_s the sound speed and u_A the Alfvén velocity.

In conclusion, scaling arguments demonstrate a counter-streaming experiment, designed within the Vulcan operating capabilities, can simulate collisionless aspects of an SNR. We have scaled the experiment to an SNR impacting the ISM 100 years after the supernova explosion. A longer-term objective is to use similar experimental methods to examine electron acceleration at collisionless magnetised shocks.

References

1. B H Rippin, *et al.* Laser Part. Beams 8, 183 (1990).
2. S J Rose, Physics World, 7(4), 56 (1994).
3. B A Remington, D Arnett, R P Drake, and H Takabe, Science 248, 1488 (1999).
4. H Takabe, *et al.* Plasma Phys. Contr. Fusion 41, A75 (1999)
5. A Levinson and R Blandford, MNRAS 274, 717 (1995).
6. A R Bell, *et al.* Phys. Rev. A, 38, 1363 (1988).
7. R A D Grundy *et al.*, Central Laser Facility Annual Report 1999/2000, pg 42.
8. A Djaoui and S J Rose J. Phys. B 25, 2745 (1992).
9. D Ryutov, R P Drake, J Kane, and B A Remington Ap. J 518, 821 (1999).

Acceleration of electrons by a laser pulse in a tube

R A Cairns

School of Mathematics and Statistic, University of St Andrews, St Andrew, Fife, Y16 9SS

B Rau

Department of Engineering Physics and Mathematics, Helsinki University of Technology, 02015 HUT, Finland

Main contact email address: *rac@st-andrews.ac.uk*

Introduction

Particle acceleration using lasers has been investigated extensively ever since the original suggestion of Tajima and Dawson [1] and an overview of the development of the subject up to 1996 can be found in a review article by Esarey et al [2] . Most of the work in this area has focused on beat wave and wake-field schemes, both proposed in the original paper, in which the acceleration is produced by plasma waves excited in a uniform plasma with phase velocities just below the velocity of light. Particles whose speed matches the phase velocity are accelerated in the longitudinal field of the wave. Some recent experiments showing effective electron acceleration rely on self modulation via forward Raman scattering, a process similar in principle to the beat wave, but with a frequency shifted wave being generated spontaneously from a single frequency pulse, rather than the pulse containing waves of two frequencies [3].

In this paper we discuss an alternative scheme of particle acceleration in which a very short, intense laser pulse is directed down a hollow cylindrical tube with a solid wall. Simulations [4] and experiments [5] have shown that when an intense laser pulse is incident on a solid target there is rapid ionisation followed by heating of the plasma to very high temperatures, of the order of hundreds of keV. On a time scale on which electrons can move but ions do not have time to respond there is a large negative potential in the electron cloud expanding from the surface, produced by the charge separation field. If the pulse is travelling along a tube and electrons expand into it, then a simple calculation [6], indicates that when thermal equilibrium is reached the negative potential in the centre of the tube, in Volts, may be several times the electron temperature, in eV. Ahead of the pulse, the potential must, of course, be zero, so the result is a longitudinal potential ramp, moving with the pulse and capable of accelerating electrons. A similar idea was given by Bulanov et al [7] some years ago, though there the emphasis was on the wake-field in a plasma contained by the tube. So far as we are aware the idea has not been pursued in any detail since.

Other work on the use of capillaries with which we are familiar, for example that of Dorchies et al [8] discusses their use to create long uniform plasmas for conventional beat wave or wake-field experiments. Here we present some computer simulations which indicate that the use of a short pulse to create an ionisation and heating front moving down a tube may be capable of generating longitudinal accelerating fields of the order of 10^{10} V/m. Initial results indicate that test particles accelerated by this field remain quite well focused in the centre of the tube. We suggest that a scheme of this sort may offer some advantages over schemes based on using pre-formed plasmas, since the velocity of the pulse is that of propagation in a waveguide and is perhaps more easily controllable than the group velocity in a plasma.

Simulations

For our numerical investigation, we used a two dimensional particle in cell (PIC) code [9] capable of simulating the propagation of laser light along a slot rather than a tube. This reduces the amount of time and memory required for the computations while reproducing the essential features of the effects we are looking at. While the particle momenta, the electric currents, as well as the electromagnetic fields, are resolved in all three dimensions, the plasma electron positions are updated in two spatial dimensions only. The plasma ions on the other hand are simulated by a uniform background charge inside the channel walls, approximating the effect of heavy (and thus comparatively slow moving) ions which do not react on the time scale of the experiment.

The simulation runs on a grid with up to 4000 x 800 grid points and about 25 macro electrons per cell along the channel walls and covers an area of about 1000 x 200 $(c/\omega_p)^2$. In these simulations, we initialise an intense, short laser pulse in vacuum and let it propagate towards a channel with walls of pre-ionised, overdense, cold plasma. The plasma electrons are allowed to move along the direction of laser pulse propagation as well as in one perpendicular direction. The polarisation of the pulse can be chosen parallel or perpendicular to the channel walls. Here we present the results from a perpendicular polarisation (TM-wave) only since such waves heat the plasma more efficiently via Brunel heating[10] for low to moderately high laser intensities. Since ionisation will take place at the leading edge of the laser pulse, it is not expected to change the characteristics of the acceleration mechanism for high intensity pulses and is therefore left out.

In our simulations, we usually chose a system with the following parameters (the values in parenthesis correspond to a laser wavelength of 800 nm): The initially cold plasma was 5.25 times overdense (1.7 x 10^{21} cm^{-3}), channel width about 9.6 λ (7.6 μm), the full length of the laser pulse ($\cos^2$ envelope) about 3.2 λ (8.5 fs), and the peak field strength $a_0 = e E_{max}/(m_e \omega c) = 3$ (I_{max}= 2 x 10^{19} W/cm^2). The pulse was initialised in vacuum and had a super-Gaussian transverse profile. As it hits the channel entrance, part of the pulse is scattered and/or reflected such that only a fraction (about 70%) of the electromagnetic energy enters the structure. Once the pulse has entered the plasma channel, it propagates stably losing energy to the heating of the plasma walls only.

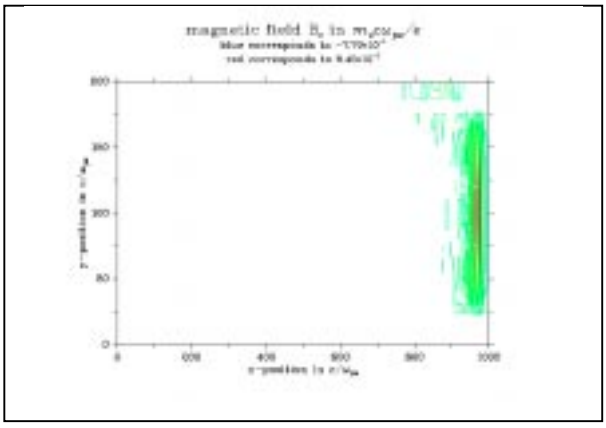

Figure 1. The magnetic field perpendicular to the plane of the diagram. This indicates the position of the pulse.

Figure 1 shows the oscillatory magnetic field of the pulse near the end of the run. As the laser pulse is propagating along the channel, hot electrons leave the channel walls and form an electron cloud with a cone-shaped edge behind the pulse as seen in Figure 2.

Negatively charged particles ahead of this cloud experience an accelerating force along the direction of laser pulse propagation.

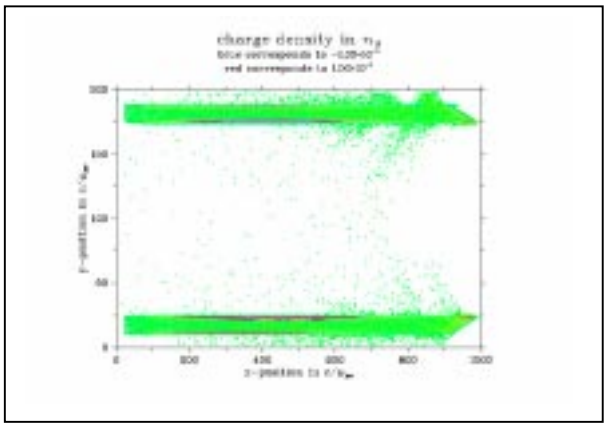

Figure 2. The electron density when the pulse has reached the right hand end of the tube. The dense areas at the top and bottom show the position of the walls.

To obtain a quantitative estimate of the accelerating field, we allowed test particles to move along the channel. These test particles did not contribute to the charge density or the electric currents but fully responded to the fields present. They can thus be thought of as a rather low density beam of electrons. This cold beam was injected right behind the laser pulse (to avoid transverse acceleration by the transverse electric field of the pulse) at a speed of 0.9c (661 keV).

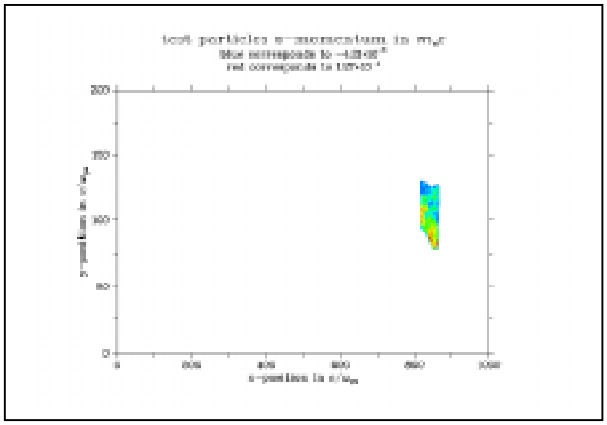

Figure 3. The position of a test particle bunch initially injected at the left hand end. The contours indicate variations in energy within the bunch.

Figure 3 shows the position of this electron beam at the end of the run, indicating that it remains focussed near the centre of the tube. It is injected so that it lies behind the pulse, and so is not disrupted by the pulse fields, and ahead of the electrons blown off the wall. This is the region in which the accelerating field is largest. As the electron cloud builds up slowly, the accelerating fields become strong only at the end of our simulation. In fact, due to scattered light, some of the test electrons undergo some deceleration and spatial defocusing at the channel mouth. However, once the cone-shaped electron cloud has formed, test particles ahead of this acceleration structure experience some spatial focusing as well as strong acceleration, as shown in Figure 4. This spatial focusing is accompanied by a spread in the energy distribution such that the beam emittance seems to be more or less conserved in the acceleration region.

Finally, as the pulse electromagnetic energy is depleted due to the heating of the plasma electrons along the walls, the formation of the accelerating structure becomes less efficient and the accelerating gradient less steep. In our numerical simulation this effect starts to become visible at the end of the run.

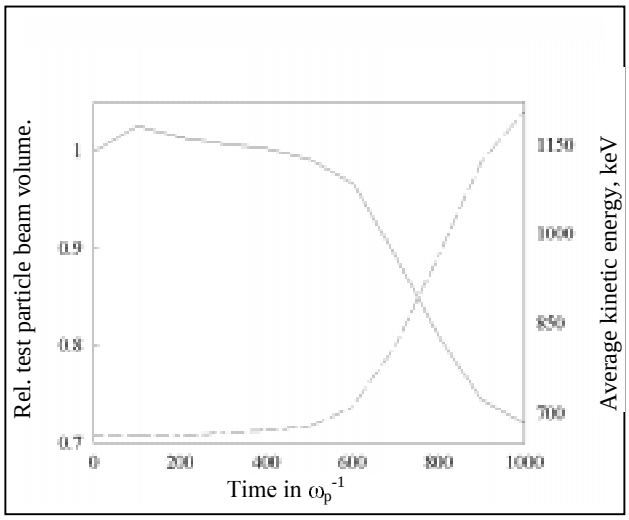

Figure 4. The change in average energy and the spatial volume occupied by the test particles. Strong acceleration is accompanied by spatial focusing.

From the acceleration of the electron bunch we can estimate the peak accelerating field in our simulation to be a few times 10^{10} V/m, a value comparable to what is generally thought to be possible in beat waves or wake-fields. Although limitations on computing resources constrained our simulations to two dimensions and short times, our results suggest that a scheme of this sort may be competitive with other laser based schemes. A possible advantage for very high energy particles is that in beat wave or wake-field schemes the density of the plasma goes down as the phase velocity of the wave increases. At the same time the maximum field obtainable, roughly proportional to the square root of the density, also goes down. Here, the velocity of the pulse is that of propagation in a vacuum waveguide, ahead of any plasma which is produced, and depends on the waveguide mode and the dimensions of the tube. In our simulations it is close to the speed of light. Also, it is possible that the timing and velocity of the pulse, or pulses in a staged device, would be more controllable in a solid tube than in a plasma. In principle it might even be possible to taper the tube in such a way as to have an increasing pulse velocity and so prevent the limitation of acceleration as the electrons outrun the accelerating potential gradient. So far as laser requirements are concerned, the need is for a pulse sufficiently intense to produce a substantial hot electron population and short enough to stay ahead of the electron cloud in the tube.

Acknowledgement

This work was supported by the European Commission through the TMR network SILASI, No. ERBFMRX-CT96-0043.

References

1. T Tajima and J M Dawson, Phys. Rev. Lett. 43, 267 (1979).
2. E Esary et al, IEEE Trans. Plasma Sci., 24, 252 (1996).
3. D Gordon et al, Phys. Rev. Lett., 80, 2133 (1998).
4. S C Wilks et al, Phys. Rev. Lett. 69, 1383 (1992).
5. F N Beg et al, Phys. Plasmas 4, 447 (1996).
6. B Rau and R A Cairns, Phys. Plasmas, to be published.
7. S V Bulanov et al, Phys. Lett. A 195, 84 (1994).
8. F Dorchies et al, Phys. Rev. Lett. 82, 4655 (1999).
9. T Zh Esirkepov, E-print archive xxx.lanl.gov/abs/physics/9901047 (1999).
10. F Brunel, Phys. Rev. Lett., 59, 52 (1987).

Propagation of light through thin overdense plasma slabs

R A Cairns

School of Mathematics and Statistics, University of St Andrews, St Andrews, Fife, KY16 9SS

B Rau, M Airila

Department of Engineering Physics and Mathematics, Helsinki University of Technology, 02015 HUT, Finland

Main contact email address: *rac@st-andrews.ac.uk*

Introduction

Anomalous transmission of laser light through thin plasma slabs has been observed in a number of experiments in recent years[1,2]. In some of these the pulse was sufficiently long that the observed transmission can be explained by a reduction in the slab density towards the end of the pulse duration [3], but in the experiments of Giulietti et al [1] the pulse is so short that the slab remains at near solid density. Motivated by these latter experiments, we have carried out simulations of transmission of short pulses through targets of thickness about one tenth of a wavelength. We have found that there may indeed be enhanced transmission under certain conditions and have developed some theoretical ideas to explain the results of our simulations. Whilst our approach relies on some simplifications which make precise comparison with experiment difficult, we hope that the phenomena we describe may have some relevance.

The simulation results

In a real laser plasma experiment the high intensity pulse heats the electrons through a variety of complicated nonlinear processes. Since we wish to concentrate on light propagation through overdense plasma we have simplified matters by starting with a pre-heated plasma and using a comparatively low intensity pulse. This allows us to separate out what is basically a kind of complex anomalous skin effect from all the nonlinear complications which would occur with a pulse of realistic intensity. Ions are assumed immobile on the time scales of interest and are simply treated as a background charge density with a step function distribution along the direction normal to the slab. The electrons, on the other hand, are initialised with a Boltzmann energy distribution in a self-consistent space charge field [4] , giving them a bell-shaped density profile.

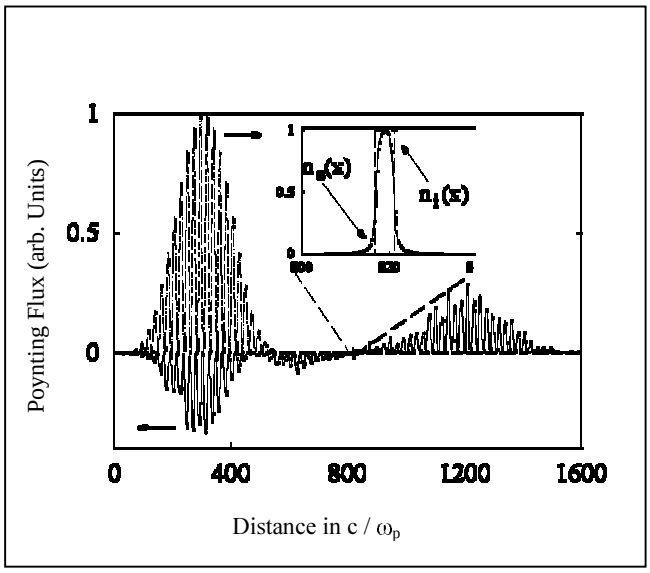

Figure 1. The initial (dotted line) and final (solid line) Poynting flux normalised to the maximum of the initial flux. The slab, positioned as indicated by the inset, is one tenth of a wavelength thick and 50 times overdense.

Figure 1 shows a typical simulation result with a hot electron distribution.

As is evident from this figure there is substantial transmission, about 33% of the incident pulse energy. This is to be compared with the transmission based on a WKB approximation with the wavenumber obtained from the familiar cold plasma dispersion relation, where the result is of the order of 10^{-4}. Another striking feature of the result is that there is emission of radiation, more or less symmetrically from the font and back surfaces, after the incident pulse has gone. Finally, it is clear that the wavelength of the transmitted radiation is the same as that of the incident pulse, so that we are not dealing with any nonlinear effect.

Some theory

Our explanation of the results presented briefly in the previous section hinges on the observation that hot electrons contained by the self-consistent space charge potential bounce between the front and back surfaces of the slab. Further, the shape of the potential for a thin slab is roughly parabolic, so a large fraction of the particle distribution has approximately the same bounce frequency. Finally, this bounce frequency for the parameters we use happens to be very close to the laser frequency. This last coincidence was not set up deliberately, but happened to be the case for parameters which we chose to be roughly in line with the short pulse experiments of the Pisa group [1].

The result of this coincidence in frequencies is the following. Suppose that at some instant the phase of the field at the front surface is such as to accelerate electrons in a particular direction transverse to the surface and generate a transverse current. Half a period later these electrons have moved to the back surface and electrons at the front surface are being accelerated in the opposite direction. A full period later, the original electrons have returned to the front surface and their initial transverse motion is being reinforced. In this way a current distribution is set up which extends across the whole width of the slab and is in the opposite direction in the front and back halves of the slab. This current can be seen in the simulations. The result of the current distribution extending over the whole width, rather than being confined to a thin skin layer, is that radiation is emitted from the back surface. Our interpretation of the crucial role of electrons with resonant bounce frequency is confirmed by the fact that the transmission with cold electrons falls to the classical level. Furthermore, even if we have hot electrons but confine them by rigid reflecting walls rather than the self consistent potential, the transmission falls to a low level.

If the transmission and the ringing which produces emission after the pulse has passed are due to the excitation of a resonant response within the slab, we would expect them to vary linearly with the duration of the driving pulse, at least for short times before some saturation effect comes into play. Figure 2 shows that this is what happens. The drop at the upper end is probably because the simulation box becomes too short for the pulse rather than being a real effect. The transmission as a function of temperature increases to a maximum, which depends on the plasma density and the slab thickness then falls off fairly gradually. We have verified that this behaviour is consistent with the fraction of electrons whose bounce period is in resonance with the wave, again lending support to our interpretation of the phenomenon.

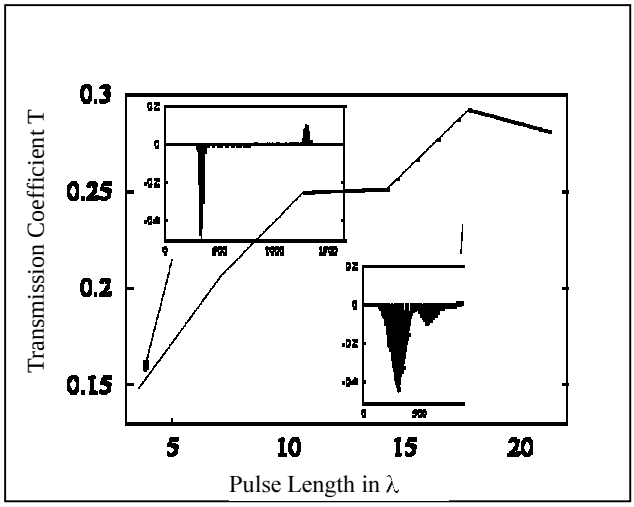

Figure 2. The transmission as a function of pulse length. The slab was 1/10 of a wavelength thick and 50 times overdense. The insets show the Poynting flux, as in Figure 1, for the lengths indicated.

The emission of radiation from the slab after the pulse has passed can be explained as the ringing of a natural mode of the thin slab. To analyse this mode we assume, following the qualitative discussion given above, that the current within the slab is antisymmetric about its centre. Taking the lowest order expansion of such a current we assume that

$$J_y = \begin{cases} Kx, & |x| < \Delta/2 \\ 0, & |x| > \Delta/2 \end{cases}$$

with Δ the slab width. We can then construct a solution of Maxwell's equation with outgoing waves on each side[4] and find that, if the slab is thin compared to the pulse wavelength, the transverse electric field inside the slab is also proportional to x. Finally we find that the perturbation to the electron velocity inside the slab is consistent with the assumed current if :-

$$\frac{1}{2}\frac{\omega_p^2}{\omega^2}\left(\frac{k\Delta}{2}\right)^2 = 1$$

a condition which is quite well satisfied for our parameters. We conclude that for a thin plasma slab there is a natural mode with an antisymmetric current distribution which radiates energy away from both surfaces. The frequency of this mode is close to the pulse frequency for our parameters so we conclude that the emission after the pulse is the result of ringing of this mode.

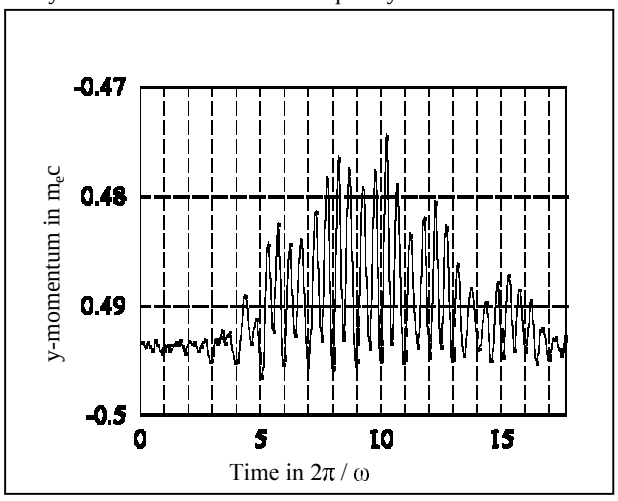

Figure 3. The transverse momentum of a resonant electron.

While the field inside the slab is oscillating at the wave frequency, a resonant electron is moving back and forth across the slab, also at the wave frequency. The result is that if we follow the motion of a particle, it feels a transverse field which oscillates at twice the wave frequency. In an Eulerian frame, the transverse current oscillates at the wave frequency, as expected in a linear analysis, while in a Lagrangian frame following a resonant electron it oscillates at twice the wave frequency.

Figure 3 illustrates this motion for a typical resonant electron. When the pulse arrives the oscillation at twice the wave frequency is set up, then persists after the pulse has passed.

We have also investigated the effect of wave intensity on transmission and a typical result is shown in Figure 4.

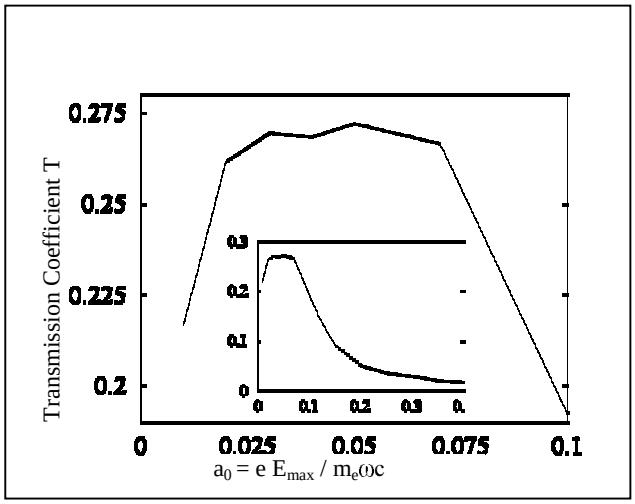

Figure 4. The transmission as a function of peak field in the pulse. The thickness was 1/10 wavelength, the plasma 20 times overdense and the pulse length 17.8 λ.

For the parameters of this run, the transmission is approximately constant over a range of intensities, then starts to decrease. We interpret this as being a result of the fact that the ponderomotive pressure on the electrons starts to become sufficient to distort the confining space charge potential and so change the bounce frequency. If this is the case then the decrease in transmission with intensity should not be regarded as a general feature, but simply the fortuitous result of the fact that we started with parameters where there was a large fraction of resonant electrons. We might equally well have a situation where the ponderomotive pressure increases the number of resonant electrons and so enhances transmission.

Conclusions

We have identified a mechanism, based on the existence of a resonance between the bounce frequency of electrons confined by the space charge field in a slab and the wave frequency, which allows greatly enhanced transmission of a laser pulse. It is basically similar to the well-known anomalous skin effect, except that an electron does not just pass through the skin layer once, but passes through it repeatedly as it is reflected from the slab boundaries. The parameters for which this occurs are approximately those of experiments where anomalous transmission is seen[1], so the effect described here may perhaps be of relevance to these experiments.

Acknowledgement

This work was supported by the European Commission through the TMR Network SILASI, No. ERBFMRX-CT96-0043.

References

1. D Giulietti et al, Phys. Rev. Lett. 79, 3194 (1997).
2. J Fuchs et al, Phys. Rev. Lett. 80, 2326 (1998).
3. J Fuchs et al, Phys. Plasmas 6, 2563 (1999).
4. R A Cairns, B Rau and M Airila, Phys. Plasmas, to be published (2000).

A versatile matrix based solution for the Two Plasmon Decay instability

A C Machacek, J S Wark

Department of Physics, University of Oxford, Clarendon Laboratory, Parks Road, Oxford. OX1 3PU

Main contact email address: *a.machacek1@physics.ox.ac.uk*

Introduction

Optical radiation emitted from laser produced plasma is relatively straightforward to collect and measure, and hence is invaluable as a diagnostic tool. Such tools are vital if plasma parameters such as density, temperature and scale length are to be known to inform developments in short pulse laser-solid target experiment and theory.

While many of the instability processes which produce such scatter have undergone rigorous theoretical study in the last twenty-five years, two assumptions have remained in much of the analysis performed. Firstly that extra modes are usually ignored, and secondly that the temperature is sufficiently low that the standard adiabatic plasmon dispersion relationship, as in equation (1), may be used. It is timely for these two assumptions to be critically reviewed with the advent of high temperature plasma at and near the focus of an ultra-intense short pulse laser such as Vulcan in CPA mode. We begin such an evaluation here, taking the Two Plasmon Decay (TPD) process as our example. This is a logical starting point, as the TPD typically has the lowest threshold for an electronic parametric instability in a laser produced plasma, and as such is likely to occur over greater regions of plasma.

$$\omega^2 = \omega_p^2 + 3v_e^2 k^2 \qquad (1)$$

The consideration of extra modes

The conventional method of determining the gain rates of instability in homogeneous plasma is to Fourier transform the Vlasov equations, and then solve for a complex frequency by determining the roots of a suitable polynomial[1]. The consideration of extra modes has already been recognised as important in a determination of the general properties of electronic parametric instabilities in a plasma subjected to relativistic intensities[2]. However in these treatments, the plasma pressure was neglected in comparison to the huge ponderomotive pressures present, and as such we may not use this model to describe TPD at lower intensities. The technique by which the multiple modes were considered is to use a Floquet transformation of the plasma perturbations; that is we transform from $n(x,t)$ to $n_q(k,\omega)$ using the integral

$$n_q(k,\omega) = \int n(x,t)\, e^{i(\mathbf{k}_q \bullet \mathbf{r} - \omega_q t)}\, d^3\mathbf{r}\, dt$$
$$\mathbf{k}_q = \mathbf{k} + q\mathbf{k}_L \qquad (2)$$
$$\omega_q = \omega + q\omega_L$$

where the L subscript denotes the frequency and wave vector of the incident laser light. Using this formalism we may write the continuity and law of motion for the electrons in the form of a matrix, as

$$A_q X_{q-1} + B_q X_q + C_q X_{q+1} + \omega X_q = 0 \qquad (3)$$

If we take the electron thermal velocity to be $v_e = \sqrt{k_B T/m}$, the local electron plasma frequency to be ω_p, and the amplitude of the quiver velocity of the electrons in the laser field as v_0, then the matrices become

$$X_q = \begin{pmatrix} \psi_q \\ \frac{1}{N} n_q \end{pmatrix}$$
$$A_q = C_q = \begin{pmatrix} -\frac{1}{2} k_y v_0 & 0 \\ 0 & -\frac{1}{2} k_y v_0 \end{pmatrix} \qquad (4)$$
$$B_q = \begin{pmatrix} q\omega_L & -i\left[\frac{\omega_p^2}{k_q^2} + \gamma v_e^2\right] \\ i k_q^2 & q\omega_L \end{pmatrix}$$

where n is the perturbation in the electron number density, the velocity perturbation is given by grad(ψ), and γ=3 for adiabatic plasma. The frequency of the plasmon and the gain rate of the process are then determined by taking the real and imaginary parts respectively of the eigenvalue of the matrix

$$\begin{pmatrix} B_{-Q} & C_{-Q} & 0 & \cdots & 0 \\ A_{-Q+1} & B_{-Q+1} & C_{-Q+1} & \cdots & 0 \\ 0 & A_{-Q+2} & B_{-Q+2} & \cdots & 0 \\ \vdots & \vdots & \vdots & \ddots & C_{Q-1} \\ 0 & \cdots & 0 & A_Q & B_Q \end{pmatrix} \qquad (5)$$

Using this technique we may include all orders up to +Q and down to –Q, choosing a value of Q commensurate with adequate convergence and acceptable computational speed.

The results are not significantly different from those generated using merely the $q = 0$ and $q = -1$ modes, and thus the neglect of these modes is justified in this case. However, we have performed additional calculations to treat the problem of the combined TPD / SRS (Stimulated Raman Scattering) instability in the presence of a strong static magnetic field. This uses methods analogous to those of Barr[3], which include an arbitrary number of modes. A marked difference in the structure of the instability in **k**-space is observed, and will be reported in a future publication.

Furthermore, we may also describe non-adiabatic plasma by using the appropriate value of the polytropic co-efficient γ for the density of plasma and value of **k** concerned. Work is currently in hand to investigate the accuracy of such a method.

References

1. W. L. Kruer *The Physics of Laser Plasma Interactions* Addison-Wesley, Redwood City (1988)

2. B. Quesnel, P. Mora, *et al.* Physical Review Letters 78, 2132 (1997) Physics of Plasmas 4, 3358 (1997)

3. H. C. Barr, T. J. M. Boyd *et al* Physics of Fluids 27, 2730 (1984)

High Energy Ions Produced from Cluster Explosions

M Eloy, R Azambuja, J T Mendonça

Grupo de Lasers e Plasmas, Centro de Física de Plasmas, Instituto Superior Técnico, Av. Rovisco Pais 1 1049-001 Lisboa, Portugal.

R Bingham

CLRC Rutherford Appleton Laboratory, Chilton, Didcot, Oxon, OX11 0QX, UK

Main contact email address: *r.bingham@rl.ac.uk*

Introduction

We report on simulations of atomic cluster explosions upon interaction with high-intensity femtosecond laser pulses. By using a 2D and 3D fully relativistic PIC code we investigate the dynamics of hydrogen and argon cluster explosions providing information about the time-resolved ion energy spectra, for different laser intensities. Multi-cluster systems are also studied and the influence of cluster distribution in ionic energy spectra is shown. Results indicate that MeV ions are produced through Coulomb explosion of the atomic clusters and the possibility of capturing most of these ions with a specially designed magnetic focusing system is discussed.

The interaction of laser pulses with atomic and molecular clusters has become a subject of great interest. Recent experiments show that the interaction of short (<ps), intense (~10^{17} W/cm^2) laser pulses with rare gas clusters is responsible for the production of highly energetic electrons and ions [1,2], X-ray emission in the keV range[3], coherent high-harmonic generation[4], plasma waveguide formation[5] and applications to nuclear fusion [6].

limitations we present a novel approach to accurately describe the dynamics of laser-cluster interaction by using a Particle-in-Cell (PIC) code, determining for each time step the position, momentum and energy of the particles under the influence of both the external laser field and the fields generated by the particles themselves, for a very large number of particles and within reasonable computational times.

We use the fully relativistic 3D PIC code KARAT to model the interaction of an ultra-short (30 fs gaussian laser pulse), high-intensity (10^{17}- 10^{20} W/cm^2), 800 nm plane wave with a 1 μm diameter plasma sphere of either hydrogen or argon with n_i = 5 x 10^{21} cm^{-3} and placed in the center of the simulation region. Code KARAT is also used in the 2D fully relativistic case, the simulation parameters being the same as for the 3D case with exception for the laser pulse, now gaussian in space with a 10 μm radius with a duration of 20 fs.

All clusters are treated as pre-formed microplasmas, the hydrogen cluster being mono-ionized, H^+, and the argon cluster having either a constant average charge, Ar^{9+}, or a different charge according to the laser intensity under study, namely Ar^{4+}

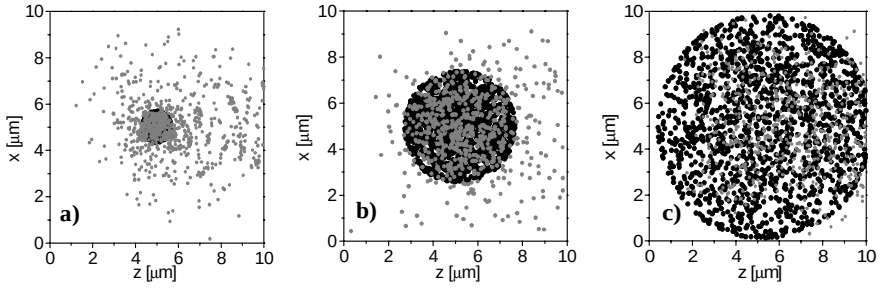

Figure 1. Dynamics of cluster expansion for I = 10^{20} W/cm^2 at a) t=50 fs, b) t=100 fs and c) t=150 fs. The ions are depicted in black and the electrons in grey. The laser pulse is plane polarised in the x-axis, propagates along z and is injected from left to right, centred with the simulation box.

The cluster expansion mechanism can be described using either a hydrodynamical model or a Coulombic repulsion model, depending on the laser intensity and pulse duration as well as on the cluster size and charge state. In the hydrodynamic regime, dominant for lower (<10^{17} W/cm^2) intensities and longer pulses, the electrons are held in the cluster via space-charge attraction from neighbouring ions and the cluster is heated to very high temperatures[1]. Pressure build-up within the core causes the cluster to expand hydrodynamically. Ion energies up to 1 MeV have been achieved[1]. In the Coulombic regime, dominant for ultra-intense (>10^{17} W/cm^2), ultra-short (<150 fs) laser pulses, a sufficient number of electrons are expelled by the laser from the cluster core, leaving behind a positively charged droplet which explodes due to electrostatic repulsion. Also, Coulomb explosions occur preferentially for smaller clusters and produce the most energetic ions (1 MeV) [2].

Numerical models using particle dynamics have been proposed to describe the Coulomb mechanism [7,8], although requiring substantial computational resources and being unable to account for large number of atoms. A fluid description [9] cannot provide such a detailed insight of the process. To circumvent these

for 1 x 10^{17} W/cm^2, Ar^{7+} for 5 x 10^{17} W/cm^2, Ar^{8+} for 10^{18} - 10^{19} W/cm^2, Ar^{10+} for 5 x 10^{19} W/cm^2 and Ar^{13+} for 1 x 10^{20} W/cm^2. Different charge states of argon were determined through 2D laser-gas interaction simulations using the ADK optical ionization model[10] and assuming that only the first 25% of the laser pulse is responsible for ionizing the cluster. Our simulation box is 10 μm x 10 μm (x z) containing 111 x 111 cells, in the 2D case, and 10 μm x 10 μm x 10 μm containing 45 x 45 x 90 cells (x y z) in the 3D case.

As the laser reaches the cluster, the electrons begin to oscillate transversally in the E-field of the laser and longitudinally via the e[**v** x **B**] force; ponderomotive blowout and trapping by the laser field generates electron expulsion from the cluster core and inertia prevents ions from responding significantly to the laser field [11]. A net positive charge builds up inside the cluster, resulting from the ions which were left behind and the cluster undergoes a Coulombic explosion, the ions expanding isotropically (Figure 1) and gaining energies that range, for H^+, from 1.5 to 7.5 MeV in the 2D case and from 0.011 to 3 MeV in the 3D case, differences due mainly to geometry effects, and also from 3 to 33 MeV for Ar^{9+} and 0.49 to 42 MeV for Ar^{4+}

and Ar^{13+}, respectively, for laser intensities varying from 10^{17} to 10^{20} W/cm^2 as shown in Figures 2a), b), c) and d). At the initial stages of the explosion, the ions gain a large amount of energy during a short (~50 fs) interval of time, due to Coulomb repulsion. However, as the cluster expands, the separation between neighbouring ions will increase and the energy gain will not be so dramatic. Eventually, the ions will be so far separated that Coulomb repulsion has little contribution to the energy curve that reaches a saturation value.

We have also looked at the current distribution throughout the explosion. Figure 3 indicates the maximum current observed in our simulations, for the case of the hydrogen cluster irradiated at 10^{20} W/cm^2. Again, due to isotropy, current yields are similar in all directions. At the early times of the explosion we observe a rapid increase of the current due to the acceleration of the ions resulting from Coulomb repulsion, followed by a decrease explained by the fact that although the energy of the ions has reached a saturation value, as stated previously, the cluster is still expanding. Eventually these effects cancel out and a saturation value is reached. Peak current yields varying from 0.31 kA to 1.44 kA are observed. Our simulations also indicate the current pulse duration to be around 100 fs.

To investigate the possibility of producing a high-energy collimated ion source we have designed a point-to-parallel focusing system, composed by a set of three quadruople magnets, based on the standard thin-lens approximation to calculate the dimensions of the system as well as the magnetic fields required[12]. This magnetic focusing system ensures the production of a circular cross-section collimated ion beam obtained from a point source, such as our cluster. We take the example of a hydrogen cluster irradiated at 10^{20} W/cm^2 and assume the ions to have an energy of 3 MeV, as our simulations indicate. We consider the collection angle of the ions to be ±5º, ±10º, ±15º and ±22.5º, thus collecting all particles that emerge from a cone centered with the cluster and with apertures of 10º, 20º, 30º and 45º respectively. The design can easily be extrapolated for different collection angles, as well as for the case of the argon cluster explosion, with only a few changes in

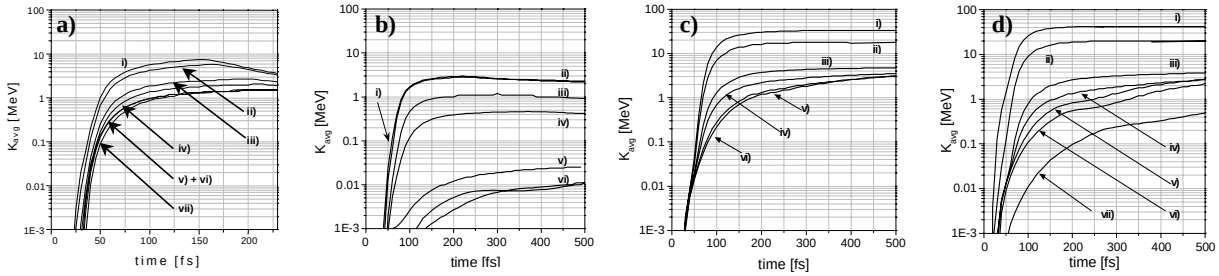

Figure 2. Average ion energy as a function of time for laser intensities of: i) 1 x 10^{20} W/cm^2, ii) 5 x 10^{19} W/cm^2 , iii) 1 x 10^{19} W/cm^2, iv) 5 x 10^{18} W/cm^2, v) 1 x 10^{18} W/cm^2, vi) 5 x 10^{17} W/cm^2 and vii) 1 x 10^{17} W/cm^2. *a)* for a H^+ cluster in 2D case, *b)* for a H^+ cluster in 3D case *c)* for an Ar^{9+} cluster and *d)* for an Ar^{n+} cluster with charge states of 4^+, 7^+, 8^+, 10^+ and 13^+ for the vii), vi), v) through iii), ii) and i) cases respectively. Difference in energy yields for the simple Ar^{9+} case is due to the difference in charge states**.**

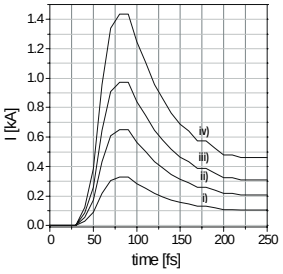

Figure 3. Maximum current observed for the case of a H cluster explosion irradiated at 10^{20} W/cm^2, corrected for collection angles of i) ± 5º, ii) ± 10º , iii) ± 15º and iv) ± 22.5º.

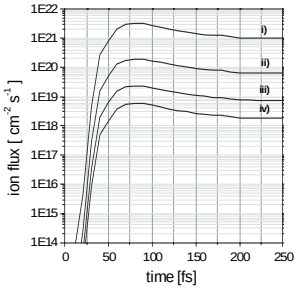

Figure 4. Ion flux observed for the case of a H cluster explosion irradiated at 10^{20} W/cm^2. These values pertain to the collimated ion beam with radius indicated in Figure 5 and for collection angles of i) ± 5º, ii) ± 10º , iii) ± 15º and iv) ± 22.5º.

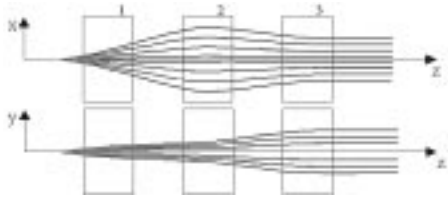

Angle [± °]	Beam Radius [mm]	B_1 [T]	B_2 [T]	B_3 [T]
5	6.5	1.5	2.2	1.1
10	26.0	1.5	2.2	1.1
15	75.2	1.5	2.2	1.1
22.5	151.5	1.5	2.2	1.1

Figure 5. Magnetic focusing system design. The quadrupoles 1, 2 and 3 are placed at a convenient distance from the exploding cluster, depending on the collection angle. Some of the cluster ion trajectories are depicted. A collimated ion beam with a circular cross-section is obtained after the last quadrupole, the overall system length, measured from the cluster position, varying from 13 cm to 64 cm, also depending on the collection angle.

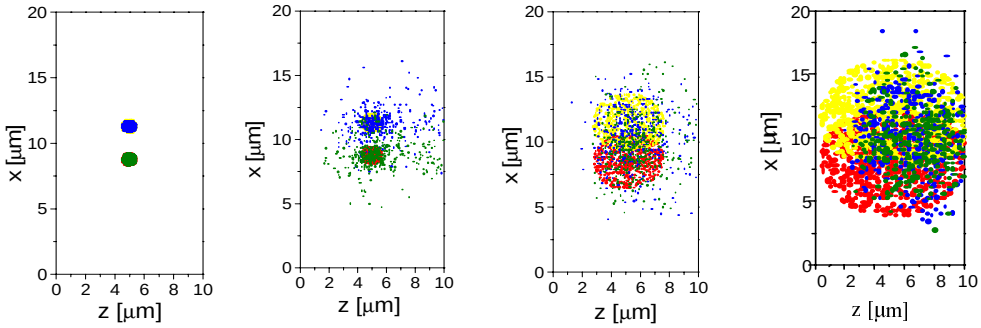

Figure 6. Dynamics of cluster expansion for a two-cluster system at I = 10^{20} W/cm^2 when (from left to right) t = 0 fs, t = 50 fs, t = 100 fs and t = 150 fs. The ions are depicted in yellow and red and the electrons in blue and green. The laser pulse is plane polarised in the x-axis, propagates along z and is injected from left to right, centred with the simulation box.

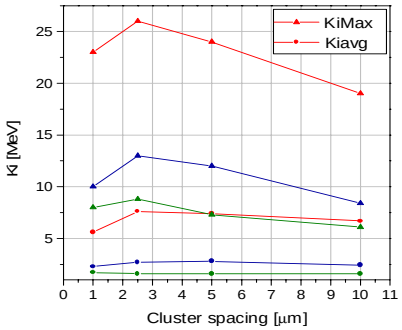

Figure 7. Maximum and maximum average ionic energy as a function of cluster spacing for I = 10^{20} W/cm^2 (red), I = 10^{19} W/cm^2 (blue) and I = 10^{18} W/cm^2 (green). Optimum separation occurs at 2.5 μm.

the parameters. As can be seen from Figure 4 and Figure 5, collimated ion beams of radius ranging from 6.5 mm to 151.5 mm and fluxes from 3.0 x 10^{21} cm^{-2} s^{-1} to 5.6 x 10^{18} cm^{-2} s^{-1} for collection angles of ±5º to ±22.5º, respectively, can be obtained with reasonable magnetic fields, so that the whole system can readily be assembled with commercially available components.

Finally, we have looked at a multi-cluster system. We use PIC-code KARAT in the 2D fully relativistic case to model the interaction of an ultra-short (20 fs gaussian laser pulse), high-intensity (10^{17}- 10^{20} W/cm^2), 800 nm, 10 μm radius gaussian pulse with two 1 μm diameter fully ionized hydrogen plasma spheres bearing n_i = 5 x 10^{21} cm^{-3}. These two clusters are separated vertically (x) with distances of 1 μm, 2.5 μm, 5 μm and 10 μm and the system centre of mass is placed in the centre of the simulation region, now 20 μm x 10 μm (x z) containing 222 x 111 cells.

Although the explosion mechanism does not differ significantly from the single-cluster case (Figure 6) a careful look at the ionic energy spectra indicates that cluster separation plays a relevant role in the maximum of the energy distribution and has a contribution to the average energy of the ions as shown in Figure 7. For large separation distances the presence of a second cluster has little effect on the energy distribution of both ion species; yet, as the spacing decreases, after electron separation from both cluster cores, a larger density of ions will be present in the inter-cluster region, which will enhance ionic repulsion. If the distance between the cores is too small, however, a larger number of electrons will stay within the cluster system, instead of being pushed from the cluster core by the laser pulse; as a consequence, the net positive charge build up will be less efficient and electrostatic repulsion between neighboring ions will decrease resulting in a lowering of both the maximum and the average of the ionic energy spectrum.

Conclusions

In conclusion, we have studied the interaction of an ultra-short high intensity laser pulse with a cluster. For our parameters, Coulombic explosion is the mechanism responsible for cluster expansion and with increasing laser intensity, the expansion approaches the pure electrostatic repulsion case, when all electrons are removed from the cluster core. We have investigated the spatial distributions and energy of the ejected ions and found that the particles have typical energies of 7.5 and 3 MeV, for hydrogen in 2D and 3D respectively, 33 MeV for Ar^{9+} and 42 MeV for Ar^{n+} at the highest intensities used, and, in the tail of the energy distribution function, for 10^{20} W/cm^2, particles with energies up to 10 MeV, 7 MeV, 130 MeV and 210 MeV, respectively, are generated. The presence of a second cluster can influence the final ionic energies, which can be increased by choosing appropriate inter-cluster distances. The possibility of manufacturing a high-current, high-energy collimated ion beam source via laser-cluster interaction is also discussed. By using standard off-the-shelf components it is possible to obtain a 3 MeV, 6.5 mm radius parallel ion beam of around 100 fs pulse duration with peak fluxes of 3.0 x 10^{21} cm^{-2} s^{-1} and peak currents as high as 1.4 kA.

M. Eloy and R. Azambuja are supported by FCT/PRAXIS XXI grants, contracts PRAXIS XXI/BD/9010/96 and PRAXIS XXI/BD/11495/97 respectively.

References

1. T. Ditmire, E. Springate, J.W.G. Tisch, Y.L. Shao, M.B. Mason, N. Hay, J.P. Marangos, M.H.R. Hutchinson, Phys. Rev. A 57 (1998) 369;

2. M. Lezius, S. Dobosz, D. Normand and M. Schmidt, Phys. Rev. Lett. 80 (1998) 261;

3. McPherson, B.D. Thomson, A.B. Borisov, K. Boyer and C.K. Rhodes, Nature 370 (1994) 631;

4. T.D. Donnelly, T. Ditmire, K. Neuman, M.D. Perry, R.W. Falcone, Phys. Rev. Lett. 76 (1996) 2472

5. T. Ditmire, R.A. Smith and M.H.R. Hutchinson, Opt. Lett. 23 (1998) 322;

6. T. Ditmire, J. Zweiback, V.P. Yanovsky, T.E. Cowan, G. Hays, K.B. Wharton, Nature 398 (1999) 489;

7. L. Poth and A.W. Castleman Jr., J. Phys. Chem. A 102 (1998) 4075;

8. T. Ditmire, Phys. Rev. A. 57 (1998) R4049;

9. M. Brewczyk, C.W. Clark, M. Lewenstein and K. Rzazewski, Phys. Rev. Lett. 80 (1998) 1857;

10. M.V. Ammosov, N.B. Delone and V.P. Krainov, Zh. Eksp. Teor. Fiz. 91 (1986) 2008 [Sov. Phys. JETP 64 (1986)1191] ;

11. M. Eloy, R. Azambuja, J.T. Mendonca and R. Bingham, Interaction of ultra-short high intensity laser pulses with atomic clusters, submitted for publication;

12. H. Wollnick, Optics of Charged Particles, Academic Press Inc., Florida, 1987.

Calculations of resonance enhanced multiphoton ionization of argon and neon

M Plummer and C J Noble

CLRC Daresbury Laboratory, Daresbury, Warrington, Cheshire, WA4 4AS, UK

Introduction

We have developed a new version of the R-matrix Floquet method for laser-atom interactions with the aim of treating many-electron inert gases in realistic laser fields. As well as performing various test calculations exploring gauge dependence for both argon and neon in different high frequency fields, we have applied this new code to detailed studies of multiphoton ionization of argon in a KrF laser field which have the possibility of direct experimental verification. These are the first such calculations at high laser intensities (100 TW / cm^2). We are presently studying neon and argon in frequency-doubled Ti-Sapphire laser fields.

The Floquet approach

Although a great deal of work has been performed both experimentally and theoretically on inert gases in laser fields[1], apart from helium the complexity of representing both the aromic systems and the multiphoton effects has limited most ab-initio calculations either to high frequencies which are incompatible with existing lasers or to low field intensities[2]. In contrast for one-electron systems and to some extent for two-electron systems both time-dependent and time-independent approaches have yielded useful results directly comparable with experiment.

For many-electron systems most ab-initio calculations use the time-independent Floquet approach[3] in which the field strength is assumed constant. The field-electron interaction is treated in the dipole approximation giving rise to potential terms which are periodic in time. This periodicity allows the time-dependent Schrödinger equation to be recast as a time-independent eigenvalue problem by expanding the wave function as a Fourier series multiplied by an overall phase factor $\exp(-iEt)$. The complex quasienergies E correspond to field-atom states of the system, called Floquet states. The imaginary part of E may be written as $(-\Gamma/2)$ with Γ the ionization rate of the state in atomic units (all states are resonances with finite lifetimes).

If a laser pulse may be represented as a dipole field of frequency ω with a relatively slowly varying amplitude then the wave function at any time may be written as a superposition of Floquet states. If the amplitude varies adiabatically then the wavefunction may be well represented by a single Floquet state corresponding to the initial atomic state in the field-free limit. Trajectories of Floquet quasienergies corresponding to different field-free states may be calculated as frequency and intensity are varied. Avoided crossings between the Floquet states are of particular interest as at these points the atomic character of the two states is exchanged if the crossing is passed adiabatically. If the field is weak the crossings represent two perturbed atomic states differing in energy by an integral number of photons (note that E is defined modulo ω).

Our calculations

The work which has been undertaken is described in three publications[2,4,6]. The R-matrix Floquet approach introduced by Burke *et al*[6] takes advantage of the fact that for single ionization all but one electron will remain close to the nucleus (forming the 'target' ion) and many-electron effects are restricted to a sphere centred on the nucleus. In this internal region the Floquet Hamiltonian is diagonalized on an antisymmetrized basis of functions using a configuration interaction expansion. For argon and neon the inner filled electronic shells are frozen leaving eight active electrons. Floquet calculations require combininations of different $LS\pi$ symmetries with dipole mixing terms for each value of the Floquet-Fourier parameter n, leading to very large matrices. The region outside the sphere is treated as a one-electron exchange-free multi-channel problem.

Our new code contains significant improvements compared to earlier work[6,7] which allow much larger problems to be treated efficiently and includes a new variational radial basis[4]. We have shown that in calculations which do not have an effectively complete description of the 'target' ion the use of the velocity gauge in the inner region may introduce serious inaccuracies[2].

New results have been obtained[5] for argon in a KrF laser field for intensties up to 100 TW / cm^2. We find a series of resonance enhanced multiphoton ionization peaks as the intensity increases and the 'ground' Floquet state interacts with 'excited' Floquet states. There is a significant increase in the ionization rate around 100 TW / cm^2. Experimental verification of these theoretical predictions is now required.

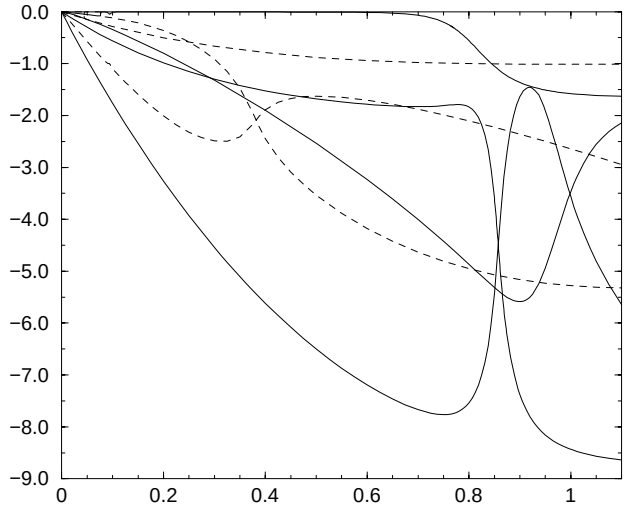

Figure 1. Imaginary parts of quasienergies (0.0001 au) versus intensity (units of 100 TW / cm^2). The solid lines show the ground state quasi-energy and others which interact with it.

References

1. C J Joachain, M Dörr and N J Kylstra
Adv. At. Mol. Phys., 42 226, (2000)

2. M Plummer and C J Noble
Proceedings of the Eighth International Conference on Multiphoton Processes, AIP Publishing (2000)

3. J H Shirley
Phys. Rev., B138 979 (1965)

4. M Plummer and C J Noble
J. Phys. B, 32 L345 (1999)

5. M Plummer and C J Noble
J. Phys. B, submitted (2000)

6. P G Burke, P Francken and C J Joachain
J. Phys. B, 24 761 (1991)

7. M Dörr, M Terao-Dunseath, J Purvis, C J Noble, P G Burke and C J Joachain
J. Phys. B, 25 2809 (1992)

Atoms, Ions and Molecules in Intense Laser Fields

D H Glass, H W van der Hart, P G Burke

Department of Applied Mathematics and Theoretical Physics, The Queen's University of Belfast, Belfast, BT7 1NN, UK

J Colgan

Department of Physics, Auburn University, AL 326830, USA

Main contact email address: *D.H.Glass@qub.ac.uk*

Introduction

Recently there has been substantial interest in the interaction of intense laser fields with molecules. While many experiments have been carried out on complex molecules, much of the theoretical work has focused on the H_2^+ ion. For this reason the R-matrix Floquet theory of multiphoton processes[1)] and the associated computer programs have been extended to treat a general diatomic molecule in the presence of an intense laser field[2)]. In the present report results are presented for H_2 at experimentally accessible laser frequencies.

Another area of interest is the study of non-linear optics using x-ray lasers. A four-wave mixing scheme has been investigated experimentally[3)] where two x-ray photons are absorbed along with an optical photon resulting in the emission of an x-ray photon which is close to the second harmonic of the initial x-rays. A theoretical study of this process is underway and preliminary results for the first stage are given below.

Finally, ionization rates are presented for Mg which, like the x-ray study, look at photoionization from excited states, but at much lower frequencies. This work emphasizes the contrast between ionization of the ground state and excited states.

Four-Photon Ionization of H_2

In this work calculations have been carried out in the fixed nuclei approximation and the laser is taken to be linearly polarized with the molecule aligned along the polarization direction, which is the case of most interest for light molecules. Results are presented for ejection of a single electron of H_2 by four-photon absorption in the approximation where a single state (the H_2^+ ($^2\Sigma_g^+$) state) is used to represent the residual molecular ion.

The potential curves for H_2 are shown in Figure 1. It should be noted that the calculations were carried out at the internuclear separation of H_2 of 1.4 au and frequencies were considered where intermediate three-photon resonances with excited bound states occur.

In Figure 2 the ionization rate is shown as a function of the laser frequency for two different intensities. At each intensity the cross marks the threshold frequency for four-photon ionization. As the frequency increases the laser sweeps through a series of resonances converging to the H_2^+ ($^2\Sigma_g^+$) ground state of the residual ion and in Figure 2 the first three of these resonances are shown. The rate is enhanced by several orders of magnitude at the resonances and as the intensity increases the frequency range over which this enhancement occurs is broadened.

Furthermore, the position of the resonances shifts and so, for example, the KrF laser frequency that is almost resonant with the second excited state at 10^{13} Wcm^{-2} is non-resonant at 3 x 10^{13} Wcm^{-2}. These shifts can be explained by the fact that the ionization threshold and the energies of the excited states are increased by approximately the ponderomotive energy in the presence of the laser field. The influence on these effects for similar frequencies and intensities have been studied in detail in helium[4)] and it is expected that many of the same features will be found in the molecular case. In particular, it can be predicted that the third harmonic of the Ti:Sapphire laser will become resonant with the lowest resonance at an intensity of about 8 x 10^{13} Wcm^{-2} while an intensity of about 1.5 x 10^{14} Wcm^{-2} is required to bring about the same effect for the KrF laser.

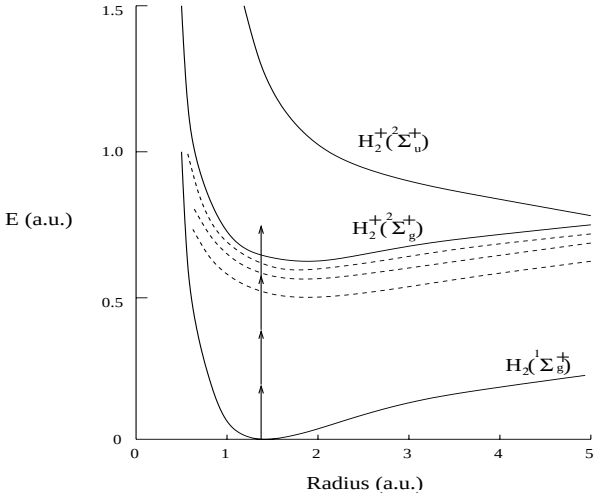

Figure 1. Potential curves for H_2.

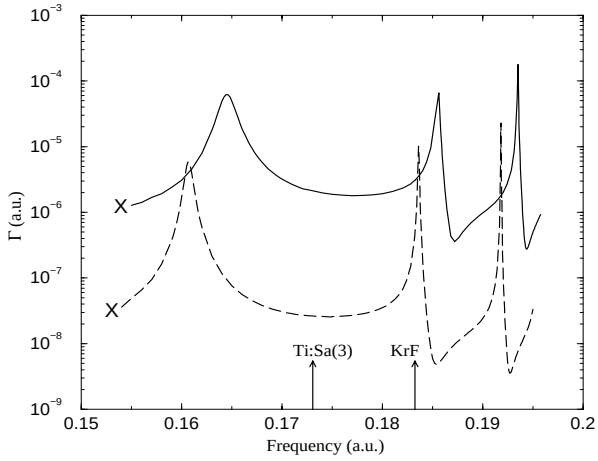

Figure 2. Ionization rate against laser frequency for intensities of 10^{13} Wcm^{-2} (dashed line) and 3 x 10^{13} Wcm^{-2} (solid line). The crosses mark the threshold for four-photon ionization and the arrows indicate the frequencies of the KrF laser and the 3rd harmonic of the Ti:Sapphire laser.

X-ray Laser Interactions with Positive Ions

Results have recently been obtained for multiphoton transitions in Na-like K, which provide the first step in the investigation of four-wave mixing. One advantage in the present approach is that one and two-photon transitions from low-lying bound states to higher states can be studied in such a way that the photoionization of the higher state is explicitly taken into account. Na-like K provides a good starting point since it has

formed the basis of earlier studies[5]. In the present work Hartree-Fock orbitals have been used to describe the system and spin-orbit effects have not been included.

Figure 3 gives the energy level diagram for the system and shows the two processes that are considered. The main focus is on the three-photon detachment of an electron from the 3p ^{2}P state of K^{8+}. This proceeds by three intermediate resonances due to two-photon excitations of the 7p ^{2}P and 7f ^{2}F states and single-photon excitation of the 4s ^{2}S state. However, since three-photon detachment is strongly mixed with two-photon detachment from the 4s ^{2}S state at a certain frequency, this process is also considered.

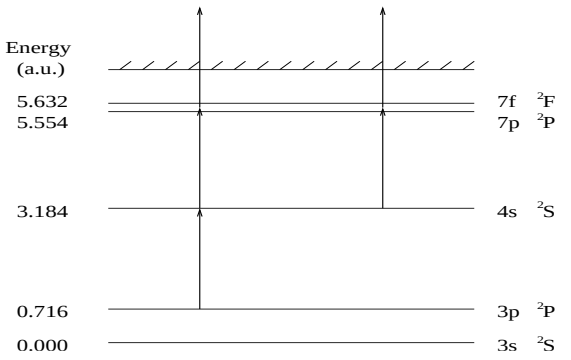

Figure 3. Energy level diagram for K^{8+}.

Preliminary results are presented in Figure 4 for a laser intensity of 10^{14} Wcm^{-2}. At the lowest frequency shown the solid line gives the detachment rate from the 3p ^{2}P state and the dashed line the rate from the 4s ^{2}S state. A resonance with the 7p ^{2}P state occurs with the former at a frequency of 2.42 au and with the later at 2.37 au. This results in an increase in the rate from the 3p ^{2}P state of several orders of magnitude.

There is a resonance between the 4s ^{2}S and 7f ^{2}F states at a frequency of 2.45 au and between the 3p ^{2}P and 7f ^{2}F states at a frequency of 2.46 au. Finally, an interaction occurs between the 3p ^{2}P and 4s ^{2}S states at a frequency of 2.47 au. At the highest frequencies shown the states have exchanged character so that now the dashed line represents the rate from the 3p ^{2}P state.

It is hoped that this work can be extended in the future by including a second laser to investigate the transition between the 7p ^{2}P and 7s ^{2}S states.

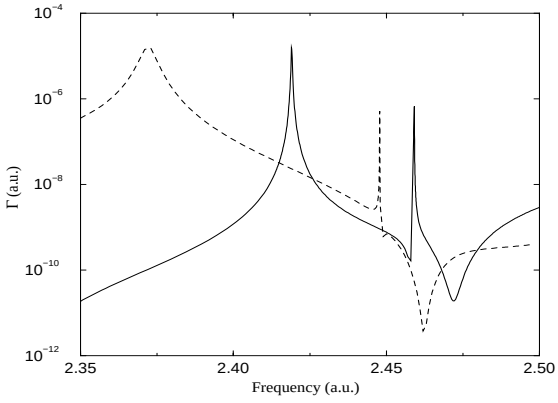

Figure 4. Ionization rates for the 3p ^{2}P (solid line) and 4s ^{2}S (dashed line) states of K^{8+}. At a frequency of 2.47 au the states exchange character.

Multiphoton Ionization of Mg

The Mg atom has been used widely to investigate the properties of atoms embedded in strong laser fields. Previously, the R-matrix Floquet approach has been applied to study the Mg atom in single and two-colour laser fields[6] and the results obtained have been compared to experimental findings[7]. Presently, our interest focuses on the multiphoton properties of excited states of Mg at the Nd-YAG frequency. At this frequency, three photons are required to detach an electron from the 3s3p ^{1}P state of Mg. Due to the presence of the Rydberg series, intermediate resonances may have a significant influence on the ionization rates. In addition, most investigations of the influence of a strong laser field on the interactions between Rydberg states have been carried out for frequencies which present experimental difficulties.

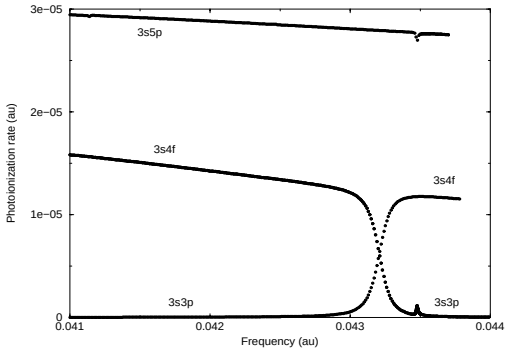

Figure 5. Ionization rates for three states of Mg at an intensity of 10^{10} Wcm^{-2}.

In Figure 5, we show photoionization rates for three states of Mg, three-photon ionization rates for 3s3p ^{1}P, and single-photon ionization rates for 3s4f ^{1}F and 3s5p ^{1}P for frequencies around the Nd-YAG frequency. The intensity of the laser was set to 10^{10} Wcm^{-2}. At a frequency of 0.0432 au, the photoionization rate from the 3s3p ^{1}P state is enhanced by the two-photon resonance with the 3s4f ^{1}F state, while at a frequency of 0.0435 au, the photoionization rate of the 3s3p ^{1}P state is enhanced by a resonance with the 3s5p ^{1}P state. It is clearly seen that the two-photon interaction between the 3s3p ^{1}P and 3s4f ^{1}F states is stronger than the interaction between the 3s3p ^{1}P and the 3s5p ^{1}P states. In fact, the three-photon ionization rate for the 3s3p ^{1}P state is dominated by the interaction with the 3s4f ^{1}F state over a wide frequency range.

The present results indicate that the presence of Rydberg series has a strong influence on the multiphoton ionization rates of excited states. The large number of Rydberg states leads to a large probability that the ionization is resonantly enhanced at each intermediate stage. This behaviour is in contrast to the multiphoton ionization behaviour of ground states, for which generally several photons need to be absorbed in order to reach the lowest excited state.

References

1. P G Burke, P Francken and C J Joachain, J. Phys. B 24, 761, (1991)
2. P G Burke, J Colgan, D H Glass and K Higgins, J. Phys. B 33, 143, (2000)
3. R M N O'Rourke et al, RAL-TR-1999-062, 52, (1999)
4. D H Glass and P G Burke, J. Phys. B 33, 407, (2000)
5. M H Muendel and P L Hagelstein, Phys. Rev. A 44, 7573, (1991)
6. N J Kylstra et al, J. Phys. B 31, 3089, (1998)
7. N E Karapanagioti et al, Phys. Rev. Lett. 74, 2431, (1995)

A Thomson Scattering Post-Processor for the MEDUSA Hydrocode

J Hawreliak, J S Wark

Department of Physics, Clarendon Laboratory, University of Oxford, Parks Road, Oxford, OX1 3PU

Main contact email address: *j.hawreliak@physics.ox.ac.uk*

Introduction

As computational power increases simulation codes have seemed to become more than just models, to almost verge on 'virtual experiments'. In these virtual experiments it has become common to add virtual diagnostics. This is an important step in simulation work because it provides a direct comparison with experimental data, gives direct insight into the physics of the diagnostic and its interaction with the plasma and aids in the development of analysis tools specific to that particular diagnostic.

Thomson scattering is a very powerful diagnostic, in principle giving simultaneous information on the density, temperature, heat flow and velocity of the plasma through a method which is relatively non-perturbative. With today's high frequency and high power lasers it is possible to probe small relatively dense regions of the plasma that have not been directly diagnosed in the past. Coupling the output of the spectrometer to a streak camera gives this information as a function of time.

Here we describe how the output from a MEDUSA hydrocode simulation run is fed into a Thomson Scattering post-processor to produce images similar to those which would be collected experimentally by a streak camera. The post-processor is also being modified to take experimental images, and output predicted time-dependent plasma parameters.

Outline of Basic Theory

The scattered radiation from the plasma can be determined by looking at the fields radiated by the free electrons under the acceleration of the electric field of the probing laser beam. The electron will have an initial velocity governed by the micro fields of the plasma in the vicinity of the electron. This will add a first order effect to the phase of the radiated field. The electron is assumed to be non-relativistic at all times so we can ignore the Lorentz force from the magnetic field of the radiation. Also the amplitude of the electron oscillation is assumed to be much smaller then the wavelength of emitted light so that the dipole approximation can be used.

A Fourier analysis of the acceleration will contain frequencies characteristic of the electron motion described by $\mathbf{r_j}(t)$ and a component at ω_0 from the probing radiation.

$$\vec{E} = \vec{E}_0 \cos(\vec{k}_0 \cdot r_j(t) - \omega_0 t) \tag{1}$$

$$\ddot{\vec{r}} = -\left(\frac{e}{m}\right)\vec{E}_0 \cos\left(\vec{k}_0 \cdot \vec{r}_j(t) - \omega_0 t\right) \tag{2}$$

These components will translate into similar components in the radiated spectrum from the electron. Using Fourier analysis to break the electron motion into a series of waves allows the physical interpretation of a three wave interaction. Having the laser wave, $\mathbf{k_0}$, scatter off the plasma waves , **k**, into the direction of the collected radiation $\vec{k}_S = \frac{\omega}{c}\frac{\vec{R}}{|R|}$, where **R** is the direction of the detector .

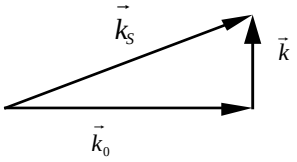

Figure 1. Vector diagram of the scattering of the waves in the plasma.

From this we can derive a scattering equation for the spectrum of the scattered waves as

$$I(\vec{k},\omega)d\omega d\Omega = NI_0\sigma(\vec{k},\omega)d\omega d\Omega$$

$$\sigma(\vec{k},\omega) = \sigma_T S(\vec{k},\omega)$$

$$\sigma_T = \left(\frac{e^2}{mc^2}\right)^2 \sin^2\beta \tag{3}$$

$$S(k,\omega) = \frac{1}{2\pi N}\int_{-\infty}^{\infty} e^{i\omega\tau}\sum_{j,l}^{N}\cos[\vec{k}\cdot\{\vec{r}_l(t) - \vec{r}_j(t+\tau)\} - \omega_0\tau]d\tau$$

The scattered intensity, *I(k,w)* is a function of the number of electrons *N*, the intensity of incoming radiation I_0 and the dynamic form factor, *S*, which takes into account the density fluctuations within the plasma. Using a dressed test particle and the Boltzmann equation for the electron distribution function an equation for the dynamic form factor can be obtained in terms of macroscopic variables of interest in the plasma.

$$S(k,\omega)d\omega =$$

$$\left|\frac{1-G_i(\frac{\omega}{k})}{1-G_e(\frac{\omega}{k})-G_i(\frac{\omega}{k})}\right|^2 F_e(\tfrac{\omega}{k})d\omega + Z\left|\frac{G_e(\frac{\omega}{k})}{1-G_e(\frac{\omega}{k})-G_i(\frac{\omega}{k})}\right|^2 F_i(\tfrac{\omega}{k})d\omega$$

$$G_e = -\alpha^2 W(x_e) \quad , \quad x_e = \frac{\omega}{kv_e}$$

$$G_i = -Z\frac{T_e}{T_i}\alpha^2 W(x_i) \quad , \quad x_i = \frac{\omega}{kv_i} \tag{4}$$

$$\alpha = \frac{1}{k\lambda_D}$$

$$W(x) = 1 - 2xe^{-x^2}\int_0^x e^{p^2}dp - i\pi x e^{-x^2}$$

where F_e and F_i are the distribution functions of the electrons and ions, v_e and v_i are the thermal velocity of the electrons and ions and λ_D is the Debye length. These are simple to program into a computer to obtain the dynamic form factor and hence the scattered spectrum.

Heat Flow

One of the benefits of Thomson scattering is that it gives a measurement of the heat flow within the plasma. The heat flow modifies the electron distribution function. For simplicity we assume here that such flow can be represented by a shift of the electron distribution function with respect to the ions. In this case the scattering cross section can be recovered by replacing

$$x_e \rightarrow x_e - y$$

$$y = \frac{\hat{k}\cdot U}{v_e} \tag{5}$$

where U is the relative velocity between the electron distribution and ion distribution.

MEDUSA gives information on overall heat flow within each Lagrangian cell, but clearly, being a hydrocode, can give no information on the actual form of the distribution function. We thus need to find a simple connection between heat flow and the gross shift in the distribution function described above. In order to do this in a simple way we assume the heat to be carried by the hotter electrons , whilst the cooler electrons at the centre of the distribution travel in the opposite direction so there is no net particle flow.

We assume that the distribution function in the presence of heat flow conserves particles, current and energy. That is to say,

$$f_{noheatflow}(v) \rightarrow f(v) = f_0(v) + \delta f^1(v) + \delta f^2(v) \qquad (6)$$

where the perturbations necessary to be able to meet all of the physical constraints placed on the equations imply

$$\begin{aligned} &\int \delta f^1(v)dv = 0, \int \delta f^2(v)dv = 0 \quad , \text{ particle conservation} \\ &\int vf(v)dv = \int vf_{noheatflow}(v) \quad , \text{ current conservation} \\ &\int v^2 f(v)dv = \int v^2 f_{noheatflow}(v) \quad , \text{ energy conservation} \\ &\int vv^2 f(v)dv = S \quad , \text{ heat flow} \end{aligned} \qquad (7)$$

The three equations require three unknowns, the two scaling factors on the perturbations and the velocity shift of the distribution function U

$$\begin{aligned} f_0(v) &= \frac{N}{v_e\sqrt{\pi}} \exp - \left[\frac{(v-U)^2}{v_e{}^2} \right] \\ \delta f^1(v) &= C_1 \frac{(v-U)}{v_e} f_0 \\ \delta f^2(v) &= C_2 \frac{2(v-U)^2 - v_e^2}{v_e^2} f_0 \end{aligned} \qquad (8)$$

The velocity shift simply reduces to

$$U = -\left(\frac{S}{N}\right)^{\frac{1}{3}} \qquad (9)$$

As expected the velocity shift of the distribution function is in the opposite direction to that of the heat flow because it represents the return current of cold particles[2]. Figure 2 shows that the distribution function does not deviate significantly from the Maxwellian distribution until the heat flow is about S = .125 N*v_e^3 which is on the order of the heat flow at which Spitzer heat flow is assumed to break down and the free streaming flux limit must be used. In future it would be of interest to investigate the effect of the non-Maxwellian nature of the distribution function on the Thomson spectrum. We emphasize that here we simply take it to be a shifted Maxwellian, with the velocity shift related to the MEDUSA heat flow in the manner described above.

Physical Considerations

There are many possible geometries that can be simulated using MEDUSA. To date the post-processor has been adapted for planar plasma geometry. The Thomson probe beam is assumed to be incident normal to the target surface.

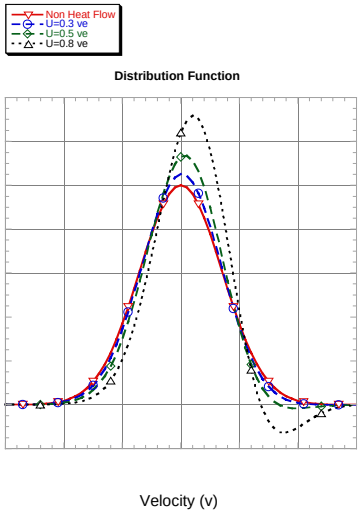

Figure 2. Showing the effect on the distribution function of different heat flows.

A finite spatial cross section of the probe beam is used with a Gaussian intensity distribution. In a similar manner the resolution of the collecting optic is taken into account. Thus the final signal incident upon the spectrometer will contain contributions from various regions of the plasma, each with slightly differing properties and weighting depending on the intensity of the beam at the particular point.

Along the same lines, the post-processor also takes into account the finite spectrometer slit width, and the streak camera's finite resolution by convolving the simulated streak image with the appropriate function that describes the dispersion of the system.

Results

We show here the simulated Thomson scattering streak image of a plasma created by irradiation of an Aluminum target with a 1053 nm beam, contained in a pulse of duration 1.0 nsec, at a peak irradiance of 1.4 x 10^{14} Wcm^{-2}. The plasma was assumed to be probed at a distance of 300 μm from the original target surface, with the probe beam operating at the 4th harmonic, 263.3 nm. The simulated streak image is binned into 512 bins in the spectra direction. The image is convolved with a gaussian function which would have an effect equivalent to the 200 μm x 100 μm slits in front of the spectrometer and streak camera.

The important time-dependent hydrodynamic parameters (which in principle may be extracted from Thomson scattering data) output by MEDUSA are shown in the graphs below (see Figures 3-6). Also shown is the predicted experimental streak image (Figure 7). The manner in which the hydrodynamics influences the observed time-dependent spectrum is readily apparent. For example, the decrease in plasma velocity after the initial expansion is evinced by the approach of the lines to the location of λ_0 (263.3 nm). Similarly, the late-time decrease in the temperature of the electrons and the ions manifests itself by the decreasing separation of the two peaks which comprise the ion feature. The electron density dependence may be inferred from the time-dependence of the overall scattered intensity. The heat flow exhibits itself as the degree of asymmetry in the intensity of the peaks. The success of the post-processor can be judged by the way in which is has proved extremely successful in modeling experimental data.[3]

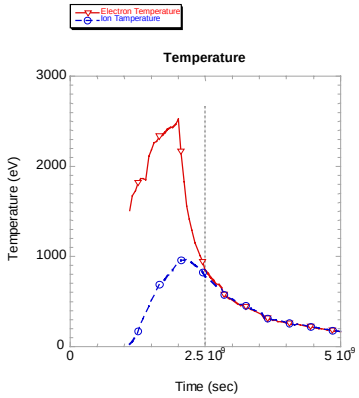

Figure 3. Ion and electron temperature at the centre of the probe beam from MEDUSA.

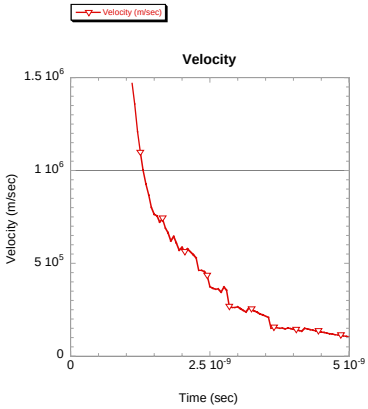

Figure 4. Velocity of the plasma at the centre of the probe beam from MEDUSA.

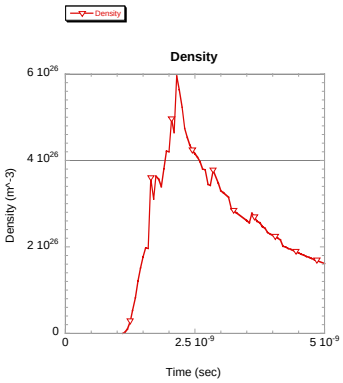

Figure 5. Density of the plasma at the centre of the probe beam from MEDUSA.

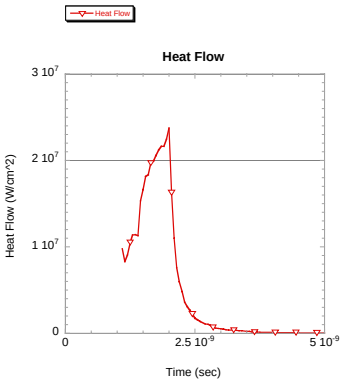

Figure 6. Heat flow of the plasma at the centre of the probe beam from MEDUSA.

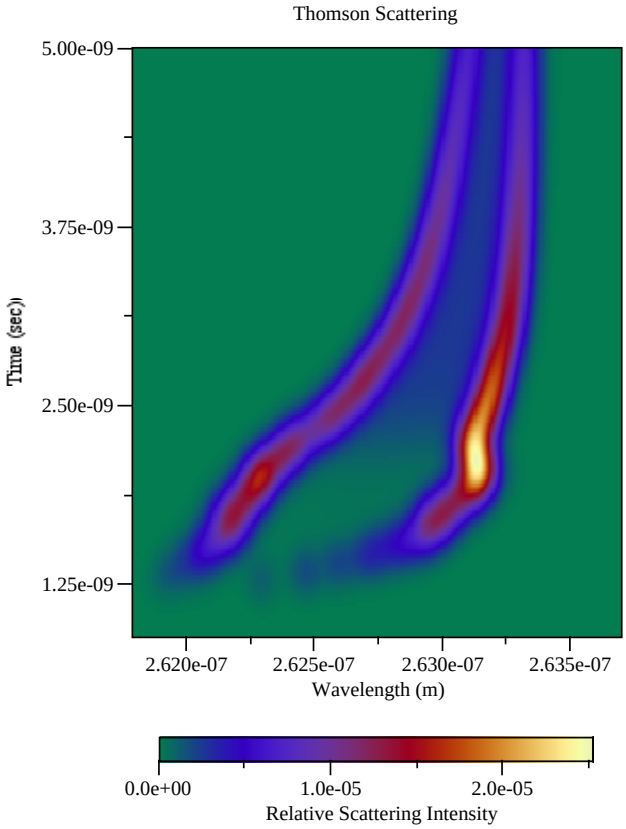

Figure 7. The simulated Thomson scattering streak image of a plasma created in MEDUSA.

Conclusion

We have written a Thomson-scattering post-processor for the MEDUSA hydrocode. The post-processor is designed to simulate, as far as is possible, experimental data in that it takes into account such details as the spatial distribution of the probe beam, and the finite resolution of the collection system. As is shown elsewhere within this volume, the code can model observed experimental data extremely successfully. The code is now being further adapted to be used as a data analysis tool. In this mode it will be possible to input an experimental image from a streak camera in TIFF format and the program with the calibrated detector parameters will output the associated density, temperature, velocity and heat flow as a function of time.

References

1. Evans D., Rep. Prog. Phys. 32,207-271 (1969)
2. Key M., SUSSP , 219 (1979)
3. J Hawreliak *et al* (Ibid)

Non-Uniformities in Planar Foil Expansion

R G Evans, N C Woolsey

Physics Department, University of York, Heslington, York, YO10 5DD, UK

Main contact email address: *r.g.evans@physics.org*

Introduction

The effects of non-uniform illumination of IFE pellets[1–4] has been well studied in the context of non-uniform drive pressure and in driving fluid instabilities such as Rayleigh-Taylor[5] and Richtmeyer-Meshkov. Essentially the plasma blow-off produces an atmosphere which can smooth out non-uniform illumination at later times but 'imprinting' at early times remains a problem.

Throughout this time there has been an implicit assumption that the effects of non-uniform illumination will be symmetrised in the expanding plasma blow-off and since this region is usually of little interest there has been no real experimental investigation of the symmetry of blow-off apart from some early optical probe experiments that found prominent features in high Z targets[6-8].

With the recent interest in the application of laser irradiated plasmas to produce conditions of interest in astrophysical applications there has emerged a need for more careful study of the assumed uniformity of the very low density plasma blow-off. We report here on purely numerical simulations of the low density plasma hydrodynamics triggered by the experimental observation of strong modulation of the low density plasma produced by an exploding thin foil.

The Basic Computer Model

Our computer model is the 2-D hydrodynamic code *POLLUX* [9] which follows the absorption of laser energy and the subsequent hydrodynamic motion of an ideal gas in cylindrical r-z geometry with the laser incident along the negative z axis. The initial condition of the simulation is shown in Figure 1.

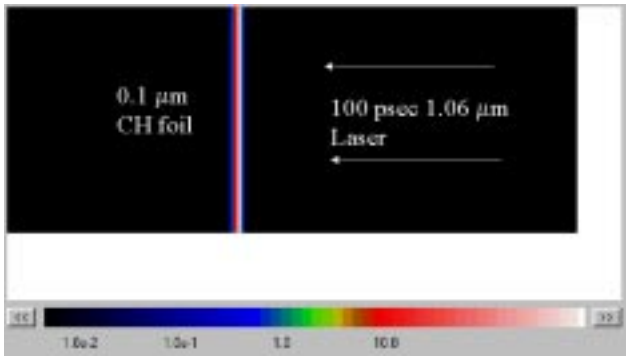

Figure 1. Initial conditions for the POLLUX simulations. The colour bar shows density and the units are multiples of critical density.

The numerical mesh is 250 (z) by 100 (r) cells covering an initial simulation region of 125 μm by 100 μm. The laser pulse rises in 70 ps to a peak intensity of 10^{14} Wcm^{-2} and the radial laser profile is spatially modulated in the form (1.0 + 0.5* rand ( )) where rand ( ) is a random number between 0.0 and 1.0. This gives an RMS deviation of intensity of 1/6. The same 'random' radial profile is used for all the runs and the radial beam profile is assumed constant in time. In order to follow the long term evolution of the expanding plasma the mesh expands in the z direction only at a constant velocity from 50 ps onwards.

The computer runs include a variable laser pre-pulse occurring 210 ps before the main pulse and there is an optional very simple model of optically thin radiative losses with a black body limit.

Simulations of the Experimental Conditions

Under the conditions of the experiment of Woolsey et al [11](ie no pre-pulse) we have run the model for simulation times up to 600 ps following the density to just below 1% of critical density. Figures 2a and 2b show the density contours during the evolution of the plasma and the surprising result is that the effect of the non-uniform illumination persists throughout the planar expansion of the plasma. The results with and without the effects of the radiative losses are visually very similar.

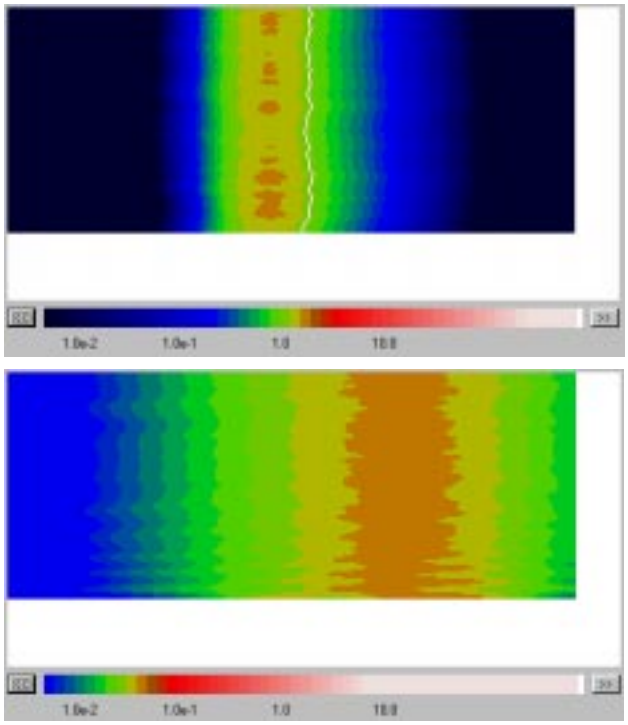

Figure 2. Density contours at (a) the peak of the laser pulse and (b) 750 ps into the simulation. Note the shift of the colour palette between the two diagrams. In (b) the mesh has expanded from its initial 125 μm to about 325 μm in the z direction.

Discussion

These results are at first sight counter intuitive in that one would expect the expanding plasma to become more uniform as time progresses. However this intuition is only partially correct inasmuch as the expansion can symmetrise only when it becomes spherical and there is a 'phase mixing' of the expansion from different apparent sources. The situation in the expanding plasma is fundamentally different from the 'cloudy day effect' that symmetrises the ablation pressure produced by non-uniform deposition of laser energy at lower densities. The cloudy day effect relies on thermal conduction in a large temperature gradient which is a strongly dissipative process while the expanding low density plasma supports non-dissipative isothermal sound waves since the low density high temperature plasma has an extremely high diffusivity. The un-damped sound waves can only be averaged out by the 'phase-mixing' effects of the ultimately spherical expansion.

Amelioration of the non-uniform expansion

Given the above argument on the non-dissipative nature of the sound waves responsible for the flow non-uniformity, the only

sure way to produce a uniform expanding plasma is to wait until the expansion has become spherical. This may not be useful if the aim is to collide two such expanding plasmas to produce a planar shock wave and some other mechanisms require to be investigated.

Improving the uniformity of the laser illumination will have practical limits and the use of hohlraum drive to explode the foil would be beneficial but has an efficiency penalty. Within the computer simulations we have investigated the effects of a laser prepulse since this will introduce some of the benefits of 'cloudy day' smoothing in the low density plasma which is produced by the pre-pulse before the main pulse heating arrives.

We have simulated a pre-pulse arriving 210 ps before the main pulse and with power levels of 5%, 10% and 15% of the main pulse. Qualitatively there is a marked improvement in the uniformity of the expansion but within the limited time window of the simulation the plasma has not expanded as far as in the runs with no pre-pulse. Figure 3 shows the comparison with and without the 5% prepulse at the same time after the main heating beam.

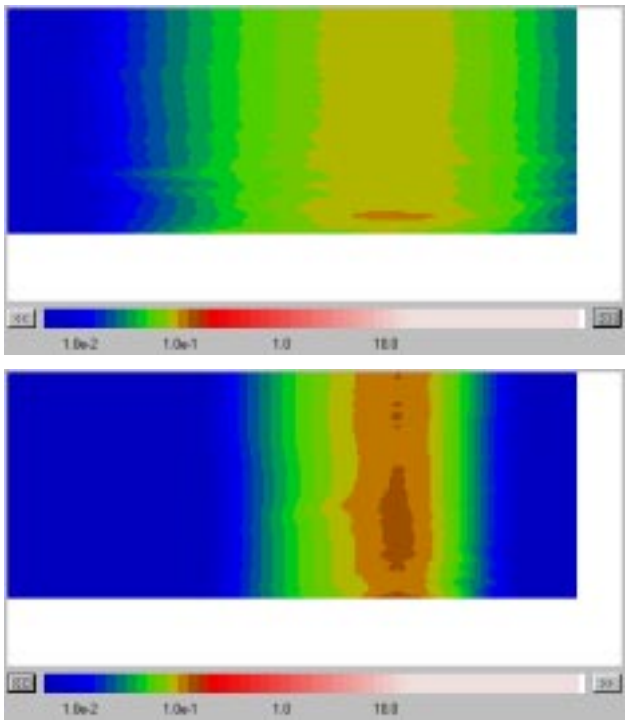

Figure 3. Simulations (a) with no pre-pulse and (b) with 5% pre-pulse at the same time after the main heating pulse. In (a) the mesh has expanded to 225 μm and in (b) to 285 μm.

Radiation Loss Effects

In contrast to the results with no pre-pulse we find that the pre-pulse simulations are sensitive to the inclusion of radiation losses from the plasma which can drive instabilities in the plasma[10] due to the quadratic dependence of radiated power on density. The effects of radiation would not normally be expected to be large in a low Z plasma such as the CH target simulated here but in the peculiar conditions of these expanding thin foils we observe an amplification of the non-uniformities which we believe to be real but which merits further and more careful study. The case of the 10% pre-pulse with radiative losses included is shown in Figure 4.

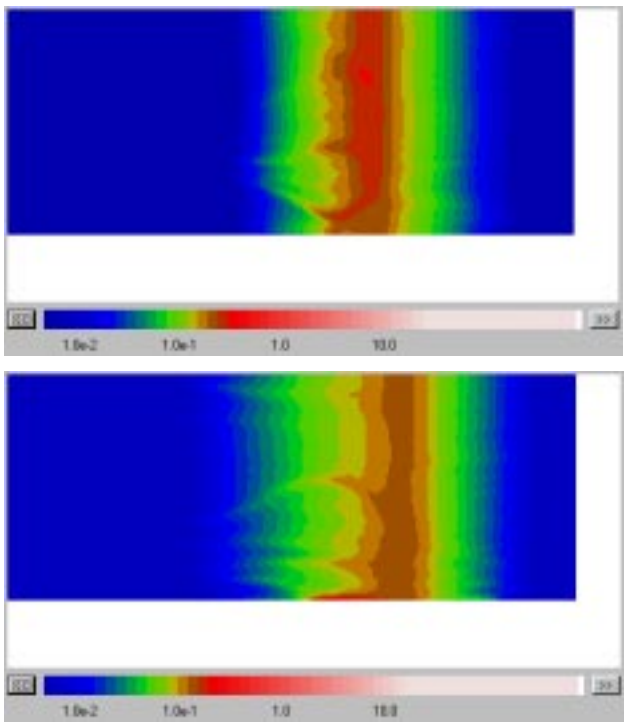

Figure 4. Simulation with a 10% pre-pulse and radiative losses included. (a) at 200 ps after the peak of the heating pulse and (b) 400 ps after the peak.

References

1. J H Gardner and S E Bodner
   Phys. Rev. Lett. 49, 1137, (1981)
2. R G Evans, A J Bennett and G J Pert
   J. Phys. D: Appl. Phys, 15, 1673, (1982)
3. R G Evans
   Lasers and Particle Beams, 3, 3, 273, (1985)
4. A J Cole, J D Kilkenny, P T Rumsby, R G Evans, M H Key,
   J. Phys. D: Appl. Phys., 15, 1869, (1982)
5. R G Evans, A J Bennett and G J Pert
   Phys. Rev. Lett., 49, 22, 1639, (1982)
6. T Mochizuki, T Yabe, K Mima, K Yoshikawa, H Azechi, A Kikuchi and C Yamanaka
   Jap. J. Appl. Phys., 19, 10, L645
7. M J Herbst, J A Stamper, R R Whitlock, R H Lehmberg, B H Ripin
   Phys. Rev. Lett., 46, 328, (1981)
8. O Willi, P T Rumsby, C Hooker, A Raven and Z Q Lin
   Opt. Commun., 41, 110, (1982)
9. G J Pert
   J. Comput. Phys., 43, 111, (1981)
10. R G Evans
    Plasma Phys. Control Fusion, 27, 7, 751, (1985)
11. N C Woolsey et al, Central Laser Facility Annual Report 1999/2000, pg 42

Extraction of Hugoniot information from time resolved x-ray diffraction data

A Loveridge, J S Wark

Sub-department of Atomic & Laser Physics, University of Oxford, Clarendon Laboratory, Parks Road, Oxford, OX1 3PU, UK

D H Kalantar

Lawrence Livermore National Laboratory, Livermore, California 94550, USA.

Main contact email address: *loveridg@ox.compsoc.net*

Introduction

Time resolved x-ray diffraction from shocked crystals is a powerful diagnostic of shock compression within a crystal lattice. It allows the non-destructive probing of the internal motion of the lattice planes at an atomistic level whilst the shock is in motion within the crystal. Since the first observation of lattice compression under shock loading by Johnson *et al*,[1] to the recent efforts of *eg.* Kalantar *et al*.,[2] much progress has been made. However, whilst such experimental efforts supply a great deal in the way of qualitative information about the material under examination, the extraction of quantitative information from time resolved x-ray diffraction data is rarely attempted. This is increasingly unsatisfactory, as the development of the technique of nonequilibrium molecular dynamics to simulate shock drive processes has now reached a stage where the interactions of 10 million shock impacted atoms can be predicted and theoretically examined.[3] A numerical technique that allows the extraction of quantitative information from time resolved x-ray diffraction data is the subject of this paper.

Experiment

A typical time resolved x-ray diffraction experiment is illustrated in Figure 1. A crystal is impacted by some pressure source (which in the present case is hohlraum-driven) and causes a shock to propagate within the crystal. Synchronous with the shock drive, a monochromatic point source of x-rays irradiates the opposite surface of the crystal. The location of the point source has been chosen such that the x-rays it generates diffract off some planes of interest within the crystal. The shock causes the lattice spacing of the crystal to change, altering the angle at which it diffracts the x-rays.

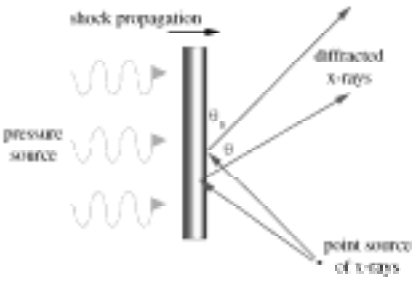

Figure 1. Schematic diagram of a typical time resolved x-ray diffraction experiment.

The example of time resolved x-ray diffraction data that we are going to use in this paper is given in Figure 2. This figure shows data taken on the Nova laser facility, LLNL, by Kalantar and co-workers. Diffraction is from the (400) planes of a 40 µm thick silicon crystal, using an x-ray wavelength of 1.859 Å.

Analysis

The dynamical theory of x-ray diffraction in crystals is the approach that must be used when perfect, single crystals are being considered. It was developed by Darwin[4] and Ewald,[5] and was modified to take into account the effects of absorption by Prins[6] and von Laue.[7] The theory solves Maxwell's equations in a medium which possesses a complex and periodic dielectric constant under the assumption of an incident and single diffracted electromagnetic wave. The elegance of the numerical technique that is the subject of this paper is that it requires very little in the way of theoretical knowledge. The reader is therefore referred to the many publications on the subject for a more complete description of the dynamical theory.[8]

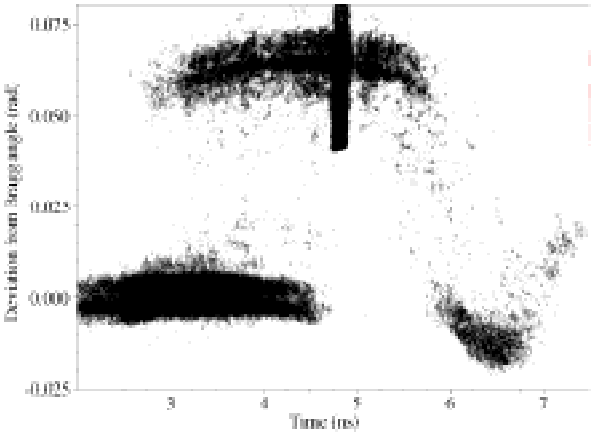

Figure 2. Time resolved x-ray diffraction image.

The theory of x-ray diffraction from shocked crystals was developed by Takagi[9] and Taupin.[10] However, we wish to extract quantitative information about the shock propagation process *without* using these theories. The main motivation for *not* using the Takagi-Taupin theory is that much can be achieved using a much simpler set of working assumptions. The main assumption made is that by the time the shock comes into view in the data it has had time to establish itself and achieve a steady state. This is a reasonable assumption for the data presented in Figure 2, as the x-rays have an attenuation length of 23.89 µm at this wavelength, and so the shock has propagated through nearly half of the crystal before coming into view.

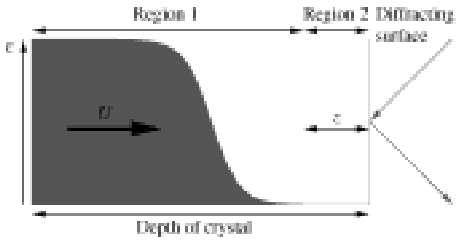

Figure 3. A simple two-region model of the shock propagating within the crystal.

The motivation behind this assumption is that it allows the crystal to be divided into two regions, as illustrated in Figure 3. The foot of the shock front, with Region 1 containing all of the shocked material, and Region 2 containing purely unshocked, virgin, material marks the boundary between the two regions. If we assume that the shock is greater than an absorption length in size, and the form of the shock front is constant in time, then the reflectivity of Region 1 (neglecting for the moment any attenuation in Region 2) must be constant in time also. The reflectivity of the shocked region appears to vary on the time resolved x-ray diffraction image, but that is *entirely* due to the fact that the diffraction is attenuated by a changing amount of

unshocked material, rather than any change in the reflectivity itself. Further, as time progresses, an increasing amount of the virgin material is consumed by the shock, so the thickness of Region 2 decreases, so the reflectivity of the unshocked region will decrease.

In order to proceed, then, we are required to know how we expect the observed integrated reflectivity of diffraction from Regions 1 & 2 to vary with motion of the interface between them. Considering Region 1 first, we can make no assumption about the functional value of the unattenuated reflectivity of Region 1, as we are not considering the effects of strain on the dynamically diffracting crystal lattice. Thus, we can only describe the variation of the integrated reflectivity of diffraction from Region 1 as a function of z by:-

$$R_S^\theta(z) = R_S^\theta(z=0)\exp\left[-2z/\Lambda_A \sin\theta\right] \qquad (1)$$

where Λ_A is the absorption length, θ is the angle of diffraction and $R_S^\theta(z=0)$ is the (unknown) unattenuated integrated reflectivity of Region 1. Region 2 can be considered rather more quantitatively, as it is simply a perfect crystal laminate of thickness *z*. The reflectivity as a function of angle of such a laminate can be calculated [8], and thus the integrated reflectivity of Region 2 can be numerically obtained. However, it would be more convenient if we knew the *analytic* function that provides the integrated reflectivity of a perfect crystal lamina of a given thickness. Thus, we choose to fit a suitable analytic function to such data. The chosen function is:-

$$R_U^\theta(z) = M\tanh Nz(\mu\text{m}) \qquad (2)$$

where M = 1.4642 x 10^{-5} rad and N = 0.37328 µm^{-1}. This function fits the calculated data with a linear correlation coefficient of 0.99989, more than sufficient for us to proceed.

Having obtained analytic functions that describe how we expect the observed integrated reflectivities of Regions 1 & 2 to vary as a function of *z*, we can now proceed with our analysis of the data presented in Figure 2. Since we have no absolute calibration of the crystal reflectivity, we must restrict ourselves to examining the ratio of the integrated reflectivities of the two regions. A parameter which is proportional to the unshocked integrated reflectivity is found by integrating the data between ±0.075 rad, and for the shocked reflectivity integration was over angles >0.075 rad.

The ratios of these parameters are plotted in Figure 4. The function fitted to these data is:-

$$\frac{R_U^\theta}{R_S^\theta} = Q\frac{\tanh N(z_0 - Ut)}{\exp\left[-2(z_0 - Ut)/\Lambda_A \sin\theta\right]} \qquad (3)$$

where $z_0 = z(t=0)$, t is time, U is the shock speed and Q is an unknown constant of proportionality.

A weighted fit performed on these data gives the result:-

Q = 0.55583 ± 0.058363
z_0 = 45.784 ± 2.9221 µm
U = 9.8625 ± 0.58805 µm ns^{-1} (= km s^{-1})

which fits the illustrated data with a reduced χ_ν^2 of 1.1702 and a linear correlation coefficient of 0.99625.

How realistic are these numbers? Firstly, we know that the crystal in which the shock is propagating is 40 µm thick, and this analysis has indicated that the shock was at a depth of ~46 µm at the time of shock initiation. However, in this model a constant shock speed has been assumed, and so no allowance has been made for the acceleration of the shock at the point of initiation. The sound speed along the (100) axis at 25˚C is 8.43322 km s^{-1} ± 0.025%,[11] so the extracted shock speed is physically plausible for an elastic shock wave.

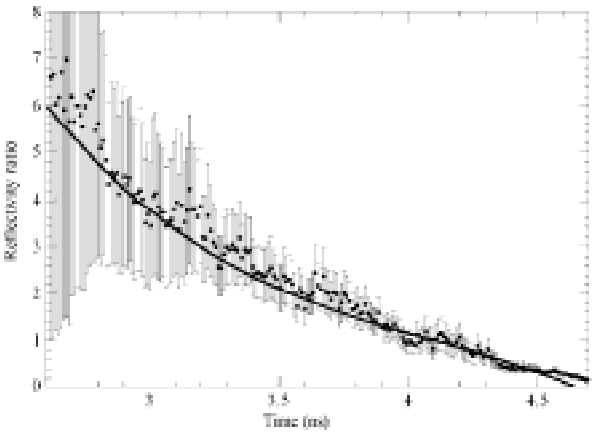

Figure 4. Plot of the ratio of the unshocked to the shocked integrated reflectivities of the data presented in Figure 2.

Development & Conclusion

Conservation of mass, energy and momentum link shock pressure, 3-D compression and shock speed by the equation:-

$$P = \frac{U^2}{V_0}\left(1 - \frac{V_1}{V_0}\right) \qquad (4)$$

where P is the shock pressure and $V_{0,1}$ are the specific volumes of the unshocked and shocked regions respectively. We know the shock speed, so all we need is the shock compression in order to extract the shock pressure. This is achieved by simultaneously recording Laue diffraction patterns from planes perpendicular to the shock front, which provides information on compression in the transverse direction which provides all the additional information we need. Thus, by using equation (4), we can use our shock speed measurement to obtain a measurement of the pressure of the shock, whilst the shock is propagating within the crystal. The shock pressure which results from the above shock speed and the observed 3-D compression is 14.246 ± 1.8645 GPa. This is a unique measurement – we have achieved the extraction of quantitative shock pressure information from time resolved x-ray diffraction data using compression and shock speed as our parameters. In more traditional Hugoniot measurements[12], it is the shock speed and the particle speed that are used as the extraction parameters, so this result, using compression and shock speed, is something which has never previously been achieved.

References

1. Q. Johnson, et al. Nature, 213,1114, 1967.
2. D.H. Kalantar et al. Rev. Sci. Inst., 70, 629, 1999.
3. B.L. Holian & P.S. Lomdahl. Science, 280, 2085, 1998.
4. C.G. Darwin. Phil. Mag., 27, 315 & 675, 1914.
5. P.P. Ewald. Ann. der Physik, 49, 1 & 117, 1916 ; 54, 519, 1917.
6. J.A. Prins. Zeitschr f. Phys., 63, 477, 1930.
7. M. von Laue. Acta Cryst., 2, 106, 1949.
8. W.H. Zachariasen. Theory of x-ray diffraction in crystals. Dover Publications, Inc., New York, U.S.A., 1994.
9. S. Takagi. Acta Cryst., 15, 1311, 1962 ; J. Phys. Soc. Jap., 26,1239, 1969.
10. D. Taupin. Bull. Soc. Franç. Miner Crist., 87 , 469, 1964.
11. H.J. McSkimin & P. Andreatch, Jr. J. Appl. Phys., 35,2161, 1964.
12. W.H. Gust & E.B. Royce. J. Appl. Phys., 45,1897, 1971.

Mechanism of the double ionisation of helium

D G Lappas, P L Knight

Blackett Laboratory, Imperial College of Science, Technology and Medicine , London SW7 2BW, UK

P P Corso

Istituto Nazionale di Fisica della Materia and Dipartimento di Scienze Fisiche ed Astronomiche dell'Università, via Archirafi 36, 90123 Palermo, Italy

Main contact email address: *d.lappas@ic.ac.uk*

Introduction

We present calculations of the double ionisation of the helium atom interacting with an intense and short laser pulse, utilising one-dimensional models. A substantial signature of non-sequential (NS) ionisation is found for all laser wavelengths, from 248 nm to 1064 nm, provided pulses of appropriate duration are employed. The "knee" structure[1)] is found not only for long wavelengths; it is also present in the "multiphoton" short-wavelength regime. The underlying mechanism of the correlated electron ionisation is investigated and discussed. In our model calculations we can easily separate the influence of the laser-electron from the electron-electron interaction in the double ionisation probability. Therefore, we can directly probe the basic mechanism of double electron ejection and rule out a shake-off mechanism[1)] in favour of the recollision process[2)]. "Exact" one-dimensional fully correlated calculations also support a recollision mechanism.

Theoretical Models and Methods

In order to study the two-electron physics, an "exact" treatment of the electron correlation is needed. We approach the problem by reducing the dimensionality of the system and solving the two-electron Schrödinger equation in one space dimension[3)]. All the Coulombic interactions avoid the singularity at the origin with a soft-core parameter. The double ionisation probability is defined here as the total probability that both electrons are at least 5 a.u. away from the origin (atomic core) at the end of the laser pulse.

Although the exact 1-D model describes the experimental features in a very good qualitative manner, it is rather computationally demanding, even in one space dimension, and cannot be used easily for very long pulses or very high electron energies. A calculation for only a single value of intensity takes a few hours on a Pentium II personal computer, depending on space-time resolution. We would also like to have more flexibility in probing separately the electron-laser and the electron-electron interactions as well. For these purposes, an approximation to the previous exact model was introduced[4)]. The basic idea of the approximate scheme comes from the fact that, in the intensity regime of the relevant experiments, i.e. before and up to the saturation of single ionisation (laser intensity < 10^{15} W/cm^2) one of the He electrons ionises rapidly, while there is only a small relative probability that the second electron also ionises. It is then possible to assume that we can distinguish between the two electrons as if they were identifiable as an *external* and an *internal* one. It has been shown[3)] that if both electrons are treated equally (as in a time-dependent Hartree-Fock or density functional theory approach), the knee structure cannot be reproduced, a fact that indicates the limitations of some standard mean-field approximations.

Here, in this approximate scheme, also known as "Crapola", the total wave function is written as a product of the wave functions of the two electrons, which are now distinguishable. Of course, at the end, the electrons are made indistinguishable with respect to the measured ionisation[5)]. The important advantage of this approach is that the two equations of motion are essentially decoupled, in the sense that the equation for the external electron does not depend on the co-ordinate of the internal one. Therefore, the two-dimensional problem is reduced to two 1-D Schrödinger equations that can be solved numerically easily and fast, even on a personal computer, for a large range of intensities.

Results and Discussion

We show in Figure 1 the double ionisation signal for a range of laser intensities from 10^{14} to 10^{16} W/cm^2, and a range of wavelengths (frequencies) from 248 to 1064 nm. We see how the knee structure, being the manifestation of saturation of the direct NS double ionisation, appears for all wavelengths. The laser pulses have a 32-cycle total duration, and their shape is a $\sin^2$ function (for a total phase of one π). The additional structure of the curves, especially for shorter wavelengths, is due to multiphoton atomic transitions. For the shortest wavelength of 248 nm a high signal for NS ionisation is evident. This result has also been confirmed by fully correlated two-electron calculations[5)]. Other S-matrix calculations[6)] have not shown any NS signal for the 248 nm wavelength. We believe that the reasons are the extremely long pulse duration that was used and the resultant saturation of the single ionisation, even at very low intensities.

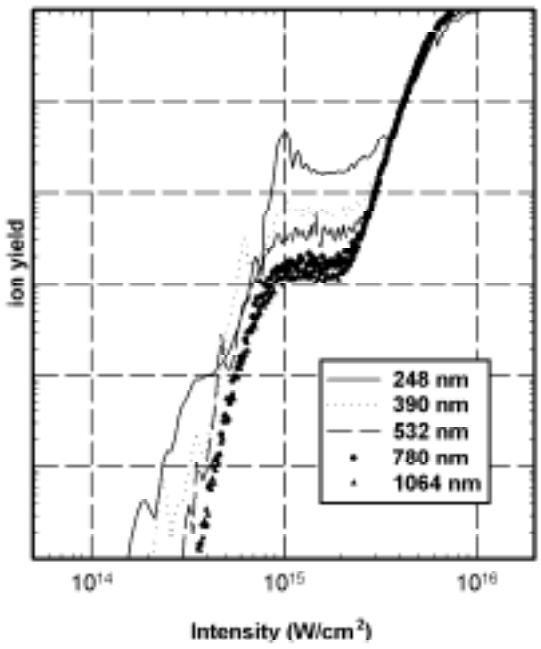

Figure 1. Double ionisation probabilities (ion yields) at the end of 32-cycle laser pulses, for the indicated wavelengths. The laser pulses do not have the same duration in time, but only the same number of laser periods for each frequency.

In order to identify the signature of the recollision mechanism of NS double ionisation, we calculate the explicit time-dependence of the single and double ionisation probabilities. In Figure 2 we see that the expected periodic sharp increases of single ionisation, due to the periodic ejection via tunneling, are followed by corresponding increases of double ionisation after

approximately one half of the laser period. This strongly suggests a periodic electron-electron collision and transfer of energy from the external electron to the internal one.

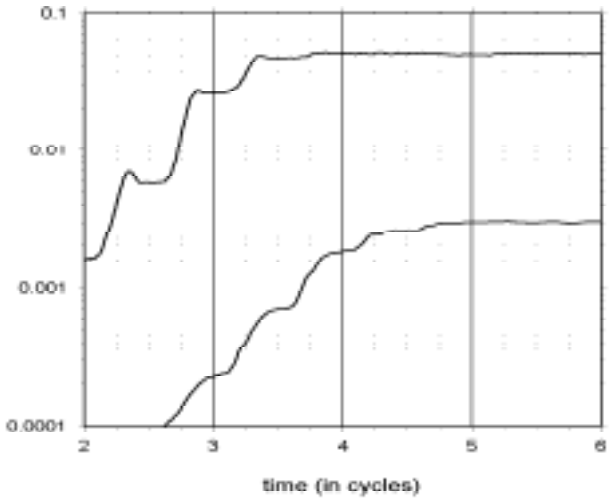

Figure 2. Single (upper line) and double (lower line) ionisation probabilities as functions of time during a 6-cycle laser pulse of 780 nm wavelength. The intensity is 7.9 x 10^{14} W/cm^2. The pulse shape is a trapezoid with 2 cycles of linear turn on, 2 cycles of constant field strength and 2 cycles of linear turn off.

A rather clearer picture of this dynamic process is shown in Figure 3, where the joint two-electron probability distribution of the 1-D fully correlated wave function is shown. This snapshot of the space probability distribution is taken at a moment around a classically expected recollision[7], at 3.5 cycles in a laser pulse of sin(ωt) form. We clearly see that the electron-electron scattering is immediately followed by double electron ejection that is occurring in the negative direction of the x-axis for each electron (lower left side of the graph). The probability along the two x-axes, in the shape of a cross, indicates single ionisation and always appears first.

The fact that the external electron seems to be mainly responsible for the ejection of the internal one, suggests that in the approximate two-electron scheme[4] that was discussed above, one should be able to reproduce almost completely the double ionisation probability, even if the internal electron is artificially made not to interact with the laser field. It has actually been shown[5] that only the interaction with the mean field of the external electron is sufficient to almost completely reproduce the total double ionisation probability, up to the intensity of saturation of the single ionisation. Moreover, it has also been shown that a half-cycle laser pulse, that does not allow even a single recollision event, does not produce any NS ionisation[5]. Also, any effect from a shake-off process would have produced an NS signal, even in the case of a half-cycle pulse.

In view of all the available evidence, we propose that the interaction of the internal (core) electron with the external one should be viewed not as a standard process of single-impact ionisation, but as an electron-electron scattering process that occurs periodically over many laser cycles, in a time interval of the order of the pulse duration. The energy that is transferred to the internal electron is provided by the returning and rescattered external electron through a three-step process: multiphoton absorption of unlimited energy from the laser pulse by the external electron, subsequent emission of radiation during rescattering of the external electron with the atomic core, and, finally, absorption of this radiation by the internal electron, which can then ionise.

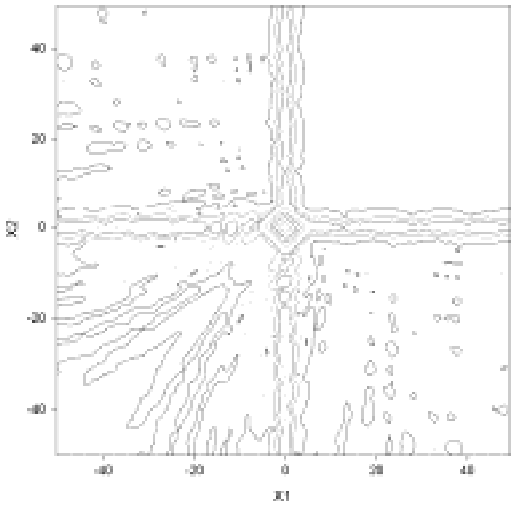

Figure 3. Contour plot of the two-electron space probability distribution $\left|\psi(x_1, x_2)\right|^2$ at time 3.5 cycles in the laser pulse of wavelength 780 nm and intensity 4.2 x 10^{14} W/ cm^2. The pulse shape is a trapezoid, as in Figure 2. The contours are spaced by one order of magnitude from each other, on a logarithmic scale. The position co-ordinates are in atomic units.

Conclusion

Significant NS ionisation has been found for a wide range of wavelengths, from 248 to 1064 nm, for laser pulses of sufficiently short duration. We calculate both the single and the double ionisation probabilities as functions of time during the laser pulse, using the fully correlated 1-D two-electron model. We demonstrate how our results are consistent with the recollision mechanism of double ionisation by using the time dependence of the ionisation probabilities and selected snapshots of the two-electron wave function. Also, by utilising our two-electron model calculations we are able to find strong evidence for the insignificance of the shake-off mechanism for the double ionisation, at least in the wavelength regime that was considered in this work.

References

1. B. Walker, B. Sheehy, L.F. Di Mauro, P. Agostini, K.J. Schafer and K.C. Kulander, Phys. Rev. Lett. 71, 1227 (1994).
2. P. Corkum, Phys. Rev. Lett. 71, 1994 (1993).
3. D.G. Lappas and R. van Leeuwen, J. Phys. B: At. Mol. Opt. Phys. 31, L249 (1998).
4. J.B. Watson, A. Sanpera, D.G. Lappas, P.L. Knight and K. Burnett, Phys. Rev. Lett. 78, 1884 (1997).
5. P.P. Corso, D.G. Lappas and P.L. Knight, submitted to J. Phys. B (2000).
6. Becker and F.H.M. Faisal, Phys. Rev. A 59, R1742 (1999).
7. M. Dörr, Optics Express 6, 111 (2000).

Modelling of Short Pulse X-ray Laser Experiments

R King, G J Pert

Department of Physics, University of York, York, Y010 5DD

Main contact email address: *rek102@york.ac.uk*

Introduction

X-ray lasers using amplified spontaneous emission are well established. The general theory underlying such laser action was established nearly thirty years ago by Casperson[1] and related authors. At this time most of the characteristic effects, such as saturation, the distinction between homogeneous and inhomogeneous broadening, line narrowing and subsequent re-broadening for in-homogeneously broadened lines, were identified. The theory was later extended to X-ray lasers by Pert[2].

A recent development in collisionally pumped lasers has been the exploitation of travelling wave systems with transient gain. The standard model of ASE lasers assumes that the laser is uniform and steady state. Clearly, this is unsatisfactory for the transient scheme described above.

In this paper we will investigate the behaviour of homogeneously broadened, uni-directional time varying ASE lasers by an extension of our earlier work. The results from the model will be compared with results from detailed simulation, which reveals the model's limitations when applied to experiment.

Analytic Model

The model is based upon the earlier work of one of the authors[2], and will not be described in detail here. The extension of the model to account for the situation where the gain has a finite lifetime, and the assumptions made in this model are described elsewhere[3], and allows the temporal profile of the output signal to be obtained for an arbitrary gain profile. In this paper we will consider only the matched case, where the pumping pulse and lasing pulse are synchronized.

The model demonstrates the characteristic pulse shortening noted by Lin et al[5], and also exhibits line narrowing in a similar manner to the long pulse case. Results for the analytical model can be found elsewhere[3].

Comparison with Simulation

The analytical model can also be compared with more detailed computational modelling. To match the analytical model to simulation we use two codes, EHYBRID and RAYTRACE, developed at York. The codes require data on the driving laser and many other parameters, so we model a typical set-up used in the experiments of MacPhee et al[4] on Ne-like Germanium lasing at 196 Å. The analytical model requires knowledge of certain physical parameters, so we use the output of the codes to provide this data.

Figure 1 shows the growth curve produced by detailed simulation with EHYBRID and RAYTRACE, by the analytical model for a Doppler broadened line, and also the experimental data produced by MacPhee et al[4].

A feature of the EHYBRID curve is the 'tail' on the curve at short target lengths (~2 mm). RAYTRACE predicts that signals emitted at later times by recombination over a wide cross section and radiated over a large solid angle contribute a large fraction of the total output for short target lengths. These are emitted from regions of relatively low gain, but high spontaneous emission. The divergence of the beam is high, and at this stage the plasma is behaving as 'floodlight'. The normal collisional output, produced over times of the order of the gain duration, is well collimated and in agreement with the analytical model.

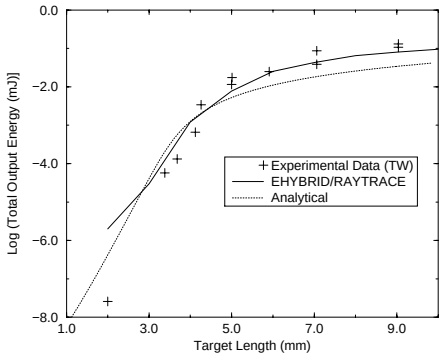

Figure 1. Total output power as a function of target length calculated by modelling (dotted line) and simulation (full line). Also shown are the experimental points relating to the data produced by MacPhee et al[4].

The output power from RAYTRACE shows the characteristic pulse shortening discussed earlier. The pulse width drops to ~0.3 of the gain duration for a target length of 5 mm. Agreement between the model and simulation is satisfactory, due to the differing time histories of other regions of gain.

At longer target lengths, the analytical curve falls significantly below the RAYTRACE curve. Simulation suggests that the area of the output beam increases by a factor ~8 between a 4 mm target and a 8 mm target. This implies that above saturation rays with smaller values of *gl* contribute strongly, and consequently additional parts of the plasma start to make a significant contribution to the overall output signal. The analytical model, which does not include this behaviour, is consequently incomplete at these longer target lengths. However, general agreement between simulation and the analytical model is good.

Agreement between simulation and experiment is excellent around and above saturation, but clearly simulation differs significantly at short target lengths. Since the experimental set-up typically receives radiation over a fraction of the total solid angle, it is possible that a substantial part of the total signal emitted at later times by recombination will be missed. The analytical model will therefore approximate the experiment more closely at small target lengths. Agreement between the analytical model and experiment is satisfactory, but differs above saturation as discussed above.

Conclusion

We have shown that the simple ASE model of laser generation can be extended to a situation where the gain has a finite lifetime. The model is capable of giving satisfactory agreement with simulation and experiment, provided suitable values of the saturation intensity, etc, are used. Discrepancies highlight the inadequacies and assumptions of the model.

References

1. L.W. Casperson, J. Appl. Phys 48 256 (1977).
2. G.J. Pert, J. Opt. Soc. Am. B 11 1425 (1994).
3. R.E. King and G.J. Pert, Compte Rendues, in press.
4. A.G. MacPhee et al, in press.
5. J.Y. Lin et al, Opt. Commun. 166 211-218 (1999).

Computational Simulations of a Ne-Like-Ar Collisionally Pumped X-UV Laser

L M Upcraft, G J Pert

Department of Physics, University of York, Heslington, York, YO10 5DD.

Main contact email address: *lmu101@york.ac.uk*

Introduction

Ne like Ar (Ar^{8+}) can be produced through optical field ionisation (OFI) by a femtosecond laser of intensity ~5×10^{16} W/cm^2 with the released electrons gaining energy in the process. Circularly polarised light produces hot electrons that should allow efficient collisional pumping. Such schemes were first suggested by Corkum and Burnett[1] with Lemoff et al later giving detailed rate calculations for noble gas systems[2].

We have performed detailed computational simulations on two aspects of Ne like Ar which is predicted to lase at 46.9 nm on the $2p^5 3p\ ^1S_0 \rightarrow 2p^5 3s\ ^1P_1$ transition. BREAKDOWN simulates the atomic and hydrodynamic process in a 1D plasma following OFI of the gas and allows the temporal evolution of the gain and output saturated intensity to be determined. PROPAGATE models the propagation of the driving laser into the plasma and calculates the dispersion of the beam and the resulting degree of ionisation.

Results

BREAKDOWN was run for a range of ion densities using an incident laser pulse of FWHM 30 fs, a focal spot size of 30 μm, a wavelength of 800 nm and a peak intensity of 10^{17} W/cm^2 giving a beam energy of 90 mJ. This produced electrons with an initial temperature of 1.8 keV.

It was immediately observed that the gains predicted were very high, of the order of 1000 cm^{-1} while the saturation intensity was fairly low (~10^7 to 10^8 W/cm^2).

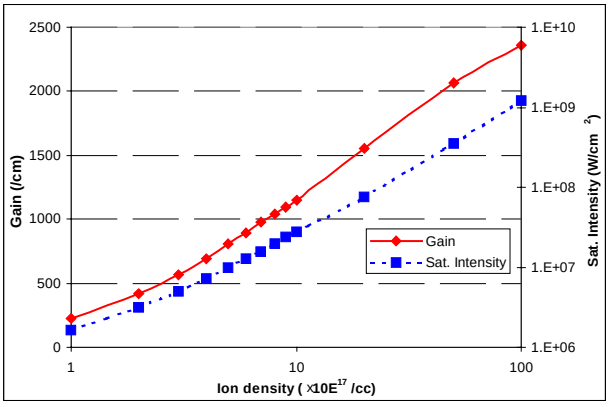

Figure 1. Peak gain and saturation intensity (at time of peak gain) plotted as a function of the ion density.

The large gains are attributable to the fact that the ions remain cold (having temperatures of a few tenths of eV) since they do not heat appreciably in the femtosecond driving laser. Although the saturation intensity reaches ~10^9 W/cm^2 at ion densities of around 10^{19} cm^{-3}, results from PROPAGATE show that driving the pump laser into the gas even at much lower densities is difficult. At these densities it was found that the population inversion was established very rapidly (less than 1 ps) but that collisional ionisation to Ar^{9+} limited the lasing time in the central region of the plasma to around 5 ps. For densities of around 5×10^{17} cm^{-3} lasing would continue for 10 to 20 ps.

Early results from PROPAGATE showed that a driving pulse identical to that used for BREAKDOWN would not produce any significant volume of the Ar^{8+} ion species required even at densities as low as 5×10^{17} cm^{-3}. The long wavelength required to generate the hot electrons is strongly scattered, the beam disperses rapidly and the intensity falls below the 5×10^{16} W/cm^2 required to produce the Ar^{8+} species and as a result a much more powerful beam is required. Only when the peak intensity is raised to 5×10^{17} W/cm^2 and the spot size increased to 50 μm is a significant channel of Ar^{8+} formed as shown in Figure 2. Here it can been seen that a channel of radius approximately 30 μm and length 4 mm is produced. In this case the energy supplied by the laser is increased significantly to 750 mJ.

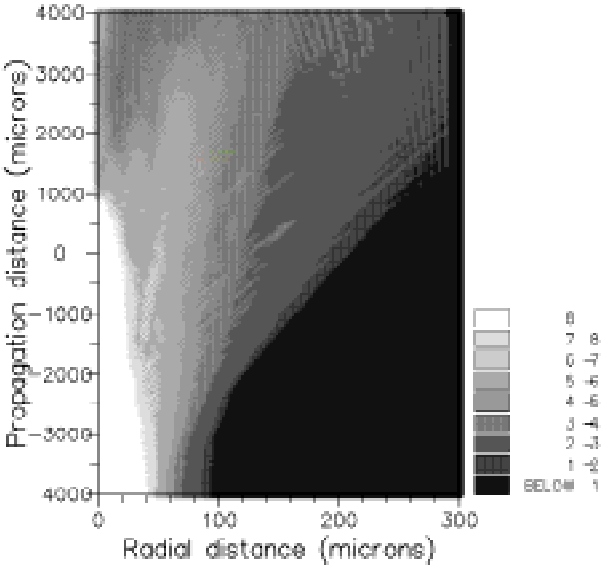

Figure 2. Contour plot of the degree of ionisation as the driving beam enters from $z = -4$ mm and propagates to the ideal focus at a distance of $z = 0$. (The structure in the upper right of the plot is due to the electric field reflecting from the limited mesh.)

In addition to the scattering problem, the long wavelength also means that the Rayleigh length is fairly long, 3.5 mm, which will present major focusing problems. This is also illustrated in Figure 2 where it can be seen that significant dispersion occurs around 2 mm before the beam reaches the ideal focus.

Conclusion

Modeling has shown that although the predicted gain of a Ne-like Ar collisionally pumped OFI laser is large, the saturated output is low (10^6 to 10^7 W/cm^2) for densities at which driving the pump beam into the gas is practicable. The long wavelength of the driving laser means that forming the plasma is difficult and even at ion densities as low as 5×10^{17} cm^{-3} intensities of the order of 10 times that required for OFI are necessary. It is probably for this reason that these schemes have been difficult to demonstrate experimentally.

References

1. P. B. Corkum and N. H. Burnett, OSA Proceedings on Short Wavelength Coherent Radiation: Generation and Applications, R. W. Falcone and J. Kirz, eds. (Optical Society of America, Washington, DC, 1988), Vol 2, p. 225.

2. B. E. Lemoff, C. P. Barty and S. E. Harris, Optics Letters, 8 569 (1994)

The Transition from Uni-directional to Bi-directional Behaviour in Amplified Spontaneous Emission Lasers

G J Pert

Department of Physics, University of York, Heslington, York, YO10 5DD

Main contact email address: *gjp1@york.ac.uk*

Introduction

Amplified spontaneous emission (A.S.E.) lasers operate by the amplification of forward travelling spontaneous emission, predominately from the back (entrance) of a large aspect cylinder of high gain. At high output irradiance the output from the front (exit) is saturated, with a consequent reduction in both the local small signal gain and spontaneous emission rates.

In the simplest picture, the laser is visualised with a single beam starting at the back and exiting at the front – uni-directional operation. However the laser is normally symmetric, and a backward beam, identical to the forward, but reversed, is generated – bi-directional operation. Near the entrance the spontaneous emission rate of the forward beam is reduced by saturation due to the backward. The consequence is that the output irradiance of each beam is reduced by saturation due to the other. This key distinction between uni- and bi- directional modes was identified in Casperson's[1] pioneering paper which gave the first detailed theory of A.S.E. lasers. Subsequent work[2] derived analytic expressions for the output taking into account line narrowing and the distinction between homogeneously and in-homogeneously broadened lines.

Practical application of these ideas was relatively limited until the advent of X-ray lasers, where the absence of high reflectivity mirrors makes A.S.E. operation essential. Measurements of line widths by Koch et al[3] showed that lasing lines are effectively homogeneously broadened despite a dominant Doppler width. The application of the bi-directional model has proved successful in a wide range of cases, where the gain is long-lived, i.e. quasi-stationary. More recently X-ray lasers have been developed using short (psec) heating pulses from a CPA pump, and this condition is no longer valid. If the gain lifetime is less than the X-ray laser pulse transit time, not all the laser line will be accessed by the laser pulse if the medium is uniformly heated. To overcome this difficulty a travelling wave pump is used, where the pump and laser beams travel in synchronism along the axis. In this case the symmetry between the forward and backward beams is lost. In particular if the gain duration is sufficiently short that the backward beam never achieves saturation, the forward beam is essentially uni-directional. The behaviour of A.S.E lasers under conditions of travelling wave pumping has been recently investigated for matched[4] and mismatched[5] conditions, and compared against detailed simulation[6].

Bi-directional Operation

If the gain lifetime is sufficiently long that the backward beam can achieve saturation, then we must include the reduction in the forward beam spontaneous emission and gain occasioned thereby. The general problem contains three characteristic times, namely the transit times for the gain pulse and the laser pulses, and the characteristic time constant of the gain. Thus we imagine the system as follows. The gain pulse with some appropriate profile $\psi(t/\tau)$ propagates along the gain axis from the entrance to the exit with speed v starting at time zero. Simultaneously a series of forward and backward pulses are generated, travelling forwards and backwards with speed c. If c>v the forward going wave runs ahead of the gain pulse, and the first pulse leaving the exit starts from the entrance. On the other hand if c<v the forward wave lags the gain, and the first pulse starts at the exit. The leading backward pulse always starts at the entrance.

The Model

To analyse this system we use the model introduced by Pert[2] and generalised for time varying gain by King and Pert[6], where fuller details are given. We consider the laser as a uniform rod of length ℓ with spontaneous emission rate, E, and gain, G, on a homogeneously broadened line, to be both given by the form: $A(0)=A_0/(1+\bar{I}/I_s)$ where $\bar{I}=\int I(\nu)f(\nu)d\nu/f(0)$ is the frequency averaged irradiance, I_s the saturation irradiance and f(ν) the line shape function. In the bi-directional case there exist two beams of irradiance: I_+ forward and I_- backward. The total irradiance at any point and time is $I=I_++I_-$. We consider the laser field made up of a series of pulses starting at different times from the appropriate end. As in our earlier work, we introduce the small signal gain length, $x=G_0z$, and the actual gain length, $X=\int_0^z G(0)\,dz$, as seen by the pulse, where z is the distance from the pulse starting point. The instantaneous irradiance is given by $I=I_0\,\alpha(X)$, and the frequency averaged $\bar{I}=\int I(\nu)f(\nu)d\nu/f(0)=I_0\beta(X)$, where $\beta(X) = d[\alpha(X)]/dX - 1$, I_0 being the spontaneous emission irradiance and $\alpha(X)$ the amplification function described in Reference 2. The irradiance of each beam is given by its individual gain-length product $X_{+/-}$.

A finite difference model is used to calculate the behaviour of the laser. The laser axis is subdivided into N elements each of length $\Delta z=\ell/N$, the time-step is chosen to be $\Delta t=\Delta z/c=\ell/cN$, so that each pulse moves one interval per time-step, and the transit time is N time-steps. At the time/space mesh point [m,n] (time m Δt and position n Δz measured from the entrance), the local gain time is $m\Delta t-n\Delta z/v = (m-n\,c/v)\,\Delta t$. Hence the local small signal gain is $G_0\psi([(m-n\,c/v)\Delta t/\tau]$. The calculation is performed by evaluating the overall gain lengths for the forward and backward beams X_+ and X_- at the point (m,n) from their previous time values, namely at the points [(m-1),(n-1)] and [(m+1),(n-1)] respectively, and taking into account the gain saturation correction. Thus we have:

$$X_+[m,n]=X_+[(m-1),(n-1)]+\tfrac{1}{2}\{g[[(m-1),(n-1)]]+g[m,n]\}$$

$$X_-[m,n]=X_-[(m+1),(n-1)]+\tfrac{1}{2}\{g[[(m+1),(n-1)]]+g[m,n]\}$$

Since g[m,n]=G[m,n] Δz depends on $\bar{I}$ [m,n] and therefore $X_{+/-}$[m,n], these equations have an implicit form, which must be evaluated by iteration. We have found that for most purposes a two-step (or predictor-corrector) iteration is sufficient. Validation tests against the analytic results of Reference 2 show that an accuracy of greater than one per cent is readily achieved.

The initial and boundary values are easily established. At time zero, n=0, both the forward and backward beams are zero everywhere. At the entrance, the forward beam is always zero, $I_+[0,n]=0$, and its output irradiance is $I_+[M,n]$. Similarly the backward beam is always zero at the exit, $I_-[M,n]=0$, and its output irradiance is $I_-[0.n]$.

Establishment of a Quasi-static Radiation Field

In this short note we will investigate cases where the gain is switched on instantaneously, and remains constant thereafter. The initial condition is one of zero irradiance everywhere. For nearly one transit each beam will be independent of the other, and the output given by the uni-directional relations. However

as the fields become established, there will be a transition to bi-directional behaviour.

We consider the case in which a gain pulse travels along the axis at a speed which is a multiple of the laser light speed. The peak gain length is sufficiently large that the pulse is rapidly saturated. In Figure 1 we present the case of an overall small signal gain length $G_0 \ell$=50 and saturation/spontaneous irradiance ratio**,** $I_s/I_0 = 10^6$, and plot the growth of the forward and backward irradiance as a function of time measured in terms of the laser beam transit time, ℓ/c.

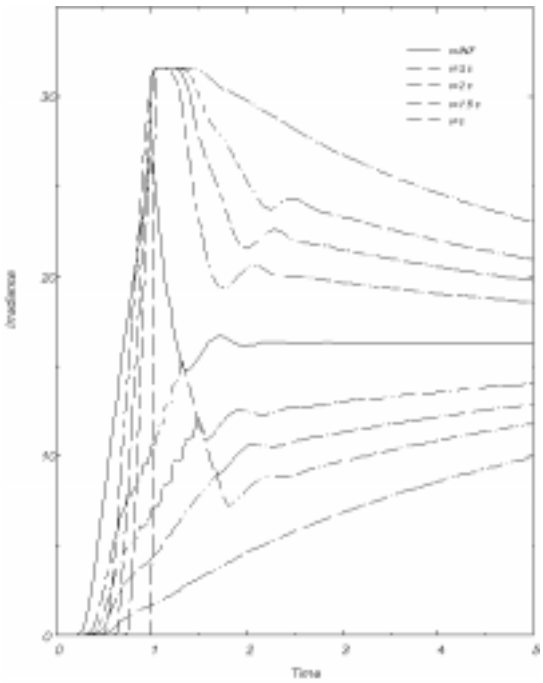

Figure 1. Output irradiance as a function of transit time for different gain wave speeds for the case $G_0\ell$=50 and $I_s/I_0 = 10^6$. The upper lines correspond to the forward wave and the lower to the backward.

Since v>c the gain runs ahead of the laser, and there is no forward output before the arrival of the gain pulse, i.e. before c/v transit times. In contrast the backward signal, although weak, starts from the onset of gain. An important parameter is the small signal gain-length at which saturation sets in, namely $x_s \approx \ell n\{ I_s/I_0 \sqrt{\ell n(I_s/I_0)}\} \approx 15$. From Figure 1 we can see that there are two different patterns of behaviour.

The first is exemplified by the uniformly pumped case, v=∞, in which the saturation of the backward pulse near the exit does not allow the forward pulse to achieve uni-directional output. Since the forward pulse on its initial transit is only modified by saturation from the backward if the latter has been saturated by the time they intersect, we require $\frac{1}{2}\ G_0\ \ell(1\text{-}c/v) > x_s$. This situation can only occur if v>c and $G_0\ \ell > 2\ x_s$. Under these conditions, as can be seen from Figure 1, overshoot occurs due to the enhanced output from the initial beam. The resulting reduction in spontaneous emission resulting from the enhanced saturation undershoots on the next transit, leading to a damped oscillation in the output signal. This effect is most strongly marked when the gain is applied uniformly (v=∞).

When the preceding condition is not satisfied, the forward wave is not modified by saturation on its first transit and is therefore initially uni-directional. It maintains its uni-directional output until the backward wave saturates near the entrance, i.e. for a fraction $x_s/\{G_0\ \ell(1+c/v)\}$ of the transit time. Since the backward wave is strongly saturated at its origin, i.e. the exit, the head of the backward wave moves slowly forward as the forward wave is also reduced by saturation at its source. The approach to the bi-directional form is therefore slow and exponential.

Uni-directional to Bi-directional Transition

We now examine the bi-directional transition directly by initiating the problem with a forward directed uni-directional beam and constant gain when the saturation/spontaneous irradiance ratio**,** $I_s/I_0 = 10^6$.

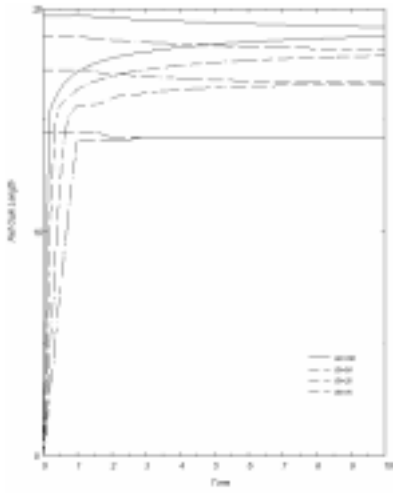

Figure 2. Plot of the actual gain length as a function of time for different gain-lengths. The upper curves refer to the forward wave and the lower to the backward.

Figure 2 shows the time development of the bi-directional output actual gain length for different small signal gain lengths as a function of the transit time. The development of the backward wave and the corresponding reduction of the forward wave are clearly seen. It can be seen that the forward wave is progressively diminished as the backward wave grows, the saturation of the latter reducing the spontaneous emission into the former. At low $G_0\ell \approx x_s \approx X(\ell)$, saturation is weak with only a small difference between uni- and bi-directional outputs. Relaxation in this case occurs over approximately two transits – the first propagates the correcting backward beam, and the second the corrected forward. As $G_0\ell$ increases the backward beam propagates a correspondingly smaller fraction of the overall length before saturating, and modifies the forward in only a fraction of the transit time. However the corresponding movement of the effective starting point of the latter is small, and therefore the overall change in its total gain-length product is also small (removing only a short length of highly saturated gain). The motion of the forward (or backward) starting point therefore proceeds as a series of small steps over times, which depend on the effective length of the backward pulse. Thus as noted earlier the relaxation is approximately exponential in form, with a decay–time, which increases with gain-length. Note that for large gain lengths the relaxation time is many transits.

References

1. L W Casperson, J. Appl. Phys., 48, 256, (1977)
2. G J Pert, J. Opt. Soc. Am. B, 11, 1425, (1994)
3. J A Koch et al, Phys. Rev. A, 50, 1877, (1994)
4. J Y Lin et al, Optics Comm. 166, 211, (1999)
5. F Strati, Central Laser Facility RAL Annual Report, RAL-1999-062, 73, (1999)
6. R E King and G J Pert, Compte Rendues A in press

Science - Astra Laser Programme

Ultrafast Time-of-Flight Mass Spectrometry: Femtosecond Ionisation of Laser-Desorbed Atoms and Molecules

S M Hankin, X Fang, K W D Ledingham, R P Singhal, T McCanny, L Robson, A D Tasker

Laser Ionisation Studies Group, Department of Physics & Astronomy, University of Glasgow, Glasgow G12 8QQ, UK

C Kosmidis, P Tzallas

Physics Department, University of Ioannina, 45110 Ioannina, Greece

A J Langley, P F Taday, E Divall

Central Laser Facility, CLRC Rutherford Appleton Laboratory, Chilton, Didcot, Oxon, OX11 0QX, UK

Main contact email address: *s.hankin@physics.gla.ac.uk*

Introduction

The emerging field of ultrafast laser-molecule interactions has highlighted new areas of physics and chemistry and is becoming an important tool for molecular analysis[1-4]. From a mass spectrometry perspective, the generation of molecular or structurally-characteristic ions is a key feature in the technique's analytical ability. Short-pulse laser radiation offers the unique attributes of very high intensities ($10^{12\text{-}17}$ W cm^{-2}) with a pulse duration shorter than the vibrational, rotational and dissociative timescales of molecules. These attributes have led to suggestions that femtosecond laser radiation can be regarded as an efficient, universal and soft ionisation source[5-7].

Comparative studies[8-11] using short-pulse (ps and fs) and nanosecond lasers have been carried out for atoms and molecules in the gas phase to show the advantages of ultrafast ionisation. Using the Astra laser facility at RAL, the Glasgow group[12-16] has carried out extensive investigations of gas-phase non-resonant femtosecond laser ionisation using ToF mass spectrometry (FLMS). However, the evolution of FLMS as an analytical technique requires the use of methods to introduce solid-phase species to the gas-phase for ionisation. In addition to studies of elemental and inorganic materials[17,18], the potential of FLMS for the analysis of biomolecules[19] and the detection of environmentally-hazardous materials is considerable[7]. Current research by the Glasgow group focuses on coupling femtosecond laser ionisation with a laser desorption source for the analysis of solid-phase labile molecules. This report describes the instrumentation employed and some initial results for the programmes of research in laser desorption femtosecond post-ionisation time-of-flight mass spectrometry.

Experimental

The instrument used in this work, schematically shown in Figure 1, was a reflectron time-of-flight (ToF) mass spectrometer comprising a sample load-lock, source chamber and flight tube. The core of the system is a spherical stainless steel chamber of 30 cm diameter. Ports on the chamber are fitted with fused quartz windows allowing laser irradiation and direct viewing of the sample. The 1.5 m long flight tube houses the reflectron and MCP detector. The source chamber and flight tube are pumped to a base pressure of ~10^{-9} Torr using two rotary-backed turbomolecular pumps. Large samples are glued to a stainless steel stub using conducting silver-epoxy adhesive. Powder samples for analysis are dissolved in a suitable volatile solvent, deposited on to the stub and allowed to dry. Following evaporation of the solvent, the stub is admitted to the source chamber by means of a rotary-pumped load-lock and transfer arm. The stub is positioned on a manipulator arm in the centre of the chamber which allows for the movement in three dimensions and rotation about the vertical axis. Micrometers control the movement in each axis for accurate and reproducible movement. Ion extraction and acceleration is achieved using the sample stage and a two-plate ion optic designed specifically for this instrument[20]. An electrostatic potential of +2.7 kV is applied to the sample stage from a HT power supply. Potentials of +2 kV and +520 V are applied to the first and second plates respectively. The ions are guided into a Reflectron electrostatic mirror using XY deflection plates mounted after the ion extraction optics. The ions are detected by a multi-channel plate detector (Galileo) maintained at +2 kV. Signal output from the detector is coupled to a digital oscilloscope (LeCroy, 9344C) for single-shot and averaged data collection. A PC installed with GRAMS/32 software (Galactic), connected to the oscilloscope through a GPIB interface, is used for data acquisition, mass calibration and analysis.

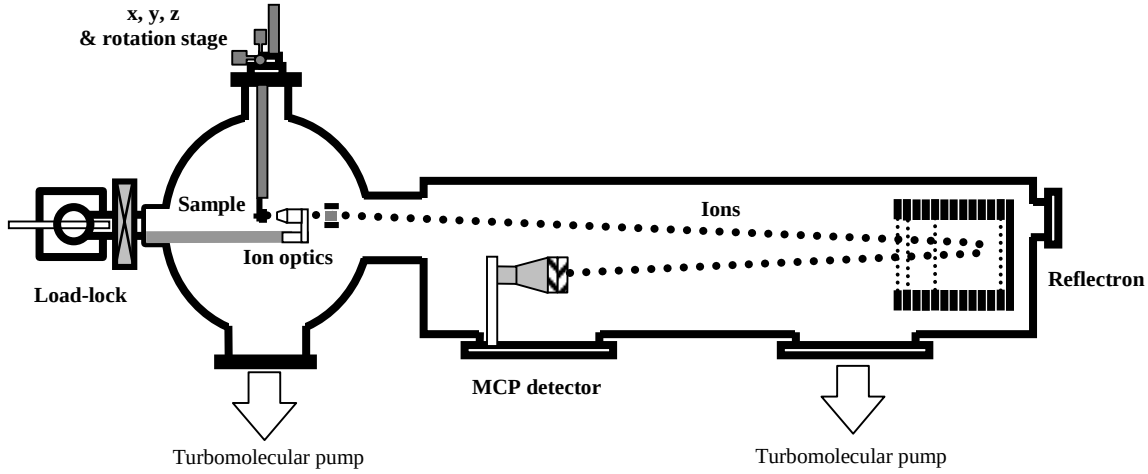

Figure 1. Reflectron time-of-flight mass spectrometer.

Laser desorption of the solid samples was achieved using the fourth harmonic output (266 nm, 5 ns) from a Nd:YAG laser (Minilite I, Continuum) focussed onto the sample stub. The energy of the desorption laser beam was controlled using an optical attenuator (Newport, 935-5) and monitored using a joulemeter (Molectron, J4-09). Focussing the ~7 mm diameter beam using a 27 cm focal length lens generated intensities up to 1 x 10^{10} W cm^{-2}.

The Astra femtosecond laser system[21], based on an Ar-ion pumped mode-locked titanium-sapphire oscillator (Spectra-Physics), produced pulses of ~9 μJ $pulse^{-1}$ at a wavelength of ~790 nm and pulse duration of 50 fs. The low-energy pulses were stretched to ~300 ps, amplified in a second Ti:Sapphire rod pumped by 140 mJ in 20 ns of the second harmonic from a Nd:YAG laser (Spectra Physics). Variable attenuation of the beam was achieved using a λ/4 waveplate and polariser positioned before the pulses were re-compressed to eliminate any non-linear effects and optical damage in the attenuator at high intensity. The amplified pulses (5 mJ $pulse^{-1}$) were re-compressed to 50 fs in a grating pair and directed into the source of the mass spectrometer for ionisation of the laser-desorbed sample. Focussing the ~1 cm diameter beam using a 30 cm focal-length lens yielded intensities as high as 5 x 10^{15} W cm^{-2}, determined by calculation and from the thresholds for Ar^{n+} ionisation.

Accurate spatial and temporal alignment of the desorption and ionisation laser pulses is critical for achieving maximum ion signal or studying the dynamics of laser desorption, schematically shown in Figure 2.

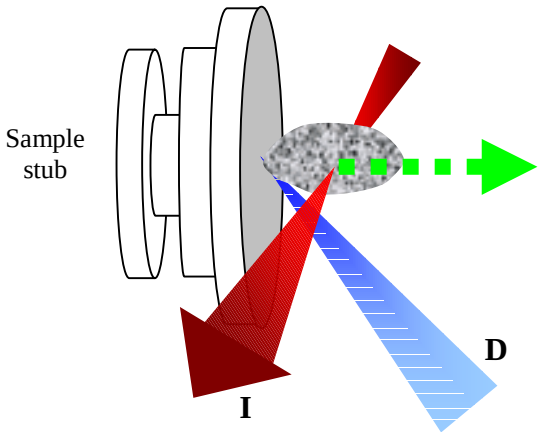

Figure 2. Nanosecond laser desorption (D) coupled with femtosecond laser post-ionisation (I) generates ions (■) that are analysed by the ToF mass spectrometer.

The timing between the desorption and ionisation laser pulses was accurately controlled using a pulse/delay generator (SRS, DG535). A master trigger (T_0) from the femtosecond oscillator was used to trigger the delay generator. A variable 37 μs delay TTL pulse fired the flashlamps of the desorption laser. The Q-switch was fired at a fixed delay of 150 μs with respect to the flashlamps for optimum energy. The delay between desorption and post-ionisation was variable from 0-37 μs.

Results & Discussion

With atoms, ionisation is the only channel. However, with molecules this is not the case. At lower intensities, dissociation may compete with ionisation and fragmentation may play an important role. In addition, multiply-charged ions formed at higher intensities may be highly unstable due to Coulombic repulsion. These initial results show the qualitative differences between atomic and molecular ionisation under strong-field laser irradiation.

Figure 3 shows the femtosecond ionisation mass spectrum of laser-desorbed Gallium Arsenide (GaAs) recorded at intensities of 1 x 10^{9} W cm^{-2} and 1.8 x 10^{15} W cm^{-2} for desorption and ionisation respectively.

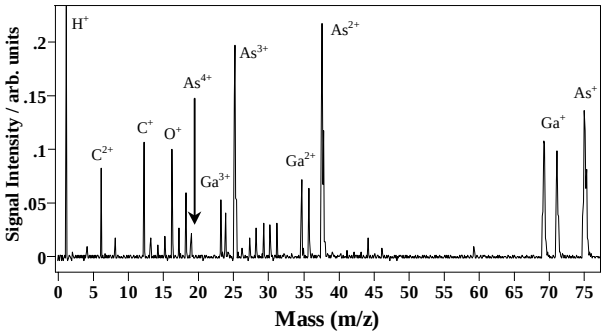

Figure 3. ToF-MS of laser-desorbed GaAs.

The spectrum exhibits singly-charged atomic ions of As (m/z=75) and the isotopes of Ga (m/z=69 & 71) in agreement with the natural abundances. Multiply-charged atomic ions were observed unambiguously up to the +3 charge-state for Ga and +4 for As. The isotopic abundances of ^{69}Ga and ^{71}Ga were resolved for all charge-states. The As^{2+} and As^{3+} signals dominate the spectra at intensities greater than 5 x 10^{14} W cm^{-2}. This is a reflection of the relative differences in the ionisation potentials for the two atoms as shown in Table 1.

Atom	1st IP / eV	2nd IP / eV	3rd IP / eV	4th IP / eV
Ga	5.99	20.51	30.71	64
As	9.81	18.63	28.35	50.13

Table 1. Ionisation potentials[22] for Ga^{n+} and As^{n+} (n=1-3).

The low mass signals assigned as H^+, C^{n+} and O^+ arise from ionisation of hydrocarbon and water surface-contamination co-desorbed with the GaAs. These ion signals decreased as the surface layers were ablated, exposing material in the bulk to desorption. At laser intensities greater than 5 x 10^{14} W cm^{-2} minor higher mass ion peaks were observed at m/z=150 and 225 and were attributed to As_2^+ and As_3^+ clusters.

Figure 4 shows the mass spectrum of trinitrobenzene (TNB) recorded at intensities of 3.3 x 10^{8} W cm^{-2} and 4 x 10^{15} W cm^{-2} for desorption and ionisation respectively.

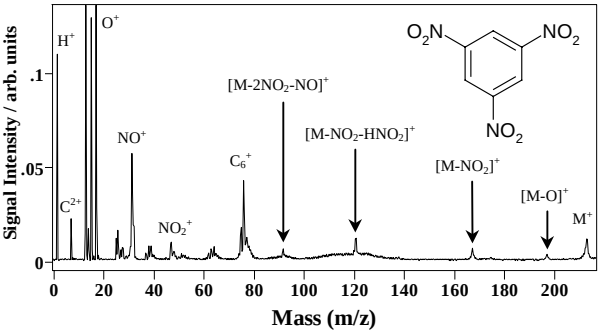

Figure 4. ToF-MS of laser-desorbed trinitrobenzene (TNB).

The spectrum exhibits a significant degree of molecular fragmentation yielding structurally-specific and non-specific fragments. In addition to the small parent ion at m/z=213, the mass spectrum shows ion signals characteristic of the TNB molecule: $[C_6H_3N_3O_5]^+$ (m/z=197), $[C_6H_3N_2O_4]^+$ (m/z=167), $[C_6H_2NO_2]^+$ (m/z=120) and $[C_6H_3O]^+$ (m/z=91). These dissociative channels arise from the loss of H, O, NO and NO_2 from the parent. Low mass fragment ions were identified as H^+, C^{2+}, N^+, O^+, C_n^+ (n=1-6), NO^+ and NO_2^+. The effect of the

desorption and ionisation laser intensities on the ion yields for TNB and other nitro-aromatic molecules was studied and will be reported elsewhere.

The laser desorption step plays as important a role as the ionisation step in terms of inducing molecular fragmentation. Molecular dissociation prior to ionisation may occur under intense desorption conditions yielding small neutral fragments. Preliminary investigations have revealed that higher ion yields of the parent ions and structure-specific fragments are accompanied by lower yields of the small fragment ions. An optimum laser desorption intensity is desirable for desorption of intact neutral species representative of the sample, prior to direct ionisation during the nanosecond laser pulse. Furthermore, the optimum laser intensity was also observed to be dependent on the molecule being analysed[23]; in these experiments the optimum intensity for TNB was found to be ~3.3 x 10^8 W cm^{-2}. Notably, the peak shapes for laser-desorbed analytes exhibit a significantly different appearance from that of gas phase analytes. This is due to the large kinetic energy distribution in the ions as a result of the desorption event and energetic fragmentation[24-26].

Conclusions

The coupling of a nanosecond laser for molecular desorption with the Astra femtosecond laser has extended the applicability of femtosecond laser mass spectrometry to the analysis of involatile solid materials. The time-of-flight mass spectra of GaAs and TNB have revealed the characteristic features and differences of femtosecond atomic and molecular ionisation of laser-desorbed species. Significant yields of multiply-charged atomic fragments, parent ions and structure-specific fragment ions of labile molecules have been obtained. An optimum desorption laser intensity for the transfer of neutral intact parent molecules into the gas phase has been observed to be molecule-dependent. This work is the first report of the femtosecond ionisation of laser-desorbed nitro-aromatic species and has significant implications for analytical studies of nitro-aromatic explosive molecules[27].

Further studies are being conducted to investigate the optimum conditions of laser ablation for the production of parent molecules without dissociation during desorption. In addition, issues of generality, uniform ionisation efficiency and high-intensity phenomena in the femtosecond irradiation of polyatomic molecules are being investigated.

The authors acknowledge EPSRC for funding and Studentships (LR and ADT) and NERC for a Postdoctoral Fellowship (SMH).

References

1. P B Corkum, M Y Ivanov and J S Wright
Annu. Rev. Phys. Chem. 48, 387, (1997)

2. K Codling and L J Frasinski
J. Phys. B: At. Mol. Opt. Phys. 26, 783, (1993)

3. A L Burlingame, R K Boyd and S J Gaskell
Anal. Chem. 70, R647, (1998)

4. K W D Ledingham and R P Singhal
Int. J. Mass Spectrom. Ion Proc. 163, 149, (1997)

5. R Möllers, M Terhorst, E Niehuis and A Benninghoven
Org. Mass Spectrom. 27, 1393, (1992)

6. J Matsumoto, C-H Lin and T Imasaka
Anal. Chem. 69, 4524, (1997)

7. C Grun, R Heinicke, C Weickhardt and J Grotemeyer
Int. J. Mass Spectrom. 185/186/187, 307, (1999)

8. R Weinkauf, P Aicher, G Wesley, J Grotemeyer, E W Schlag, J. Phys. Chem. 98, 8381, (1994)

9. K W D Ledingham, C Kosmidis, S Georgiou, S Couris, RP Singhal, Chem. Phys. Lett. 247, 555, (1995)

10. J Matsumoto, C-H Lin and T Imasaka
Anal. Chim. Acta 343, 129, (1997)

11. N P Lockyer and J C Vickerman
Int. J. Mass Spectrom. 176, 77, (1998)

12. DJ Smith, K W D Ledingham, R P Singhal, H S Kilic, T McCanny, A J Langley, P F Taday and C Kosmidis
Rap. Comm. Mass Spectrom. 12, 813, (1998)

13. K W D Ledingham, R P Singhal, D J Smith, T McCanny, P Graham, H S Kilic, W X peng, S L Wang, AJ Langley, P F Taday and C Kosmidis, J. Phys. Chem. A 102, 3002, (1998)

14. K W D Ledingham, D J Smith, R P Singhal, T McCanny, P Graham, H S Kilic, X Peng, A J Langley, P F Taday and C Kosmidis, J. Phys. Chem. A 103, 2952, (1999)

15. D J Smith, K W D Ledingham, R P Singhal, T McCanny, P Graham, H S Kilic, P Tzallas, C Kosmidis, A J Langley and P F Taday, Rap. Comm. Mass Spectrom. 13, 1366, (1999)

16. X Fang, K W D Ledingham, P Graham, D J Smith, T McCanny, R P Singhal, A J Langley and P F Taday
Rap. Comm. Mass Spectrom. 13, 1390, (1999)

17. C He, J N Basler and C H Becker, Nature 385, 797 (1997)

18. G K Nicolussi, M J Pellin, K R Lykke, J L Trevor, D E Mencer and A M Davies, Surf. Interface Anal. 24, 363, (1996)

19. V Vorsa, K F Willey and N Winograd
Anal. Chem. 71, 574, (1999)

20. C J McLean, P T McCombes, R Jennings, K W D Ledingham and R P Singhal, Nuc. Instrum. Meth. Phys. Res. B 62, 285, (1991)

21. A J Langley, N Girard, I Mohammed, I N Ross and P F Taday, 1998-99 CLF RAL Annual Report (RAL-TR-1999-062), 187

22. Handbook of Chemistry and Physics, CRC Press: Boca Raton, Florida, 1988

23. G R Kinsel, J Lindner, J Grotemeyer and E W Schlag
J. Phys. Chem. 95, 7824, (1991)

24. S A Reid, Chem. Phys. Lett. 301, 517 (1999)

25. J C Miller and R F Haglund (Eds.) “Laser Ablation: Mechanisms and Applications”, Springer: Berlin, 1991

26. H Dang and Q Qin
Appl. Surf. Sci. 151, 180 (1999)

27. J I Steinfeld and J Wormhoudt
Annul. Rev. Phys. Chem. 49, 203, (1998)

Proton Production from a Terawatt, Compact, High Repetition-Rate Laser Interacting with Thin Solid Targets

I Spencer, K W D Ledingham, T McCanny, R P Singhal

Department of Physics and Astronomy, University of Glasgow, Glasgow G12 8QQ, United Kingdom

E L Clark*, K Krushelnick, M Zepf, A E Dangor

Blackett Laboratory, Imperial College of Science,Technology, and Medicine, London SW7 2BZ, UK

R Allott, D Neely, R J Clarke, A J Langley, P F Taday, E J Divall, P A Norreys

Central Laser Facility, CLRC Rutherford Appleton Laboratory, Chilton, Didcot, Oxon, OX11 0QX, UK

Main contact email address: *i.spencer@physics.gla.ac.uk*

Introduction

Great interest has developed recently in the generation of energetic ions, and especially protons using high-intensity, compact, high-repetition rate lasers. Although measurements of laser-plasma produced ion emission have been made as early as 1994[1], the recent excitement has been caused by the possibility of using "table-top" lasers as a source of energetic proton beams for cancer therapy. It has already been demonstrated that high-power lasers can be used to generate positron-emitting nuclides via (γ,n) reactions[2]. However the prospect of producing these nuclides via (p,n) reactions is more promising to the nuclear medicine community because isotopes produced in this manner can be separated from their parent isotopes using fast chemistry. Proton beams and positron emitters are currently produced using cyclotrons, which are expensive and cumbersome, so the prospect of using table-top, high-power, high-repetition rate lasers instead appears most promising. This technique has previously been demonstrated theoretically[3].

When a high-intensity laser pulse interacts with matter, the electric field component of the pulse causes electrons to be accelerated in the direction of the E-field. Space charge separation effects then cause ions to be accelerated. Recent experiments have used both gas targets[4], and solid targets[5]. These experiments were carried out on the large-scale, single-shot laser system, Vulcan[6]. The motivation for the work described in this report was to demonstrate proton production on a much smaller, high-repetition rate laser, to assess the viability of the commercial applications described above. This report describes preliminary measurements of proton production on such a laser system.

Experimental

The experiment used the ultra-high intensity branch of the Astra titanium: sapphire laser[7,8,9]. Astra uses chirped pulse amplification (CPA)[10,11] technology. This system delivered pulses on target of 150 mJ, duration 70 fs, at a rate of 1 Hz with a wavelength of 800 nm, and when focused to a spot size of 12 μm, yielded intensities on target of 5 x 10^{17} Wcm^{-2}. A pre-pulse, possibly from imperfect compression of the pulse was measured and found to have an intensity 10^{-4} that of the main pulse, and arriving on target 14 ns before the main pulse. This is sufficient to produce a pre-plasma on the target surface, before the arrival of the main pulse. The laser light was incident on either 18 μm thick magnetic TDK tape, or 23 μm thick CH tape, at 45° with p-polarised light within an evacuated target chamber. The experimental set-up is shown in Figure 1. Two 95 % reflecting turning mirrors were used to steer the beam on target, focused by a f/3 off-axis parabolic mirror. The first turning mirror permitted 5 % transmission of the laser energy to allow measurements of the pulse duration to be taken by a single shot autocorrelator, and to view the far-field image of the laser focus via a CCD camera. A second CCD camera was positioned above the tape target in order to view plasma emission from the laser interaction. A tape target was used so that the tape was advanced after every laser pulse, and hence the laser interacted with a fresh piece of target for every laser shot.

CR-39 is a plastic nuclear track detector which is sensitive to ions with energies greater than 100 keV / nucleon. When a nucleon is incident on a piece of CR-39, it causes structural damage, which, after etching with sodium hydroxide, produces a pit of definite dimensions. The larger the incident ion, the greater the pit size. CR-39 is not sensitive to electrons, or other ionising radiation such as X-rays. Pieces of CR-39 were placed in the target chamber, behind the target, in the "straight-through" direction at a distance 40 mm from the target, and in front of the target, directed along the target normal, at a distance 180 mm from target, in the "blow-off " direction.

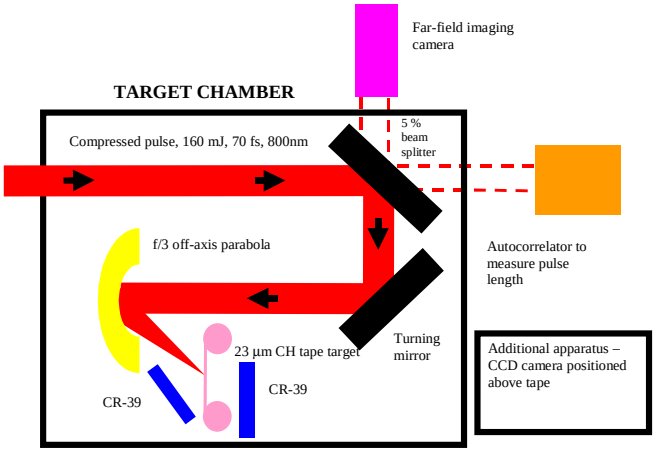

Figure 1. Schematic diagram of experimental arrangement.

Results and discussion

The first experiment carried out was to observe proton and possibly heavier ion emission from the laser-solid interaction. Laser pulses were directed at 18 μm thick TDK tape for this experiment. This magnetic tape was composed of a 12 μm thick CH layer, plus a 6 μm thick layer of fine grained ferric particles.

During some of our runs it was noticed that when CR-39 samples were placed in both the blow-off and straight-through directions, proton and carbon ion pits were identified in both positions, plus much larger pits which we think are iron ion pits in only the straight-through position.

This was a very interesting observation which only occurred when the fine grained ferric particle layer faced the straight-through position. The CR-39 samples in the blow-off position did not contain these iron pits. We have explained these observations in the following way. When the electrons and protons were accelerated in the straight-through position the iron ions are accelerated by charge separation in this direction. Any iron ions going in the blow-off direction due to coulomb repulsion would not have sufficient energy to traverse the 12 μm CH layer. Table 1 lists the various ions, and their approximate abundance.

Ion species	Position	Abundance/sr
Protons	Blow-off	7.95×10^5
Carbon	Blow-off	4.21×10^4
Protons	Behind target	3.63×10^6
Carbon	Behind target	1.26×10^6
Iron	Behind target	5.58×10^5

Table 1. Detected ions above 100 keV/nucleon, and their abundance/sr.

Once proton emission was detected, the next experiment was to obtain an estimate of the energies of the protons being emitted. This was done by covering the CR-39 in mylar filters of different thickness, ranging from 3 μm to 12 μm, and directing the laser at a CH tape target. Thicker filters stop protons of higher energy, and so using filters of varying thickness, it was possible to build up an energy spectrum of the protons emitted in the laser-solid interaction. Figure 3 shows a typical proton spectrum of protons in the "straight-through" direction. This shows a maximum proton energy of around 600 keV, and a mean energy of about 250 keV. This is in good agreement with previous observations on the Vulcan laser[1)].

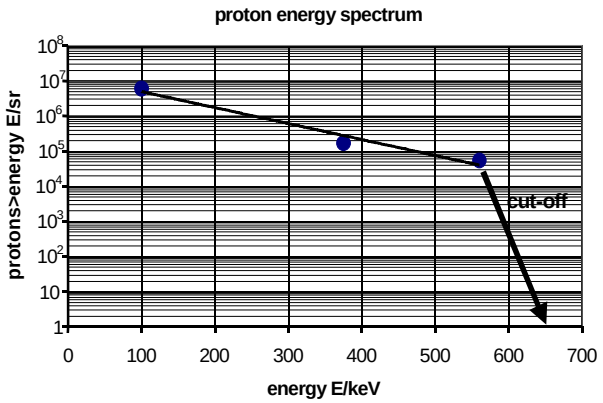

Figure 2. Spectrum of proton energies. This shows an energy cut-off at about 600 keV, and a mean energy of 250 keV.

In addition, a CCD camera positioned above the tape target was used to take images of the plasma emission from the laser-solid interaction. Figure 3 shows a typical emission profile. It is clear that there are several plasma "jets" going in different directions, both from the front of the target, and from the back. This is indicative of several different competing electron acceleration mechanisms[12)]. This occurs when the plasma density scale-length is relatively long, which is brought about by a long laser pre-pulse. As mentioned previously, the pre-pulse in this experiment was measured and found to have an intensity 10^{-4} of that of the main pulse, arriving 14 ns before the main pulse.

Conclusion

This paper reports preliminary measurements of proton emission from a high power, high repetition-rate laser interacting with thin solid targets. It has been shown that protons, as well as heavier ions such as carbon and lead are emitted during such an interaction, although the principal particles emitted are protons. The energies of these protons have been measured and are found to have a mean energy of 250 keV and a cut-off energy of 600 keV when a laser pulse of intensity 5×10^{17} Wcm^{-2} is incident on target. The plasma was also imaged, and was found to produce electron (and hence proton) "jets" in all directions, front and back.

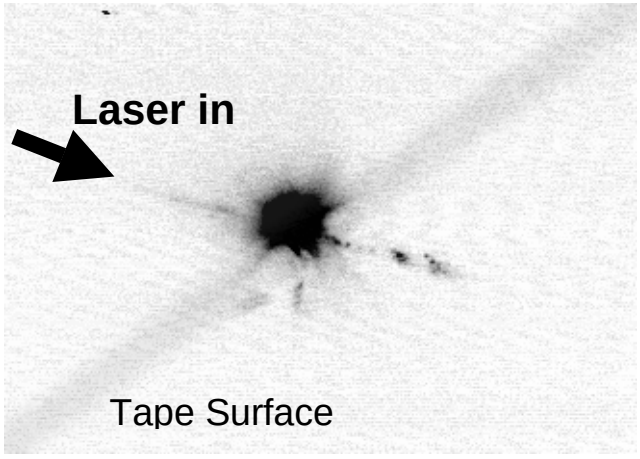

Figure 3. Image of plasma emission from the laser-solid interaction. It is clear that there are several plasma jets present.

This experiment has shown that proton production using a compact, high power, high repetition-rate laser operating at 5×10^{17} Wcm^{-2} is feasible. However, when the upgrade to the Astra laser is completed, intensities of $10^{18} - 10^{19}$ Wcm^{-2} will be achievable. At these intensities, it will be possible to produce protons of much higher energy (mean energy around 10 MeV) and in greater abundance. The magnetic fields induced from a laser-solid interaction of this type will lead to much more collimated proton beams. Also, at these proton energies, nuclear reactions come in to play, and in particular, the reaction $^{18}O(p,n)^{18}F$ (reaction threshold 2.44 MeV) will be investigated, because the isotope ^{18}F is used widely in nuclear medicine. These future experiments are an exciting prospect, and the work described in this paper has laid the groundwork for new research and applications.

* E L Clark is also at Radiation Physics Department, AWE plc, Aldermaston, Reading RG7 4PR, United Kingdom

References

1. A P Fews *et al*, Phys. Rev. Lett. 73, 1801 (1994)
2. K W D Ledingham *et al*, Phys. Rev. Lett. 84, 899 (2000)
3. M Yamagiwa and J Koga, J. Phys. D. 32, 2526 (1999)
4. K Krushelnick *et al*, Phys. Rev. Lett. 83, 737 (1999)
5. E L Clark *et al*, Phys. Rev. Lett. 84, 670 (2000)
6. C N Danson *et al*, J. Mod. Opt. 45, 1653 (1998)
7. A J Langley *et al*, CLF Annual Report 1998/1999, pp 186
8. A J Langley *et al*, CLF Annual Report 1998/1999, pp 187
9. C J Hooker *et al*, CLF Annual Report 1998/1999, pp 190
10. D Strickland and G Morou, Opt. Commun. 56, 219 (1985)
11. M A Perry and G Morou, Science 264, 917 (1994)
12. M I K Santala *et al*, Phys. Rev. Lett. 84, 1459 (2000)

The angular distributions of fragment ions arising from tetrahedral CH_3I

P Graham, K W D Ledingham, R P Singhal, T McCanny, S M Hankin, X Fang

Department of Physics & Astronomy, University of Glasgow, Glasgow, G12 8QQ, Scotland, UK.

P F Taday, A J Langley

Central Laser Facility, CLRC Rutherford Appleton Laboratory, Chilton, Didcot, Oxon, OX11 0QX, UK

P Tzallas, C Kosmidis

Department of Physics, University of Ioannina, GR-45110, Ioannina, Greece.

Main contact email address: *K.Ledingham@physics.gla.ac.uk*

Introduction

The ability to control the relative spatial positions and orientations of groups of molecules is important enough to warrant intensive investigation into the various ways envisioned to achieve this. One such technique to align molecules termed the "brute-force" method [1] uses strong static fields to align and orient the molecules. The disadvantages of this however, is that this method is only applicable to polar molecules. A more versatile technique is to use intense linearly polarised laser pulses to effect an alignment.

Angular distributions of the fragment ions that arise from dissociation of the parent ion can be measured as a function of polarisation angle to determine if the molecule is aligning. However, as pointed out by Ellert et al. [2] the anisotropy observed in the distributions may alternatively be interpreted as an ionisation-rate dependent on the angle made with the laser field. In order to discriminate between the two effects non-resonant nanosecond pulses have been used to align neutrals and a fs laser used to dissociate the parent, then ionise the fragments for detection [3-5]. This way, if the fragment ions show an anisotropy it can only be due to the parent aligning with the ns laser field. However, if using an intense fs laser the fragment distributions narrow with increasing charge-state, it may then be concluded that the parent is aligning with the intense field.

Various heavy molecules such as CS_2 [3, 4], I_2 [3, 5] and CH_3I [3, 4, 6, 7] have been aligned using a nanosecond laser beam. However, as the rotational period for CH_3I^+ is likely to be of the order of picoseconds, alignment within the 50 fs laser pulse of the Astra facility laser, based at RAL, is not thought likely, even with the intense laser fields used. Thus, the anisotropies observed are interpreted to arise from an angle-dependent ionisation-rate. This is the first time that the angular distributions of a tetrahedral have been presented using fs laser pulses only and for fragments other than CH_3^+ and I^+ from the CH_3I molecule.

Experimental

The CH_3I vapour was admitted effusively from an inlet system into a (baked) high-vacuum chamber, which was pumped to a base pressure of 1×10^{-8} Torr. The CH_3I pressure was of order 1×10^{-6} Torr. The ToF system is a conventional linear system, the field-free length being 1.2 m. Ion optics are based on a Wiley-McLaren design and mass resolution is 200 at 100 Da.

The laser system is based on the chirped pulse amplification (CPA) technique [8], and produces pulses of about 5 mJ per pulse at 790 nm at a rate of 10 Hz. The laser pulse enters the ToF perpendicularly to the molecular beam and is focussed using a f/3 spherical mirror mounted on a rotateable x-y-z vacuum bellows. The polarisation vector of the laser is rotated by placing a $\lambda/2$ wave-plate in the beam, just before the Quartz window of the ToF vacuum chamber.

Results

Results from the study of the tetrahedral CH_3I molecule are presented for laser intensity of about 10^{16} W cm^{-2} and 50 fs.

The fragment ion angular distributions are shown in Figures 1 and 2. The parent ion distribution is characteristically isotropic and is not shown. It is immediately obvious that, as in the case for the peripheral ions from CS_2 and CO_2 [9] and N_2O [10], the I-ion distributions are peaked in the direction of collinearity between the polarisation and ToF-axis, (0° and 180°).

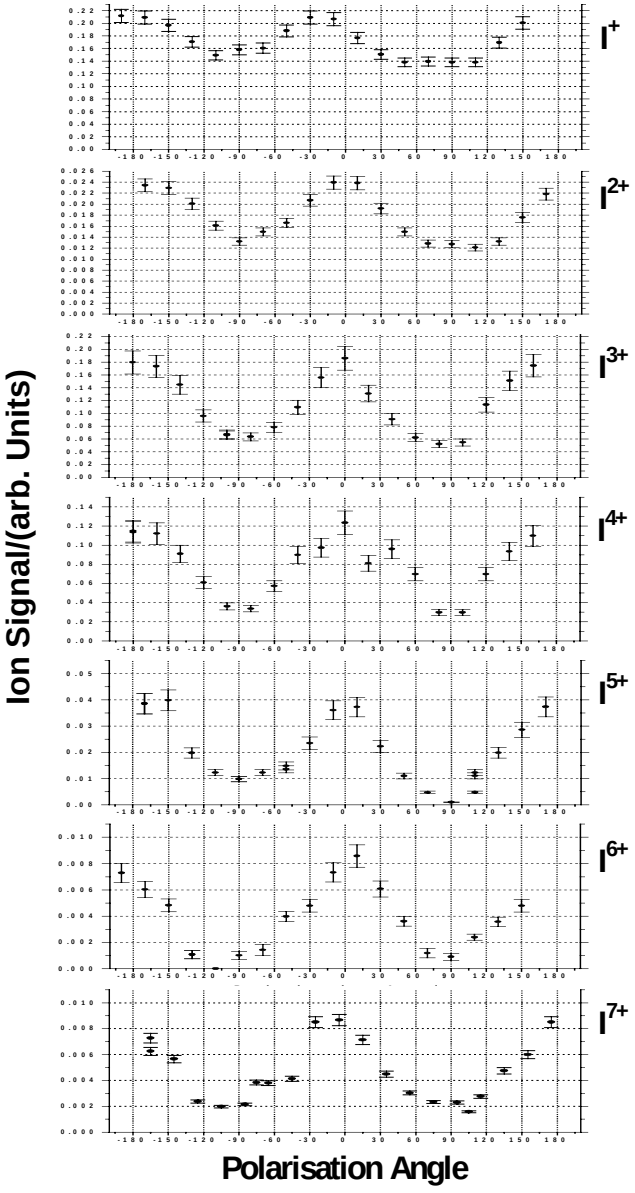

Figure 1. Angular distributions of Iodine fragment ions.

The I-ion distributions (Figure 1) appear to be of equal width, and that minimum ion peak intensity occurs at (± 90°). It is likely that the CH_3I molecule would be too massive for the laser field to induce rotation within the 50 fs laser pulse duration, despite the field strength of the laser pulse.

Another important feature of the I-ion distributions is that, although all I-fragment distributions show a distinct anisotropy, there is also an isotropic component that gradually disappears as the charge-state increases. This suggests that the lesser-charged fragments are likely to come from 'soft' fragmentation of meta-stable parent precursors giving rise to low kinetic energy fragments that are able to be 'captured' by the extraction field. The higher-charged fragments come from highly charged and unstable transient states of the parent molecule, leading to Coulomb explosion and hence higher kinetic energies. This decreases the probability of detecting them when the molecule is orthogonally orientated to the ToF-axis, and so reduces the isotropy of the distribution. Furthermore, molecules oriented perpendicular to the laser field will not achieve the ionisation-state possible when oriented parallel to the field and ionisation is more 'atom-like'.

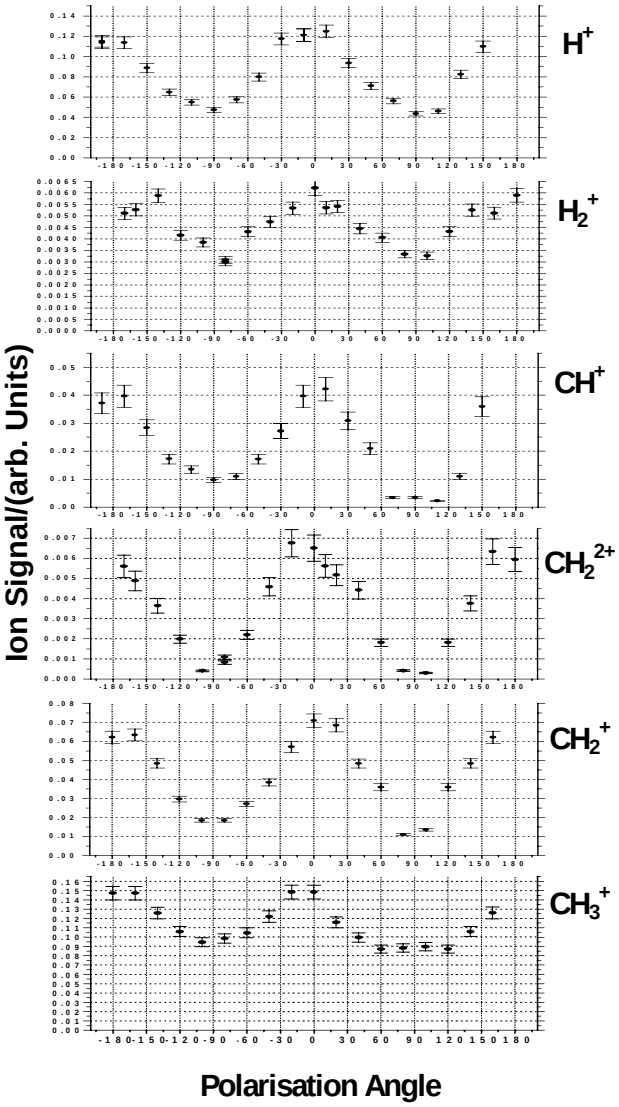

Figure 2. Angular distributions of other fragment ions.

Distributions of CH_m^+ ions ($m \leq 3$), H^+ (fig. 2) and C^{p+} ($p \leq 4$) ions (not shown) were also measured, and their appearance is very similar to those for the I-fragments. This may suggest that the CH_3I molecule is distorted in the presence of the intense laser field prior to dissociating. As each of the ions is peaked along the 0°/180° direction, the CH_3I ion may be excited to a state with a structure similar to that of an umbrella blown inside-out, a so-called umbrella bend mode [7]. The molecule then behaves as a diatomic with an I atom at one end and one of the other fragment ions at the other.

Conclusions

In conclusion, the angular distributions of tetrahedral CH_3I molecules were studied at laser intensities of about 10^{16} W cm^{-2} and in the fs-regime (50 fs). It is shown that for molecules such as CH_3I, whose rotational period is longer than the laser pulse duration, that the observed anisotropies of the fragment ions most likely comes about because the ionisation and dissociation is enhanced for those molecules with their axes initially parallel to the laser field. Alignment would be more pronounced as the charge-state or polariseability of the parent increases, which would result in a narrowing of the distributions. The ions are more efficiently detected along the ToF-axis. All fragment ions are peaked along the ToF-axis direction (0°/180°) which suggests that the tetrahedral molecule behaves as a diatomic molecule in the laser field, i.e. the I-ions are ejected in one direction and all other fragment ions are ejected in the opposite direction. Furthermore, all possible fragment ions are present in mass spectra such that the parent ion can access all dissociation channels and I-ion peaks up to I^{7+} are observed.

All I-fragment distributions show a distinct anisotropy, but there is also an isotropic component that gradually disappears as the charge-state increases. This suggests that the lesser-charged fragments are likely to come from 'soft' fragmentation of meta-stable parent precursors giving rise to low kinetic energy fragments that are able to be 'captured' by the extraction field. The higher-charged fragments come from highly charged and unstable transient states of the parent molecule, leading to Coulomb explosion and hence higher kinetic energies. This is also the first time that I^{7+} from CH_3I has been observed.

References

1. Loison JC, Durand A, Bazalgette G, White R, Audouard E 1995 J. Phys. Chem., 99, 13591-13596
2. Ellert CH and Corkum PB 1999 Phys. Rev. A, 59, R3170-R3173
3. Sakai H, Safvan CP, Larsen JJ, Hilligsoe KM, Hald K, Stapelfeldt H 1999 J. Chem. Phys., 110, 10235
4. Larsen JJ, Sakai H, Safvan CP, Wendt-Larsen I, Stapelfeldt H 1999 J. Chem. Phys., 111, 7774
5. Larsen JJ, Wendt-Larsen I, Stapelfeldt H 1999 Phys. Rev. Lett., 83, 1123
6. Sugita A, Mashino M, Kawasaki M, Matsumi Y, Gordon RJ, Bersohn R 2000 J. Chem. Phys., 112, 2164
7. Samartzis PC, Bakker BLG, Parker DH, Kitsopoulos TN 1999 J. Phys. Chem. A, 103, 6106-6113
8. Strickland D and Mourou G 1985 Opt. Commun., 56, 219
9. Graham P, Ledingham KWD, Singhal RP, McCanny T, Hankin SM, Fang X, Smith DJ, Kosmidis C, Tzallas P, Langley AJ, Taday PF 1999 J. Phys. B: At. Mol. Opt. Phys., 32, 5557-5574
10. Graham P, Ledingham KWD, Singhal RP, McCanny T, Hankin SM, Fang X, Tzallas P, Kosmidis C, Taday PF, Langley AJ 2000 *to be published*

The Analysis of Nitro-PAHs using Laser Desorption / Femtosecond Laser Mass Spectrometry (LD / FLMS)

A D Tasker, L Robson, S M Hankin, K W D Ledingham, R P Singhal, X Fang, T McCanny

Department of Physics and Astronomy, University of Glasgow, Glasgow G12 8QQ

C Kosmidis, P Tzallas

Department of Physics, University of Ioannina, GR-45110, Ioannina, Greece.

A J Langley, P F Taday, E J Divall

Central Laser Facility, CLRC Rutherford Appleton Laboratory, Chilton, Didcot, Oxon, OX11 0QX, UK

Main contact email address: *k.ledingham@physics.gla.ac.uk*

Introduction

Interest in nitrated polycyclic aromatic hydrocarbons (nitro-PAHs) has grown ever since it was shown that PAHs react with oxides of nitrogen to form nitro-PAHs[1]. It has also been found that some nitro-PAHs have high mutagenicity and can be present in a variety of environmental media such as diesel exhaust[2] and urban air particulates[3].

One method of detecting PAHs in environmental samples which allows the sensitivity and selectivity required is two-step laser desorption / ionisation mass spectrometry. Until recently the majority of work in this field has been carried out using nanosecond laser pulses. Dotter *et al*[4] have looked at 4 nitro-PAH standards and concluded that competing photofragmentation pathways were able to produce the NO^+ ion. A parent ion, however, was not always observed. Unfortunately, laser pulses of nanosecond duration are unable to analyse nitro-PAHs due to the rapid dissociation of the molecules before they can be detected. The intense, short pulses of a femtosecond laser, however, may be able to ionise the nitro-PAHs thus reducing the probability of the molecules dissociating before being detected in a mass spectrometer[5].

The aim of the present work is to apply femtosecond laser mass spectrometry (FLMS) to the detection of nitro-PAHs with a view to analysing 'real-world' environmental samples.

Experimental Section

The nitro-PAHs studied are shown in Figure 1.

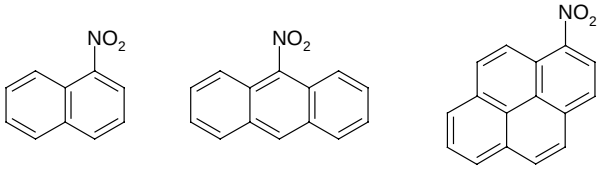

Figure 1. Nitro-PAHs: 1-nitronaphthalene, 9-nitroanthracene and 1-nitropyrene.

The reflectron time-of-flight (ToF) mass spectrometer used in this work has been described previously[6, 7]. Briefly, the source chamber and flight tube are pumped using rotary-backed turbomolecular pumps to a base pressure of 10^{-9} Torr. The sample for analysis is deposited on a stainless steel stub and transferred to the source chamber by means of a load-lock. Laser desorption of the solid samples was achieved using the fourth harmonic output (266 nm) from a nanosecond Nd:YAG laser (Minilite I, Continuum) focussed onto the sample stub using a 27 cm focal length lens. The Astra femtosecond laser system was used for post-ionisation of the desorbed molecules. The delay between desorption and ionisation was variable from 1-37 μs using a delay generator (SRS, DG535). The ions, extracted from the source using purpose-designed ion optics, were guided into the reflectron after which they are detected by a multi-channel plate (Galileo). The signal output from the detector was coupled to a digital oscilloscope (LeCroy, 9344C) for single-shot and averaged-data collection. A PC installed with GRAMS/32 software (Galactic) was connected to the oscilloscope through a GPIB interface and was used for data acquisition and analysis.

Results and Discussion

Laser desorption / femtosecond ionisation mass spectra were obtained for 1-nitronaphthalene, 9-nitroanthracene and 1-nitropyrene over a range of ionisation laser intensities ($1.74 - 8.4 \times 10^{14}$ W/cm^2 at 400 nm and $2.2 - 4.5 \times 10^{15}$ W/cm^2 at 800 nm). All spectra contained an abundance of fragmentation at high intensities and each of the molecules displayed a similar contrast in the mass spectra between 400 and 800 nm.

To illustrate the general behaviour observed, Figure 2 shows the mass spectra of 1-nitropyrene at both 400 and 800 nm. Each spectrum displays ions although there are considerably more high mass ions in the 400 nm case. This is particularly evident in the fact that the 400 nm spectrum displays a large parent peak (a) at m/z = 247 whereas the 800 nm spectrum does not.

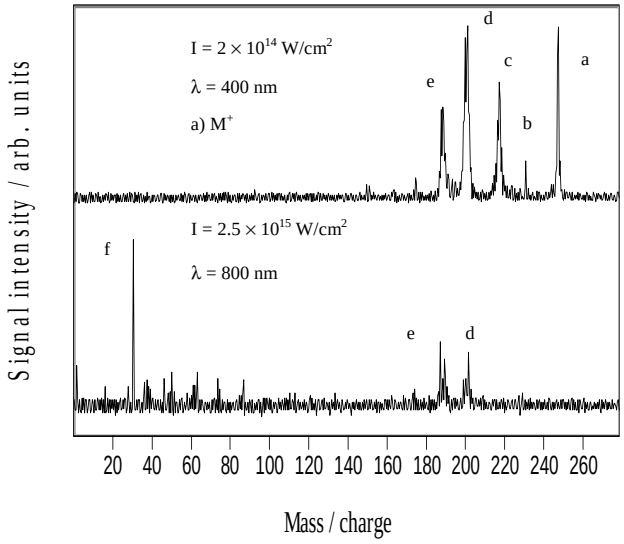

Figure 2. Mass spectra of 1-nitropyrene.

In the 400 nm mass spectrum, the next discernible peaks of lower mass correspond to the $[M–O]^+$ fragment ion (b) at m/z = 231 followed by the $[M–NO]^+$ fragment (c) at m/z = 217. It can be seen that, while the 800 nm spectrum displays far more low mass fragmentation, including a large NO^+ ion at m/z = 30 (f), it does not contain the three high mass ions, including the large parent peak, that were observed at 400 nm. The other significant high-mass peaks in both spectra are the $[M–NO_2]^+$ (d) and $[M–NO–CO]^+$ (e) fragments.

The greater abundance of high-mass ions at 400 nm could be due to the fact that at the lower intensity used at this wavelength, multiphoton processes cannot be ruled out. It is

also possible that a change in the shape of the pulse, as a result of frequency doubling, may also contribute to the higher mass peaks. It is apparent, however, that as ions can be detected at considerably lower energies at 400 nm than at 800 nm, then changing the wavelength of the ionising radiation leads to a change in the abundance of high mass fragments.

The features observed in Figure 2 are very similar to those found in the LD/FLMS of 9-nitroanthracene and 1-nitronaphthalene. Molecular ions were observed in both cases and an intact parent ion was found at 400 nm for each molecule. As with 1-nitropyrene, the mass spectra for these molecules also displayed peaks at high mass corresponding to the $[M–NO]^+$ fragment at m/z = 143 for 1-nitronaphthalene and m/z = 193 for 9-nitroanthracene. The other observable peaks at high-mass once again corresponded to the $[M–NO_2]^+$ and $[M–NO–CO]^+$ ions.

The spectra observed for the three nitro-PAHs used in this study imply that the major mechanism for the decomposition of these molecules involves the dissociation of the parent to yield $[M–NO]^+$ and NO^+ fragments[8, 9] along with the $[M–NO_2]^+$ and $[M–NO–CO]^+$ ions.

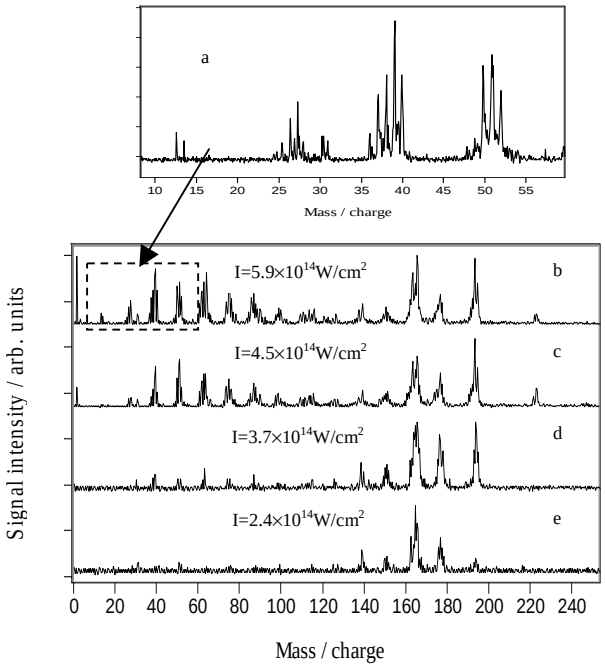

Figure 3. Mass spectra of 9-nitroanthracene at 400 nm.

Figure 3 shows mass spectra for 9-nitroanthracene recorded at four different intensities. At the highest intensity level the mass spectrum shows considerable fragmentation and an abundance of carbon clusters, as was also the case with the other nitro-PAHs. The high resolution of these clusters (a) compared with the higher mass fragments suggests that there is a direct correlation between the position in the laser pulse that the ions are formed and their time of flight. The sharper resolution of the lower mass peaks implies that they were ionised in the central area of the laser focus whereas the broader high mass peaks suggest an energy distribution in any neutral products from laser desorption.

It can be seen in Figure 3 that as the intensity of the ionising beam is lowered (5.9×10^{14} W/cm^2 $\rightarrow$ 2.4×10^{14} W/cm^2), the degree of fragmentation decreases significantly until there is virtually no low mass ions (e). Lowering the intensity leads to a situation where there is not enough energy available to ionise the carbon clusters that are formed after any photo-rearrangement or dissociaton of the molecule.

Conclusions

The nitro-PAHs 1-nitronaphthalene, 9-nitroanthracene and 1-nitropyrene have been studied at wavelengths of 400 and 800 nm using both femtosecond (ionisation) and nanosecond (ablation) lasers coupled to a ToF mass spectrometer. Analysis of mass spectra taken over a range of laser intensities has demonstrated that high mass ions can be observed for each molecule. It was also found that an intact parent ion can be detected at 400 nm in each case. The greater abundance of high mass ions at 400 nm may be due to multiphoton processes taking place during ionisation.

There is evidence, as is the case under nanosecond conditions, that the predominant mechanism for the fragmentation of these nitro-PAHs involves the dissociation of the parent to produce $[M–NO]^+$, $[M–NO_2]^+$ and $[M–NO–CO]^+$ ions.

It was observed that, in all spectra, the resolution was considerably higher in the lower mass carbon clusters than it was at the higher mass fragments, thus giving an indication as to where in the laser pulse these ions were formed. It was also found that, as the intensity of the ionising laser beam was lowered, the degree of fragmentation decreased, yielding parent ion dominated mass spectra ($I = 2.4 \times 10^{14}$ W/cm^2 for 9-nitroanthracene).

In conclusion, this work demonstrates the potential use of LD / FLMS as a tool for the detection of nitro-PAHs and other labile environmental pollutant molecules including pesticides and PCBs.

References

1. J. N. Pitts, K. A. V. Cauwenberghe, D. Grosjean, J. P. Schmid, D. R. Fitz, W. L. Belser, G. B. Knudson Science, 202, 515, (1978)

2. S. M. Hankin, P. John Anal. Chem., 71, 1100, (1999)

3. M. Dimashki, S. Harrad, R. M. Harrison Atmos. Environ., 15, 2459, (2000)

4. R. N. Dotter, C. H. Smith, M. K. Young, P. B. Kelly, A. D. Jones, E. M. McCauley, D. P. Y. Chang Anal. Chem., 68, 2319, (1996)

5. K. W. D. Ledingham, R. P. Singhal Int. J. Mass Spectrom, 163, 149, (1997)

6. I. S. Borthwick Ph.D. Thesis, University of Glasgow, August, (1993)

7. S. M. Hankin *et al* CLF Annual Report 1999-00, pg 89.

8. H. S. Kilic, K. W. D. Ledingham, C. Kosmidis, T. McCanny, R. P. Singhal, S. L. Wang. D, J. Smith, A. J. Langley, W. Shaikh J. Phys. Chem., 101, 817, (1997)

9. D. B. Galloway, J. A. Bartz, L. G. Huey, F. F. Crim J. Chem. Phys., 98, 2107, (1993)

Analysis of PAHs Using Laser Desorption/Femtosecond Laser Mass Spectrometry

L Robson, A D Tasker, S M Hankin, K W D Ledingham, R P Singhal, X Fang, T McCanny

Department of Physics and Astronomy, University of Glasgow, Glasgow G12 8QQ, Scotland, UK

A J Langley, P F Taday, E J Divall

Central Laser Facility, CLRC Rutherford Appleton Laboratory, Chilton, Didcot, Oxon, OX11 0QX, UK

C Kosmidis, P Tzallas

Department of Physics, University of Ioannina, GR-45110, Ioannina, Greece

Main contact email address: *K.Ledingham@physics.gla.ac.uk*

Introduction

Laser desorption / femtosecond laser mass spectrometry (LD/FLMS) allows ultra-sensitive detection and trace analysis of atoms and molecules. The technique involves two steps: desorption of intact neutral molecules from the sample surface and post ionisation of the desorbed analyte using high intensity femtosecond laser pulses (10^{14}-10^{15} W/cm^2). The ions are mass-separated and detected according to their mass-to-charge ratio using a reflectron time-of-flight mass spectrometer. The intense, ultrafast laser pulses from the femtosecond laser are able to ionise virtually any class of molecule and almost eliminate the chance of dissociation prior to detection. Separating desorption and ionisation allows each step to be optimised independently, maximising the sensitivity and selectivity of the technique.

In this study, the technique is applied to the analysis of polycyclic aromatic hydrocarbons (PAHs). These molecules are fused aromatic rings and are environmental pollutants. They are formed during the incomplete combustion of organic material. The most common sources include traffic, industrial processes and tobacco smoke. The analysis of PAHs and their oxy- and nitro- derivatives is of increasing importance since it is now well established[1)] that they have carcinogenic, mutagenic and teratogenic effects on humans and animals.

In contrast to similar studies[2)], the spectra presented for the PAHs anthracene, tetracene and pentacene upon interaction with 50 fs, 790 nm and 395 nm intense femtosecond laser pulses are in some cases dominated by parent ion peaks. The generation of intact parent ions unambiguously identifies the analyte providing strong evidence for the potential of LD/FLMS as a fundamental analytical technique for the detection of environmental pollutants.

Experimental

Details of the reflectron time-of-flight (ToF) mass spectrometer used have been described in detail elsewhere[3,4)]. Briefly, the source chamber and flight tube are pumped using rotary-backed turbomolecular pumps to a base pressure of 10^{-9} Torr. The sample for analysis is deposited on a stainless steel stub and transferred to the source chamber by means of a load-lock. Laser desorption of the solid samples was achieved using the fourth harmonic output (266 nm) from a nanosecond Nd:YAG laser (Minilite I, Continuum) focussed onto the sample stub using a 27 cm focal length lens. The Astra femtosecond laser at the Rutherford Appleton Laboratory system was used for post-ionisation of the desorbed molecules. A variable delay from 1-37 μs was set up between desorption and ionisation using a delay generator (SRS, DG535). The ions, extracted from the source using purpose-designed ion optics, were guided into the reflectron after which they are detected by a multi-channel plate (Galileo). The signal output from the detector was coupled to a digital oscilloscope (LeCroy, 9344C) for single-shot and averaged-data collection. A PC installed with GRAMS/32 software (Galactic) was connected to the oscilloscope through a GPIB interface and was used for data acquisition and analysis.

The molecules studied here are anthracene, tetracene and pentacene, formed from 3, 4 and 5 fused aromatic rings respectively.

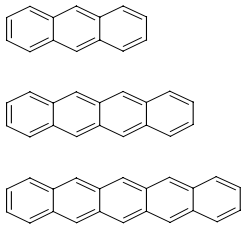

Figure 1. Molecular structures of PAHs investigated: anthracene, tetracene and pentacene.

Results and Discussion

Each molecule was studied at 790 nm and 395 nm over a range of intensities. The mass spectra of signal intensity versus mass-to-charge ratio (m/z) for tetracene at maximum and minimum ionisation intensities using 395 nm and 790 nm wavelengths are shown in Figures 2 and 3 respectively.

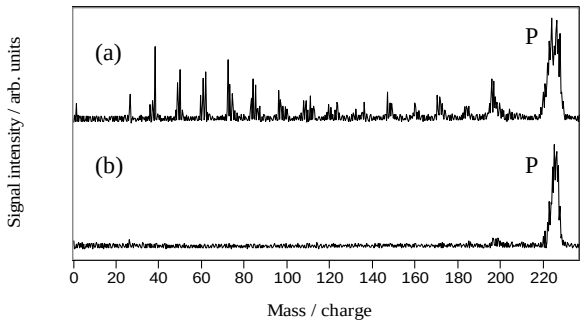

Figure 2. Time of flight mass spectra for tetracene at 395 nm. Ionisation intensities: (a) 4.6 x10^{14} W/cm^2 (b) 2.7 x10^{14} W/cm^2. Desorption intensity: ~ 6.1x10^9 W/cm^2.

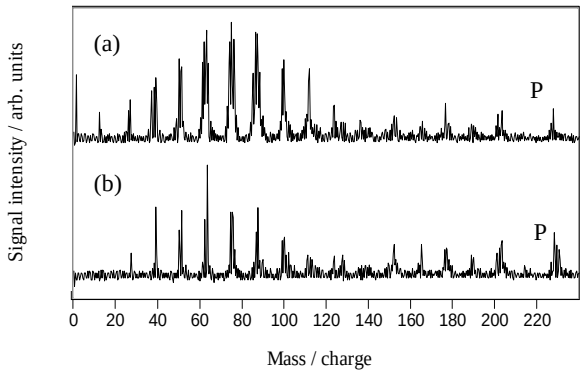

Figure 3. Time of flight mass spectra for tetracene at 790 nm. Ionisation intensities (a) 3.9 x 10^{15} W/cm^2 (b) 2.2 x 10^{15} W/cm^2. Desorption intensity ~5.2 x 10^9 W/cm^2.

Figure 2(a) shows extensive fragmentation; carbon clusters are dominant with C_2^+ to C_{16}^+ readily resolved, but not at the expense of detecting the parent ion, denoted by P, at m/z=228 which is the largest peak in the spectrum. The most interesting feature of the spectra obtained for tetracene at 395 nm is that when the peak intensity of the ionising laser is reduced to 2.7 x 10^{14} W/cm^2 almost no fragmentation is observed and the parent ion dominates the spectra. In contrast to this, at 790 nm ToF spectra for tetracene do not yield exclusively parent ions at the minimum ionisation intensity. As shown in Figure 3, extensive fragmentation occurs with a much smaller yield of parent ion at a maximum intensity of 3.9 x 10^{15} W/cm^2. Although the relative yield of parent ion increases as the intensity of the ionisation laser is lowered to 2.2 x 10^{15} W/cm^2, at no intensity do the spectra show parents only as is the case at 395 nm.

The results described above were common to all three molecules. At intensities of 2.2 – 4.0 x 10^{15} W/cm^2 it is believed that field ionisation is the mechanism for molecular ionisation[5]. Using 395 nm, 50 fs laser pulses the intensity range is reduced to 1.9 – 3.7 x 10^{14} W/cm^2. It is believed at these intensities molecular ionisation could be attributed to multiphoton ionisation processes and/or to a field ionisation mechanism. Also, the shape of the laser pulse at both wavelengths has to be considered when identifying the differences between the spectra, in addition to where in the laser pulse the parent and low mass fragments are ionised. The high resolution of the carbon clusters indicates that ionisation takes place at the focus of the laser beam where the intensity is at a maximum, whereas ion production of the parent reflects the energy spread in neutral production from the ablation process.

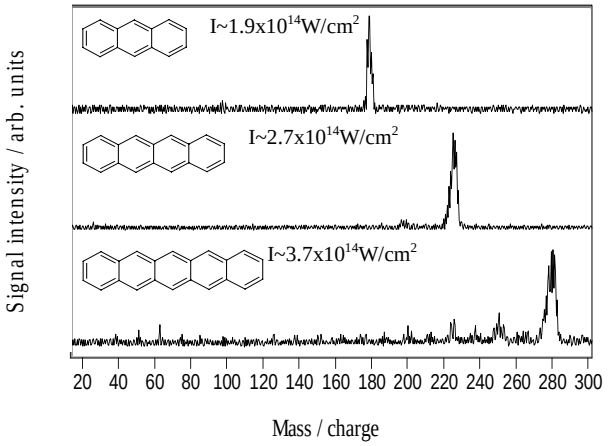

Figure 4. Time-of-flight mass spectra for anthracene, tetracene and pentacene at 395 nm, 50 fs pulses at corresponding threshold intensities.

A comparison of the time-of-flight mass spectra for the three molecules at 395 nm using the minimum ionisation intensity required for detection of ions is shown in Figure 4. It can be seen that the threshold intensity required for the production of ion signals increases with chain length. A small amount of fragmentation is observed for pentacene, the highest mass molecule studied, but the parent ion dominates the spectrum. De Witt and Levis[2,6] have used 780 nm, 170 fs laser pulses and concluded that as the number of atoms in a series increases, an increase in the dissociation probability is observed.

Conclusions

Using nanosecond laser desorption / femtosecond ionisation laser mass spectrometry (LD/FLMS) the PAHs anthracene, tetracene and pentacene were studied. Mass spectra at 395 nm and 790 nm of varying intensity (I ~ 1.6 x 10^{14} – 1.6 x 10^{15} W/cm^2) and 50 fs pulse duration were produced. Although parent ions were detected at both wavelengths, the 395 nm regime yielded parent-ion dominated ToF mass spectra.

The Glasgow group has reported that at 790 nm FLMS was highly efficient for the analysis of various molecules including aromatics, nitroaromatics and organometallics[7], but not all molecules produced parents[8]. However, the data presented for these three molecules has shown that the optimum regime to operate FLMS for PAHs may be at 395 nm and not 795 nm in terms of parent ion production.

This work has provided ToF mass spectra of high-mass PAH molecules that have not previously been analysed. In conclusion, the combination of nanosecond ablation and post ionisation with fs pulses has been shown to be an effective way of analysing environmentally-sensitive, solid phase materials.

References

1. International Agency for Research on Cancer Monographs on the Evaluation of Carcinogenic Risks to Humans, Volume 32, Part 1, IARC, Lyon, France, (1983)
2. M J DeWitt, R J Lewis J. Phys. Chem. 23, 110, (1999)
3. I Borthwick PhD thesis, Glasgow University, (1993)
4. S M Hankin et al CLF Annual Report 1999-00, pg 89.
5. K Codling, L J Frasinski J. Phys. B 26, 783, (1993)
6. M J DeWitt, R J Levis J. Chem. Phys. 110, 23, (1999)
7. K W D Ledingham, R P Singhal Int. J. Mass Spectrom. Ion Proc. 163, 149-168, (1997)
8. P Tzallas et al to be published

Science - Lasers *for* Science Facility Programme

1) Chemistry

2) Biology

3) Physics

Photophysical Properties of Phenothiazine and Pyrene Based Dyades Studied by Picosecond Time-Gated Raman Spectroscopy

S Schneider, J Kurzawa, A Stockmann

Institut für Physikalische und Theoretische Chemie, Friedrich-Alexander-Universität Erlangen-Nürnberg, D-91058 Erlangen, Germany

R Engl, J Daub

Institut für Organische Chemie, Universität Regensburg, D-93040 Regensburg, Germany

P Matousek, M Towrie

Central Laser Facility, CLRC Rutherford Appleton Laboratory, Chilton, Didcot, Oxon, OX11 0QX, UK

Main contact email address: *schneider@chemie.uni-erlangen.de*

Introduction

The investigation of systems in which electron donor and acceptor are separated by a spacer group with well-defined properties (aliphatic – aromatic, rigid – flexible, short – long, etc.) has greatly contributed to a better understanding of photoinduced charge separation and recombination. One reason for this is that important parameters which govern the rates can be varied at will, e.g. the distance and orientation of donor and acceptor moiety or the strength of the electronic coupling between them. But the spacer can also introduce restrictions in that donor and acceptor cannot approach each other to reach a geometry in which electron transfer is an exergonic process. The chemical nature of the donor and acceptor moiety determines the so-called polar driving force

$$PDF = e\,(E^{D}_{ox} - E^{A}_{red}) - E_{00}$$

where E^{D}_{ox} and E^{A}_{red} represent the oxidation potential of the donor and the reduction potential of the acceptor measured in the polar solvent applied. E_{00} corresponds to the lowest excitation energy of the actually excited species.

In order to estimate the change in free enthalpy connected with the photoinduced electron transfer process one has to take into account the energy necessary for the charge separation across the distance R_{DA}. In polar solvents, this contribution is usually negligible, in nonpolar solvents it can be, however, so large that despite a large polar driving force the electron transfer process becomes endergonic.

Because of their good photophysical properties, the systems investigated in this contribution apply phenothiazine as donor and pyrene as acceptor. Furthermore, the phenyl group is introduced as spacer allowing for various stereoisomers with pronouncedly different spatial arrangements of donor and acceptor moieties, i.e. different distances R_{DA} across which charge is shifted (Scheme 1). If geometrical information is taken from semiempirical model calculations using the program package VAMP one finds that ΔG_{et} in nonpolar solvents should be negative for all compounds except for **4**. Since there are a number of assumptions and approximations involved in this estimate it is worthwhile to investigate by proper experimental techniques whether these predictions are correct.

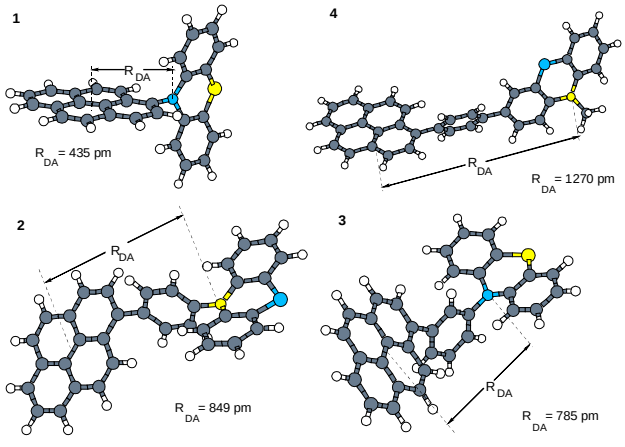

Scheme 1. Geometry optimization via AM1 of 1 - 4 .

Materials and Methods

The synthesis of the compounds under investigation is described elsewhere in detail [1]. Because only a time window of less than 500 ps was investigated, no attempts were made to free the solutions from oxygen.

The experimental set-up for recording the transient absorption spectra is described in detail by M. Towrie et al.[2]. For monitoring the time-resolved resonance Raman spectra the newly developed technique employing a fast Kerr-gate for fluorescence rejection was applied[3]. In both experiments the excitation wavelength (267 nm) matched the $S_0 \rightarrow S_2$ absorption band of pyrene.

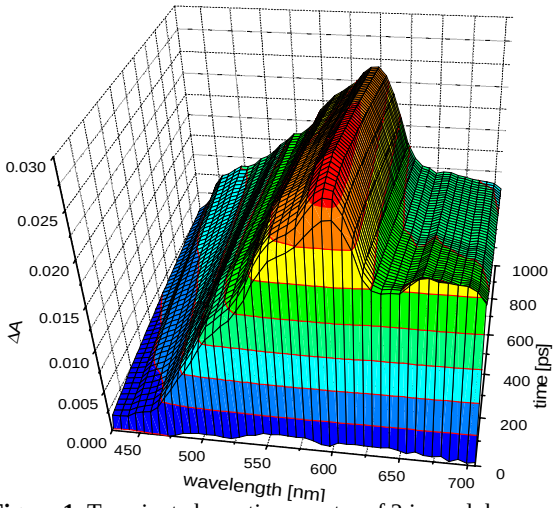

Figure 1. Transient absorption spectra of 2 in cyclohexane recorded at different delay times (λ_{ex}= 267 nm).

Results

In Figure 1, the evolution of the transient absorption measured for the compound **2** in cyclohexane solvent is displayed as an example. Within the cross correlation time of pump and probe pulses, a strong absorption with broad maxima around 580 nm and 670 nm develops. In the following approx. 20 ps one observes an increase in absorbance at around 590 nm and decrease at around 670 nm, both changes being related to the formation of the charge separated state. Since, as one can expect, the compound **3** exhibits a very similar behaviour which is, however, quite different from that of the directly linked system **1** (with strong absorption peak at around 480 nm) one must conclude that the appearance of the absorption spectrum of the bridged radical ion pair is modified by partial conjugation across the phenyl bridge. To illustrate this difference, the transient spectra recorded 25 ps after the excitation pulse are

displayed in Figure 2. The great similarity of the transient absorption spectrum of **1** with the absorption spectrum of the pyrene anion radical allows a unique assignment and the

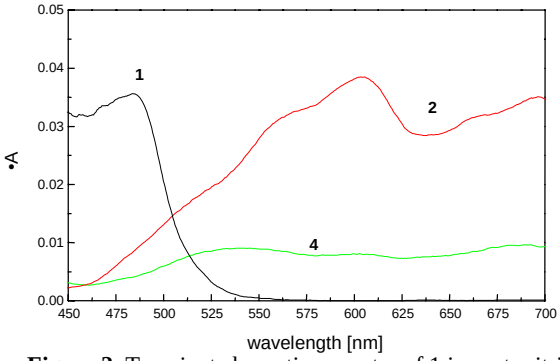

Figure 2. Transient absorption spectra of 1 in acetonitrile, 2 and 4 in cyclohexane at Δt = 25 ps (λ_{ex}= 267 nm).

postulation of complete photoinduced charge separation. If in the phenyl-bridged systems **2** and **3** the different shape of the transient absorption spectra is caused by partial electron delocalization, then the question immediately arises whether in the compound **4** the photolytically created state is one with more or less complete delocalization of the unpaired electrons. To delve deeper into this problem we have recorded time-resolved Raman spectra with the probe laser wavelength within the transient high absorption region.

The TR^3 spectra recorded for the directly coupled system **1** in cyclohexane (Figure 3) show nicely fast formation of a species characterized by a strong vibrational band at around 1597 cm^{-1} and three bands of medium intensity located at about 1345, 1298 and 1216 cm^{-1}. Noteworthy is the fact that band positions are unchanged up to 250 ps delay.

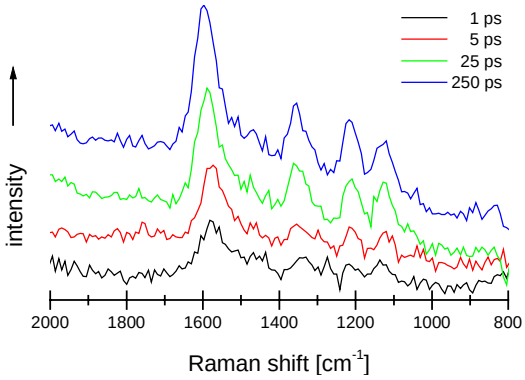

Figure 3. Transient Raman spectra of 1 in cyclo-hexane (λ_{ex}= 267 nm, λ_{probe}= 480 nm).

For the phenyl-bridged systems **2** and **3** we get TR^3 spectra (Figure 4) with a similar band pattern, but slightly shifted band positions. Since we find, in addition, a higher signal intensity for acetonitrile than for cyclohexane as solvent, the assignment of these bands to the pyrene radical anion is well-founded. It is also obvious that the build-up time of the Raman signal is slower for compounds **2** and **3** than for **1** (for which $-\Delta G_{et}$ is the largest !) and that the maximum signal intensities are lower. Also the peak position of the 1597 cm^{-1} band is the same for both phenyl-bridged systems **2** and **3**, whereas the relative intensities vary in accordance with the topology of the bridge.

In acetonitrile, the compound **4** exhibits a very weak, strongly Stokes-shifted emission which can be assigned to a CT fluorescence thus indicating that in polar solvents a photoinduced charge transfer occurs.

Unfortunately, the solubility of **4** in acetonitrile was too low for the TR^3 spectroscopy and we were unable to record a reference spectrum which would provide structural information about the suspected CT state. In cyclohexane, the compound **4** produced a

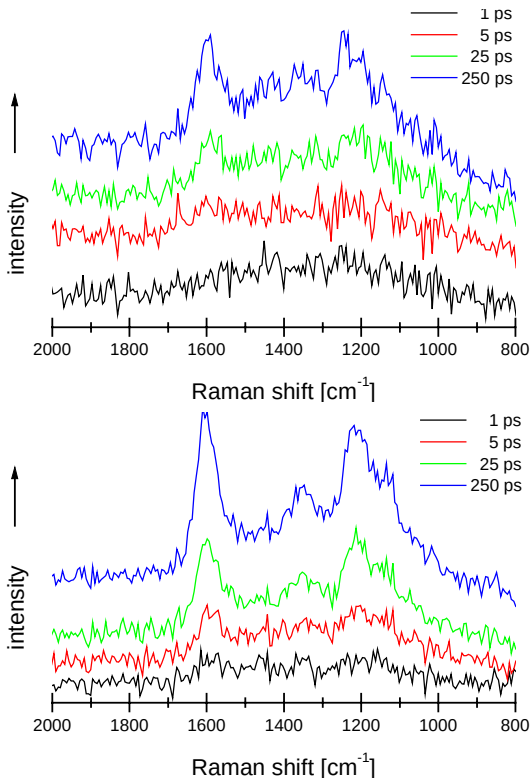

Figure 4. Transient Raman spectra of 2 and 3 in cyclohexane (λ_{ex}= 267 nm, λ_{probe}= 590 nm).

TR^3 spectrum (not shown) which was essentially featureless if one ignores an extremely weak band around 1600 cm^{-1}. On the other hand, the transient absorption spectra of the compound **4** showed a clear evolution within the first 25 ps (not shown). In contrast to acetonitrile solvent, in cyclohexane the absorption induced in the range around 700 nm was substantially more intense. Since phenyl-substituted phenothiazine exhibits a strong S_1–S_n absorption band in this region, the transient absorption observed for **4** could be due to absorption from a state with largely delocalized charge superimposed on an absorption band originating from a locally excited phenothiazine group. Since both states should have similar energies, thermal equilibration between them could lead to a concerted decay.

Conclusion

Application of the Kerr-gate technique allowed the measurement of TR^3 spectra characterizing the photoinduced CT state in a series of electron donor-acceptor systems. It was shown that in nonpolar solvents - in accordance with the estimates for ΔG_{et} - formation of a species in which the electron is localized on the pyrene moiety occurs only in the systems **1 – 3**. For the more extended system **4**, photoinduced electron transfer is either not occurring or leads to a state in which the electron is largely delocalized.

Acknowledgement

Financial support by Volkswagenstiftung, Fonds der Chemie and via the European Union TMR Large Scale Facility Access Programme is gratefully acknowledged.

References

1. R Engl, PhD thesis, Universität Regensburg (1999)
2. M Towrie, P Matousek, A W Parker, S Jackson,Dual Diode Array System for Transient Absorption Spectroscopy, Annual Report of the Central Laser Facility, RAL-TR-1998-080, (1998)
3. P Matousek, M Towrie, A Stanley, A W Parker Appl. Spectrosc., 53 1485, (1999)

Picosecond Dynamics of Monodisperse Nanometer-Sized Silver Colloids

S Schneider, K Pöppl, G Sauer

Institut für Physikalische und Theoretische Chemie, Friedrich-Alexander-Universität Erlangen-Nürnberg, D-91058 Erlangen, Germany

P Matousek

Central Laser Facility, CLRC Rutherford Appleton Laboratory, Chilton, Didcot, Oxon, OX11 0QX, UK

Main contact email address: *schneider@chemie.uni-erlangen.de*

Introduction

Since the absorption spectrum of colloidal gold and silver exhibits a band with high extinction in the visible region, such metal particles have been used since the medieval age, e.g. to stain glass windows. During the past decade, nanometer-sized particles have attracted considerable interest because of their potential to prepare new materials with unique electronic, optical and magnetic properties.

The visible absorption band of gold and silver metal colloids is attributed to surface plasmon oscillation modes of the conduction electrons which are coupled through the surface (roughness) to the external electromagnetic field. Within the framework of Mie theory [1] which applies to particles much smaller than the wavelength of light, dipole and higher order transitions can be treated in principle, but usually only dipole modes are considered. In a quasi-static approximation the extinction coefficient κ is given by:

$$\kappa = (9V\varepsilon_m^{3/2} / c) \cdot [\omega\varepsilon_2(\omega) / (\varepsilon_1(\omega) + 2\varepsilon_m)^2 + \varepsilon_2(\omega)^2]$$

where V is the particle volume, ω the angular frequency of the electromagnetic field, $\varepsilon_1(\omega)$ and $\varepsilon_2(\omega)$ denote the real and imaginary part of the dielectric function of the metal, ε_m represents the dielectric constant of the surrounding medium. The width and peak position of the plasmon band which is determined by $\varepsilon_1(\omega) \approx -2\varepsilon_m$ is in this approximation independent of the particle size. However, in the extinction spectra of monodisperse colloids one observes a strong dependence of both properties on particle size. The experimental findings can be modelled if the dielectric function of the metal is assumed to be size-dependent [2]. For particles with diameters $d \geq 25$ nm, like the ones investigated in this study, higher order multipole absorption as well as scattering contribute to the extinction spectra.

Optical excitation into the plasmon band creates hot electrons as manifested by bleaching of this band. The bleach recovery can be described by a biexponential [3-5]. The first component with a decay time between about 1 and 10 ps is attributed to electronic energy relaxation through electron-phonon coupling. The second component with a decay time of several tens of picoseconds originates from the subsequent cooling of the lattice by phonon-solvent interaction. It is still a matter of debate, whether the first decay time is dependent on particle size or on the excitation intensity. It is also still unclear how the layers of stabilizing agents influence the lattice cooling. In part, this lack of knowledge is connected with the difficulties encountered in the preparation of proper samples, i.e. monodisperse colloids of appropriate size and shape. In this contribution we describe the results of pump-probe experiments performed with nearly monodisperse gelatine-stabilized silver colloids of about 50 nm diameter.

Materials and Methods

The synthesis of the monodisperse silver hydrosols was described in detail earlier [6, 7]. Stabilization against aggregation induced by van der Waals forces was achieved by addition of either 0.1 M KCl (Coulombic repulsion due to negative surface charge) or approximately 0.7% (by weight) gelatine to the fresh colloid. In additional experiments both stabilizers were added.

The changes in the dielectric properties of the surrounding cause small but significant changes in the extinction spectra (Figure 1).

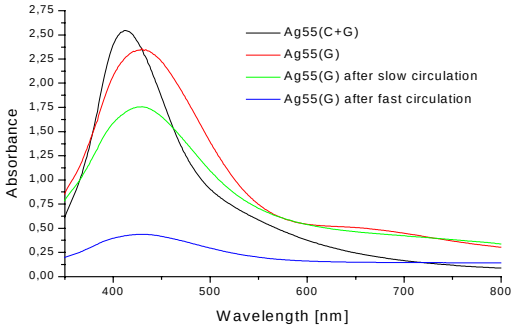

Figure 1. Absorption spectra of 50 nm Ag colloids stabilized with gelatine (G) and both chloride and gelatine (C+G).

The experimental set-up for the pump-probe experiments is described in detail elsewhere [8].

For optical excitation, the second harmonic at λ = 400 nm was used. The transient absorption was measured in the wavelength range 380 to 700 nm applying a white light continuum generated in H_2O using an 800 nm pump pulse. The colloid was circulated by a peristaltic pump through the sample cell with 1 mm path length. Because the mechanical stress in the pump causes sample deterioration (cf. Figure 1), low pumping speeds were used. In order to achieve a sufficiently high S/N ratio an absorbance at 400 nm greater than 2 per cm was necessary.

Results and Discussion

The shape of the extinction spectra displayed in Figure 1 and especially the wavelength of the absorption maximum provide clear evidence that the colloids under investigation are indeed monodisperse and not aggregated. Noteworthy is also the fact that, in contrast to other reports, the shape of the extinction spectra does not change in the course of the experiment.

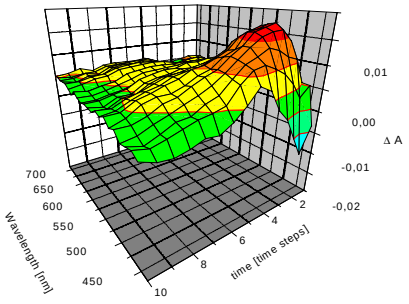

Figure 2. Time- and wavelength-resolved transient absorption of Ag55(G), laser power 100%.

In Figure 2, the absorbance changes induced at full pump power (peak irradiance 1.5 x 10^9 Wcm^{-2}) are shown in dependence on

the probe delay. At the shortest wavelengths accessible, an instantaneous strong bleaching is observed. In the wavelength region above approx. 450 nm, the absorbance is increased. Both transient features disappear on a picosecond time scale. Around 700 nm, a weak transient is observed which exhibits rise and decay on longer time scales.

The transient absorbance changes are strongly dependent on the pump power as demonstrated in Figure 3. Upon increasing pump intensity, the induced absorbance around 500 nm increases but at the same time a bleach of increasing intensity appears at shorter wavelengths. This behaviour can be rationalized by keeping in mind that upon excitation of the conduction electrons the dielectric properties of the silver particles change. The plasmon band of the hot material is lower in peak extinction but larger in width. This implies that the wavelength of equal absorbance moves bathochromically if the pump power is increased and consequently also the point of zero crossing in the ΔA spectra (Figure 3).

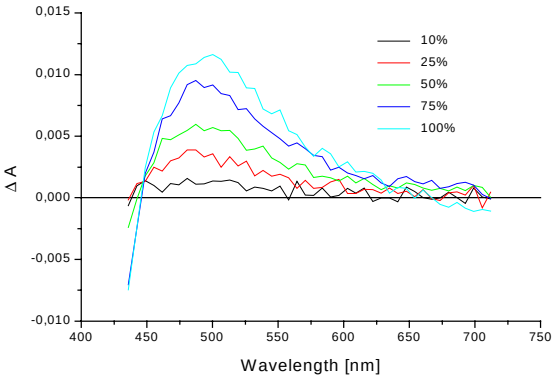

Figure 3. Pump-power dependence of transient absorption of colloid Ag55(G) recorded 2 ps after photolysis.

In Figure 4, the power dependence of the initial rapid relaxation of the induced absorbance (λ ~ 500 nm) is shown. We find that for our 50 nm particles the decay kinetics are dependent on pump power.

Generally, a biexponential fit is sufficient for a proper fit. Figure 5 summarizes the decay constants 1/τ of the fast component. It demonstrates that there is a pronounced dependence on pump power (the solid lines represent an inverse

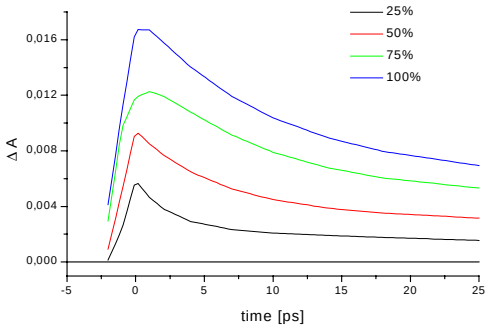

Figure 4. Kinetics of the transient absorption of colloid Ag55(G) in dependence in pump power.

intensity dependence). Furthermore, it is shown that the nature of the stabilizing shell has, at low pump powers, a significant effect on the electronic energy relaxation due to electron-plasmon coupling.

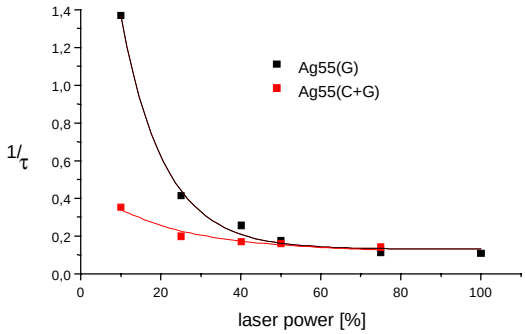

Figure 5. Correlation between rate of absorption recovery and pump power.

Acknowledgement

Financial support by Deutsche Forschungsgemeinschaft, Fonds der Chemie and the access awarded via the European Union TMR Large Scale Facility Access Programme are gratefully acknowledged.

References

1. G Mie
Ann. Phys. (Leipzig), 25 377, (1908)

2. U Kreibig and M Vollmer
Optical properties of metal clusters; Springer Verlag Berlin (1995)

3. T W Robert, B A Smith, J Z Zhang
J. Chem. Phys., 102 3860, (1995)

4. J H Hodak, I Martini, G V Hartland
J. Phys. Chem. B, 102 6958, (1998)

5. S Link and M A El-Sayed
J. Phys. Chem. B, 103 8410, (1999)

6. H Gliemann, U Nickel, S Schneider
J. Raman Spectr., 29 89, (1998)

7. N Shirtcliffe, U Nickel, S Schneider
J. Colloid Interface Sci., 211 122, (1999)

8. M Towrie, P Matousek, A W Parker, S Jackson
Dual Diode Array System for Transient Absorption Spectroscopy, Annual Report of the Central Laser Facility, RAL-TR-1998-080, (1998)

Reorganisation Dynamics of DMABN Intramolecular Charge Transfer Reaction

C Ma, W M Kwok, D Phillips

Department of Chemistry, Imperial College, London SW7 2AY, UK

P Matousek, A W Parker, M Towrie

Central Laser Facility, CLRC Rutherford Appleton Laboratory, Chilton, Didcot, Oxon, OX11 0QX, UK

W T Toner

Department of Physics, Clarendon Laboratory, Parks Road, Oxford, OX1 3PU, UK

Main contact email address: *A.W.Parker@rl.ac.uk*

Introduction

DMABN (4-dimethylaminobenzonitrile) is an archetypal donor-acceptor molecule that performs intramolecular charge transfer (ICT) reaction accompanied by structural reorganization in solution phase[1)]. Since its discovery in 1951, the solvent dependent dual fluorescence phenomenon of DMABN has been interpreted in terms of a forward charge transfer reaction from a molecular B state to an A state occurring only in polar solvents[1)]. In non-polar solvents only the B state is formed and 'normal' fluorescence is seen. Time-resolved fluorescence (TRF) techniques have been widely applied to study the dynamics of this ICT reaction[2)] and various models have been proposed for structures of the B and A states[3)]. The structure of the A state has begun to be confirmed using time-resolved vibrational spectroscopy with results lending support to the TICT model[4,5)]. Based on the observation of absence of dual fluorescence in the gas phase, it is believed that solvent plays a crucial role for the ICT reaction and formation of the A state[3)]. From previous TRF studies, consistent results have been obtained for DMABN in aprotic solvents. However, conflicting data was presented in alcohol solvents[2)], possibly due to combinative influences of solvent dynamic reorientation processes, viscosity and H-bonding. In spite of the large amount of work, systematic experimental investigations on reorganization dynamics and solvent effects are still lacking.

To monitor structural evolution of the excited state of DMABN and the solvent influence, ps-time-resolved resonance Raman (TR^3) spectra of DMABN in several solvents at different delay times is now possible using the newly developed Kerr gate to reject the fluorescence[6)]. Initial transient absorption (TA) measurements were carried out to find the optimum probe wavelength for the TR^3 experiments.

Experimental arrangements

Kerr gated ps-TR^3 experiments were carried out using 90° collection configurations based on the optical parametric amplifiers (OPAs) system [6)]. Setup arrangement for the TA experiments are described elsewhere [7)]. The pump wavelength was 267 nm for all experiments. In the TR^3 measurements, probe wavelength of 460 nm was used to monitor the B and A state simultaneously, 330 nm were used to monitor only the A state[5)]. The TA and 460 nm probe TR^3 spectra presented here were obtained by subtracting a negative time-delay background signal from the positive time-delay signals. TA spectra were calibrated using a 10 nm band-pass filter. Acetonitrile Raman bands were used to calibrate the TR^3 spectra with an absolute frequency accuracy of +/- 10 cm^{-1}. TR^3 bands below 750 cm^{-1} were attenuated by the Rayleigh cut off.

DMABN and spectroscopic grade solvents were used as received. Sample concentrations were 1 to 3 x 10^{-3} mol dm^{-3}.

Results and discussion

TA spectra of DMABN in acetonitrile for several delay times from 2 to15 ps are shown in Figure 1. These show clearly a broad and intense absorption across the visible (450-720 nm) which decreases, whilst intensity around 430 nm increases with increasing time delay. The appearance of an isosbestic point suggests conversion between two distinct states, which are attributed to the B (visible absorption) and A (~430 nm absorption) states based on comparison with previous results obtained in non-polar solvents where only the B state was detected and polar solvents where only the A state was detected[7)]. The time constant for the conversion from B to A state (the ICT reaction) was calculated to be ~5 ps and this is consistent with TRF results of other groups[2)] and ourselves[7)]. Similar spectra were found in other polar solvents but these gave different conversion time constants[2)]. It is seen that, dependent on delay time, both the B and A state absorb at 460 nm (see arrow in Figure 1). It is therefore a suitable excitation wavelength for monitoring time-dependent structural reorganization accompanying the ICT reaction.

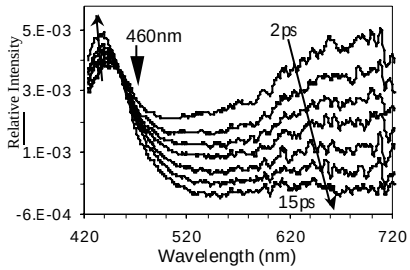

Figure 1. Transient absorption spectra of DMABN in acetonitrile at 267 nm excitation.

TR^3 spectra of DMABN in polar methanol and decanol solvent and non-polar solvent cyclohexane with 267 nm pump and 460 nm probe wavelengths are displayed in Figure 2.

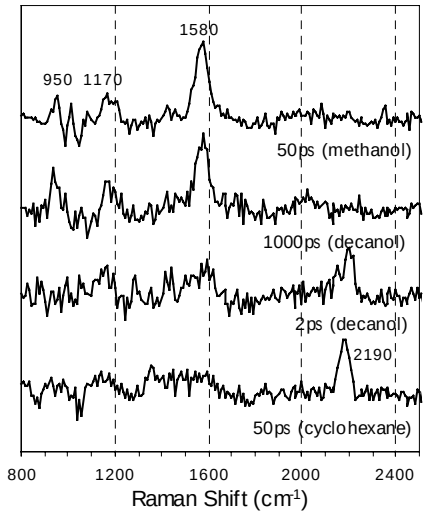

Figure 2. TR^3 spectra of DMABN in methanol, decanol and cyclohexane with 267 nm pump, 460 nm probe wavelengths.

Based on observed band frequencies, spectral patterns and comparison with our earlier TR^3 results obtained in cyclohexane and methanol at different probe wavelengths, the 50 ps spectra

in corresponding solvents shown in Figure 2 are attributed to the B and A state, respectively. In decanol solvent, DMABN undergoes a slow ICT reaction which makes it possible to record TR^3 spectra with enough contributions from B, A or both states at different delay times. The Figure shows that early (2 ps) and later time (1000 ps) spectra recorded in decanol resemble that of the B and A state spectra respectively. Spectra at delay times between 2 and 1000 ps contain contributions from both states. The observed band frequency shifts (down-shift of ~1580 cm^{-1}) and differences in spectral distribution from the early to later time delay spectra reflect substantial changes in geometry as well as difference of electronic density caused by the excitation pulse as time progresses. The results provide direct evidence for the dynamic structural reorganization accompanying the B to A ICT reaction.

By using 330 nm excitation to probe the A state exclusively, it is interesting to observe down shift of CN stretching frequency (~30 cm^{-1} from 25 to 1000 ps) in decanol with an increasing delay time. This is shown in Figure 3(a), where both ~2215 cm^{-1} ground state and ~2100 cm^{-1} the A state CN bands are displayed (no background subtractions were made for the spectra). The dynamic down-shift of the A state CN frequency (obtained from unconstrained Lorentzian fitting) is illustrated by a correlation function C(t) in Figure 3(b). It gives a ~288 ps average time constant, which is similar to the 245 ps decanol solvation time.

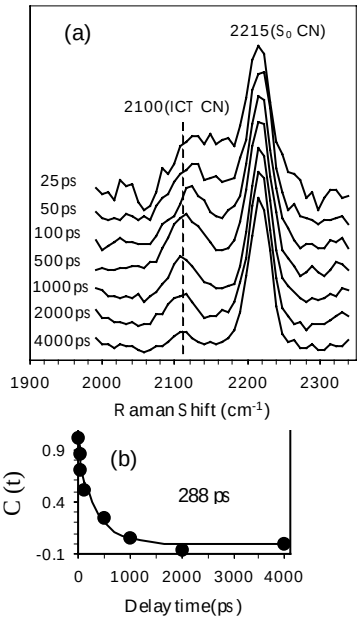

Figure 3. (a) TR^3 spectra of DMABN in decanol with 267 nm pump, 330 nm probe. (b) Time-dependent CN frequency shift.

Similar experiments performed in other alcohol solvents revealed the same picture but the time constants of the shift were found to be solvent dependent. Besides the CN band, one ring C=C stretching mode also shows a frequency shift. However, no band shifts were observed in low viscosity aprotic solvents, such as THF whose dielectric constant is similar to decanol. This solvent-dependent Raman band frequency shift in alcohol solvent is not expected if the ICT reaction leads only to population increase of the A state and decrease of the B state. It implies that solvent-dependent relaxation occurs for the initially formed A state. Longer solvent reorientation time, larger viscosity and possibly H-bonding between the solute and solvent molecules in alcohol solvents, but absent in normal aprotic solvents, cause a slowing of the A state relaxation process which occurs on the pico-second time scale and resolved by our apparatus.

The A state relaxation was confirmed by our Kerr gated TRF experiments. In aprotic solvent the decay of the A state was found to be exponential, but was non-exponential in alcohol solvents. It is known that non-exponential fluorescence decay is predicted for a barrierless large amplitude motion of excited molecules [8]. A shear viscosity dependence of fluorescence quantum yield is expected in this case[8]. Being a flexible molecule, dimethylamino group of DMABN is free to twist and as indicated by theoretical calculations, the potential governing the twist motion is somewhat flat in gas phase or non-polar solvents but develops into a low energy stable well centered at a 90^o twist angle in polar solvents[9]. It is found also[10] that the dipole moment of the excited state molecule increases as twist angle changes from 0^o to 90^o. Therefore, if the CN frequency is taken as gauge of charge separation, the relaxation process could be interpreted in terms of a solvent-controlled barrierless adiabatic charge transfer accompanied by twist motion of dimethylamino group. However, solvation, viscosity and H-bonding dependent experiments, our future work, are required to clarify this interesting argument.

Summary

The DMABN structural reorganization dynamics accompanying ICT reaction and the solvent influence on the process have been studied by Kerr gated TR^3 and TA techniques in several solvents. The TA measurements and TR^3 spectra obtained with 267 nm pump, 460 nm probe provide direct evidence for electronic and geometric structure conversion between the B(LE) to A(ICT) state. A frequency down shift of the A state CN stretching mode with time constant similar to solvent reorientation time was found by 330 nm probe TR^3 experiments in decanol. The observation implies a relaxation of the initially formed A state, which is possibly a solvent-controlled barrierless adiabatic charge transfer accompanied by twist motion of dimethylamino group.

References

1. E. Lippert, W. Rettig, V. Bonacic-Koutecky, F. Heisel, J. A. Miehe and references therein Adv. Chem. Phys., 68 1, (1987)

2. P. Changenet, P. Plaza, M. M. Martin, Y. H. Meyer J. Phys. Chem. A, 101 8186, (1997).

3. W. Rettig, B. Zietz Chem. Phys. Lett., 317 187, (2000).

4. C. Chudoba, A. Kummrow, J. Dreyer, J. Stenger, E. T. J. Nibbering, T. Elsaesser, K. A. Zachariasse Chem. Phys. Lett., 309 357, (1999)

5. W. M. Kwok, C. Ma, P. Matousek, A. W. Parker, D. Phillips, W .T. Toner, M. Towrie Chem. Phys. Lett., 322 395, (2000)

6. P. Matousek, M. Towrie, A. Stanley, A. W. Parker Appl. Spectrosc., 53 1485, (1999)

7. W. M. Kwok, C. Ma, P. Matousek, A. W. Parker, D. Phillips, M. Towrie J. Phys. Chem. A, 104 4188, (2000)

8. B. Bagchi, G. R. Fleming J. Phys. Chem., 94 9, (1990)

9. P. Gedeck, S. Schneider J. Photochem. Photobio. A: Chem., 165 105, (1997).

10. T. Fonseca, H. J. Kim, J. T. Hynes J. Mol. Liq., 60, 161, (1994)

Kerr Gated TR^3 Study of DMABN

W M Kwok, C Ma, D Phillips

Department of Chemistry, Imperial College, London SW7 2AY, UK

P Matousek, A W Parker, M Towrie

Central Laser Facility, CLRC Rutherford Appleton Laboratory, Chilton, Didcot, Oxon, OX11 0QX, UK

W T Toner

Department of Physics, Clarendon Laboratory, Parks Road, Oxford, OX1 3PU, UK

Main contact email address: *A.W.Parker@rl.ac.uk*

Introduction

DMABN (4-dimethylaminobenzonitrile) is an archetypal intramolecular electron donor-acceptor molecule that has attracted the interest of both experimentalists and theoreticians during the last 40 years because of its solvent dependent dual fluorescence[1)]. Explanations fall into four main classes: TICT (Twisted Intramolecular Charge Transfer)[2)], WICT (Wagged ICT)[3)], PICT (Planar ICT)[4)], and RICT (Rehybridisation ICT)[5)]. Despite a substantial body of investigation devoted to the issue, discrimination between proposed models still remains unanswered or in dispute.

Most theoretical work supports the TICT model[6)]. However, direct experimental evidence for the structure of the excited states of DMABN in solution is required. Its importance is illustrated by the recent observation of the C≡N stretching mode of the A state at ~2100 cm^{-1} in time-resolved infra-red spectra, which rules out the RICT model[7,8)]. However, no other vibrational bands of this state have yet been reported. Applying the time-resolved resonance Raman (TR^3) technique to this molecule was impossible because of the intense dual fluorescence signals swamping the much weaker Raman scatter. By using a newly developed Kerr gate of 3 ps resolution[9)] to reject the fluorescence, TR^3 spectra of the A state DMABN and DMABN-d_6 (the methyl groups are deuterated) in methanol solvent have been obtained for the first time. The results provide new evidence for discriminating between the other models and determining the underlying mechanisms.

Experimental arrangements

The experiments were carried out using a TR^3 system based on optical parametric amplifiers (OPAs), described elsewhere[10)] with 90^o collection configuration[11)]. The pump wavelength was 267 nm. Probe wavelengths of 400 and 330 nm were used in resonance with two different electronic transitions. Pump and probe beams had 5-10 and 1-5 μJ energy/pulse, respectively, ~1 ps pulse-length, and parallel polarisations. Solution filters of *trans*-stilbene (330 nm probe) and 9-cyanoanthracene (400 nm) were placed in front of the spectrometer to block the Rayleigh lines and scattered pump light. Details of acquisition methods and the Kerr gate are given elsewhere [9)]. Here we used an improved system based on CS_2 (400 nm) and benzene (330 nm) with throughput up to 60 % (excluding polariser losses).

Each spectrum shown is the sum of 5-10 individual background-subtracted spectra having accumulation times of typically 1000 seconds. Acetonitrile Raman bands were used to calibrate the spectra with an estimated accuracy of +/- 10 cm^{-1} in absolute frequency. The filters attenuated all bands below 750 cm^{-1}. DMABN and spectroscopic grade solvents were used as received. DMABN-d_6 was synthesized according to Reference 3 and its purity confirmed by NMR and mass spectroscopic analysis. Sample concentrations were 1 to 3 x 10^{-3} mol dm^{-3}.

Results

TR^3 spectra of the A state of DMABN and DMABN-d_6 in methanol are shown in Figures 1 and 2, for probe wavelengths of 400 and 330 nm, respectively, at 50 ps delay time between pump and probe pulses. The dotted lines are unconstrained fits to Lorentzian band shapes. Weak features in Figure 1 at ~2040 cm^{-1} are stray light artifacts. Band frequencies and intensities for DMABN and DMABN-d_6 are the same within experimental error. The three prominent bands, ~1580, ~1160 and ~957 cm^{-1}, were also observed in our earlier experiment using a 415 nm probe[11)].

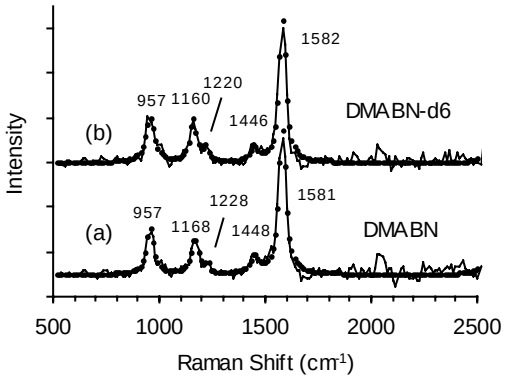

Figure 1. Ps-TR^3 spectra of the A state of (a) DMABN and (b) DMABN-d_6 obtained with 267 nm pump, 400 nm probe.

Using 330 nm probe wavelength (Figure 2), prominent bands that are insensitive to deuteration are seen at 2096, 1581 and ~750 cm^{-1}. However, bands at 1250, 1164 and 1007 cm^{-1} are recorded in the spectrum of DMABN-d_6 while only one broad asymmetric peak at ~1125 cm^{-1} is observed for DMABN in the same region. Fits indicate that this peak comprises two overlapping bands at ~ 1119 and ~ 1160 cm^{-1}. Weak features below 1581 cm^{-1} may correspond to the 1448 cm^{-1} band in the 400 nm spectra.

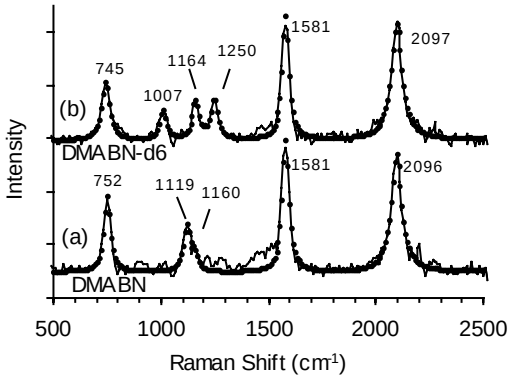

Figure 2. Ps-TR^3 spectra of the A state of (a) DMABN and (b) DMABN-d_6 obtained with 267 nm pump, 330 nm probe.

Band frequencies and relative intensities are listed in Table 1. The provisional assignments considering mainly totally

symmetric vibrations are also included. Some ground state DMABN frequencies are listed for comparison.

Assignment	Vibrational frequency (cm^{-1}) (relative intensity)				
	S_0	A state (TR^3)			
	DMABN	DMABN		DMABN-d6	
	632.8nm	400nm	330nm	400nm	330nm
ring breath	790	~	752(54)	~	745(56)
C-H bend	946	957(33)	~	957(39)	~
	~	~	~	~	1007(23)
	~	~	1119(36)	~	~
C-H bend	1184	1168(25)	1160(11)	1160(30)	1164(33)
	~	1228(3)	~	1220(6)	~
	~	~	~	~	1250(32)
	~	1448(14)	~	1446(11)	~
C=C stretch	1610	1581(100)	1581(100)	1582(100)	1581(100)
CN stretch	2220	~	2096(141)	~	2097(155)

Table 1. Vibrational frequencies and provisional assignments of resonance Raman bands of A state DMABN and DMABN-d_6.

Discussion

The probe wavelengths of 330 and 400 nm were selected to coincide with two strong transitions from the A state of DMABN identified by Okada et al[12]. According to previous studies, it is believed that in methanol, after 50 ps, conversion from the B to A state (the ICT reaction) is complete and all fast relaxation processes involving intramolecular structural change and solvent reorientation have finished[1]. We therefore attribute the recorded spectra to the A state.

The strong C≡N stretching band at 2096 cm^{-1} in only the 330 nm spectra shows ~114 cm^{-1} down-shift from the ground state frequency, in agreement with time-resolved infrared studies[7,8]. The ~1581 cm^{-1} phenyl ring C=C stretching vibration (Wilson 8a) and the 752/745 cm^{-1} ring breathing mode is shifted down by ~30 cm^{-1} and ~38 cm^{-1}, respectively, from corresponding ground sate frequencies (Table 1). The large frequency downshifts of these ring modes together with the downshift of the C≡N mode imply a loosening of the ring structure in the A state with the transferred charge delocalising over the whole benzonitrile group[7]. Indeed, the frequencies we report for the Wilson 1 and 8a modes and the C≡N stretch are very close to those of the benzonitrile radical anion[13] (760, 1592 and 2093 cm^{-1}, respectively), implying almost complete decoupling of the dimethylamino group in the A state of DMABN. This strengthens the argument made on the basis of transient absorption measurements[12] and therefore lends support to the TICT model.

Substantial changes due to methyl group deuteration are only observed in the 1000-1300 cm^{-1} region of the 330 nm probe spectra (Figure 2). Pure methyl vibrations may occur in the 1100-1500 cm^{-1} region but would be expected to show larger changes on deuteration than any observed. We therefore conclude that there are no bands associated with pure methyl vibrations. It is clear, from Table 1, that the dominant modes in the 460 nm spectra are resident on the ring, while modes associated with all three sub-groups, dimethylamino, the ring and cyano, are observed at the stronger 330 nm resonance. This implies the changes in electron density caused by the two excitation wavelengths are different and that at the 330 nm probe wavelength the transition dipole moment is parallel to the long axis of the molecule.

Structural data relating to C_{ring}-N_{amino} stretching mode is crucial to discriminate between the proposed models[1,4,8]. This mode is expected to occur in ~ 1000 to ~ 1400 cm^{-1} region and would be resonance enhanced by the 330 nm long-axis transition and sensitive to deuteration. The 1007 and 1250 cm^{-1} bands of DMABN-d_6, and the 1119 cm^{-1} band of DMABN, at 330 nm probe, have these properties. The enhancement of two bands of this kind in the deuterated molecule at frequencies bracketing that of the single band in DMABN indicates a large difference in the potential energy distributions in either the A state or the upper electronic state, or both. As indicated by ground state normal mode analysis[14], the C_{ring}-N_{amino} stretching vibration may contribute to as many as six modes and may not be dominant in any of them. This therefore prevents unambiguous assignment of this mode at present. However, the absence of a deuteration-sensitive band in the 1250 - 1900 cm^{-1} range, at either probe wavelength, casts doubt on the PICT model. This model predicts a frequency up-shift for the Wilson 13 mode, relative to its ground state value of 1373 cm^{-1} (due to its ~23% ring-N content). However, the PICT model cannot be entirely ruled out since the ground state may not be a reliable guide. The WICT model cannot be ruled out based on the present data.

Conclusion

Using a Kerr gate to reject fluorescence, picosecond time-resolved Raman spectra of the intramolecular charge transfer state of DMABN and DMABN-d_6, have been obtained in resonance with two different electronic states, using probes at 330 and 400 nm. Several resonance Raman bands in the 750-2200 cm^{-1} region are reported for the first time. The prominent C≡N stretch at 2096 cm^{-1} and bands sensitive to amino group deuteration are only observed using the 330 nm probe. At 400 nm, bands assigned to modes localised on the ring dominate the spectrum**.** The results support the TICT model.

References

1. E. Lippert, W. Rettig, V. Bonacic-Koutecky, F. Heisel, J. A. Miehe, Adv. Chem. Phys., 68 1, (1987)
2. K. Rotkiewicz, K. H. Grellmann, Z. R. Grabowski Chem. Phys. Lett., 19 315, (1973).
3. W. Schuddeboom, S. A. Jonker, J. M. Warman, U. Leinhos, W. Kuhnle, K. A. Zachariasse, J. Phys. Chem., 96 10809, (1992).
4. K. A. Zachariasse, M. Grobys, T. Von der Haar, A. Hebecker, Y.V. Ilchev, Y.-B. Jiang, O. Morawski, W. Kuhnle, J. Photochem. Photobiol. A: Chem., 102 59, (1996).
5. A. L. Sobolewski, W. Sudholt, W. Domcke Chem. Phys. Lett., 259 119, (1996)
6. L. Serrano-Andres, M. Merchan, B. O. Roos, R. Lindh, J. Am. Chem. Soc., 117 3189, (1995)
7. M. Hashimoto, H. Hamaguchi, J. Phys. Chem., 99 7875, (1995).
8. C. Chudoba, A. Kummrow, J. Dreyer, J. Stenger, E.T.J. Nibbering, T. Elsaesser, K.A. Zachariasse, Chem. Phys. Lett., 309 357, (1999)
9. P. Matousek, M. Towrie, A. Stanley, A. W. Parker, Appl. Spectrosc., 53 1485, (1999)
10. M. Towrie, A. W. Parker, W. Shaikh, P. Matousek, Meas. Sci. Technol., 9 816, (1998)
11. W. M. Kwok, C. Ma, P. Matousek, A. W. Parker, D. Phillips, M. Towrie, J. Phys. Chem. A, 104 4188, (2000)
12. T. Okada, M. Uesugi, G. Kohler, K. Rechthaler, K. Rotkiewicz, W. Rettig, G. Grabner, Chem. Phys., 241 327, (1999).
13. I Juchnovski, C. Tsvetanov, I. Panayotov Monatsh. Chem., 100 1980, (1969),
14. P. N. Gates, D. Steele, R. A. R. Pearce, K. Radcliffe J. Chem. Soc., Perkin Trans. II**,** 1607**, (**1972)

Reactions of HydroxyCinnamates as Antioxidants

R H Bisby

Division of Biological Sciences, University of Salford, Salford M5 4WT, UK

A W Parker

Central Laser Facility, CLRC Rutherford Appleton Laboratory, Chilton, Didcot, Oxon, OX11 0QX, UK

Main contact email address: *r.h.bisby@salford.ac.uk*

Intoduction

There is growing interest in naturally occurring phenolic compounds that display biological antioxidant properties[1]. These include hydroxycinnamates (4-hydroxycinnamic acid [4HC], ferulic acid [FA], curcumin and caffeic acid or 3,4-dihydroxycinnamic acid [DHC]) which are components of many plant-derived foods [2] and spices [3]. Such compounds have been demonstrated to react with aqueous free radicals [4], inhibit lipoprotein oxidation [5] and to react with oxidising ·OH adducts of pyrimidines [6]. Foley et al [7] have shown that these compounds are also modest singlet oxygen quenchers (second order quenching rate constant, k_q = 4 x 10^6 to 4 x 10^7 dm^3 mol^{-1} s^{-1}) compared with the tocopherol analogue Trolox C (k_q = 4.4 x 10^8 dm^3 mol^{-1} s^{-1} [8]). The same authors have shown the one-electron reduction potentials of the radicals from these hydroxycinnamates to be between 50 to 100 mV more positive that of the Trolox C radical, confirming them to be rather weaker antioxidants than Trolox.

Results and Discussion

a) Oxidation of hydroxycinnamates by triplet duroquinone

On laser flash photolysis (360 nm) of solutions of duroquinone (DQ) the first excited state converts rapidly to the highly oxidising triplet state (^{3}DQ). Rates of reaction of ^{3}DQ with the solutes were determined from measurements of the decay of the ^{3}DQ absorption at 490 nm in deaerated (argon purged) solutions containing phosphate buffer (25 mmol dm^{-3}, pH 7.0) in ethanol/water (50/50 v/v).

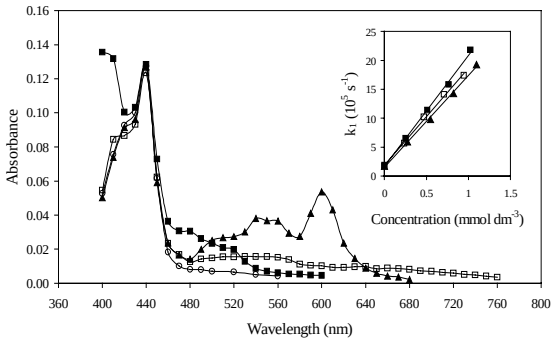

Figure 1. Transient spectra measured 10 μs after the laser flash (360 nm) following reaction of ^{3}DQ with 4HC (▲), FA (□) and DHC (■) in ethanol/water (50/50 v/v) buffered to pH 7 with phosphate (25 mmol dm^{-3}). The transient spectrum of $DQ^{-\cdot}$ obtained from solutions containing ascorbate is shown for comparison (O). INSET:- First order rate constants (k_1) for decay of the ^{3}DQ absorption at 490 nm and 25 ºC as a function of solute concentration, symbols as in the main figure.

The inset to Figure 1 shows the first order rate constants plotted against solute concentrations. The intercepts indicate the lifetime of ^{3}DQ to be ~5 μs in deaerated solution in the absence of reactive solute. The slopes of these plots give the second order rate constants for reaction of ^{3}DQ with 4-HC, 3,4-DHC and FA to be (1.59 ± 0.04) x 10^9, (1.69 ± 0.05) x10^9 and (1.93 ± 0.06) x 10^9 dm^3 mol^{-1} s^{-1} respectively. These values are approaching the diffusion-controlled limit in accord with the high oxidation potential for ^{3}DQ (2.17 V)[9].

The transient absorption spectra of the corresponding hydroxycinnamate radicals are shown in Figure 1. At λ > 480 nm, they are similar to those observed previously by free radical oxidation of hydroxycinnamates in pulse radiolysis experiments[7,10] and show that reaction of ^{3}DQ is by electron transfer to give the corresponding phenoxyl radical:-

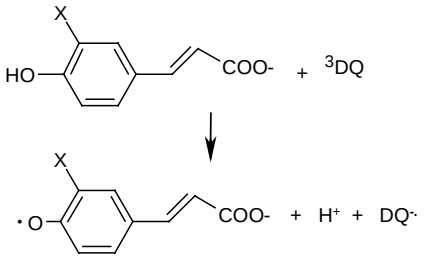

X= -H, 4-hydroxycinnamate (4HC)
-OMe, ferulic acid (FA)
-OH, 3,4-dihydroxycinnamate (DHC)

The absorption peak at 440 nm arises from the simultaneous formation of the durosemiquinone radical anion ($DQ^{-\cdot}$).

b) Time-resolved resonance Raman spectra of the radical from 4-hydroxycinnamate

Of the three hydroxycinnamates investigated, resonance Raman spectra could be obtained only from the radical of 4HC. The spectra in Figure 2 were obtained using a probe laser wavelength of 600 nm to be in resonance with the long wavelength absorption of the radical (Figure 1). The TR[3] spectrum of the cinnam-4-oxyl radical in methanol/water (50/50 v/v) contains two dominant bands at 1543 and 1593 cm^{-1}, in addition to some weaker bands at 1280 – 1320 cm^{-1}. When probed within the long wavelength absorption band (λ ≈ 400 nm), aryloxyl radicals generally show a strong band at 1500-1520 cm^{-1}assigned to the C-O (Wilson ν_{7a}) stretching vibration [11,12]. The ring C-C (Wilson ν_{8a}) mode is absent in phenoxyl[11], but appears at ca. 1580-1620 cm^{-1} in 4-substituted phenoxyl radicals where radical site delocalisation is enhanced[13,14]. Comparison with these data clearly identifies the cinnam-4-oxyl radical resonance Raman band at 1543 cm^{-1} to be the C-O stretching vibration. This may be compared[15] with the vibrational frequencies of a typical C=O double bond (bond order 2, at 1700 cm^{-1}), a C-O single bond (ca. 1200 cm^{-1} in phenols) and the symmetric C-O stretching vibration at in carboxylate ions (bond order 1.5, 1360-1450 cm^{-1}). This suggests that the C-O bond in the cinnam-4-oxyl radical has considerable single bond character. Nevertheless the band at 1543 cm^{-1} is at significantly higher frequency than in the phenoxyl radical (1505 cm^{-1}) and the 4-methoxyphenoxyl radical (1518 cm^{-1}) and shows that the resonance form B (Scheme 1) contributes significantly. The charge separated form

(C) probably does not contribute in this case, although it has been proposed for such as the p-aminophenoxyl radical where the polar substituents stabilize the charge separation[15]. The band at 1592 cm^{-1} may also be readily assigned to the C-C ring stretching vibration by analogy with previous examples of phenoxyl radical spectra[11-16]. The observation of this C-C band in the cinnam-4-oxyl radical also implies substantial delocalisation of the unpaired electron to the 4-substituent, in this case the ethylenic bond. Figure 2 also shows that the cinnam-4-oxyl radical may be observed in less polar solvents, but there is little effect of solvent on relative band intensities or position.

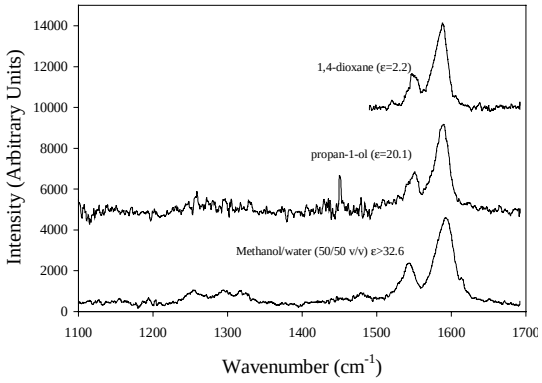

Figure 2. Time-resolved resonance Raman spectra of the cinnam-4-oxyl radical in solvents of varying relative permittivity. The spectra were measured in solutions containing DQ (2.5 mmol dm^{-3}) and 4HC (1 mmol dm^{-3}) excited at 360 nm and probed at 600 nm, with a pump-to-probe delay of 2 μs.

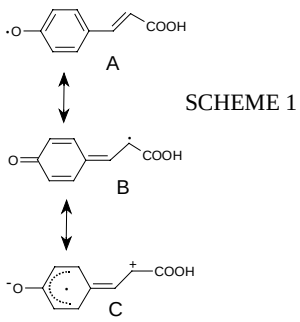

SCHEME 1

The TR^3 spectra show that in the cinnam-4-oxyl radical the conjugated ethylenic bond serves the same purpose as the chroman oxygen atom in α-tocopherol, allowing the radical site to delocalise[17]. The increased stability of the radical is a major factor in increasing the antioxidant activity of these compounds.

References

1. K.Herrmann Crit.rev.Food Sc.Nutr. 28 315 (1989)
2. J.H.Chen and C.T.Ho J.Agric.Fodd Chem. 45 2374 (1997)
3. K.I.Priyadarsini, S.N.Guha and M.N.A.Rao Free Radic.Biol.Med. 24 933 (1998)
4. C.Rice-Evans, N.Miller and G.Pagana free Radic.Biol.Med. 20 933 (1996)
5. M.Nardini, M.D'Aquino, G.Tomassi, V.Gentili, M.Di Felice and C.Scaccini Free Radic.Biol.Med 19 541 (1995)
6. W.Wang, J.Luo, Z.Zuo, J.Zhang and N.Lin Radiat.Phys.Chem. 46 41 (1995)
7. S.Foley, S.Navaratnam, D.J.McGarvey, E.J.Land, T.G.Truscott and C.A.Rice-Evans Free Rad.Biol.Med. 26 1202 (1999)
8. R.H.Bisby, C.G.Morgan, I.Hamblett and A.A.Gorman J.Phys.Chem.A 103 7454 (1999)
9. E.Amouyal and R.Bensasson J.Chem.Soc.Farday Trans I 72 1274 (1976)
10. P.Hapiot, A.Neudeck, J.Pinson, H.Fulcrand, P.Neta and C.Rolando J.Electroanal.Chem. 405 169 (1996)
11. G.N.R.Tripahi and R.H.Schuler J.Chem.Phys. 81 113 (1984)
12. G.N.R.tripathi in Time Resolved Spectroscopy (eds R.J.H.Clark and R.E.Hester) Wiley 1989, pp. 157-218.
13. G.N.R.Tripahi and R.H.Schuler J.Phys.Chem. 92 5129 (1988)
14. A.W.Parker and R.H.Bisby J.Chem.Soc.Faraday Trans 89 2873 (1993)
15. G.N.R.Tripathi J.Phys.Chem.A 102 2388 (1998)
16. R.H.Bisby and A.W.Parker J.Am.Chem.Soc. 117 5664 (1995)
17. G.W.Burton and K.U.Ingold Acc.Chem.Res. 19 194 (1986)

Probing the Light-Switch Mechanism of $[Ru(phen)_2dppz]^{2+}$ by Picosecond TR^3

C G Coates, M Coletti, J Hamilton, J J McGarvey

Department of Chemistry, The Queen's University of Belfast, Belfast, BT9 5AG.

P Matousek, A W Parker

Central Laser Facility, CLRC Rutherford Appleton Laboratory, Chilton, Didcot, Oxon, OX11 0QX, UK

Main contact email address: *j.mcgarvey@qub.ac.uk*

Introduction

The 'light-switch' complex $[Ru(phen)_2dppz]^{2+}$ **(1)** (phen = 1,10-phenanthroline; dppz = dipyridophenazine) has been of particular interest over recent years,[1] due to the marked luminescence enhancement which it undergoes upon intercalation of the dppz ligand within the stacked bases of double and single-stranded nucleic acid. On the basis of a recent investigation into the photophysical response of the complex to solvent environment, employing single-channel, picosecond time-resolved luminescence and absorption techniques, Barbara. et al. proposed a possible mechanism for the light-switch effect.[2] The model involves two close-lying ^{3}MLCT states (formally $Ru^{III}(phen)_2(dppz^{\cdot-})$) – $MLCT^{/}$ and $MLCT^{//}$ – the relative energies of which are sensitive to the polarity of the solvent environment. In water, it was proposed that decay following excitation progresses rapidly (~ 3 ps) through $MLCT^{/}$ to $MLCT^{//}$ from which a largely non-radiative, rapid (250 ps) decay to ground state ensues. In a less polar medium, such as acetonitrile or bound to DNA, it was suggested that the $MLCT^{//}$ state lies sufficiently high in energy relative to $MLCT^{/}$, that intense luminescence from the $MLCT^{/}$ state (τ > 500 ns) becomes the dominant process. Following earlier investigations by our group using nanosecond excited state resonance Raman spectroscopy to probe the excited state nature of **(1)** and the interaction of the complex with nucleic acid,[3] the current studies at RAL involve a comprehensive investigation by picosecond TR^3, transient absorption (TA) and fluorescence spectroscopies into the photophysical nature of the complex in solvent environments of varying polarity.[4]

Also undertaken were preliminary ultrafast spectroscopic studies on the DNA-binder $[Ru(tap)_2dppz]^{2+}$ (tap = 1,4,5,8,9,12-hexaphenanthrene). Previous nanosecond time-resolved and steady-state studies have shown that whilst binding to DNA persists through the more favoured dppz ligand, electron localization in the ^{3}MLCT state appears to be on the tap ligand. Upon photo-excitation of the bound species, an electron transfer from guanine base ensues, resulting in significant quenching of the excited state.

Results and Discussion

Ps-TR^3 Raman spectra were recorded of **(1)** in water, d^3-acetonitrile and d^4-methanol at both 390-390 nm and 400-350 nm pump and probe combinations. For example, Figure 1 shows the ps-TR^3 spectrum of **(1)** in water recorded with 390 nm pump and 390 nm probe wavelengths. The Kerr cell technique[4] was implemented for this wavelength combination in order to avoid collection of any Raman signal from the pump beam. The spectra shown, over a time delay range from 4 to 1000 ps, have each been corrected for ground state species through careful subtraction of the spectrum

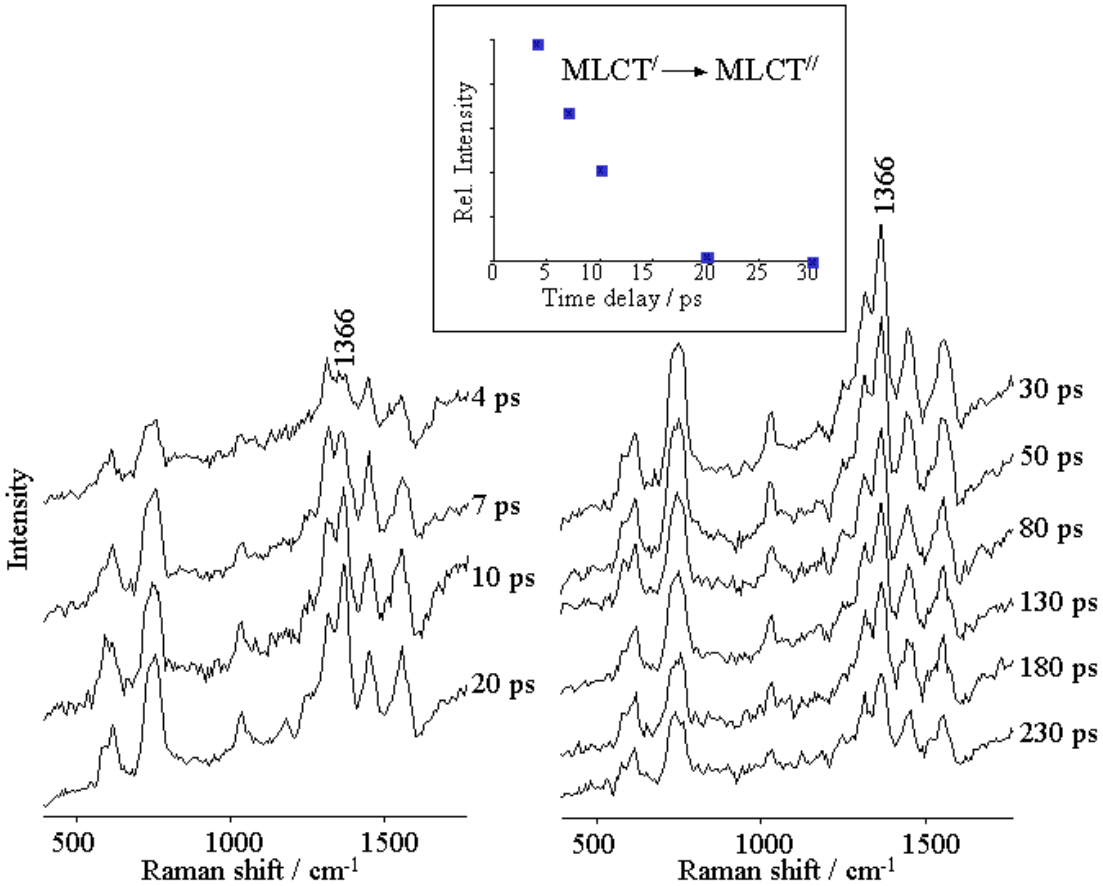

Figure 1. TR^3 spectra of **(1)** in water at 390/390 nm pump and probe at various delay times. Inset: Kinetics of MLCT interconversions derived through spectral subtractions.

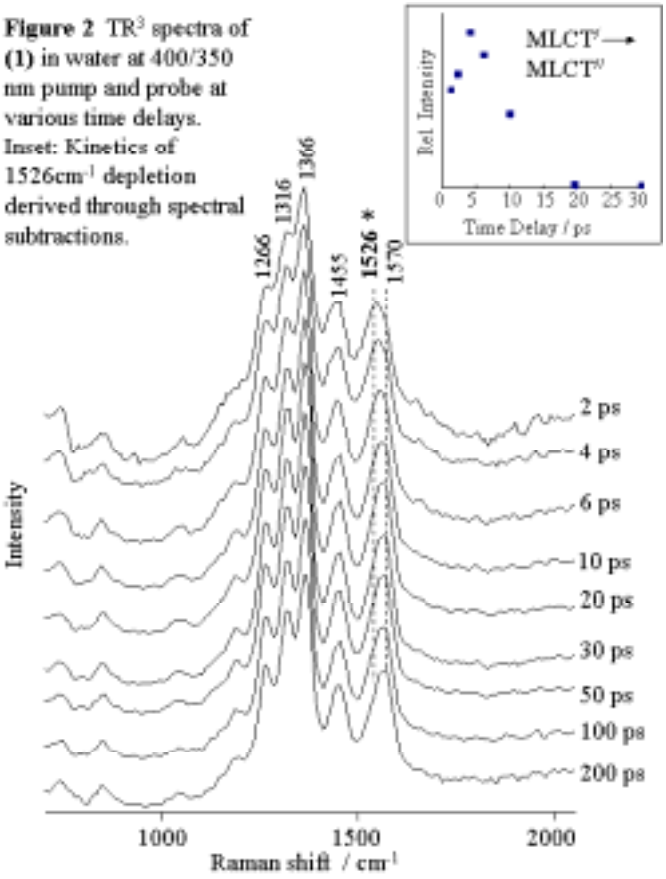

Figure 2 TR^3 spectra of **(1)** in water at 400/350 nm pump and probe at various time delays. Inset: Kinetics of 1526cm^{-1} depletion derived through spectral subtractions.

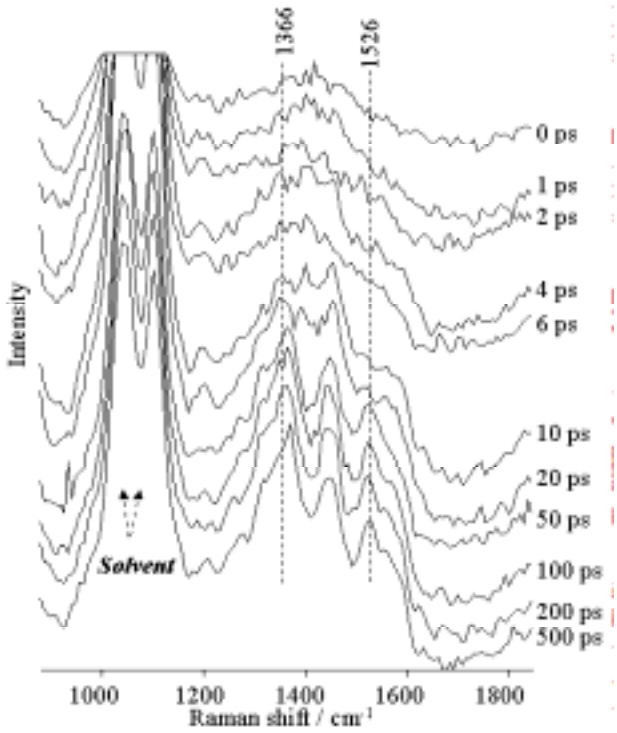

Figure 3 TR^3 spectra of **(1)** in d^7-acetonitrile at 400/350 nm pump and probe at various time delays.

obtained at -20 ps, scaled on removal of the known ground state feature at 1409 cm^{-1}. In general, the spectra shown display features which are in good agreement with excited state spectra of **(1)** in water from previous single-colour transient RR studies, recorded with 396 or 355 nm laser pulses of approx. 8 ns duration.[3)]

The spectral series of Figure 1 can be divided into two phases of decay following excitation. The first phase is apparent between approx. 4 - 20/30 ps, exhibiting a grow-in of the dppz^{-} 1366 cm^{-1} feature, relative to neighbouring dppz^{-} peaks, accompanied by an initial increase in absolute intensity of all the features across the spectrum. The subsequent phase of decay is characterised by a general reduction in intensity of the excited state spectra over the time delays studied between 30 -230 ps. The first phase is attributed to conversion from MLCT$^{/}$ to MLCT$^{//}$ states. The kinetics derived from the spectral changes are shown in Figure 1 inset. Figure 2 shows spectra recorded of **(1)** in water using a 400 nm pump – 350 nm probe combination. The inter-conversion in this case was followed through monitoring of the intensity of a band at 1526 cm^{-1}, a feature which has been previously identified by nanosecond RR at 355 nm excitation for the complex in non-aqueous environments only, and proposed to be associated with the MLCT$^{/}$ state. Indeed, subtractions performed on the current picosecond series show evidence of the band at early times, decaying fully by approx. 20 ps into a state, MLCT$^{//}$, which does not exhibit the feature. Kinetics derived from such subtractions are shown in Figure 2 inset. Further, there is good agreement between the kinetics plots derived from both wavelength combinations in the picosecond studies.

Importantly, spectra of **(1)** in non-aqueous environments revealed that the longer-lived state shows features characteristic of the initial state probed in aqueous environment, consistent with the premise that the MLCT$^{/}$ state is the enhanced luminescent state in such environments (e.g. acetonitrile or DNA-bound). For example, Figure 3 shows spectra recorded of the complex in d^3-acetonitrile at 400 nm pump -350 nm probe, at a series of time delays between 0 - 500 ps, revealing that the long-lived state exhibits the signature feature at 1526 cm^{-1}.

Of additional significance however, are low intensity spectra evident at early times for **(1)** in non-aqueous environment at this 350 nm probe wavelength, suggesting progression through a state which is not resonantly enhanced at this wavelength, unlike either of the MLCT states probed thus far. Switching to a 390 nm probe wavelength revealed spectra at earlier times exhibiting features which have not previously been assigned to a dppz^{-}- based MLCT state.[3)] Thus, this initial 'precursor state' which, with the current time-resolution, is probed in non-aqueous environment only, is apparently more resonantly enhanced at slightly longer wavelengths than is evident for the MLCT states. Further evidence of a delayed grow-in of the MLCT$^{/}$ state has been gathered by picosecond TA and fluorescence measurements for **(1)** in acetonitrile, methanol and DNA. Also, picosecond TA measurements of the complex in water showed a distinction between the long-wavelength absorptions (> 500 nm) of MLCT$^{/}$ and MLCT$^{//}$ states. Interestingly, time-resolved luminescence measurements not only gave evidence for a delayed grow-in of the triplet MLCT$^{/}$ state in non-aqueous media, but also exhibited rapid luminescence decay from the initially populated singlet MLCT state, occurring within the Kerr-gate duration (< 3 ps), in all environments.

Thus, the lowest excited states of **(1)** have been thoroughly characterised by the present studies at the ultrafast facility, supporting the proposal of environment-sensitive tuning of two triplet MLCT states.[2)] In contrast to the Barbara proposal however, evidence for a 'precursor state' emerges from the studies in non-aqueous media but which is not thought to be directly involved in the light-switch mechanism.

Very recently, picosecond TA studies on the photophysical pathways of the complex [Ru(tap)$_2$dppz]$^{2+}$ are beginning to

reveal a progression through an intermediate state before occupation of the final tap$^{\cdot-}$-based MLCT state (formally $Ru^{III}(tap^{\cdot-})(tap)(dppz)$). This latter state, when the complex is intercalated to DNA through the dppz ligand, is responsible for oxidising the guanine base of the polynucleotide, yielding $Ru^{II}(tap^{\cdot-})(tap)(dppz)$ and $G^{\cdot+}$. The rate of cross-over from the intermediate to the active MLCT state seems to be quite insensitive to environment (~ 1-2 ns), the intermediate itself having insufficient redox potential to oxidise the strand, thus constituting a rate-determining step in the photo-induced electron transfer process when bound to DNA. Further picosecond TR^3 investigations on this system are in progress.

Acknowledgements

We wish to thank Dr F. Kirsch-de Mesmaeker for a sample of $[Ru(tap)_2dppz]^{2+}$ and Prof. J.M. Kelly for useful discussions.

We acknowledge support of this work by EPSRC (Grant no. GR/M45696).

References

1. A E Friedman, J C Chambron, J P Sauvage, N J Turro, J K Barton, J. Amer. Chem. Soc., 112, 4960, (1990).
2. E J C Olson, H D Hormann, A M Jonkman, M R Arkin, E D A Stemp, J K Barton, P F Barbara, J. Amer. Chem. Soc., 119, 11458, (1997).
3. C G Coates, L Jacquet, J J McGarvey, S E J Bell, A H R Al-Obaidi, J M Kelly, J. Amer. Chem. Soc., 119, 7130, (1997).
4. C G Coates, E Tuite, M Coletti, P Lincoln, B Onfelt, J Olofsson, P Matousek, A W Parker and J J McGarvey, J. Am. Chem. Soc. (2000), manuscript in preparation.

ps-TR^3 of [Ru(phen)$_2$dppz]$^{2+}$ in Aqueous and Organic Media, and Bound to DNA

J Olofsson, B Önfelt, P Lincoln, B Nordén, E Tuite

Department of Physical Chemistry, Chalmers University of Technology, SE-412 96 Göteborg, Sweden.

A W Parker, P Matousek

Central Laser Facility, CLRC Rutherford Appleton Laboratory, Chilton, Didcot, Oxon, OX11 OQX, UK

Main contact email address: *etuite@ncl.ac.uk*

Introduction

The interaction of substitution-inert metal complexes with DNA has generated considerable interest with respect to development of DNA conformational probes, artificial nucleases, hybridisation sensors, and anti-cancer drugs.[1)] More than any other compound, complexes with the dipyridophenazine (dppz) ligand have provoked intense investigation because of their environmentally-sensitive photophysics. [Ru(phen)$_2$dppz]$^{2+}$ (phen = phenanthroline) is a fluorescent probe for DNA since it luminesces moderately in the presence of dsDNA while displaying no background emission in water – termed the "light-switch effect". When bound to DNA by intercalation of the dppz ligand, the emission is complex and multi-exponential with lifetimes of hundreds of nanoseconds. The emission properties, including lifetimes and spectral maxima and profile, are very sensitive to the enantiomer and base sequence used[2)] although the origin of this variation is not yet understood.

Recently, the effect of environment on the photophysics of this complex has been investigated on faster time-scales to investigate the origin of the light-switch effect.[3,4)] Picosecond transient absorption and time-resolved emission studies[3)] found that in water an initially populated state (termed MLCT') emitting with λ_{max} *ca.* 615 nm rapidly decayed (2.5 ps) to a second state (MLCT") emitting with λ_{max} *ca.* 800 nm which provided a route for efficient non-radiative decay to the ground state (250 ps). No such kinetics were observed for the complex in acetonitrile or bound to DNA, and it was proposed that in both these media MLCT" was too high in energy to be populated: hence, the complex decayed to the ground state from MLCT' on the nanosecond timescale with features typical of MLCT states of ruthenium(II)polypyridyl complexes. It was suggested that in alcohols, MLCT" might be close in energy to MLCT' and could be thermally populated to provide a pathway for rapid non-radiative decay, although radiative decay from MLCT' at *ca.* 615 nm dominates the emission spectrum. More recently,[4)] ps-transient absorption and anisotropy (with photoselection) studies have revealed that the fast decay can be better described as biexponential (700 fs and 4 ps), the first of these being accompanied by a large anisotropy change but not the second. These lifetimes are very similar to those reported for water reorganisation,[5)] suggesting that changes in electron distribution in the excited state are connected with solvent reorganisation. It was also found that when bound to DNA the transient absorption of the complex evolved with lifetimes of 7 ps and 37 ps, with small accompanying changes in anistropy, which was suggested to reflect the timescale of reorientation of the DNA basepairs about the intercalated excited state molecule. Additional findings [B. Önfelt, unpublished results] indicated that in alcohols also the transient absorption spectrum evolved in hundreds of picoseconds. This was accompanied by large anisotropy changes and a linear correlation between the lifetime and the dielectric constant of the medium was found.

Our goal was to investigate the nature of the excited states that we have identified in ps-transient absorption and anisotropy studies, by employing the technique of picosecond time-resolved resonance Raman (TR^3) spectroscopy on the same timescale.

Results & Discussion

To investigate the basis of the "light-switch" effect, we studied the solvent dependence of the picosecond-TR^3 spectra of [Ru(bpy)$_2$dppz]$^{2+}$ and [Ru(phen)$_2$dppz]$^{2+}$, and also the modified complex [Ru(phen)$_2$cpdppz]$^{2+}$, and its dimer. The studies focussed on a comparison between the behaviour of [Ru(phen)$_2$dppz]$^{2+}$ in acetonitrile, water, D_2O, and DNA with preliminary studies also in ethanol. A number of pump/probe combinations were tested before choosing 390 nm / 390 nm as the experimental configuration that allowed the best quality data to be collected and compared for all the media studied. Because of luminescence from the ruthenium complex in this spectral region, it was necessary to employ the ps-Kerr gate to enable Raman spectra to be collected. The Kerr gate also acted as a temporal discriminator blocking the Raman light originating from the pump beam in this single colour TR^3 experiment.

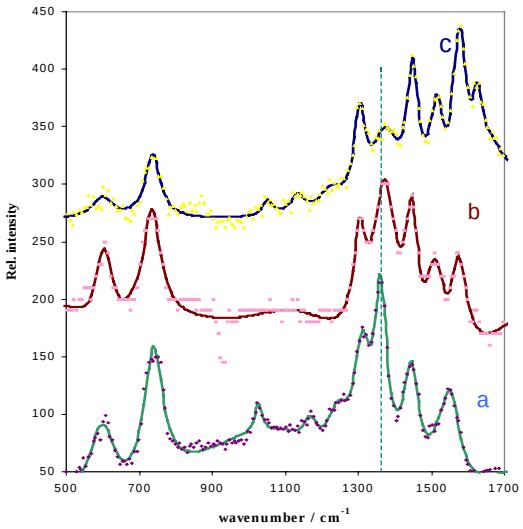

Figure 1. ps-TR^3 spectra of [Ru(bpy)$_2$dppz]Cl$_2$ in (a) water, (b) MeCN and (c) bound to DNA. Pump and probe wavelengths were both 390 nm and all spectra are at 20 ps time delay.

Figure 1 compares the TR^3 spectra obtained for [Ru(phen)$_2$dppz]$^{2+}$ in water, acetonitrile and when bound to DNA. The TR^3 spectrum for the complex bound to DNA grows in intensity with time (with a lifetime similar to changes observed in transient absorption) but does not change in shape and the spectrum resembles closely that observed in ns-TR^2 experiments.[7)] The spectrum in acetonitrile did not appear to show any evolution under our conditions. The kinetic behaviour for the transient observed in water is illustrated in Figure 2: the spectrum clearly changes with time, with a lifetime similar to that measured by transient absorption.[4)] The spectral band positions, in wavenumbers, for the three environments studied are summarized in Table 1.

Since the complex is strongly luminescent in both acetonitrile and DNA (λ_{max} *ca.* 615 nm) one might assume that a common excited electronic state is responsible for this emission. Indeed,

the similarity of certain features in the spectra could be interpreted to support this, especially as the spectrum after equilibration to the lowest excited state in water is notably different. Quantitatively, the spectra in environments that stabilise the luminescent state are characterised by bands at *ca.* 1360 cm^{-1} and *ca.* 1560 cm^{-1} that are shifted to higher wavenumber compared to the spectrum of the lowest excited state in water, and a band at *ca.* 1510 cm^{-1} that is much more intense in non-aqueous environments.

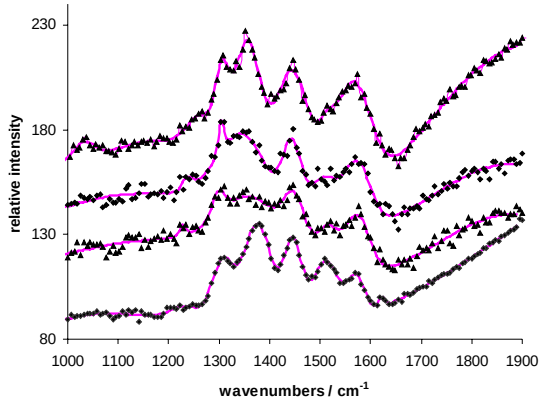

Figure 2. Evolution of TR^3 spectrum for $[Ru(phen)_2dppz]Cl_2$ in H_2O (ambient air). The time delays are from top 20, 6 and 4 ps. Also shown for comparison is the spectrum collected at 20 ps delay in acetonitrile (lowermost trace). Pump 390 nm / Probe 390 nm. The excited state spectra at 4 ps and 6 ps delay were first corrected for leakage through the Kerr gate. All spectra in aqueous solution were then corrected by subtraction first of the ground state spectrum (recorded with a delay of –20 ps) and then of the solvent spectrum.

If the hypothesis proposed by Olsen *et al.*[3] for the existence of two states is correct (MLCT' being the initial state occupied in all solvents, and the only state occupied in acetonitrile), then we would expect to observe in water a different spectrum at 1-4 ps than at 20 ps, and an initial spectrum identical to that in acetonitrile. The two features identified in the literature as being characteristically distinct in the different solvents are the position of the *ca.* 1360 cm^{-1} band[6] (*vide supra*), and the intensity of the *ca.* 1526 cm^{-1} band[7] which has been described as a marker for the luminescent state. With respect to both these features, when probing at 390 nm, we observe that the spectrum at 4 ps has features more similar to the spectrum in acetonitrile than that at 20 ps in water, with a band shifted to higher wavenumber at 1368 cm^{-1} and a stronger relative intensity at 1515 cm^{-1}, suggesting that the initial state is indeed closer in nature to that observed in acetonitrile. However, the 4 ps spectrum in water is *not identical* to the spectrum in acetonitrile, which means that conclusive assignment as the same state is not possible. However, whilst it has been assumed that the same state is populated in MeCN and DNA, since the complex luminesces strongly at *ca.* 615 nm in both cases, neither do they produce identical TR^3 spectra. At this stage of our investigations we cannot distinguish whether this is due to different environments leading to different resonance enhancement patterns through changes in the higher resonant state or there being two different excited states.

What is most remarkable in this study is that the spectrum of $[Ru(phen)_2dppz]Cl_2$ observed in water at short time delays (4 ps), closely resembles that of the complex bound to DNA. In light of this, we suggest that there is a common precursor state, that evolves into a different state when solvated by water which cannot be produced when bound to DNA because the medium of surrounding basepairs cannot adapt to effect "solvation" of the MLCT state. We suggest that the precursor state may also occur initially in MeCN but on too fast a timescale to be resolved within these experiments. On such short timescales solvation dynamics may well be responsible for the evolution of a slightly different state in MeCN from that in DNA.

Conclusion

These ps-TR^3 studies have complemented investigations by our group described in the introduction to this article using time-resolved isotropic and polarised absorption measurements on this set of compounds in water, alcohols and DNA.

From the observed tri-exponential decay to the ground state in water with lifetimes of 700 fs, 4 ps and 250 ps, we have proposed that initial excitation leads to metal-to-ligand-charge transfer (MLCT) to all ligands and that the 700 fs lifetime represents localisation of the MLCT state onto the dppz ligand. Although the TR^3 technique is not applicable for such short time delays, it was possible to confirm (from comparison of different compounds, data not shown) that after 1-2 ps the electron is indeed localised on the dppz ligand. It has been postulated that the equilibrated species in water that decays with a 4 ps lifetime is the same state as observed in acetonitrile. TR^3 spectra collected on this timescale suggest this may not be the case since they have features that are similar to those observed in acetonitrile but not identical. The spectrum recorded in water at 20 ps was very different however, as anticipated if a second MLCT state is involved as postulated. The TR^3 spectra for $[Ru(phen)_2dppz]^{2+}$ in both MeCN and bound to DNA (showing luminescence in both cases) were also similar but not identical, which could indicate that the same state shows different enhancements in different media. However, it is remarkable that the spectrum in water at short times resembles strongly that for the compound bound to DNA, suggesting that this is a common precursor state (prior to solvation, a process that cannot be accommodated by intercalation in DNA) that has not been identified in acetonitrile. Computational efforts are currently underway to provide an interpretation of the spectral changes.

solvent	delay	cm^{-1}	cm^{-1}	cm^{-1}	cm^{-1}	cm^{-1}	cm^{-1}	cm^{-1}
MeCN	20 ps	1236	1307	1377	1456	1509	1572	1622 (w)
CT-DNA	20 ps	–	1304	1391 (br)	1450.5	1515.5	1577.5	1626.5
H_2O	4 ps	1227	1299	1368	1450	1514	1573.5	–
H_2O	20 ps	1251.5	1306	1356	1444.5	1512 (sh)	1564	–

Table 1. Raman band positions in wavenumbers based on preliminary spectral fitting. All data produced from 390 nm pump and probe for $[Ru(phen)_2(dppz)]Cl_2$ in acetonitrile, bound to DNA, and in water at short and long delays.

References

1. Norden, B.; Lincoln, P.; Åkerman, B.; Tuite, E. Metal Ions in Biological Systems 1996, 33, 177-252.

2. Tuite, E., Lincoln, P., Nordén, B. *J.* Am. Chem. Soc. 1997, 119, 239-240.

3. Olsen, E. J. C.; Hu, D.; Hörmann, A.; Jonkman, A. M.; Arkin, M. R.; Stemp, E. D. A.; Barton, J. K.; Barbara, P. F. J. Am. Chem. Soc. 1997, 119, 11458-11467.

4. Önfelt, B.; Lincoln, P.; Nordén, B.; Baskin, J. S.; Zewail, A. H. Proc. Natl. Acad. Sci. *USA* (2000) 97, 5708-5713.

5. Waterson, S. Bakker, H. J. Nature (1999) 402, 506-507.

6. Benniston, A. C., Matousek, P, Parker, A. W. J. Raman Spectroscopy (2000), 31, 503-507.

7. Coates, C. G., Jacquet, L., McGarvey, J. J., Bell, S. E. J., Al-Obaidi, A. H. R., Kelly, J. M. J. Am. Chem. Soc. 1997, 119, 7130.

ns-TR^3 Study of TTF-Anthraquinone Hybrids

A Beeby, M R Bryce, A E Jones, C Christensen, P J Low, D F Peripichka

Dept of Chemistry, Univ of Durham, Durham, DH1 3LE, UK

AW Parker, I P Clark

Central Laser Facility, CLRC Rutherford Appleton Laboratory, Chilton, Didcot, Oxon, OX11 0QX, UK

Main contact email address: *andrew.beeby@durham.ac.uk*

Introduction

Over the past decade a number of systems containing tetrathiafulvalene, TTF, functionality have attracted a great deal of attention as electron donors in solid state charge-transfer materials, which themselves are potentially of interest as organic conductors and new photonic materials. A great deal of work on these and related materials has been carried out by Prof. Bryce's group at Durham[1].

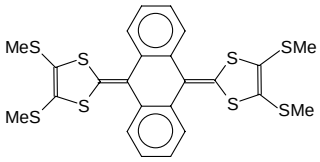

(**1**)

In recent years this has led to the synthesis of hybrid materials containing the TTF moiety such as compound (I).

Cyclic voltammetry studies of compound **1** have shown a single, two electron oxidation wave, arising from the generation of the dication, $\mathbf{1}^{2+}$. Solid state studies of salts of this material show that in the dication the anthracene ring has become planar and aromatised, and it is thought that this is a driving force for the formation of the dication. The single electron oxidation product, $\mathbf{1}^{+\cdot}$, has not been detected in such experiments and is assumed to be thermodynamically unstable with respect to the dication and ground state. It was our intention to study photoinduced electron transfer reactions involving **1** as an electron donor to investigate whether the radical cation could be observed.

Results and discussion

ns-Laser flash photolysis experiments showed that upon irradiation at 266 nm solutions of **1** in halogenated solvents a new species showed the formation of a transient with an absorption maximum at 650 nm. This transient has a lifetime of the order of 80 μs, and is insensitive to the presence of oxygen. The same transient is also observed, albeit with a lower intensity when 355 nm radiation is used. The transient cannot be observed in other, non-halogenated polar solvents, or in hydrocarbon solution. During the course of steady state photolysis experiments we have observed that **1** undergoes photooxidation to give the oxide, **2,** which is also fluorescent, λ_{max} = 600 nm.

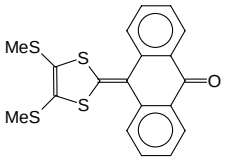

2

It is proposed that the transient species was the radical cation, $\mathbf{1}^{+\cdot}$ and hence the characterisation of this species became a key objective. Using ns-TR^3 we have obtained the resonance Raman spectrum of this species and monitored the kinetic behavior of this species. Again this method showed that the transient could only be detected in halogenated solvents. Attempts to record the resonance Raman spectrum of the electrochemically generated dication using 514 nm radiation were prevented due to fluorescence from the sample. From this observation we can conclude that the observed transient is not the dication or the oxide, **2**.

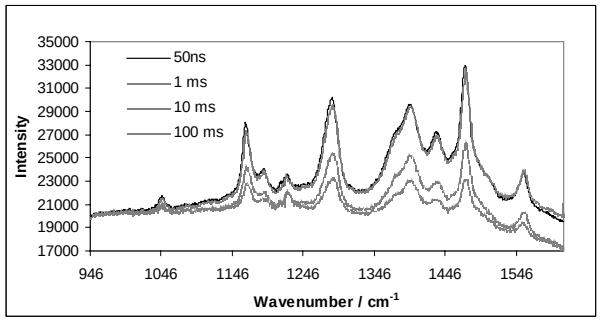

Figure 1. ns-TR^3 spectra of $\mathbf{1}^{+\cdot}$ in $CHCl_3$ solution. Pump 266 nm, probe 650 nm.

By changing the wavelength range over which the scattered light and fluorescence were collected the ns-TR^3 spectrometer was reconfigured to allow the acquisition of the fluorescence spectra induced by the 514 nm 'probe' pulse following the 266 nm 'pump' pulse. Monitoring the fluorescence spectrum over a range of delay times showed a growth of the fluorescence centred at 680 nm. Preliminary analysis of the data obtained in this fashion indicates that the intensity of fluorescence increases with the time delay between the pump and probe pulses and, significantly, that the spectra are similar to those obtained from the dication. By contrast the λ_{max} of the oxide is at 630 nm. We propose that the radical ions, $\mathbf{1}^{+\cdot}$ which are formed immediately by the 266 nm pump pulse undergo disproportionation to give the dication, with shows its characteristic fluorescence, and that this process occurs over a period of tens of microseconds.

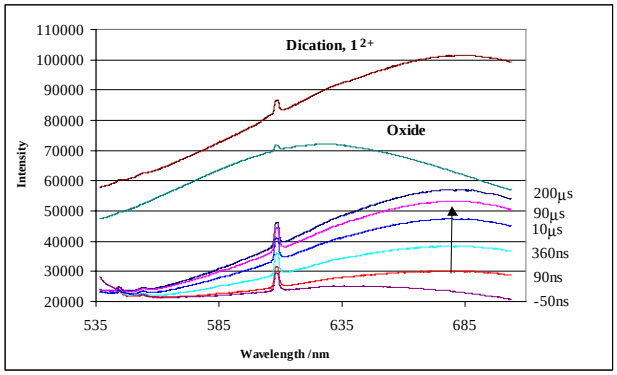

Figure 2. Fluorescence spectra obtained by pump (266 nm) - probe (514 nm) of 1 in degassed $CHCl_3$ solution, showing increase in intensity at 680 nm with time (0 – 200 μs). The dication, 1^{2+} and oxide 2 are shown offset for reference. Note: spectrum is uncorrected for spectral response of detection optics

During the course of this work we have developed cells and a portable potentiostat for the recording of UV-vis and Raman spectroscopies of electrochemically generated species. These are useful for a number of applications since they allow the facile generation of radical ions and allow the acquisition of their spectra.

References

1. M.R.Bryce, J. Mater. Chem., 1995 5 1481-1496 and M.R.Bryce, Adv. Mater., 1999 11 11-23.

Temperature Jump Time-Resolved Infrared Spectroscopy: Measuring Bovine Ubiquitin Protein Folding Kinetics at Low pH

C S Colley, S R Griffiths-Jones, M W George, M S Searle

School of Chemistry, University of Nottingham, University Park, Nottingham, NG7 2RD, UK

I P Clark, A S Wilkinson

Central Laser Facility, CLRC Rutherford Appleton Laboratory, Chilton, Didcot, Oxon, OX11 0QX, UK

Main contact email addresses: *mark.searle@nottingham.ac.uk* and *mike.george@nottingham.ac.uk*

Introduction

The protein folding process, in which a disordered polypeptide chain assembles into a compact three-dimensional structure, is a central problem in structural biology. Protein folding is a highly complex process involving numerous weak co-operative interactions yet despite the complexity of the problem, many small proteins (< 100 residues) fold on a timescale of only a few milliseconds. Current models suggest that folding proceeds through a hierarchical process[1)] in which the lower limit to the kinetics of folding is determined by local structural events such as the formation of α-helices, β-turns and β-hairpins that nucleate the collapse and folding of the polypeptide chain. There has been a considerable amount of experimental effort devoted to determining the kinetics of protein folding using a variety of techniques including stopped-flow, ultrafast mixers, laser temperature jumps and laser-initiated photochemical triggers.[2)] Infrared spectroscopy is a particularly important technique for studying protein structure[3-5)] since the position of the amide I stretching vibration (1610-1680 cm^{-1}) has been shown to be strongly correlated with protein secondary structure because of its sensitivity to hydrogen bonding, dipole-dipole interactions and the geometry of the peptide backbone. Dyer and Woodruff have pioneered the application of fast time-resolved IR spectroscopy (TRIR) together with a laser induced temperature-jump to probe protein folding kinetics.[6)]

In this paper we examine the protein folding of bovine ubiquitin at low pH using TRIR. Bovine ubiquitin is a small protein (76 residues) free of disulphide bridges and has been studied as a model system since it consists of both α-helix and β-sheet. It forms a highly stable, compact structure that has been shown to fold in a two-state process[7)] (Figure 1). We have been investigating the mechanism of folding by examining the conformational propensity of protein fragments for evidence of possible nucleation sites for folding of the native structure.

Figure 1. Structure of bovine ubiquitin from the X-ray co-ordinates (PDB accession code 1ubq).

Experimental

FTIR spectra

Data were collected (1000 scans, resolution of 2 cm^{-1}) using a Nicolet Nexus 670 FTIR spectrometer equipped with MCT detector. A 100 μm IR cell (Harrick) with CaF_2 windows was used. The temperature of the cell was maintained using a circulating water bath and measured with a type-J thermocouple inside the cell. All protein solutions (1 $mmoldm^{-3}$) were made in D_2O with the pH uncorrected for the deuterium isotope effect.

Temperature-Jump TRIR measurements

A diagram of the experimental setup is shown in Figure 2.

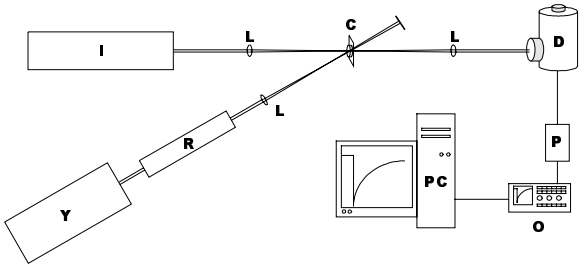

Figure 2. Schematic of Temperature-Jump TRIR Setup: (C) Infrared solution cell, fitted with a thermocouple and connected to a circulating water bath; (D) HgCdTe Detector (Laser Monitoring Systems); (I) continuous wave infrared diode laser (Mutek); (L) Lens; (O) Digital Oscilloscope; (P) Pre-amplifier; (PC) Computer; (R) raman shifter; and (Y) Nd:YAG laser (Continuum Powerlite).

The fundamental Nd:YAG laser emission (1064 nm, 10 ns pulse duration) is Raman shifted using a 1 m Raman shifter (10 bar H_2), producing a high energy pump beam (~5 mJ/pulse) at ~ 1.9 μm. This wavelength corresponds to a weak near-IR absorption band of the solvent, D_2O and induces a temperature jump of ca. 8 ºC. The T-jump was calibrated from the change in absorbance of the D_2O band at 1620 cm^{-1}, providing an internal thermometer. To generate a significant temperature jump it is essential to overlap the pump and probe beams in a small volume and we have used CaF_2 lenses to focus both infrared beams. Beam overlap is achieved using a 200 μm pin-hole giving an interaction volume of ca. 4 nL. The TRIR apparatus used in these experiments has been described elsewhere[8)] Briefly, the pulsed pump laser initiates the reaction and a cw IR diode laser and fast MCT detector are used to monitor the transient IR absorptions at a fixed frequency. IR spectra are built up on a "point-by-point" basis by repeating this measurement at several different IR frequencies.

Results & Discussion

Steady-State FTIR

FTIR spectra have been measured as a function of temperature for a solution of Ubiquitin in D_2O at pH 1. Lowering the pH enables observation of both the folded and unfolded states by reduction of the melting temperature (T_m). NMR studies have shown that the folded structure is not significantly altered relative to pH 7. The FTIR difference spectra, Figure 3(a), shows that the amide I absorption profile changes significantly with temperature. Figure 3 also shows the conventional (b) and deconvolved (c) FTIR spectra of native folded ubiquitin at 25°C**.** The deconvolved spectrum is fitted to 8 Gaussian bands which have been assigned according to the literature precedent.[5)] Monitoring thermal unfolding from the change in integrated intensity of the principal β-sheet band observed at

1629 cm^{-1} at 25°C, demonstrates a reversible co-operative sigmoidal melting process with a T_m of ~65°C at pH 1.0.

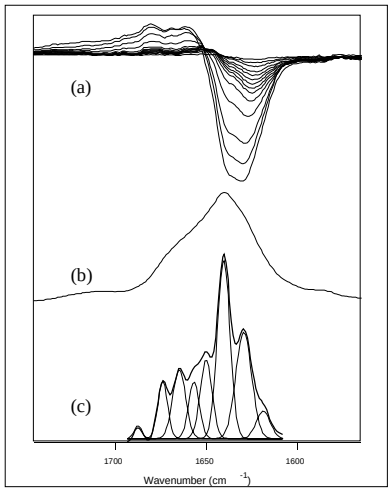

Figure 3. (a) FTIR difference spectra, showing the change in the amide I absorption envelope, relative to the lowest temperature, over the range 278 to 363 K. (b) Conventional and (c) deconvoluted FTIR spectra (assuming Lorentzian band shapes with a full width half maximum of 18 cm^{-1} and using a resolution enhancement factor of 2.5) of bovine ubiquitin at 25°C, pH 1.0 showing 8 principal bands.

Kinetics by TRIR

After an instantaneous temperature-jump of ca. 8°C initiated at 67°C, changes in the IR spectrum, corresponding to transient perturbation of the equilibrium between folded and unfolded states, were used to measure fast folding kinetics. The transient IR spectrum obtained 4 ms after the T-jump between 1600 and 1667 cm^{-1} is in good agreement with the IR difference spectrum obtained from the steady-state spectra collected at 67 and 75°C (Figure 4(a)).

The change in IR absorbance with respect to time was monitored at 1635.5 and 1667 cm^{-1}, corresponding to the disappearance of bands due to ordered secondary structure, and appearance of the weak band due to random coil structure, respectively. Subtraction of the solvent absorption, collected in an identical T-jump experiment in D_2O alone, reveals an exponential decay/growth curve at these wavelengths, which we are readily able to fit to a single rate process consistent with a two-state folding model (Figure 4(b) and (c)). Both kinetic traces yield the same observed rate constant $k_{obs} \approx 1000\ s^{-1}$ although the signal-to-noise ratio is significantly lower at 1670 cm^{-1}. Assuming that k_{obs} is the sum of the folding and unfolding rate constants, $k_{obs} = k_F + k_U$, and that the equilibrium constant at a given temperature is given by $K_{eq} = k_F/k_U$, then we are able to estimate a rate of folding at 75°C (at the T_{max} of the T-jump) of ~400 s^{-1}. As far as comparisons are possible, this rate constant is in broad agreement with previous fluorescence and amide NH exchange kinetic experiments.[7-9)]

Conclusions

The development of a new laser temperature jump TRIR apparatus at RAL has allowed measurement of protein folding kinetics outside the normal time-range accessible using rapid mixing techniques. Our preliminary data suggest that infrared spectroscopy provides a sensitive probe for thermodynamic and kinetic studies We plan to exploit this in detailed future work with other structurally modified ubiquitin variants.

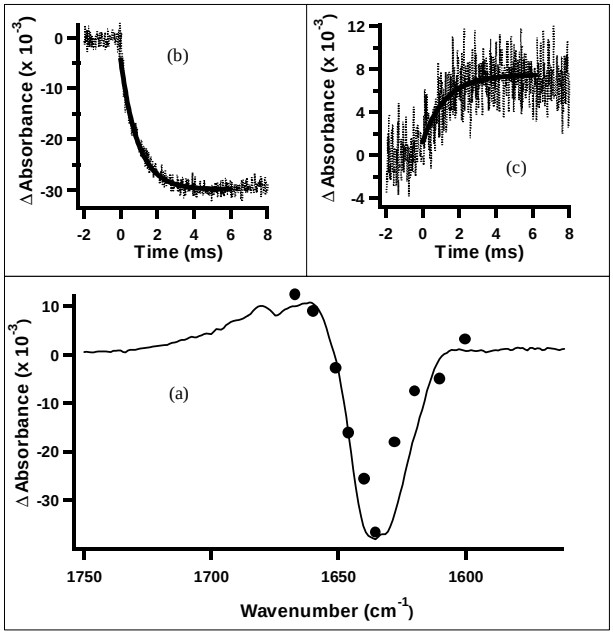

Figure 4. (a) Time-resolved IR spectrum (dots) obtained 4 ms after temperature-jump of 8°C (67°C to 75°C); steady state IR difference spectrum (continuous line) from data at 67°C and 75°C. The decay/growth of the signals due to (b) disappearance of protein secondary structure at 1635.5 cm^{-1} and (c) appearance of random coil at 1667 cm^{-1} are monitored as the protein unfolds following the T-jump. The best-fit line is shown, assuming a single exponential process.

Acknowledgements

We are grateful for access to the EPSRC-funded Central Laser Facility at the CLRC Rutherford Appleton Laboratory in Oxfordshire. We thank M Towrie, P Matousek and A W Parker for helpful discussions. We acknowledge the financial support of the EPSRC for studentships to CSC and SRG-J, and to Roche Discovery, Welwyn, UK for a CASE award to SRG-J.

References

1. R L Baldwin and G D Rose, Trends Biochem. Sci., 24, 77, (1999)
2. M Gruebele, J Sabelko, R Ballew and J Ervin, Acc. Chem. Res., 31 699 (1998)
3. C S Colley, S R Griffiths-Jones, M W. George, M S Searle, Chem. Comm., 593, (2000)
4. J L R Arrondo, A Muga, J Castresana and F M Goni, Prog. Biophys. Mol. Biol., 59, 23, (1993)
5. W K Surewicz, H M Mantsch and D Chapman, Biochemistry, 32, 389, (1993)
6. R B Dyer, F Gai, W H Woodruff, R Gilmanshin, R H Callender, Acc. Chem. Res., 31 709 (1998)
7. S Khorasanizadeh, I D Peters, T R Butt and H Roder, Biochemistry, 32, 7054, (1993)
8. M W George, M Poliakoff and J J Turner, Analyst, 119, 551, (1994)
9. M S Briggs and H Roder, Proc. Natl. Acad. Sci., USA, 89, 2017, (1992)

Picosecond Time-resolved Infrared Investigation into the Photochemistry of (2,4,6-Trimethylbenzoyl)diphenylphosphine Oxide

D C Grills, M W George

School of Chemistry, University of Nottingham, University Park, Nottingham, NG7 2RD, UK

M Towrie, P Matousek, A W Parker

Central Laser Facility, CLRC Rutherford Appleton Laboratory, Chilton, Didcot, Oxon, OX11 0QX, UK

Main contact email address: *Mike.George@nottingham.ac.uk*

Introduction

(2,4,6-Trimethylbenzoyl)diphenylphosphine oxide **(1)** is one of a large family of acylphosphine oxides which have found extensive commercial use as photoinitiators in free radical polymerisation processes.[1)] The acyl-phosphinoyl chromophore has a strong absorption extending well into the visible part of the spectrum. This has made these compounds particularly suited to the curing of white lacqeurs. Photolysis of **1** causes highly efficient α-cleavage ($\phi \sim 0.6$) from a short lived ($\tau < 1$ ns) triplet excited state and the formation of 2,4,6-trimethylbenzoyl **(2)** and diphenylphosphinoyl **(3)** radicals (see Scheme 1).[2)] The phosphinoyl radical **3** has been found to be more reactive towards unsaturated compounds than the benzoyl radical **2**.[3)] Consequently, its reactivity towards a number of substrates has been extensively studied using a variety of techniques including laser flash photolysis (LFP)[4)] and time-resolved ESR.[5)]

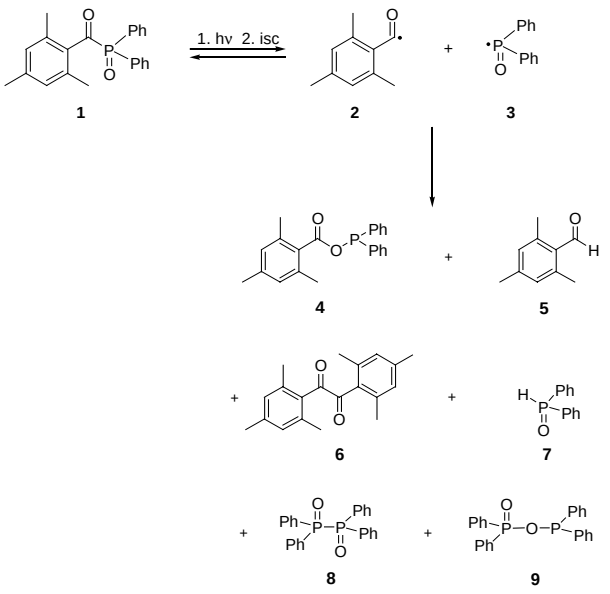

Scheme 1. The photoproducts obtained upon photolysis of **1**.

However, the reactivity of **2** has not been so extensively investigated. The UV absorption of **2** in solution is expected to be very weak (similar to that of the benzoyl radical), thus preventing its detection by LFP. Ingold and co-workers first demonstrated the characterisation of benzoyl radicals using nanosecond time-resolved infrared (TRIR) spectroscopy.[6)] Benzoyl radicals have a characteristic infrared band at 1790 - 1830 cm^{-1} depending upon the nature of the substituents on the benzene ring. We recently used nanosecond TRIR spectroscopy to directly detect **2** in solution and measure its reactivity towards a series of substrates.[2)] **2** has a strong IR absorbance centred at 1800 cm^{-1}. Steady-state photolysis studies showed that a number of photoproducts are produced upon photolysis of **1** in the absence of a radical trapping agent (see Scheme 1). However, in the presence of $BrCCl_3$, in addition to the expected trapped products (2,4,6-trimethylbenzoyl bromide and diphenylphosphinic bromide), the rearrangement product, diphenyl[(2,4,6-trimethylbenzoyl)oxy]phosphine **(4)** was persistently formed. This supported the conclusion obtained previously[7)] from ^{31}P CIDNP experiments that **4** is rapidly produced via an *in-cage* recombination of radicals **2** and **3**. An *in-cage* formation of **4** would compete with the formation of the polymerisation-initiating radicals **2** and **3**, considerably reducing the efficiency of the UV curing process. Therefore, in order to gain further insights into the photochemistry and mechanisms of reactivity of commercial acylphosphine oxide polymerisation photoinitiators, we have performed a preliminary picosecond TRIR (ps-TRIR) investigation of **1** in acetonitrile solution using the recently developed ps-TRIR facility at the Rutherford Appleton Laboratory.

Experimental

The details of the experimental apparatus for the new Picosecond TRIR Spectroscopy Laboratory at RAL will be published elsewhere.[8)] Briefly, part of the output from a Ti:sapphire oscillator/regenerative amplifier (800 nm, 1 ps, 3 mJ) was used to pump a BBO OPA. This OPA amplified the idler (ca. 1400 nm) from our existing 400 nm pumped picosecond OPA.[9)] The signal and idler output were then passed directly into a single $AgGaS_2$ crystal, generating tunable narrowband mid-infrared pulses (ca. 25 cm^{-1} FWHM, 1 ps, ca. 5 μJ) by difference frequency generation. Residual 400 nm light, with polarisation at the magic angle, was used to excite the sample, which was flowed in acetonitrile solution through a 1 mm nozzle producing an open jet at the focus of the pump and probe beams. The delayed probe beam was split into signal and reference beams before the sample and then focussed onto a matched pair of liquid N_2 cooled HgCdTe detectors. The outputs of the detectors were sampled by boxcar integrators in single sample mode and their difference was measured by a lock-in amplifier. Chopping of the pump beam permitted measurement of the detector outputs with pump-on and pump-off, allowing the change in infrared absorption of the sample upon excitation to be measured at various time delays.

Results and Discussion

Figure 1(a) shows the kinetic trace obtained at 1800 cm^{-1}, following 400 nm excitation of **1** in acetonitrile. A strong transient absorption is observed to grow in with a time constant of 130 ps. This is assigned to the formation of the benzoyl radical **2**, the decay of which has previously been monitored[2)] at this wavenumber by TRIR on the microsecond timescale. This growth constant is similar to those[10)] obtained by Turro and co-workers with LFP for the decay of the singlet excited state of **1** (τ = 128 ps) and the formation of the phosphinoyl radical **3** (τ = 123 ps). However, there is extensive evidence from magnetic field effects, CIDNP experiments and triplet quenching experiments that implicates the role of the triplet excited state of **1** as the dominant pathway for α-cleavage to produce benzoyl radicals.[10)]

The results from the picosecond LFP experiments were reconciled by suggesting that photolysis of **1** initially produces the singlet excited state which intersystem crosses to the excited triplet state, which in turn α-cleaves to form the radicals **2** and **3** (see Scheme 2). The triplet excited state is present but cannot

be easily detected by time-resolved methods because it decays as quickly as it is formed. The rate limiting step in this process is therefore the intersystem crossing from singlet to triplet and thus the measured rate of growth of **2** is actually that of the intersystem crossing.

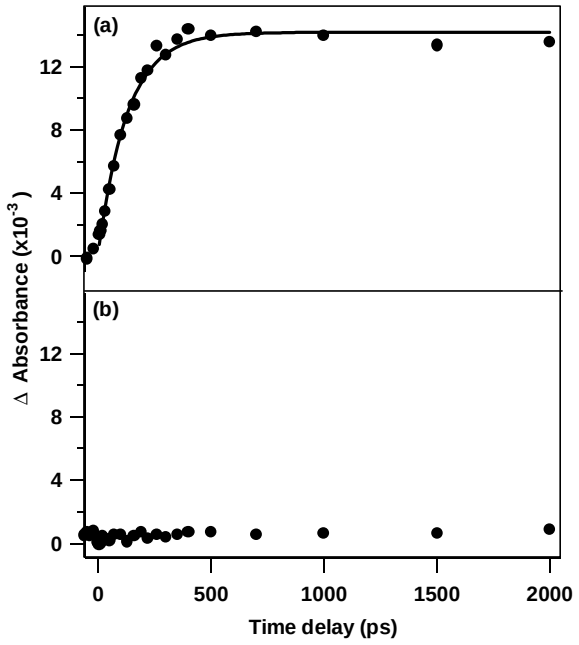

Figure 1. Transient absorption kinetics observed following photolysis (400 nm, 1 ps) of **1** in acetonitrile solution at room temperature, monitored at (a) 1800 cm^{-1} and (b) 1735 cm^{-1}. The absorption at 1800 cm^{-1} is assigned to the benzoyl radical **2**.

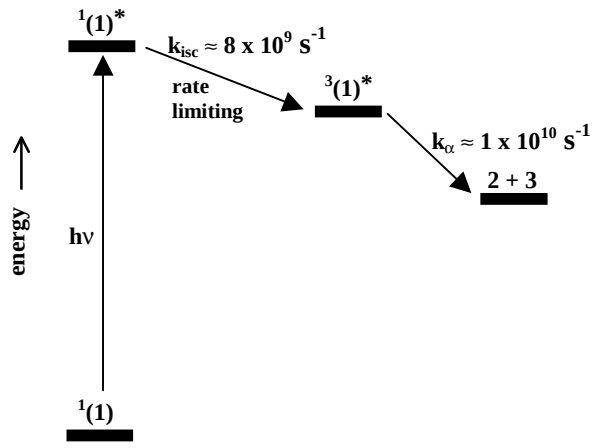

Scheme 2. Energy level diagram for α-cleavage of **1**. Reproduced from ref. 10.

The growth of the benzoyl radical **4** determined by ps-TRIR is in good agreement with the mechanism proposed by Turro and co-workers.[10)]

There is evidence that the formation of the rearrangement product **4** occurs via an *in-cage* recombination process. Therefore, we have probed the formation of **4** using ps-TRIR. **4** has been shown previously[2)] to have a strong IR absorption at 1735 cm^{-1}. Figure 1(b) shows the kinetic trace obtained at 1735 cm^{-1}. We find no evidence on the picosecond timescale for the generation of a transient species at 1735 cm^{-1}. These results appear at first to disagree with the original assumption that **4** is formed extremely rapidly via an *in-cage* recombination of **2** and **3**. In order to rationalise this we must consider the difference between the ps-TRIR experiments and experiments performed with ns-Nd:YAG lasers. One possibility is that the formation of **4** is a secondary photochemical process. The higher photon-flux in the nanosecond/steady-state experiments may result in a detectable concentration of **4** only being observed under these experimental conditions. However this does not easily explain why **4** seems to be formed via an *in-cage* process. Further investigations are underway to fully understand the photochemistry of this important class of polymerisation photoinitiators.

Acknowledgements

We are grateful to the EPSRC (GR/M40486) for financial support for the picosecond infrared facility. We thank Mr K. Stanley for technical assistance.

References

1. A Barca
Farbe Lack, 96, 422, (1990)

2. G W Sluggett, C Turro, M W George, I G Koptyug, N J Turro, J. Am. Chem. Soc., 117, 5148 (1995)

3. T Sumiyoshi, W Schnabel and A Henne
Polymer, 26, 141, (1985)

4. T Sumiyoshi and W Schnabel
Makromol. Chem., 186, 1811, (1985)

5. M Kamachi, A Kajiwara, K Saegusa and Y Morishima
Macromolecules, 26, 7369 (1993)

6. A G Neville, C E Brown, D M Rayner, J Lusztyk, K U Ingold, J. Am. Chem. Soc., 113, 1869, (1991)

7. W Rutsch, K Dietliker, D Leppard, M Koehler, L Misev, U Kolczak and G Rist, Proceedings of the XXth International Conference in Organic Coatings-Science and Technology, p 467, (1994)

8. M Towrie, D C Grills, P Matousek, A W Parker, M W George, Appl. Spect., to be submitted

9. M Towrie, A W Parker, W Shaikh and P Matousek Meas. Sci Tech., 9, 814, (1998)

10. S Jockusch, I V Koptyug, P F McGarry, G W Sluggett, N J Turro and D M Watkins, J. Am. Chem. Soc., 119, 11495, (1997)

Structural landscapes in hydrogen-bonded biomolecular clusters: resonant ion-dip spectroscopy

E G Robertson, L C Snoek, J P Simons

Physical and Theoretical Chemistry Laboratory, South Parks Road, Oxford, OX1 3QZ

M Mons

Service des Photons, Atomes et Molecules, Commissariat a l'Energie Atomique, CEN Saclay, 91191 Gif-sur-Yvette Cedex, France

Main contact email address: *jpsimons@physchem.ox.ac.uk*

Introduction

Molecular conformation plays a crucial role in the selectivity and function of pharmacologically active molecules. Molecular shape and the interactive forces between the molecule and its nearest neighbours, also control molecular recognition processes. These are involved in virtually all aspects of biological function, ranging from neurotransmission and specific drug-receptor interactions, to enzyme catalysis. Enzyme function, in its turn, is dependent upon specific interactions between neighbouring molecules, bound together at the active site of the enzyme and between the active site and the reactive substrate. It can also be dependent upon the formation of chemically reactive intermediates (transition states) and charge migration within the enzyme-substrate complex.

The factors which control the conformational landscape involve a subtle balance between 'through bond' and 'through space' interactions within the molecule, and their modification by 'non-bonded' interactions with the environment. Hydrogen-bonding interactions are ubiquitous, operating both within the molecules and externally, especially with neighbouring water molecules. Together, these interactions determine the molecular architecture, the electronic charge distributions and the network of pathways for electron and proton transfer within the molecular structure. Their relative influence and the way in which their cooperative behaviour may control conformational and supra-molecular structure and the specificity of molecular function remain very unclear.

In the last few years, very powerful strategies have been developed and exploited for exploring and mapping the conformational landscapes of model biomolecules, including neurotransmitters, amino-acids, amides and enzyme inhibitors, and the supra-molecular structures of their size-selected hydrates. *Ab initio* structural computation provides crucially important theoretical input, through which experimental data can be analysed and interpreted. Theory provides the 'à la carte menu' of structural possibilities and the experiments tell us which ones are actually chosen. The recent development of IR-UV ion depletion spectroscopy[1-3] has proved to be an especially elegant tool for the structural assignment of isolated H-bonded molecules, because of its great sensitivity to the local environment of H-bonded chromophores, such as –OH or $–NH_2$. It is a 'hole-burning' method that monitors the infrared spectrum of each species selectively, *via* dips in their mass-selected, resonant two photon ionisation spectral intensity. Zwier and co-workers have applied the technique with spectacular success, determining structures for clusters as large as $(benzene)_2(H_2O)_8$.[2] Crucially aided by a loan laser from the LSF, a series of IR-UV experiments were commenced in the authors' laboratory to probe conformation and hydration in flexible organic molecules.

2-Phenylethanol (PEAL)

2-phenylethanol (PEAL) is a system that we have studied extensively by R2PI and LIF techniques, assigning molecular conformers and 1:1 water clusters, by band contour analysis.[4,5] One of the considerations in selecting PEAL was the need to 'calibrate' OH stretching vibrations to help interpret spectra of molecules less well understood. PEAL and its water clusters offer at least three types of OH environment: OH···O, OH···π and 'free' OH.

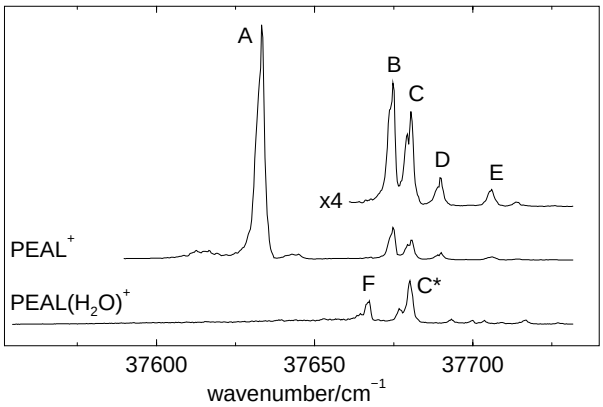

Figure 1. R2PI spectra of PEAL and its 1:1 hydrate.

The five monomer features A-E in Figure 1 were initially thought to be associated with four or five different conformers. Infrared spectra measured for each of them revealed a surprising result - several of the spectra were identical (A=B=E, C=D). Prompted by this discovery, UV-UV holeburning spectra were measured, confirming that only *two* conformers were present in the jet. They are assigned to the structures shown in Figure 2, on the basis of their UV band contours and their IR-UV spectra shown in Figure 3a.

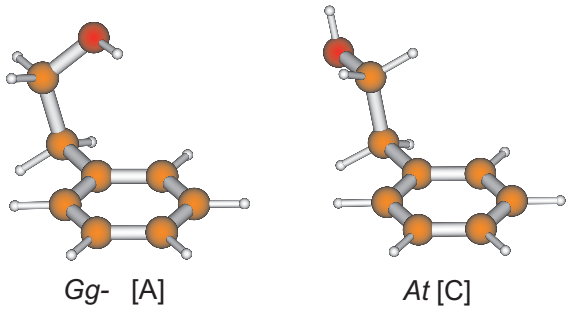

Figure 2. Conformers of PEAL observed in the jet expansion, labelled according to the arrangement of the side chain with respect to CCCO (gauche/anti) and CCOH (gauche/trans).

The most populated molecular conformer *Gg*-π (origin 'A') is a folded structure, stabilized by an intramolecular π -type H-bond between the terminal OH group and the aromatic ring. Its OH stretch frequency is red-shifted relative to that of the *At* conformer (origin 'C') which has an extended *anti* side chain. A re-examination of the previous band contour work revealed in turn some complexities previously unsuspected such as tunnelling of the terminal OH and vibronic coupling involving motion of the side chain.[6]

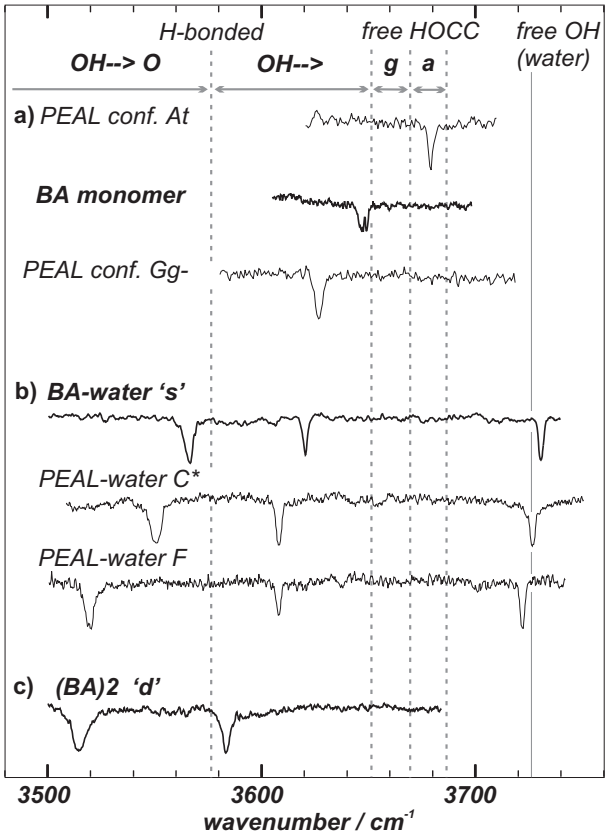

Figure 3. IR-UV ion depletion comparing PEAL and BA species: (a) monomer (b) 1:1 hydrates (c) BA dimer.

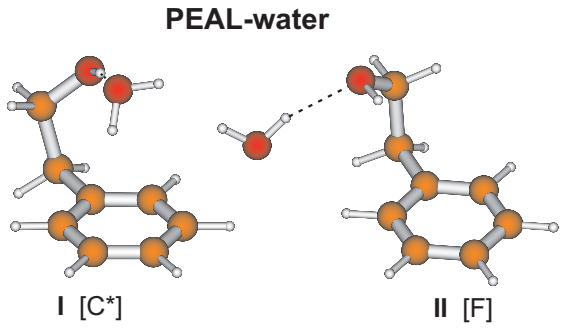

Figure 4. *Ab initio* (MP2/6-31G*) structures for 1:1 hydrates of 2-phenylethanol.

Infrared spectra were also measured for the two 1:1 water complexes of PEAL, see Figure 3b. Comparison with *ab initio* predictions allowed them to be assigned to two different structures based upon PEAL in its folded conformation. In one, water binds to one of the oxygen lone pairs and the intramolecular π -type H-bond is preserved; in the other, the π-type intramolecular H-bond is disrupted and the water molecule inserts between the terminal OH group of PEAL and the aromatic ring, thus bridging the two ends of the molecule. Their structures are shown in Figure 4.

Benzyl alcohol (BA)

The conformational properties of aryl alcohols, and especially benzyl alcohol, have been the subject of numerous spectroscopic investigations.[7-12] The extent to which a flexible side chain allows the possibility of OH···π type intramolecular hydrogen bonding has been of particular interest.

The conformation of benzyl alcohol (BA) may be defined by two dihedral angles of the side chain, τ_1(OCCC) and τ_2(HOCC). IR [7] and n.m.r.[8] studies of BA in condensed phase generally conclude that the predominant component has a *gauche* conformation about τ_2(HOCC), with some indication of a minor component with τ_2(HOCC)=180°. The lack of consensus concerning conformation about τ_1(OCCC), however, is a common introductory theme in a series of experimental investigations.[7-10] In the molecular structure determined by gas-phase electron diffraction,[11] τ_1(OCCC) is 54° (and τ_2(HOCC) is either +60° or -60°). In a detailed examination of the electronic spectroscopy of BA,[10] evidence was found for only one conformer in the supersonic jet; analysis of low frequency torsional progressions and the number of observed conformers in a series of structural analogues led to the assignment of BA to a single structure with τ_1(OCCC)= 90°. Very recently, the IR-UV ion dip spectroscopic study of BA led to the assignment of *two* conformers through comparison with *ab initio* calculations at the HF/6-31G level.[9] The dominant feature in the electronic spectrum, with an OH stretch frequency of 3650 cm^{-1} was assigned to a planar conformer with τ_1(OCCC)≈ 0° and τ_2(HOCC)≈ 0°, while a much weaker feature, with a red-shifted OH stretch frequency of 3585 cm^{-1}, was assigned to a structure similar to conformer *g* in Figure 3. The large red-shift was attributed to a strong OH···π interaction in the molecule, a finding which is surprising given that the species responsible is barely populated in the jet. While BA might display varying behaviour in solution phase, depending on solvent and concentration, it is clear that the gas-phase studies of BA should converge on the unique structure corresponding to the global potential minimum. In this work, the IR-UV spectroscopy of BA is re-examined, and UV band contour data obtained in order to resolve the current ambiguities.

Ab initio calculations on benzyl alcohol (BA) indicate two minima in the potential energy surface at each level of theory employed, one with a *gauche* and the other with a *trans* arrangement of the HOCC side chain: the MP2/6-31+G** structures are shown in Figure 5.

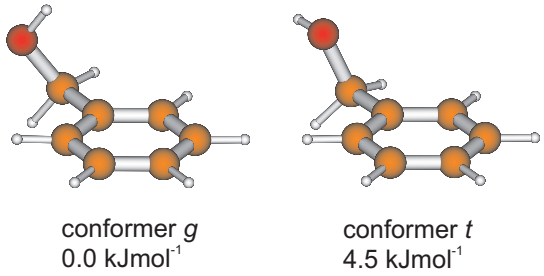

Figure 5. Conformers of benzyl alcohol predicted by MP2/6-31+G** calculations with their relative energies. The labelling (*g/t*) refers to a *gauche* or *trans* conformation about the CO bond.

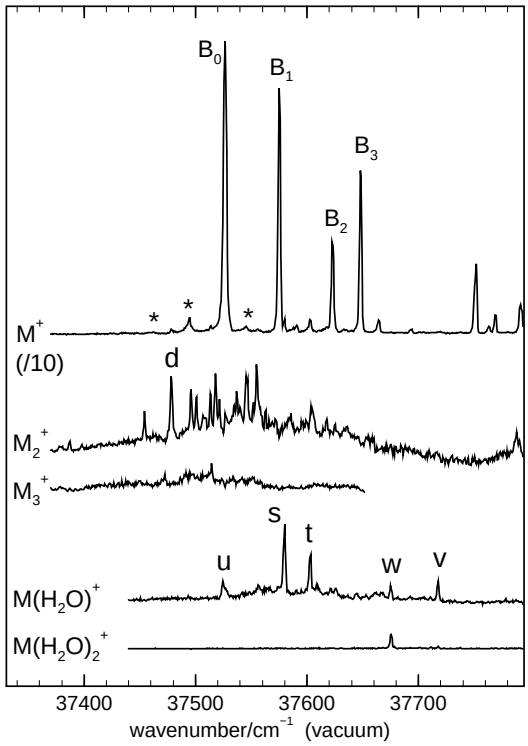

Figure 6. Mass-selected R2PI spectroscopy of benzyl alcohol and associated clusters. The peaks marked with an asterisk appear with much greater intensity in a warm expansion. The water complex bands are labelled in accord with an earlier study.[12)]

The mass-selected R2PI spectrum of the BA molecule in the region of its $S_1 \leftarrow S_0$ band origin is shown in Figure 6. The dominant peaks in the monomer mass channel, labelled B_0 - B_3, have been assigned previously to a single conformer on the basis of isotope shifts.[10)] The ion depletion IR spectrum recorded with the probe laser centred on the origin band B_0 is shown in Figure 3a, together with the corresponding IR spectra of the two observed conformers of PEAL, for comparison. The OH stretch band of BA (3649 cm^{-1}) lies closer to the frequency of the H-bonded *Gg*-π conformer of PEAL than the all *trans At* conformer, suggesting its association with a *gauche* HOCC side chain conformation. The position at 3649 cm^{-1} indicates a very weak H-bond interaction, which induces a red-shift of *ca.* 11 cm^{-1}, much less than the 36 cm^{-1} red-shift seen in the *Gg*-π conformer of PEAL. This analysis is confirmed by comparison with *ab initio* calculations at the B3LYP/6-31+G* level. The predicted OH stretch frequency for BA conformer *t* is 3676 cm^{-1}, but for conformer *g* it is 3648 cm^{-1}, in excellent agreement with the observed frequency, 3649 cm^{-1}. Analysis of the UV band contour also allows a good evaluation of [*A*-(B+C)/2]".

To summarise, high level ab initio calculations suggest *the most stable conformer of BA has a gauche arrangement of the HOCC atoms and that the dihedral angle τ_1(OCCC) is ca. 50-60°, with non-negligible barriers at 0° and 90°.* Such a structure is consistent with all our experimental data on the observed conformer: the OH stretch frequency (3649 cm^{-1}), the [*A*-(B+C)/2]" parameter (0.1151 ± 0.0020 cm^{-1}), and the appearance of hot-bands in the electronic spectrum suggesting a low frequency S_0 vibrational mode around 32 cm^{-1}. In the light of this analysis, the gas-phase electron diffraction determination that τ_1(OCCC) ≈ 54° [11)] should be regarded as reliable and the most accurate experimental measurement to date.

The labelled features in the $M(H_2O)^+$ mass channel of Figure 6 were assigned to clusters with one (s,t), two (u), three (v) and four (w) water molecules by Bernstein *et al.* [12)] on the basis of pulsed nozzle/laser timing delay studies. The IR-UV ion dip spectrum obtained with the probe laser centred on the water complex band 's' is shown in Figure 3b; an identical spectrum was also obtained by probing band 't', suggesting that 's' and 't' are separate vibronic transitions of one complex. The observation of three distinct bands in its OH stretch region confirms its association with a 1:1 water complex, and comparison with other systems indicate the following assignments: OH→O (3566 cm^{-1}), OH→π (3621 cm^{-1}) and free OH_{water} (3731 cm^{-1}) in agreement with the most stable *ab initio* predicted structure shown in Figure 7. The equivalent water complex **I** in PEAL (Figure 4) gives rise to the spectrum labelled PEAL-water C* in Figure 3b, which is very similar.

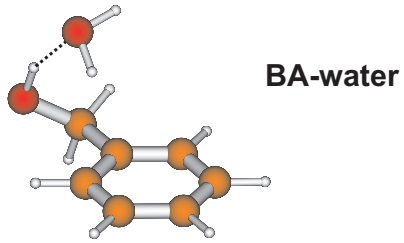

Figure 7. *Ab initio* (MP2/6-31G*) structure for the most stable 1:1 hydrate of benzyl alcohol.

In the R2PI spectra of Figure 6, a series of bands appear in both the dimer and monomer mass channels, suggesting their association with BA dimer species which partially dissociate. The peak labelled 'd' was previously probed by IR/UV ion dip spectroscopy.[9)] In the region 3530 - 3750 cm^{-1} only one band was evident, which led to the erroneous assignment of 'd' to the *gauche* monomer of benzyl alcohol. In Figure 6c, our more extended IR/UV ion dip spectrum shows an additional feature at 3515 cm^{-1}, as well as the previously observed band at 3584 cm^{-1}. The large linewidth of the new feature and its highly red-shifted position are both characteristic of an OH bound to a strong acceptor, which could only be the oxygen of the other BA molecule. Assignment of the 3515 cm^{-1} band to an OH→O oscillator implies that the 3584 cm^{-1} band is associated with a strong OH···π bond, since it is not geometrically possible for both alcohol groups to form OH···O hydrogen bonds. These assignments are consistent with the structure of the most stable dimer at the HF/6-31G* level, see Figure 8. It benefits not only from OH···O and OH···π H-bonds, but also from a weak $O\cdots HC_{ring}$ interaction.

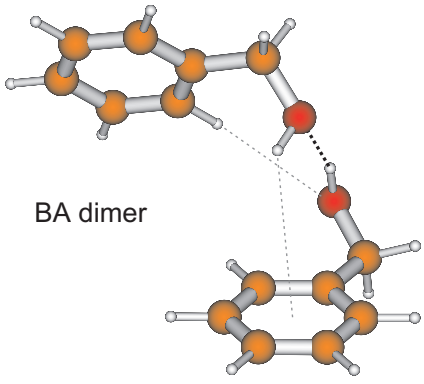

Figure 8. *Ab initio* (HF/6-31G*) structure for the most stable dimer of benzyl alcohol.

2-Amino-1-phenylethanol (APE)

2-amino-1-phenylethanol (APE) is an analogue of noradrenaline (α-(aminomethyl)-3.4-dihydroxy benzyl alcohol), a molecule which is involved among other functions in neuronal communication. It is also related to the ephedra molecules (methyl substituted APE on the second carbon of the tail), an important class of pharmaceuticals. The flexible side chain allows the possibility of a large number of alternative conformers and their relative stabilities may be influenced by intramolecular hydrogen-bonded interactions between the neighbouring hydroxyl and amino groups. The two groups present both donor and acceptor sites and their presence also introduces the possibility of H-bonded or 'non-bonded' interactions between the side chain and the aromatic ring. The relative conformer populations, stabilised in the free jet expansion, reflect their relative energies. The APE molecule provides an opportunity to study the interplay of inter- and intramolecular H-bonding, in a case where the functional groups are attached to a flexible framework and bound water molecules may influence the preferred conformation.

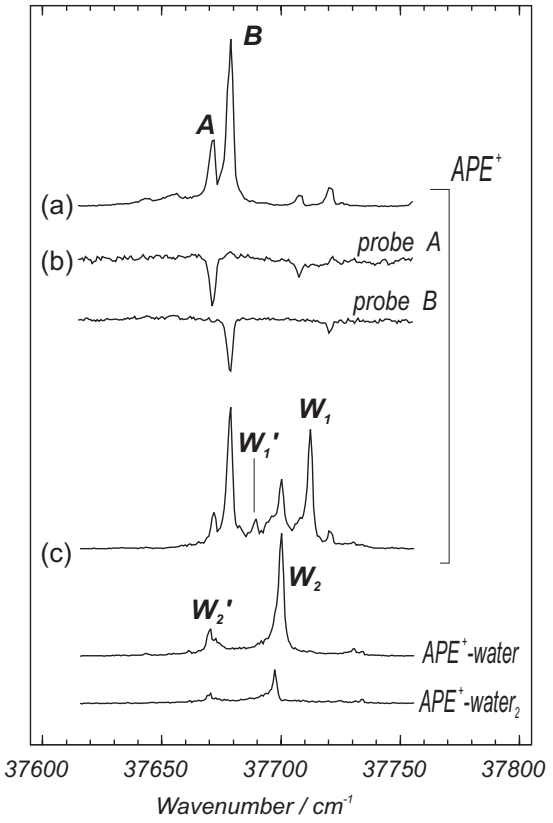

Figure 9. Mass-selected R2PI spectra of APE in the absence of water (a), (b) and with water entrained in the carrier gas (c). (b) UV-UV hole-burning spectra of the APE monomer obtained by probing depletion either on band A or B. The mass channel in which the signal was collected in indicated on the right hand-side. Bands assigned to 1:1 complexes are labelled W_1 and W_1', and to 1:2 complexes, W_2 and W_2'.

The mass-selected R2PI spectrum of the APE molecule in the region of its $S_1 \leftarrow S_0$ band origin, recorded in the absence of water (Figure 9a), shows two main bands at 37685 and 37693 cm^{-1}, labelled respectively A and B. The small splitting between these features suggests their assignment to the origin bands of two separate conformers, an assignment supported by the UV-UV hole-burning spectra which were generated by tuning the probe laser first onto A and then onto B (Figure 9b).

IR-UV ion depletion spectra recorded with the probe laser centred on bands A and B are shown in Figure 10a. Each conformer exhibits an intense, red-shifted OH stretch band around 3530 cm^{-1} and a much weaker antisymmetric NH stretch band near 3430 cm^{-1}. The clear implication is that both conformers possess an intramolecular OH…N hydrogen bond. When the observed red-shifts (≈140 cm^{-1}) are compared with that in the phenol-ammonia complex (363 cm^{-1}),[3] it is evident that the intramolecular H-bond of the APE molecule is weaker, presumably because of the geometrical constraints exerted by the side chain. Combining the IR data with the UV band contours permits an unambiguous assignment of A and B to the GG_1 and AG_1 structures shown in Figure 11.

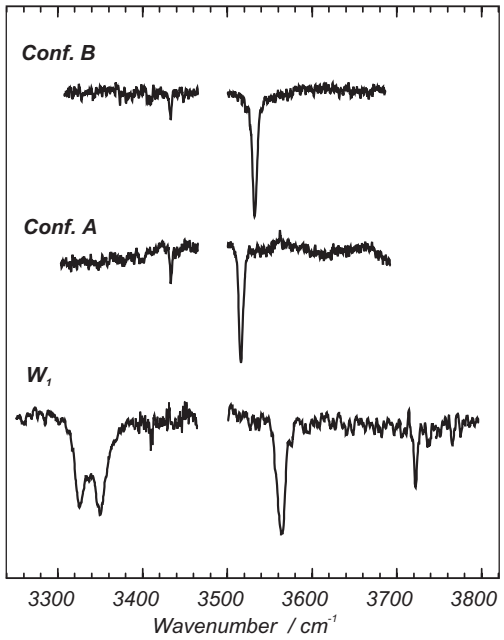

Figure 10. IR ion-dip spectra probing (a) the monomer bands A and B, and (b) the complex band W_1. The gap in the IR spectrum of the complex is a consequence of IR absorption by the $LiNbO_3$ crystal.

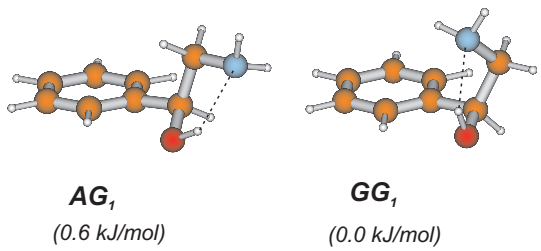

Figure 11. The most stable conformers of APE at the MP2/6-311G**//MP2/6-31G* level with their relative energies. The conformers are labelled according to the arrangement of the side chain with respect to CCCN (*Gauche/Anti*) and OCCN (*Gauche/Anti*).

When water was present in the carrier gas, the R2PI spectrum in the region of the $S_1 \leftarrow S_0$ monomer band origin, obtained by monitoring the APE+ mass channel, exhibited two additional features labelled W_1 and W_1' in Figure 9. The IR/UV ion depletion spectrum of the more intense band, W_1, is shown in Figure 10b. It exhibits three intense features readily ascribed to the OH oscillators of a 1:1 water complex: OH→N (3349 cm^{-1}), OH→O (3562 cm^{-1}) and free OH (3722 cm^{-1}). The strained intramolecular H-bond of the isolated conformer has been replaced by two strong, nearly linear H-bonds. Insertion of the water molecule between the two polar groups changes the geometry of the host with respect to dihedral angles in the side chain, see figure 12. As a consequence, the terminal amino group in the GG-W complex is pushed towards the ring, thus energetically favouring this form over AG-W by the enhancement of a π H-bond.

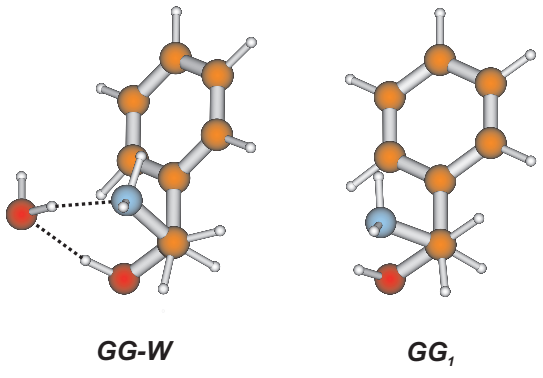

Figure 12. The most stable 1:1 complex of APE at the MP2/6-311G* level, shown with its corresponding GG_1 monomer for comparison.

Conclusions

Mass-selected R2PI and IR-UV ion depletion spectroscopic techniques provide key data for the assignment of molecular conformers and complexes, the interpretation of which is greatly facilitated by high level *ab initio* calculations. The data are often complementary; in the present case of aryl alcohols, for example, UV band contours reveal the position of the heavy atoms in the side chain, while the OH stretch frequencies are sensitive to the HOCC conformation. The spectral shifts induced in OH stretch frequencies by H-bonding has helped to reveal the role played by OH...π interactions in determining conformation.

The results on the APE, which are relevant for the description of the more complex neurotransmitter, noradrenaline, show that *intra*molecular H-bonding controls both the conformational structure and the relative conformational abundance. The theoretical study confirms the H-bonded structure revealed experimentally, and in particular, the disruption of the *intra*molecular H-bond by the first bound water molecule. It also reveals the key role of side chain flexibility and cooperative effects in this neurotransmitter analogue.

Acknowledgements

The authors gratefully acknowledge the EPSRC for grant support (MM) and the Leverhulme Trust for postdoctoral support (EGR). We also thank the Laser *for* Science Facility at the Rutherford Appleton Laboratory for the loan of the IR laser system.

References

1. R.N. Pribble, T.S. Zwier, Science 265, 75 (1994)
2. C.J Gruenloh, J.R. Carney, F.C Hagemeister, C.A. Arrington, T.S. Zwier, S.Y. Fredericks, J.T. Wood, K.D. Jordan, J. Chem. Phys. 109, 6601 (1998).
3. A. Iwasaki, A. Fujii, T. Watanabe, T.Ebata, N. Mikami, J. Phys. Chem. 100, 16053 (1996)
4. J.A. Dickinson, M.R. Hockridge, R.T. Kroemer, E.G. Robertson, J.P. Simons, J. McCombie, M. Walker, J. Am. Chem. Soc. 120, 2622 (1998)
5. M.R. Hockridge, E.R. Robertson, J. Phys. Chem. A 103, 3618 (1999)
6. M. Mons, E.G. Robertson, L.C. Snoek, J.P. Simons, Chem. Phys. Lett. 310, 423, (1999)
7. T. Visser, J.H. van der Maas, Spectrochim. Acta, 42A, 599 (1986) and references therein.
8. T. Schaefer, R. Sebastian, J. Peeling, G.H. Penner, K. Koh, Can. J. Chem. 67, 1015 (1989)
9. N. Guchhait, T. Ebata, N. Mikami, J. Am. Chem. Soc. 121, 5705 (1999)
10. H.-S. Im, E.R. Bernstein, H.V. Secor, J.J. Seeman, J. Am. Chem. Soc. 113, 4422 (1991)
11. M. Trætterberg, H. Østensen, S. Ragnhild, Acta Chem. Scand. A34, 449 (1980)
12. S. Li, E.R. Bernstein, J. Chem. Phys. 97, 7383 (1992)

Reaction kinetics of atomic carbon, C(^{3}P), with O_2 and NO down to 15 K

D Chastaing, S D Le Picard, I R Sims

School of Chemistry, The University of Birmingham, Edgbaston, Birmingham, B15 2TT, UK

Main contact email address: *i.r.sims@bham.ac.uk*

Introduction

Ground state atomic carbon, C ($2p^2\ ^3P_J$), is particularly abundant in dense interstellar clouds, where its reactions are thought to be important in the synthesis of long-chain carbon-containing radicals. There is, therefore, considerable interest in the measurement of the rate coefficients for C(^{3}P) reactions down to the temperatures prevailing in these dense clouds (10—50 K).

We recently performed the first ever measurements on the kinetics of C(^{3}P) reactions below room temperature, using an indirect chemiluminescence technique to detect C(^{3}P) in a CRESU (Reaction Kinetics in Uniform Supersonic Flow) apparatus.[1)] Reaction rates were determined by observing the chemiluminescence from NO($B^2\Pi$) which is generated in the reaction between C(^{3}P) atoms and NO_2. As C(^{3}P) was not observed directly, it was not possible to confirm experimentally that any excited spin-orbit population C(^{3}P) formed in the photolysis was relaxed. It was argued that, as the spin-orbit splittings in C(^{3}P) are rather small, relaxation would be very rapid. Furthermore, it was necessary to consider the possibility that other photolysis products of C_3O_2 were responsible for the observed signal. It was concluded that they were not. However, experimental confirmation of these points awaited the current work employing direct detection of atomic carbon. We had also hoped to measure the rate of reaction of C(^{3}P) with NO in our previous study, but this proved impossible owing to the reaction of NO with NO_2 present in excess as part of the chemiluminescence detection scheme.

Apart from the results published in our earlier paper, kinetic measurements on reactions of carbon atoms have been confined to room temperature or above. Husain and co-workers have performed kinetic measurements on the widest variety of reactions using atomic resonance absorption to detect C(^{3}P). Becker and co-workers are the only group to have used LIF detection, via a two-photon transition. Some dynamical studies have also been carried out using crossed molecular beams. References to this work may be found in our previous article.[1)]

Experimental

In order to measure the rate of the prototypical atom-diatomic radical reaction between C and NO, as well as to confirm our earlier results, we sought to devise a scheme for directly detecting the relative concentration of C(^{3}P) formed in the CRESU flow, using one-photon vacuum ultraviolet (VUV) laser-induced fluorescence, employing the (3s ^{3}P – 2p ^{3}P) transitions around λ = 166 nm. One-photon VUV LIF detection of C(^{3}P) has been demonstrated previously,[2)] but never in a kinetic study. Generation of the required 166 nm radiation is not possible using standard frequency-tripling techniques in rare gas mixtures, and so we chose instead to employ two-photon resonant frequency mixing in xenon.[3)]

The CRESU technique[4,5)] has at its heart an axisymmetric Laval nozzle, mounted on a moveable reservoir within a vacuum chamber. All the temperatures (apart from 295 K) in the gas flows were achieved by the isentropic expansion of the gas mixture prepared in the reservoir through the nozzle and into the main chamber. This expansion generates a supersonic flow of gas in which the Mach number, the temperature, the density of the gas, the mole fraction of the co-reagent and the velocity of the gas stream are constant along the axis of the flow. A range of nozzles was employed in the present work, each providing a particular temperature and density for the selected carrier gas. Experiments were carried out in He, Ar and N_2.

C(^{3}P) atoms were created by the 10 Hz pulsed laser photolysis of carbon suboxide, C_3O_2, using the 193 nm radiation from an excimer laser (Lambda-Physik, Compex 102), which propagated through the throat of the Laval nozzle and along the axis of the flow. The fluence of the beam was about 50 mJ cm^{-2} in the CRESU chamber. C_3O_2 was synthesised and used as before.[1)]

Detection of C(^{3}P) atoms was achieved using VUV LIF at wavelengths around 166 nm, corresponding to the [3s ^{3}P – 2p ^{3}P] electronic transition. 166 nm radiation was generated by two-photon resonant four-wave frequency mixing[3)] in xenon. A gas cell, with a path length of around 20 cm, was equipped with a quartz input lens (10 cm focal length) and a CaF_2 recollimation lens (10 cm focal length) at the output, leading directly into the CRESU chamber. Two tuneable dye laser beams were introduced into the cell, which contained 35 mbar of Xe. The first, at a wavelength 255.94 nm was the frequency-doubled output of a 355 nm Nd:YAG-pumped dye laser (LAS, LDL 205). The output energy was ~2 mJ. The UV frequency (ν_{UV}) was set to the Xe $5p^5 6p[2½, 2]$ two-photon resonance. Excitation of this resonance was ensured by monitoring the Xe^+ multiphoton ionisation signal in a separate cell. Another, visible dye laser beam (pulse energy ~20 mJ) at a wavelength of around 560 nm (corresponding to frequency ν_{vis}) was generated in a second identical dye laser pumped by the same Nd:YAG laser (Spectra Physics, GCR 170), but at 532 nm, and combined and co-propagated into the Xe cell. VUV radiation resulted at a frequency $\nu_{VUV} = 2\nu_{UV} - \nu_{vis}$. Tuning the visible dye laser in the range λ_{vis} = 560 - 565 nm, corresponded to λ_{VUV} = 165.44 - 165.88 nm. The resultant VUV beam intersected the CRESU flow and the photolysis beam at the focus of an optically fast CaF_2 condenser lens pair, which imaged any resulting fluorescence onto the photocathode of a VUV solar blind photomultiplier tube (Electron Tubes, type 9403) after passing through a VUV interference filter (Acton Research) centred at 159.8 nm (23.4 nm bandwidth).

Relaxation of the nascent spin-orbit distribution was seen at the lowest temperatures studied, and was observed to take place very rapidly (in ~ 1 - 2 μs). Kinetic measurements were only started after this relaxation had taken place. For each co-reagent concentration, a C(^{3}P) kinetic decay trace was recorded by systematically varying the time delay between the photolysis and probe laser pulses. Each decay consisted of 100 points, and was averaged for 6 laser shots per point. They were fitted to yield values of k_{1st} for each gas mixture on which experiments were carried out at a particular temperature. The flows of co-reagent (O_2, or NO; Air Products), and the carrier gas (He, Ar or N_2; Air Products) were taken directly from the cylinders and regulated by means of mass flow controllers (MKS). Knowledge of the total gas density from Pitot-tube measurements and of the individual gas flows enabled the concentrations of the co-reagent, and hence the corresponding second-order rate coefficient, to be calculated.

Results and Discussion

Experiments to determine the kinetic behaviour of carbon atom reactions with O_2 and NO were performed both at room temperature in a subsonic flow, and at low temperatures ranging from 15 K to 204 K in He, Ar or N_2 buffer gases, using a number of Laval nozzles. Results are displayed in Figure 1.

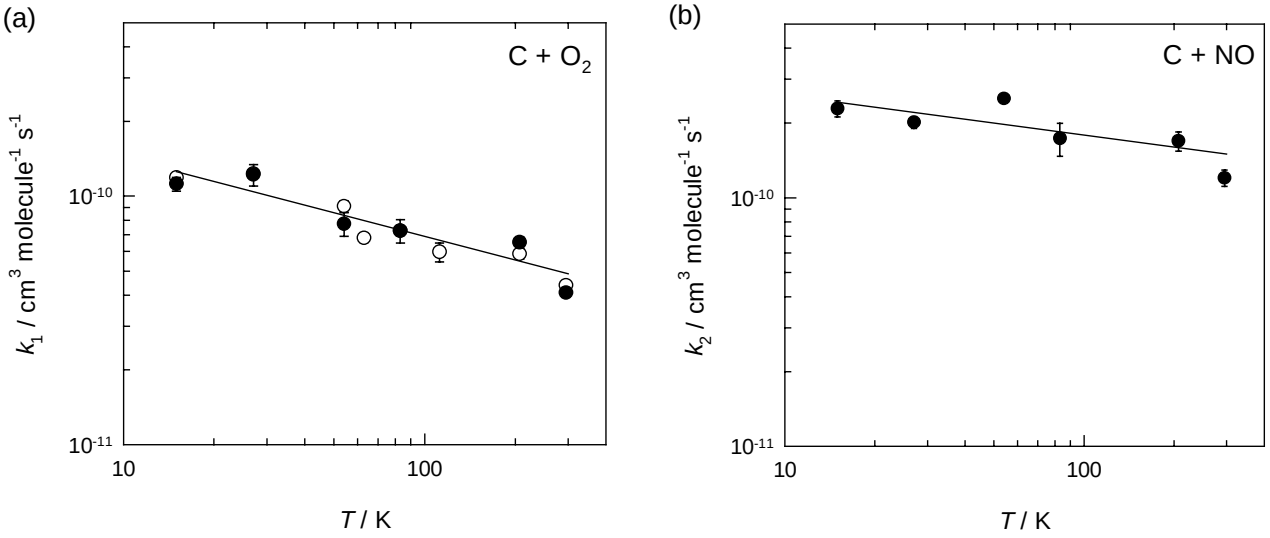

Figure 1. Rate coefficients for the reactions of **(a)** $C(^3P_J)$ with O_2 and **(b)** $C(^3P_J)$ with NO plotted on a log-log scale against temperature. The open circles (○) in (a) show the results of experiments in which chemiluminescence from $C(^3P_J)$ + NO_2 was used to follow the kinetics, the filled circles (●), in (a) and (b), the results of experiments in which kinetic decays of $C(^3P_J)$ atoms were recorded using VUV-LIF. The solid lines show the results of non-linear least-squares fits as described in the text.

The new results for the reaction

$$C(^3P) + O_2 \rightarrow CO + O \qquad (1)$$

display a remarkably good agreement with our previous measurements using the indirect chemiluminescence detection technique. This lends confidence to both sets of measurements. An unweighted non-linear least-squares fit to the combined data set yields the following temperature dependence:

$$k_1 = (4.9 \pm 0.8) \times 10^{-11} (T / 298\ \mathrm{K})^{-(0.32 \pm 0.08)}\ \mathrm{cm^3\ molecule^{-1}\ s^{-1}},$$

with errors quoted as ±2σ, where σ is the standard error. This compares favourably with the temperature dependence determined previously ($k = 4.7 \times 10^{-11} (T / 298\ \mathrm{K})^{-0.34}$ $\mathrm{cm^3\ molecule^{-1}\ s^{-1}}$). Possible explanations for the observed negative temperature dependence were discussed elsewhere [1].

Our results for the reaction

$$C(^3P) + NO \rightarrow CN + O \qquad (2a)$$
$$\rightarrow CO + N \qquad (2b)$$

are in only fair agreement with the rather scattered results of previous studies at room temperature. An unweighted non-linear least-squares fit over the temperature range 15 - 295 K yields the following temperature dependence for the overall rate coefficient: $k_2 = (1.5 \pm 0.4) \times 10^{-10} (T / 298\ \mathrm{K})^{-(0.16 \pm 0.14)}$ $\mathrm{cm^3\ molecule^{-1}\ s^{-1}}$, with errors quoted as before. The rapid rate at room temperature, combined with the mild negative temperature dependence, is characteristic of radical-radical or atom-radical reactions occurring on attractive potential surfaces.[1] In such cases, some collisions may occur over surfaces that do not lead to thermodynamically accessible products. The observed mild negative temperature dependence may then result from an increase in the proportion of collisions which occur on surfaces that do lead to products. The $^3P_1$ and $^3P_2$ spin-orbit states of $C(^3P)$ lie at energies equivalent to 23 K and 62 K respectively above the ground state $^3P_0$. The populations in the individual spin-orbit states change markedly through the range of temperature covered in the present experiments. Therefore, if reaction is more probable from lower spin-orbit states this alone could lead to a negative temperature-dependence, independent of the dynamics of the reactive collisions.[6]

In contrast to the reaction between C and O_2, recent ab initio potential surface and rate coefficient calculations have been performed on the C + NO system. Beghin et al.[7] employed the ACCSA method on a long range electrostatic/dispersion potential, giving a rate coefficient at room temperature of 3.43×10^{-11} $\mathrm{cm^3\ molecule^{-1}\ s^{-1}}$, with a marked negative temperature dependence. Andersson et al.,[8] in a very recent study, present quasiclassical trajectory calculations on a new ab initio potential surface. They obtain a rate coefficient of $\sim 8 \times 10^{-11}$ $\mathrm{cm^3\ molecule^{-1}\ s^{-1}}$ at room temperature, and almost no temperature dependence. However, they took a constant correction factor of 1/9 to allow for the non-reactive collisions as explained above. At room temperature, and certainly below, this factor is temperature dependent, and a fuller treatment could bring their results into agreement with our data.

We are grateful to EPSRC for a substantial research grant to construct the CRESU apparatus. We thank the EU (under its TMR programme) for a studentship (DC) and postdoctoral fellowship (SDLP, as part of the Research Network on Astrophysical Chemistry). The EPSRC Laser Loan Pool at the Rutherford Appleton Laboratory provided an Nd:YAG-pumped dye laser system, for which we express our thanks. We are also very grateful to Professor Ian WM Smith for valuable discussions, and to Stuart Arkless, Tony Rothin and Steve West for their skilled technical assistance.

References

1. D. Chastaing, P. L. James, I. R. Sims, and I. W. M. Smith, Phys. Chem. Chem. Phys., 1 2247, (1999)

2. M. Rowekamp, A. Goehlich, and H. F. Dobele Appl. Phys. A, 54 61, (1992)

3. R. Hilbig and R. Wallenstein IEEE J. Quantum Electron., 19 194, (1983)

4. R. Sims, J. L. Queffelec, A. Defrance, C. Rebrion-Rowe, D. Travers, P. Bocherel, B. R. Rowe, and I. W. M. Smith, J. Chem. Phys., 100 4229, (1994)

5. P. L. James, I. R. Sims, I. W. M. Smith, M. H. Alexander, and M. B. Yang, J. Chem. Phys., 109 3882, (1998)

6. R. A. Brownsword, S. D. Gatenby, L. B. Herbert, I. W. M. Smith, D. W. A. Stewart, and A. C. Symonds J. Chem. Soc., Faraday Trans., 92 723, (1996)

7. Beghin, T. Stoecklin, and J. C. Rayez Chem. Phys., 195 259, (1995)

8. S. Andersson, N. Markovic, and G. Nyman Phys. Chem. Chem. Phys. 2 613, (2000)

Laboratory investigation of kinetics of reactions of IO radicals

C E Canosa-Mas, M J Scott, D Shah, A Vipond, K Wagner, R P Wayne

Physical and Theoretical Chemistry Laboratory, University of Oxford, South Parks Road, Oxford, OX1 3QZ, UK

Main contact email address: *dina@physchem.ox.ac.uk*

Introduction

Iodine chemistry in the atmosphere continues to receive much attention. Iodine compounds, such as CH_3I, CH_2I_2 and C_2H_5I, are released into the atmosphere from several natural sources including oceanic plankton and burning of biomass. Anthropogenic sources, such as CF_3I, which has been proposed as a substitute for halons for use as a fire retardant and in the etching industry, also exist. In addition biomass burning is an ever increasing contributor to atmospheric trace gases.

It has generally been assumed that the short tropospheric lifetime of the iodine source compounds would preclude their transport into the lower stratosphere in any significant concentration. However, CH_3I has been observed in small, but detectable, concentrations in the lower stratosphere[1]. A possible means of rapid transport of alkyl iodides from low altitudes to the upper troposphere and lower stratosphere, particularly in the tropics, *via* strong localised convective clouds has been proposed[2].

Iodine compounds are more photolabile than their chlorine or bromine counterparts and, once emitted, the alkyl iodides are quickly degraded by photolysis to release an iodine atom.

$$RI + h\nu \rightarrow R + I \qquad (1)$$

Unlike chlorine or bromine atoms, which may be scavenged by reaction with various organic species, iodine atoms, by virtue of their low electronegativity, are unable to abstract H atoms from saturated hydrocarbons, or, add to double bonds of unsaturated species. Consequently their main reaction is with ozone.

$$I + O_3 \rightarrow IO + O_2 \qquad (2)$$

The IO formed can then take part in numerous reactions involved in catalytic ozone destruction cycles such as the reaction of IO with X where X includes NO, IO, BrO and ClO.

$$IO + X \rightarrow I + XO \qquad (3)$$
$$O_3 + XO \rightarrow 2O_2 + X \qquad (4)$$

The reservoir species for I and IO, such as HOI, $IONO_2$, HI and I_2O_2 are more photolabile than those of bromine and chlorine meaning that a larger proportion of iodine in the atmosphere will be in the active form.

Under low ozone conditions, the reaction of Cl atoms with methane is favoured leading to the formation of CH_3O_2 which in turn may react with IO in an ozone depleting cycle forming active iodine, or a reservoir species that can be recycled into active iodine.

$$IO + CH_3O_2 \rightarrow I + CH_3O + O_2 \qquad (5a)$$
$$IO + CH_3O_2 \rightarrow HOI + CH_2O_2 \qquad (5b)$$

The reaction of IO with CH_3O_2 may be of potential importance in the stratosphere and the marine boundary layer.

The study of the reactions of CH_3O_2 in the laboratory also requires the investigation of possible side reactions involving the CH_3O radical; the latter species is always present in non-negligible concentrations when CH_3O_2 is produced in low pressure reactors such as the one used in this work. CH_3O itself is also a key intermediate in the atmospheric oxidation of methane and also in combustion systems. However there are relatively few kinetic data available for its reaction with other radicals and none for its reaction with I atoms or IO radicals.

In this work the reactions

$$CH_3O + I \rightarrow \text{products} \qquad (6)$$
$$CH_3O + IO \rightarrow \text{products} \qquad (7)$$

have been investigated at room temperature. The study of these reactions is detailed in the first section of this paper.

Some exploratory investigations into the kinetics of the reaction of IO with isoprene, *trans*-2-butene and dimethylsulphide (DMS) which are found in the marine boundary layer, are detailed in the second section.

$$IO + \text{isoprene} \rightarrow \text{products} \qquad (8)$$
$$IO + \textit{trans}\text{-2-butene} \rightarrow \text{products} \qquad (9)$$
$$IO + DMS \rightarrow \text{products} \qquad (10)$$

The reaction of IO with DMS has been thought to explain the short atmospheric lifetime of DMS in coastal areas[3]. The reaction of IO with isoprene and *trans*-2-butene has not been studied before.

Experimental details

All experiments were carried out using a discharge-flow tube (Figure 1) equipped with a double sliding injector and six static side ports, described previously[4]. Experiments were conducted at P = 2 – 2.3 Torr and T = (296 ± 1) K.

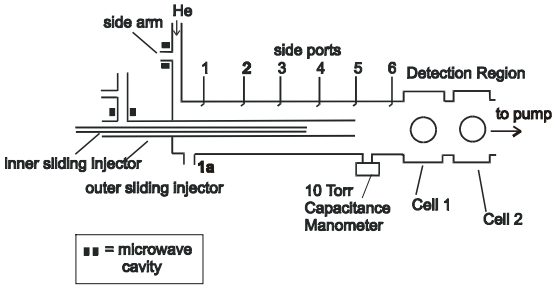

Figure 1. Schematic diagram of apparatus.

Section 1. The reaction of CH3O with I and IO.

Generation of species

The methoxy radical, CH_3O, was generated by the reaction of F atoms with methane in the presence of NO_2:

$$F + CH_4 \rightarrow CH_3 + HF \qquad (11)$$
$$CH_3 + NO_2 \rightarrow CH_3O + NO \qquad (12)$$

The F atoms were generated in the outer sliding injector by subjecting a mixture of F_2 in helium to a microwave discharge. Methane was delivered through the internal injector in sufficient excess to consume all the F atoms and enough NO_2 was added to just surpass the maximum of the CH_3O signal, ensuring complete consumption of the CH_3 radicals. Typical concentrations of F_2, CH_4, and NO_2 were $< 5 \times 10^{11}$, 4×10^{14} and 5×10^{12} molecule cm^{-3} respectively. Typical concentrations of CH_3O were $(0.5 – 1.5) \times 10^{11}$ molecule cm^{-3}.

Br atoms were generated by the reaction of Cl atoms with vinyl bromide, C_2H_3Br, introduced *via* port 1.

$$Cl + C_2H_3Br \rightarrow Br + C_2H_3Cl \qquad (13)$$

I atoms were generated by the reaction of Cl atoms with ICl added at port 1a.

$$Cl + ICl \rightarrow I + Cl_2 \qquad (14)$$

In both cases the Cl atoms were generated in the side arm by subjecting a mixture of Cl_2 in helium to a microwave discharge, the precursor was then added in excess to completely consume the Cl atoms. Typical concentrations of I and Br were (0.5 – 1.5) $\times 10^{12}$ molecule cm^{-3}.

IO radicals were formed by the reaction of excess ozone with I atoms, the latter being generated by the method described above.

$$I + O_3 \rightarrow IO + O_2 \qquad (2)$$

Ozone, (*ca.* 5 $\times$ 10^{13} molecule cm^{-3}) was delivered through port 2. Typical concentrations of IO were (0.5 – 2.5) x 10^{12} molecule cm^{-3}.

Detection of species

The flow tube was coupled to two detection cells. The first permitted detection of CH_3O radicals by laser induced fluorescence (LIF) of the ($\tilde{A}^2A_1 \leftarrow X^0E_1$) transition at λ = 292.8 nm. The excitation beam was produced using a dye laser, (Spectra Physik PDL-2) with rhodamine 610 chloride dye solution, pumped by a Nd-YAG laser (Quanta ray, GCR-11). The fluorescence passed through two filters (Schott UG11 λ = 270 – 380 nm band pass and Andover Corporation $\lambda \geq$ 305 nm) and was detected by a photomultiplier (EMI B2F/RF16443) positioned orthogonal to the laser beam. The signal was processed through a box car integrator (EG & G 162) and output to a chart recorder.

In order to quantify the concentration of CH_3O, the LIF signal was calibrated through a series of experiments. It should be emphasised that, since CH_3O was the kinetic species in the experiments, only an approximate concentration was required. In each calibration experiment, a constant excess of CH_3 was allowed to react over a fixed contact time with a range of concentrations of NO_2 (reaction 12). A different concentration of CH_3 was used in each experiment to determine the maximum slope, *m*, from the series of plots of LIF signal *versus* [NO_2]. The value of 1/*m* yields the approximate calibration factor. The sensitivity of the LIF detection system was *ca.* 6×10^{9} molecule cm^{-3}.

The second cell allowed the detection of Cl, Br or I atoms by resonance fluorescence (RF). The atoms were observed at wavelengths of 138 nm, 148 – 158 nm and 170 – 200 nm respectively. A lamp, in which a dilute flow of Cl_2, Br_2 or I_2 in argon was subjected to a microwave discharge, provided the exciting radiation. The radiation passed through a window of CaF_2 (for chlorine), sapphire (for bromine) or Spectrosil quartz (for iodine) into the centre of the cell. The RF from the Cl, Br or I atoms passing through the detection zone of the flow tube were detected by a photomultiplier (Hamamatsu, R1459) positioned orthogonal to the lamp.

Experimental procedure

The reaction of CH_3O with I

All experiments were performed under *pseudo*-first-order conditions with excess Br or I formed in the main flow of the tube. The kinetic species, CH_3O, was generated in the sliding injector and introduced into the main flow at a number of different positions, corresponding to contact times of up to 30 ms. It was not possible to calibrate accurately the RF system for I, hence the rate constant of CH_3O with I was obtained by a 'relative' method. The LIF signal was measured in the absence and presence of Br and I consecutively. The concentrations of Br and I were equal; both were generated by complete conversion of a fixed concentration of Cl to Br or I by reaction with excess ICl or vinyl bromide (reactions 13 and 14).

Treatment of data and results

The experimental data obtained were treated using a simple *pseudo*-first-order approach

$$\ln\left\{\frac{S_0}{S_t}\right\} = k'_X t \qquad (I)$$

where X = Br or I, and $k'_x = k_x[X]$. The slope of a plot of $\ln\{S_0/S_t\}$ *versus* contact time, *t*, yields the value of the first-order rate constant k'_X. The ratio of the rate constants is expressed

$$\frac{k'_I}{k'_{Br}} = \frac{k_I[I]}{k_{Br}[Br]} \qquad (II)$$

Since the concentrations of Br and I are the same, equation II can be simplified so that the ratio of the *second-order* rate constants, k_I/k_{Br}, is equal to that of the first-order rate constants, k'_I/k'_{Br}.

Figure 2 shows the plot of k'_{Br} as a function of k'_I.

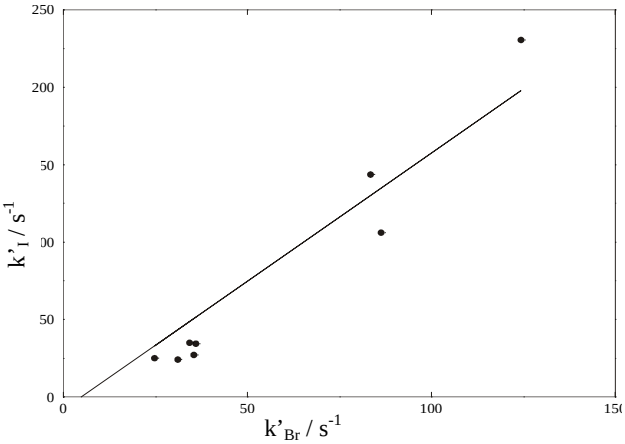

Figure 2. Relative plot of k'_i *versus* k'_{Br}.

The ratio of k_I/k_{Br} was found to be (1.66 ± 0.24), where the errors are the 95% confidence limits of the line of regression. Inserting the value previously obtained in this laboratory [5], for k_{Br} of k_{Br} = (5.0 ± 0.3) $\times$ 10^{-11} cm^3 molecule^{-1} s^{-1} into the ratio yields a value of k_I = (8.3 ± 1.8) $\times$ 10^{-11} cm^3 molecule^{-1} s^{-1}. Errors include the 95% confidence limits of the gradient in figure 2 and the errors in k_{Br}.

Co-reactant	Rate constant / 1×10^{-11} cm^3 molecule^{-1} s^{-1}
Cl	(9.0 ± 0.9) [5]
	20 [6]
	(10 ± 2) [7]
	(1.9 ± 0.4) [8]
Br	(5.0 ± 0.3) [5]
	4.9 [9]
	(7.0 ± 0.4) [10]
I (this work)	(8.3 ± 1.8)

Table 1. Rate constants for the reaction of CH_3O with Cl, Br and I atoms.

This is the first determination of the rate constant for this reaction. Comparison of the result obtained with the rate constants for the analogous reaction of CH_3O with Cl and Br (Table 1) shows no apparent trend.

There are two possible channels for this reaction (data from DeMore *et al.* [11]):

$$CH_3O + I \rightarrow H_2CO + HI \qquad \Delta H_r = -206 \text{ kJmol}^{-1} \quad (15a)$$
$$CH_3O + I + M \rightarrow CH_3OI + M \quad (15b)$$

The products of the reaction have not been observed in this kinetic study. However, it seems likely that HI will be a major product as the other plausible channel is pressure dependent and thus unlikely to occur to any significant extent under the low pressure conditions of our system.

The reaction of CH_3O with IO

This reaction was also studied under *pseudo*-first-order conditions, with CH_3O as the kinetic species. Again a relative method was used whereby the reactions of CH_3O with I and IO were studied consecutively. CH_3O signals were recorded in the absence and presence of I and IO. IO radicals were generated by the reaction of I with excess ozone.

Treatment of data and results

Again the data obtained was treated with a simple *pseudo*-first-order approach (equation I). The slopes of the plots of $\ln\{S_0/S_t\}$ *versus* contact time, *t*, yielded the first-order rate constants, k'_{IO} and k'_I. However, it was not possible to obtain the *second-order* rate constant from the ratio of first-order rate constants, as the concentration of I and IO was not equal. The difficulty is a consequence of the rapid self-reaction of IO which causes some of the IO and I to be lost

$$IO + IO + M \rightarrow I_2O_2 + M \quad (16a)$$
$$IO + IO \rightarrow 2I + O_2 \quad (16b)$$
$$\rightarrow OIO + O \quad (16c)$$
$$\rightarrow I_2 + O_2 \quad (16d)$$

$$k_{16} = (9.3 \pm 1.0) \times 10^{-11} \text{ cm}^3 \text{ molecule}^{-1}\text{s}^{-1}$$ [12]

A model that took into consideration the rapid self-reaction of IO, was therefore used to calculate the ratio of the concentration IO to the concentration of I at various contact times during a kinetic run. The ratios obtained were used to calculate the average concentrations of I, $[\bar{I}]$, and IO, $[\overline{IO}]$, during each kinetic run. In this case the ratio of the first-order rate constants, R, is expressed as

$$R = \frac{\ln(S_0/S_t)_{IO}}{\ln(S_0/S_t)_I} = \frac{k_I[\bar{I}] + k_{IO}[\overline{IO}]}{k_I[I]_0} \qquad (III)$$

where k_I and k_{IO} are the *second-order* rate constants for the reaction of CH_3O with I and IO respectively, and $[I]_0$ is the initial concentration of I.

Equation III can be rearranged to

$$\frac{k_{IO}}{k_I} = \frac{R[I]_0 - [\bar{I}]}{[\overline{IO}]} \qquad (IV)$$

Values of R, $[I]_0$ and average concentrations of I and IO were entered into the model to produce values for the ratio k_{IO}/k_I. The ratios obtained for k_{IO}/k_I were then averaged to yield a value of (0.9 ± 0.1) where the error represents the 95% confidence limits of the average. The ratio and the value of k_I obtained in this work were used to calculate a *second-order* rate constant of $k_{IO} = (7.5 \pm 2.5) \times 10^{-11}$ cm^3 molecule^{-1} s^{-1}. The error includes the 95% confidence limits on the ratio and the errors in k_I.

This is the first determination of this rate constant. By analogy with the reaction of CH_3O with ClO and BrO, the reaction of CH_3O with IO may have four possible product channels

$$CH_3O + IO \rightarrow CH_2O + HOI \quad (17a)$$
$$\rightarrow CH_3O_2 + I \quad (17b)$$
$$\rightarrow CH_2O_2 + HI \quad (17c)$$
$$\rightarrow CH_3I + O_2 \quad (17d)$$

It was not possible to conduct any product studies in our study; however, by analogy with the reaction of CH_3O with ClO, for which HOCl was found to be the major product[8], it seems likely that HOI will be the major product. Comparison of the rate constant obtained in this work with those for the reaction of CH_3O with ClO and BrO (Table 2) show a trend of reactivity of the form $k_{IO} > k_{BrO} > k_{ClO}$.

Co-reactant	Rate constant/ 1×10^{-11} cm^3 molecule^{-1} s^{-1}
ClO	(4.1 ± 0.5) [5]
	(2.3 ± 0.3) [8]
BrO	(5.2 ± 0.5) [5]
	(3.8 ± 0.4) [10]
IO (this work)	(7.5 ± 2.5)

Table 2. Literature values for the rate constants for the reaction of CH_3O with ClO, BrO and IO.

It may be postulated that the reaction proceeds *via* a five membered transition state (Figure 3), where it is the oxygen of the XO which abstracts the H atom from the CH_3O, generating HOX as the major product, a process which would be more favoured by the less electronegative I atom. The transition state may also be less strained for the larger IO radical than the smaller BrO radical, which, in turn would be more stable than the five membered structure incorporating the smaller ClO radical leading to higher reactivity.

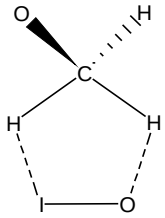

Figure 3. Five-membered transition state.

Section 2. Exploratory study of the reaction of IO with isoprene, *trans*-2-butene and DMS.

Generation of species

The IO radical was generated by one of two methods; the reaction of O atoms with trifluoromethyliodide, CF_3I

$$O + CF_3I \rightarrow CF_3 + IO \quad (18)$$

or by the reaction of O atoms with I_2

$$O + I_2 \rightarrow I + IO \quad (19)$$

The O atoms were generated in the outer sliding injector by subjecting a mixture of oxygen in helium to a microwave discharge. The CF_3I or I_2 was delivered through the internal injector in sufficient excess to consume all the O atoms.

Isoprene (99%), *trans*-2-butene (>99%) and DMS (99.5%) were all used as supplied. Typical concentrations of isoprene, *trans*-2-butene and DMS were $(0.16 - 1.8) \times 10^{14}$ molecule cm^{-3}.

Detection of species

In these experiments IO LIF detection, which has never previously been used in conjunction with a discharge flow system, was employed. The set-up of the LIF system was similar to the one used for CH3O LIF (described above) with the two main differences being the use of a different dye (Coumarin 440) and the use of a different filter (Coherent 35–3425–000 λ = (470 ± 7) nm interference filter). Since IO radicals were the kinetic species in these experiments it was not necessary to know accurately the concentration of the IO radicals. The LIF system for IO was therefore not calibrated.

Experimental procedure

The reaction of IO with isoprene, *trans*-2-butene and DMS were studied under *pseudo*-first-order conditions with IO as the kinetic species. Known concentrations of the organic co-reactant were introduced *via* port 1. The IO radicals were generated in the sliding injector and introduced into the main flow at a number of different positions, corresponding to contact times of up to 30 ms. The IO LIF signal was measured in the absence and presence of organic species.

Treatment of data and results

The experiments on the reaction of IO with *trans*-2-butene showed very little or no change in IO LIF signal on addition of organic reactant, leading to the conclusion that reaction does not occur to any significant extent under the conditions of our system.

The exploratory experiments on the reaction of IO with isoprene and DMS showed the reactions to be very slow, requiring large concentrations of isoprene or DMS and very long contact times to show changes in the LIF signal.

From the few experiments performed, upper limits of $k_8 \leq 2 \times 10^{-12}$ cm^3 molecule^{-1} s^{-1}, $k_9 < 1.5 \times 10^{-12}$ cm^3 molecule^{-1} s^{-1} and $k_{10} \leq 2 \times 10^{-12}$ cm^3 molecule^{-1} s^{-1} were obtained.

A summary of the present literature values for the rate constants and the results obtained in this work are given in Table 3.

Reaction	This work k / cm^3 molecule^{-1} s^{-1}	Literature k / cm^3 molecule^{-1} s^{-1}
IO + *trans*-2-butene	$< 1.5 \times 10^{-12}$	—
IO + isoprene	$\leq 2 \times 10^{-12}$	—
IO + DMS	$\leq 2 \times 10^{-12}$	$(3.0 \pm 1.5) \times 10^{-11}$ [3] $(1.5 \pm 0.5) \times 10^{-11}$ [13] $(8.8 \pm 2.1) \times 10^{-15}$ [14] $(1.5 \pm 0.2) \times 10^{-14}$ [15] $< 3.5 \times 10^{-14}$ [16]

Table 3. Summary of results

The reaction of IO with *trans*-2-butene or isoprene has not been investigated before.

The values obtained by Barnes *et al* [3] and Martin *et al* [13] were derived from numerical modelling. The study by Barnes *et al* [3] was conducted at 760 Torr total pressure, in a FT-IR steady state photolysis system. The investigation by Martin *et al* [13] employed a discharge flow system coupled to mass spectrometry. Three more recent studies [14 – 16] have been made using a more direct method of observing the IO radical, including a re-investigation by Maguin *et al*[15] using an improved discharge-flow mass spectrometry technique[13]. These studies report much lower values for the rate constant, with which our upper limit is in agreement.

Acknowledgements

D Shah and K Wagner thank the NERC for funding under grants GT 04/97/273/MAS and GT 04/99/AS/211. We also thank the Rutherford Appleton Laboratory for loaning the laser system.

References

1. H B Singh, L J Salas and R E Stiles
J. Geophys. Res., 88, 3684, (1983)

2. S Solomon, R R Garcia and A R Ravishankara
J. Geophys. Res., 99, 20491, (1994)

3. I Barnes, K H Becker, P Carlier and G Mouvier
Int. J. Chem. Kinets., 19, 489, (1987)

4. P Biggs, C E Canosa-Mas, D E Shallcross, A Vipond and R P Wayne
J. Chem. Soc. Faraday Trans., 93, 2701, (1997)

5. C E Canosa-Mas, N J Hendy, J Maclennan, M J Scott, D Shah, A Vipond and R P Wayne
in preparation (2000)

6. P Biggs, C E Canosa-Mas, J M Fracheboud, G Marston, D E Shallcross and R P Wayne
J. Chem. Soc. Faraday Trans., 91, 3045, (1995)

7. T Jungkamp, A Kukui and R N Schindler
Ber. Bunsenges. Phys. Chem., 99, 1057, (1995)

8. V Daële, G Laverdet and G Poulet
Int. J. Chem. Kinets., 28, 589, (1996)

9. I Szilágyi, S Dobe and T Bérces
Presentation at the 15th International Symposium on Gas Kinetics, Bilbao (1998)

10. A Aranda, V Daële, G Le Bras and G Poulet
Int. J. Chem. Kinets., 30, 249, (1998)

11. W B DeMore, S P Sander, C J Howard, A R Ravishankara, D M Golden, C E Kolb, R F Hampson, M J Kurylo and M J Molina
JPL Publication, 97–4, (1997)

12. C E Canosa-Mas, M L Flugge, D Shah, D E Shallcross, A Vipond and R P Wayne, in preparation (1998)

13. D Martin, J L Jourdain, G Laverdet and G Le Bras
Int. J. Chem. Kinets., 19, 503, (1987)

14. I Barnes, V Bastian, K H Becker and R D Overath
Int. J. Chem. Kinets., 23, 579, (1991)

15. F Maguin, A Mellouki, G Laverdet, G Poulet and G Le Bras, Int. J. Chem. Kinets., 23, 237, (1991)

16. E P Daykin and P H Wine
J. Geophys. Res., 95 D11, 18547 (1990)

Spectroscopic studies of doubly charged transition metal complexes in the gas phase

L Puskar, P E Barran, R R Wright, D A Kirkwood, A J Stace

School of Chemistry, Physics, and Environmental Science, University of Sussex, Falmer, Brighton BN1 9QJ, U.K.

Main contact email address: *A.J.Stace@Sussex.ac.uk*

Introduction

A number of recent experiments have sought to extend the realm of gas phase transition metal ion chemistry to examples where the ion occupies an oxidation state that is more characteristic of the metal concerned, i.e. Cu(II), Fe(II), Mg (II) etc., when found in solution.[1-11)] Arguably one of the most interesting prospects for these new experiments is a detailed understanding of the electronic properties of multiply charged transition metal complexes, and how, for example, d – d and metal/ligand electronic transitions evolve as a function of the nature and number of coordinating molecules.

For a given $[M.L_n]^{2+}$ complex in solution, electronic excitation within the metal ion centre could result in metal-to-ligand charge transfer (MLCT), whereas a similar transition in a ligand could lead to ligand-to-metal charge transfer (LMCT).[12,13)] Either process will depend on the degree of overlap between the orbitals involved, and may also depend indirectly upon the rates of radiative and non-radiative relaxation. For the first time, it has been possible to photoexcite size-selected $[M.L_n]^{2+}$ ions, and examine the competition between LMCT processes and neutral ligand loss induced by rapid non-radiative decay. Two systems have been studied: $[Cu\ (pyridine)_n]^{2+}$ and $[Ag\ (pyridine)_n]^{2+}$, and tunable UV radiation at ~ 280 nm has been used to promote a $\pi \rightarrow \pi^*$ transition in the pyridine molecule. The two metal-ligand systems behave differently in their response to ligand excitation; they both, however, display a marked correlation between fragmentation pattern and the underlying presence of a stable $[M.L_n]^{2+}$ configuration. The experiments have been performed on an apparatus which combines high resolution mass spectrometry with a facility for generating metal-containing clusters. Neutral clusters of pyridine are formed via the adiabatic expansion of a mixture with argon through a pulsed supersonic nozzle. After passing through a 1 mm diameter skimmer the cluster beam enters a drift region where a Knudsen cell is located that contains the metal of interest. The cell is heated to either 1400ºC (Cu) or 1150ºC (Ag) to provide a vapor pressure of approx. 10^{-2} mbar, which is sufficient for the neutral clusters to 'pick-up', on average, a single metal atom.

Clusters emerge from the 'pick-up' region and pass into the ion source of a high resolution double focusing mass spectrometer (VG ZAB-E) where they are ionized by 100 eV electron impact. The use of a high-resolution double focusing mass spectrometer has proved invaluable in this series of experiments.[9)] The instrument has the capability to separate out individual multiply charged ions containing up to thirty solvent molecules. In addition, the geometry of a magnetic sector followed by an electrostatic analyser means that size-selected ions can be photoexcited using a laser, and any subsequent fragmentation detected via a change in kinetic energy. Laser radiation with a tuning range of 275 – 285 nm was generated by frequency-doubling the output from a dye laser (SIRAH – PrecisionScan) pumped with a Nd:YAG laser (Spectron SL805) operating at 532 nm. To maximize the possibility of detecting a response from a weak ion signal (~ 10^{-11} A), the laser beam was passed through the mass spectrometer orientated co-axially with the ion beam. With the ion source potential fixed at 5 kV, singly charged decomposition products originating from charge transfer within a mass-selected doubly charged parent ion, were identified by sweeping the voltage on the electrostatic analyser between $2E_0$ and zero, where E_0 is the value used to transmit the main ion beam.[14)] Data collection on individual photofragments employed a multichannel scalar (Stanford Research SR400) which was triggered, together with the YAG laser, via a delay generator (Stanford Research DG 535). The use of a scalar made it possible to accommodate the large variations in the arrival times of fragments that may result from either Coulomb explosion and/or photoexcitation at different positions over the 1.5 m that the ion and laser beams overlap.

Following the photoexcitation at 280 nm of size-selected $[M\ (pyridine)_n]^{2+}$ complexes for n in the range 4 – 7, two quite separate processes are observed:

photo-induced unimolecular decay –

$$\mathbf{[M\ (pyridine)_n]^{2+} \rightarrow [M\ (pyridine)_{n-k}]^{2+} + k\ (pyridine)}$$

and

photo-induced charge transfer (LMCT) –

$$\mathbf{[M\ (pyridine)_n]^{2+} \rightarrow M^{+}(pyridine)_{n-k} + pyridine^{+} + k\text{-}1(pyridine)}$$

No significant differences in behavior were observed at other wavelengths within the available tuning range of 275 – 285 nm. Radiation at UV wavelengths is known to promote pyridine to either the $S_1(n\pi^*)$ state (~ 287 nm in the gas phase) or the $S_2(\pi\pi^*)$ state (~260 nm in the gas phase). It has been shown that excited pyridine molecules can undergo very rapid nonradiative deactivation (≤ 20 ps) either via intersystem crossing or through the formation of a valence isomer of pyridine. No charge transfer bands exist for complexes with either Cu(II) or Ag(II) because of the large differences in ionisation energy for step Cu(I) → Cu(II) (20.29 eV) or Ag(I) → Ag(II) (21.5 eV) compared with pyridine (9.26 eV).

Two observations lead us to believe that for pyridine molecules in the first solvation shell surrounding either Cu(II) or Ag(II) we are probably exciting the $S_2(\pi\pi^*)$ state at ~280 nm: (i) absorption spectra for the pyridinium ion show the $n\pi^*$ states are missing because the lone-pair electrons on the nitrogen atom are participating in bond formation with the proton.[15)] Similarly, Cu^{2+} and Ag^{2+} can be expected to polarise electron density away from the nitrogen atom on pyridine; however, this effect may not extend to molecules in the second solvation shell; (ii) bulk phase spectra show the $\pi \rightarrow \pi^*$ transition in Cu(II)/pyridine complexes to be shifted to longer wavelengths when compared with the free ligand.[16,17)]

Each $[M\ (pyridine)_n]^{2+}$ ion responds differently to excitation of the ligand. Given the presence of a fast radiationless transition,[15)] the most obvious outcome would be for the complex to undergo unimolecular decay, using the excess energy provided by the photon to overcome the binding energy of the ligand. Since both metals have stable $[M\ (pyridine)_3]^{2+}$ ions,[9,18)] the loss of one molecule from each tetramer should not, in itself, promote dissociative charge transfer. In this respect, the data presented for the $[Cu\ (pyridine)_n]^{2+}$ ions match expectations; the photoexcited tetramer loses one neutral molecule with only slight evidence of charge transfer accompanying the loss of two pyridines. As the complexes increase in size, the fragmentation pattern undergoes a series of very abrupt transitions in a way which always leaves $[Cu\ (pyridine)_4]^{2+}$ as the dominant (> 80%) photofragment.

Thus, the larger complexes always decay in a very precise fashion to what is perceived to be the most stable structure.[18)]

The data recorded for $[Ag(pyridine)_n]^{2+}$ ions contrasts with that given for Cu(II), in that both $[Ag(pyridine)_4]^{2+}$ and $[Ag(pyridine)_5]^{2+}$ show very strong evidence of charge transfer. However, for complexes containing six or more pyridine molecules, photoexcitation leads to the loss of neutral molecules. The fact that the Ag(II) tetramer is recognised as being stable both in the gas phase experiments and in the condensed phase,[9,19,20)] means that the observation of charge transfer in $[Ag(pyridine)_5]^{2+}$ is unexpected if the mechanism is purely dissociative. The most obvious alternative, is to propose that one or more of the 4d orbitals on Ag(II) lie close in energy to the pyridine π^* orbital which receives the electron in the initial excitation step. Under these circumstances, the extremely short time scale for direct electron transfer would be very effective at reducing Ag(II) to Ag(I), even when compared with the rapid radiationless decay rate exhibited by pyridine in the π^* state.[15)] An increased level of interaction between the π orbitals on pyridine and a 4d as opposed to a 3d orbital, would certainly be consistent with both the spectroscopic observations and calculations of Schläfer and König.[16,17)] Likewise, the ease of reduction of Ag(II) compared to Cu(II), follows the trend seen in condensed phase chemistry as represented, for example, by the standard reduction potentials for the metals concerned,[21,22)] which in turn is associated with the significantly lower free energy of solvation of Ag(II) compared with Cu(II).[22)]

It is possible that the marked change in behaviour seen for the silver(II) complexes as a function of size, is associated with a switch in electronic transition on going from the first to the second solvation shell. Thus, in the second shell present in $[Ag(pyridine)_{6,7}]^{2+}$, the reduced polarizing influence of the positive charge could lead to pyridine being excited to the $S_1(n\pi^*)$ state. At ~280 nm the $S_1(n\pi^*)$ absorption coefficient for neutral pyridine in solution is a factor of ~ 100 larger than that of the $S_2(\pi\pi^*)$ transition;[15)] therefore, the increased magnitude of the former could compensate for the smaller numbers of molecules occupying a second shell. The data recorded for $[Ag(pyridine)_5]^{2+}$ could be seen as representing a transition between the two patterns of behaviour: with charge transfer coming from $S_2(\pi\pi^*)$ excitation and leading to the most stable Ag(I) arrangement,[12)] and the loss of neutral pyridine resulting from $S_1(n\pi^*)$ excitation and giving the most stable doubly charged configuration[9,19,20)] Such a switch would not be seen in condensed phase spectra because traditional Ag(II) complexes never contain more than four pyridine ligands.[19,20)]

These preliminary experiments demonstrate the potential for spectroscopic/charge transfer studies on size-selected multiply charged metal – ligand complexes, with the differences seen here between Cu(II) and Ag(II) equating with their behavior in the condensed phase.[23)] The results also provided very strong support for an assumption adopted to interpret data on the relative intensities of $[M.L_n]^{m+}$ complexes;[3,7-9)] namely, that large excited ions preferentially fragment down to the most stable structure. Such a correlation between fragmentation pattern and stability on the part of the ions, removes any ambiguity regarding the method of cluster preparation and the influence it may have on a typical mass spectrum.[24)] Additional details regarding these experiments can be found elsewhere [23)].

References.

1. T. Blades, P. Jayaweera, M. G. Ikonomou, P. Kebarle, Int. J. Mass Spectrom. Ion Processes 102, 251 (1990).
2. T. Blades, P. Jayaweera, M. G. Ikonomou, P. Kebarle, J. Chem. Phys. 92, 5900 (1990).
3. J. Stace, N. R. Walker, and S. Firth, J. Am. Chem. Soc. 119, 10239 (1997).
4. M. Peschke, A. T. Blades, and P. Kebarle, J. Phys. Chem. A. 102, 9978 (1998).
5. S. E. Rodrigeuz-Cruz, R. A. Jockusch, E. R. Williams, J. Am. Chem. Soc. 120, 5842 (1998).
6. S. E. Rodrigeuz-Cruz, R. A. Jockusch, E. R. Williams, J. Am. Chem. Soc. 121, 1986 (1999).
7. Woodward, M. P. Dobson, and A. J. Stace, J. Phys. Chem. A 101, 2279 (1997).
8. N. R. Walker, S. Firth, and A. J. Stace, Chem. Phys. Lett. 292, 125 (1998).
9. N. R. Walker, R. R. Wright, and A. J. Stace, J. Am. Chem. Soc. 121, 4837 (1999).
10. T. G. Spence, T. D. Burns, G. B. Guckenberer, V and L. A. Posey, J. Phys. Chem. 101, 1081 (1997).
11. T. G. Spence, B. T. Trotter, and L. A. Posey, J. Phys. Chem. 102, 7779 (1998).
12. F. A. Cotton and G. W. Wilkinson, Advanced Inorganic Chemistry (Wiley, London, 1988).
13. G. L. Geoffroy and M. S. Wrighton, Organometallic Photochemistry (Academic Press, New York, 1979).
14. R.G. Cooks, J.H. Beynon, R.M. Caprioli, and G.R. Lester, in Metastable Ions, (Elsevier, Amsterdam, 1973).
15. M. Chachisvilis and A. H. Zewail, J. Phys. Chem.,103, 7408 (1999).
16. E. König and H. L. Schläfer, Z. physik. Chem. Neue Folge 26, 371 (1960).
17. H. L. Schläfer and E. König, Z. physik. Chem. Neue Folge 30, 145 (1961).
18. N. R. Walker, R. R. Wright, and A. J. Stace, unpublished results.
19. H. N. Po, Coord. Chem. Rev., 20, 171 (1976).
20. W. Levanson and M. D. Spicer, Coord. Chem. Rev., 76, 45 (1987).
21. P. W. Atkins, Physical Chemistry (Oxford University Press, Oxford, 1998), 6th ed., page 936.
22. J. Burgess, Metal Ions in Solution (J. Wiley, New York, 1978).
23. L. Puskar, P. E. Barran, R. R. Wright, D. A. Kirkwood, and A. J. Stace, J. Chem. Phys. 112, 7751 (2000).
24. J. Stace and C. Moore, Chem. Phys. Lett., 96, 80 (1983).

Time-resolved fluorescence spectroscopy of 2-aminopurine in a protein-DNA complex

D T F Dryden, A C Jones

Department of Chemistry, University of Edinburgh, The King's Buildings, Edinburgh, EH9 3JR, UK

Email address: *David.Dryden@ed.ac.uk, a.c.jones@ed.ac.uk*

Introduction

The double helical structure of DNA displays a range of features which can be recognised by ligands such as drugs and proteins (enzymes)[1]. These features can be of a fairly general nature such as the electrostatic field produced by the charged phosphate backbone of the DNA, a change in helical pitch and physical bending, or more specific, involving the potential of different DNA nucleotide sequences to display different hydrogen bonding patterns to potential ligands. In response to the interaction of these agents, the DNA may undergo structural or conformational changes which facilitate their function. Fluorescence spectroscopy is finding increasing application for probing interactions of DNA with ligands and monitoring changes in DNA conformation, by introducing fluorescent probes into specific locations within the DNA chain. The natural bases of DNA are not useful as fluorescent probes because of their extremely low quantum yields[2], and thus the use of extrinsic probes is necessary. The fluorescent analogue of adenine, 2-aminopurine (2-AP), is one such probe [3-5] which, because of its structural similarity to adenine (6-aminopurine), can be introduced into DNA with minimal perturbation to the system.

In this project we were particularly interested in the use of 2-AP to probe the methylation of DNA by the *Eco*KI methyltransferase, a component of the *Eco*KI type I DNA restriction and modification (R/M) system. The methylation of cytosine and adenine nucleotides within specific DNA sequences is found in many organisms, from bacteria to man. Methylation of DNA fulfils many functions including gene regulation, DNA replication, and the marking of host chromosomal DNA at specific target sequences to distinguish it from foreign unmethylated DNA. This last process is widespread in bacteria and protects the bacterial DNA from degradation by host restriction endonucleases which destroy invading viral DNA containing unmethylated target sequences [6].

The interaction of methyltransferases and repair enzymes with DNA has been found to induce an astonishing localised deformation in the DNA structure, known as nucleotide "base flipping" [7]. This deformation involves the 180^{o} rotation of the target nucleotide around the phosphate backbone, out of the DNA helix and into the reactive site of the enzyme. Apart from the movement of the flipped nucleotide, the conformation of the remainder of the DNA is largely unchanged.

EcoKI is the archetypal member of the type I DNA R/M systems [6]. EcoKI maintains the methylation of both strands of specific target sequences within the bacterial DNA and detects the absence of methylation on the same target sequences found on viral DNA. The absence of the methyl markers triggers cleavage of the viral DNA and ''restricts" viral propagation. The EcoKI enzyme, in contrast to those studied so far with 2-AP, can simultaneously monitor the methylation of two adenine nucleotides within its target sequence, one adenine on each strand of the DNA. If one adenine is already methylated, the enzyme methylates the second adenine efficiently. If neither adenine is methylated, the enzyme remains bound to the DNA and methylates the DNA 50-fold more slowly, taking hours to produce significant methylation. This allows the efficient discrimination of unmethylated DNA for the restriction reaction. The ability to switch between methylation and restriction endows EcoKI with the properties of a "smart" molecular machine.

Results

The fluorescence of 2-AP is strongly quenched within the base-stacked structure of double-stranded DNA but is enhanced if the base stacking or base pairing is perturbed [8,9]. 2-AP fluorescence emission intensity has been used for monitoring DNA polymerases[10], helicases[11], DNA repair enzymes[12-14] and DNA methyltransferases[15-18]. Previous time-resolved fluorescence studies of 2-AP in DNA revealed a complex fluorescence decay which could be described by 4 exponential decay times (and pre-exponential factors) of approximately 40 ps (0.6), 0.4 ns (0.2), 2 ns (.15) and 9 ns (0.05) [8,9]. These fluorescence decay measurements were only performed at a single emission wavelength. In our work at the LSF, we used a picosecond-pulsed dye laser and time-correlated single-photon counting to measure the fluorescence decay as a function of emission wavelength. Our results confirmed the multiexponential decay function, Table 1, and indicated even greater complexity in that the decay times are wavelength-dependent, data not shown. The complexity of the decay behaviour of 2-AP in DNA (in contrast to its simple photophysics in aqueous solution) suggests that the environment of the 2-AP in DNA is extremely heterogeneous.

It has been found that the simplest DNA adenine methyltransferases cause a dramatic increase in fluorescence intensity when they bind to a DNA duplex containing 2-AP at the methylation site [15-18]. This enhancement was attributed to a flipping of the base out of the DNA helix into the catalytic site of the enzyme and 2-AP has rapidly been adopted as a probe of base flipping by methyltransferases. The large increase in fluorescence intensity of 2-AP has been explained by suggesting that the enzyme active site provides a similar environment to that in aqueous solution. However, this interpretation is questionable on a number of grounds: (i) the active site of methyltransferases contains various hydrophobic aromatic rings which might be expected to interact with 2-AP in a manner similar to the stacking of nucleotides within DNA which is proposed to quench the fluorescence; (ii) the presence of positively charged and hydrogen-bonding groups in the active site would be expected to perturb the 2-AP fluorescence; (iii) our lifetime measurements described below on 2-AP in an EcoKI-DNA complex show that the 2-AP environment is greatly perturbed, but is certainly not equivalent to free aqueous solution.

We have found that the addition of EcoKI to DNA containing 2-AP at the location targeted for methylation by the enzyme dramatically changes the amplitudes of the four lifetime components of 2-AP. The amplitude of the 40 ps component decreases by about an order of magnitude and that of the 9 ns components increases by about an order of magnitude, Table 1. A multiexponential decay is still observed indicating the persistence of a heterogeneous environment for the 2-AP probe.

We have also studied EcoKI-DNA complexes in which 2-AP is located adjacent to the adenine targeted for methylation by the putative base flipping mechanism. Once again, we observe an increase in the fluorescence intensity and a multiexponential decay of the 2-AP probe, data not shown. Thus a perturbation of base stacking, rather than breakage of Watson-Crick base pairing and subsequent flipping, appears sufficient to produce large changes in fluorescence lifetime. Thus, there is no clear

correlation between a change in fluorescence intensity of 2-AP and base flipping. Other perturbations such as a distortion of nucleotides adjacent (including base flipping) to the 2-AP location, an interaction with 2-AP via the minor groove of the DNA by amino acid side chains or some other distortion of the DNA may also cause similar fluorescence intensity and lifetime changes. However, we have observed the formation of a new fluorescent species upon addition of the methylation cofactor, S-adenosyl methionine (SAM), to the *Eco*KI-DNA complex. This modified form of 2-AP, which we will refer to as M-AP, is only formed when the 2-AP replaces the adenine which would normally be methylated and not when placed at the adjacent position. This new species has excitation and emission spectra which are red-shifted relative to those of 2-AP. The observation of a new excitation spectrum indicates the formation of a new ground-state species. The fluorescence lifetimes of M-AP are longer than those of 2-AP, Table 1, however the available excitation wavelengths at the LSF do not currently permit the exclusive excitation of M-AP, hence the calculated lifetimes arise from a mixture of 2-AP and M-AP. The formation of M-AP in a DNA sequence-specific manner may represent firm evidence for base flipping by *Eco*KI.

Conclusion

The use of time-correlated single-photon counting to analyse the fluorescence decay of 2-AP incorporated in DNA and the effect of protein binding to the DNA has revealed highly complex behaviour not apparent from fluorescence intensity measurements. The environment of the 2-AP is perturbed by the binding of *Eco*KI adenine methyltransferase in a manner dependent upon the location of the fluorophore within the DNA and on the presence or absence of the methylation cofactor SAM.

Acknowledgements

We gratefully acknowledge the assistance of Stan Botchway and Mike Towrie at the LSF and Neil Speirs and Peter Jennings in Edinburgh.

References

1. Rhodes, D., Schwabe, J.W.R., Chapman, L., Fairall, L. Phil. Trans. Roy Soc. Ser. B-Biol. Sci., 351 501-509, (1996)
2. Holmen, A., Broo, A., Albinsson, B., et al. J. Am. Chem. Soc. 119 2240-12250, (1997)
3. Broo, A. J. Phys. Chem. A 102 526-531, (1998)
4. Holmen, A., Norden, B., Albinsson, B., J. Am. Chem. Soc.119 3114-3121, (1997)
5. Ward, D.C., Reich, E., Stryer, L. J. Biol. Chem. 244 1228-1237 (1969)
6. Dryden, D.T.F, Davies, G.P., Martin, I., Powell, L.M., Murray, N.E., Ellis, D.J., Berge, T., Edwardson, J.M., Henderson, R.M. Biochem. Soc. Trans. 27 691-696, (1999)
7. Roberts, R.J. & Cheng, X., Annu. Rev. Biochem. 67 181-198, (1998)
8. Guest, C.R., Hochstrasser, R.A., Sowers, L.C., et al. Biochemistry 30 3271-3279, (1991)
9. Nordlund, T.M., Anderson, S., Nilson, L. et al. Biochemistry 28 9095-9103, (1989)
10. Beechem, J.M., Otto, M.R., Bloom, L.B., et al. Biochemistry 37 10144-10155, (1998)
11. Raney, K.D., Sowers, L.C., Millar, D.P., Benkovic, S.J. Proc. Natl. Acad. Sci, USA 91 6644-6648, (1994)
12. McCullough, A.K., Dodson, M.L., Scharer, O.D., et al. J. Biol. Chem. 272 27210-27217, (1997)
13. Stivers, J.T., Pankiewicz, K.W., Watanabe, K.A. Biochemistry 38, 952-963 (1999)
14. Stivers, J.T. Nucl. Acids Res. 26 3837-3844, (1998)
15. Allan, B.W., Beechem, J.M., Lindstrom, W.M. & Reich N.O., J. Biol. Chem. 273 2368-2373, (1998)
16. Allan, B.W., Reich, N.O., Beechem, J.M. Biochemistry 38 5308-5314, (1999)
17. Allan, B.W., Reich, N.O. Biochemistry 35 14757-14762, (1996)
18. Holz, B., Klimasauskas, S., Serva, S., et al. Nucl. Acids Res. 26 1076-1083, (1998)

Sample	τ_1 ns (%)	τ_2 ns (%)	τ_3 ns (%)	τ_4 ns (%)	τ_5 ns (%)
2-AP alone, emission at 365 nm	-	-	-	10.6 (100)	-
2-AP-DNA, emission at 365 nm	0.04 (33)	0.18 (45)	2.10 (8.5)	9.13 (12)	-
2-AP-DNA + *Eco*KI, emission at 365 nm	0.05 (5.2)	0.70 (9.0)	4.15 (30)	10.31 (56)	-
2-AP-DNA +*Eco*KI +SAM, emission at 365 nm	0.04 (9.0)	0.81 (7.8)	4.87 (37)	12.19 (47)	-
2-AP-DNA +*Eco*KI +SAM, emission at 450 nm	-	0.40 (0.6)	3.92 (6.8)	12.86 (53)	18.21 (40) (M-AP)

Table 1. Fluorescence decay parameters of 2-AP located at the methylation site in the *Eco*KI recognition sequence, excitation at 318 nm with picosecond-pulsed dye laser. The addition of SAM causes the appearance of the longer lifetime species, M-AP, at long emission wavelengths.

Fluorescence lifetime imaging of photosensitizer distributions in mammalian cells using a picosecond gated laser line scanning confocal microscope

S W Botchway, A W Parker

Central Laser Facility, CLRC Rutherford Appleton Laboratory, Chilton, Didcot, Oxon, OX11 0QX, UK

J P Connelly L Kunz, A J MacRobert

University College London Medical Laser Centre, UK

Main contact email address: *S.Botchway@rl.ac.uk*

Introduction

Photodynamic therapy (PDT)[1-3], as it is termed, is already becoming established as a treatment for some cancers. Fluorescence monitoring during PDT is proving very useful as exposure to light initiates the photoreactions and fluorescence of the photosensitiser. A line scanning confocal microscope system has been developed at the Rutherford Appleton Laboratory[4] to image fluorescence and this has been extended using a gated optical detector to allow time-resolved confocal fluorescence microscopy[5]. We have previously shown using steady state confocal microscopy that in V79 Chinese hamster fibroblasts, metal phthalocyanines (eg $AlPcS_2$) localize in perinuclear sites [4,5]. With rapid scanning confocal microscopy giving both fluorescence intensity and lifetime data we are able to study photosensitizer environment, and the changes accompanying PDT and photobleaching. We have extended these studies and present confocal lifetime images of AlPcS2 compared with mTHPC, two photosensitizers with different biochemical characteristics, in mammalian cells.

Experimental

Instrumentation - Bilateral confocal laser scanning fluorescence microscope

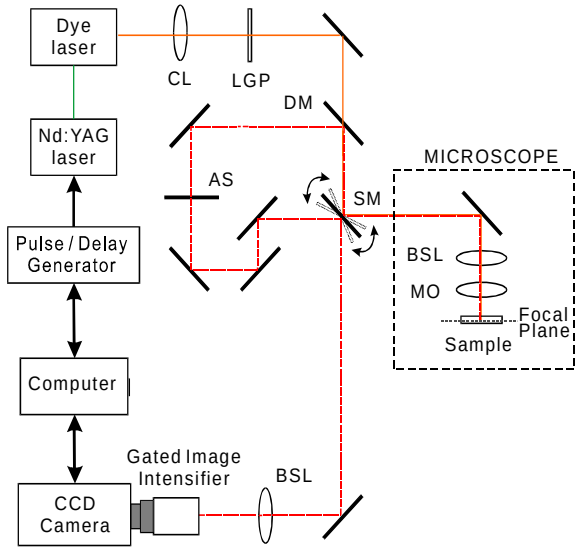

Figure 1. Layout of the confocal apparatus and optics.

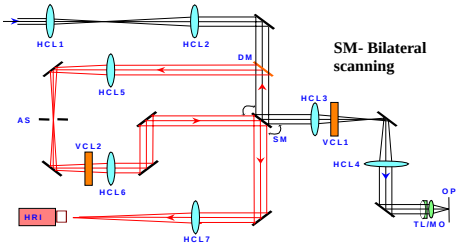

Figure 2. Optical path for laser excitation and sample fluorescence. VCL and HCL are cylindrical lens;LPF, long pass filter.

A picosecond laser consisting of a cavity-dumped dye laser (Spectra Physics, model 3500) pumped synchronously by a mode-locked Nd^{3+}/YAG laser (Spectron, model SL903) was used. The excitation wavelengths used in this work were 610 nm for AlPcS2 and 590 nm for mTHPC. The laser excitation beam was focused to a vertical line and collimated into an expanded beam, transmitted through a dichroic mirror (DM, Omega Optical 660DCSP) and scanned by reflection into the microscope using a double-sided scanning mirror (SM, General Scanning, M3H). The emitted fluorescence (dashed line) was collected by the same objective and focussed on to the semi-reflective scanning mirror and a slit, adjustable to control the depth of focus, to project an image of the slit on to the 2-D detector. Any extraneous scattered excitation light was further attenuated using a long-pass filter (Schott RG630) placed in front of the gated optical detector. Images were collected on an 8-bit scientific grade CCD camera capable of on-chip integration (Cohu, 4910). The bilateral scanning mirror was made to oscillate at 25 Hz by a sawtooth signal matched to the video frame rate of the CCD camera. This resulted in two complete scans of the laser excitation line across the microscope field per video frame, yielding real-time fluorescence images on the video monitor for samples that were sufficiently fluorescent. All images presented in this work were recorded by integrating for up to 4 seconds (100 video frames) on the CCD chip.

The average laser excitation power was about 6 µW during image acquisition to give minimum photobleaching of the intracellular AlPcS2 fluorescence. The fluorescence images were obtained using a 63x oil-immersion objective (Nikon PlanAchromat, 1.4 NA). Optimal axial resolution (1 µm) was determined by calibration using 1 micron diameter fluorescent spheres (Molecular Probes F-8826), whilst the lateral resolution was less than 1 µm measured with a graticule. The gated high rate imager (HRI, Kentech Instruments Ltd., UK) was operated at 800 kHz to match the pulse repetition rate of the dye laser. The peak-to-peak jitter of the HRI is less than 40 ps. Temporal resolution of the confocal microscope is 120 ps so that many biomolecular probes with lifetimes down to 0.1 ns can be investigated. Lifetime measurements were performed in nanosecond steps with 0.7 ns gate width of the HRI and an experimental series took only 3 seconds to accumulate. Fluorescence lifetime maps were generated by calculating the fluorescence decay time at each pixel from images collected over 0-4 ns for $AlPcS_2$ and 0-10 ns for mTHPC after arrival of the excitation pulse at the sample.

Sample preparation and cell culture

Disulphonated aluminium phthalocyanine (AlPcS2) was prepared according to the method of Ambroz et al [6]. mTHPC was provided by Scotia Quantanova, UK. V79-4 Chinese hamster fibroblasts were cultured in the presence of phenol-red free minimal essential medium (MEM) supplemented with 10% foetal calf serum (Sigma Biochemicals), 1% penicillin and 1% L-glutamine in a petri dish with a cover slip base. The cells were grown over a period of 40 - 60 hr in a humidified 5% CO_2 incubator at 310 K to allow the cells to flatten. Cells were then incubated with $AlPcS_2$ or mTHPC in MEM for 1- 2 hr at 310 K. The concentration of AlPcS2 or mTHPC in the medium was

~25mM. The cells were washed thoroughly with phosphate buffer solution prior to measurements.

Results and Discussion

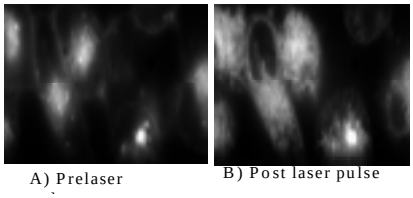

Figure 3. Confocal Fluorescence Imaged section of V79-4 cells (stained at 37 ^{o}C). Redistribution of $AlPcS_2$.

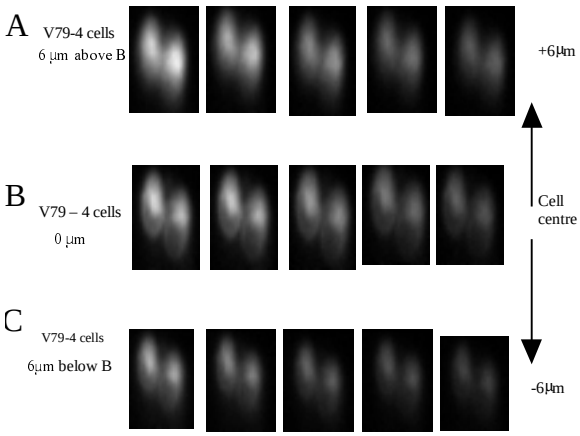

Figure 4. Subnanosecond gated confocal fluorescence images of the same V79-4 cells incubated with AlPcS2 at laser power of 70 μW.

Figure 5. Subnanosecond gated confocal fluorescence images of the V79-4 cells incubated with mTHPC at laser power of 7 μW.

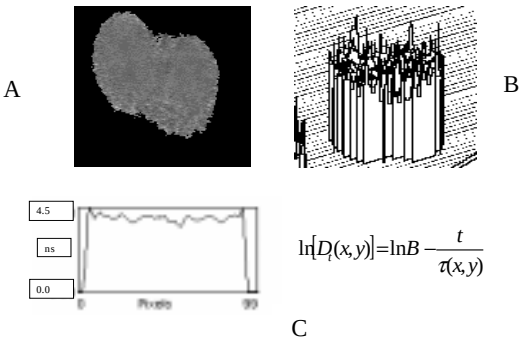

Figure 6. A) Fluorescence life time map calculated by a linear least square analysis of the intensities at each of the five image pixels of figure 4. B) Surface plot of A; C) Cross section through the centre of the lifetime map (A).

We have shown previously that the AlPcS2 drug localizes within perinuclear sites most probably comprising of the Golgi apparatus and the endoplastic recticulum rather than mitichondria[5)]. Following laser irradiation, the drug redistributes to fill the cell cytoplasm (Figure 5) and producing an increase in fluorescence intensity. This effect can be minimized at low drug concentration and low laser intensity although photobleaching becomes a competing effect under these conditions.

The lifetime map provides more quantitative evidence for the independence of the fluorescence lifetime of $AlPcS_2$ and mTHPC on its location within the cell. The fluorescence lifetime map (Figure 5) does not show significant dependence on intracellular distribution. Lifetimes from different confocal planes are all similar. This suggests similar and homogenous environments of the drugs throughout the cell. Average lifetimes of 4.1 ± 1 ns and 5.5 ns were obtained for $AlPcS_2$ and mTHPC respectively. Solution studies of the $AlPcS_2$ showed a lifetime of 4.5 ns and 6 ns in PBS and methanol respectively. The lifetime of mTHPC also changed from 6.5 ns to 8 ns in PBS and methanol solution respectively. This suggests that physical effects such as quenching due to aggregation or photobleaching may be shortening the lifetimes in the cells.

Conclusions

a. We have constructed a tuneable time resolved (TR) laser line-scanning confocal fluorescence microscope with sub-nanosecond high repetition rate optical imager allowing resolution of lifetimes down to 100 ps.
b. TR-Confocal confocal fluorescence images of mammalian cells shows no evidence for the dependence of the fluorescence lifetime of AlPcS2 and mTHPC on their location within the cell.
c. The PDT drugs studied in this work showed similar lifetimes across all cellular compartments of ~4.1 ns and 5.5 ns for AlPcS2 and mTHPC + < 10% respectively.
d. The results highlight the potential usefulness of this setup in the study of fluorescence dynamics of intracellular drug localisation.
e. Interestingly the environmentally dependent lifetimes observed for these drugs in differing solvents is not observed within the cell. This enforces the need to move towards in vivo studies to understand fully the action of these important drugs.

Acknowledgements

We thank Mrs C. deLara (RAGSU, MRC, UK) for providing the cells and Drs M.Towrie and P. Matousek for their help with the lasers.

References

1. R. Bonnett, Reviews in contemporary Pharmacotherapy 1999, 10, 1-17
2. R. Bonnett, Chemical Society Reviews 1995 24 19-33.
3. D. Phillips, Progress in Reaction Kinetics, 1997, 22, 175-300.
4. A.D. Scully, R.B. Ostler, D. Phillips, P. ONeill, A.W. Parker, A.J. MacRobert, Bioimaging 1997, 5, 9-18.
5. A.D. Scully, R.B. Ostler, A.J. MacRobert, A.W. Parker, C. deLara, P. ONeill, D. Phillips, Photochemistry and Photobiology, 1998, 68 199-204.
6. M Ambroz, A. Beeby, A.J. MacRobert, M.S.C. Simpson, R.K. Svenson and D. Phillips (1991). J. Photochem. Photobiol. B*: Biol.* 9, 87-95.

Development of the RAL laser-plasma x-ray source for biological irradiations: characterisation and preliminary results

M A Hill, D L Stevens, S Cunniffe, D T Goodhead

MRC Radiation & Genome Stability Unit, Harwell, Didcot, Oxon, OX11 0RD, UK

W Shaikh, J Westhall, C J Reason, G J Hirst, I C E Turcu*

Central Laser Facility, CLRC Rutherford Appleton Laboratory, Chilton, Didcot, Oxon, OX11 0QX, UK

**Now at JMAR Research Inc., San Diego, CA, USA*

Main contact email address: *m.hill@har.mrc.ac.uk*

Introduction

A new MRC high-flux biological irradiation facility has been designed for use with the RAL laser-plasma induced ultrasoft x-ray source (Figure 1). The high intensity and broad beam, together with the reduced x-ray source-to-sample distance has been used to overcome the high attenuation of low energy x-rays and produce high dose rates in the sample, enabling a range of biological and chemical end points to be studied.

Ultrasoft x-rays can be used to probe the energy and spatial requirements for specific types of radiation damage and biological response and so provide much needed data for understanding and modelling the processes involved. They interact via the photoelectric effect producing low energy, isolated electron tracks randomly throughout the irradiated material. These electrons have well defined energies and short tracks comparable in size to those of critical structures in the cell, such as DNA, nucleosomes and chromatin fibres. Also, these tracks are similar to the numerous secondary electrons and electron 'track ends' produced in the slowing down spectrum of more energetic electrons and are therefore representative of a substantial component in any ionising radiation.

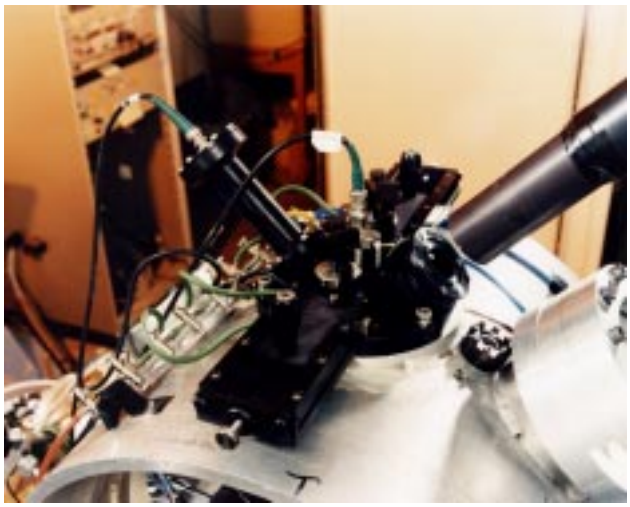

Figure 1. The new MRC biological irradiation facility.

For x-rays in the energy region of 0.28 keV to 4.55 keV the biological and chemical response varies significantly due to changes in the spatial distribution of energy deposition events along the resulting electron tracks[1-2]. The range of the single photo-electron produced by the 0.28 keV x-ray is < 7 nm, while the combined range of the photo- and Auger-electron produced by 4.55 keV x-rays is ~ 500 nm. The polypropylene target is of particular interest, producing carbon x-rays of ~400 eV, which are above the carbon K, but below the oxygen K absorption edges. These x-rays will preferentially interact with carbon in DNA rather than the surrounding water. Recent mammalian cell survival experiments have indicated an increase in effectiveness of a factor of 2 compared to energies just below the carbon edge, due to localisation of photon interactions on the DNA[3].

Irradiation of biological samples

The target and tape drive mechanism has been redesigned to maximise the x-ray flux by reducing the target-to-sample distance from 30 cm to 5.4 cm through helium at atmospheric pressure. A schematic of the irradiation configuration is shown in Figure 2.

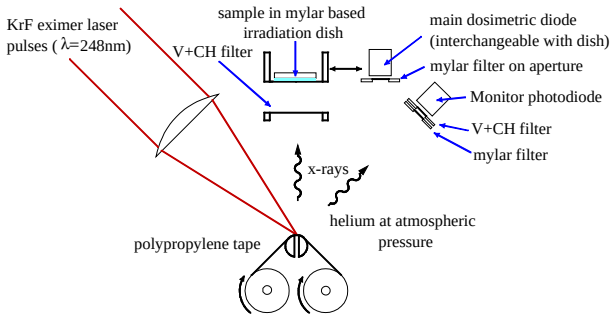

Figure 2. Schematic of the biological irradiation set up.

Samples are irradiated in glass walled irradiation dishes (3 cm internal diameter) with a 0.9 μm mylar base. These samples typically include mammalian cells grown on the mylar base as an attached monolayer (~5 μm thick). Alternatively, lymphocytes or plasmid DNA are spread evenly across the mylar base under a CR39 disc to form a uniform layer (typically 7.8 μm thick). The samples are positioned horizontally, directly above the source of x-rays. These x-rays are produced by focusing KrF eximer laser pulses (λ = 248 nm) onto a moving target tape. The incident angle of the laser is 45° to the target tape surface, which is parallel to the irradiation dish. A UV/light filter (0.5 μm V on 0.5 μm CH), spanning a circular area of 3 cm diameter, is positioned between the target and the dish. The three-position irradiation slide allows one sample to be changed while another is being irradiated. Air beneath each dish is flushed with helium prior to moving into position for irradiation. For dosimetric purposes the central position on the slide is occupied by a photodiode with a 0.9 μm mylar dish base filter mounted on a 6.5 mm diameter aperture. This is cross calibrated before and after each exposure with a second monitor photodiode with identical filters positioned at 45° from the normal of the target tape. The charge signals from these diodes are fed into an analogue-to-digital converter interfaced to a computer. The monitor diode is used to determine when the required dose to the sample has been delivered. A second slide has also been made which allows samples to be cooled.

Characterisation

The stability of the lasers and careful optimisation was found to be important for accurate dosimetry and for minimising the variation of dose per shot. Figure 3 gives examples of shot by shot comparisons between the signals from the main dosimetric diode and the monitor diode. There is a significant difference between the non-optimised and optimised beams. This distribution was checked before and after each sample irradiation and reoptimised if necessary. The improvement in the distribution of dose per shot is given in Figure 4.

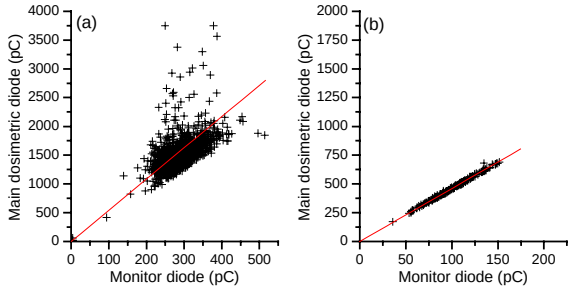

Figure 3. Shot by shot comparison between signals from the main dosimetric diode and the monitor diode (a) sub-optimal (b) optimal**.**

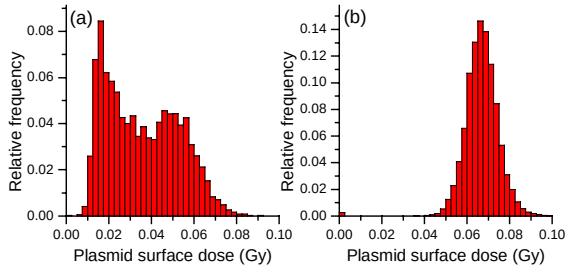

Figure 4. Distribution of dose per shot obtained (a) sub-optimal, (b) optimal.

The dose distribution across the sample was assessed with a disc of GafChromic® HD-810 radiochromic dye film in an irradiation dish. The area-weighted average optical density over the 28 mm diameter of the sample, compared to the 6.5 mm diameter area at the centre viewed by the photodiode, was experimentally determined to be 0.91.

Plasmid DNA studies using a polypropylene target

A 7.8 μm thick plasmid sample was irradiated with 50 Hz x-ray pulses from the polypropylene target. The dose rate at the incident surface of the sample was calculated as 0.06 Gy per shot on average, giving a dose rate of 3 Gy s^{-1} at 50 Hz. Polypropylene tape was used as a target to produce carbon x-ray emission lines. This was used in preference to mylar tape, which would also produce higher energy oxygen lines. The dose calculations were based on the relative intensity of the carbon emission lines (G J Tallents and A Nottola, personal communication), the attenuation of these carbon x-rays through the helium, filter and mylar was calculated. This results in a dose averaged x-ray energy of ~450 eV in the sample. Due to attenuation of the x-rays, the ratio of mean absorbed dose to surface absorbed dose in the plasmid sample was calculated to be 0.56. Accurate dosimetry is reliant on a good knowledge of the emission spectra, the reliability of which will be checked in future studies.

These preliminary studies used pUC18 plasmid DNA (2686 base pairs) irradiated in a solution of Tris (0.66 mmol dm^{-3}) with an OH scavenging capacity of 10^{-6} s. Initially >95% of the plasmid was in the supercoiled form. Relaxation to the open circular form results from a DNA single-strand break (ssb), which can be produced either by the radiation interacting directly with the DNA or indirectly by reaction with an OH radical produced by the interaction of radiation with a nearby water molecule. The production of a DNA double-strand break (dsb) results in the linearisation of the plasmid. The relative proportions of the different plasmid forms can be determined by gel electrophoresis due to their different mobilities.

Results

The dose dependence for the loss of supercoiled plasmid from a single preliminary experiment is shown in Figure 5. From the slope of this response, a D_{37} value was calculated to be 73 Gy which, assuming Poisson statistics, represents the radiation dose required to give on average one ssb per plasmid molecule. With 2686 base pairs in the pUC18 plasmid and assuming an average mass of 650 Da per base pair, gives an ssb yield of 7.9×10^{-9} ssb Gy^{-1} Da^{-1} (given by $1/(D_{37} \times 2686 \times 650)$). This is in line with previously determined yields[2] (Figure 6).

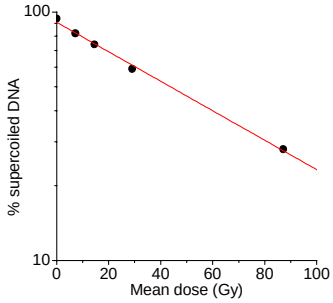

Figure 5. Dose dependence for the loss of supercoiled pUC18 plasmid irradiated in aqueous solution containing 0.66 mmol dm^{-3} Tris.

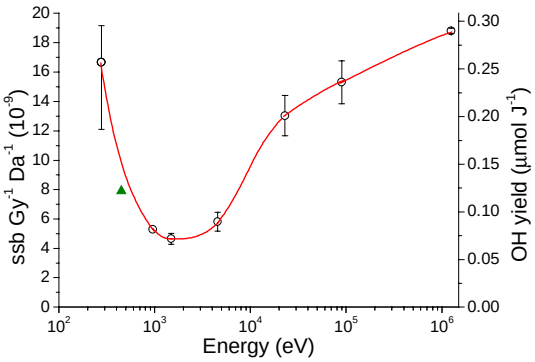

Figure 6. Experimental dependence of the yield of single-strand breaks in pUC18 DNA and calculated OH yield with incident photon energy (▲ this work, O previous experimental values[2], —— line to guide the eye through previous experimental values).

Discussion

The passage of ionising radiation through water and mammalian cells leads to the production of reactive chemical species along its path. Many of these reactive species are formed in close proximity and so have a high probability of interacting with each other as they start to diffuse, with a higher probability for smaller initial separations. After ~ 1 μs the reactive species remaining have moved so far apart that the intra-track reactions are unlikely. The scavenging capacity of 0.66 mmol dm^{-3} Tris corresponds to a mean OH radical lifetime of 1 μs, sufficiently long for the OH radical to become homogeneously distributed and so the yield of ssb induced may be used as a measure of the yield of OH radicals escaping radiation tracks. A yield of homogeneous OH radicals of 0.12 μmol J^{-1} was calculated by normalising the yield of ssb to the yield for ^{60}Co γ-rays (18.8×10^{-9} ssb Gy^{-1} Da^{-1})[2] with a correspond OH yield of 0.29 μmol J^{-1} at 1 μs [4].

This data provides information in an important energy region between the 278 eV C_K x-ray data and the single experimental point from ~956 eV Cu_L x-rays. As the energy decreases in this

region a large increase in the yield of ssb was observed with an inferred increase in OH radicals escaping the radiation track.[2] In general, decreasing photon energy results in a reduction of the initial separation of the reactive species and therefore a decrease in OH yield, due to the decrease in mean free path and increased angular scatter of the photo- and Auger-electrons. However at low photon energies the number of OH radicals escaping the track rises due to the probability of reaction now being limited by the reduced initial yield of reactive species per track at these much reduced energies.

The reported variation in yields with photon energy[2] illustrates the importance of electron track structure and localised ionisation density on the chemical and ultimately biological consequences. Increasing ionisation density would be expected to lead to a corresponding increase in complexity of DNA damage resulting from local clustering of ionisation in DNA and its immediate surroundings.

Summary

The successful irradiation of both plasmid and mammalian cells (data not presented) with ~450 eV x-rays demonstrates the feasibility of cellular radiobiology and DNA biochemical experiments with the new setup. At 50 Hz the surface dose rate of 180 Gy min^{-1} (480 Gy min^{-1} for cellular irradiations) is significantly higher than the values of 2, 1, 50 and 4 Gy min^{-1} obtained for C_K (278 eV), Cu_L (956 eV), Al_K (1.49 keV) and Ti_K (4.55 keV) x-rays respectively from the MRC cold cathode ultrasoft x-ray source. This high dose rate allows the scavenger concentration in the plasmid system to be varied in order to give information on the inhomogeneous spur kinetics of the low energy electron tracks produced. This should provide invaluable benchmark data for computer models of radiation spur kinetics and radiation induced DNA damage.

References

1. D T Goodhead and H Nikjoo
Radiat. Prot. Dosim. 31, 343 (1990)

2. J Fulford, P Bonner, D T Goodhead M A Hill,
P O'Neill, J. Phys. Chem. A, 103, 11345 (1999)

3. M A Herve du Penhoat, B Fayard, F Abel, A Touati,
F Gobert, I Despiney-Bailly, M Ricoul, L Sabatier,
D L Stevens, M A Hill, D T Goodhead and A Chetioui
Radiat. Res. 151, 649 (1999)

4. G V Buxton
In: Radiation Chemistry: Principles and Applications
(Farhataziz and M A J Rogers, Eds.). VCH Publications
Inc., p321 (1987)

Electromagnetic Noise Tests in the CLF X-Ray Laboratory

A G Michette, C J Buckley, S J Pfauntsch, Z Wang

Department of Physics, King's College London, Strand, London WC2R 2LS

G J Hirst, W Shaikh

Central Laser Facility, CLRC Rutherford Appleton Laboratory, Chilton, Didcot, Oxon, OX11 0QX, UK

Main contact email address: *Alan.Michette@kcl.ac.uk*

Introduction

As described in the Annual Report for 1998/99[1)] the King's College x-ray microscope has been successfully installed and used in the CLF x-ray laboratory. However, the quality of the images obtained was severely limited by electromagnetic noise picked up by the modified electron multiplier (EM) detector[2)]. Electromagnetic noise in the detector system reduces the contrast, i.e., the number of grey levels in an image and, therefore, indirectly makes the resolution worse.

The extent of the problem is shown in Figure 1, which is a typical EM detector output pulse. Here, the pulse height is ~300 mV and the noise has an amplitude of ~50 mV. For more absorbing parts of specimens, the pulse heights would be considerably lower than 300 mV. Under favourable circumstances, the noise amplitude could be reduced to ~2 mV which, if reproducible, would have been acceptable. However, despite attempts to achieve reproducible noise and to limit its effects, the amplitude varied in an unpredictable way.

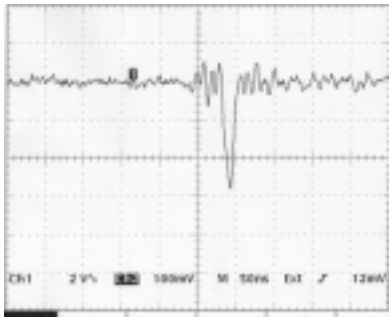

Figure 1. An output pulse from the EM detector.

Because of the problems caused by the noise a series of experiments was carried out to identify the main sources.

Noise Survey

The electromagnetic noise was surveyed by monitoring the EM detector amplifier output with a storage oscilloscope and selectively switching off different components, as summarised in Table 1.

Table 1. Noise survey experiments

	Final laser amplifier	Remaining laser components	Detector	Plasma	Noise level [mV]
1	On	On	On	On	40–50
2	On	Off	On	On*	20–25
3	Off	On	On	On*	~10‡
4	Off	Off	On	On*	~10‡
5	On	On	On	Off¶	20–25
6	On	On	Off†	On	40–50
7	On	On	Off†	Off¶	20–25

*With one or more laser components switched off, no plasma is formed; "On" here means that the target drive was on.
‡The oscilloscope traces for these configurations were essentially identical.
¶Target drive on, but card in beam.
†Detector power switched off, but detector amplifier on.

From the noise levels shown in Table 1 three main conclusions can be drawn, as summarised below.

i) The noise seems to be picked up through the detector amplifier (or connecting leads) rather than by the detector itself, since the noise level does not decrease when the detector power is off (compare 1 & 6 and 5 & 7).

ii) Of the laser components, only the final amplifier contributes significantly to the noise (compare 2,3 & 4).

iii) There is a significant amount of noise associated with the plasma itself (compare 1 & 5 and 6 & 7).

The first of these can be reduced by using a detector with larger intrinsic gain, thus requiring less external amplification. A multiplier with a dynode chain current an order of magnitude larger than that of the original EM at the same voltage is being prepared. This also has external voltage stabilisation on the last few dynodes and an adjustable voltage between the first and second dynode. As well as providing a considerable improvement in signal level the linearity will also be improved. Alternatively, other types of detector, such as cooled diodes, SiLi detectors or proportional counters, can be considered.

The noise associated with the laser amplifier can be removed by shielding or, ideally, situating the x-ray microscope target chamber in a different laboratory from the lasers, with the laboratories connected by a beam pipe.

The noise associated with the plasma is thought to be due to long wavelength (microwave or radio) emission as the plasma expands which is transmitted via electrical feedthroughs to the outside of the target chamber. It was demonstrated that long wavelength radiation can be transmitted in this way by two experiments. In the first, the number of a mobile telephone placed inside the chamber (which was closed but not evacuated) was dialed, and the telephone rang. In the second, the telephone was replaced by a radio, which continued to pick up FM signals (Fox FM) but not AM signals (Radio Five Live) when the chamber was closed. It still remains to measure the frequencies involved in the plasma noise so that suitable filters can be inserted into the feedthroughs to remove it.

References

1. A G Michette et al.,
Annual Report of the Central Laser Facility p151 (1999)

2. C J Buckley et al.,
X-Ray Microfocusing: Applications and Techniques,
SPIE Proceedings 3449 208 (1998)

UV-Laser Photo-induced Refractive Index Changes in Poly Methyl Methacrylate and Plastic Optical Fibres for Application as Sensors and Devices

P J Scully, S Caulder, R Bartlett

Liverpool John Moores University, School of Engineering, Byrom Street, Liverpool, L3 3AF

Main contact email address: *p.j.scully@livjm.ac.uk*

Introduction

Initial attempts to photo-induce refractive index changes in bulk poly methyl methacrylate (PMMA) and in PMMA based plastic optical fibres (POF) using UV light are described. Optimum changes have been achieved at 216 nm, causing path length changes of 10π, corresponding to possible refractive index modulation of between 5 and 14 % over thicknesses up to 100 μm. The effects of refractive index changes on the far field modal distribution of tapered PMMA plastic optical fibres are described. *A major portion of this paper has been submitted to OFS 2000, 14th International Conference on Optical Fiber Sensors, October 2000.*

Background and Previous Work

POF has traditionally been considered to be inferior to silica fibre, but its cheapness, ease of termination, and robustness, is rapidly increasing its credibility for LANs etc. New graded index POF fibres have become available[1)], and advances in materials and manufacturing have increased the POF bandwidth up to GBps and reduced losses down to 10 dB/km [2)]. It is expected that as POF becomes more widely accepted, its advantages in ease of preparation and termination, and easy coupling to detectors and emitters will make it highly attractive for sensing applications. POF is typically 1mm diameter, step-index with core made from pure PMMA (refractive index 1.492) and cladding from fluorinated PMMA (refractive index 1.405).

Periodic UV-induced refractive index changes in mono-mode glass optical fibres have led to in-fibre Bragg gratings for applications such as mirrors and wavelength division multiplexers for communications applications, and as strain and temperature sensors as well as taps and couplers. Gratings in multimode fibres were anticipated [3)] and realised by Peng et al[4)] in a fluorescein doped multimode POF.

Previous work at Liverpool John Moores University (LJMU) demonstrated the feasibility of photo-inducing physical surface gratings using a loaned UV excimer laser at 248 nm after a number of incubation pulses (about 90 at 1 - 2 Hz) in the pre-ablative regime (below 90 mJ/cm^2) [5)]. The gratings were revealed by washing with isopropyl alcohol (IPA), which reacts with photoproducts or oligomers of PMMA, to remove the fragments and expose the periodically perturbed surface. This procedure was used to write end gratings and side cladding gratings. The disadvantage of the technique is that because of the revealing process, optical feedback to enable control and optimisation of the procedure is not possible. Refractive index changes at the wavelength investigated were not detected, nor were any other wavelengths investigated.

Following on from this work, the effect of a number of different UV wavelengths on the refractive index of PMMA was investigated, in order to moderate the optical properties of POF to form useful sensors and devices.

UV Irradiation of PMMA Slabs

For ease of handling and alignment, refractive index changes were induced in PMMA slabs. The UV wavelengths were generated using a Lumonics Pulsemaster Excimer laser emitting at 308 nm, pumping a Lambda Physik FL3002 dye laser and SHG in the Nanosecond Laboratory at Rutherford Appleton Laboratory, and a Spectra Physics GCR-170 Nd:YAG laser emitting at 335 nm and pumping a Lambda Physik LAS20505 dye laser and SHG at LJMU.

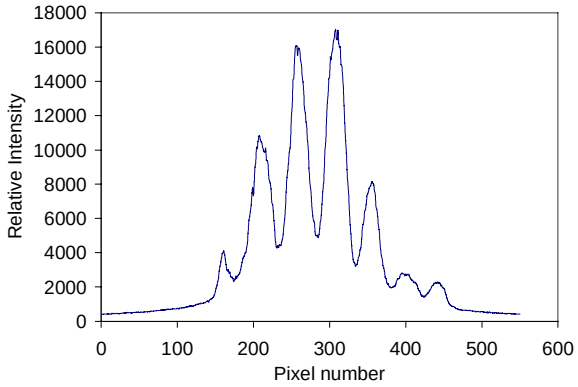

Figure 1. Cross-section of Fabry-Perot Fringes produced by illumination of PMMA slab with He Ne laser.

Optical path length changes at a selection of UV wavelengths were measured using a 3 mm thick PMMA slab as a Fabry Perot etalon. When the UV irradiated area was illuminated with a green He-Ne laser at 548 nm, shifts in reflected interference fringes (Figures 1,2) were observed using a CCD camera, indicating changes in sample thickness, refractive index and penetration depth in agreement with other researchers [6,7)]. The Fabry-Perot method was simple to set up and repeatable, and was used to measure small changes in optical path length in the sample as a function of laser power, fluence, repetition rate and total accumulated energy or number of pulses. Temporary path length changes due to thermal expansion and contraction could be distinguished from permanent changes resulting from photochemical effects. Fringe distortion and reduction in visibility was used to identify the ablation threshold, confirming those in the literature, and enabling the onset of ablation for wavelengths to be identified for those wavelengths not reviewed in the literature. This enabled the laser fluence to be kept below the ablation threshold for new wavelengths.

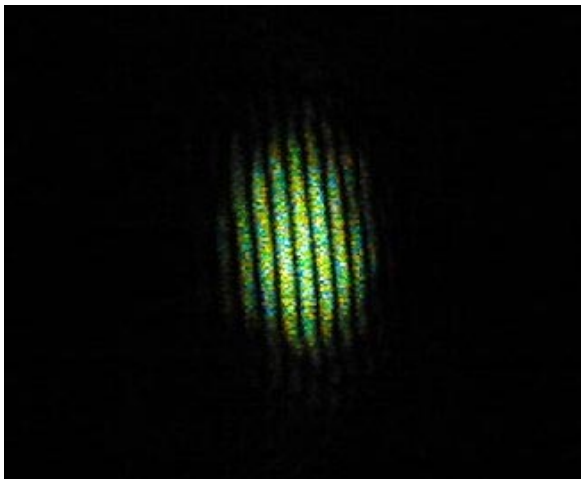

Figure 2. Photograph of fringe pattern obtained by reflected interference of green He Ne laser from 3 mm thick slab.

Other interferometric methods of measuring refractive index, such as the Michelson Interferometer were investigated and found to be unsuitable, being too unstable to measure small fringe shifts (2 or less) in PMMA slabs, as it was affected by air currents and building vibrations.

Experiments at the YAG wavelengths and 308 nm as well as tunable dye wavelengths were performed. 351, 363, 308, 266, 240, 237.5, 230, 220, and 216 nm were investigated. Some of these wavelengths had been reported in the literature for ablation of PMMA, but not for refractive index changes except for 216 nm [7]. Hence a database was built up of the effect of different wavelengths and output powers of various laser wavelengths. The UV and IR spectra of the PMMA slabs were measured to confirm chemical changes.

248 nm and 216 nm were identified as giving the greatest permanent fringe shifts. 248 nm gave an overall permanent fringe shift of 3 at a fluence of 26 mJ/cm^2, for 1847 pulses at a repetition rate of 5 pulses per second. 216 nm gave a fringe shift of 5 fringes at a fluence of 1 mJ/cm^2 at a repetition rate of 10 Hz for 50, 000 pulses (Figure 3). The fringe shift, Δm, was used to calculate possible changes in refractive index, n_1, and penetration depth, t_1, for the PMMA slabs, using $\Delta m = 2 (n_1 - n) t_1/\lambda$, where n is 1.488. If the refractive index change reported by Baker and Dyer, [6] in thin films (2 µm thick) of PMMA, at 248 nm (1.488 to 1.492 or 0.5%) at similar rep rate and fluence had been achieved in our samples, then the penetration depth would be 81 µm. Frank [8] reports a penetration depth of 4 to 10 µm giving respective refractive index changes of 1.488 to 1.6916 (14%) and 1.488 to 1.568 (5%). Samples of PMMA irradiated at 216 and 242 nm showed changes in their UV and visible absorption spectra, indicating that photochemical changes had taken place.

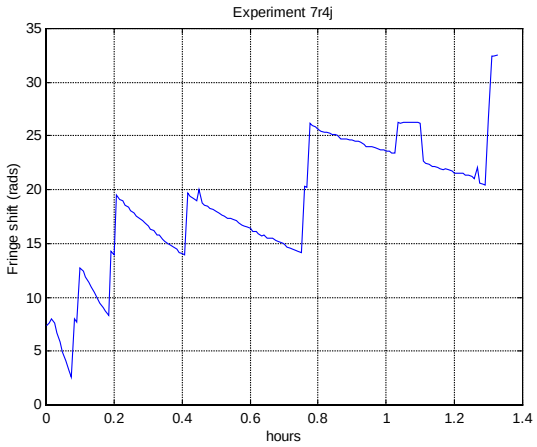

Figure 3. The shift of the interference fringe as the PMMA slab was irradiated at 216 nm. Fluence 1mJ/cm^2.

Grating Formation in PMMA

Periodic refractive index changes in slabs of PMMA were generated, using a phase mask of period 575 nm to produce UV laser interference fringes at the optimum wavelength of 216 nm. The maximum intensity of the interference pattern was carefully controlled to generate maximum refractive index change without causing ablation or thermal effects. The presence of the grating in the PMMA slab was detected by observation of diffraction maxima, formed by illumination of the slab with a low power He-Ne laser, and by observation of diffractive rainbow effects when illuminated by intense white light.

UV Irradiation of PMMA Optical Fibres

The Fabry Perot PMMA slab method was applied to 3 mm long portions of PMMA fibres with core diameter 0.98 mm and cladding thickness of 20 µm, by inserting the sections in holes drilled in a PMMA slab, or metal slab and polishing to achieve a highly reflective finish. This treatment enabled the fibre segments to be illuminated using the He-Ne laser, so that reflective interference took place and fringe shift could be observed during UV irradiation, in order to show that similar refractive index changes can be achieved in fibre samples as in bulk PMMA slabs.

The fluence and exposure times that gave the largest refractive index shift in PMMA slabs at 216 nm were identified and used to irradiate the sides of POF optical fibres which had either their claddings chemically removed or their cores chemically tapered [9] (Figure 4).

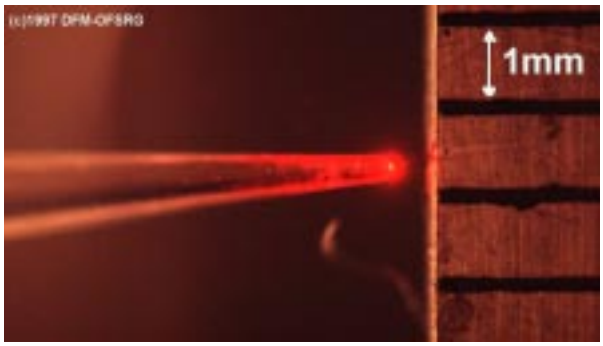

Figure 4. Photograph of 1mm diameter POF tapered using chemicals.

The change in refractive index caused a change in the the far field modal distribution, which could be measured using a goniometer before and after irradiation, or an on-line CCD camera arrangement during irradiation. It was necessary to carefully control the UV irradiation because ablation, melting or thermal changes in the fibre would also cause modal changes. In order to enhance the observation of modal changes, the outer-most modes of the POF were excited by coupling parallel light from a He-Ne laser into the fibre using a microscope objective, but setting it off-axis so that the far field distribution from the outer modes formed a circular annulus with dark centre, projected onto a paper screen [10]. The far field modal distribution was observed as a function of UV irradiation exposure time, using a CCD camera. A cross-section profile of the image was taken at various times during irradiation, and a one dimensional non-causal filter was applied using MATLAB (Figure 5).

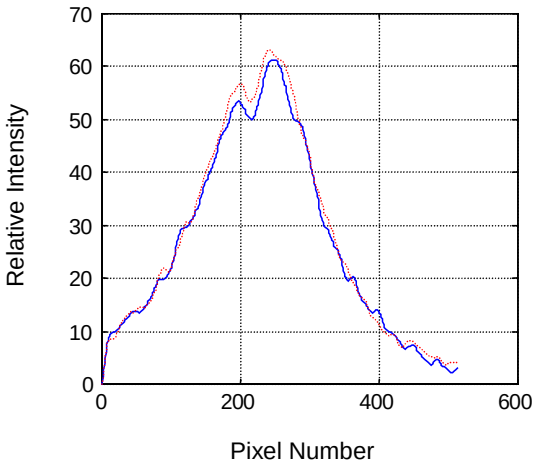

Figure 5. Plot of cross-sectional profile of far field modal distribution of POF taper before and after UV irradiation on the side of the taper at 216 nm; 1 mJ/cm^2 for about 50,000 pulses, 10 Hz (..... initial intensity, _____ final intensity).

The use of tapered POF fibres enabled refractive index changes to be written in reduced diameter POF, at the waists and tips. Since the fibre can be tapered down to 0.1 mm or 100 μm, the refractive index change can be induced across the entire fibre core. This procedure tackles the problem of asymmetrically writing refractive index changes into large diameter POF by reducing the effective numerical aperture and thus the number of modes involved in interaction with the photo-induced perturbation.

Conclusions, Discussion and Further Work

The photo-induction of refractive index changes in PMMA using UV laser light at 216 and 248 nm has been demonstrated, and optimised in terms of fluence and exposure time. Periodic refractive index changes were induced in PMMA slabs, and the effects of photo-induced refractive index changes on the far field modal distribution of POF tapers were measured. The next step in the investigation is to photo-induce a periodic refractive index change into the core of a reduced diameter POF, and to photo-induce graded refractive index profiles in the cores of POF tapers and declad fibres.

Gratings in POF tapers will be measured by observation of the spectral transmission of the taper using an optical spectrum analyser, and by observation of the redistribution of transmitted modes, using a CCD camera or by measurement of the numerical aperture. Such devices will have applications as mode strippers, redistributors and couplers, and sensors for measuring strain. Fibre-end gratings have applications in wavelength division multiplexing and de-multiplexing, as well as wavelength modulated fibre sensors. Fibre cladding gratings have applications in fibre couplers and mode redistributors. Photo-induced graded refractive index changes in POF are of interest as an alternative method for manufacture of graded index POF.

Acknowledgements

The support of the Engineering and Physical Sciences Research Council is acknowledged. (GR/M48031), as well as Corning (Formerly BICC) Corning Cable Systems RD&E for the loan of a phase mask, and staff at CLRC Rutherford Appleton Laboratory, Lasers *for* Science Facility for use of their Nanosecond Laser Laboratory and EPSRC Laser Loan Pool. Thanks are due to Ian Clark, Mike Towrie, Tony Parker and Stan Botchway of CLRC, as well as Rekha Chandy, Piers Eldridge, Vasilis Alexiou and Jim MacTavish of Liverpool John Moores University.

References

1. Polishuk P. (1998). FibreSystems March 1998 17-21.
2. Kalish D. & Clayton J.B. (1997). POF Conference ’97. Kauai, Hawaii. Sept 22-25. 1997.
3. Wanser K.H., Voss K.F (1994). Tenth International Conference on Optical Fibre Sensors. Conference Proceedings. B. Culshaw, J.D.C.Jones, Editors, Proc SPIE 2360, 265-268.
4. Peng et al (1999). Optical Fiber Technology 5, 242-251.
5. Schmitt N.F. (1999) UV photo-induced grating structures on polymer optical fibres. PhD Thesis. Liverpool John Moores University .
6. Baker A.K. and Dyer P.E. (1993). Appl. Phys. A57, 543-544.
7. Bityurin N. et al (1997). Applied Surface Science 109/(1997), 270-274.
8. Frank W.B (1998). Passive components in plastic materials using surface modification by ionizing radiation. 7th International Plastic Fibres Conference ’98. Berlin, Oct 5-8.
9. Merchant D.F., Scully P.J., Schmitt N.F. (1999), Sensors & Actuators, 76, 365-371.
10. Radhakrishnan & El-Sherif (1996). Optical Fibre Technology 2, 114-126.

High Resolution Patterning by the UV Irradiation of Organometallic Films

J A Cairns, M R Davidson, G J Berry, Y C Fan

Department of Electronic Engineering and Physics, University of Dundee, Dundee, DD1 4HN, UK

J Thomson, A Fzea, A Johnson, J Lobban, P McGivern

Department of Chemistry, University of Dundee, Dundee, DD1 4HN, UK

W Shaikh, G J Hirst, M Towrie, I P Clark

Central Laser Facility, CLRC Rutherford Appleton Laboratory, Chilton, Didcot, Oxon, OX11 0QX, UK.

Main contact email address: *j.a.cairns@dundee.ac.uk*

Introduction

The ability to generate high-resolution metal patterns has many applications, not least in the microelectronics industry. The technology currently used in the production of high-resolution metal patterns involves many complex lithographic processes. One such method involves the deposition of a layer of metal followed by a film of resist. The resist is then patterned by optical lithography thus exposing the underlying metal film. The exposed metal areas can then be etched to produce the metal pattern. Finally, the resist is removed. Each of these steps has the potential to introduce errors into the final pattern. A more straightforward approach is to use a direct write method. Here, a material such as a thin film of an organometallic material is irradiated with electrons, ions or photons. To produce a pattern in the organometallic using light two general methods can be adopted. In one method the light beam is focused to a fine spot and rastered across the photosensitive material. Alternatively, the sample is exposed through a mask which consists of the desired pattern.

At the University of Dundee we have been investigating the production of metal patterns by the irradiation of organometallic compounds by deep UV[1, 2].

Experimental

A range of organometallic compounds has been synthesised for this work. These include:

- cis-Dichlorobis(triphenyl-phosphine)platinum(II)
- cis-Dichlorobis(dimethylphenyl-phosphine)platinum(II)
- chlorotriphenyl phosphine gold(I)
- chloro(1,5-cyclooctadiene) platinum(II)

Thin films (~1 μm) were deposited by thermal evaporation *in vacuo* onto silicon wafers. This method of deposition results in films with excellent mechanical properties. The adhesion of films deposited by thermal evaporation is very good in comparison to those deposited by spin-coating, which is thought to be a result of the absence of solvent molecules competing for bonding sites. Thermal evaporation also allows the deposition of films onto fragile and/or non-wettable substrates such as those used in X-ray and projection electron lithography.

The organometallic films were exposed through a chromium-on-quartz photomask to ultraviolet radiation from a Lambda Physik 210iF excimer laser. The experimental setup is shown in Figure 1. The laser had an output of up to 150 mJcm^{-2} per pulse at 248 nm (KrF) or 100 mJcm^{-2} per pulse at 193 nm (ArF). The pulse length in both cases was approximately 20 ns and the laser could be pulsed at up to 100 Hz. The beam intensity was controlled by the insertion of appropriate attenuators in the form of thin quartz plates (Hoya), and was measured using a large area photodiode (Gentec ED500) and joulemeter (Sun EM1). An aperture of typically 8 mm in diameter controlled the size of the beam on the sample. Exposures were carried out by opening the shutter, which was controlled electro-mechanically, for the desired length of time. Pulse energies at the film ranged from 10 to 100 mJcm^{-2} per pulse and total exposures ranged from 50 to 3000 mJcm^{-2}. Following exposure the unexposed organometallic was removed by rinsing in acetone. The samples were then analysed by scanning electron microscopy (JEOL JSM T300 and JSM 6310) and X-ray Photoelectron Spectroscopy (VG HB 100 Multilab).

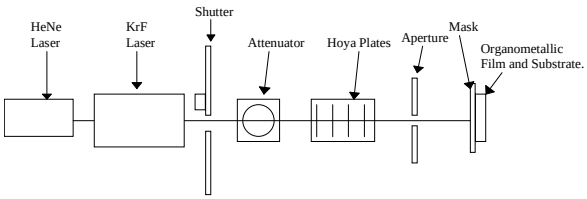

Figure 1. Experimental setup used for UV exposure of organometallic films.

To elucidate the mechanism for UV-induced decomposition, films were irradiated with radiation of various wavelengths ranging from 200 to 350 nm. These experiments were performed at the Nanosecond Laboratory and used the experimental set up shown in Figure 2. The UV was delivered by the dye laser in the form of 15 ns pulses. The radiation induced changes in the films were studied by measuring the change of transmission of a fixed wavelength (365 nm).

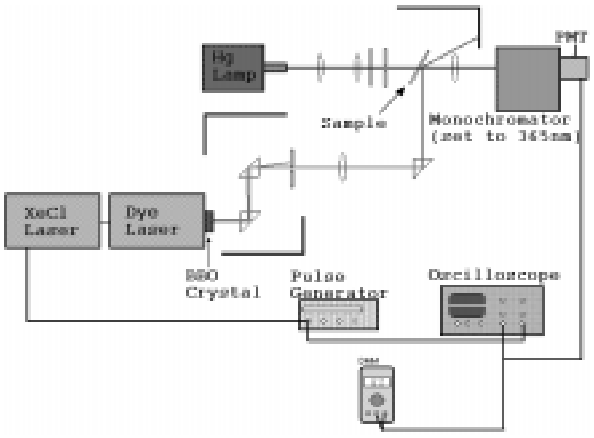

Figure 2. Experimental setup used to monitor transmission changes as a function of irradiation dose.

As shown above, the sample was held at approximately 45 deg with respect to both the laser beam and the interrogation beam. Both beams were incident on the sample at approximately the same position. Films were exposed to various wavelengths of UV including 200 nm, 250 nm, 290 nm, and 343 nm. The choice of these wavelengths was made because the films used absorbed strongly below 310 nm and it would be beneficial to collect data from either side of the absorption edge.

Results and Discussion

A number of samples were produced by irradiating films of cis-Dichlorobis(triphenyl-phosphine)platinum(II) through a chromium-on-quartz photomask which consisted of 2 μm line/spaces. A typical transfer is shown below in Figure 3.

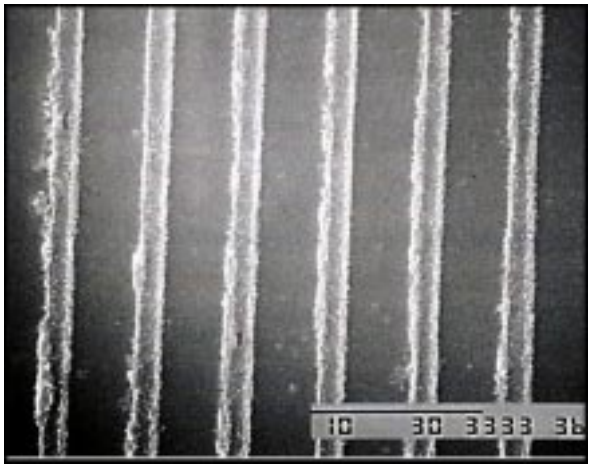

Figure 3. Pattern produced cis-Dichlorobis(triphenyl-phosphine)platinum(II) in by 248nm UV irradiation.

On exposure to UV, the organometallic decomposes which results in a shrinkage of the film. Figure 4, which shows a cross-section of an irradiated film of chlorotriphenylphosphine gold(I), demonstrates this.

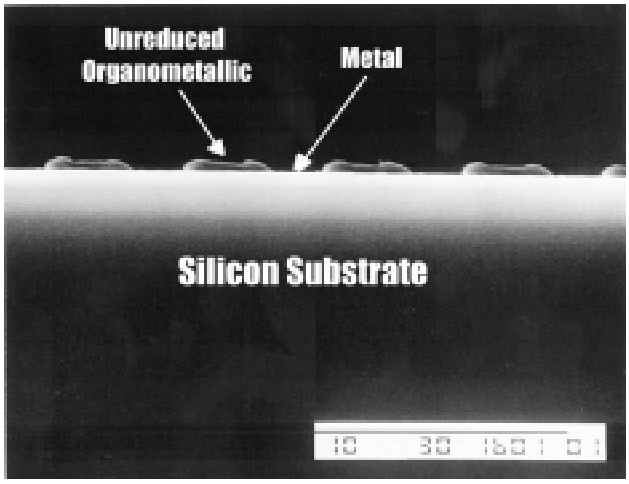

Figure 4. Cross section of irradiated film of chlorotriphenyl phosphine gold(I).

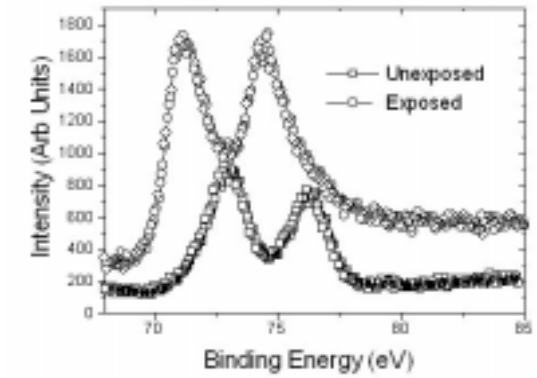

Figure 5. XPS spectra of the Pt 4f peaks before and after exposure of a film of cis-Dichlorobis(triphenyl-phosphine)platinum(II).

Once exposed, any unreduced organometallic can be removed by rinsing the sample in a solvent such as acetone. This removal of unexposed organometallic is very efficient and little residue remains on the substrate. Ultrasonic cleaning of the substrate can also be used with little damage caused to the pattern.

The chemical composition of the UV deposited material was studied by X-ray photoelectron spectroscopy. The samples for this study were prepared by exposing a film of cis-Dichlorobis (triphenyl-phosphine)platinum(II) on a silicon substrate directly to UV. In this case no mask was used. Figure 5 shows the shift in the binding energy of the platinum 4f peaks following exposure to a dose of 32J cm^{-2} of 248 nm radiation.

[Note that the binding energy has been referenced to the carbon 1s peak to take into account shifts due to surface charging]

The position of the Pt $4f_{7/2}$ peak before irradiation is at approximately 72.88 eV. After exposure, the peak shifts to a lower binding energy of 71.28 eV which agrees well with the published value of 71.2 eV for metallic platinum.

Figure 6, below, shows the change in transmission of an organometallic film when irradiated with different wavelengths of UV.

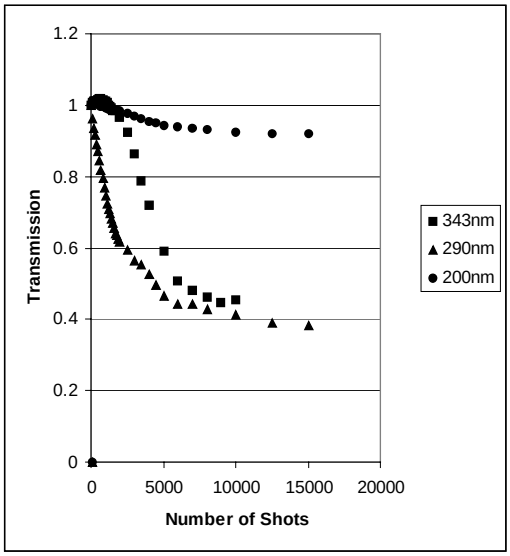

Figure 6. Graph of transmission vs number of shots for an organometallic film exposed to increasing doses of UV at various wavelengths.

The analysis of the results is ongoing but several interesting observations have been made. It can be seen that there is a distinct difference between the changes in transmission at the various wavelengths. At 200 nm, the change in transmission is slight. This may be explained by the fact that 200 nm UV is strongly absorbed by the film. The relatively low drop in transmission could be explained if only the upper surface of the film was decomposed to metal. A more dramatic change in transmission is observed at 290 nm. Here a 60% change in transmission is observed. Exposure of the films with wavelengths above the absorption edge at 310 nm (e.g. 343 nm) produces a different result. In this case there is little change in transmission with exposure until over 2500 shots. It has been shown that the films absorb only very weakly at this wavelength. However the high peak power used may result in the formation of metal particles by processes such as two-photon capture etc. Once produced these metal centres may 'catalyse' the decomposition process and once initiated the transmission would fall as before.

Acknowledgements

This work was funded by an Engineering and Physical Sciences Research Council grant, number GR/M41223. The project was also part funded by the European Community, European Regional Development Fund through the Eastern Scotland Objective 2 Programme, and further financial assistance was provided by Scottish Enterprise and the Scottish Higher

Education Funding Council. The authors would also like to thank Compugraphics International Ltd for the production of photomasks used in this work.

References

1. G.J. Berry, J.A. Cairns, M.R. Davidson, Y.C. Fan, A.G. Fitzgerald, J. Thomson and W. Shaikh, Appl. Surf. Sci., in press.

2. G.J. Berry, J.A. Cairns, M.R. Davidson, Y.C. Fan, A.G. Fitzgerald, A.H. Fzea, J. Lobban, P. McGivern, J. Thomson and W. Shaikh, paper presented at the Spring Meeting of the Materials Research Society, 2000.

Production of crystalline silicon thin films on glass by laser irradiation

S D Summers, H S Reehal

School of Electrical, Electronic & Information Engineering, 103 Borough Rd., South Bank University, London. SE1 0AA, UK.

G J Hirst

Central Laser Facility, CLRC Rutherford Appleton Laboratory, Chilton, Didcot, Oxon, OX11 0QX, UK.

Main contact email address: *summersd@sbu.ac.uk*

Introduction

Amorphous silicon thin films have been used to produce commercial solar cells for two decades. However widespread application of this technology for power generation has not occurred. The material is metastable, and device performance degrades significantly during the lifetime of the solar cell. To overcome this problem the silicon can be crystallised. To do so cost-effectively requires cheap substrates such as glass that require low thermal budget processing during cell production. Excimer lasers have been identified as a tool for crystallising the silicon films without subjecting the entire system, including substrate, to a high thermal budget.

We have shown this approach to be successful in crystallising large areas rapidly[1]. In this report we outline progress in all aspects of the technique, as we apply it, from in-situ material monitoring during irradiation, to the resultant material characterisation.

Thin Film Production

Silicon films have been produced by electron cyclotron resonance plasma enhanced chemical vapour deposition (ECR PECVD) and RF magnetron sputtering. The latter have been useful in determining structural characteristics of hydrogen-free films after KrF excimer laser irradiation but are electrically inactive and so will not be covered in this report. The ECR PECVD films have been found to be electrically useful and the electrical resistivity characteristics of the films change substantially after crystallisation[2].

Hydrogen in films produced by PECVD can be problematic if present in high quantities, this is due to the silanic (Si-H) bond energy of 3.9 eV being less than the photon energy of excimer lasers (the KrF laser operating at 248.6 nm has a photon energy of 5 eV). When the silicon film melts and the silanic bonds are broken explosive hydrogen release occurs, and 'bubble' defects form throughout the film. However the hydrogen can be minimised during film growth if the substrate temperature is at least 300 - 400°C, and/or removed thermally by a temperature treatment above 500°C after film growth. The silanic bond can be broken at these relatively low temperatures due to its reactivity associated with charge transfer along the bond.

Time Resolved Melt Observation

One of the difficulties for research of, and indeed prospective mass production of, crystalline silicon by excimer laser crystallisation (ELC) is an *in situ* knowledge of the melt. This has been achieved in the past by time-resolved reflectivity measurements (TRM)[3]. We have undertaken such measurements on silicon with the substrate heated to ~400°C, and without additional substrate heating. In addition time-resolved electrical resistivity measurements (TERM) have been taken, working on the principle that molten silicon has much lower electrical resistivity than the solid precursor. Both measurements have yielded interesting and useful results.

TRM

The reflectivity measurements were taken using a 588 nm He-Ne laser and photodiode. Reflectivity of solid silicon is in the range of 0.3 to 0.4, for single crystal to amorphous silicon respectively. The actual starting reflectivity of the amorphous/microcrystalline films deposited was not independently measured prior to the measurements. Reflectivity of molten silicon is ~0.7 at 588 nm. The photodiode was light shielded to avoid stray contamination and a filter was used to avoid triggering by the KrF excimer or resultant fluorescence.

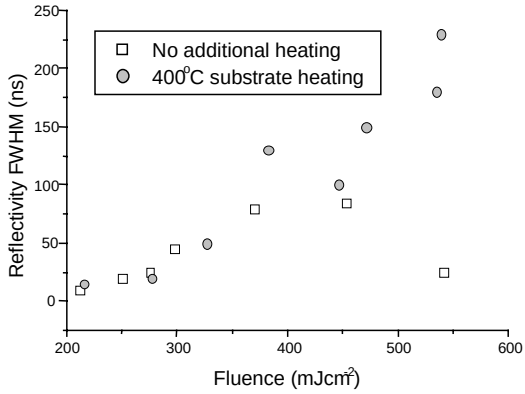

Figure 1. Surface melt duration as measured by TRM as a function of fluence.

Figure 1 shows the reflectivity full-width half-maximum (FWHM) estimated from the CRO traces obtained from the photodiode. The trace maxima were constant and so the FWHM gives a more meaningful insight into the effects of fluence and additional substrate heating on the melt duration. Figure 2 shows a typical reflectivity CRO trace. The output laser pulse length is nominally 30 ns. It is evident that for fluences above ~300 mJcm^{-2} the melt duration becomes longer than the incident pulse duration. Substrate heating acts to enhance melt duration substantially at higher fluences even up to the "damage" threshold found for the unheated film of ~540 mJ cm^{-2}; the damage evident on this sample is probably due to hydrogen release as this sample was not dehydrogenated prior to irradiation. A large drop in reflectivity FWHM is then observed. It is likely that increased melt durations give rise to larger grain sizes; further work is being done to quantify this.

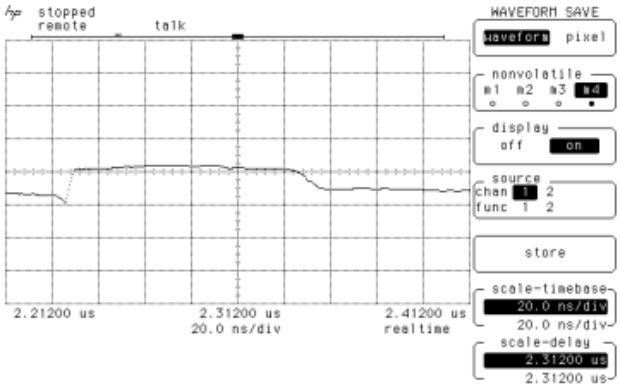

Figure 2. Typical TRM waveform as captured by a fast capture oscilloscope.

Interestingly a drop in reflectivity is usually seen as a small, short-lived dip in the trace prior to the maximum reflectivity plateau. This is a known interference effect that occurs on a short time-scale within the pulse duration. It is associated with

the movement through the film of a narrow melt front driven by the explosive crystallisation of the amorphous material. This explosive crystallisation occurs because the silicon melt is supercooled, i.e. the temperature is above the melting point of amorphous silicon but below that of polycrystalline silicon[4].

TERM

The resistivity measurements were made using a fast capture oscilloscope. Figure 3 shows the voltage traces taken for increasing fluence from 180 to 450 mJ cm^{-2}. The drop in starting voltage (i.e. at time zero) is due to the change in the material from the previous shot(s).

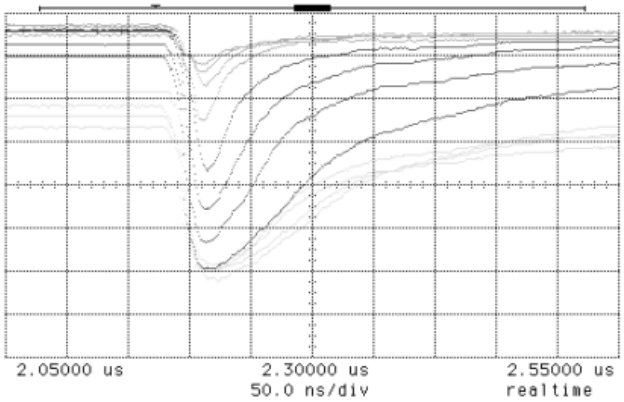

Figure 3. Voltage traces showing the drop in film resistivity as the fluence increases (top trace corresponds to the lowest fluence).

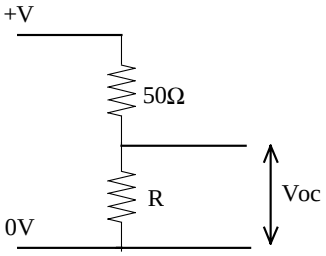

Figure 4. Equivalent circuit of TERM set-up valid for ~400 ns.

Figure 4 shows the equivalent circuit of the TERM set-up where R is the resistance of the silicon during irradiation and Voc is the voltage reading on the oscilloscope. The resistivity measurements were made using a fast capture oscilloscope and a length of d.c.-charged 50 ohm co-axial cable acting as a prompt voltage source. This analysis is valid for ~400 ns after irradiation due to the use of ~ 40 m co-axial cable. The value of R can be found from,

$$R = \frac{50 \times Voc}{(Vi - Voc)}$$

where Vi is the initial steady-state Voltage reading at time zero.

Figure 5 shows the change in the melt resistance at the 'peak', with fluence. If the material melts uniformly then the change of the voltage trace, indicating resistance, could give an indication of melt depth.

At the higher fluences (>375 mJ cm^{-1}) the resistance values appear to level indicating full melt has been achieved.

For these fluences a molten resistivity of 3 – 4 x 10^{-4} Ωcm can be estimated; this is within a factor of two agreement with values for pure silicon in the literature (7.5 x 10^{-5} Ωcm found by Schnyders *et al.*)[5].

At fluences less than 150 $mJcm^{-2}$ a drop in resistance is still seen which may be associated with excited charge carriers.

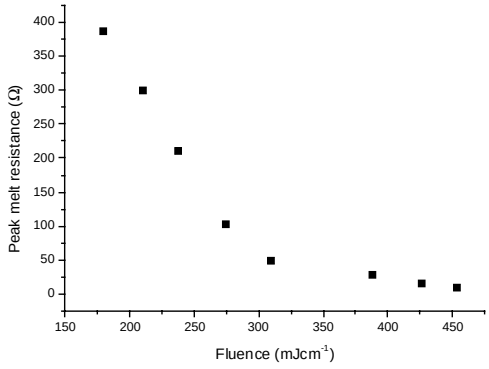

Figure 5. Peak melt resistance as a function of fluence.

Preferential orientation enhancement

After crystallisation the silicon films have been analysed by Raman micro-spectroscopy and X-ray diffraction (X-RD). Both techniques show the change in material from either amorphous or microcrystalline (a partly crystalline and partly amorphous material) to polycrystalline material. X-RD also indicates a randomly oriented polycrystalline material from standard deposited material. However we have found that if the film is deposited as a microcrystalline material with preferred orientation then the laser crystallisation process acts to enhance this preferred orientation (Figure 6).

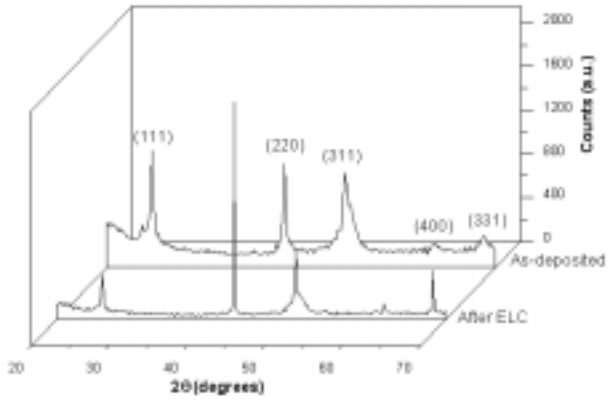

Figure 6. X-RD spectra showing preferred orientation enhancement.

Surface melt features

Above a certain fluence some films take an iridescent appearance to the eye. Figure 7 shows optical micrographs of (A) as a deposited film and (B) a film irradiated at 346 $mJcm^{-2}$. The number scales are in microns.

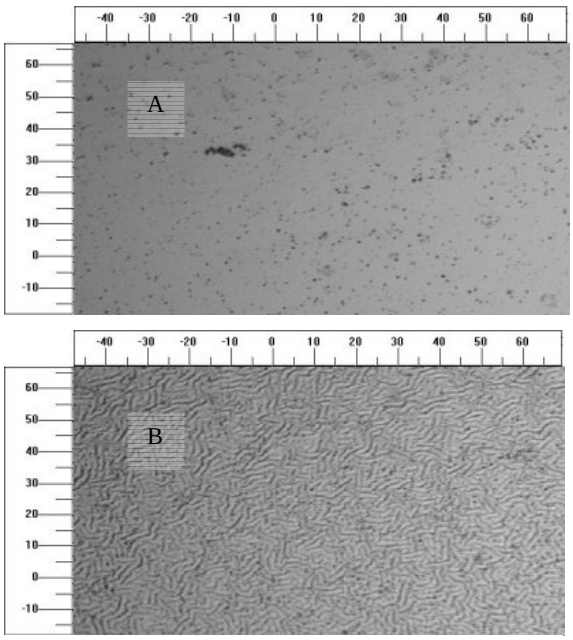

Figure 7. Optical micrographs of film before (A) and after (B) ELC.

It is clear form Figure 7B that a surface pattern has been formed. This may be the result of melt fronts interacting and being frozen during the rapid solidification process.

Acknowledgements

This work has been funded by the EPSRC and supported by BP Solarex. We acknowledge the provision of time on DARTS, the UK national synchrotron radiation service at the CLRC Daresbury Laboratory, through funding by the EPSRC.

References

1. S D Summers *et al.*
Accepted for publication in J. Mat. Sci.: Mat. Elec. (2000).

2. S Summers *et al.*
To be published in Proc. of 16th European PVSEC (2000).

3. J Boneberg and P Leiderer
phys. stat. sol. (a) 166 643 (1998).

4. J S Im *et al.*
Appl. Phys. Lett. 63 1969 (1993)

5. H S Schnyders and J B VanZytveld
J. Phys. - Cond. Mat. 8 10875 (1996).

Laser annealing of micro-mirror based thin film electroluminescent devices

D C Koutsogeorgis, W M Cranton, C B Thomas

The Nottingham Trent University, Dept of Electrical and Electronic Engineering, Burton Street, Nottingham, NG1 4BU, UK.

G Hirst, W Shaikh

Central Laser Facility, CLRC Rutherford Appleton Laboratory, Chilton, Didcot, Oxon, OX11 0QX, UK.

Main contact email address: *demosthenes.koutsogeorgis@ntu.ac.uk*

Introduction

Inorganic thin films of ZnS:Mn have dominated the field of thin film electroluminescent devices (TFELs) being the core of alternating current thin film electroluminescent (ACTFEL) devices. Recently, the Displays Research Group at the Nottingham Trent University have developed a micromirror based structure for display devices, forming laterally emitting thin film electroluminescent (LETFEL) devices[1)]. Critical to the fabrication of LETFELs, as for any TFEL device, is an annealing process that is carried out in order to activate the dopant in the phosphor thin film, by effectively incorporating the luminescent dopant ions in the host lattice. This annealing process is conventionally carried out as a post-deposition thermal treatment in vacuum, typically at 500°C for ~1 hour. However previous work[2)] has shown that thermal annealing of electro-luminescent devices also results in a modification of the electron transport properties within the device, limiting the performance. In order to overcome the limitations that thermal annealing introduces, laser annealing has been proposed and after determining the optimum experimental conditions we have successfully produced laser annealed LETFELs with better characteristics than thermal annealed.

Experimental conditions

The LETFEL device, developed by the Displays Research Group at Nottingham Trent University, consists of a ZnS:Mn phosphor layer sandwiched between two Y_2O_3 insulating thin films, grown onto silicon substrates patterned with micro-mirrors (SiO_2). Initially a thin film of SiO_2 is deposited by PECVD onto 4 inch n-type Si wafers. Using photolithographic techniques the SiO_2 layer is dry etched (plasma etched) to form the micro-mirrors, typically 1.5 μm wide at the base and 1.5 μm tall (Figure 1). Then the 'sandwich' structure of two 300 nm Y_2O_3 layers and a 800 nm ZnS:Mn layer are deposited via RF magnetron sputtering. Prior to deposition of the second insulating layer the phosphor thin film is laser annealed. Finally, the top electrode is deposited and is dry etched to form the individual devices. This structure of electroluminescent devices permits surface viewing by reflecting laterally emitted light due to internal waveguiding effects and while allowing resolutions up to 1200 lines per inch.

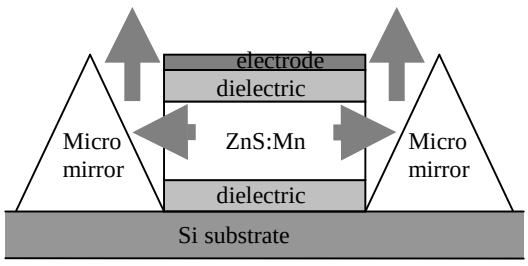

Figure 1. Schematic cross section of Laterally Emitting Thin Film Electroluminescent (LETFEL) device, showing the principle of reflected light emission.

In the past, aluminium has been used as the top electrode but for the present work Ti/W was also investigated. Aluminium, having a melting point (660°C) close to the thermal annealing temperature, has been found to diffuse into the dielectric, leading to EL devices that break down easily. On the other hand, Ti/W has a very high melting point (melting points are Ti:1660°C, W:3410°C)[3)], allowing thermal annealing after completing the fabrication (deposition, masking and plasma etch). Hence, with Ti/W as a top electrode both thermal and laser annealed LETFEL devices can be fabricated from the same wafer for direct comparison.

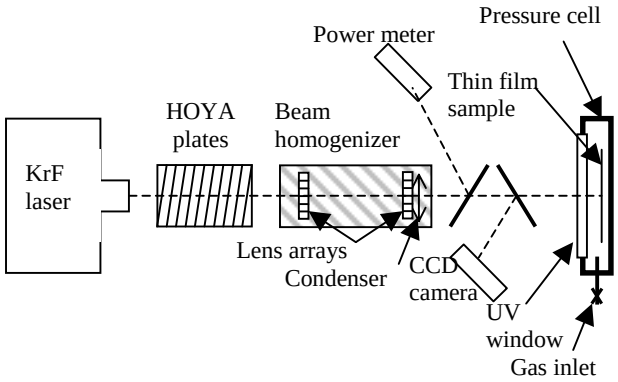

Figure 2. Optical bench for laser annealing with KrF laser.

For the purposes of laser annealing the experimental system illustrated in Figure 2 was used. The KrF laser (LAMBDA Physik) in the X-ray lab (LSF in RAL) delivers 248 nm pulses of 20 ns duration. A variable number of Hoya plates (fused silica plates) are used to attenuate the beam. This results in the ability to provide different values of fluence. An excimer laser beam homogenizer (Exitech ltd., type EX-HS-700D) was used providing 80% deliverability and uniformity better than 2% throughout the laser spot. In this manner a spot size of 5 x 5 mm is obtained with any fluence up to 1.5 Joules/cm^2. Two additional Hoya plates are introduced after the beam homogenizer to reflect a small portion of the beam to the on-line diagnostics: a photo-thermal converter (GENTEC ED-200) for monitoring the energy of each pulse and a CCD camera for monitoring the quality (uniformity) of the laser spot.

In order to have high performance laser annealing, ablation must be limited by housing the sample in a stainless steel pressure cell allowing high pressurized environments (150 psi) of an inert gas (Ar). For accurate positioning of the sample the cell is mounted on an X-Z translation stage, with motions driven by two stepper motors controlled by a computer.

Finally the LETFEL devices are tested in terms of electroluminescence, by measuring the luminance vs voltage characteristics. Measurements are performed on a probe station located in a dark enclosure and while driven by a sinusoidal wave the luminance is measured by coupling the emitted light to a photomultiplier tube via an optical fibre positioned 1 cm above the test device.

Results and discussion

In Figure 3 the characteristic luminance vs voltage curves are shown, with the drive voltage at 5 Khz. For the laser annealed devices an increase of electroluminescence with increasing fluence of the laser annealing pulse is observed. With incident fluences >1 J/cm^2, the laser annealed devices exhibit luminances in excess of that produced by the thermal annealed devices. Furthermore, the laser annealed devices can be driven at higher voltages than the thermal annealed without breaking

down. Also the voltage threshold is found to decrease with increasing fluence of the annealing pulse. The lower threshold voltage for laser annealed devices could be attributed to some surface ablation. At the same time the laser annealed devices were found to be more stable than the thermally annealed. This technique is thus of interest both in terms of increasing luminance and device reliability.

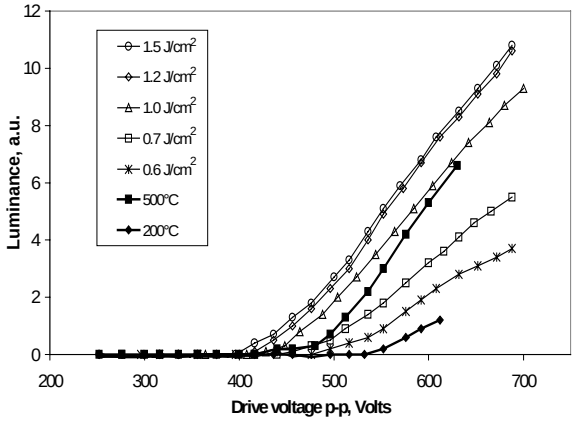

Figure 3. Characteristic luminance vs voltage curves of LETFEL devices with different annealing conditions.

In the past thermal annealing of ZnS:Mn thin film has been investigated. In Figure 4 the results of thermal annealing are shown in terms of photoluminescence and electroluminescence, normalised to the as-deposited films. These as deposited samples are considered to be thermally annealed at 200°C because of being grown at this temperature. The thermal annealing took place, as a post deposition process, in vacuum for an hour at 400°C, 500°C, 600°C and 700°C. It is clear that higher temperatures of annealing improve the photoluminescence, whereas the electroluminescence is not significantly enhanced above 500°C. This behaviour was investigated and finally the saturation in electroluminescence improvement with increasing the annealing temperature was found to be a result of the inevitable annealing of the interfaces between the phosphor thin film with the insulators. Although the phosphor itself has been improved, as the photoluminescence indicates, the overall performance of electroluminescent devices is limited due to the destruction of the interface states that act as donors of hot electrons.

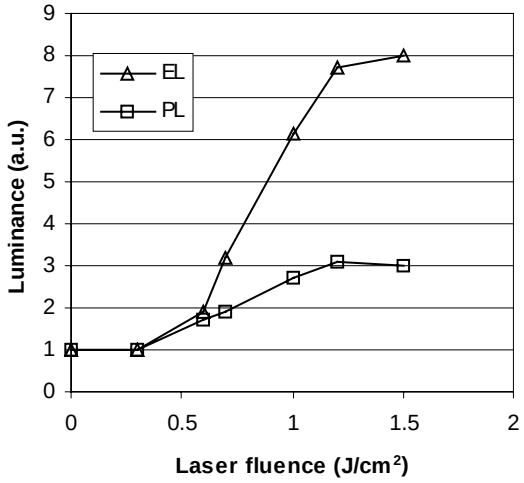

Figure 4. Photoluminescence and electroluminescence improvement with increasing temperature of thermal annealing.

After more than three years investigation of laser annealing, in the LSF and funded by EPSRC, we are now able to perform the same evaluation for laser annealing. In Figure 5 the photoluminescence and electroluminescence of laser annealed films are shown. Both PL and EL start being enhanced above a threshold fluence of 0.3 J/cm^2, after which the higher the fluence the better the improvement. Above ~1.2 J/cm^2 the enhancement saturates for *both* PL and EL, indicating that laser annealing does not introduce any side effects like thermal annealing.

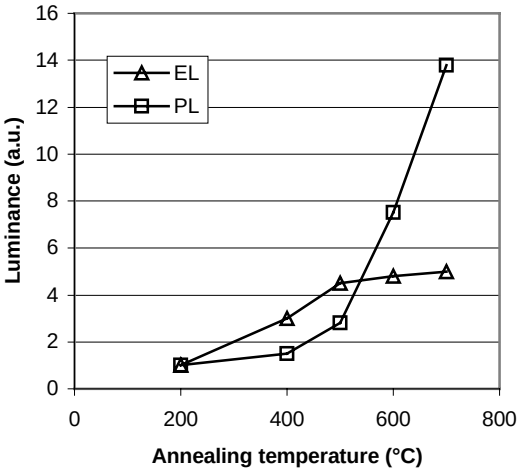

Figure 5. Photoluminescence and electroluminescence improvement with increasing the fluence of the laser pulse.

The above graphs (Figures 4 and 5) show that with a laser pulse of adequate fluence highly localised annealing can be achieved, where only the phosphor film is annealed and not the insulators or the interfaces between them. Laser annealing of phosphor thin films for electroluminescent devices is proven to be viable, with comparable or better characteristics than thermal annealed devices.

References

1. C B Thomas, W M Cranton, R Stevens
SID International Symposium 96 Digest, 1996.

2. W M Cranton, R Stevens, C B Thomas, A H Abdullah, M R Craven, Proc. IEE Colloquium on Materials for Displays, 1995.

3. D R Lide (ed) in: CRC Handbook of Chemistry and Physics, 71st edition, pp.4-35, 1990-1991.

Source Modification for Imaging X-ray Fluorescence Spectrometry

G J Price, A N Brunton, A P Martin, G W Fraser

Space Research Centre, Department of Physics and Astronomy, University of Leicester, Leicester LE1 7RH

W Shaikh

Central Laser Facility, CLRC Rutherford Appleton Laboratory, Chilton, Didcot, Oxon, OX11 OQX, UK

Main contact email address: *gwf@star.le.ac.uk*

Introduction

Work carried out on the RAL laser plasma X-ray source in February 1997 proved the concept of an Imaging X-ray Fluorescence Spectrometer (IXRFS) based on microchannel plate (MCP) X-ray "lenses" and large area charge coupled device (CCD) detectors [1)]. Whereas conventional XRF techniques yield chemical compositions averaged over the illuminated sample area, an imaging spectrometer allows the determination of the spatial distribution of low-Z elements in inhomogeneous samples without the need for sample scanning. Further studies in the laboratory at Leicester led to the award, in early 1999, of a major EPSRC Instrument Development grant (GR/M51550) for the construction and characterisation of a prototype IXRFS system for use with either lab X-ray sources or the laser plasma X-ray source.

A key experiment in the EPSRC programme is the localisation of carbon and other low-Z contaminant particles on silicon wafers. For such an experiment, the maximum X-ray energy from the source must be less than the Si K absorption edge energy of 1839 eV, otherwise tailing from the substrate fluorescence peak may swamp the desired signal. The LSF laser plasma source, shooting steel tape in normal operation, does not meet this criterion. Although the bulk of the emission is in a line complex around 1 keV, a significant high energy bremsstrahlung tail extends beyond 2 keV.

We report here on attempts made during our laser plasma source run between July 19th and 30th 1999 to "soften" the Fe source spectrum and eliminate the high energy spectral tail, ideally without loss of ~1 keV flux. The experimental arrangement was as described in Reference 1 with the addition of a gate valve to allow isolation of the end-chamber holding the CCD. The optical blocking filter was 2.0 μm mylar plus 0.8 μm Al. Three methods were used to attempt to cool the plasma :

(i) reduction of laser intensity by the insertion of Hoya plates into the optical path

(ii) blocking a selected number of pulses in the pulse train

(iii) defocusing the laser spot on the target tape. The degree of defocusing was quantified by monitoring the decrease of the signal current in a fixed Si(Li) diode, which actually measures the output X-ray flux, rather than the geometric size of the focal spot.

Three distinct composite fluorescent targets were employed :

(1) Cu, Si on Al substrate. Measurements with this target were made with a 12 Hz laser repetition rate.

(2) Cu, Si, Ni plus multielement target (B,C,N,O,F,Al and Si – MicroAnalysis Consultants, St.Ives) on Mo substrate (20 Hz)

(3) As 2, except Al substrate and 50 Hz.

Since the minimum laser repetition *time* is much longer than the plasma lifetime, the laser repetition rate should not, in principle, affect the results. An Oxygen K peak should be present in all spectra due to the presence of oxide layers in all targets.

Results

Table 1 summarises the experimental configurations for which CCD pulse height spectra were recorded (see Figure 1). CCD images confirmed the basic principles of the imaging spectrometer and will not be discussed further here.

Expt. No	Source Frequency (Hz)	Target	Softening Procedures
1	12	1	None
2	12	1	10 Hoya neutral density plates in laser beam path
3	12	1	Pulse train limited to one pulse
4	12	1	Pulse train limited to two pulses
5	20	2	None
6	20	2	Times 2 defocusing
7	20	2	Times 10 defocusing
8	50	3	Times 10 defocusing
9	50	3	None

Table 1. Summary of spectral softening experiments.

Table 2 summarises the line intensity ratios (uncorrected for filter transmission or CCD quantum efficiency) which indicate the degree of spectral softness for the various experimental configurations. The Cu Lα (0.93 keV) to Si Kα (1.74 keV) ratio is the best measure of the relative intensity of the bremsstrahlung tail. Comparing experiments 1 and 2 with Target No.1 indicates that reduction of laser intensity, while maintaining spot size, has the desired effect in that both the O/Si and Cu/Si line intensity ratios increase when the Hoya filter plates are inserted. Comparing experiments 1 and 4 indicates that limiting the pulse train from eight to two pulses has a marginal effect. Experiments 5-7, however, show that a marked improvement in both ratios is obtained by defocusing the source with Target 2. Confusingly, this marked improvement in spectral softness is not repeated with Target 3 (Experiments 8 and 9), which differs from Target 2 only in respect of the substrate material.

Expt. No.	O/Si	Cu/Si
1	0.42	1.36
2	0.77	2.15
3	-	-
4	0.55	1.48
5	6.5	4.4
6	14.2	7.6
7	23.8	10.3
8	14.7	7.8
9	10.3	6.2

Table 2. Line intensity ratios from O Kα (0.525 keV), Cu Lα (0.93 keV) and Si Kα (1.740 keV) peaks in CCD pulse height spectra. For experiment 3, with only one pulse in the train, the signal-to-noise ratio of the X-ray spectrum was too poor to give meaningful ratios.

Further analysis is resolve this discrepancy. Further experiments are necessary to optimise the laser plasma source operating mode for the IXRFS development programme.

Acknowledgement

APM and GJP acknowledge the receipt of PPARC studentships.

Reference

1. A.P. Martin and ten co-authors, *X-ray Spectrometry* 28, 64-70 (1999).

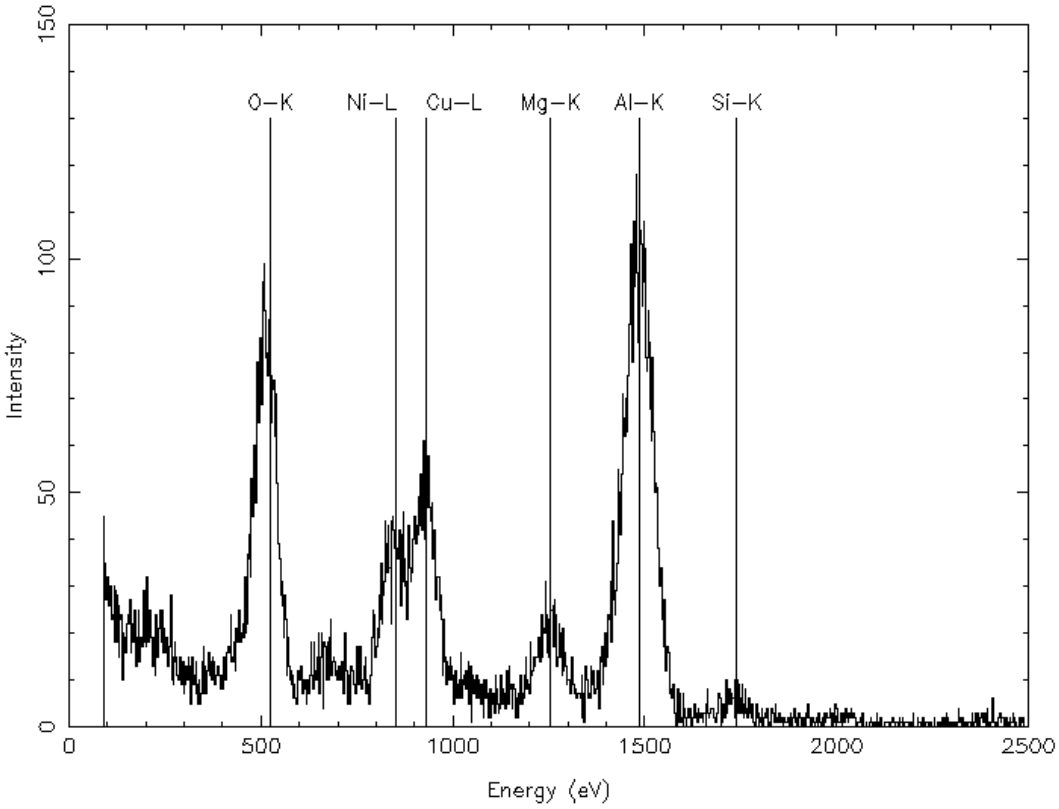

Figure 1. CCD pulse height spectrum for Experiment No. 9. Named fluorescent emission lines indicated by vertical lines.

Bolometric Detection of Monochromatic Acoustic Phonons Generated by Femtosecond Pulse Laser Excitation of a GaAs/AlAs Superlattice

A J Kent, P Hawker, L J Challis

School of Physics and Astronomy, University of Nottingham, University Park, Nottingham NG7 2RD UK

A Bartels, T Dekorsy, H Kurz

Institut für Halbleitertechnik, Sommerfeldstr. 24, 52074 Aachen, Germany

K Köhler

Fraunhofer-Institut für angewandte Festkörperphysik, D-79108 Freiburg, Germany

Main contact email address: *Anthony.Kent@Nottingham.ac.uk*

Abstract

We have used pulse time-of-flight techniques to examine the phonon emission from an optically excited GaAs/AlAs superlattice structure. For laser excitation wavelengths shorter than 767 nm (the energy of the E1-HH1 transition) we detect a significant longitudinal acoustic phonon component directed in a narrow beam normal to the structure. Under identical excitation conditions generation of coherent longitudinal acoustic phonons has previously been observed confined within this structure. We suggest that the excitation wavelength and angular characteristics of the LA emission is consistent with those of propagating modes produced as coherent phonons 'leak' from the superlattice structure.

Introduction

Phonon spectroscopy is a powerful technique for studying defects in materials and the properties of low-dimensional electrons and holes in semiconductors. This is because interactions with phonons are normally much stronger than with photons and also phonons can probe directly excitations at finite wave vector. However, in the past, applications of the technique have been limited by the lack of availability of pulsed sources of monochromatic, coherent phonons with frequencies of a few hundred GHz for use in experiments. Most work has had to be done using broadband (Planckian) phonon sources and energy detectors (bolometers) which do not obtain detailed spectroscopic information. A method of producing monochromatic phonon beams of usable intensity would revolutionize phonon spectroscopy. Such beams when used in conjunction with recently developed wafer bonding and nanometre scale fabrication techniques open the way for a new field of "phonon optics".

In recent years a number of experiments have been reported in which coherent phonons have been generated in semiconductor structures using ultrafast laser pulses. In the first experiments [1)] coherent optical phonons were generated. However, more recently, coherent THz acoustic phonons have been generated by ultrafast excitation of electrons and holes in GaAs/AlGaAs quantum wells [2)] and superlattices [3,4)] and detected by surface deflection [2)] and time-resolved reflectivity [3,4)].

It has been shown that coherent zone-folded longitudinal acoustic phonons are excited when a femtosecond laser pulse is shone onto a superlattice (SL) [3,4)].The excitation process has been attributed to impulsively stimulated Raman scattering in which the formation of an electron-hole pair is accompanied by the creation of a longitudinal acoustic (LA) phonon. The acoustic mini-band structure of the SL permits the creation of relatively high frequency phonons of low q with the principal feature being a triplet of phonon modes centered around $q \approx 0$ with side-bands at $q \approx 2k_{laser}$ produced by back-scattering. The central frequency corresponds to the unfolded zone boundary at $q = 2\pi/d_{SL}$ where d_{SL} is the period of the SL, leading to $\omega \approx 2\pi v/d_{SL}$ where v is the velocity of the LA phonons and hence $\nu = v/d_{SL}$ which is typically around 500 GHz for the structures used. A triplet of modes centered on twice this frequency corresponding to the unfolded zone boundary at $q = 4\pi/d_{SL}$ is also observed but with an intensity more than 10 times weaker.

The presence of the phonons confined in the SL has been observed by studying the reflection of a probe pulse from the sample surface following the excitation pulse [3,4)]. The reflected signal amplitude oscillates at a few hundred GHz which is attributed to modulation of the refractive index by the lattice vibrations. The modulation amplitude decays in a few ns and it seems likely that this is the result of the confined modes leaking into propagating monochromatic phonons. This process has been observed in optical 2-color pump-probe experiments but only over small distances (500 nm) [5)] and not in phonon spectroscopy using incoherent detection schemes. In this work our aim has been to observe these propagating phonons as they reach the surface of the GaAs wafer opposite the SL using bolometric detection and pulsed time-of-flight measurements. We also aimed to assess the suitability of the optically excited SL as a source for phonon spectroscopy applications.

Experiment

The sample was fabricated from a GaAs/AlAs superlattice consisting of 40 periods each comprising 22 monolayers (ML) of GaAs with 4 ML of AlAs, grown by MBE on a 500μm (100) semi insulating GaAs substrate. On the opposite surface to the superlattice was fabricated a 10 x 10 μm^2 thin film superconducting aluminium bolometer to detect the emitted phonons. The sample was mounted in an optical access liquid helium cryostat and maintained at a constant temperature on the bolometer's superconducting transition (~2.4 K). Phonons incident on the bolometer raised its temperature slightly causing a small increase in its resistance. With a small bias current flowing, this gave a transient voltage signal that could be averaged to produce a phonon time-of-flight signal.

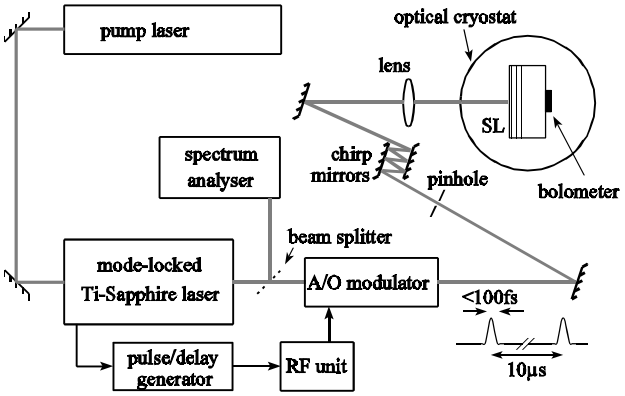

Figure 1. Optical arrangement, see text for a description.

The superlattice was excited with femtosecond pulses from a tunable Ti:sapphire laser. Figure 1 shows the optical arrangement. The repetition rate of the mode-locked laser was

about 82 MHz (one pulse every 12 ns). For reasonable temporal resolution in the phonon time-of-flight measurements, the time interval between pulses should be much longer than the phonon flight time to the bolometer (about 100 ns). It was necessary therefore to use an external acoustic-optic modulator to isolate individual pulses from the laser.

Dispersion of the laser pulses due to propagation through the modulator, lens and cryostat windows was corrected by chirp mirrors. A f = 100 mm lens was used to focus the laser to a spot on the sample of approximately 50 μm diameter. Using an adjustable mirror, the laser excitation spot could be moved over the surface of the sample to investigate the angular distribution of the emitted phonons.

Results and discussion

Figure 2 shows the results of surface reflectance measurements (made at RWTH Aachen) of the SL after femtosecond pulse excitation at λ = 767 nm corresponding to the E1-HH1 transition. The refractive index is modulated at 600 GHz by the coherent LA phonons. The amplitude modulation of the signal is due to beating between the phonon modes generated by forward ($q \approx 0$) and back ($q \approx 2k_{laser}$) scattering of the laser beam.

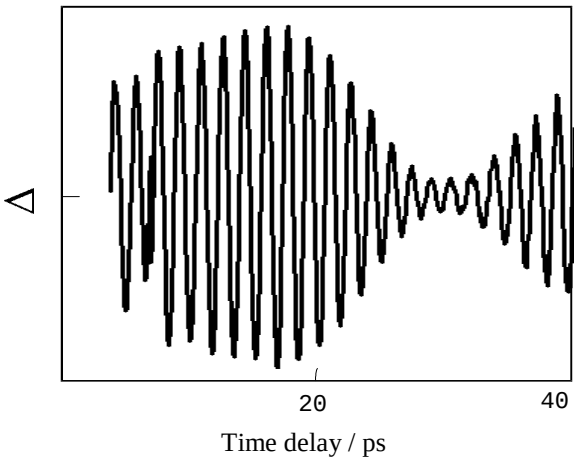

Figure 2. Surface reflectance measurements of the SL used in this experiment.

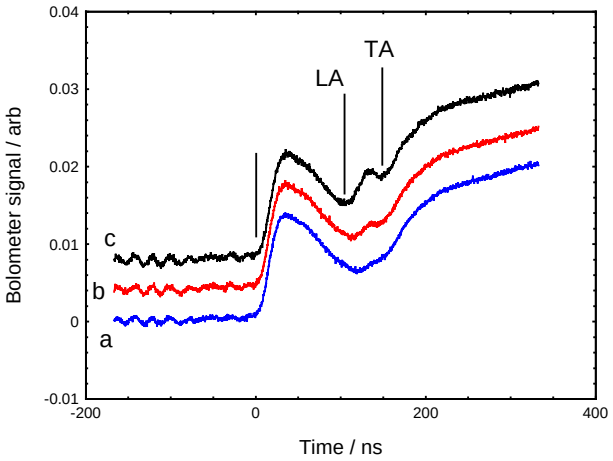

Figure 3. Time resolved signals. The start of the rise of the LA and TA phonons signals correspond to the ballistic arrival times (marked).

Figure 3 shows a number of phonon time-of-flight traces taken at various excitation wavelengths with the laser spot directly opposite the bolometer. At time zero the excitation pulse hits the sample producing electrons and holes in the superlattice and surrounding GaAs substrate/capping layer material. A large peak is observed coincident with the laser pulse which changes little with laser wavelength. We attribute this to direct optical excitation of the bolometer. This instantaneous signal had maximum intensity when the excitation spot was directly opposite the bolometer and so we attribute it to sub-GaAs band gap luminescence, probably arising from defects. Relaxation of the free carrier density occurs with a time constant of some 100 ps accompanied by emission of incoherent phonons, normally observed as carriers relax to the band edges, and generation of coherent longitudinal acoustic (LA) modes. A short time later the emitted phonons arrive at the bolometer and are detected. The expected ballistic LA and transverse acoustic (TA) phonon arrival times are marked.

For laser wavelengths, λ, longer than 767 nm excitation is in the GaAs substrate only (the bandgap of GaAs at liquid helium temperatures corresponds to an excitation wavelength of 816 nm). We observe negligible LA emission but a strong TA mode signal rising to a delayed peak at about 0.5 μs. This is followed by a long slowly tail. The signal is consistent with previous measurements [6] in bulk GaAs and is indicative of strong LO phonon emission in the substrate. Highly excited carriers relax by emitting a cascade of LO phonons before reaching the GaAs band edge, recombining with holes and emitting a band-gap photon. The LO phonons decay rapidly via a series of steps to high frequency TA modes (ν ~ 1.5 THz). Strong isotope scattering within the substrate then gives rise to some diffusive propagation and the observed long time tail to the signal.

For excitation at wavelengths below 767 nm (carriers now excited in the superlattice as well as the substrate), we observe in addition, the appearance of a sharp LA mode peak. Using a trace taken at a wavelength much longer than 767 nm as a reference we can subtract off the signals due to direct optical excitation of the bolometer and the phonons generated by relaxation in the GaAs substrate to reveal the SL phonon signals more clearly, Figure 4. At λ = 767 nm the LA mode signal turns-on. At shorter wavelengths the carriers are generated with a larger excess energy in the SL and so the TA and "tail" signals increase while the LA signal saturates.

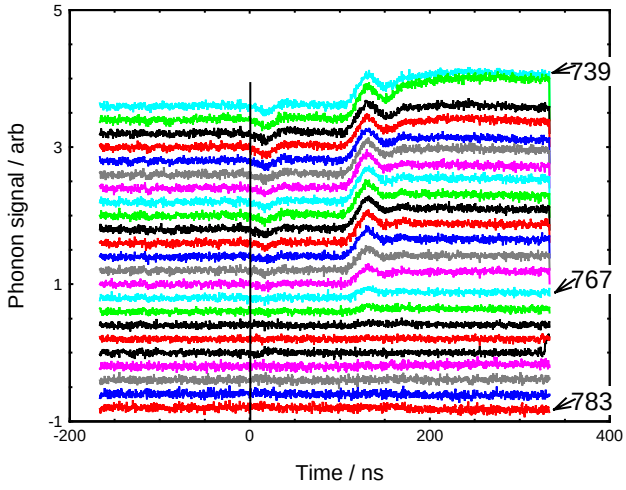

Figure 4. Time resolved traces after subtraction of luminescence contribution.

The rapid increase of the LA mode emission as carriers become excited in the superlattice is shown more vividly in Figure 5, where we plot the integrated LA mode intensity versus λ at constant excitation power. Negligible LA emission occurs for λ > 767 nm. LA emission increases rapidly as carriers become excited in the superlattice (λ = 767 nm) and then the emission

intensity remains approximately constant as λ decreases further. The weak structure present in the region λ < 767 nm was reproducible and we note that the peak at λ = 750 nm is separated from the ground state superlattice resonance (E1-HH1) by 36 meV, or the energy of a bulk GaAs LO phonon. We have no definitive explanation but suggest that it may be associated with a resonant absorption process; carrier excitation in the well accompanied by emission of a GaAs LO phonon. Such a process would increase the capture cross-section for carrier generation resulting in an increased detected signal.

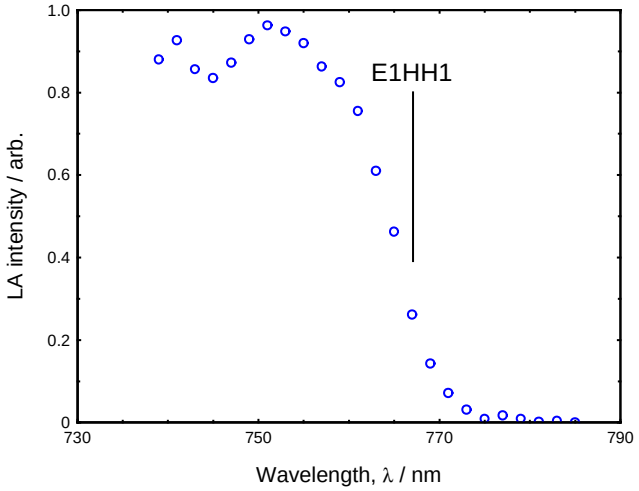

Figure 5. Integrated LA signal as a function of excitation wavelength.

Figure 6 shows the angular dependence of the LA mode signal at λ = 760 nm. The emission is strongly peaked normal to the plane of the superlattice. This angular dependence cannot be due to phonon focussing which arises due to the acoustic anisotropy of GaAs. Focussing of the LA mode is weak and gives a slight enhancement of the LA signal at θ ≈ 45°.

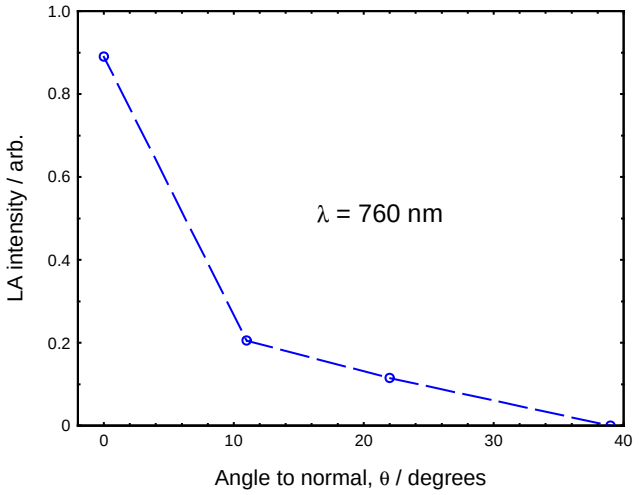

Figure 6. Angle dependence of the LA emission from the SL, θ = 0 corresponds to the laser being directly opposite the bolometer.

One possibility that has to be considered is that the observed LA emission is due to relaxation of hot electrons and holes confined in the quantum wells (QWs). In this case the emitted phonons have to have a thermal distribution up to a cut-off frequency determined by energy and momentum conservation rules. Such emission is expected to be directed close to the normal to the quantum wells due to in-plane ($2k_F$) momentum conservation and momentum non-conservation perpendicular to the wells. However, we have measured the phonon emission from a 5 nm-wide GaAs quantum well (similar to the well width in the SL sample) and found that the emitted LA intensity falls to half of its maximum at θ ~ 30°. The width of the emitted phonon beam in Figure 6 is much less than this. We suggest the observed angular distribution of LA emission from the SL is consistent with that from a coherent source with a lateral extent large on the scale of the phonon wavelength (~ 8 nm at 600 GHz). For such a source diffraction effects would be insignificant, and the phonons would be emitted in a narrow beam normal to the source plane. Assuming that in our case the source size equals the diameter of the focussed laser spot (~ 50 μm) then a very narrow beam of emission would be expected (angular divergence = 0.2 radians). We suggest therefore that the observed LA signal present for excitation wavelengths below 767 nm is due to the propagating component produced as coherently generated phonons 'leak' from the superlattice structure.

Conclusions

We have detected the LA phonons emitted by an optically excited GaAs/AlAs superlattice using a superconducting bolometer on the opposite face of the substrate. The laser wavelength and angular dependence of the emitted phonons have been studied and the observations are consistent with the signal being due to coherent LA phonons excited in the superlattice leaking into propagating modes.

Further experiments are planned to examine the LA emission in greater detail using a detector with spectral discrimination. Using such a detector it should be possible to unambiguously confirm that the frequency of the detected propagating phonons is the same as that of the coherent modes generated in the previous optical studies.

We would like to thank the School of Physics and Astronomy, University of Nottingham for financing the visit of A Bartels to Nottingham and additional financial support of the project. We also thank to Miss R Bellingham for assisting with the data taking.

References

1. W.E. Bron, J. Kuhl and B.K. Rhee, Phys. Rev. B34, 6961 (1986); G.C. Cho, W. Kütt and H. Kurz, Phys. Rev. Lett. 65, 764 (1990); also see for an overview T. Dekorsy, G.C. Cho and H. Kurz, in *Light Scattering in Solids VIII*, edited by M. Cardona and G. Güntherodt, (Springer, Berlin, 2000), and references therein.
2. J.J. Baumberg, D.A. Williams and K.Kohler, Phys. Rev. Lett 78, 3358 (1997).
3. A. Yamamoto, T. Mishina and Y. Masumoto, Phys. Rev. Lett. 73, 740 (1994).
4. A. Bartels,T. Dekorsy, H. Kurz and K. Kohler, Phys. Rev. Letts. 82, 1044 (1999).
5. K. Mizoguchi, M. Hase and S. Nakashima, Phys. Rev. B. 60, 8262 (1999).
6. R.G. Ulbrich, V. Narayanamurti and M.A. Chin, Phys. Rev. Lett. 45, 1432 (1980).

Acoustic Instability of Fully Pre-mixed Flames

C M Coats, Z Chang, P D Williams

Department of Engineering, University of Leicester, University Road, Leicester LE1 7RH

Main contact email address: *cmc7@le.ac.uk*

Introduction

As a result of the widespread introduction of stringent emissions standards in European countries there is considerable interest in the development of fully premixing burners for use in gas-fired domestic water heaters[1]. Burners which mix the whole of the combustion air with the fuel before combustion commences offer a number of potential advantages over conventional partially premixing designs in terms of reduced emissions of NO_x and CO_2 and increased thermal efficiency, compactness and flexibility. They also possess one very undesirable characteristic, however, viz. their propensity to excite unacceptable vibrations when incorporated within sealed heating systems. This vibration problem is the principal obstacle to the successful utilisation of fully premixing burners in these systems at the present time.

It is known that the vibration problem is caused by the establishment of a resonance between a fluctuation in the rate of the heat release in the premixed flame and one or more of the natural acoustic modes of the burner enclosure and flue. Fluctuations in the rate of heat release are accompanied by movements of the flame front which generate sound, a proportion of which is reflected back towards the burner by the containing enclosure. If the reflected sound has the effect of amplifying a particular flame fluctuation then it closes a positive feedback loop with the amplification of the original fluctuation as the system gain. The oscillation is thus self-amplifying until non-linear effects cancel any further gain and a limit cycle is established which repeats itself indefinitely.

Whilst the general dynamic character of such unstable couplings is well understood, the analysis and prediction of resonant behaviour in any given circumstances remains problematical because little is known about the mechanisms by which the flame responds to the acoustic feedback. A programme of fundamental research has therefore been embarked upon at Leicester in which fully premixed flames, stabilised on practical designs of burner, are to be subjected to simulated acoustic feedback of variable frequency and amplitude. It is hoped that, by imaging the flames at different phases of the incoming sound waves, qualitative and quantitative information will be provided about both the mechanism of the flame response and the resultant system gain. The present article is concerned with the visualisation technique which is to be used in this work and which was developed during the year under review using equipment made available from the Loan Pool under Loan LP15E299.

Experimental details

The flames it is required to visualise in these experiments are laminar fully premixed methane-air flames, typically supplied with a quantity of air which is 20-30% in excess of the stoichiometric requirement. They are to be stabilised on test burners replicating the essential features of practical designs. For the preliminary experiments reported here the burner head was a plaque of refractory ceramic containing a parallel array of closely spaced slots, each approximately 1.25 mm in width. The reactant mixture issued from the slots with a velocity of up to about 3 m/s, each slot supporting a separate flame a few mm in height and shaped, in cross section, like an inverted vee (Figure 1).

The part of the flame it is required to image is the flame front - a region less than 1 mm in thickness in which essentially all of the parent fuel is consumed and the bulk of the heat release takes place. This zone is faintly luminous, being characterised by chemiluminescence from free OH and, to a much lesser extent, from free CH radicals. Because cross-sectional views of the oscillating flame are required, however, the use of a planar laser-induced fluorescence (PLIF) technique is essential for this work.

It is relatively straightforward to induce fluorescence from OH in the UV using either an excimer laser or the frequency-doubled output from a dye laser operating with Rhodamine dye and this method has been employed fairly widely in recent years to visualise both premixed and diffusion flames[2]. Its limitation, so far as the visualisation of premixed flame fronts is concerned, is that the population of ground-state OH radicals declines only slowly in the burned gases downstream of the flame front, resulting in a poorly defined image. The decision was therefore taken to attempt the more difficult task of visualising the flame front by inducing fluorescence from CH, a species which is present in only very small concentrations in lean premixed flames and which does not survive to any appreciable extent in the burned gas. So far as we are aware, PLIF from CH has been used previously only to visualise diffusion flames in which the concentrations of this radical are significantly higher[3-5].

The Loan Pool system made available for this work was NSL-2, comprising a Spectron SL805G Nd:YAG laser pumping a Sirah PrecisionScan dye laser. The system was configured to use the third harmonic of the Nd:YAG to pump Exalite 392A dye in the Sirah, the output being tuned to one of the lines in the *Q* branch of the $B^2\Sigma^- \leftarrow X^2\Pi(0.0)$ absorption band of CH at a wavelength close to 390 nm. Because the available pump energy at 355 nm was limited to a maximum of about 130 mJ per pulse, some initial adjustment of the energy split between the oscillator and amplifier stages of the Sirah was necessary to achieve lasing action in the former. Thereafter, however, good results were achieved with this dye, fresh solutions providing an output in excess of 10 mJ per pulse.

The beam was expanded, apertured and formed into a thin vertical sheet approximately 10 mm in width immediately above the top of the burner. To discriminate against scattered laser light it was important to be able to detect the laser-induced fluorescence at a wavelength different from that used for the excitation. Fortunately there is relatively rapid electronic energy transfer in the flame from the excited $\nu=0$ vibrational level of the *B* state to the $\nu=1$ vibrational level of the *A* state[6]. The transition $A^2\Delta \rightarrow X^2\Pi(1,1)$ then produces fluorescence which can be detected at wavelengths near 430 nm. The fluorescence in this band was collected with an f/2 lens, separated with a narrow band-pass filter and focussed onto a 385 x 578 intensified CCD array. Because of the weakness of the fluorescence at the detection wavelength it was necessary to integrate the fluorescence generated by several hundred identically phased pulses of the laser to produce a clear image of the flame front. The image intensifier was gated off between pulses to reject background emissions at the detection wavelength from the flame and burner.

An unexpected finding, given the relatively low intensity ($< 5 \times 10^5$ W/mm^2) of the laser sheet, was a tendency for the fluorescence to saturate in the waist region. It was therefore advantageous, when imaging these two-dimensional flames, to increase the strength of the fluorescence signal by offsetting the imaged region slightly from the waist of the sheet.

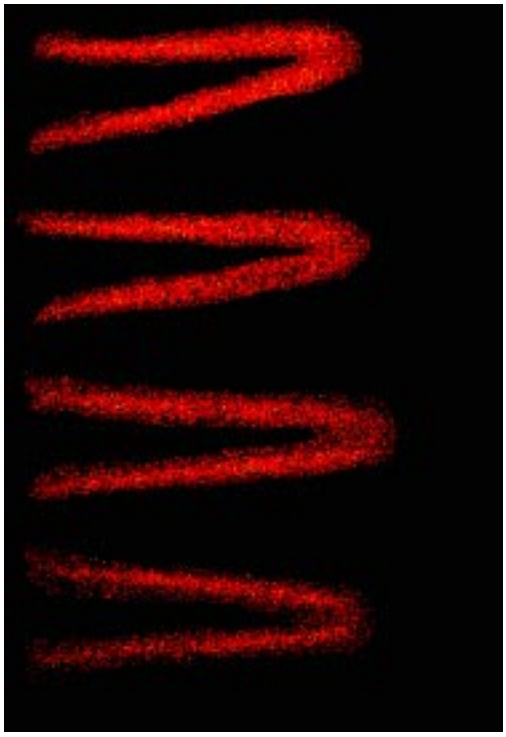

Figure 1. Undisturbed flames.

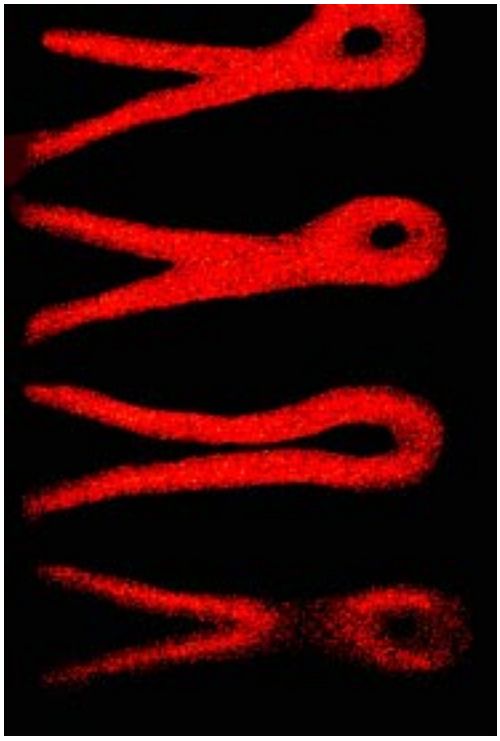

Figure 2. Oscillating flames.

As is often the case in flame imaging applications, the most difficult problem to be overcome in the development of this technique was that of achieving a high enough signal-to-noise ratio. Much of the noise was fluorescence induced in surrounding objects by scattered laser light. This could be separated from the flame image to some extent by the subtraction of a reference background produced by running the system for an identical number of pulses with the flame extinguished. Extreme measures were still necessary, however, to eliminate as much as possible of the noise at source.

Results

Two representative flame images, slightly enhanced by post-processing, are presented as Figures 1 and 2. In each case the imaged area is approximately 10 x 15 mm and encompasses the flames formed by four adjacent slots in the burner which is to the left of the picture. The apparent differences between the individual flames are the result of small variations in the widths of the slots, buoyancy effects and lateral deflection of the flames, caused by the thermal expansion, away from the centre of the burner. In Figure 1 the flames are undisturbed and burning in a steady manner. In Figure 2 they are oscillating with large amplitude at a frequency of 600 Hz under the influence of sound waves incident normally on the burner with a sound pressure level of slightly over 130 dB. The oscillating flames have been imaged at the point in the acoustic cycle at which the flame tips are becoming detached from the main bodies of the flames. 700 pulses of the laser were used to produce each image. The images are clear and detailed and, when produced for different phase angles of the incoming sound waves, provide the required phase-resolved information on the dynamic behaviour of the flame front.

Conclusions

(i) PLIF from CH is a viable technique for visualising the fronts of lean premixed methane-air flames in situations where multiple pulses can be used to build up clear images.

(ii) Saturation of the fluorescence signal at atmospheric pressure is readily achieved with modest pulse energies.

(iii) The multipulse imaging technique developed during the period of the laser loan, employed in synchrony with controlled acoustic forcing of the experimental flames, has the potential to yield valuable information of a fundamental nature concerning the problem of thermo-acoustic vibration in practical heating systems and will be employed in this way in continuation work.

References

1. T H Twist and K J A Hargreaves
   Proc. 2nd Int. Conf. on Combustion and Emissions Control, London, p. 011/1, (1995)
2. A C Eckbreth
   Laser Diagnostics for Combustion, Temperature and Species, Abacus, (1988)
3. S H Starner, R W Bilger, R W Dibble, R S Barlow, D C Fourguette and M B Long
   24 th Symp. (Int.) on Combustion, The Combustion Institute, p. 341, (1992)
4. R W Schefer, M Namazian, E E J Filtopoulos and J Kelly
   25th Symp. (Int.) on Combustion, The Combustion Institute, p. 1223, (1994)
5. K A Watson, K M Lyons, J M Donbar and C D Carter
   Comb. Flame 117 257, (1999)
6. N L Garland and D R Crosley
   Appl. Optics, 24 4229, (1985)

Conventional and far-infrared modulated photoluminescence of nitride based semiconductors in high magnetic fields

P A Shields, R J Nicholas

Clarendon Laboratory, Department of Physics,University of Oxford, Parks Road, Oxford, OX1 3PU. UK

N Grandjean, J Massies

CNRS, Centre de Recherche sur l'Hétéro-Epitaxie et ses Applications, Valbonne, F-06560, France

Main contact email address: *r.nicholas1@physics.ox.ac.uk*

Introduction

Quantum well (QW) structures based on the nitride materials system have already been successful in developing a blue emitting laser, by using an InGaN alloy as the well material with GaN as the barrier [1] . In order to coincide with the blue region of the spectrum, the indium content was tailored to achieve emission around 400 nm. UV emitters can also be envisaged, by using AlGaN alloys for the barrier material with GaN in the wells. This combination can bring the emission wavelength down towards 320 nm [2] , where for example there are potential uses in spectroscopy.

The optical quality, as determined from the emission efficiency, is better in the InGaN/GaN system compared to the GaN/AlGaN structures, whereas for the emission linewidth the opposite is true. The latter is likely to be related to the position of the tertiary alloy in the structure, it being in the active region in InGaN structures where an inhomogeneous composition would have a greater effect. Typically the best emission linewidths in InGaN/GaN structures are about 40 meV [3] , which can be compared with about 20 meV for GaN/AlGaN wells [4] . The development of these high quality AlGaN/GaN QW's by Grandjean et al. has allowed us to make some of the first measurements of the magneto-optical properties in nitride based quantum wells.

Due to the linewidths already mentioned, the large effective masses and the large exciton binding energies in these materials, to see any effects from the magnetic field, it is necessary to use very high fields which leads us to use pulsed field magnets which can currently give fields of up to 55 T.

Experiment

We have attempted both far-infrared modulated photoluminescence (FIRM-PL) along with conventional photoluminescence on a range of nitride-based materials. The PL was generated with a frequency doubled Argon laser, producing output powers up to 200 mW. For the FIRM-PL, no modulation was observed above the noise level of ~2% from a selection of infrared wavelengths between 37-570 μm generated from a CO2-laser-pumped molecular gas cavity.

However we have also performed low and high excitation photoluminescence (PL) in both steady and pulsed magnetic fields on a AlGaN/GaN sample with single quantum well widths of 4, 8, 12, and 16 monolayers (ML) separated by 100 Å $Al_{0.13}Ga_{0.87}N$ barriers strained to the GaN lattice constant. For the pulsed fields, the sample was immersed in liquid helium (4.2 K), in the bore of the resistive magnet, through which is passed the energy stored in a 8 μF bank of capacitors, charged up to ~5000 V. For the steady fields, a superconducting magnet capable of 19 T was used.

For the high excitation density PL the source was a pulsed frequency-quadrupled Nd:YAG laser at 266 nm, whereas for the low excitation density it was the 244 nm line from a CW frequency-doubled Argon laser. For the latter in the pulsed fields, a masked chopper wheel was used to produce a train of short laser pulses, ~0.3 ms duration, at ~100 ms intervals. A pulse from this train triggered the magnet system so that the next laser pulse coincided with the maximum of the pulsed field, where there is little change in the field (<1%) over a 0.3 ms timescale. A CCD cooled to -700C attached to a quarter metre spectrometer was used to detect the PL.

Results

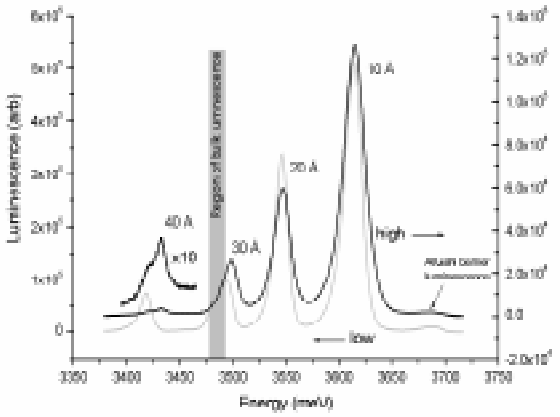

Figure 1. High and low excitation photoluminescence from four separate quantum wells, of widths 4, 8, 12, 16 monolayers.

Figure 1 shows the low and high excitation PL for this sample. Several PL peaks can be seen and have been attributed to the different wells. In-built electric fields play an important role in this sample via the quantum confined Stark effect, having been measured to be ~550 kV/cm [4] . The consequences of this are easily seen through the observation of PL from the widest well at 3.42 eV below the band gap energy of bulk GaN. However the PL from the 12 ML QW coincides with the luminescence from the bulk template, and thus makes it difficult to draw conclusions for this well width. Between the low and high excitation, we have observed a large screening of the electric field that is strongly dependent on the width of the wells, in qualitative agreement with theory and previous deductions.

The effect of the magnetic field on the 4ML QW can be seen in Figure 2, which shows a shift of the luminescence to lower energy. The form of this shift is dependent on the width of the wells, and is shown in Figure 3. For the widest wells there is a diamagnetic blueshift of the transition energy, but as the well width decreases we observe a transition to a redshift, which for the 4 ML well is approximately 2 meV at 50 T. Eventually at the highest field the redshift stops and appears to be overtaken by a smaller diamagnetic term. In addition, there is a change in both the intensity and overall peak width, with a strong narrowing seen at the highest fields for the wider wells.

For the widest well, two components are observed that have different dependencies on magnetic field. The observation of two peaks has previously been suggested to be due to fluctuations in the well width, corresponding to 16 and 17 MLs. We see an enhancement of the 16 ML peak with field, which is consistent with this proposal and the suppression of the in-plane transport. The excitons are then less able to find the potential minima caused by the fluctuations before recombining.

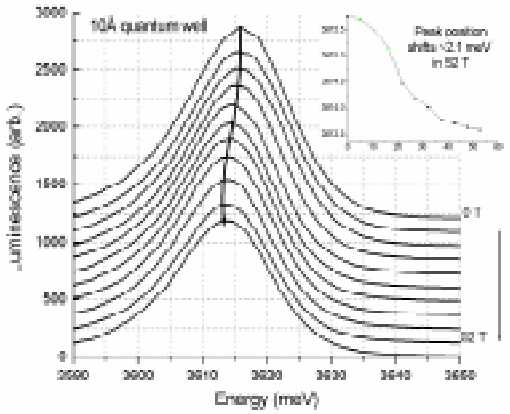

Figure 2. Magnetic field dependence of the low excitation photoluminescence for the 4 monolayer quantum well. The spectra are offset for clarity.

The shifts for all the wells can be fitted using $E(B) = E_0 + \gamma_1 B + \gamma_2 B^2$, and the overall dependence is determined by the relative magnitudes of the linear Zeeman and quadratic diamagnetic terms. The linear Zeeman shift causes the transition to split into two, of which we only see the lowest energy component. The peculiar S-shape for the narrower wells at the lower fields can be explained as coming from a significant thermal population in the upper component whilst the Zeeman splitting is still small. In fitting the data to this equation only the higher field values were used where the lower branch is expected to dominate the emission. The following table shows the parameters used to fit the data, along with the corresponding effective g-factors from the Zeeman term.

Transition	γ_1 (μeV/T^2)	g^*	γ_2 (μeV/T^2)
Bulk	0	-	2.04(3)
4 ML QW	-74(3)	2.6(1)	0.62(5)
8 ML QW	-76(7)	2.6(1)	1.0(1)
16 ML QW	-36(16)	1.2(5)	1.6(3)

Discussion

The observation of a Zeeman splitting through a clear redshift is surprising, since in the magneto-reflectivity of GaN epilayers, no splitting is seen in the A valence band when the magnetic field is parallel to the c-axis [5,6]. For bulk GaN this is due to a cancellation of the electron and hole g-factors. Even for the B valence band there is a similar compensation leading to an excitonic g-factor, g* = 1.24. So as both theoretical and experimental work on AlGaN heterojunctions [7] suggest that the electron effective g-factor should not change due to confinement, we conclude that instead the hole g-factor must have drastically changed in the narrow quantum wells due possibly to a significant change in the valence band structure, which we relate to the properties of the AlGaN barriers.

The effect of the internal electric fields is to separate the electrons and holes at opposite sides of the QW, which causes a significant proportion of the wavefunction to extend into the barrier region and makes them more sensitive to the barrier properties. X-ray measurements on these samples show that the AlGaN barriers have the same lattice constant as the GaN template, it being larger than if they were unstrained, resulting in them having a tensile biaxial strain. It is also known that in AlN the crystal field splitting has the opposite sign to that of GaN thus inverting the order of the states, so that at some critical value of x in AlxGa1-xN, a reversal of the states would be expected [8]. Both of these effects cause a re-ordering of the crystal field split states. Modeling the valence band spin splitting using the conventional Luttinger Hamiltonian, shows that this reordering causes a return to the spin order of the conventional zinc-blende pattern, changing the sign of the g-factor for the lowest Γ_7 hole band and lowering its energy below the Γ_9 A-valence band.

Our results suggest therefore that the ordering of the valence band has changed for narrow quantum wells, as a result of the lower barrier height for the Γ_7 bands. The re-ordering of these states will cause the ground state to have a Γ_7 character and the inverted spin splitting would account for the observed enhanced effective g-factor.

We now move to a discussion of the magnitude of the diamagnetic shift, which is related to the exciton binding energy and the excitonic wavefunction. The effect of a magnetic field can be considered as an extra confining potential on the already localised excitonic system.

The bulk data can be fitted very well to a full numerical calculation for a 3-dimensional hydrogen atom in a magnetic field [9], using 24.1 meV as the exciton binding energy and fitting a value of 0.180(2) me for the reduced mass as the only free parameter. The binding energy, taken from elsewhere [10] from identifying an excited state, was determined from the same sample used in our magneto-reflectivity. This numerical calculation reduces to a B^2 dependence in the low field limit, so that by fitting the low field data we obtain a coefficient, γ_2=2.04(3) μeV/T2 that we can use in a direct comparison between the bulk and QW data.

The diamagnetic coefficient for a quantum well is given by,

$$\gamma_2 = \frac{e^2}{8\mu}\left\langle \rho^2 \right\rangle$$

where μ is the reduced mass of the exciton and ρ is the separation of the electron and the hole in the plane of the quantum well [10]. Therefore the diamagnetic coefficient contains information about the zero-field properties of the exciton and can give a value for the in-plane extent.

From the 1s orbital in the hydrogen atom, the expectation value of r^2 is, $\left\langle r^2 \right\rangle = 3a_0^{*2}$, where is the effective Bohr radius. r^2 can then be converted to an in-plane size through $\left\langle \rho^2 \right\rangle = \frac{2}{3}\left\langle r^2 \right\rangle$. If the exciton is assumed to remain essentially three dimensional, the effective binding energy, R*, can then be deduced through scaling with respect to the hydrogen atom,

$$R^* = \frac{1}{\varepsilon_r}\frac{a_0^H}{a_0^*}R^H$$

where a_0^H is the Bohr radius and R^H is the Rydberg constant. This gives the following expression

$$R^* = \sqrt{\frac{e^2}{4\mu}\frac{1}{\gamma_2}}\frac{a_0^H R^H}{\varepsilon_r}$$

The deduced values have been summarised in the following table (ε_r = 9.8 1[11], μ=0.18). The similarity of the binding energy for the bulk deduced in this way, 25.3 meV compared to 24.1 meV from the 1s-2s separation, illustrates the accuracy of this technique.

Transition	Width (Å)	In-plane extent of exciton, (Å)	Exciton binding energy (meV)
Bulk	-	41.9(5)	25.3(3)
4ML	10	23(1)	46(2)
8ML	20	29(2)	36(2)
16ML	40	36(4)	29(3)

This table shows that as the well width is reduced, the exciton size is also reduced resulting in a strong enhancement of the binding energy for the narrow wells, in agreement with published figures [4, 13]. The values compare well with the theoretical values[13] when the electric field is included in the calculation, with the 16 ML QW approaching the bulk value. For wells much wider than 16 ML, it is expected that there will be a reduction of the exciton binding energy due to the separation of the electron and hole to the separate interfaces of the QW.

Although the model uses the approximation of the 3D exciton, this remains a reasonable approximation due to both the shrinkage of the in-plane wavefunction extent caused by the increased binding and the considerable leakage of the bound state wavefunction out of the wells into the barriers as evidenced by both the change in the valence band ordering and the calculated maximum in the excitonic binding energy at around 4 ML.

To conclude, our data shows that by observing an enhanced g-factor for the narrow wells, the valence band must have changed significantly compared with bulk GaN. We have attributed this to a re-ordering of the valence band states in the strained AlGaN barriers, giving different barrier heights for the different QW hole states. We have also observed an increase in the exciton binding energy with the reduction of the well width in agreement with theory.

References

1. S. Nakamura, M. Senoh, S. Nagahama, N. Iwasa, T. Yamada, T. Matsushita, H. Kiyoku, Y. Sugimoto, Jap. J. App. Phys., 35, (1B) L74 (1996)
2. T. Nishida and N. Kobayashi, phys. stat. sol. (a) 176, 45 (1999)
3. T. Wang, D. Nakagawa, J. Wang, T. Sugahara, S. Sakai, Appl. Phys. Lett. 73, 3571, (1998)
4. N. Grandjean, B. Damilano, S. Dalmasso, M. Leroux, M. Laügt and J. Massies, J. Appl. Phys 86, 1 (1999)
5. P. A. Shields, R. J. Nicholas, B. Beaumont, P. Gibart, Phys. Stat. Sol. (b) 216, 17 (1999)
6. R. Stepniewski, M. Potemski, A. Wysmolek, K. Pakula, J. M. Baranowski, J. Luusakowski, I. Grzegory, S. Porowski, G. Martinez, P. Wyder, Phys. Rev. B, 60, 1 (1999)
7. W. Knap, E. Frayssinet, M. L. Sadowski, C. Skierbiszewski, D. Maude, V. Falko, M. Asif Khan, M. S. Shur, App. Phys. Lett. 75, 3156 (1999)
8. K. Kim, W. R. L. Lambrecht, B. Segall, Phys. Rev. B, 56, 7363 (1997)
9. P. C. Makado and N. C. McGill, J. Phys. C: Solid State Phys. 19, 873 (1986)
10. G. Neu, M. Teisseire, B. Beaumont, H. Lahreche, P. Gibart, Phys. Stat. Sol. (b) 216, 79 (1999)
11. S. N. Walck and T. L. Reinecke, Phys. Rev. B, 57, 9088 (1998)
12. S. Barker, Jr and M. Ilegems, Phys. Rev. B, 7, 743 (1973)
13. P. Bigenwald, P. Lefebvre, T. Bretagnon, B. Gil, Phys. Stat. Sol. (b) 216, 371 (1999)

Vacuum-UV Resonant Photoabsorption Imaging of Laser Produced Plasmas

J S Hirsch, O Meighan, J-P Mosnier, P van Kampen, W W Whitty, J T Costello

National Centre for Plasma Science and Technology, School of Physical Sciences, Dublin City University, Ireland

C L S Lewis, A G MacPhee

School of Mathematics and Physics, Queens University of Belfast, Belfast BT7 1NN, Northern Ireland

G J Hirst, J Westhall, W Shaikh

Central Laser Facility, CLRC Rutherford Appleton Laboratory, Chilton, Didcot, Oxon, OX11 0QX, UK

Main contact email address: *jtc@physics.dcu.ie*

Introduction

The Dual Laser Plasma (DLP) method [1-3] is a well established and extremely versatile technique for measuring photoabsorption spectra of almost all atoms and singly/multiply charged ions. In DLP spectroscopic experiments, one laser plasma constitutes the absorbing 'sample' while the other forms the VUV (continuum) backlighting source. VUV light passing through the sample plasma is dispersed by a spectrometer and recorded on a VUV sensitive array detector. Varying the delay between the formation of the 'sample' and 'light source' plasmas one can measure the time resolved photoabsorption spectrum of the sample plasma. By recording photoabsorption spectra in different spatial zones of the sample plasma it is possible to build up a picture of how the plasma evolves in space and time. Unfortunately conventional DLP technique as a plasma diagnostic is somewhat limited due to the necessity to probe sequentially the different plasma spatial zones**.**

We show here that probing a laser ablated/plasma plume with quasi-monochromatic VUV light can overcome this limitation. In contrast to the usual DLP spectroscopy experiment we pass a VUV beam, tuned to an atomic or ionic resonance, through a laser-plasma plume and measure the resultant transmitted image (or shadow). In this way we are able to obtain directly the spatial-temporal distribution of plasma species. This method has a number of attractive features for application to laser ablated/plasma plume characterisation – namely:

- VUV light can access resonance lines of all atoms and moderately charged ions up to the photon energy limit of the VUV source and any associated optics.
- VUV light can access the higher density regimes that are excluded from visible light photoabsorption/shadowgraphy techniques.
- The pulsed laser plasma light source emits VUV radiation typically for 1 - 50 ns, depending on the heating pulse duration.

However, the most important point is that the laser plasma source makes analysis of the transmitted light distribution relatively uncomplicated; it is, to a very good approximation, a direct image of photoabsorption within the plume. The main reasons for this are:

- The dimension and effective relative bandwidth of the laser plasma source means that it is essentially an incoherent source and hence image analysis is not complicated by the presence of interference patterns.
- Refraction of a VUV beam in a plasma with given density gradient is significantly reduced compared to the case for a visible beam, with beam deviation angles scaling approximately as $(\lambda_{probe})^{-2}$.
- The use of VUV radiation as a probe has another very important advantage – it can be used to photoionize atoms or ions. In particular, tuneable VUV radiation can be used to induce *resonant photoionization* in e.g., Ca^+ via the path [4]

$$Ca^+ (3p^6 4s\ ^2S) + h\upsilon \rightarrow Ca^{+*} (3p^5 4s\ 3d\ ^2P) \rightarrow Ca^{2+} (3p^6\ ^1S) + e^-$$

The branching ratio for fluorescence to electron emission processes for such VUV excited (inner-shell) resonances, tends to be significantly less than 10^{-4}. Hence, almost all absorbed photons are converted to electrons and one does not have to be concerned about multiple photon absorption/re-emission cycles in the plasma plume. Further, excitation energies for different stages of ionization tend to be displaced slightly from each other. Thus, keeping all other experimental conditions identical, one can readily image different ionization stages of the same atom in one experiment by tuning the monochromator energy to the relevant resonance lines.

We have chosen to showcase this technique by imaging the temporal and spatial distribution of ground state of Ca, Ca^+ and Ca^{2+} in a laser plasma plume using the 3p-3d resonance line for each species. In particular, Ca^+ was chosen since its absolute VUV cross-section has been measured [5] permitting us to construct a column density map of Ca^+ in the plasma plume. We have also been able to track in time and extract the expansion velocity of the Ca^+ component of the plume, which turns out to be in good agreement with the model of Singh and Narayan [6]. We have also measured on the $3p^6(^1S) \rightarrow 3p^5 3d\ (^1P)$ resonance of Ca^{2+} which is accessible only with this VUV method.

Experiment

A schematic of the experiment is shown in Figure 1.

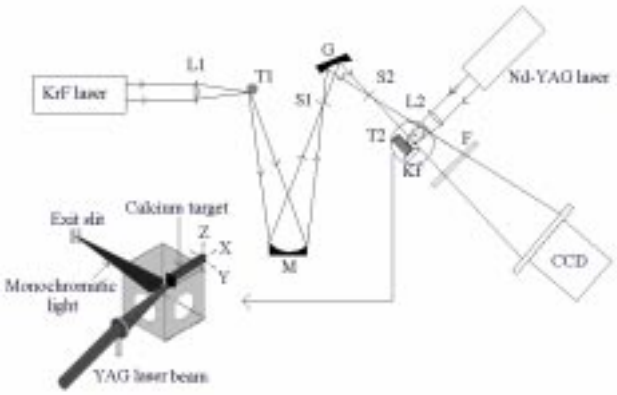

Figure 1. Experimental arrangement.

A tungsten plasma, generated by a KrF excimer laser (248 nm, 0.17 J, 20 ns) focused to a ~100 μm point by a 10 cm focal length f/5 fused silica lens, acted as a VUV continuum light source. This point plasma was located 1 m from a f/10 iridium coated mirror of focal length 0.5 m with which it made an angle of incidence of 7.5°. The plasma source was imaged with unit magnification onto the entrance slit of a 0.2 m focal length vacuum f/4.5 monochromator (Acton™ VM-502). An exit slit width of 250 μm yielded a bandwidth of ~ 0.9 eV. Due to the near normal angle of incidence on the focussing mirror, we observed no plasma radiation with a photon energy > 35 eV.

The VUV pulse duration was observed to be 50 ± 5 ns in the 20 – 35 eV photon energy range.

VUV radiation emanating from the exit slit was directed through a calcium plasma produced by a time synchronised Nd-YAG laser (1064 nm, 0.3 J, 10 ns). The Nd-Yag laser was focused to a horizontal line of length 8 mm and width ~ 0.25 mm by a 15 cm focal length cylindrical lens. The on-target irradiance was ~ 5 x 10^8 W/cm^2. In order to shield the detector from both scattered 248 nm laser light and direct calcium plasma emission, a 0.4-micron thick aluminium filter was placed in front of the CCD camera. When combined with the near normal incidence iridium coated mirror, the composite filter restricted the monochromator transmission to light with a photon energy between 16 and 35 eV.

The VUV shadowgrams were recorded on a 2048 x 1024 pixel ANDOR™ CCD camera with a pixel size of 13 μm x 13 μm, placed 50 cm from the exit slit of the monochromator and ~ 38 cm from the calcium plasma. In practice we found that the typical source flux was only 20 counts per pixel and hence all images were recorded using "superpixels" of 8 x 8 pixels size in order to improve the image signal to noise ratio. Since these 'superpixels' yielded an effective pixel size ~100 μm x 100 μm, the spatial sampling frequency of the CCD was reduced to 10 samples/mm for all images shown here.

The procedure we followed was to record an image of the background signal without firing any laser. The KrF laser was fired and an image of the continuum was recorded with background subtraction $\int I_0(E)dE$ where $I_0(E)dE$ is the VUV fluence (Jcm^{-2}) between E and E + dE falling on each pixel. A calcium plasma was created and an image of any residual VUV emission from it was saved as a background signal. Finally both lasers were fired at a set time delay and a photoabsorption image was recorded with background and front plasma emission subtraction $\int I(E)dE$ where I(E)dE represents the transmitted VUV fluence (Jcm^{-2}) between E and E + dE. The spatially resolved absorbance was obtained by evaluating:

$$A = \log_{10}\left(\frac{\int I_0(E)dE}{\int I(E)dE}\right)$$

Results

The 'footprint' of the VUV beam emerging from the monochromator was measured at different distances (11.5 cm, 28 cm and 50 cm) from the exit slit. The dimensions (full widths and heights) are 3.8 mm x 2.6 mm at 11.5 cm, 9.1 mm x 0.8 mm at 28 cm and ~15 mm x 2.7 mm at 50 cm. The calcium target was located at the 11.5 cm position for all photoabsorption measurements and hence the area of plasma sampled was ~ 3.8 mm x 2.6 mm. The VUV beam diverges in the horizontal plane with an angle of ~ 0.03 rads and in the vertical plane with an angle of ~ 0.014 rads.

To measure the magnification of the system in the horizontal plane we used a moveable knife-edge as shown in Figure 1. Starting at the cut-off position (i.e., blocking all VUV radiation from the backlighter) the knife edge was retracted from the VUV beam in steps of 200 μm and the corresponding change in image size recorded. The results yielded a value of 3.4 ± 0.1 for the horizontal magnification. The magnification in the vertical plane was also measured using a moveable knife-edge and a value of 1.0 ± 0.1 obtained. In addition we were able to use the same knife edge data to estimate the horizontal and vertical resolution of the system. From the shape of the knife edge traces in both the vertical and horizontal directions we measured values of 0.25 mm in the horizontal direction and 0.30 mm in the vertical direction. Further details are given elsewhere [7].

In Figure 2 (top panel) we show time resolved absorption images (shadowgrams) recorded by tuning the monochromator to the 3p - 3d resonances line of atomic Ca at 31.4 eV. The data are absorbance distributions and reflect the spatial distribution of ground state Ca in the plasma plume at times of 100 ns - 3 μs after calcium plasma generation. The sharp edge at the top of each image is the shadow of the knife-edge located close to the Ca target (Figure 1) while the sharp cut-off at the bottom of the image is due to the edge of the thin film aluminium holder. An area of intense absorption (and hence atomic Ca concentration) remains close to the surface of the Ca target until approximately one microsecond at which point the Ca atoms have expanded outwards to a dimension comparable to the horizontal extent of the VUV beam. For time delays in excess of one microsecond the region of greatest Ca atomic number density becomes detached from the target surface and overall the absorption decreases. However, even at three microseconds there is still a measurable absorption signal. The apparent region of low absorption at the bottom of all the images shown in the paper is an artefact resulting from damage to the Al-VUV filter.

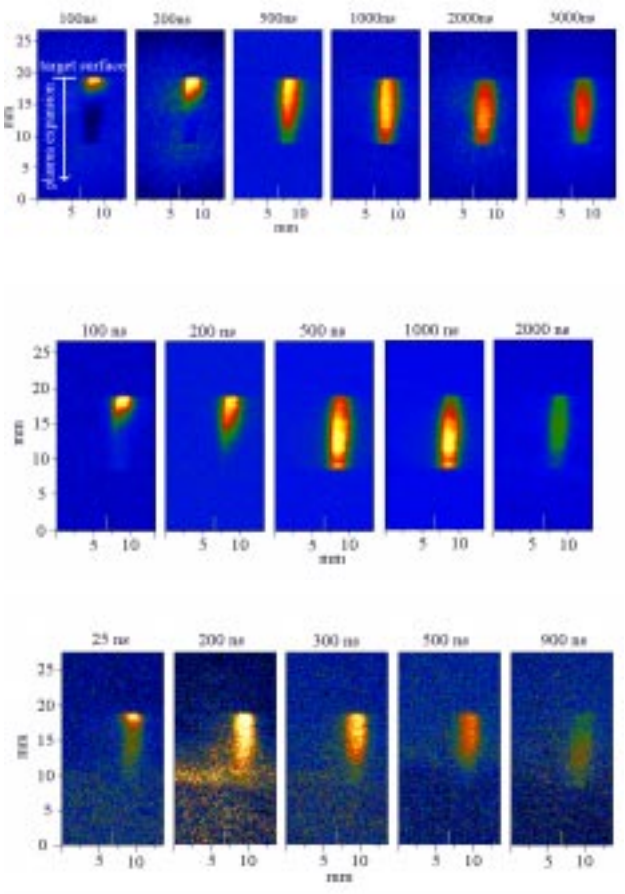

Figure 2. Time resolved shadowgrams of Ca, Ca^+ and Ca^{2+}.

In Figure 2 (middle panel) we show time resolved absorbance distributions recorded at the 3p - 3d (33.2 eV) resonance of Ca^+ for time delays ranging from 100 ns to 1 μs. Here again we observe a behaviour similar to that of atomic calcium. However, it is clear that the hotter Ca^+ ions have a larger horizontal velocity component and as a consequence the plume expands more quickly and the Ca^+ absorption signal drops more rapidly than in the atomic calcium case.

In Figure 2 (bottom panel), we show VUV shadowgrams recorded at the 3p (^{1}S) – 3d (^{1}P) resonance (34.7 eV) of Ca^{2+} for time delays ranging from 25 ns to 900 ns. These shadowgrams were recorded at the short wavelength limit of the system where the continuum signals I_0 and the transmitted signal I were both very weak. In addition, in the cases of Ca and Ca^+ the 3p-3d resonance linewidths are in the order of 100 meV and hence

they absorb a significant portion of the 0.9 eV width VUV beam. For Ca^{2+}, the 3p-3d resonance linewidth is very much narrower (meV) and hence only a small part of the VUV radiation is absorbed by these ions. As a result, there is only a small difference between the I and I_0 signals. These effects resulted in poorer quality images. However the Ca^{2+} shadowgrams show that it is possible to record multiply charged ion distributions and track their evolution in time. We will refine our experiment, further explore and develop this aspect of the work in future experiments.

Discussion

(a) Ca plasma expansion velocities

The recorded shadowgrams embody information concerning the size of the expanding plasma plume at different time delays and hence may be used to extract plasma expansion velocities. A spatial scan of the plasma plume in the horizontal plane at a 200 ns time delay for the Ca^+ 3p-3d resonance line at 33.2 eV showed that the absorption signal dropped to zero following translation of the calcium target by 1 mm on which we have to add 200 μm due to the initial position of the target relative to the knife-edge. Hence, we conclude that the size of the Ca^+ component of the plasma was 1.2 ± 0.2 mm at 200 ns. To check this result, the Ca^+ plume size was directly read off the shadowgram with the calcium target restored to its initial position. Knowing that the magnification of the system is 3.4 and that the dimension (full extent) of the plasma plume normal to the Ca^+ target on the shadowgram is 3.95 mm one again obtains ~1.2 mm for the horizontal dimension in agreement with the knife edge measurements.

We have found that the intensity distribution of each image along an axis normal to the target is usually a slightly asymmetric bell shaped function. For our current purposes we take the FWHM of this distribution to represent the plasma dimension normal to the target surface. In practice we used this measurement of the image full width at half maximum to estimate the velocity of the Ca^+ ions at defined time delays above 50 ns. Based on uncertainties in measurements of the plume size, the projection magnification and the probing time, the velocity was estimated to an accuracy of ± 15 %.

These measurements are compared with calculations obtained by solving numerically the equation describing the adiabatic phase of the plasma expansion as illustrated in Figure 3. The adiabatic expansion equation can be written as [6],

$$X(t)\left[\frac{d^2X}{dt^2}\right]=Y(t)\left[\frac{d^2Y}{dt^2}\right]=Z(t)\left[\frac{d^2Z}{dt^2}\right]=\frac{kT_0}{M}\left[\frac{X_0Y_0Z_0}{X(t)Y(t)Z(t)}\right] \qquad (1)$$

where X_0, Y_0, Z_0 are the initial orthogonal edge positions of the plasma after the termination of the laser pulse, M is the atomic mass, k is Boltzmann's constant and T_0 is the isothermal temperature. The velocity calculations were performed using as initial spatial conditions a line plasma of size of 8 mm x 0.25 mm with an initial velocity of 10^5 cm s^{-1} for different plasma temperatures.

The measured velocities are in good agreement with the results of the theoretical model. The plasma velocity increases rather slowly with time going from 6 x 10^5 cm s^{-1} at 50 ns to 7.15 x 10^5 cm s^{-1} at 200 ns. The effect of lowering the laser energy from 300 mJ to 200 mJ is a reduction in plasma expansion velocity from 6 x 10^5 cm s^{-1} to 5.2 x 10^5 cm s^{-1} at 50 ns after calcium plasma initiation. Even though the model is designed to predict the motion of the entire plasma, it is interesting to see that there is a good agreement between calculated plasma velocity and observed ground state Ca^+ velocity evolution. For a measured Nd-YAG laser pulse of energy 300 mJ, a model plasma temperature of 45000 K yields a good fit. For a 200 mJ laser pulse we obtain a good agreement for a model plasma temperature of 35000 K. These results are consistent with a plasma temperature dependence on the laser pulse energy scaling as $E_{laser}^{3/5}$.

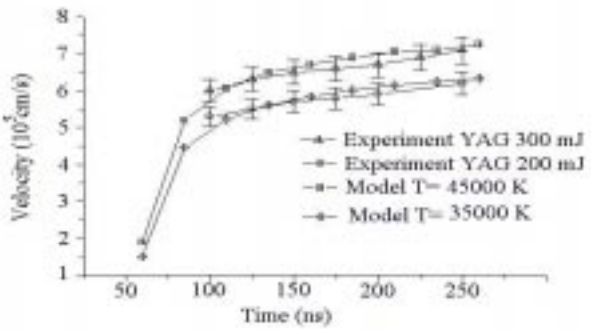

Figure 3. Evolution of plasma plume expansion velocity.

(b) Column density map of Ca^+.

To determine values of the column density NL, the equivalent width W_E of the 3p-3d Ca^+ absorption resonance line has to be determined. It can be found by inserting the shadowgram data values, i.e., $\int I_0(E)dE$ and $\int I(E)dE$, into

$$W_E=\Delta E\left(\frac{\int_{\Delta E}[I_0(E)-I(E)]dE}{\int_{\Delta E}I_0(E)dE}\right) \qquad (2)$$

with $$\int I(E)dE=\int I_0(E)\exp[-\sigma(E)NL]dE$$

Using the numerical solution of equation (2) we can then associate a value of NL with every value of W_E found experimentally to create a map of column density within the plasma plume. The interval ΔE was 0.89 eV which in turn sets the limits of the integration. Finally $I_0(E)$ is approximately constant over ΔE and hence (2) simplifies to:

$$W_E=\int[1-\exp[-\sigma(E)NL]]dE \qquad (3)$$

In particular cases, e. g., when dealing with an optically thin plasma, it can be shown that the equivalent width varies linearly with the product NL. In contrast, in the optically thick case, it can be shown to follow a square root dependence on NL. We can then express the equivalent width in these two specific cases

(i) Optically thin plasma:

$$W_E=\left(\frac{\pi e^2}{mc}\right)\times h\times f\times NL \qquad (4)$$

(ii) Optically thick plasma:

$$W_E=\left(\frac{2\pi e^2\times h\times f\times NL\times\Gamma}{mc}\right)^{\frac{1}{2}} \qquad (5)$$

where m is the atom/ion mass, c is the velocity of light, h is the Planck constant, f the oscillator strength and Γ is the half width of a Lorentzian curve which best approximates the atomic lineshape function. Figure 4 shows three plots of the equivalent width as a function of the product NL, for the 3p-3d transition of Ca^+ which has an oscillator strength f = 2.3.

As expected, for small column density (NL) values, (NL < 1 x 10^{14}), the general expression of the equivalent width varies linearly with NL in agreement with the optically thin case. However for large values of NL, the optically thick approximation diverges quite dramatically and for NL > 1 x 10^{16} cm^{-2} the curve tends to an asymptotic value of 0.35 eV.

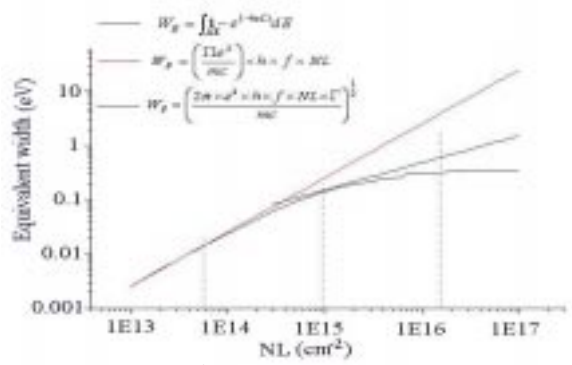

Figure 4. W_E for Ca^+ 3p – 3d (thin, thick and exact).

This behaviour can be explained by noting that the 3p-3d Ca^+ resonance is very strong, (peak cross section of 2200 Mb), and the values obtained when solving $W_E = \int [1 - \exp[-\sigma(E)NL]dE$ reach saturation for NL > 2 x 10^{15} cm^{-2}. This is clear from Figure 5 where we plot 1 – exp[-σ(E)NL] for different NL.

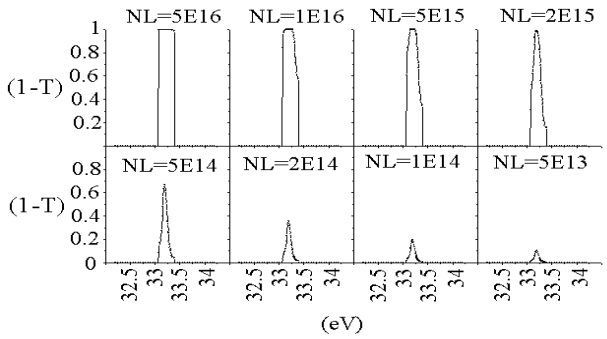

Figure 5. 1-T (Ca^+ 3p – 3d) for various column densities.

As a result, except for very long time delays (Δt > 2500 ns), shadowgrams display saturated absorption and values of equivalent width (obtained using equation (3)) W_E are all greater than 0.3 eV. Hence we only extract column densities from the shadowgram taken at 2500 ns and this is shown in Figure 6.

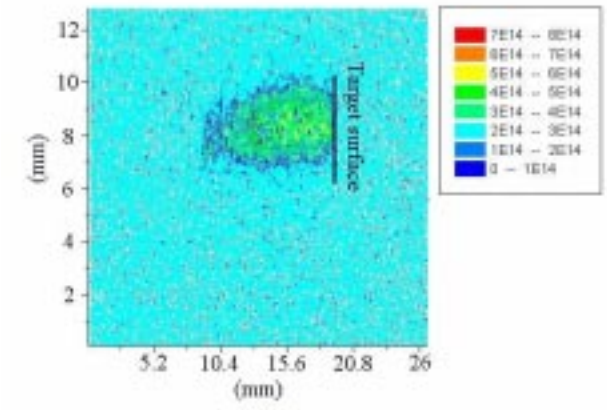

Figure 6. Column density map of Ca^+ at 2500 ns.

Since at this time delay the plume is now larger than the VUV beam footprint and also quite homogeneous we do not see any spatial variation in NL. However we have the advantage of broad tuneability over a wide VUV photon energy range we may choose from one of the many weaker Ca^+ resonances in order to probe higher ion-density regions of the plume. We will explore this option in future experiments.

Conclusions

We have recorded time and space resolved VUV absorbance distributions using the 3p – 3d resonances of ground state Ca, Ca^+ and Ca^{2+}. From these shadowgrams we have extracted values of the plasma plume size at different time delays and hence plasma expansion velocities. These results are in good agreement with computed plasma expansion velocity predictions. We have also shown that with appropriate choice of inner-shell resonance it is possible to extract time resolved maps of column densities for ions from the recorded images.

Looking to the future, on the development of the basic technique one could also make measurements in the non-resonant part of the photoionization continuum. This has the advantage that the spectral resolution needed is significantly smaller than in the case of resonances. In addition, the number of atoms and ions for which absolute photoionization cross-sections are available is very small. However, the *non-resonant* part of the photoionization continuum cross-section of all atoms and ions can be computed with an accuracy of better than 10%. Hence one could potentially apply the non- resonant 'photoionization' imaging technique to almost all atoms and ions to obtain number/column densities with good accuracy. We have already shown how this can be done using DLP spectroscopy [8]. We intend to explore this direction in future experiments. Looking even further ahead we will explore the use of a grazing incidence monochromator based system to cover the 35 – 400 eV photon energy range and also experiments with sub-nanosecond continuum light sources [9]. This will help bridge the diagnostic gap between the present work and earlier work with crystal (keV photons) dispersion and ~100 ps frametimes which required access to large laser facilities [10].

Acknowledgement.

This work was funded by the European Union under the TMR Facilities Access Program.

References

1 P. K. Carroll and E. T. Kennedy, Phys.Rev.Lett, 38, 1068, (1977)

2 J. T. Costello, E. T. Kennedy, J-P. Mosnier, P. K. Carroll and G. O'Sullivan, Physica.Scripta T34, 77 (1991)

3 E. Jannitti, M. Gaye, M. Mazzoni, P. Nicolosi, P. Villoresi, Phys.Rev.A., 5, 4033 (1993)

4 J. M. Bizau, D. Cubaynes, M. Richter, F.J. Wuilleumier, J. Obert, J.C. Putaux, T.J Morgan, E. Kallne, S. Sorensen and A Damany, Phys. Rev. Lett, 67, 576 (1991)

5 I.C. Lyon, B. Peart, K. Dolder, and J.B. West, J. Phys. B, 20, 1471 (1987)

6 R. K. Singh and J. Narayan, Phys. Rev. B, 41, N 13, 8843 (1990)

7 J. S. Hirsch, O. Meighan, J-P. Mosnier, P. van Kampen, W. W. Whitty, J. T. Costello, C. L. S. Lewis and A. G. MacPhee, G. J. Hirst, J. Westhall and W. Shaikh, J.Appl.Phys (Submitted for publication June 2000)

8 W.W. Whitty, J.T. Costello, E.T. Kennedy, C. Moloney, and J-P. Mosnier, Appl. Surf. Sci., 127-129, 686 (1998).

9 O. E Meighan, A. Gray, W. Whitty, J-P. Mosnier, C.L.S. Lewis, A MacPhee, R. Allot, I.C.E. Turcu, 27A. Lamb and J.T. Costello, Appl. Phys. Lett, 70, p 1497, (1997)

10 J. Balmer, C.L.S. Lewis, R.E. Corbett, E. Robertson, S. Saadat, D. O'Neill, J.D. Kilkenny, C.A. Back and R.W. Lee, Phys. Rev. A, 40 (1), 330, (1989)

Facility Development

1) **Vulcan**
2) **Astra**
3) **Lasers *for* Science Facility**
4) **Instrumentation**
5) **Laser Research and Development**

Vulcan Petawatt Upgrade Overview

C B Edwards

Central Laser Facility, CLRC Rutherford Appleton Laboratory, Chilton, Didcot, Oxon, OX110QX, UK

Main contact email address: *c.b.edwards@rl.ac.uk*

The project to upgrade the ultra-short pulse beam of Vulcan to the Petawatt level began formally on 1st April, 1999. The 3 year project is funded through an EPSRC Research Grant and made possible by an agreement with Lawrence Livermore National Laboratory (LLNL), California to provide components following the closure of the NOVA laser facility. The upgrade will deliver target irradiance in the 10^{21} W cm^{-2} regime, with first beam on target for users in June 2002. Work on the project in the year to the end of March 2000 has been concentrated in five main areas as summarised below. Further details are described in articles following.

Upgrade Specification

The detailed specification and optical design has been completed. This includes original work on the modeling of the performance of the pulse compressor, optimisation of the optical train and amplifier architecture, and calculations of the building stability requirements. The final specification adopted for the project is an energy on target of 500 J in a pulse of 500 fs duration with a target irradiance of 10^{21} W cm^{-2}.

Target Area Building

Following detailed design and a competitive tendering process, a contract for the construction of the new target area building was placed at the end of January 2000. Work commenced immediately and excavations for the foundations were completed by the end of March. The building specification required a detailed assessment of the requirements for radiation shielding which has been designed to avoid the need to classify users of the new facility as radiation workers.

Components from Livermore

The first shipment of ex-NOVA components to the CLF from LLNL took place in July 1999. These included the first of the 208 mm diameter amplifiers, pulsed power components needed for the construction of an amplifier test facility in building R2 and large optical components (see Figure 1).

Capacitor Bank

The reconstruction of the Vulcan capacitor bank using high energy density capacitors from NOVA is central to the upgrade project. The new system will store sufficient energy to drive the additional disc amplifiers needed for the upgrade and the current disc amplifiers within the existing floor space. The charging units will also be replaced with state of the art units designed specifically for the Vulcan requirement. During the year a test facility was commissioned in building R2 to enable system components and complete disc amplifiers to be tested prior to installation on Vulcan.

Clean Room Infrastructure

A large clean room has been established in R2 to enable the clean assembly and optical testing necessary to commission and maintain the Petawatt beam line. This was made possible by the acquisition from Space Science Dept. of a number of large area clean air hoods which were surplus to requirements.

Project Management

Underpinning the project is a well-defined management structure which reports to the Project Management Committee (PMC), chaired by Dr T G Walker, Chief Executive of CCLRC. The PMC also includes Professor O Willi and Dr J Wark as principle users of Vulcan, Ms D Watson (EPSRC Associate Programme Manager for Physics) and Mr D Harman (EPSRC Finance Dept.). The CLF is represented by Henry Hutchinson (Director, CLF) and Chris Edwards (Project Manager).

Figure 1. Steve Hawkes of the CLF inspects one of the large mirrors required for Petawatt beam delivery in the new R2 clean room.

CPA Design Considerations for the Vulcan Petawatt Upgrade

J Collier, R Allott, C N Danson, C B Edwards, S Hancock, D Neely, D A Pepler, D A Rodkiss, I N Ross, T B Winstone, B E Wyborn

Central Laser Facility, CLRC Rutherford Appleton Laboratory, Chilton, Didcot, Oxon, OX14 0QX, UK

Main contact email address: *J.Collier@rl.ac.uk*

Introduction

The specification for the single beam Petawatt upgrade of Vulcan is 500 J on target delivered in 500 fs. This is a specification that pushes to the limit the capabilities of the Vulcan system and this article details some of the issues that arose.

Compressed Pulse Length

Fundamental to the Petawatt upgrade specification, and in many ways the starting point for the design, is an evaluation of the minimum pulse length that is achievable from a combination of Vulcan, the upgrade components and the CPA scheme. There are a number of important parameters that will ultimately dictate this pulse length and these include : the output pulse bandwidth and spectral shape; the stretcher and compressor design; the B-Integral, wavefront and optical component quality; chromatic aberration; alignment errors; and spatial spectral dispersion.

Bandwidth

The amplification medium used in Vulcan is Neodymium doped phosphate glass (Nd:glass). It has a fluorescence bandwidth of approximately 20 nm and is centred at 1053 nm. To amplify the CPA seed pulse from the nano-Joule level when leaving the stretcher to the hundreds of Joules level on target requires a net energy gain of greater than 10^{11}. Given the various static losses in passing through Vulcan the gross gain required increases to more than 10^{14}. This very high gain means that direct amplification in the Nd:glass of the seed pulse with its 16 nm input spectral "top hat" bandwidth profile causes a severe "gain narrowing". The resultant output spectral profile is calculated to be of an asymmetric $sech^2$ shape with a FWHM bandwidth of less than 2 nm. This has been confirmed by measurements in TAW. An exact prediction of the amplified pulse bandwidth and shape is limited by a lack of knowledge of the exact types and distributions of the Nd:glass (phosphate) used in Vulcan. Importantly, this 2 nm bandwidth is only sufficient to support upon compression pulse lengths upwards of 700 fs, excluding any additional detrimental effects. Clearly, to reduce this pulse length one of the most important aspects is to increase the gross gain bandwidth of Vulcan. For the Petawatt upgrade, this will be achieved in two ways.

First, the initial amplification of the CPA pulse, currently undertaken in phosphate 9 mm Nd:glass rods will be replaced by amplification in a new OPCPA Front End preamplifier. This system[1)] will increase the seed pulse energy from about 1.5 nJ to approximately 10 - 20 mJ – a gain of 1 - 2 $x10^7$ – using a novel technique based on optical parametric amplification. Importantly, this will occur without any loss of the 16 nm injected bandwidth. In using this system there is also an intrinsic reduction in the level of the static losses. This pulse is then directly injected into the rod amplifier chain.

The second change will be to replace or introduce additional rod amplifiers using Neodymium doped *silicate* glass. The silicate glass has similar bandwidth to the phosphate glass but with the centre of the fluorescence peak shifted to ~1062 nm. This combination of gain in silicate and phosphate will generate a larger gain bandwidth overall. Calculations show that the introduction of a modest amount of silicate glass into the Vulcan rod chain in addition to the OPCPA Front End should be sufficient to achieve an output pulse bandwidth slightly more than 4 nm.

CPA Scheme

Following the changes detailed above to the amplification scheme, Vulcan is expected to produce an output pulse bandwidth of ~ 4 nm. This bandwidth needs to be sufficiently stretched in time prior to amplification to ensure that the self-phase modulation accumulated during amplification and propagation (the so called "B-Integral") is not so high that it unduly prevents compression of the chirped pulse. Additional effects arising from propagation through the compressor that modify the pulse bandwidth must be considered.

Starting with the compressor, an important effect that occurs is "spectral apodization" of the pulse spectrum, which arises from the angular dispersion of the first grating causing the partial loss of spectral components on the second due them simply missing the finite sized grating. This is, of course, a result of the gratings being the same size as each other and indeed as the input beam. The effect of this spectral apodization results in both a partial loss of bandwidth after passing through the compressor and a reduction in the compressor energy efficiency due to bandwidth "overspill". Therefore the effect of increases to the amplification bandwidth of Vulcan detailed previously need to be determined after propagation through the compressor.

Finally, the fact that this apodization occurs as a near field "clip" that varies with wavelength, the effect of which is evaluated in the far field means that consideration must be given to the effective far field amplitude of any particular wavelength as opposed to just a geometric loss factor. This is included in the calculations.

A number of CPA schemes have been evaluated, essentially attempting to provide the required 1 PW on target with various energies and pulse lengths. Following detailed calculation, the CPA scheme that has been decided upon will use gratings of line density 1480 mm^{-1} operated at a 47.9 degree incidence angle. The diffracted angle will be 54.7 degrees and they will be separated by 13.0 m. This combination will provide a linear dispersion of 300 ps nm^{-1} and a non-linear dispersion of ~ 8 ps nm^{-1}**.** It will therefore result in a CPA pulse duration at the exit of the Vulcan chain of ~1.2 ns for the ~4 nm bandwidth. Following propagation through the compressor the pulse bandwidth will be 4.0 nm. By contrast, the pulse duration at injection (following the pre-amplifier) will be 4.8 ns deriving from the 16 nm injected bandwidth.

Due to the inclusion of silicate glass, the pulse centre wavelength after amplification will be close to 1054.5 nm and the maximum compressor energy efficiency will depend on an appropriate setting of its centre wavelength. This means that the stretcher –compressor will not be set at the traditional 1053 nm centre wavelength but closer to 1054.5 nm, with the exact value being determined following appropriate spectral measurement.

B-Integral

The B-Integral accumulated using this scheme will be approximately 1.3. The effect of the B-Integral is to increase the pulse duration on high energy shots to that obtained on low energy shots. If the B-Integral becomes too high then the pulse actually breaks up in time. Ideally the B-Integral should be kept as low as possible. A B-Integral of 1.3 is higher than one would like and will cause the 300 fs bandwidth limited pulse to be increased to approximately 380 fs. Figure 1 below

diagrammatically summarises the effect of bandwidth and B-Integral changes.

Wavefront Quality

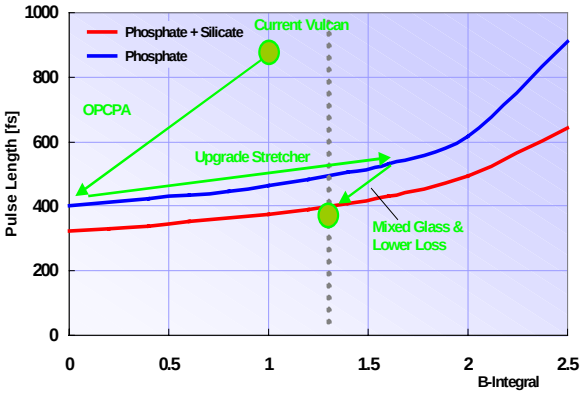

Figure 1. The bandwidth and B-Integral changes that are necessary for the upgrade specification. The B-Integral falls with the inclusion of silicate glass because the greater optical bandwidth means the stretched pulse is longer for the same dispersion.

Another important aspect that will affect the pulse length is the pulse wavefront quality entering the compressor. This may seem unusual, given the normal association of wavefront quality to focal spot quality, but with the beam size and grating separation needed for the specification, an intrinsic sensitivity to wavefront quality is inevitable. This can be understood with reference to Figure 2 by considering perturbations to the wavefront as pointing errors into the compressor.

These pointing errors, that vary spatially, take slightly different

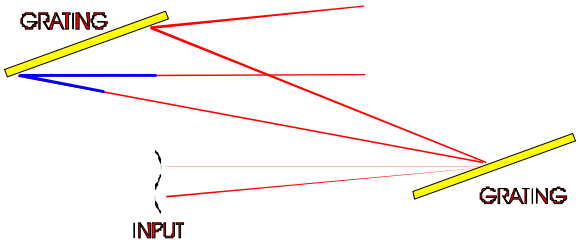

Figure 2. Wavefront gradients regarded as localised pointing errors into the compressor have slightly different path lengths through the system.

paths, and thus slightly different path lengths, through the compressor in the dispersion plane of the gratings. Without an exact knowledge of the wavefront aberration and an appropriate propagation code that takes into account diffraction it is difficult to make definite prediction of the effect. However, an estimation can be made of the temporal effect of pointing errors. This shows that pointing errors that equivalently lie outside the first Airy minimum for the beam will have path length differences that exceed 200 fs. It is therefore important to minimise the amount of power that is contained at these higher gradients. Previous measurements conducted on the Vulcan beam quality show that it is "3 times diffraction limited" [2], indicating that appreciable powers do indeed extend beyond this point. The installation therefore of a wavefront correction system to bring the beam to as close to the diffraction limit as possible is essential to ensure that as much of the beam power is as compressible as possible. There is of course the added

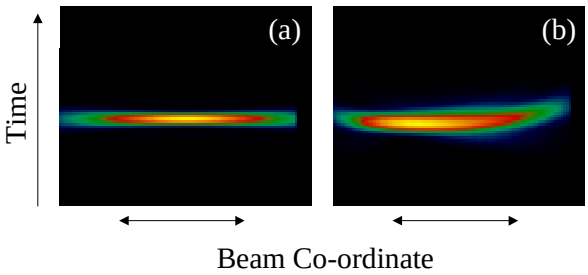

Figure 3. A graphical comparison of the pulse leaving the compressor with (b) and without (a) spectral phase aberrations arising from B-integral and aberrations. The horizontal axis is a horizontal beam co-ordinate. Vertical is time, and the colour an arbitrary intensity level.

benefit that with wavefront correction the spot will be close to diffraction limited in spatial extent as well.

Chromatic Aberration

One aspect of wavefront aberration that is difficult to correct for is chromatic aberration. Ordinarily, with the relatively small bandwidths that are in use, chromatic aberration is of little importance. However, the need to expand the beam to large diameter to maximise the illuminated area of the compression gratings means that in the final vacuum spatial filter, approximately 1 wave of defocus aberration develops across the 16 nm total bandwidth, as shown. A relatively large percentage of the beam power is thus contained in wavefront gradients that have appreciable path length variations throughout the compressor. An estimation of this effect can be made which shows that this aberration will increase the pulse duration from the 380 fs above to approximately 440 fs.

Figure 3 is the result of a simulation that includes all of the effects discussed so far and provides a graphical representation of a pulse that has been amplified in Vulcan as described above and fully traced through the compressor. The figure represents the pulse as it emerges from the compressor and is brought to a line focus by a horizontal axis cylindrical lens.

Alignment Errors

Other sources of pulse length increase are alignment errors in the compressor and mis-alignments between the stretcher and compressor. The effect of these mis-alignments is to provide an additional source of temporal aberration. Alignment tolerances of : grating parallelism of ±18 µrad, grove parallelism of ±80 µrad, input angle matching of 2 mrad and grating separation of ±1.1 mm each correspond to additional group delays of 100 fs which would result in a 10 fs per parameter increase in the 450 fs pulse length above. However, pulse length increase through misalignment should be minimal because extensive optical diagnostics will be available to assist in the alignment and monitoring process.

Spatial Spectral Dispersion

One final contribution to pulse length increase, although somewhat semantic, is that due to spatial spectral dispersion. This arises because after passage through the compressor the various wavelengths are now no longer superimposed spatially, but rather displaced laterally by some 39 mm nm^{-1}. This means that upon focussing, the different wavelengths are spatially displaced in the near field of the 'beam' and cause a pulse front tilt in the far field. The pulse in the far field is locally short but if spatially integrated over the far field plane then the pulse length would increase to just under 500 fs.

Stretcher and Pulse Contrast

Another important aspect that could adversely affect the pulse duration is the design of the stretcher. The stretcher has to be

spectrally phase conjugate to the compressor. It is important in the design of the stretcher to ensure that this conjugation is maintained and that the stretcher does not impose spectral phase structure that is different from that of the compressor. Additionally, in order to prevent degradation of the pulse contrast it is also important to ensure that there is no severe spectral amplitude or phase clipping and that a degree of spectral apodization occurs. It is interesting to note that generally the spectral apodization of the compressor does cause a reduction in pulse contrast and that in the stretch a contrast increase. There is a balance therefore to be achieved, as detailed elsewhere in this CLF Annual Report [3].

Spectral apodization in the stretcher is most readily achieved by ensuring that the beam passing through the stretcher is relatively large in diameter (of the order 30 - 40 mm) and a similar type of "gentle" clip occurs as described earlier in the compressor. Large beams and off axis propagation however mean that spectral phase errors could easily develop. An analysis has been conducted of the proposed design, which is based on an all reflective Offner triplet, which shows that the spectral phase errors are present but are acceptable . The result of these simulations for a 40 mm beam is shown in Figure 4 illustrating the spectral phase as a function both of the wavelength and the position in beam for an on axis case (0 mm) and the off axis case (40 mm). The results are shown after 2 passes of the four pass stretcher.

Energy and Fluence

A pulse length of 500 fs will require an on target energy of 500 J to generate the required 1 Petawatt of power. The combined efficiency of the compressor grating pair to be used is 76%. This arises from 90% diffraction efficiency per grating and an additional 93% efficiency through spectral bandwidth 'spill over' on the 2nd grating. The required output energy from Vulcan is thus 670 J.

Use of similar gratings at the Lawrence Livermore National Laboratories (LLNL) on the Nova facility has established an operating fluence of approximately 320 mJ cm^{-2}. The shot repetition rate however was significantly lower than that of Vulcan, as was the required lifetime. This, combined with previous operational experience of Jobin-Yvon diffraction gratings used on Vulcan, leads to a maximum grating fluence of 160 mJ cm^{-2}. The required beam area on the first grating is thus

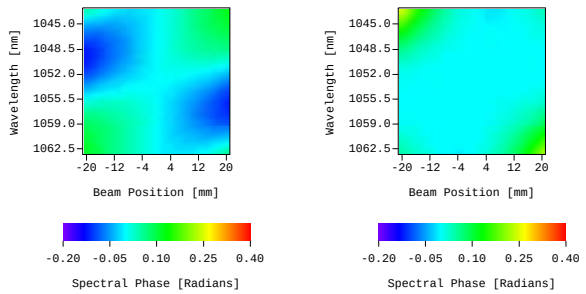

0 mm 40 mm

Figure 4. Spectral phase results of stretcher simulations for on axis (0 mm) and off axis (40 mm) propagation.

4190 cm^2. The gratings operate most efficiently at or close to the Littrow angle, which for the 1480 lines mm^{-1} gratings is 51.2 degrees. The operating grating input angle of 47.9 degrees is close to this value. A circular near field incidence beam is thus transformed into an ellipse of major axis: minor axis of 1.49:1.0 and eccentricity 0.74. The required beam diameter to satisfy the area requirement is therefore 600 mm. This is ideally suited to the dimensions of the LLNL supplied grating.

Ghosts and Back Propagation

Ghosts within a laser system are spurious reflections from convex/concave surfaces producing focused images. Although these reflections can contain a very small fraction (10^{-6}) of the energy of the input beam they can be brought to a very small focal spot generating flux densities which could damage expensive laser components. Ghosts therefore have an important role to play in designing the beam line layout. The only ghost producing elements within the proposed layout for the upgrade of the Vulcan beam line are the input and output lens for the 180 / 600 vacuum spatial filter. Although these optics will have anti-reflection coatings on each surface they could potentially produce ghosts that would cause significant damage within the system. It is essential therefore that they focus in open space i.e. not within an optic or are imaginary. The ghost positions have been calculated using a commercial optical design software package.

The input lens of the Vacuum Spatial Filter (VSF) has a focal length of 4.44 m and therefore its reflected ghosts will occur at 2.22 m and 0.55 m. They have a sufficient energy density to cause damage and thus the closest components to this lens are positioned more than 2.5 m away. The output lens has a primary transmitted ghost at 2.236 m and a secondary ghost at 1.044 m. The energy density contained within the first of these spots would be enough to cause damage, so again components are positioned so as to avoid it.

The control of pulses, possibly reflected from the target is important in preventing damage to components within the amplifier chain. A 10% reflectivity from target was assumed with no change in polarisation and 95% transmission through each VSF. The returning beam will be amplified by the 208 mm amplifier (peaking to 130 J) but this will be mostly rejected by the 208 Faraday. Any residual leakage will be still in the normal polarisation state and will see gain from the 150 disc, whereas the 108 Faraday / Back Lighter Lower combination will, overall, have a loss factor of 3.5. Leakage from the double pass system will be further rejected by the Pockels cell and Faradays in the rod chain. The most vulnerable part of the system to back propagation is the area around the pre-amplifiers. With a maximum of 500 J on target, the fluence at this point would be 3 Jcm^{-2}, which is below normal damage thresholds.

References

1. J. Collier, C. Hernandez-Gomez, I N Ross, P Matousek, C Danson, J. Walczak, Applied Optics, 38, No. 36, 7486, (1999)

2. C. Hernandez-Gomez, J. Collier, S. Hawkes, C N Danson, CB Edwards, D. Pepler, I N Ross, T B Winstone, Applied Optics, 39, No.12, 1954, (2000)

3. I N Ross, J. Collier, "Improved contrast and power from a chirped pulse amplification laser system", Central Laser Facility Annual Report 1999-2000, pg 224.

Vulcan Petawatt Upgrade: The Radiological Perspective

R Allott, P Wright, C Danson, C Edwards, D Neely, P Norreys, D Rodkiss, B Wyborn

Central Laser Facility, CLRC Rutherford Appleton Laboratory, Chilton, Didcot, Oxon, OX11 0QX, UK

Main contact email address: *r.allott@rl.ac.uk*

Introduction

The Vulcan Petawatt upgrade programme in which 500 J will be delivered to target at intensities up to 10^{21} Wcm^{-2} gives Vulcan access to the next generation of high intensity plasma physics experiments. A direct consequence of these relativistic intensities is a spectrum of high energy particles and photons which constitutes a potential radiological hazard from which experimenters, visitors and other persons at RAL must be protected.

This report details the formulation of a source term for the ultra-high intensity interaction and the specification of the shielding requirements based on this source term.

Formulating a Source Term for the Interaction

The source term was generated using the following methodology. Experimental data and theoretical predictions of the gamma spectra and hot electron distributions were provided for intensities on target of 10^{19}, 10^{20}, 10^{21} Wcm^{-2}. The lower intensities were included in order to allow comparisons to be made between the calculated dose and existing experimental data. The distributions were then used to calculate the dose per shot by the application of two distinct models. One based on the hot electron distribution using formulae developed for electron accelerators and another based on simple absorbed energy considerations using the fraction of electron energy converted to bremsstrahlung.

Hot Electron Distribution

The Hot Electron Distributions for the intensity scaling are given in Table 1.

The results are based on the assumption that (a) 50% of the laser energy is converted into fast electrons and (b) the mean kinetic energy of a relativistic Maxwellian plasma is 3 times the electron temperature.

I (Wcm^{-2})	Energy on Target (J)	Energy in Hot Elec (J)	kT_{Hot} (MeV)	Av Energy (MeV)	N° Elec.
10^{19}	20	10	2	6	1.04×10^{13}
10^{20}	500	250	4	12	1.3×10^{14}
10^{21}	500	250	13	39	4×10^{13}

Table 1. Hot Electron Distributions.

The number of electrons and the hot electron temperatures given in Table 1 for the different intensities allow the electron distributions to be plotted. The integrated curve is multiplied by the total number of electrons in order to obtain the number of electrons per MeV. The results are shown for the three intensities of interest in Figure 1.

The *calculated* gamma dose per shot is given in Table 2.

The dose is given at 5 m as this is the distance to the closest occupied area and where the forward "peak" component is located. In all cases the lateral dose component is 10 - 100 x lower compared to the forward component.

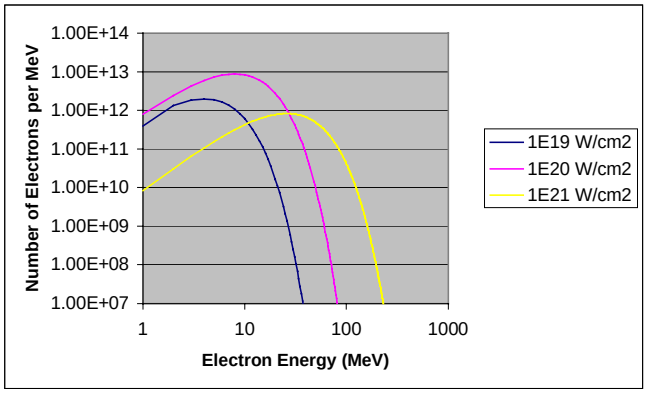

Figure 1. Hot Electron Distributions.

Intensity	Energy on Target	Distance from Target	Dose per Shot	Target Material and Thickness	Direction
10^{19} Wcm^{-2}	20 J	5 m	1 mSv	Lead 3mm	Forward Peaked
10^{20} Wcm^{-2}	500 J	5 m	40 mSv	Lead 3mm	Forward Peaked
10^{21} Wcm^{-2}	500 J	5 m	130 mSv	Lead 3mm	Forward Peaked

Table 2. Calculated Gamma Dose Per Shot.

The spectral dose in the forward cone is heavily weighted in the 1 - 10 MeV region, whereas the lateral distribution is predicted to have a much softer energy spectrum. These predictions have been verified on recent Vulcan experiments for intensities up to 10^{20} Wcm^{-2} via TLD dosimetry.

The full source term is derived by multiplying the dose per shot by the annual shot frequency. The total number of ultra-high intensity shots per year is estimated as 300, based on three experiments per year and 100 shots per experiment. Taking the highest intensity case 10^{21} Wcm^{-2} this implies a total annual dose of 39 Sv per year @ 5 m from the target in the forward direction.

This forward directed cone is of full angle ~ 30 degrees. Results from LLNL[1)] suggest that the direction of this cone varies from shot-to-shot in a random fashion within the forward 2π. Recent work at the CLF [2)] indicates that the variation in pointing is due to the level of pre-pulse. This can be controlled reliably on a shot-to-shot basis provided the laser system is performing under normal conditions. However, since a fault in the laser amplifier chain may result in a change in the pre-pulse level it must be regarded as essentially uncontrollable. In this case the full solid angle must be shielded.

This total annual dose is then used in conjunction with the maximum permissible annual dose limit in accordance with the Ionising Radiations Regulations 1999 (IRR99) in order to define the level of shielding required. The Maximum Permissible Annual Dose for a member of the public is 1 mSv (IRR99). It was decided that the design level should be a factor of 2 lower than this @ 0.5 mSv per year.

Taking the ratio of the total annual dose with the design limit gives the attenuation required which is then used to define the level of shielding.

Attenuation Required = 39 Sv / 0.5 mSv ≈ 8 x 10^4.

Neutron Dose Calculation

The neutron dose per shot is given in Table 3.

Intensity on Target	Energy on Target	Distance from Target	Dose per Shot	Direction
10^{19} Wcm^{-2}	20 J	5 m	0.000mSv	Isotropic
10^{20} Wcm^{-2}	500 J	5 m	0.065 mSv	Isotropic
10^{21} Wcm^{-2}	500 J	5 m	0.082 mSv	Isotropic

Table 3. Calculated Neutron Dose per Shot.

Calculation of the neutron dose was again by a method developed for electron accelerators and is in general agreement with the induced activity levels found on targets. The neutron energy distribution will be similar to a fission spectrum with a mean energy of ~2 MeV. In order that the neutron dose does not add significantly to the annual gamma dose the maximum permissible dose for neutrons has been set at 0.01 mSv per year. Taking the highest intensity case of 10^{21} Wcm^{-2} the Total Annual Neutron Dose is 24.6 mSv at 5m. This implies an attenuation of **24.6 mSv / 0.01 mSv ~2.5 x 10^3** is required.

Specifying Shielding Requirements Based upon the Source Term

The level of shielding required for a certain attenuation factor depends upon the shielding material and upon the energy of the ionising radiation. In this specification the gamma energy is taken as 10 MeV and the average neutron energy 2 MeV.

The shielding required to provide the appropriate level of attenuation for both gamma and neutron doses is listed below:

- Target Area Walls to be built from **60 cm concrete**.
- Target Area floor to be at least **30 cm concrete.**
- Internal shielding entirely enclosing Target Chamber (including roof): **15 cm lead backed by 10 cm high-density polythene.**
- **2 cm of aluminium** to line the inside of the target chamber to reduce radiation from scattered electrons and activation of the interaction chamber walls.

15 cm lead is equivalent to 30 cm steel at 10 MeV, so there is a considerable saving in valuable space around the interaction chamber. Although lead has a slightly higher (γ,n) cross section compared to steel, the increased secondary neutron production within the shielding material is not considered to be significant. Lead also has a lower activation threshold but there are fewer products and the decay half-lives of these products are shorter than for steel.

This shielding specification also accounts for the neutron dose due to the addition of 10 cm thick polythene which moderates and absorbs the neutrons.

Applying Shielding Requirements to the Specification and Design of the TA Building

There are a number of issues to be considered in terms of Target Area operational capacity and additional safety requirements such as laser safety and fire safety when designing the internal geometry of the target area for shielding. A diagram of the proposed TA building is shown in Figure 2.

Fire safety dictates that there are two fire escape doors in addition to the main entrance. These doors by definition have to

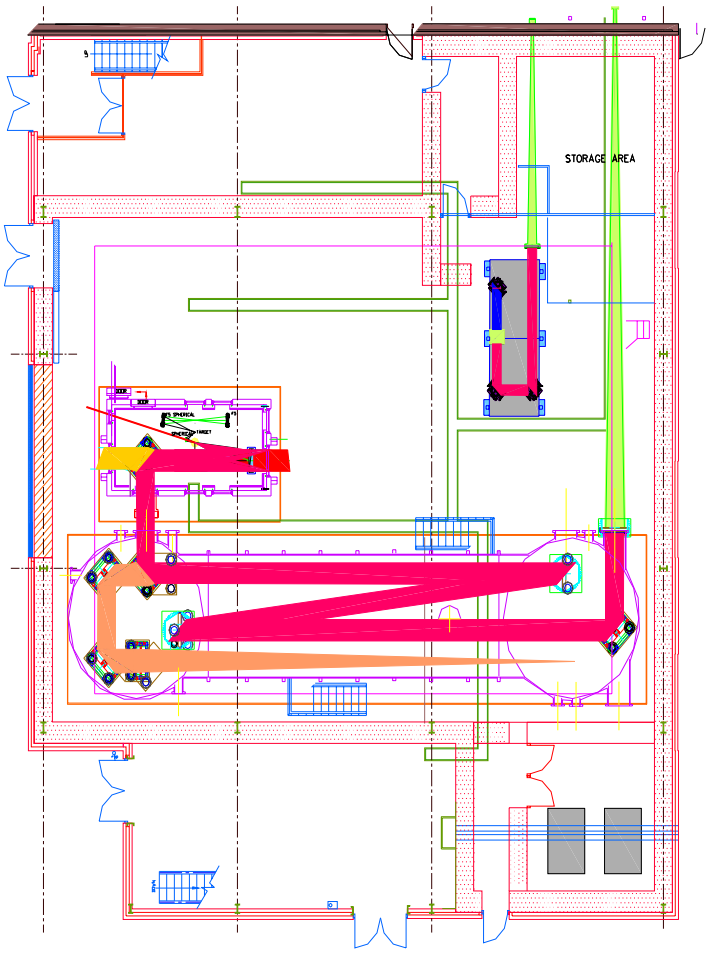

Figure 2. Possible Layout of Upgrade Target Area.

be easily accessible and opened without restriction. Such doors clearly represent a potential leakage path for ionising radiation. In order to provide the appropriate shielding a 7 cm thick lead door will be installed in front of the double access doors in the forward direction. Concrete labyrinths will be constructed in order to provide the required shielding for the main access door, the fire escape on the east wall on the ground floor and the upper level access door. The lead door will be open during occupancy of the area and then closed after shot set-up. The door will be interlocked such that it is impossible to fire a shot with it open.

The construction of a 15 cm thick lead house to enclose a target chamber of volume ~20 m^3 is a major engineering task. Consideration must be given to the manner in which the house is constructed, the provision of suitable support and the transportation of the lead. Alternative schemes whereby the shielding is positioned as close as possible to the interaction point to reduce the mass of lead required will also be considered. It is suggested that the best way to construct the housing is from standard 5 x 10 x 20 cm lead bricks. Once the lead is in place the 10 cm layer of polythene must be added and secured to the outside of the housing. Any ports required for diagnostic access must be blocked by the appropriate level of shielding behind the instrumentation. By way of good practice, the number and diameter of these ports must be kept to a minimum.

Careful consideration has been given to the design of service ducts, trenches and beam entry points. In particular the service trenches have been designed to include at least two 90^o 'dog-legs', see Figure 2. This prevents any 'direct shine' radiation escaping from the area. The duct covers adjacent to the walls should be substantial with a recommendation of 20 mm thick steel as a minimum. An internal shielding wall of 60 cm

concrete has been included to prevent direct line of sight to the points where the beams enter from the laser area.

The air conditioning and vacuum system ducts must be positioned such that there is no direct shine path to occupied areas outside the upgrade building.

Activation of Interaction Chamber and Targets

The recommendation to line the interaction chamber with 2 cm aluminium is to minimise any gamma and/or neutron activation of the target chamber. Calculations performed at LLNL indicate that for 10^{13} neutrons per shot the dose rate at the surface of an aluminium chamber wall 2 m from the interaction point would be ~10 μSv/hr. This is at least an order of magnitude more neutrons than the worst case for the upgrade. Any chamber activation would be correspondingly lower. Previous experiments on Vulcan at 10^{19} Wcm^{-2} have produced activities of 3 kBq in copper targets. With the upgrade this is anticipated to increase to ~10 MBq. A full risk assessment will be conducted incorporating safe working procedures for chamber and target activation.

Consideration of Surrounding Buildings and Areas of Occupancy

Preliminary calculations showed that "skyshine" could be significant. For this reason the philosophy of local and remote shielding was adopted to reduce skyshine and eliminate direct line of sight radiation to occupied areas.

Verification of Dose Calculations

The Petawatt laser at LLNL was capable of delivering 10^{20} Wcm^{-2} to target. Experimental results from LLNL have been used to verify the dose calculations up to 10^{20} Wcm^{-2} , the highest achievable intensity at the present time.

The highest dose per shot recorded in a "peak" forward directed cone is 20 mSv @ 1 m, for 500 J, 10^{20} Wcm^{-2} incident on a 2 mm thick gold target [3]. This is a factor of 50 lower than EWG calculated dose per shot of 1 Sv @ 1m for equivalent laser and target parameters.

However the following points should be noted:

- The calculated dose assumes 100% of energy contributes to 10^{20} Wcm^{-2} whereas in the experiment ~ 10% of the energy contributed to $I > 10^{20}$ Wcm^{-2}. Further taking into account that 50% contributes to $I > 10^{19}$ Wcm^{-2} based on reasonable assumptions of the intensity distribution these effects account for at least a factor of 5 difference.
- The calculated dose assumes that the entire dose is in the "peak" forward directed cone. The dose in the backward direction is a factor of 10 - 100 lower than the forward peak, but integrating the total dose over 4π would account for a factor of ~2 decrease.
- The calculations assume 50% conversion of laser energy into hot electrons. In the experiment the actual conversion is ~30 - 40%. This accounts for a factor of 1.5 decrease.

Taking account of all of these factors requires that the calculated dose is divided by 15 to "normalise" it to the experimental case giving ~ 65 mSv @ 1 m. This is only a factor of 3 in excess of the "peak" dose measured during experiments.

Vulcan Results

Comparison of the calculated γ dose with experimental results at 10^{19} Wcm^{-2} obtained with Vulcan show that measured values of the dose per shot are generally lower than the model predicts. A dose of ~0.5 mSv @ 1 m was recorded using TLD dosimeters in the forward direction. This is a factor of 50 lower than the calculated dose. However similar arguments can be applied to "normalise" this to the conditions assumed in the calculations.

Very recent results on Vulcan using TLD detectors to define the absolute dose and angular distribution are in strong support of the calculations. Here 10 - 20 mSv @ 1 m was measured in a forward cone of 30^{o} angle (FWHM) at 10^{20} Wcm^{-2} with ~ 90 J on target.

Conclusion

The philosophy and recommendations contained within this report is such that visiting scientists will not be required to be classified radiation workers. The shielding design is such that the occupied areas surrounding the upgrade target area do not have to be declared as controlled or supervised radiation areas. By distributing the shielding between the walls and chamber, experimental flexibility is maintained in a cost effective manner.

References

1. Perry *et al* Rev. Sci. Instrum., 70, 265, (1999)
2. Norreys *et al*, Phys Plasmas, 6, 2150, (1999)
3. Private Communication with LLNL Staff, (1999)

Vulcan Petawatt Upgrade Chamber Specification

D Neely, R Allott, C Danson, C Edwards, A MacPhee, P Hatton, P Norreys, D Rodkiss, B Wyborn

Central Laser Facility, CLRC Rutherford Appleton Laboratory, Chilton, Didcot, Oxon, OX11 0QX, UK

Main contact email address: *D.Neely@rl.ac.uk*

Introduction

The petawatt (PW) upgrade to the Vulcan laser facility will deliver a 500 J, 500 fs near diffraction limited interaction beam to target. The project covers the construction of a new target area and the necessary laser and interaction facilities. This report outlines the experimental and operational requirements for the PW interaction chamber. It has been compiled through substantial discussion with the UK High Power Laser user community and CLF staff.

The target area is required to deliver suitable facilities for experiments envisaged using the 600 mm diameter PW beam. It must also be compatible with an upgrade strategy involving primarily high energy synchronous long pulse beams and additional probing beams. The interaction facility is designed on a 'do not preclude' basis within the spending envelope of the grant.

The experiments which the new facility will accommodate cover a broad range of topics including; particle acceleration, overdense propagation, solid target interactions, nuclear interactions, magnetic field generation and measurement, X-ray lasers, harmonic and particle production, particle probing, fast ignitor studies, X-ray scattering, high field physics and astrophysically relevant studies. In each category of experiment the users provided an outline of the required laser and experimental interaction conditions.

Choice of Focusing Optic

Several distinct focusing requirements for the main PW beam were identified. These included: on and off-axis with maximum possible intensity; travelling wave line focus; double sided illumination; and long Rayleigh range.

Discussions with optical manufacturers indicated that F/1.5 was the smallest F number on-axis parabola that could be cost-effectively manufactured to achieve the required reflected wave front accuracy i.e. 0.9 m focal length. Such an optic would deliver the highest possible irradiance. However, it would also be the most likely to suffer debris damage from material ejected from the interaction region. Also, as the interaction point is situated in the middle of the incident beam this option poses the most restricted diagnostic access and would have the tightest and most difficult alignment tolerances to achieve. The optic would be unsuitable for a significant number of experimental investigations and would therefore have limited applicability.

The smallest F number off-axis parabola has a diagnostic and laser requirement for the beam after it passes through focus. The off-axis distance must scale with the focal length such that it is sufficient to allow good access to the transmitted photons or generated particles. Through engineering design studies of the experimental geometries and discussions with optical manufacturers a final specification was drawn up for such an optic. The recommended focal length and off-axis distance for the F/3.1 off-axis parabola (OAP) is 1.8 m and 0.450 m respectively.

The F/3.1 OAP is the first choice for the majority of experimental configurations and is an acceptable initial substitute for the highest interaction intensity experiments. It has therefore been recommended that a single F/3.1 parabola be acquired on the project and an F/1.5 parabola be purchased at a later date through additional grant funding. The design of the interaction chamber is such that it can accommodate all experimental geometries involving an F/1.5 on-axis parabola.

Achieving interactions lengths over ~ cm scales, with near planar wavefronts and almost uniform peak intensities necessitates using focusing optics with large F numbers. Table 1 shows the range of focusing conditions, which could be achieved within the physical constraints of the building. The table also demonstrates that a focusing optic with an F number of 50 to 100 would be required to achieve a ~cm Rayleigh ranges. Such an optic would have a focal length of 30 to 60 m and could not be fitted within the target area even if the beam was folded back on itself due to optical damage considerations. A novel idea is to use small ~ 50 mm diameter spherical optics to reimage and magnify the focal spot. Such optics are low cost and although they would have to be replaced on every shot they would permit conditions to be achieved otherwise impossible within the area. These optics could be dielectric coated either to act as high efficiency mirrors or plasma mirrors. Such disposable optics could also be used to achieve a travelling wave line focus and double sided illumination. The necessary facilities for using such advanced optical designs are included within the target chamber design.

F number	**Diameter μm**	**Raleigh range mm**	**Intensity W/cm^2 /10^{19}**
3.1	5	0.03	130
15	24	0.7	6
30	40	3	1.4
50	80	8	0.5
100	160	32	0.1

Table 1. Spot diameter D, and interaction Raleigh length R and Intensity I obtained using different F/# illumination optics.

Beam requirements

The PW CPA beam will have a duration of 500 fs or less and contain 500 J of energy. In the majority of experiments it will have a bandwidth of ~4 nm centered at 1054 nm. Optimal pulse compression of the system will be achieved by tuning the stretcher and diagnosing the compressed pulse. The diagnostic beam will be obtained from a leakage through a dielectric mirror prior to the interaction chamber. To avoid non-linear effects reflective optics situated within a vacuum system will be used to deliver and focus the beam onto the target.

To deliver a 500 J, 500 fs compressed beam using existing gold coated grating technology requires a beam diameter of 600 mm necessary because of the grating damage threshold.

Some future experiments will benefit from the delivery of a frequency doubled beam of high contrast. To obtain high contrast between the doubled and unconverted components, Type 1 doubling is recommended as the components are orthogonally polarised and reflection from four ~45° mirrors would be adequate. Tests have already demonstrated that a 2 mm KDP crystal will produce high conversion efficiency for CPA pulses. At present manufacturing techniques could not produce a single crystal of sufficient size to cover the whole

beam. However, a segmented array is within current manufacturing and technological capabilities. The interaction and compressor design should include a configuration compatible with delivering a frequency doubled beam.

The CPA beam will be highly linearly polarised. By inserting a suitable waveplate at a future date, the polarisation of the beam can be controlled.

Both the waveplate and frequency doubling crystal are transmissive optics that may be required in the compressed CPA beam line in future. These optics should be locatable within the compression chamber.

Additional beam requirements

The present Vulcan CPA user experimental campaigns rely on the provision of multiple synchronous short and long pulses. These beams have a variety of uses, from probing the interaction region to pre-heating and achieving suitable plasma conditions for the main CPA beam. It is essential that the PW Target Area and chamber is designed such that additional beams can be accommodated in future upgrades of the facility. Details of the additional user beam requirements are given below in Table 2.

Access to inject a long pulse beam through the back of the last turning mirror within the compressor chamber should be included within the area design.

Beam Type	**Details**	**Technical requirement**
Long pulse	2 x 108 minimum requirement upgradable to 2 x 208	500 J Total, 1 ns 2 kJ Total, 1 ns 1ω, 2ω, 3ω
Second CPA probe beam	108 beam capable of being doubled/Raman shifted	5 J, 1 ps 20 J, 10 ps 50J, 100 ps
Long pulse probe	108 beam	50 J, 100 ps - 1 ns 2ω, 3ω, 4ω
Pre-pulse options	Ability to have variable pre-pulse options for all configurations	
Long pulse for target cleaning		20-100 ns, 10 J ~ns, < 1J, 2ω
Optical trigger	Low energy CPA probe	1 ps, delivered up to 80 ns before main CPA pulse

Table 2. Additional beam requirements.

Alignment

A full aperture 1054 nm CW alignment beam must be provided for off line alignment in the target area. To minimise costs this beam should be injected when the CPA beam aperture is < ϕ208 mm. To accurately set collimation of this beam the output collimating lens of the injection system should be on a micrometer controlled stage with the option of upgrading to motorized control at a later date. The beam should be independent of the main Vulcan amplification chain and should be controllable from the target area. The beam should have variable power over the range 100 mW to 1 μW.

Access to the retro reflected beam from the target plane must be provided for alignment and diagnostic purposes. To minimise costs, access when the beam aperture is ϕ208 mm should be made available. An access port to the reflected undiffracted beam from the first grating as the beam travels back up the system from the target is also included within the design of the area.

Petawatt laser diagnostics

A full range of petawatt beam laser diagnostics should be provided on every shot. The characteristics to be measured are energy, pulse duration, bandwidth, minimal focal spot size, focal location and energy distribution. Additional diagnostics such as contrast and pulse fidelity should be considered for addition as soon as financially possible.

Debris issues

Target debris on full energy shots will be a significant issue in the upgrade. The technology for producing thin (between 0.1 and 3 mm) sufficient quality protective optics over the full petawatt beam aperture is not readily available. Effort to obtain such optics or suitable alternatives will be made at a later date. To minimise the potential amount of material, which could propagate towards an optic, special consideration to target design will be made.

Design philosophy

After evaluating a number of design strategies it was decided to adopt many of the successful ideas incorporated into Target Area West and include them within the context of the Petawatt upgrade.

- Internal optics, diagnostics and alignment systems should be mounted from a vacuum stable platform.
- The interaction point should be movable and located to give maximum experimental benefit in each required geometry within the environmental recommendation limits.
- Good experimental and diagnostic access must be provided and the chamber must be capable of adapting to and meeting new experimental configurations.
- The compressor and interaction chambers should be vacuum isolated using a gate valve, which can accommodate an alignment beam when access to the interaction chamber is required.

Interaction vessel

After reviewing a number of possible layouts it was decided that the chamber will be rectangular: 5 m long, ~2.2 m wide and ~2 m high. This design was arrived at after considering the experimental and operational requirements of the upgrade project and is considered the most satisfactory, as it most readily fulfils the upgrade requirements within the available budget.

Geometric considerations

To satisfy environmental requirements the interaction chamber should contain a turning mirror within it to eliminate the direct line of sight from the interaction point to the input port. In combination with the turning mirror, suitable shielding will also be located within the chamber to block the line of sight to the laser beam entrance. The chamber has also been designed to house an internal Al shield and external lead and plastic shielding. The locus of possible interaction points must satisfy the requirements of the environmental working group report, which stipulates the possible locations.

The chamber must be capable of providing a number of different geometries to cater for the diverse experimental requirements. The three main examples of these are shown in Figure 1.

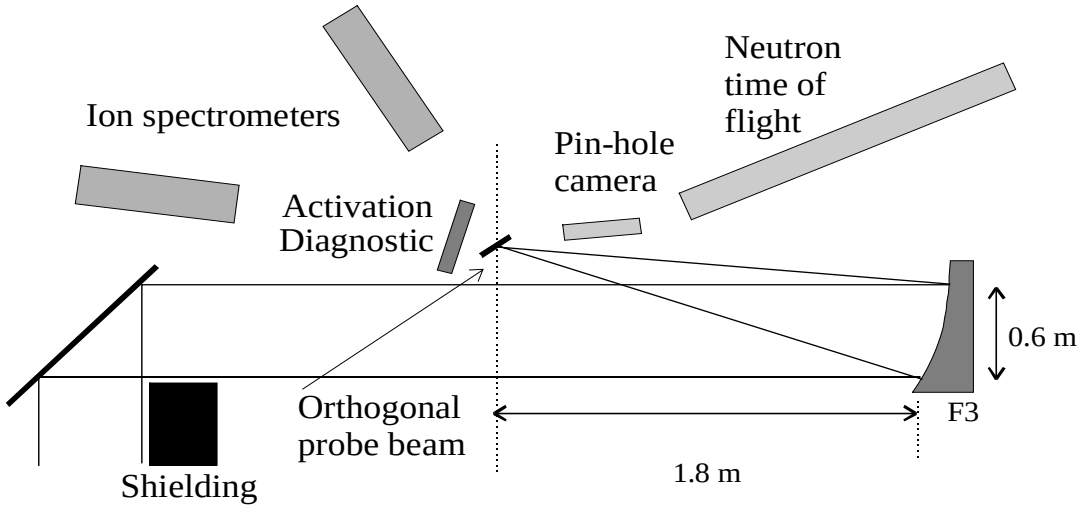

Figure 1(a). Solid target experimental set-up using an F/3.1 off-axis parabola.

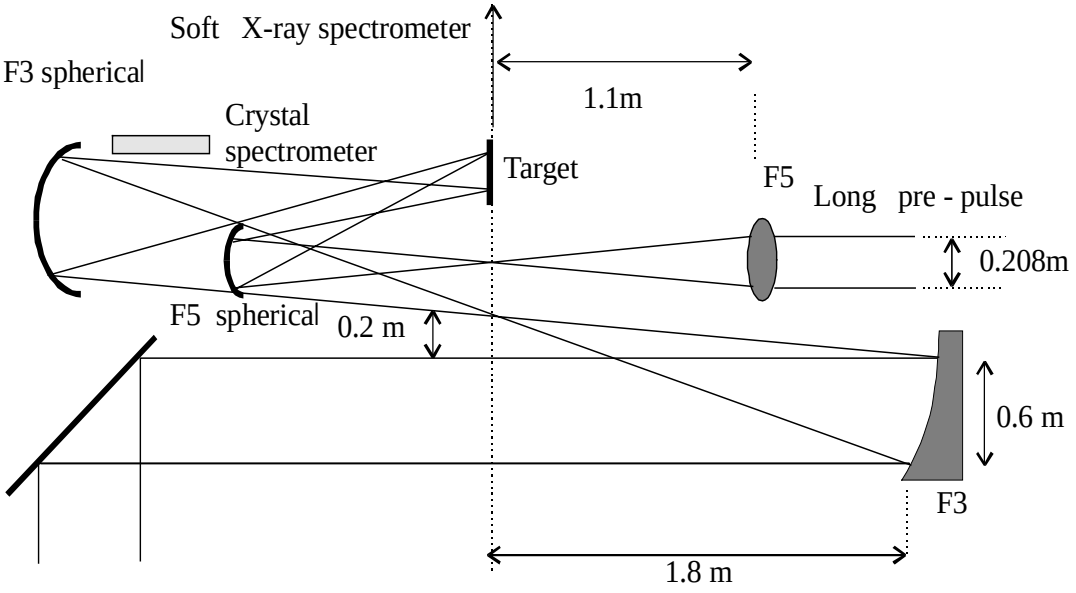

Figure 1(b). X-ray laser geometry using F/3.1 OAP and a Large spherical mirror.

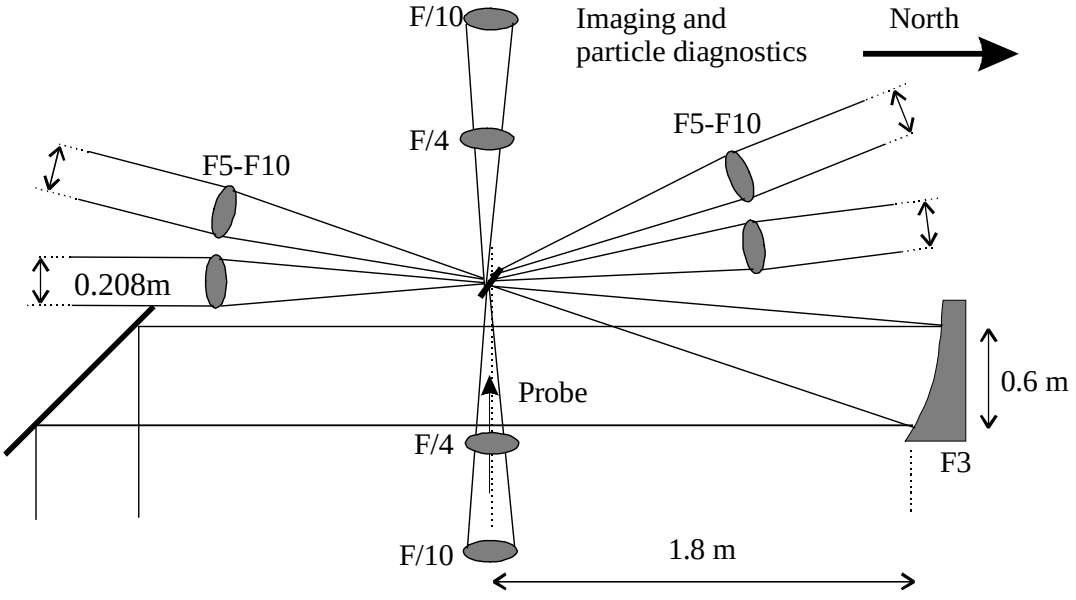

Figure 1(c). Combined F/3.1 OAP and long pulse interaction geometry.

For solid and gas target high intensity interactions a geometry similar to that in Figure 1(a) is used. This geometry is based on using a ϕ 600 mm F/3.1 off-axis parabola to generate a suitable focal spot for solid target interaction experiments. A synchronous ϕ 50 mm frequency shifted probe pulse is required to diagnose the plasma interaction. Co-axial beam illumination may also be required in some cases.

The travelling wave x-ray laser geometry shown in Figure 1(b) is based on using a combination of ϕ 600 mm F/3.1 parabola and ϕ 600 mm F/3.1 off-axis spherical mirror to generate a 10 - 20 mm line focus. A ϕ 208 mm F5 lens and off-axis spherical mirror are used to generate an overlapping long-pulse line focus to pre-form the plasma. Due to the requirements for the 208 mm beam to generate a 20 mm focus the 208 beam will be brought in above the parabola at about 20 degrees to the horizontal. The geometry of bringing the long pulse beam in on the horizontal from the other side of the target was examined and rejected, as it requires an additional 0.4 m width to be added onto the chamber.

The multi-beam geometry shown in Figure 1(c) is based on using a ϕ 600 mm F/3.1 off-axis parabola and two synchronous long pulse beams to generate a suitable focal spot for interaction with long scale length, shocked, Hohlraum or driven plasma. The long pulse beams may come in a number of different geometries depending on the exact experimental requirements. In the above diagram a number of the options for the two ϕ 208 mm beams are shown. In the case of beams transverse to the CPA axis (East-West) if the long pulse focusing lens is to be housed within the chamber an F/4 to F/5 lens can be used or ports are present to allow F/10s to be housed externally. With the energy being deposited on the target, great care must be taken to minimise debris damage, possibly requiring the use of plasma mirrors. An optical probe would be required but its direction would strongly depend on the experimental geometry. In some cases the above geometry would be used with an on-axis parabola but the F/3.1 would be the principal choice for focusing optic due to the better diagnostic access.

Control system requirements

An external drive system will be provided for moving the parabola, target mount, additional XYZ translation units, diagnostic shutters and insertion mechanism. Provision for electronically monitoring the position of the translation units should be provided. In the case of the parabola mount, angular alignment sensitivity of 10 μrad is required and for the target mount, micron position accuracy is required.

Trenches link the chamber and a control desk and user control room, permitting diagnostic monitoring and control externally to the area.

Diagnostics

The interaction chamber and area must be designed to facilitate the use of the following diagnostics: Pinhole and penumbral imaging cameras; Crystal spectrometers; Grazing incidence soft X-ray spectrometers; Protons, Neutrons and ions detectors; X-ray and γ-ray measurements; Probe beams for interferometry, shadowography and schlieren deflectometry and optical emission and laser scatter.

Vacuum system requirements

A suitable vacuum environment is required in the interaction chamber for the propagation of the Petawatt beam, radiation, particles and the use of certain targets and diagnostics. Adequate ports have been provided on the chamber to ultimately meet pumping timescales of: 10^{-3} Torr in 15 minutes; 10^{-4} Torr in 1 hour; 10^{-5} Torr in 24 hours; and with a let up time of 15 minutes.

The recommended approach for diagnostics requiring 10^{-4} Torr or better is that the interaction chamber should be maintained under vacuum for a number of shots or that secondary localised pumping units be used. An additional important requirement in terms of stability is that the vacuum system components should not introduce vibrations into the interaction chamber sufficient to affect beam pointing.

Ports and access doors

Sufficient and adequate ports to meet the beam and diagnostic experimental requirements must be provided. An additional port capable of housing a vacuum insertion mechanism has been provided. The chamber has three hinged door ports to meet access requirements. The roof of the chamber has two large ports for inserting or replacing the parabola or turning mirror. These ports are located to minimise the amount of disruption caused by replacing an optic during an experiment. One wall of the chamber is detachable to facilitate placing large mechanical items within the chamber. Adequate ports have been provided for the vacuum system. These ports should be situated to facilitate the minimum conduit length between the ports and the backing/roughing system. There are adequate ports for electrical control and diagnostic feed-throughs. To minimise EM noise pickup, these ports should be optimally situated around the chamber. Two of these ports are situated in close proximity to the service ducts.

Mounting and stability issues

A stable base for mounting the optics, target, alignment systems and diagnostics within the vacuum chamber must be provided. The bottom of the chamber will be bolted to the concrete plug, which should restrict relative movement of components to less than 4 microns.

Building issues

A double door through which a 1.5 m wide surface table could be moved into the area should be provided to allow the movement of large diagnostics to and from the area. The slope of the ramp through this door should be minimised to allow easy movement of heavy objects.

In light of the increasing use of CR39 radio-chromic film, X-ray film, activation and thermoluminescent detectors automatic developers and analysis units should be allocated space close to the target areas for a dedicated facility.

Conclusion

Through substantial discussions with the UK high intensity laser interaction user community, a detailed Petawatt interaction target chamber specification has been drawn up. A rectangular interaction chamber of ~ 20 m^3 volume has been designed to meet the wide variety of Petawatt user experimental requirements. A future report will give details of the interaction vessel geometry and engineering considerations involved in its design, manufacture and commissioning. A tender exercise for this chamber is currently underway.

Building Design for Vulcan Petawatt Upgrade

B E Wyborn, S Hancock, C N Danson, R M Allott, D Neely, D A Rodkiss, R W W Wyatt, C B Edwards
Central Laser Facility, CLRC Rutherford Appleton Laboratory, Chilton, Didcot, Oxon, OX11 0QX, UK

R J Mason, J Skrzyniarz, R Lascelles, J P H Bradley, J M Henstridge
Engineering Department, CLRC Rutherford Appleton Laboratory, Chilton, Didcot, Oxon, OX11 0QX, UK

Main contact email address: *B.E.Wyborn@rl.ac.uk*

Introduction

This article sets out the design of the building and services for the Vulcan Petawatt Upgrade Project.

The building and services have been designed to be capable of meeting the needs of multi-users for a wide variety of experiments. They will be constructed to a baseline specification and may in future years be modified and expanded as necessary. Where possible the buildings and services have been designed to accommodate these possible changes and use has been made of existing buildings and facilities.

The building plan is shown in Figure 1 and is described in more detail in the following sections.

Modifications to existing buildings and services

The wall between Laser Area 3 and Target Area 2 will be removed to make the areas contiguous. This will necessitate the re-siting of some air conditioning plant and the YLF Oscillator Room will be truncated by about 1m.

The stairs over Target Area 2 from the Vulcan Control Room to the South Control Room will be moved, and the wall between Target Area 2 and the Users Area removed to make the areas contiguous and form the new Laser Area 4 (LA4).

Target Area 2 already has air conditioning and clean air plant but other existing Vulcan services such as cooling water and N_2 systems will need to be modified.

An area of the mezzanine storage area above the new LA4 will be partitioned off to form a corridor from the South Control Room to the new Target Area Control Room 2nd floor.

New buildings and services

The following features have been incorporated into the design of the buildings and services:

- The ability to bring long pulses from Vulcan to the new Target Area in the future;
- The provision of satisfactory means of ingress and egress and convenient routes between areas as necessary for both personnel and equipment, including emergency situations;
- The provision of conveniently sited services, and equipment removal, storage and maintenance space.

The new building will be approximately 21.5 m x 24.5 m in size. It will consist of a brick faced external skin with insulated cavity walls, a concrete inner skin around the new Target Area and an aluminium skin roof. Entrance and escape doors will be provided as shown. Adequate emergency lighting and fire alarms will be incorporated. Finishes will consist of heavy duty vinyl tiling to all floors except plant rooms which will be painted concrete; plastic coated suspended ceilings to all areas except plant rooms which will have exposed roof deck; painted plaster walls to all areas except plant rooms which will be painted concrete.

The new Target Area will be built to a standard similar to the existing Target Area West (TAW) and Target Area East (TAE). The floor will be concrete covered with heavy-duty vinyl tiling incorporating 0.3 m x 0.3 m service ducts as shown. Two 1m deep ultra stable concrete plinths will be installed for the compression chamber and target chamber respectively. The area will be air conditioned to 20^0C ± 1 and have clean air plant designed to operate at Class 100,000. A remotely controlled 5 T crane with a hook height of 4.3 m will be installed. Lighting will be similar to existing in TAW and TAE with additional dimmable fluorescent (low infrared) corner lighting. An adequate number of power distribution outlets will be installed. There will be a temporary panel left in the south wall to allow installation of the large Compression and Target Chambers after the building is complete. This opening will be sealed up after the equipment has been installed.

A new Control Room will be built immediately adjacent to the new Target Area. It will be a 2-storey area with stairs between. Air conditioning, lighting, power, telephone and data outlets will be similar to the existing South Control Room. It will incorporate viewing and storage areas on the 2nd floor and space for instrumentation areas, dark rooms and user rooms. In the initial build these rooms will be omitted.

The new Plant Room will be a 2-storey area. Downstairs will be for the CLF plant i.e. vacuum plant, compressed air / N_2 let up system, cooling water etc. and upstairs for the site services plant ie HVAC, electrical distribution etc.

A single lane diverted road and footpath to the south of the new Target Area will be included and the site electrical supply and fire alarm systems will need to be extended.

The following building requirements for radiation protection have been included:

- Internal walls are a mixture of 0.6 m cast in situ concrete or concrete blocks all round. The walls will be 6.5 m high to prevent direct shine onto surrounding buildings.
- Access doors are shielded via concrete labyrinths apart from the double door in the south side of the Target Area which will have an additional door equivalent to 7cm lead installed.
- No special roof is necessary.
- The service ducting will have doglegs in it as shown.
- The control room and ancillary rooms are outside the radiation area and will be shielded fully from the new Target Area.
- The viewing area and storage area on the 2nd floor are inside the radiation area and therefore will have interlocked door access.
- The Target Area floor will be at least 30 cm thick concrete.

Programme

The building work has been programmed to minimise down time and disruption to Vulcan operations.

Vibration caused by the building work may cause a problem for the CLF's ongoing experimental programme therefore digging foundations, knocking through holes in walls etc. will be scheduled in silent hours or in Vulcan maintenance or set up weeks in preference to experimental weeks.

Initial building work commenced at Christmas 1999. The building will be weather-tight by 1st September 2000 and complete with all services by 1st January 2001.

Figure 2 shows building progress as at the end of March 2000 and Figure 3 is an impression of what the final building will look like in 2001.

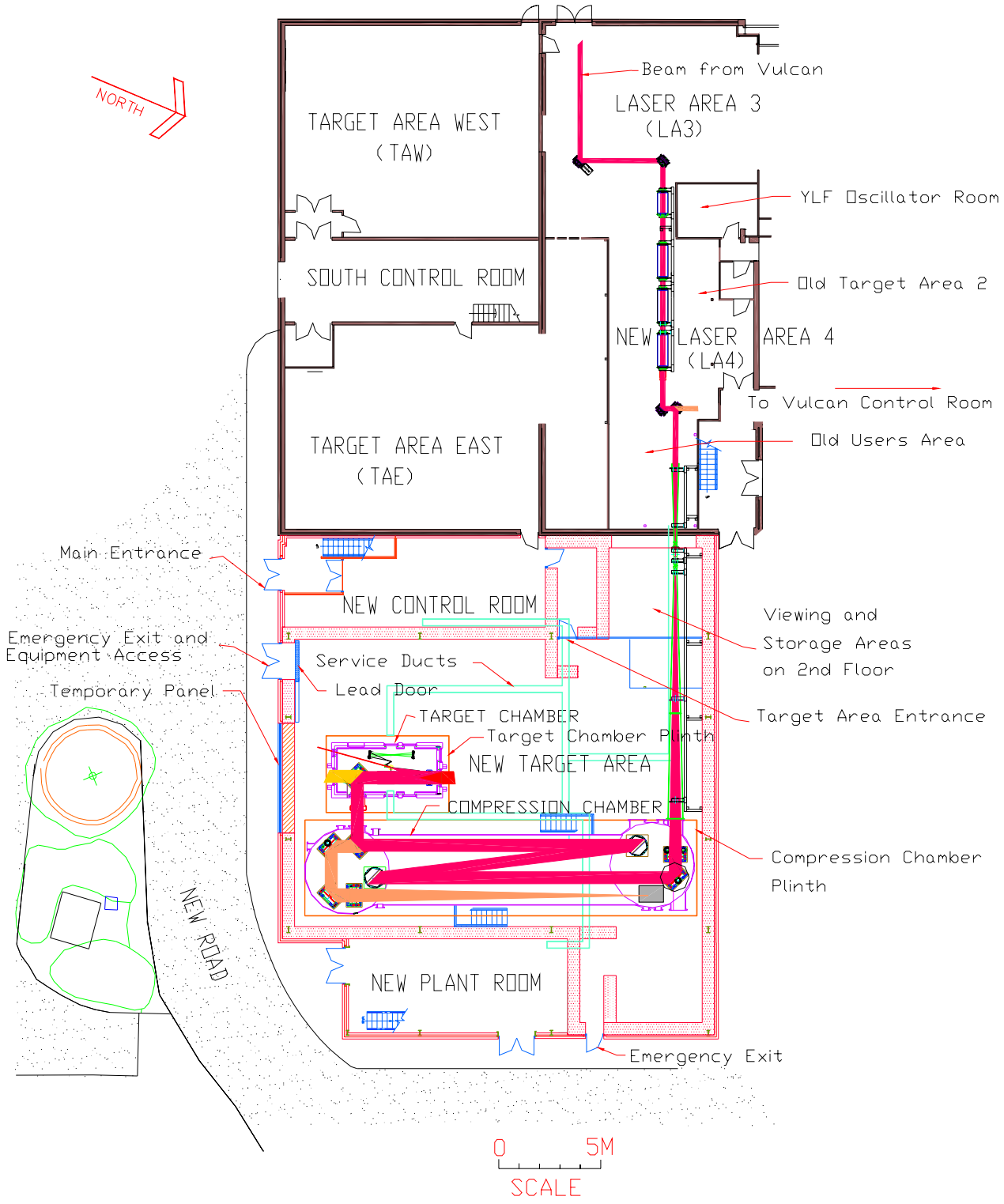

Figure 1. Plan of Vulcan Petawatt Building.

Figure 2. Progress on Vulcan Petawatt Building as at the end of March 2000.

Figure 3. Impression of finished Vulcan Petawatt building.

Gain Measurements on a 208 mm Amplifier

D Pepler, C Danson, J Collier, C Edwards, S Hawkes, A Kidd, T Spencer, T Winstone, R Wyatt

Central Laser Facility, CLRC Rutherford Appleton Laboratory, Chilton, Didcot, Oxon, OX11 0QX, UK

Main contact email address: *D.A.Pepler@rl.ac.uk*

Introduction

The disc amplifiers used on Vulcan at 108 mm and 150 mm aperture, originally to US design, were modified some years ago to operate with larger bore lamps and fewer lamp circuits. This design has proved to be very efficient and reliable over many years of operation. It was proposed to modify the ex-NOVA 208 mm amplifiers, operating with 8 lamp circuits, for compatibility with Vulcan's existing amplifiers and to operate them with 4 lamp circuits. The first amplifier has been modified and its performance tested on one of the Vulcan beam-lines.

Experimental Set-up

In order to measure the saturated gain of the 208 mm amplifier an apodised beam of 90 mm diameter was generated using the 150 mm lower beamline of Vulcan. The beam was directed from the end of laser area three (LA3) through the 208 mm amplifier, (which was situated in LA2) and the resultant beam energy measured by a whole-beam calorimeter situated further 'downstream'.

Figure 1 shows a photograph of the basic 208 mm amplifier under test, alongside the standard 150 mm amplifiers. This was a convenient position to test the amplifier as, firstly, the 208 mm amplifier was to be powered from the 150 mm amplifier supply, and the power supply contacts are situated here, secondly, the beamline was easy to arrange and thirdly, it allowed the normal system calorimetry to be used for the 150 Lower beamline.

Figure 2 shows a schematic of the test arrangement from the end of the rod amplifier chain of Vulcan through the standard 108 mm and 150 mm disc amplifiers and into the 208 mm disc and whole-beam calorimeter. The calorimeter was situated several meters away from the 208 mm amplifier in order to reduce the amount of fluorescence and amplified spontaneous emission (ASE) that it would see. A circular apodiser approximately 40 mm in diameter was placed before the 108 mm to 150 mm expanding Vacuum Spatial Filter (VSF). This compensates for the magnification of the following VSFs, bringing the beam up to the required 90 mm diameter.

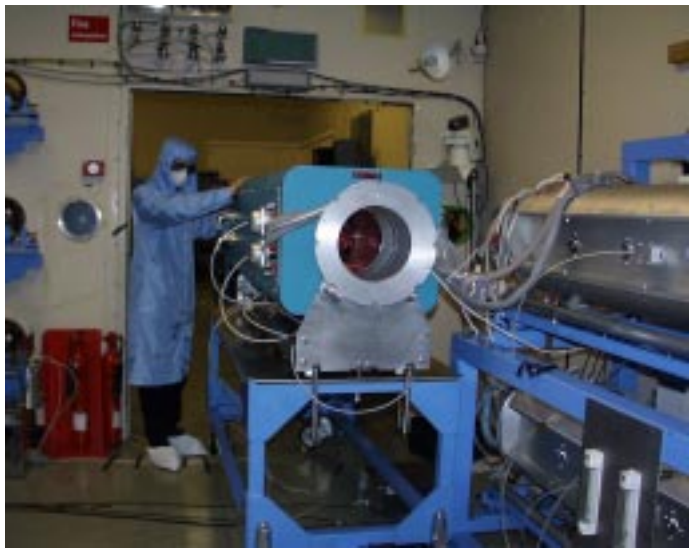

Figure 1. The 208 mm amplifier during gain tests on Vulcan.

Experimental Results

The data obtained has been corrected for the small energy offset of the ASE level on both calorimeters and for cross calibration effects and the final gain profile is shown in Figure 3. The 90 mm beam is a quarter of the area of the full beam size that will be used in the upgrade and this is shown in the graphs by normalising to 'equivalent beam energy'. The solid line on the graph is a best-fit curve using a saturation fluence of 4 J cm^{-2}. From this data, a small signal gain of 2.23 is obtained which reduces to a saturated gain (at 670 J output) in excess of 1.90. This is well above the minimum necessary to achieve the Petawatt design specification which is based on a small signal gain of 2.0, and exceeds expectations.

Operational Issues

Currently, laser operations require individual beams to have independent control of the amplifier gain in order to meet certain experimental requirements. This has normally been achieved through the deliberate delaying of the ignitron firing time for each amplifier (typically in the range 0 - 300 µs). An alternative method might be to reduce the firing voltage of the flashlamps in order to reduce the pumping and hence the gain. As the capacitor bank power supply is to be upgraded prior to installation of the 208 mm amplifiers these gain reducing mechanisms were investigated as part of the power supply specifications.

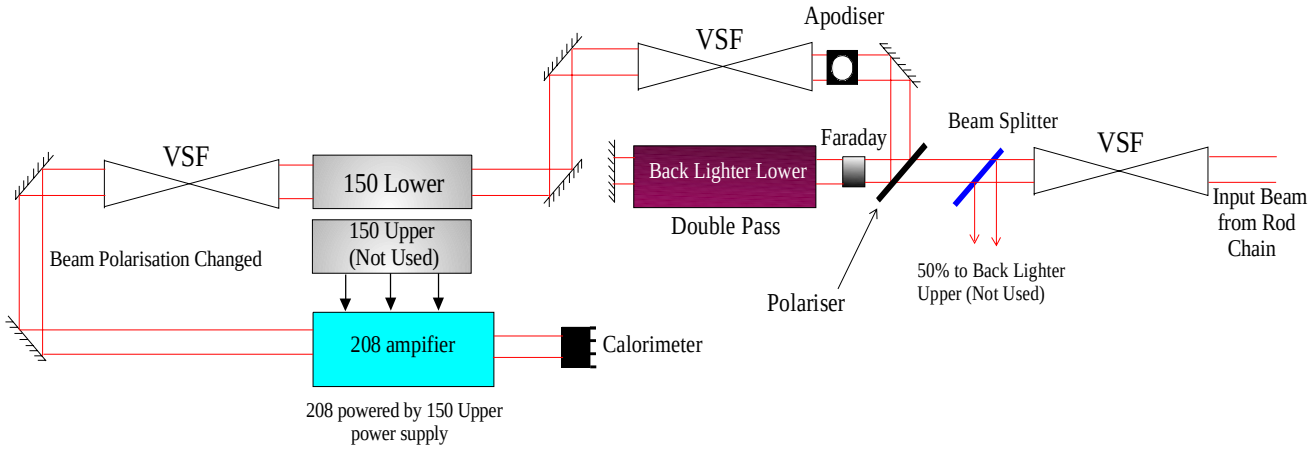

Figure 2. Schematic of the beamline used for the 208 mm amplifier gain measurements.

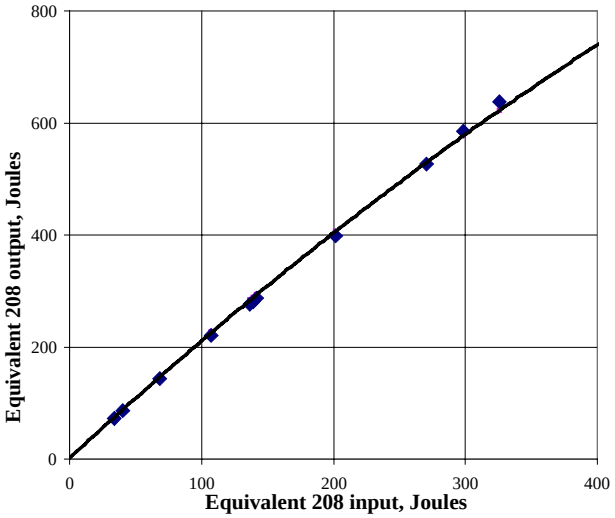

Figure 3. Input / Output performance of the modified 208 mm amplifier.

Ignitron Delay

The ignitron delays are simply achieved through computer control associated with the capacitor control system which is based on CAMAC. Every amplifier has an independent channel in a CAMAC module providing 0 to 1 ms delays in single microsecond steps. These signals then feed units to trigger the ignitron for each amplifier. Although it is usual to delay an amplifier to reduce gain, because of an inherent 400 μs bias in the trigger timing, it is actually possible to fire each amplifier up to 400 μs early. This is shown in Figure 4 which demonstrates the normalised gain profile of the standard 108 mm disc amplifier system. Although as stated this is using the standard disc amplifier system, the purpose of this test is to demonstrate both the principle of the technique and that the electronics built to control this function for the 208 mm amplifier actually works. This clearly is the case.

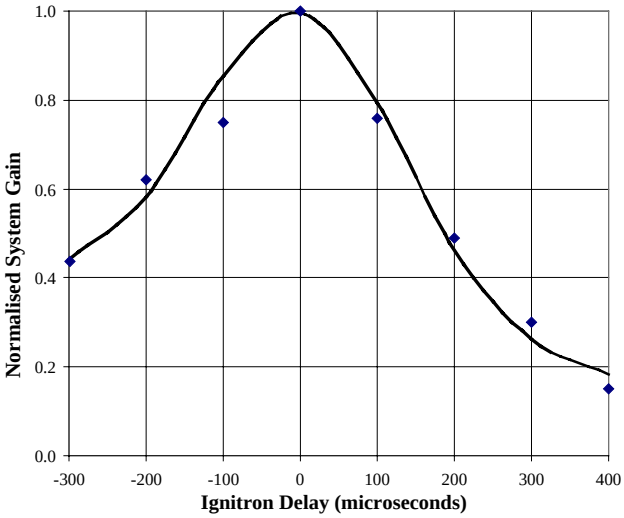

Figure 4. Normalised gain profile of the 108 mm amplifier system.

Voltage Reduction

The firing voltage of the disc amplifiers is normally 20 kV with a bank of between 2 and 6 amplifiers being fired from the same power supply unit (PSU). The new PSUs are modular with an individual PSU per amplifier so voltage reduction is possible on a more selective basis. Obviously as the voltage reduces the amount of energy available for pumping reduces, thus resulting in less gain. The single pass gains of a 108 mm and of a 150 mm disc amplifier are different so one would expect differences in these gains for the same voltage reduction.

As the voltage is reduced one ultimately reaches a point where the flashlamps no longer fire reliably. This point is approximately 12 kV, with 15 kV being chosen as a working lower limit.

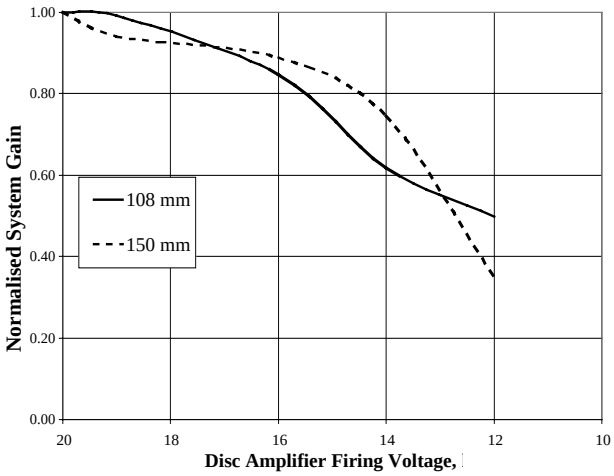

Figure 5. Graph demonstrating reduced system gain with decreasing firing voltage for the 108 mm and 150 mm diameter disc amplifiers.

As shown in Figure 5, from 20 kV down to 15 kV there is a gradual reduction in useable gain with the 108 mm amplifier losing approximately 25% (solid line) and the 150 mm amplifier about 15% (dotted line).

As the individual 208 mm amplifier modules have even smaller gain coefficients than that of the 150 mm amplifier, it seems likely that the gain reduction for the 208 mm amplifier would be small.

Conclusion

The modifications to the flashlamp arrangements in the 208 mm amplifier has been shown to be viable, giving higher than expected saturated gain (1.90).

The gain reduction techniques demonstrated here show that small differences (10% - 15%) in beamline energy balance can be accommodated with voltage reduction but that a higher degree and depth of control is achieved with the ignitron delay changes. This latter technique is thus the main gain reduction mechanism to be used on the 208 mm amplifier controls.

High Voltage Test Bank for Vulcan Petawatt Upgrade

R Wyatt, C Aldis, C Danson, B Eltham, J Govans, B Gray, S Hancock, P Holligan, A Jackson, A Kidd, T Knott, W Lester, D Neville, M Pitts, C Reason, D Rodkiss, K Rogers, J Theede, G Warner, G Wiggins, B Wyborn

Central Laser Facility, CLRC Rutherford Appleton Laboratory, Chilton, Didcot, Oxon, OX11 0QX, UK

N Symcox

Hickmans, Electrical Engineers and Contractors Ltd., Swindon, Wilts., SN1 4DE

Main contact email address: *R.Wyatt@rl.ac.uk*

March 31st 2000 saw the completion of an important milestone in the Petawatt programme - the successful charging to 20 kV of a HV test bank for the powering of disc amplifiers. An essential part of the upgrade is the smooth transition between the decommissioning of the existing capacitor banks and the installation of the new higher density storage banks. The test bank will allow the off-line testing of power supplies, charging units, computer control, capacitor storage banks, triggering circuits, and Pulse Forming Networks (PFNs), as well as the amplifiers themselves.

The bank was constructed using ex-NOVA capacitors, ignitrons and new, purpose designed charging units. When fully commissioned, the test bank will verify the new design for the capacitor banks which enables the pulsed power requirements of the upgrade to fit into the Vulcan capacitor room. The test bank is shown in Figure 1. It consists of two amplifier circuits of ~200 kJ each and will allow each to be tested individually and in parallel.

A block diagram showing the basic pulsed power circuit is shown in Figure 2. The control, charging and monitoring of the bank is performed using a PC which communicates through a Camac system to the power supplies and interlock system.

The power supplies were specially designed for the Vulcan installation and manufactured by Universal Voltronics in the US. The charging system, which is modular and designed for low maintenance, replaces the obsolete hardware currently used in the Vulcan capacitor room as well as providing for the upgrade.

Each amplifier is charged from a single unit which has independent control of the charging voltage up to 22 kV and the ignitron triggering delay. This will give improved control of the beam balance.

Figure 1. Pulsed power test bank assembled using NOVA components.

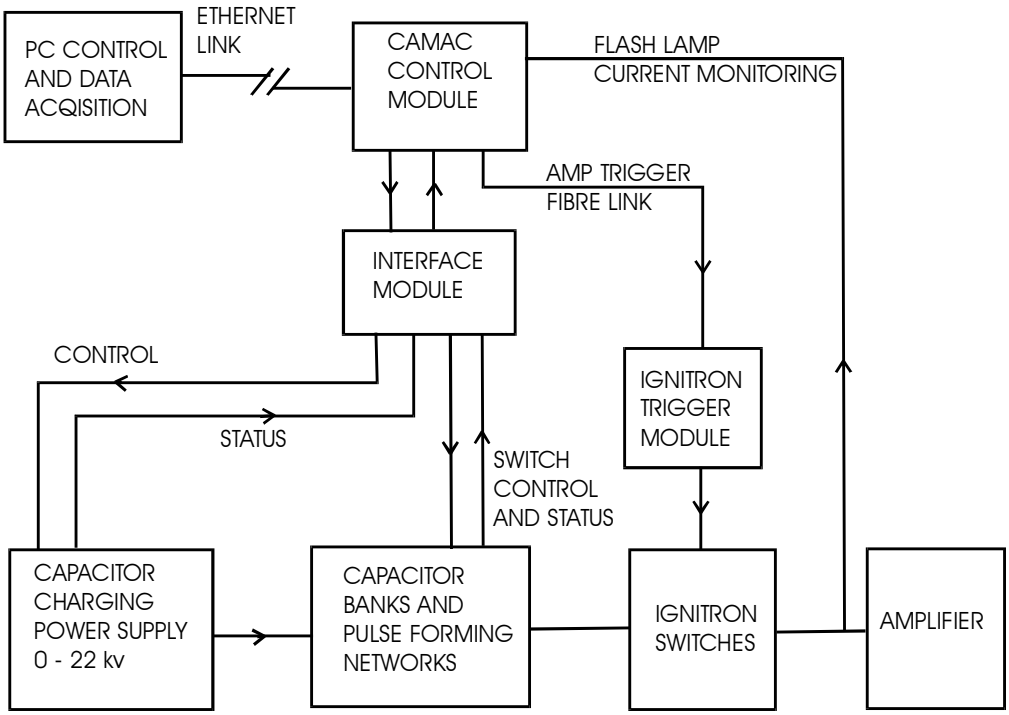

Figure 2. Block diagram of the test bank pulsed power circuit.

An overview of the Vulcan Petawatt control system

C Reason, D Pepler, J Collier, C Danson, C Edwards, A Kidd, D Neely, R Wyatt, B Wyborn

Central Laser Facility, CLRC Rutherford Appleton Laboratory, Chilton, Didcot, Oxon, OX11 0QX, UK

Main contact email address: *C.J.Reason@rl.ac.uk*

Introduction

The project to upgrade Vulcan clearly requires that the control system will need to be extended and it was decided that this should be done in such a way that it will be compatible with what exists at present and allow for further development with applications being able to communicate and save their data in a controlled and consistent manner.

The Vulcan Control System Working Group investigated the present system and future options and presented guidelines to an internal management committee.

General considerations

The environment around Vulcan after the upgrade is likely to be more harsh that at present in terms of high voltage, electrical noise and radiation. Therefore the computer system and it's connections should be well shielded, earthed to avoid earth loops and located away from sources of hazard.

The hardware should be based on PC architecture of an appropriate and cost effective specification for the particular task at the time of installation. It should run either NT or DOS as appropriate. In principle the application can be written in any language supported by the operating system but there should be a preference for Turbo Pascal in DOS and Delphi in NT.

Interfacing between the computer and the laser hardware (control and diagnostics) can be through any suitable interface that is supported by the operating system and application language as appropriate, a preference being for CAMAC. Care should be taken to minimise diversity.

Communication between computers should use Ethernet (co-ax or UTP) and transfer non application dependent files of data.

The data should be archived in a form that is either application independent (e.g. text) or in a form that is easily read by Microsoft Office applications (e.g. XLS). Image data must be stored in a form that allows exact restoration (e.g. raw, bit map or uncompressed TIFF but not, for example, JPEG).

The interlock system

The 'new' interlock system Cerberus has been written in such a way that changes can be incorporated by changing the data table that drives the system rather than changing the code itself. This has already proved invaluable as areas of Vulcan have changed their function or have been removed from the system. With the incorporation of TA2 into the laser room, the interlock computer freed from TA2 will be used to provide the interlocks for the new Target Area.

Implementation

A schematic of the proposed control system is shown in Figure 1 below. The links between the Interlock Network and the Laser Control Network are already in place, as is the PC / CAMAC interface which provides most of the current control capacity. To expand the control network to cope with the Petawatt control and data acquisition-rate requirements means that direct Ethernet links to CAMAC will be needed. A DOS driver for this task has been purchased commercially (Hytec Electronics Ltd) and is expected to be commissioned for system testing and development shortly.

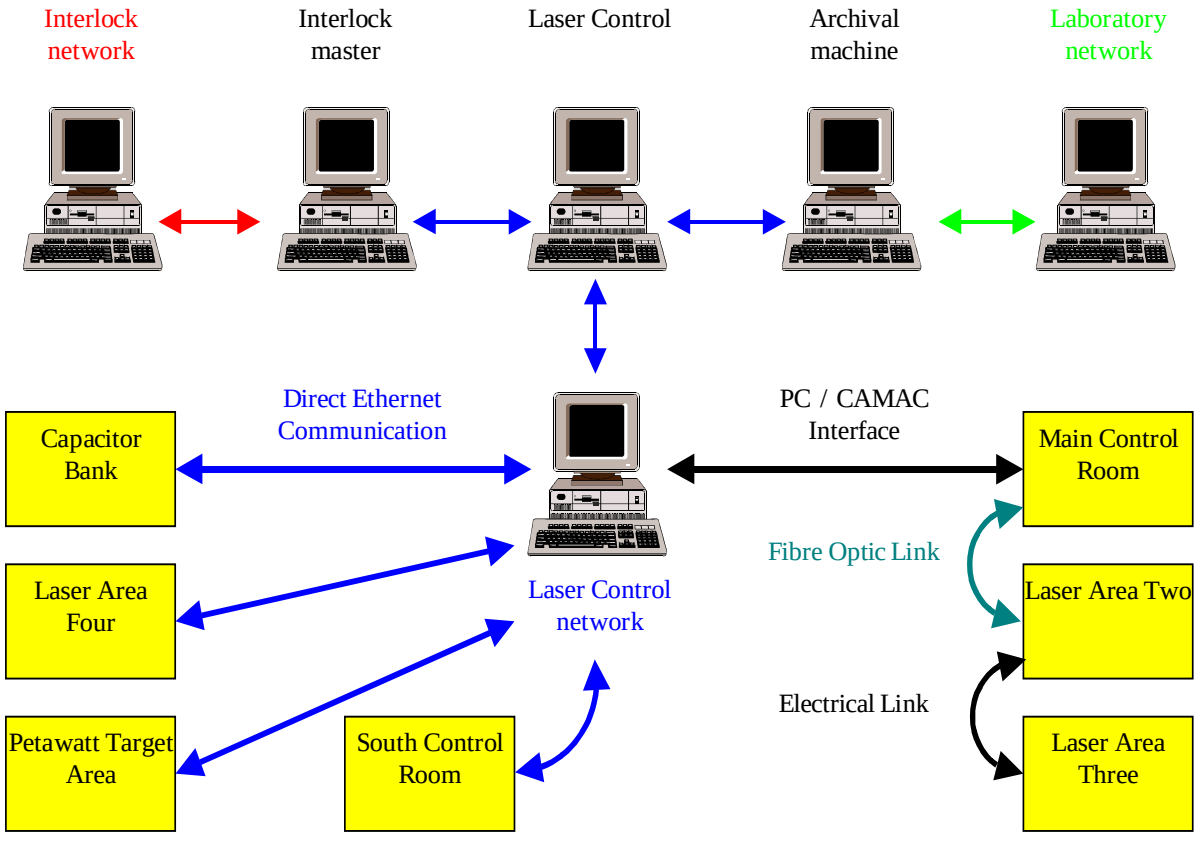

Figure 1. Schematic of the computer interlock and control systems including the new CAMAC networking arrangements.

CPA Beat-wave Configuration on Vulcan

D Neely, J L Collier, R Allott, R Clarke, C N Danson, S Hawkes

Central Laser Facility, CLRC Rutherford Appleton Laboratory, Chilton, Didcot, Oxon, OX11 OQX, UK

Z Najmudin, R J Kingham, K Krushelnick, AE Dangor

Imperial College of Science, Technology and Medicine, Prince Consort Road, London, SW7 2AZ, UK

Main Contact email address: *D.Neely@rl.ac.uk*

Introduction

Since the beat-wave scheme was first proposed[1)] as a possible electron accelerator, it has generated much interest[2)]. The beat-wave acceleration scheme is based on two laser beams of different frequencies resonantly driving a plasma wave at the difference frequency. Extremely large electric fields > GVcm^{-1} can be envisaged. Experiments have been conducted using microwaves[3)], CO_2 lasers [4,5)] and glass lasers [6,7)] as the drive beams. In the experiments the plasma wave was not driven to its limiting relativistic saturation level due to the growth of modulation instabilities which have a growth rate determined by the ion plasma frequency. We here describe the generation of CPA laser pulses [8,9)] of sufficiently short duration and intensity to drive the plasma wave to saturation before modulation instabilities can grow. The scheme generates two pulses, which are separated everywhere in time in the amplification system and temporally overlapped only in the interaction region. The system is inherently jitter free, which is an essential requirement to use short pulses. The system also avoids any non-linear optical interaction between the pulses in the beam line, which can generate unwanted sidebands, complicating diagnostics.

A requirement for a practical accelerator is that the radial gradients in the plasma wave should be smaller than the longitudinal field. To achieve this, a laser spot size comparable to or larger than the plasma wavelength λ_p is required. In Figure 1 the plasma wavelength λ_p as a function of wavelength separation $\Delta\lambda = \lambda_0 - \lambda_1$ of the two laser components is plotted and also the required electron density for resonant excitation. Since λ_p is inversely proportional to $\Delta\lambda$ the required laser energy will scale as $1/\Delta\lambda^3$, favouring operation at the maximum possible wavelength separation. One dimensional modeling[10)] has shown that the modulation instability does not inhibit the plasma wave growth provided $I\lambda^2 > 10^{16}$ Wcm^{-2} μm^2. Thus, for $\Delta\lambda$ and pulse lengths of the order 10 nm and 5 ps, the required laser energy per pulse is of the order 10 J. This would give a relativistic saturated plasma wave amplitude $\delta n/n$ in the region of 10 %.

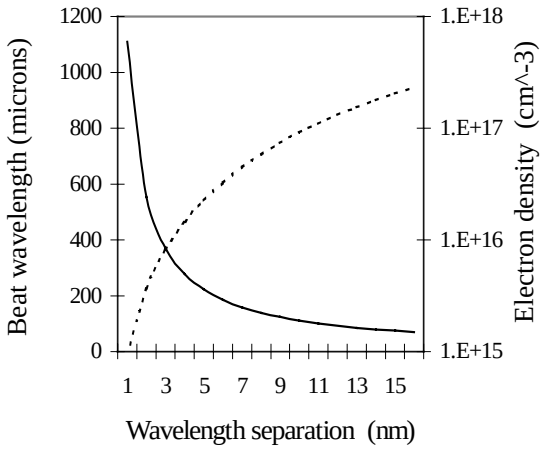

Figure 1. Graph showing the beat wavelength (solid line) and the required electron density (dashed line) as a function of the wavelength separation of the two drive wavelengths centered on 1054 nm.

Laser Scheme

A layout of the Vulcan CPA system is shown schematically in Figure 2. The initial oscillator pulse is generated by a commercial Kerr lens modelocked oscillator using Ti:Sapphire as the active medium. It produces an 80 MHz pulse train of 5 nJ, 120 fs pulses of which one is used. The sech^2 pulse has a full width half maximum bandwidth of 16 nm centred at 1054 nm.

The pulses are injected into a double pass grating stretcher as shown in Figure 3. An amplitude filter is used to select two narrow bandwidth portions of the input pulse. The bandwidth of each pulse is selected via the width of the slits, whilst the separation of the slits defines the wavelength difference and hence the beat frequency. The required amplitude filter is placed in the dispersed beam of the stretcher away from the Fourier plane. It is important to place the slits away from the Fourier plane since slits in this plane impose an extremely hard spectral clip on each pulse. Upon temporal compression, these hard clips would generate a pulse with a very poor temporal contrast after amplification, typically no better than 100: 1 many tens of pulse lengths away from the peak. By placing the slits away from this plane, the pulses are clipped in the near field and are thus selected with 'softer' spectral edges and have better contrast ratios. This results in contrast ratio improvement of the amplified pulse of 4 to 5 orders of magnitude as illustrated in Figure 4.

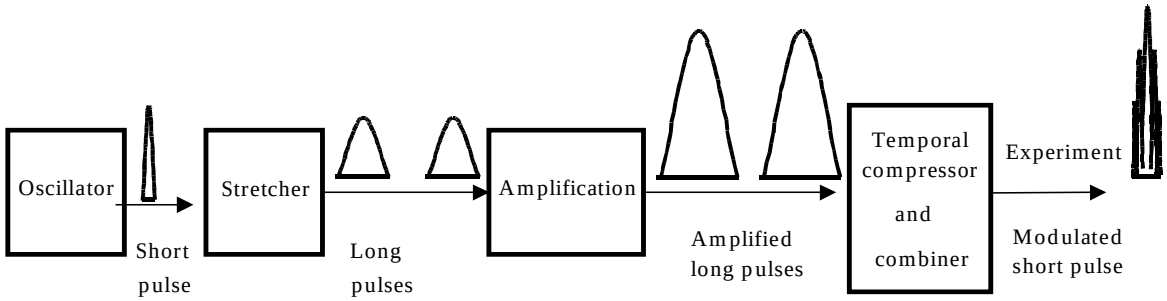

Figure 2. Schematic diagram of the two pulse CPA scheme.

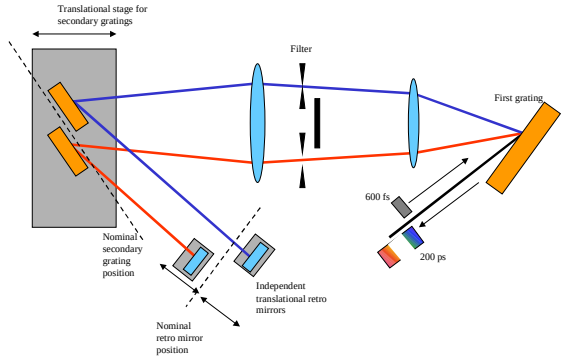

Figure 3. Schematic diagram showing the stretcher.

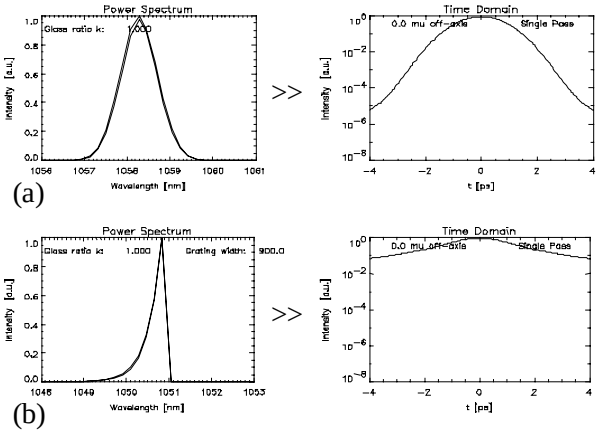

Figure 4. Comparison of the power spectrum and pulse shape of a soft and hard clipped pulse after amplification (a) filter away from the Fourier plane and (b) in the Fourier plane.

Amplification

The two pulses produced by the stretcher are temporally separated. The pulses are amplified in a single beam line. The propagation and amplification of these pulses by the Vulcan Nd:glass laser [15] has been modelled numerically. In the simulation a fluorescence curve for the phosphate glass amplifier, centred at 1053.5 nm, is used as the gain curve. A top hat function simulates the spectral filter of the stretcher.

The amplifier chain gain bandwidth significantly reduces the amplification available for the spectrally separated pulses the further they are located from the centre wavelength.

Figure 5 shows the gain required as a function of wavelength to maintain a constant output of 20 J for a narrow bandwidth of 0.1 nm and a constant input energy from the oscillator of 1 nJ. However, such a narrow bandwidth cannot be amplified to the 20 J level through the Vulcan system. This is because if the bandwidth is too narrow the stretched pulse length is short and the energy is limited by damage thresholds and B-integral effects.

Taking these factors into account, the wavelength separation as a function of bandwidth is presented in Figure 6. This illustrates that larger separations necessarily need larger bandwidths. The gain available in the Vulcan amplifier chain is such that pulses at the 20 J level can be generated for $\Delta\lambda \sim 9$ nm with a bandwidth of ~1.3 nm. The use of mixed phosphate and silicate glass amplifiers could in future allow pulses of greater wavelength separation to be used in the system.

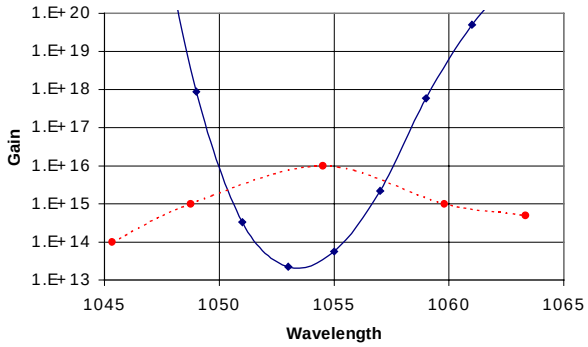

Figure 5. Graph showing the required gain (solid line) in the Vulcan Nd:glass as a function of wavelength to maintain constant output energy of 20 J for a 0.1 nm bandwidth pulse. The dashed line shows the system gain with an additional 9 mm diameter rod amplifier. The intersection represents the maximum wavelength difference the system can be used at.

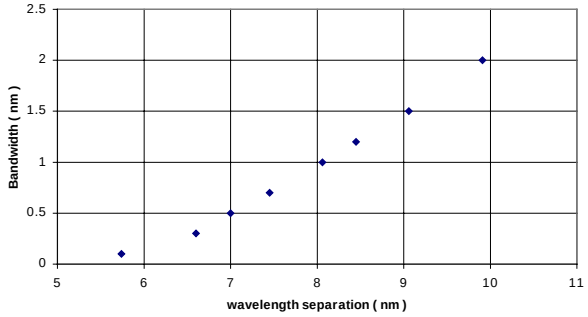

Figure 6. Graph showing the minimum pulse bandwidth necessary to maintain ~20 J of energy per pulse as a function of the wavelength separation between the laser pulses on Vulcan. This limit is set to avoid damage thresholds in the amplifier chain and B-integral effects.

Pulse compression and combining

A two grating compressor is shown in Figure 7. Both laser pulses are incident onto the first grating and overlap only partially on the second grating, as they diffract apart after leaving the first grating due to their different wavelengths. Thus, in the interaction region not all the initial energy in the pulses is used to drive the beatwave. Defining D as the distance between the grating centres, L the length of the gratings, p the grooves density per m and N the diffraction order we can define a cut-off wavelength λ_{cut}. For a single beam illuminating the first grating composed of two monochromatic components equally spaced about a central wavelength by $\sim\lambda_{cut}/2$ they will diffract out to such an extent that they both just miss the second grating and no energy is transmitted through the system. λ_{cut} is given by:-

$$\lambda_{cut} \approx \frac{2\,L\cos^2\phi_{out}}{NpD} \qquad (1)$$

Each wavelength component will fill a fraction $(1-\Delta\lambda/\lambda_{cut})$ of the final grating resulting in an overlap fraction of $(1-2\Delta\lambda/\lambda_{cut})$. If we require the beams to overlap significantly (i.e. at least overlap over the central half of the final grating) we can define a maximum wavelength separation $\Delta\lambda \le \lambda_{cut}/4$.

The present Vulcan compressor uses two 1740 lines per mm CPA gratings which have a surface ruling across 390 x 190 mm

and are used in first order with a grating separation of 3.5 m and at an input angle of 73.2 degrees. This gives $\lambda_{cut} \sim 30$ nm. Therefore, to use the existing system would give a maximum wavelength separation of $\Delta\lambda \leq 7$ nm. This corresponds to a plasma wave $\lambda_p \geq 158$ μm..

The three grating compressor shown in Figure 8 does not suffer from the problem of limited beam overlap. In this scheme the two input pulses must be on different beam lines which are incident onto two separate input gratings. In this scheme, the beams must diffract sufficiently that when the two input gratings are just touching, full beam overlap is obtained on the final grating. This condition can be expressed as $\Delta\lambda = \lambda_{cut}$. By appropriately increasing the separation between the input gratings, full overlap on the second grating can be achieved at $\Delta\lambda \geq \lambda_{cut}$. An additional degree of freedom is available in that it is possible to move the input gratings in opposite directions and introduce temporally dependent opposite chirps on the two pulses. It should be noted that the three grating compressor requires amplification of the pulses in separate chains or a suitable method of separating the pulses before the input gratings.

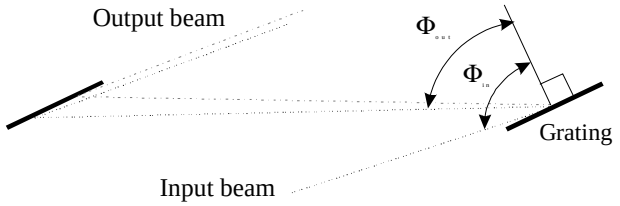

Figure 7. Schematic layout showing a two grating pulse compressor and combiner.

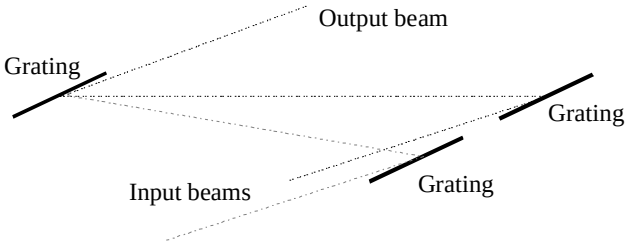

Figure 8. Schematic layout showing a three grating pulse compressor and combiner.

The maximum intensity I_{max} in the focal region which can be delivered using a two grating compressor for a beat wave experiment, is given to a first order approximation by: -

$$I_{\max} = S\, D_T\, e_d^2 \left(1 - \Delta\lambda / \lambda_{cut}\right)\left(\tau\, \pi \lambda_p^2\right)^{-1} \qquad (2)$$

Where S is the surface area of the gratings, e_d the diffraction efficiency and D_t the damage threshold energy density of the gratings. Experience[11] with the 1740 lines per mm, 1053 nm blazed, gold overcoated holographic gratings[12] in the Vulcan CPA system has shown that sustainable long term (hundreds of shots) average drive fluence is approximately 130 mJcm^{-2} for no detectable surface degradation. The diffraction efficiencies of the two wavelengths are equal to within a few percent. Setting the gratings at an input angle of 73.2 degrees gives a measured first order diffraction efficiency e_d of 89 %. For $\Delta\lambda = 7$ nm this gives $I_{max} \sim 7 / \tau$ (ps) x 10^{16} Wcm^{-2} with a Rayleigh length ~ cm. In adapting the Vulcan system to support two narrow spectral components, self phase modulation effects limit the maximum deliverable energy per pulse, reducing the above to $I_{max} \sim 3 / \tau$(ps) x 10^{16} Wcm^{-2}. This estimate is approximate since it does not account for the fact that the beam has different sizes in the horizontal and vertical planes due to the beam aperture being non circular.

The two grating compressor is much simpler to set up and is ideal in situations where the spectral separation is small. This was used in a beat-wave interaction experiment on Vulcan in April / May 2000. The laser reliably delivered 10 J of energy in two pulses separated by ~6 nm.

The Vulcan CPA system is currently being upgraded[13] to the PW level and when completed in 2002 the system will be capable of delivering pulses suitable for a beat-wave drive. The system will use 1480 lines per mm gratings separated by 13.5 m which gives $\lambda_{cut} \sim 31$ nm, very similar to the present configuration. However, with an increase in grating size to ~ 0.9 m diameter, the system will be able to support energies of ~ 100 J per pulse, enabling much longer interaction lengths to be achieved.

Summary

A novel laser configuration capable of generating the necessary conditions to drive a plasma beat wave into saturation before modulation instabilities can grow to cause significant disruption has been implemented on Vulcan. The scheme relies on generating a single sub ps, broad bandwidth pulse and spectrally stretching and filtering to select two wavelength components which are inherently synchronous. The two laser pulses have been amplified on the Vulcan CPA Nd:glass chain to greater than 20 J per pulse and have been used for a beat-wave experimental investigation.

References

1. T. Tajima and J. M. Dawson, Phys. Rev. Lett. 43 267, 1979
2. E Esarey, P Sprangle, J Krall and A Ting, IEEE Transactions on Plasma Science 24 2 p252-288 1996.
3. J. H. Rogers, D. Q. Hwang, J. C. Thomas, R. L. Horton, J. Killeen and G. Dimonte, Phys. Fluids B 4 1920, 1992.
4. C. E. Clayton et al, Phys. Rev. Lett. 54 2343, 1985.
5. C. E. Clayton et al, Phys. Rev. Lett. 70 37, 1993.
6. F. Amiranoff et al, Phys. Rev. Lett. 68 3710, 1992.
7. A. Dyson et al., Plasma Phys. Control Fusion 38 505, 1996.
8. D. Strikland and G. Mourou, Opts. Comm. 56, 219-221, 1985.
9. C. Danson *et al.* J Mod Opt. 45, 8, 1653-1669, 1998.
10. P. Mora, D. Pesme, A. Heron, G. Laval and N. Silvestre, Phys. Rev. Lett. 61 14, 1988.
11. C. N. Danson et al, 'Well Characterised 10^{19} Wcm^{-2} Operation of a high power Nd:glass laser', Accepted by J. Mod. Opt. 1998.
12. Supplied by Jobin Yvon, 16-18 Rue du Canal BP118, 91163 Longjumeau Cedex, France.
13. C. Danson et al, Accepted for publication in International Fusion Science Applications, conference proceedings, Bordeaux, France, 1999.

The implementation of the CLF Interlock System 'CERBERUS' on Vulcan

C Reason, E Divall, W Lester, D Pepler, R Wyatt

Central Laser Facility, CLRC Rutherford Appleton Laboratories, Chilton, Didcot, Oxon, OX11 0QX, UK

Main contact email address: *C.J.Reason@rl.ac.uk*

Introduction

The interlock system 'CERBERUS' was originally written for the Sprite and Titania laser systems[1,2] and as reported two years ago[3] was installed on the Astra laser with a proposal to install it on Vulcan. Since then it has been installed on Vulcan and also on the Pirate laser. A typical screen layout for Vulcan is shown in Figure 1 with the laser area hazardous. Figure 2 shows the network configuration for Vulcan.

Rules

The interlock system implements a set of rules that have been defined independently of the system. These are described in the references above. These have had to be extended to take account of different configurations found on Vulcan as it is a much more complex system compared with other lasers. In particular, three main rules have been added. These are the addition of enclosures, of Castel keys and the ability of the Laser Responsible Officer (LRO) to define the rooms in which a particular laser can produce a hazard.

The rule for enclosed lasers within a room allows lasers to be housed in a small box (enclosure) with removable interlocked panels and a shutter such that they provide no hazard in the room while the shutters and panels are shut. This has been implemented by describing the enclosure as a type of room within a room (which clearly can not contain a person, so does not need a search procedure or need to be declared as unoccupied). The rules for opening the shutter are the same as those for a room. The maintenance panel can be opened at any time and will trip the laser in the enclosure. However, once the enclosure is open, the laser can be brought back on obeying the rules for any other lasers in the room.

In order to implement the rule for Castel keys, a number of patterns of locked Castel keys can be defined and named which must match locked and empty rooms before the high voltage can be activated for a high power shot.

To implement the rule for 'Laser Hazard in Room', a table has been set up for each laser defined in the interlock system specifying the rooms in which it can produce a hazard. This is interrogated when setting rooms hazardous. For example the LRO can set the interlock system such that an active laser in the oscillator room can never produce a hazard in the target areas even if there is a potential beam path between the two rooms (on the assumption e.g. that the laser does not follow that beam path or the mirror reflectivities are wrong).

Hardware overview

The hardware currently consists of a basic (but fast) PC running the DOS operating system, a standard Ethernet network card and one or more Amplicon 192 way I/O card(s). The 'master' station is basically the same as the 'slave' stations. The communication over the network is done using the MAC address and publicly available application to application software drivers running under Turbo Pascal. The screens show the current state of the whole interlock system and a remote

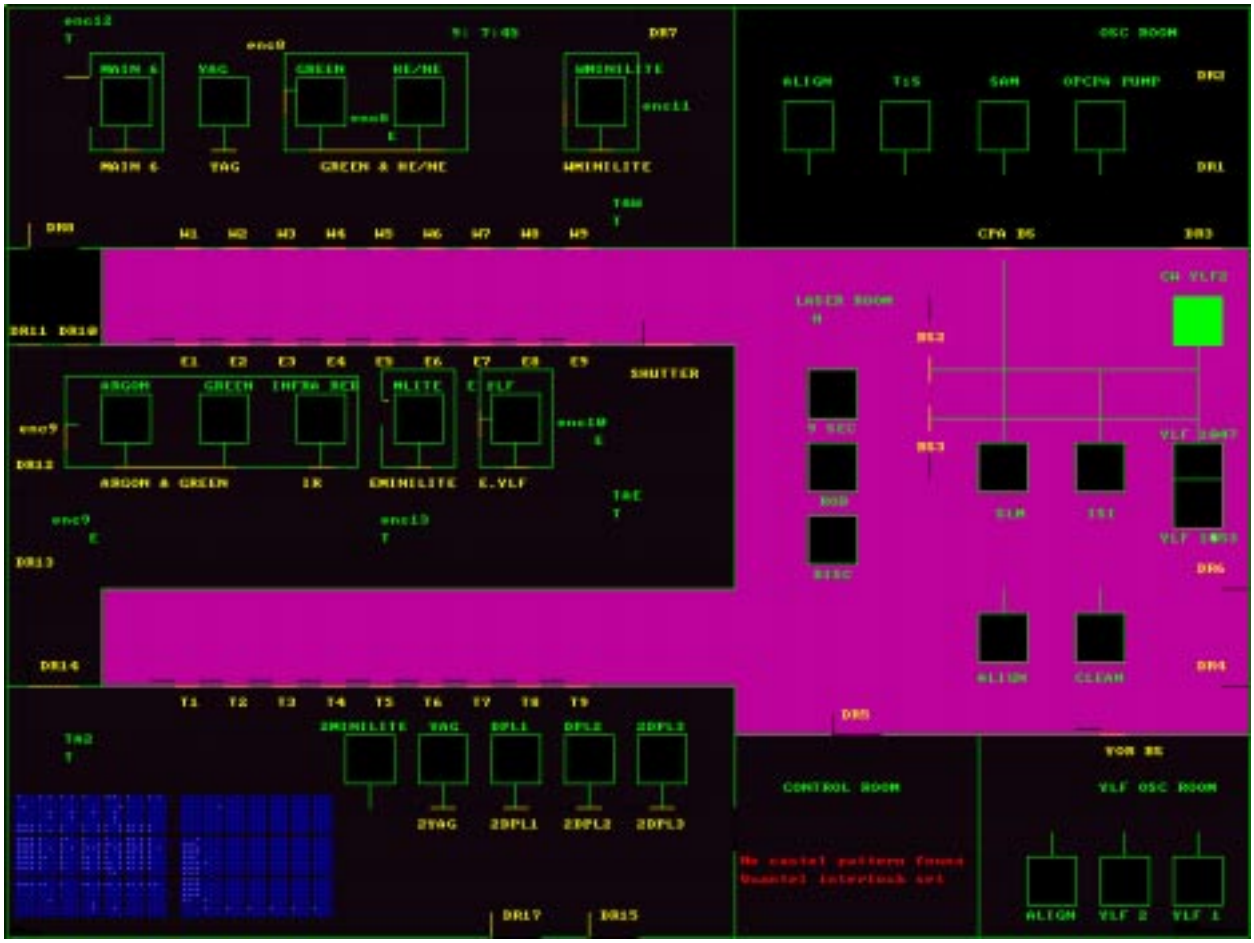

Figure 1. Interlock screen layout with the main laser area hazardous. Note the bit pattern diagnostics in the lower left hand corner.

indicator board is driven from the Amplicon card to show the state of the lasers in a particular room.

The signal conditioning between the Amplicon card and the environment has been completely redesigned and implemented using a EuroCrate system in a highly modular format. The door displays have also been redesigned to incorporate a flexible LCD backlit display also driven through the Amplicon I/O card. This allows more information to be presented at the entry door and gives an indication that the program is active.

A number of hardware upgrades are under discussion, in particular – the use of a panel (or series of panels) of multi coloured LEDs driven down an RS232 interface to provide a more informative room display. There are issues of brightness and cost and also of what and how much information can be reliably and safely given – and – the use of voice output from a sound card in the computer to replace sirens and bells, again to give more information. The issues here are the provision that it does not slow the program down and also that it does not constitute a high annoyance level.

Software overview

The software has been completely re-written in Borland Turbo Pascal V 7 running under DOS. This operating system was used because of concerns about multi-tasking in windows operating systems. However an increased knowledge of Windows NT 4 (and higher) and the ability to set 'real time' mode suggests in future implementations, NT is a possible route forward.

The scheme of the code implementing the interlock rules and a separate table (with a special editor) describing a particular instance of an interlock system has been retained and this has proved invaluable, both in installing the interlock system on different lasers and in coping with the changes on Vulcan during the run up to the upgrade and when the new target area is commissioned.

Changes to the code have been implemented to take into account the different operating requirements on Vulcan without compromising the safety of the system. In one case a table change has been made to add an authorisation key in the control room and this has been covered by issuing written standing orders.

The installation on Vulcan with the increased number of stations (7 in all), increased number of lasers and more complex operations has had an effect on the response time of the system. During normal operation, the system checks the interlocks at a rate approaching 10 Hz but during times of high activity this can drop by a factor of two or three. At present this is still acceptable but it did result in the watchdog timeouts having to be extended.

Operating experience

Initially, on all laser systems and also after any modification to the system, a series of tests are executed to ascertain the system is performing correctly. These have thrown up some problems with the system, one of which remains. If an enclosure is open in one target area it trips the lasers in the other target area. This still has to be investigated but, as it is a rare occurrence, a work around has been agreed without compromising the safety of the system.

It has been found that the new door displays are susceptible to static electricity when people are leaving the laser areas in their nylon clean coats. This occasionally causes the door displays to freeze or blank. There is an ongoing program of providing better earthing and a patch has been put into the software to re-start a door display remotely using the CERBERUS master computer.

References

1. 'Cerberus, a computerised interlock system for the Sprite laser' by C J Reason, C Hooker, P Gottfeldt, W J Lester. CLF Annual Report 1992 (RAL-92-020) p 143.

2. 'Cerberus: a laser interlock system using Arcnet' by P Gottfeldt and C J Reason. Computing and Control Engineering Journal. December 1993 p 281.

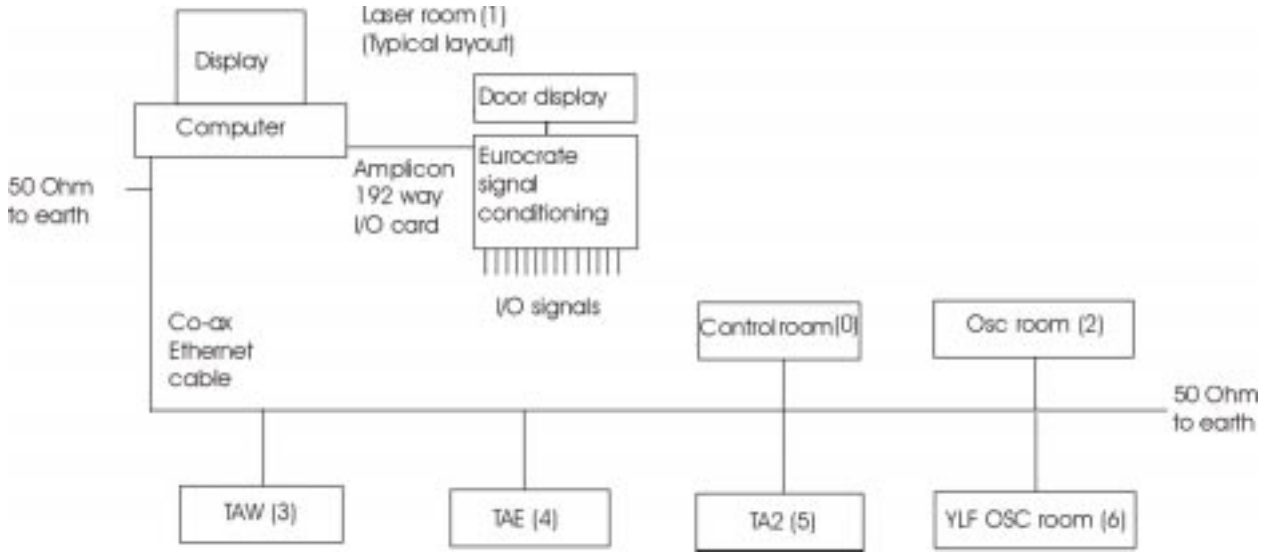

Figure 2. Cerberus network configuration for Vulcan.

The Development of a Multi-Terawatt Femtosecond Laser Facility - Astra

A J Langley, E J Divall, C H Hooker, M H R Hutchinson, A J-M P Lecot, D Marshall, M E Payne, P F Taday

Central Laser Facility, CLRC Rutherford Appleton Laboratory, Chilton, Didcot, Oxon, OX11 0QX, UK

Main contact email address: *M.H.R..Hutchinson@rl.ac.uk*

Introduction

The main objectives of the Astra development programme were to:

- Build an ultrafast femtosecond laser facility capable of delivering focused intensities up to 10^{19} Wcm^{-2}
- Design and commission a target chamber suitable for high intensity femtosecond experiments
- Enhance the laboratory facilities to provide two experiment or target areas to operate simultaneously.

This report shows that these objectives have been achieved. The facility is now supporting a programme of user experiments.

Technical issues and objectives

The Astra multi-terawatt upgrade built upon an earlier EPSRC funded programme to build a femtosecond terawatt (TW) laser within the CLF's *Lasers for Science Facility* at RAL. It may be helpful to review briefly the construction of the terawatt laser before considering the multiterawatt upgrade. The terawatt laser consisted of a 20 fs TiS oscillator providing pulses for amplification in two multipass titanium-sapphire amplifiers. Before amplification the pulses were stretched to 300 ps duration in an all-reflective two-grating stretcher. This stretch was sufficient to maintain the B-integral at or below unity during the amplification process – an important factor in maintaining pulse fidelity. After amplification the pulses were recompressed in a conventional two-grating compressor. The pulses used in experiments were of sufficiently low power to be compressed and transported to experiments in air rather than under vacuum as is required at higher pulse energies.

Many components from the terawatt laser were incorporated into the Astra upgrade including the oscillator, the two titanium-sapphire amplifiers and their Nd: YAG pump lasers, optical components, mounts and other associated equipment.

The six main areas of development carried out to achieve the multi-terawatt performance target of the Astra facility were:

1. Construct a grating stretcher to stretch the 20 fs oscillator pulses to 600 ps. (The 300 ps pulse duration used in the TW system was too short to maintain a sufficiently low B-integral with the additional refractive material present in the Astra system.)
2. Build a third multi-pass amplifier to boost the 100 mJ uncompressed output of the terawatt amplifier
3. Purchase and commission a high energy laser to pump the third amplifier
4. Design and construct two pulse compressors, one for each target area
5. Design and have built a vacuum chamber to house the compressor delivering ultra-high intensity pulses in Target Area 2 (ATA2). Compression in vacuum is essential to maintain pulse fidelity at the TW/cm^{-2} intensity of the compressed pulses and could not be attained by compression in air
6. Design and build a target chamber for ultra-high intensity experiments in ATA2.

Stretcher and compressors

Figure 1 is a schematic diagram of the Astra facility showing the laser and target areas. Pulses for amplification are derived from the existing mirror-dispersion-controlled titanium sapphire oscillator (Femto, Technische Universitat, Vienna) pumped by a frequency-doubled cw diode-pumped Nd: YVO4 laser (Millennia, Spectra-Physics). This oscillator provides pulses at a repetition frequency of 76 MHz centered at 790 nm with sufficient bandwidth to support pulses of 20 fs duration. Before amplification the pulses are stretched to 600 ps in an all-reflective gratings pulse stretcher. A Faraday isolator is placed before the stretcher to minimise the likelihood of back reflections disrupting the oscillator.

The stretcher and compressor consist entirely of reflective optics to minimise the contribution of higher order phase terms and thus maintain pulse fidelity. All the gold coated gratings were made at the Lawrence Livermore National Laboratory because the largest gratings were required to be of a size (300 x 100 mm) not available from commercial manufacturers. The gratings were manufactured to the following specifications: 1/8 wave peak-to-valley (at 632 nm) over 90 % of the aperture, 90 % efficiency at 830 nm.

The stretcher, shown in Figure 2, is an all-reflective analogue of a simple dual-grating stretcher with single relay lens [1)]. A line spacing of 1480 lines/mm was chosen in order to provide pulse stretch to 600 ps in one double-pass. This provides less pulse front distortion and transmission loss compared with multipass systems while also ensuring that the stretcher remains of practicable size. A paper describing the stretcher in more detail is published following this article.

The best pulse fidelity after recompression is obtained with the stretcher and compressors in near Littrow configuration. This also provides optimal transmission efficiency and eases alignment because beams are, by definition, retro-reflected in the dispersion plane. The stretcher is designed with a bandpass of 4x the fwhm bandwidth of a 30 fs, pulse and ray tracing analysis of the stretcher/compressor design showed that 20 fs pulses should be stretched to 600 ps and recompressed to 30 fs with a contrast ratio of at least $1{:}10^{-4}$. The stretched pulse duration was confirmed with a fast photodiode and oscilloscope. A compressed pulse duration measurement is presented below.

The most cost-effective approach to the mechanical design of the stretcher and compressors was to use commercial optical mounts. Where this was not possible, components were designed at RAL for manufacture elsewhere. The stretcher and air compressor were assembled on breadboards for ease of modification, though the vacuum compressor components were mounted on an aluminium plate to minimise outgassing.

Particular attention was paid to ensuring systems were sufficiently rugged to provide good stability during laser operations but with sufficient fine control for the alignment of optical components when optimising pulse stretch and compression. The optical components in the vacuum compressor can be controlled remotely via 13 computer-driven motor actuated micrometers. The air compressor is controlled manually.

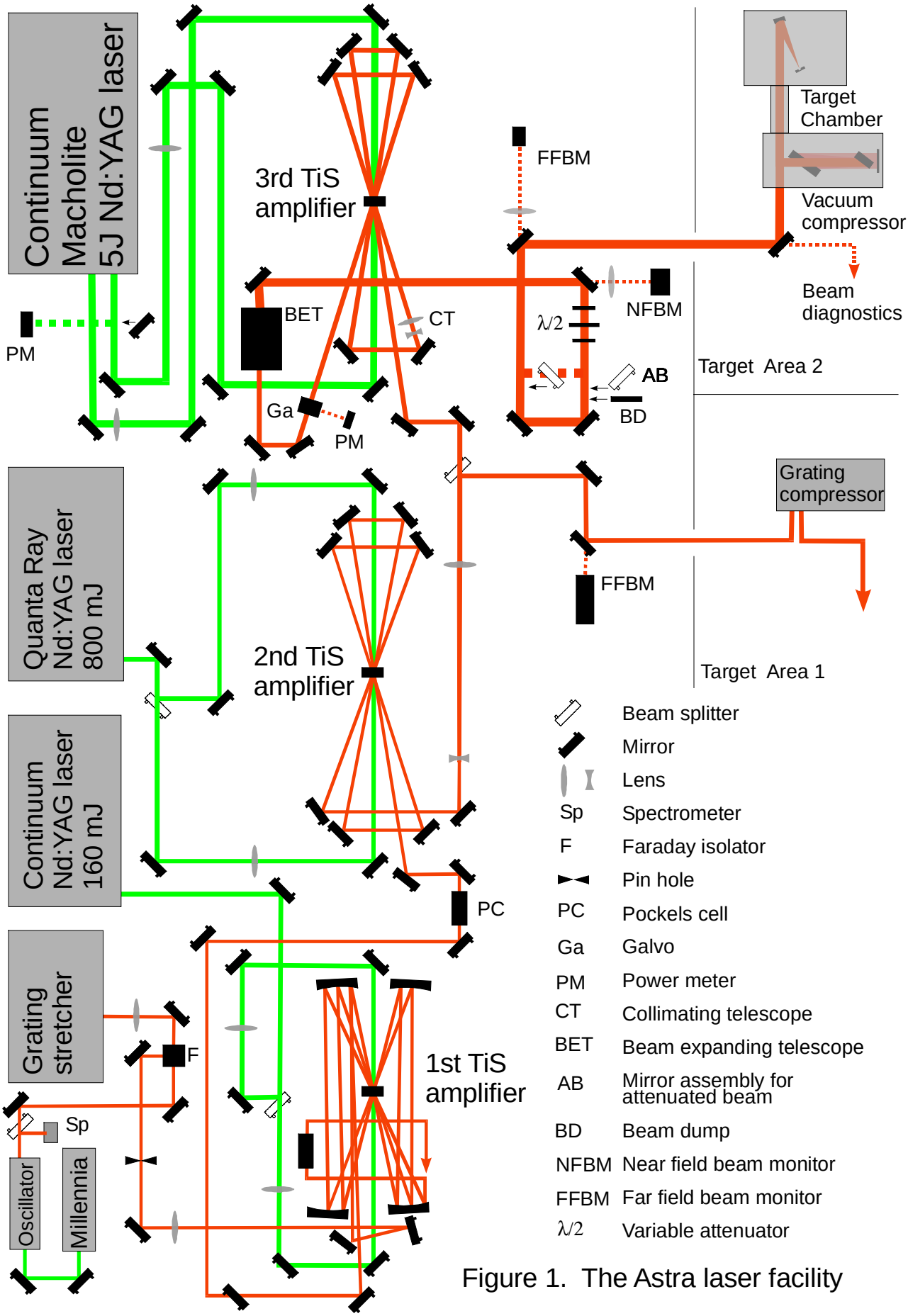

Figure 1. The Astra laser facility

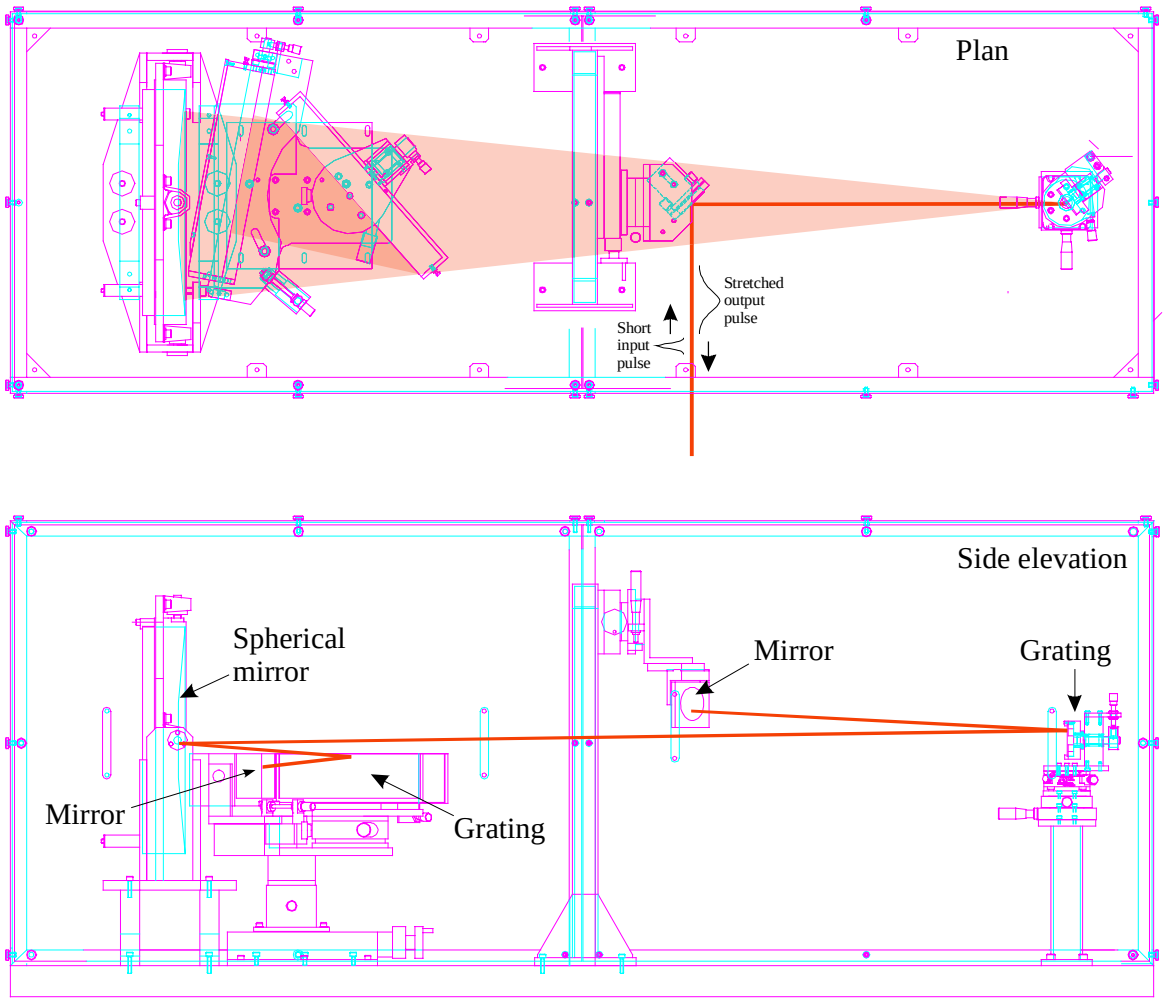

Figure 2. All reflective grating stretcher used to stretch the short (~20 fs) input pulses to a duration of 600 ps before amplification.

The 600 ps stretched pulses are amplified in two multipass TiS amplifiers that were built as part of the terawatt upgrade. The amplified uncompressed energy after the second amplifier is 100 mJ per pulse. The 800 nm beam is expanded to a diameter of 16 mm after the second amplifier and 40 % is split off at this stage and directed to Target Area 1 where pulses are compressed for user experiments. The remaining energy is directed to the third TiS amplifier for further amplification.

The 5 J Nd: YAG power amplifier pump laser

In order to amplify to energies in excess of a Joule in Ti: S at a repetition rate of a few Hertz it is necessary to use a pump laser capable of providing pulses of several Joules at green wavelengths. As several groups have demonstrated, frequency doubled Nd: YAG lasers are the lasers of choice for this application. However, off-the-shelf commercial Nd: YAG lasers are limited to energies around 1 J per pulse. When the objective is to amplify to high energies the choice is between pumping the TiS crystal with several 1 J YAG lasers simultaneously or using a single, custom built system capable of generating all the pump energy required. For the Astra upgrade several large Nd: YAG systems were considered in a competitive tender process and from amongst these was chosen a custom-built laser manufactured by Continuum Inc, USA.

The Continuum laser provides a total of 5 J per 30 ns pulse in two 532 nm beams at a repetition rate of 10 Hz. It is important to maintain a uniform beam profile when pumping the TiS crystal, and measurements of the output beams showed that the best profiles were obtained near the output faces of the final Nd: YAG amplifiers. In each beam this plane is imaged to the TiS crystal by an A/R coated 2.2 metre focal length lens. For reasons of safety both pump beams are contained where possible in black-anodised aluminium pipes, and the sections of pipe near the foci are fed with filtered N2 to minimise breakdown caused by dust particles in the high-intensity regions.

Design and construction of the TiS Power Amplifier

There were several inter-related variables which influenced the design of the high-power amplifier, and a computer simulation was written to simplify the task of evaluating different possibilities [2,3]. The main values to be determined were the dimensions of the crystal, the dopant concentration, the diameters of the pumped region and the infra-red beam and the number of passes made through the crystal. The first two are constrained somewhat by cost and by the technical limitations of the crystal-growing process, and another important constraint was the thickness of the crystal, as this is the principal contribution to both higher-order dispersion and B-integral in the laser. It was important to keep the total thickness (i.e. physical thickness times the number of passes) to a minimum: even with an increased pulse length of 600 ps fwhm, the expected increase in output energy restricted the maximum length of the crystal to around 1 cm if the B-integral was not to exceed unity. Efficient use of the available pump energy was also regarded as essential. Lastly, the relationship between the length and diameter of the crystal affects the extent of losses due to parasitic oscillations, and a separate computer model was written to analyse this problem.

The requirements of efficiency and minimum path in the material pushed the design in the direction of a relatively short, highly-doped crystal with a small number of passes. Computer

simulations with a range of diameters of the pumped region showed that efficient extraction of the energy and good saturation on the fourth pass of the crystal were achievable with the available input, using a pumped region 18 mm in diameter and an extracting beam of 16 mm diameter. In this operating regime outputs up to 1.8 J were predicted and the intensities involved were comfortably below the damage thresholds of the materials and coatings to be used. Finally the analysis showed that for pulses stretched to 600 ps the non-linear contribution of all refractive optics present in the system would result in a B-integral close to unity.

The basic layout of the new amplifier (See Figure 1) is a bow-tie arrangement, similar to the preceding ones. The infra-red beam makes four passes through the water-cooled crystal (12 mm thick, 24 mm dia.) with a maximum off-axis angle of about 3 degrees. At the pump energies used in the amplifier, the radial temperature gradient set up in the crystal causes a significant amount of thermal lensing, so the crystal becomes a positive lens with a focal length of typically 16 to 18 metres. To correct this the amplifier has a negative/positive lens pair at the input to the third pass, and their spacing is adjusted to give accurate collimation of the output beam: this is also essential if the pulse compressor is to work correctly.

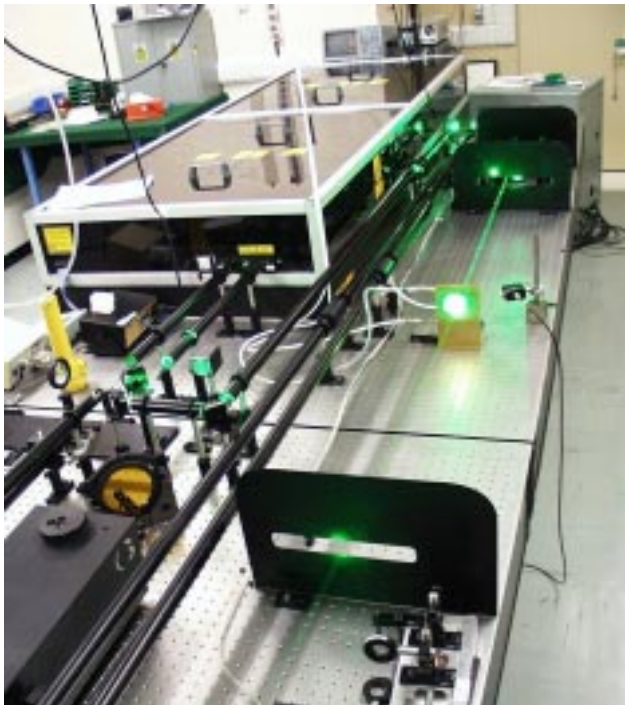

Figure 3. Astra's third amplifier. The TiS crystal (centre right) is being pumped both sides by 5 J of frequency-doubled 532 nm light from the Macholite Nd:YAG laser (rear left).

At the output of the amplifier the intensity is too high for either long-distance propagation in air or the survival of gold-coated compressor gratings, so the beam diameter is increased from 16 mm to 60 mm by a commercially-made all-reflective beam expander. The convex primary mirror of the expander is spherical, with a dielectric coating for damage resistance, and the secondary is an off-axis paraboloid coated with gold, which can withstand the lower fluence in the larger beam.

The raw output from the amplifier is a train of pulses at 10 Hz at a maximum energy of 1.8 J. For flexibility and for operational reasons, several controls have been introduced which can vary these parameters. Since single pulses or trains of pulses at a lower frequency may be required, a commercial beam-switching device is installed at the output. The experimenters can program any sequence of pulses they require from a computer in the target area control room.

The second control is a variable attenuator, consisting of a half-wave plate followed by a pair of polarising mirrors. The angle of the half-wave plate is also under computer control from the target area control room, and will allow the experimenters to adjust the laser energy on target as required. For safety reasons, the target area must be vacated when the full-power beam is present, so for alignment purposes a corner reflector consisting of a pair of uncoated glass plates can be inserted into the beam just ahead of the high reflectors in the delay trombone. These provide a fixed attenuation factor of 100. There is no change of beam direction, but the pulse arrives on target about 1 ns earlier. Beam dumps behind the plates absorb the unwanted laser energy.

Compressor and Target chambers

Figure 4 shows schematically a plan of Astra target area 2 showing the compressor and target chambers. Also shown is the path of the 800 nm uncompressed pulse beam from the laser into the compressor chamber and the path of the compressed pulse beam from the compressor to the target chamber through an adjoining pipe.

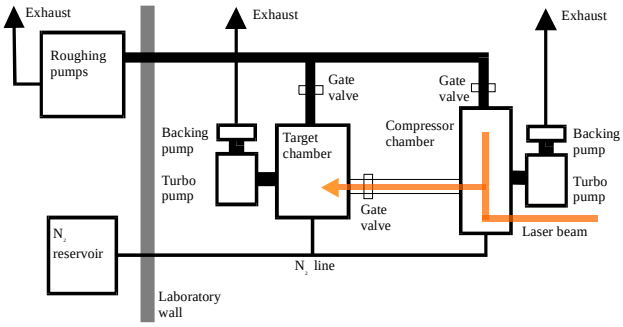

Figure 4. Schematic plan of the compressor and target chambers vacuum system.

There are a number of reasons why the two-chamber arrangement is necessary:-

- The quantity of debris generated from high repetition-rate solid target interactions would lead to the destruction of any unshielded optical component. In particular the expensive compressor gratings must be kept as far from the interaction area as possible, and this is best achieved if they are situated in a separate chamber joined only by a long tube.
- Gratings are also susceptible to damage by volatiles or dust from user experimental equipment, so to minimise this the compressor chamber can be isolated from the target chamber by a gate valve. This also enables the vacuum in the compressor chamber to be preserved when the target chamber is opened to air for sample changing, maintenance etc. The gate valve need only be opened to let pulses through once the target chamber is evacuated.
- A separate and smaller target chamber also improves the cycle time (the time required to let-up and pump down) the target chamber since the volume is less.
- The alignment of the compressor gratings is very critical, and separating them from the interaction region reduces the risk of them being knocked accidentally.

Large roughing pumps are placed outside the laboratory to reduce noise and heat. Each chamber has its own turbo pump, capable of a minimum pressure of 10^{-6} Torr. To prevent debris falling into the turbos and damaging them, they are mounted on the side and top of their respective chambers. For experimental operations the pump-down time of the target chamber to a few times 10^{-5} Torr is about 20 minutes.

Figure 5. Target Area 2 showing the compressor chamber (foreground) and target chamber.

Astra building upgrade

In order to house the new Astra laser, and provide two laboratories for user experiments, it was necessary to provide a larger area than had been available to the terawatt system. The building chosen for the upgrade (R7) consisted of low quality workshop space, and almost all the upgrade work consisted of enhancing the area to the high standards required of a central laser laboratory.

To ensure stable and reliable operation the laser area is air-conditioned with filtered air and the temperature maintained to a temperature of ± 0.5 C. It is a semi-clean area requiring personnel to wear over-shoes and coats to minimise the risk of damage to optics caused by dust. The target areas are also air-conditioned to maintain constant temperature. The laser beams are sent to the target areas from the laser via shuttered ports in the adjoining wall. A thin fused silica window at the port maintains the cleanliness of the laser area and removes air turbulence which could introduce beam pointing instabilities.

For safety reasons the laser area, ATA1 including its control area and ATA2 are maintained as an interlocked area to restrict access to authorised personnel. The computer based interlock system Cerberus is based upon the system developed for the Vulcan laser. During operations Cerberus constantly monitors the status of the area and ensures that only permitted combinations of laser hazards are present. The system protects personnel by preventing disallowed combinations of hazards and by rendering an area safe if its integrity is compromised by, for example, non-authorised entry at a door.

A considerable part of the upgrade involved the provision of the type of services required of a modern laboratory. These include water cooling for lasers and target area equipment; gas pipes to supply clean N2 for equipment purging and for other gases used in experiments; an external gas cupboard; 13 and 32 A single and three-phase power supplies; fixed BNC cable links within and between areas to carry essential signals. Many of these supplies are carried on overhead gantries to the required location within each area. The services specific to the compressor and target chambers are described above.

Astra performance

Pulses with energies of 1.8 J in 600 ps have been obtained from Astra's final TiS amplifier which is in line with theoretical modelling. Of equal importance is the final beam quality and this is influenced by the optical quality of the TiS crystal used in the amplifier. The best quality crystals of the size required for Astra often have long manufacture and delivery times. For the Astra project a suitable high-quality crystal is currently on order and hence all the data presented here derive from tests carried out with an inferior crystal.

Given the inferior beam quality obtained with this crystal, which also produced non-uniformities in the spatial profile of the beam, it was decided to run the amplifier at lower gain to avoid damage to the compressor gratings. The maximum amplified energy was restricted to 800 mJ. Figure 6 shows a second-order autocorrelation of 600 mJ pulses compressed in the vacuum compressor. The autocorrelation fwhm is 72 fs, which implies a pulse duration of 50 fs assuming a Gaussian pulse profile. Measurements with a photodiode have demonstrated a contrast ratio of 5 x 10^{-6} between the amplified pulse and the preceding oscillator pulse.

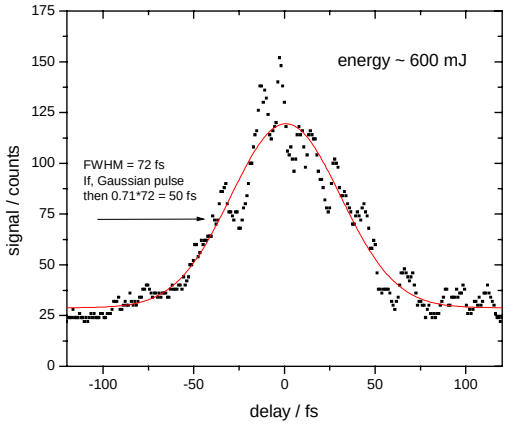

Figure 6. Autocorrelation measurement of compressed pulse.

Focusing measurements on the compressed pulse beam have obtained a focal spot diameter of 30 μm using an *f*/17 optic. This implies an M^2 of approximately 2 for this focusing arrangement and a focused intensity of 5 x 10^{17} Wcm^{-2}. Initial measurements have obtained intensities in excess of 10^{18} Wcm^{-2} with an *f*/3 off-axis paraboloid (OAP). Further work to optimise the focusing is in progress. With the good quality crystal (now on order) it will be possible to operate the amplifier at full gain which, coupled with the *f*/3 OAP, will enables us to obtain focused intensities ≥ 10^{19} Wcm^{-2}.

Summary

This upgrade programme has successfully built an ultrafast femtosecond laser facility capable of delivering focused intensities up to 10^{19} Wcm^{-2}. A target chamber suitable for high intensity femtosecond experiments has been successfully built and commissioned for user experiments. The laboratory facilities have been enhanced to enable two femtosecond experiments to operate simultaneously in two target areas. The facility is now supporting a programme of user experiments and a number of novel applications have been approved for future studies.

Acknowledgement

The authors would like to acknowledge the UK's Engineering and Physical Sciences Research Council for funding this upgrade.

References

1. D. Strickland and G. Mourou, Opt. Comm. 56 219 (1985)
2. C. P. J. Barty, C. L. Gordon and B. E. Lemof, Opt. Letts. 19(18) 1442 (1994)
3. A. Antonetti, F. Blasco, J. P. Chamberet, G. Cheriaux, G. Darpentigny, C. Le Blanc, P. Rousseau, S. Ranc, G. Rey, F. Salin, Appl. Phys. *B* 65 197 (1997)

A Simple Achromatic Pulse Stretcher

I N Ross, A J Langley, P Taday

Central Laser Facility, CLRC Rutherford Appleton Laboratory, Chilton, Didcot, Oxon, OX11 0QX, UK

Main contact email address: *I.N.Ross@rl.ac.uk*

Introduction

With the development of ever shorter pulse laser oscillators and the demand for ever increasing power using chirped pulse amplification, it has been necessary to develop pulse stretchers with very large spectral bandwidth and high fidelity. There are a number of published designs[1-3] using only reflective optics and giving good performance. However it was felt that there was some room for improvement since these designs could be difficult to manufacture to the required tolerances, could be far from easy to set up to the required accuracy, and did not always minimise the size of optic for a given bandwidth. In consequence, a simpler design has been investigated and tested and appears to be a feasible and possibly preferable alternative to the earlier designs.

Description

The principle of this design is similar to that of the Offner design in which two spherical mirrors are used to provide high quality imaging at unity spatial and angular magnification over a significant field area. However a high fidelity stretcher does not necessarily require all these properties and in consequence there is the possibility of a simpler design. Let the starting point be the minimum requirements for any achromatic stretcher. The first is that, in order for there to be zero dispersion in the output beam, the optical system must give exactly unity angular magnification from first to second grating for all wavelengths. The second requires that the chirp introduced by the stretcher be such that it may be exactly cancelled by a grating compressor. The third requires that the chromatic and spatial aberrations are sufficiently small to be acceptable. Since we do not need to use large beams in the stretcher[4] it is possible to use an arrangement simpler than the Offner system. This uses a single spherical mirror working at exactly one to one magnification, as shown in Figure 1. The specification used for this design was for a wavelength window of 130 nm at 800 nm and a stretched pulse duration of 1ns corresponding to the full 130 nm. The arrangement operates in double pass and in autocollimation. The important properties of this arrangement are that it has unity angular magnification and zero output spectral dispersion for the beam axis ray, and that, although the field size (or acceptable beam size) of this scheme is small, the modest length of the arrangement allows the use of small diameter beams (as limited by diffraction) and hence the aberration is kept to an acceptable level. These properties are discussed in detail in the following section.

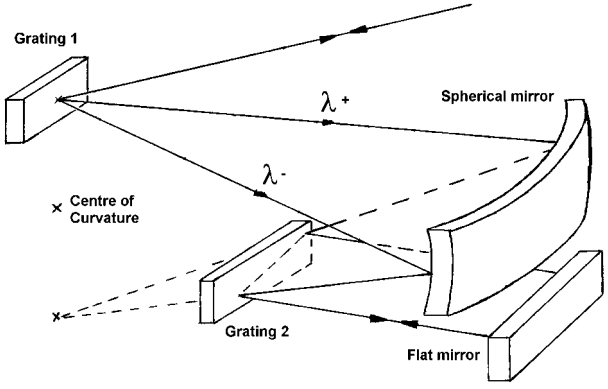

Figure 1. Grating stretcher.

Analysis

1) Axial ray geometry

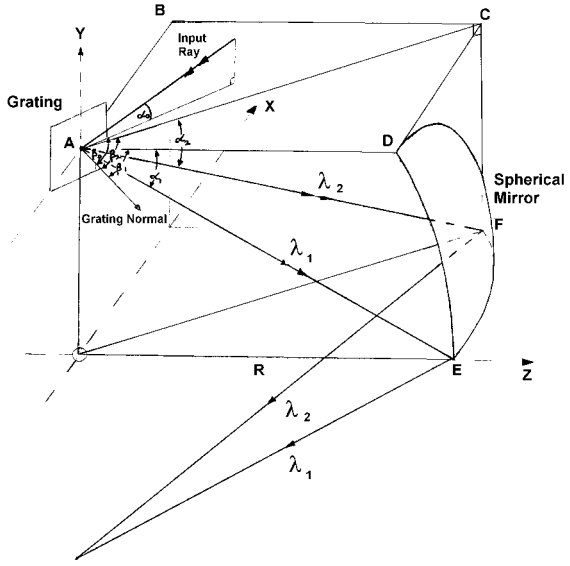

Figure 2. Stretcher geometry.

Figure 2 shows the three dimensional axial ray geometry for both a central and marginal wavelength leading up to the spherical mirror, and for a grating with grooves parallel to the Y-axis. The beam is incident on the first grating at angles β_0 in the plane of dispersion and α_0 out of this plane. More precisely:

α_0 = the angle between the incident ray and the plane normal to the grating grooves

β_0 = angle between the grating normal and the projection of the input ray onto the plane normal to the grating grooves

In Figure 2 the dispersion plane is given by ABCD.

If for the central wavelength λ_1 the diffracted beam direction is given by the angles β_1 and α_1 respectively, the grating equations give:

$$\sin\beta_0 + \sin\beta_1 = N\lambda_1/\cos\alpha_0 \qquad (1)$$

$$\alpha_1 = -\alpha_0 \qquad (2)$$

and similarly for the marginal wavelength λ_2.

Using equation 2 it follows that:

$\alpha_1 = \alpha_2 = -\alpha_0$

However from figure 2 it can be seen that:

$$\tan\alpha_1 = AO/R; \quad \tan\alpha_2 = AO/OF \qquad (3)$$

Consequently:

$$OF = AO/\tan\alpha_2 = AO/\tan\alpha_1 = R$$

Thus for the spherical mirror, which has its centre of curvature at O, the diffracted rays for all wavelengths meet the mirror in the central horizontal plane Y = 0 irrespective of the values of β_0 and α_0 . It then follows that, after reflection, all wavelengths focus to an aberration-free point at Y = -AO with an angular magnification of exactly unity.

2) Gaussian beam analysis

Having demonstrated zero aberration for the axial ray for all wavelengths, it is necessary to consider the wavefront aberration for finite-sized beams. Ray tracing is not adequate for the proposed arrangement since the beams are small and

propagation is strongly influenced by diffraction. However a full diffraction calculation would be complex and may not be justified since it is possible to carry out a much simplified Gaussian beam analysis which is able to assess the magnitude of the astigmatism. This is acceptable since the proposed design contains just gratings and an off-axis mirror and for small beam diameter the aberration is dominated by astigmatism. Gaussian beams follow the well-known propagation equations for the beam parameters for a particular cross-section of the beam. The beam propagation can be followed through an optical system for two orthogonal cross-sections (say parallel to the x- and y-axes) and, if the resulting beam has different parameters in these two cross-sections, the beam has astigmatism and the wavefront aberration can be calculated. The analysis follows the method of Kogelnik[5] in which the beam is specified by the complex parameter q given, for the x-plane, by:

$$q_x = z_x + j(\pi w_{0x}^2/\lambda) \quad \text{and similarly for the y-plane} \quad (4)$$

where z = distance after the beam waist; w_0 = waist radius at the $1/e^2$ points

The propagation is now given by the following operators:

propagation of a distance d in air: $q_{out} = q_{in} + d$ (5)

a thin lens or spherical mirror: $1/q_{out} = 1/q_{in} - 1/f$ (6)

where f = focal length

For a spherical mirror tilted by an angle θ about the x-axis,

$f_y = R\cos\theta/2$; $f_x = R/2\cos\theta$

for an in-plane grating ($\alpha_0 = 0$):

in the plane of diffraction $q_{out} = q_{in}/\gamma^2$ (7)

in the orthogonal plane $q_{out} = q_{in}$

where $\gamma = \cos\beta_0/\cos\beta_1$

If the grating is out-of-plane ($\alpha_0 \neq 0$) as in the proposed design, the ellipticity is no longer aligned parallel to the coordinate axis but at some angle to it and the transformation equations are more complex.

An initial analysis was carried out using the above in-plane grating transformations, and optimised geometries were evaluated for the exact out-of-plane geometry using CODE V.

The output beam parameters were calculated and optimised for different geometries and different input beam parameters. The phase aberration was then calculated as follows:

The out-of-flatness error δ of a wavefront having radius of curvature ρ and radius w is approximately $w^2/2\rho$, or (as a fraction of the wavelength) $w^2/2\rho\lambda$. The astigmatic wavefront error between the x- and the y-planes is $w^2/2\lambda.(1/\rho_y - 1/\rho_x)$ and if the error is taken to be that at a long distance from the beam waist this error can be written $w^2\Delta/2\lambda\rho^2$, where Δ is the distance separating the waists in the two planes. Making use of the relationship for a Gaussian beam that $\pi w^2/\lambda\rho = \lambda z/\pi w_0^2$:

$\delta/\lambda = 1/2\pi.\Delta/z_0$ (8)

where z_0 = confocal distance $\pi w_0^2/\lambda$

Figure 3 plots the astigmatic error (as calculated using equation 8) and the ratio of the x- and y-plane beam waist sizes for a variation of the input beam waist radius.

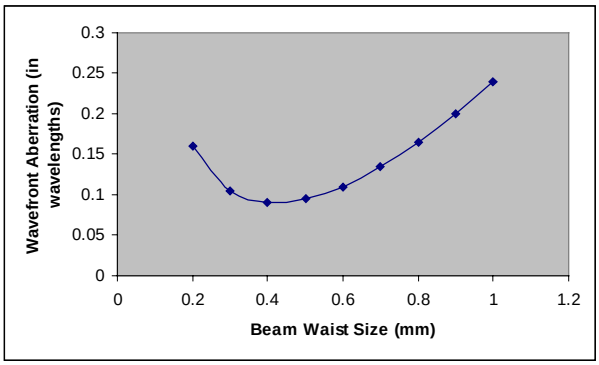

Figure 3. Calculated aberrations of the stretcher.

It can be seen that as expected it is best to use a radius close to that with minimum variation through the system. Further conclusions of the analysis were that:

a) the best plane for the input beam waist is midway between the first grating and the spherical mirror, and the best position for the flat mirror is close to the beam waist. Both these conditions lead to beams with minimum variation through the system.

b) it is best to work as close as possible to the Littrow condition for the grating, again as expected [4]

It can be seen that the minimum aberration as shown in Figure 3 is approximately λ/10, well within acceptable tolerances.

Having established the optimum arrangement the final check was to calculate, for this arrangement, the astigmatic error for the actual design in which the gratings operate slightly out of plane by an angle of 1.5 degrees. This calculation was carried out using the CODE V program. Table 1 shows comparative output beam parameters for in-plane and CODE V calculations. The effect of the out-of-plane geometry is seen to increase the aberration but not to a significant extent.

Wavelength	735 nm		800 nm		865 nm	
	in plane	code V	in plane	code V	in plane	code V
Wavefront Aberration (wavelengths)	0.054	0.083	0.011	0.019	0.074	0.088

Table 1.

Experiment

A titanium sapphire oscillator (Tsunami) generated pulses of duration 50 fs. These pulses were directed into the pulse stretcher and stretched to approximately 160 ps. They were amplified to the millijoule level in a multipass amplifier and recompressed using a conventional double pass compressor.

Figure 4 shows the autocorrelation trace of a stretched, amplified and recompressed pulse (single-shot). The measured pulse duration assuming a sech^2 profile was 50 fs, and the output compressed pulses showed excellent fidelity down to the 10^{-2} level. We can conclude that for this pulse, which had a bandwidth at half intensity of ≈ 20 nm, there is negligible distortion in the stretcher.

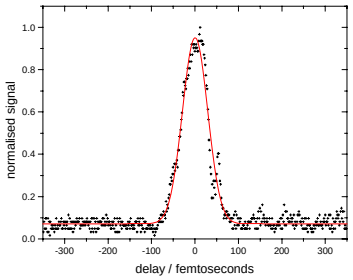

Figure 4. Autocorrelation trace of recompressed 50fs pulse.

Conclusions

The proposed new design of pulse stretcher offers the prospect of low distortion over bandwidths commensurate with the largest that can be envisaged with titanium sapphire chirped pulse amplification lasers while minimising its cost, size and manufacturing difficulty. Chromatic and wavefront aberration has been shown to be less than $\lambda/10$ over the full range of 130 nm and the design can be scaled up to accept larger bandwidths. A stretcher has been built and tested and was shown to work well. However a more critical test remains to be carried out using much shorter pulses with greater bandwidths, since this design should be capable of supplying high fidelity stretched pulses which can be recompressed to 20 fs with contrast ratio greater than 10^6.

References

1. B.E.Lemoff and C.P.J.Barty, Opt. Lett. 18, 1651 (1993)
2. G.Cheriaux et al. Opt. Lett. 21, 414 (1995)
3. J.Ititani et al. Opt. Commun. 134, 134 (1997)
4. O.E.Martinez, JOSA B3, 929 (1986)
5. H.Kogelnik, Bell Syst. Tech. J. XLIV, 455 (1965)

Development of the PIRATE Facility

M Towrie, R Barton, P Matousek, A W Parker, A Stanley

Central Laser Facility, CLRC Rutherford Appleton Laboratory, Chilton, Didcot, Oxon, OX11 0QX, UK

M W George, D C Grills

School of Chemistry, University of Nottingham, Nottingham, NG7 2RD, UK

Main contact email address: *m.towrie@rl.ac.uk*

Introduction

Over the past three years the LSF has developed high repetition rate picosecond/femtosecond (ps/fs) optical parametric amplifier systems[1,2] for investigating ultrafast dynamics of molecules in condensed phase[3-5]. The current dual OPA system is capable of delivering complete tuneability from the UV to the near IR (ca. 200 to 2200 nm (4545 cm^{-1})) suitable for transient absorption and TR[3] spectroscopy. In 1999 the EPSRC awarded funding to build the PIRATE (Picosecond IR Absoption and Transient Excitation) facility which extends the current OPA capabilities to provide high brightness spectral coverage in the Mid IR down to ~10 µm, 1000 cm^{-1}.

Two types of MIR laser sources are available, a narrowband, ~20 cm^{-1}, and a broadband OPA covering several hundred wavenumbers. The narrowband OPA enables a precise choice of IR laser frequency to specifically excite (pump) photochemical and photophysical processes. The potential of this approach has already been demonstrated by Heilweil and co-workers[6] for probing hydrogen bonding dynamics and by Woodruff and co-workers for elucidating protein folding[7]. The broadband OPA will allow transients to be studied through monitoring of a broad spectral window enabling much faster data acquisition times at high sensitivity. Heilweil and co-workers[8] have recently demonstrated the potential of such arrays for time resolved IR (TRIR) spectroscopy.

Narrowband type II $AgGaS_2$ OPA

In this design (Figure 2) the 800 nm pumped BBO OPA amplifies the idler output of the narrowband 400 nm pumped picosecond OPA of the type described elsewhere [1, 2]. The signal and idler output from the 800 nm OPA is passed directly into a single $AgGaS_2$ OPA to create MIR output by difference frequency generation (DFG). Type II $AgGaS_2$ is favoured over type I due to its 40 % higher non-linear coefficient (deff=12.9 pm/V) and 50 % lower acceptance bandwidth (25 cm^{-1}/cm).

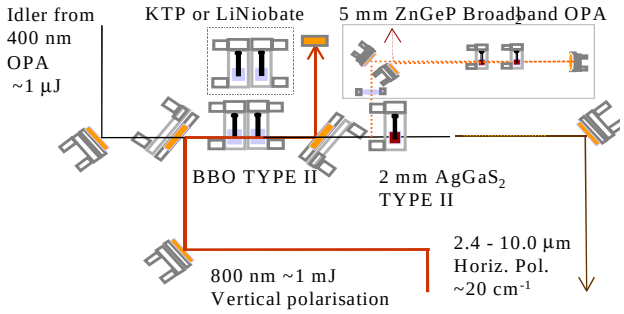

Figure 2. Narrowband and broadband OPA designs based on 800 nm pumped OPAs.

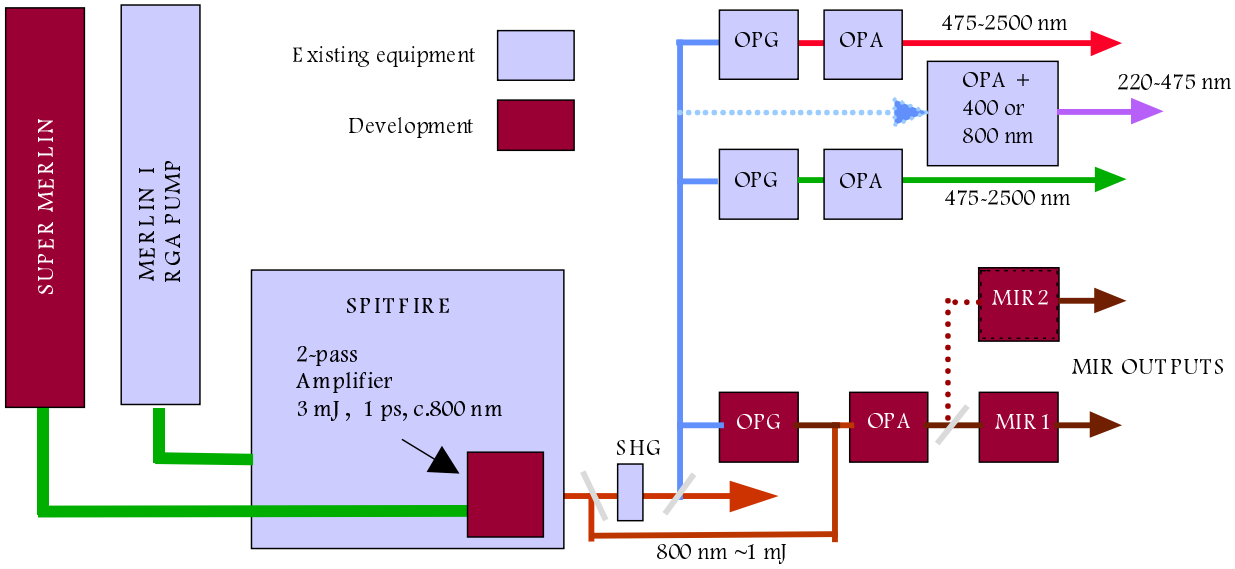

Figure 1. PIRATE Layout.

Equipment development

Figure 1 shows the layout of the PIRATE system. The original 0.8 mJ titanium sapphire regenerative amplifier has been upgraded to ~3 mJ by the addition of two new Merlin pump lasers and a two stage titanium sapphire amplifier. This system is tuneable from 780 - 840 nm with either 150 fs or 1 ps pulse duration options. The c. 800 nm and second harmonic c. 400 nm outputs are used to pump MIR and visible OPAs respectively. The new pump lasers and MIR OPAs are shaded darkly.

The 800 nm pumped BBO OPA uses 2 type II crystals with orientation:

800.0(e) = 1400.0(e) + 1866.7(o)

Phase velocity = c/1.628, c/1.616 & c/1.641 resp.

Group velocity = c/1.650, c/1.639 & c/1.673 resp.

This has the advantage that the “angle walk-off” is compensated and group velocity mismatch delays the idler with respect to the signal by ~ 100 fs. This increases DFG efficiency.

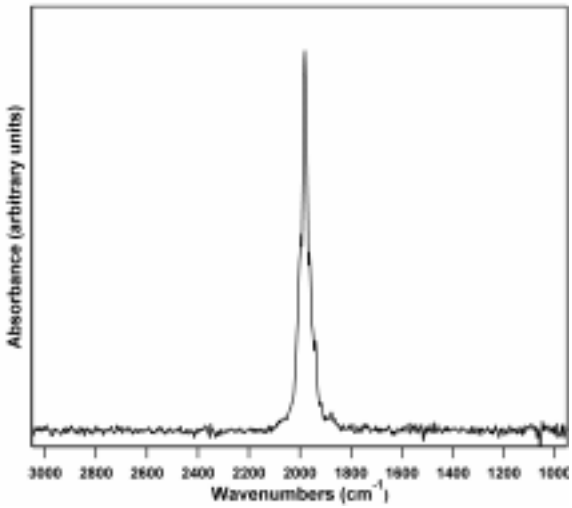

Figure 3. FTIR spectrum of narrowband (~25 cm^{-1}) picosecond IR pulses.

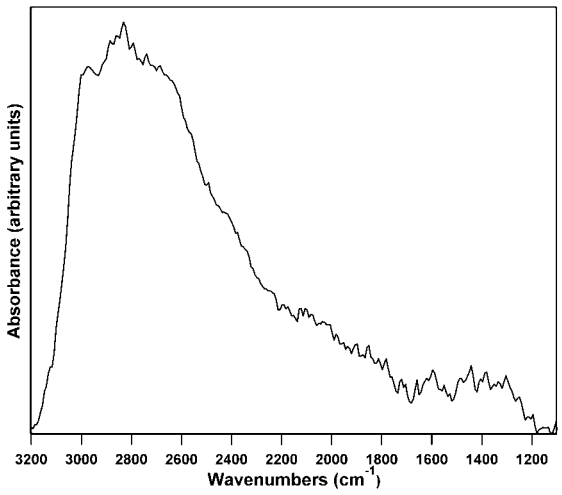

Figure 4. FTIR spectrum of broadband picosecond IR pulses covering >2000 cm^{-1}.

Broad band type I $ZnGeP_2$ OPA

$ZnGeP_2$ has one of the highest non-linearity coefficients among any crystal of ~70 pm/V with a transparency in the range 2-10 μm. Broadband output is obtained by pumping a type I $ZnGeP_2$ OPG/OPA at degeneracy with the 2 - 3 mm wavelength idler output of an 800 nm pumped BBO or KTP OPA. We have measured bandwidths of several hundred wavenumbers by this method (see Figure 4).

Pump-Probe Capability of PIRATE system

The multiple pulse configurations possible with the PIRATE set-up makes it suitable for many types of time resolved spectroscopy, including time resolved resonance Raman, coherent anti-Stokes Raman, difference frequency generation and single channel transient absorption or time resolved IR absorption. The following lists the possibilities available:

Pump & Narrowband MID IR Probe > 1 μJ

2 outputs	0.2 - 2.5 μm
1 output	2.5 - 3.5 μm
1 output	3.5 – 10 μm

Pump and Broadband Probe ~300 nJ

400 nm WLC	~0.3-0.5 μm
800 nm WLC	~0.4-1.1 μm
ZnGeP2 OPA	~1000 cm^{-1} bandwidth (3-10 μm range)

The overall tuning range of the PIRATE system is shown in Figure 5.

Multi-channel TA and TRIR Detectors

We are currently developing a dual detector system based on two custom mercury cadmium telluride 64 channel diode arrays to provide a sensitive multi-channel detector system for TRIR measurements. The set-up will be similar to our existing dual silicon diode array system used for UV-NIR transient absorption spectroscopy.

The detectors were built to our specifications by IR Associates and are each based on 64 diodes with individual pre-amplifiers. The diode array is 2 mm high by 30 mm wide. The outputs from each of the arrays are multiplexed through analogue

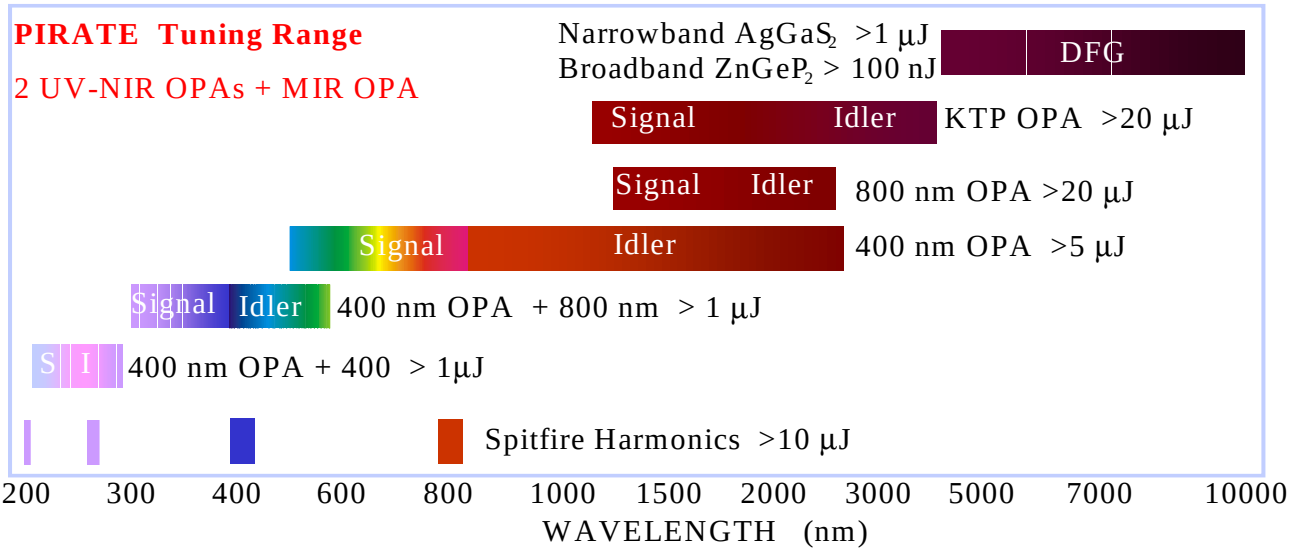

Figure 5. PIRATE capabilities and methods used to generate wavelengths.

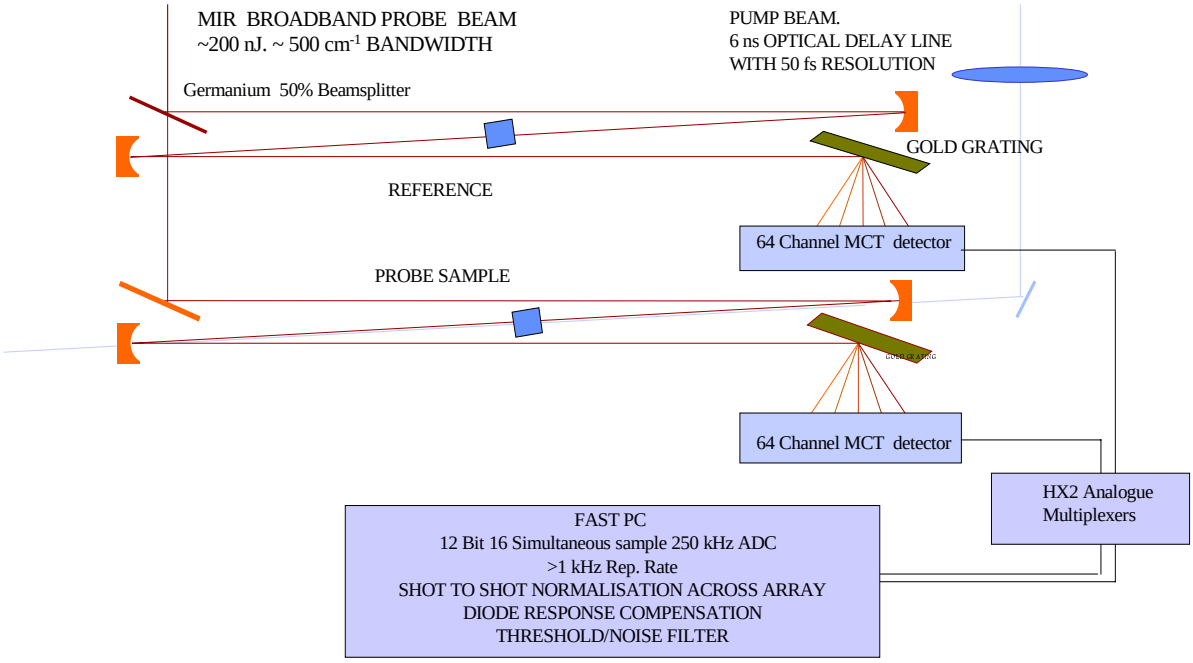

Figure 6. Broadband TRIR dual diode array detector ray diagram .

multiplexers adapted from the HX2 chip designed by the RAL Instrument Development Group. The multiplexers both have 64 simultaneous inputs with 10 microsecond integration time and give single analogue output streams at a rate of up to 200 kHz. The outputs from the HX2 units are connected to two simultaneous inputs of a Datel 250 kHz ADC card inside a 500 MHz PC. The digitised data is then analysed on a shot to shot basis to allow normalisation and discrimination.

An optical arrangement is given in Figure 6. The probe and reference beams are produced by splitting the IR beam using a 50% beamsplitter consisting of a 2 mm thick germanium plate AR coated on one side. The probe and reference beams are then focused into samples using ~30 cm focal length gold spherical mirrors. Further mirrors and an approximately 100 l/mm gold grating are then used to image and spectrally disperse the IR beams onto the detector arrays. The pump beam may be delivered to the sample at a small angle to the probe.

References

1. P. Matousek, A. W. Parker, P. F. Taday, W. T. Toner & M. Towrie. Opt. Comm. 127, 307 (1996).
2. M. Towrie, A. W. Parker, W. Shaikh & P. Matousek Meas. Sci. Tech. 9, 814 (1998).
3. P. Matousek, A. W. Parker, W. T. Toner & M. Towrie, J. Chem. Phys. 107, 9807 (1997).
4. G. Scholes, P. Matousek, , W. M. Towrie, D. Phillips & A. W. Parker J. Phys. Chem. 102, 4131 (1997).
5. P. Matousek, A. W. Parker, D. Phillips, G. D. Scholes, W. T. Toner et al, Chem.Phys Letts. 278, 56 (1998).
6. S. M. Arrivo & E. J. Heilweil, J. Phys. Chem. 100, 11975 (1996).
7. R. Gilmanshin, S. Williams, R. H. Callender, W. H.Woodruff & R. B. Dyer, Biochemistry. 36,15006 (1997).
8. S. M. Arrivo, V. D. Kleinman, T. P. Dougherty, E. J. Heilweil, Optics Letts. 22, 1488 (1997).

Generation of narrow bandwidth nanosecond pulses using an optical parametric amplifier and CW laser seed beam

M Towrie, P Matousek

Central Laser Facility, CLRC Rutherford Appleton Laboratory, Chilton, Didcot, Oxon, OX11 0QX, UK.

R Devonshire, A Buckley

High Temperature Science Laboratories (HTSL), Department of Chemistry, University of Sheffield, Sheffield, S3 7HF, UK.

Main contact email address: *m.towrie@rl.ac.uk*

Introduction

A simple nanosecond pumped optical parametric amplifier (OPA) with a small signal gain of 3 x 10^9 is described. The system generates a near transform limited output of <0.02 cm^{-1} (540 MHz) bandwidth and ~15 mJ pulse energy by the amplification of a cw titanium sapphire laser. The scheme is suitable for the amplification of CW diode lasers for applications in high resolution and non-linear spectroscopy in the near infrared.

The output is suitable for nanosecond high resolution spectroscopy such as the spectroscopy of the hyperfine structure of atoms. It comprises of a compact beta-barium borate, BBO, OPA pumped by a commercial frequency doubled Nd:YAG laser to amplify a titanium sapphire seed laser and generates several millijoules pulses with near transform limited bandwidth in the 700 - 900 nm wavelength range. The output compares favourably with dye and titanium sapphire amplifiers operating in the visible and near IR.

Experimental arrangement

The experimental arrangement is shown in Figure 1. Our scheme uses a pre-amplifier and amplifier stage and two uncoated type I 28^o cut BBO crystals with dimensions of 5 mm high, 10 mm aperture and 15 mm length. The crystals were set ~0.3 cm apart with inverted crystal geometry to compensate for the angle walk off effect.

The vertically polarised second harmonic output of an injection seeded Continuum 8000 series Nd:YAG pumped the OPA. The Nd:YAG output has pulse to pulse stability of better than +/- 1.5 %, <200 MHz bandwidth ~8 mm diameter Gaussian spatial profile and pulse duration of 5 - 6 ns fwhm. Two telescopes gave pump beam size reductions of 5 and 1.7 times in the pre-amplifier and amplifier respectively. The telescopes also help retain the beam characteristics by image relaying the Nd:YAG output into the OPA. A helium filled cell with Brewster windows was set in the focus of the main amplifier telescope to prevent plasma breakdown. The cw seed beam was provided by an etalon narrowed Spectra-Physics 3900 Ti:sapphire laser pumped using a 5 W argon-ion laser. The TEM_{00} output was horizontally polarised with power in excess of 200 mW in the 710 - 900 nm spectral range, linewidth of ~200 MHz and etalon scan range of 1.5 cm^{-1}. The CW seed and pump beams were aligned co-axially in both stages using the beamsplitter mirrors, M1 and M2. The CW laser beam was collimated and approximately 2 mm FWHM to fill the pump beam. After amplification in the pre-amplifier the signal beam is separated at M2, expanded in an X3 magnification telescope and counter propagated parallel but horizontally offset 6 mm to the pre-amplifier beams. The signal and amplifier pump beams are combined using M2 and temporally overlapped with an appropriate optical delay.

Gain measurements were made for a configuration with seed power of 50 mW @ 890 nm and 55 mJ and 150 mJ pump energy, at the crystal faces, for the pre-amp and amplifier respectively. Under these conditions the pre-amplifier had a gain in excess of 65 dB to give an amplified signal energy of ~0.6 mJ. The amplifier gave an additional small signal gain in excess of 20 dB. After separation the signal energy was ~10 mJ and idler (@1322 nm) ~ 6 mJ with shot to shot energy fluctuation of approximately +/- 10 %. For a configuration with seed powers of 0.16 mW and pump energies of 83 mJ and

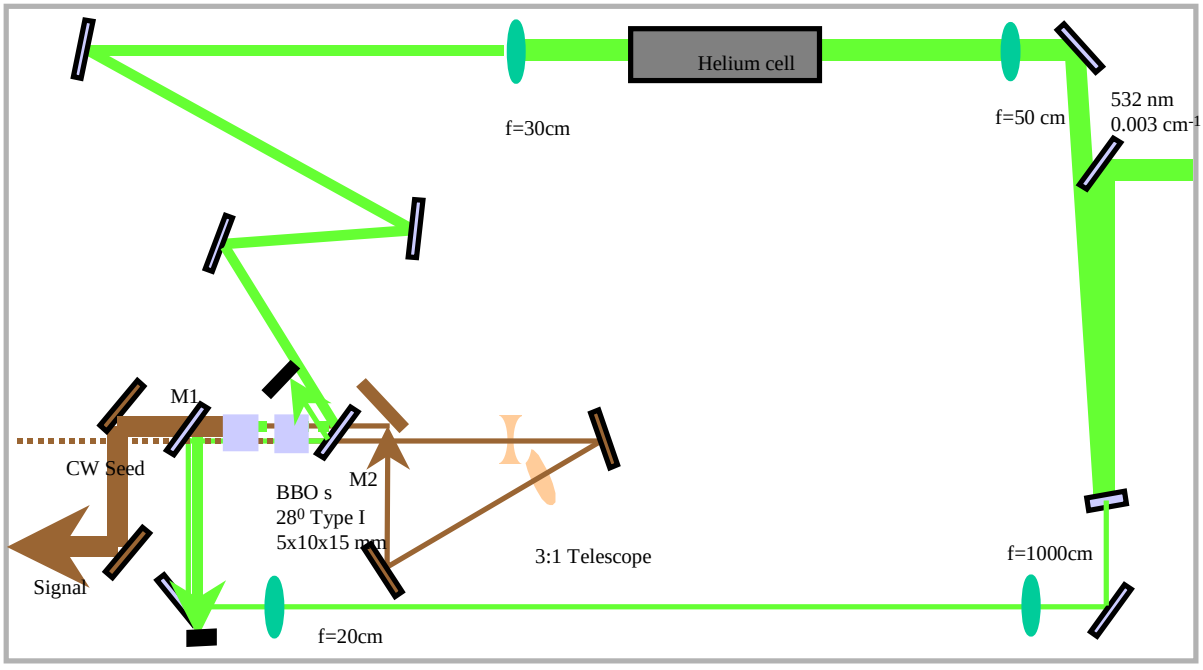

Figure 1. Layout of nanosecond OPA.

140 mJ respectively the OPA gave an overall small signal gain of 95 dB and an amplified signal output of 1 mJ. Thus for seed energies >1 mW the OPA is operated in saturation.

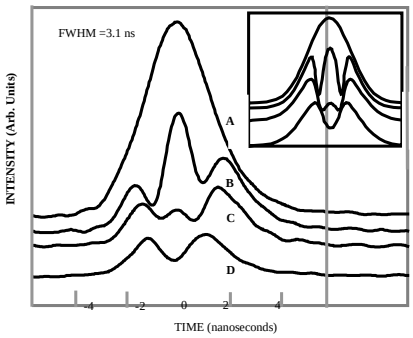

Figure 2. Experimental and theoretical gain saturation in the second stage of the OPA.

Saturation is illustrated by measurements of temporal profile using a 2 GHz photodiode and 500 MHz digital oscilliscope. Figure 2 shows the effect of back conversion of the signal and idler to the pump, for a small area in the centre portion of the beam, as the OPA output is driven into harder saturation with increasing the pump intensity. This compares well with theoretical model shapes derived for a Gaussian beam. The slight asymmetry in the saturation is due to a small temporal mismatch between the pre-amplifier seed and the main amplifier. The overall amplifier output was measured to be ~ 2 ns fwhm. However, spatially resolved measurements of the pulse showed the pulse to be temporally skewed by two nanoseconds with the output pulse length actually < 2 ns. The skew was found to derive from the pump laser. In fact the degree of saturation observed had large spatial and temporal variation which reflected the combined effects of the spatial and temporal variations in the pump and pre-amplifier signal beam.

The spectral performance of the OPA for the 83 and 140 mJ configuration was monitored using a 2 cm^{-1} resolution spectrometer to characterise the gain and bandwidth of the OPA.

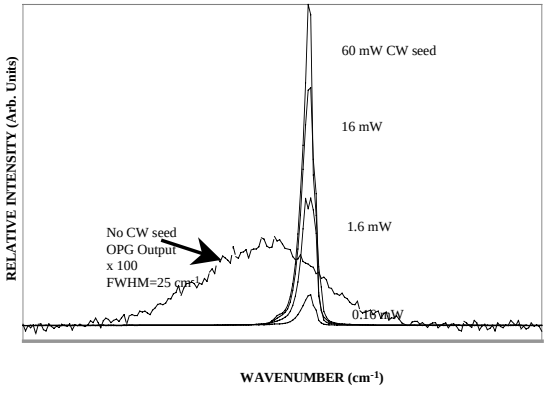

Figure 3. The OPA output for different seed powers at 800 nm. The narrow peak represents the amplified signal.

With no seed light a weak broadband spectrum attributed to spontaneous parametric generation, OPG, is observed. It has a bandwidth of 25 cm^{-1} with a total energy of about 1.5 mJ. This bandwidth is close to the OPA gain bandwidth of 20 cm^{-1} calculated for type I BBO. The bandwidth of the OPG gives the effective tuning range of the OPA without crystal adjustment which easily exceeds the 1.5 cm^{-1} scan range of the seed laser. This condition will hold over the wavelength range of the CW titanium sapphire laser. At 0.16 mW the integrated amplified seed peak and OPG peak are of comparable intensity. However, for powers of > 1 mW the OPG is suppressed and OPA dominates.

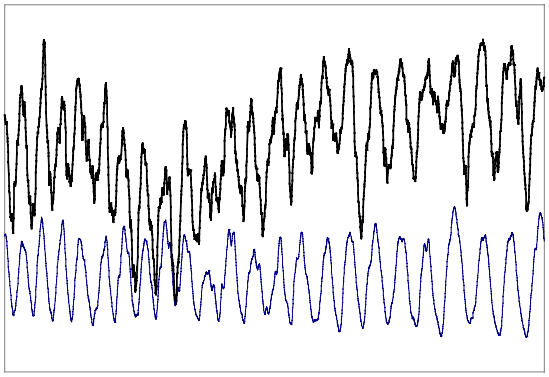

Figure 4. Simultaneous CW and OPA scan traces.

The linewidth measurements were made at OPA gain centre. Figure 4 shows a simultaneous CW and OPA scan trace over 0.76 cm^{-1} as the temperature of the etalon is allowed to cool. The fwhm of CW seed laser trace is 0.016 +/- 0.002 cm^{-1} (480 MHz) and of the OPA trace is 0.018 cm^{-1} +/- 0.004 cm^{-1} (540 MHz). Deconvolution of the instrument resolution gives 0.012 cm^{-1} linewidth. We estimate that the output pulse is around 1.3 times the transform limit assuming a Gaussian pulse. The main contribution to broadening stems from temporal modulation due to saturation and back conversion to the pump leading to perturbation of the spectral envelope. The linewidth of the idler output was not measured however, energy conservation dictates that it too is stable and near transform limited since both pump and seed are stable.

Finally, the full operating wavelength range of the OPA was not sampled. However, a similar energy performance was demonstrated at 710, 750, 800, 890 and 900 nm. At the higher phase matching angle required for 710 nm parasitic oscillation was evident. BBO crystals cut to an angle of 18^{o} would reduce or eliminate this parasitic operation.

Conclusion

A simple OPA pumped by a Nd:YAG laser has provided intense coherent narrow linewidth in the output by the direct amplification of a CW titanium sapphire seed beam. CW powers of only down to a milliwatt were sufficient to produce millijoule OPA output energies. The OPA would therefore operate with alternative CW sources such as tunable diode lasers. The source is suitable for high resolution spectroscopic applications in the near infrared.

Development of Laser Tweezers

D Nees, S W Botchway, M Towrie, A D Ward, A W Parker

Central Laser Facility, CLRC Rutherford Appleton Laboratory, Chilton, Didcot, Oxon, OX11 0QX, UK

A Burgess

ICI PLC, PO Box 90, Wilton Centre, Middlesbrough, Cleveland, TS90 8JE, UK

Main contact email address: *a.w.parker@rl.ac.uk*

Introduction

Laser tweezers have been developed and used mainly in the biosciences for free holding and manipulation of biological objects such as single living cells. In recent years calibrated laser tweezers have evolved to sophisticated force transducers, which are able to measure and apply pico-Newton forces with nanometer spatial resolution and better than milli-second temporal resolution. Dielectric particles with a higher refractive index than the surrounding medium and sizes between ~10 nm and ~50 µm can be trapped with a tightly focussed laser beam.

Milk is a well-known example of a colloidal system, being composed of small fat droplets dispersed in a bulk water medium. Similar to other colloidal systems milk is thermodynamically unstable and over a period of time, the dispersed microscopic fat droplets will coagulate and form a homogeneous macroscopic fat phase, i.e. a layer of cream. The relative stability of colloid systems stems from an energy barrier which must be overcome before two approaching fat droplets can merge. The repulsive forces, mainly electrical or sterical in nature are in the order of pico-Newtons (pN) to nano-Newtons (nN) and thus small enough to challenge even atomic force microscopy.

The investigation of the behaviour of solid particles adsorbed at fluid/fluid-interfaces is of particular interest in regard to Pickering emulsions, which are emulsions stabilized by finely dispersed solids. These are gaining increasing importance in industrial production ranging from body care to food preparations. In collaboration with ICI, we have adapted and constructed a laser tweezers apparatus to investigate topics in colloid science where pN forces need to be determined. In particular we have developed a new method of optical trapping colloidal particles resting at fluid/fluid interfaces known as the Interfacial Laser Trap Method.

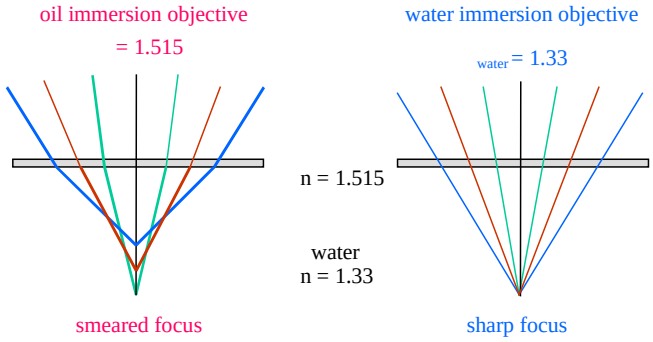

Spherical aberration occurs at the cover slip of oil immersion objectives so that the focus spreads into a cylindrical shape with depth below the glass/water interface.

Water immersion objectives provides a sharp diffraction limited focus spot independent of the depth of the aqueous sample.

Figure 2. Superior focussing of water immersion objectives in aqueous media.

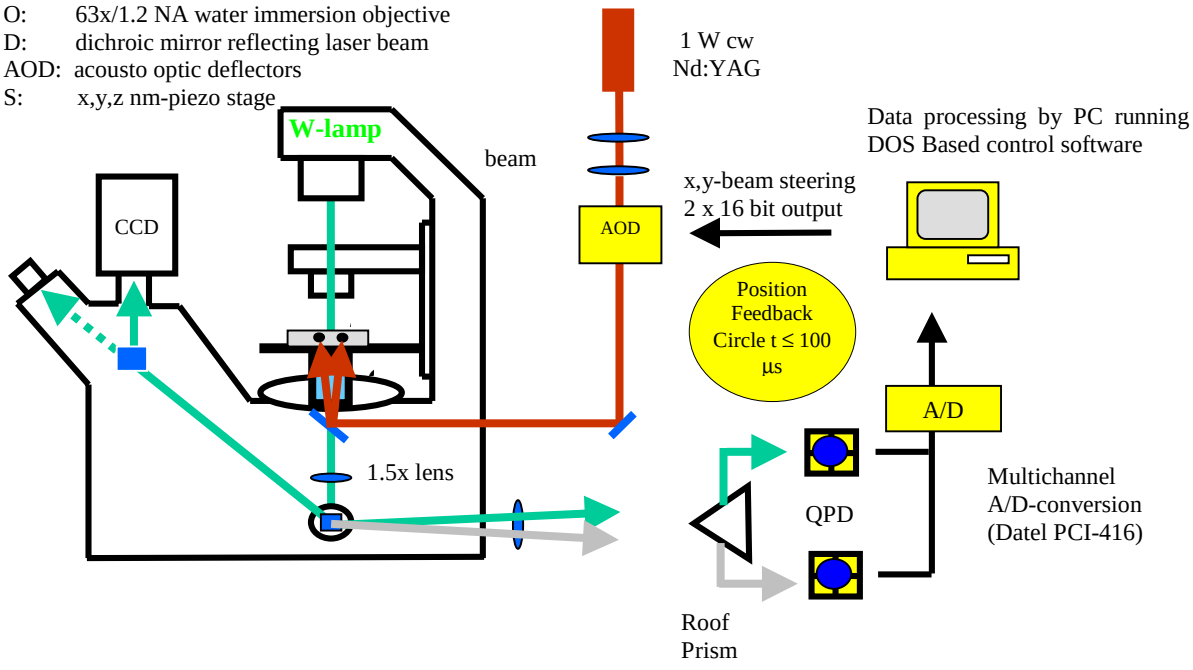

Figure 1. Laser Tweezers Setup.

Experimental.

The laser tweezers set up is shown in Figure 1. The long working distance water immersion objective (63x/1.2 NA) has been chosen, because it provides a sharp focus and thus constant trap stiffness up to 200 μm into an aqueous colloidal solution. This is a great advantage, because the trap stiffness of commonly used oil immersion objectives decreases rapidly with depth into aqueous solutions (Figure 2) and allows stable trapping only up to a few tens of μm away from the cover slip.

However, for preliminary set up and interfacial trapping, a He-Ne laser beam (632 nm 30 mW) is coupled to a microscope (Leica IRB) through a port directly below the nosepiece and focussed by a relatively low numerical aperture objective (40x, 0.5 N.A.) on a custom made anti-vibration table. The specimen is viewed upon illumination with white light using a CCD-camera. A large fraction of the viewing light is reflected onto a quadrant photo diode for nm-position detection. The analogue signals are digitized by a PC based acquisition board (Datel PCI-416). The x-y position of the particle(s) is calculated with nm accuracy from difference of the signals from adjacent diode segments (Figure 3). A special sample holder has been designed to reduce the effects of meniscus and to create either a flat horizontal water/oil – or water/air-interface. This has been achieved by constructing a composite cell of Teflon and steel. Water preferentially wets the stainless steel whereas oil or air preferentially wets the Teflon. The interface is therefore fixed at the border between steel and Teflon. Using a computer controlled piezo electric stage (100 μm in x ,y and 20 μm in the z directions), we can define precise positions with constant velocity dx/dt (dy/dt) and acceleration dx/dt2 or (dy/dt2). It is also possible to drive the stage with predefined wave signals, e.g. sinusoidal, rectangular and triangular – with full control of frequency and amplitude.

Results and future work

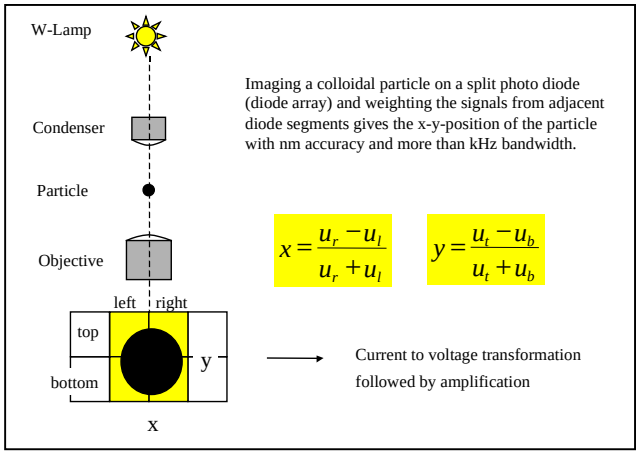

Figure 3. Particle position measurement with nm-resolution weighting rather than counting.

Figure 4 shows an optically trapped polystyrene latex particle (1 -2 μm) in a lattice. We have also trapped oil lenses (dodecane and decanol) and droplets resting at (below) fluid/fluid-interfaces –i.e. water/air and water/alkane.

Microscopic objects resting at a fluid/fluid-interface are already fixed in the x-y-plane. This eliminates the need to create an optical potential minimum in the z-plane. This potential minimum in the z-plane is the most difficult part in creating a conventional 3-dimensional optical trap in bulk systems and requires an expensive set up.

The scattering and reflective forces of the focussed laser beam with a convergence angle of 60 degrees in our experiment did not appear to influence the equilibrium resting position of the objects at the interface.

Using this set up and further modifications, we hope to investigate the effects of (i) trans-locating of the trapped polystyrene latex particle along the interface and (ii) modifying the crystal lattice environment with charged species, e.g NaCl, so that subsequent changes in lattice pN forces can be determined.

It may also be possible to calculate the actual scattering forces involved in the laser trap[1,2].

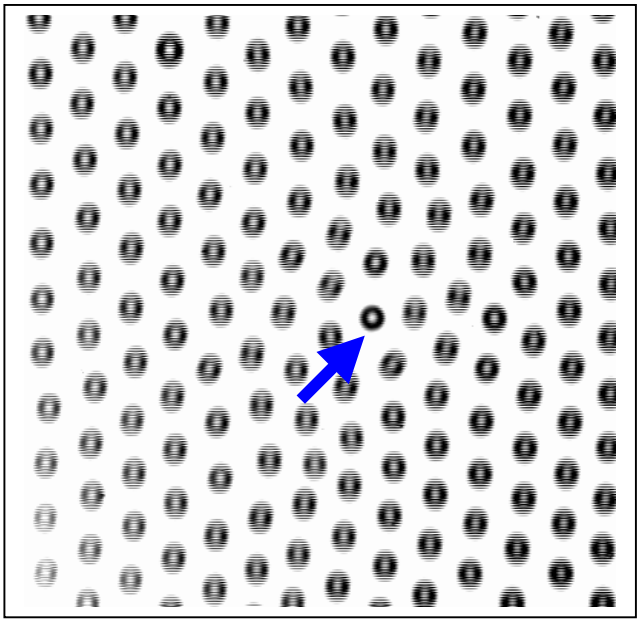

Figure 4. A trapped single particle (arrow) from a crystalline latex monolayer. Surrounding particles are blurred due to their motion.

References

1. A. Ashkin et al : Proc. Nat. Acad. Sci. *USA* 94 (1997) 4853-4860

2. (a) M.P. Sheetz: Methods in Cell Biology, 55 , Academic Press, San Diego 1998: (b) Karl Otto Greulich: Micromanipulation by Light in Biology and Medicine, Birkhauser Verlag, Berlin, 1999

Temperature and Time-Resolved Resonance Raman Spectroscopy

I P Clark, A S Wilkinson, M Towrie, A W Parker

Central Laser Facility, CLRC Rutherford Appleton Laboratory, Chilton, Didcot, Oxon, OX11 0QX, UK

P O'Neill

DNA Damage Group, MRC Radiation & Genome Stability Unit, Harwell, Didcot, Oxon, OX11 0RD, UK

Main contact email address: *I.P.Clark@rl.ac.uk*

Introduction

For many years now there has been considerable interest in the study of protein folding[1-5], the aim of much of the research being to predict a protein's secondary and tertiary structures from its primary sequence. To date this remains one of the hottest topics in biochemistry.

Rearrangement of protein secondary structures is known to take place on nanosecond timescales while for tertiary structures this occurs in the millisecond time-domain. Recently[6,7] time-resolved resonance Raman spectroscopy has been successfully applied to measuring the early timescale events (ns) of α–helical (secondary structure) folding/unfolding (or melting) of peptides following thermal activation. An infrared pulse (3 ns, 1.9 μm) was used to provide a rapid solvent temperature-jump, required for the melting of the peptide, and was followed by a time delayed UV (3 ns, 204 nm) Raman probe pulse allowing structural changes to be monitored.

To provide the Central Laser Facility with the capability to study protein dynamics requires a source of pulsed infrared radiation coincident with the near-infrared water absorption band. This report outlines how this was achieved and provides evidence for the rapid temperature-jump.

Experimental

There are two possible options available to produce the required infrared pulse: one is to use the current Nd:YAG pumped OPO (seeded Continuum *Power Lite 8000* YAG with Continuum *Sunlite* OPO) idler output at 1650 cm^{-1} already available in the Nanosecond Laboratory; the second is to install a hydrogen filled Raman shifter and to use the first stokes shift of the Nd:YAG fundamental, ie shift the fundamental by 4155 cm^{-1}, the vibrational frequency of H_2, to produce 1.9 μm. The latter option was chosen for two reasons. First, the idler output of the OPO is only specified to be 10 mJ at this wavelength while it is estimated that ca. 40 mJ could be obtained from a Raman shifter. The second choice is also preferred because of less shot-to-shot variation in pulse energy.

The optical arrangement of the H_2 filled Raman shifter is shown in Figure 1. Two 1064 nm mirrors, M1 and M2, are used to steer the YAG fundamental to the Raman shifter, entering through L1, a CaF_2 lens f = 500 mm, acting as the front window which focuses the beam into the centre of the 1 m Raman shifter. After exiting the shifter through a plane CaF_2 window, W1, the output is recollimated by a second CaF_2 lens, L2, f = 500 mm. Finally a 60˚ prism, P1, is used to disperse the various output wavelengths and a beam dump is used to isolate the desired wavelength.

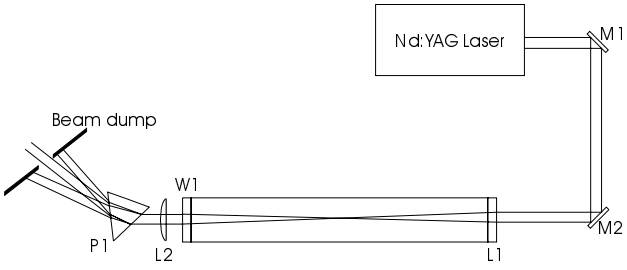

Figure 1. The experimental set-up showing the Nd:YAG pumped H_2 filled Raman shifter.

The efficiency of a Raman shifter is known to be dependent on the pump energy and the gas pressure[8-10]. The maximum energy obtained at 1.9 μm was 35 mJ. This was achieved with a pump energy of ca. 1 J at 10 Hz and a pressure of 1216 kPa (the maximum pressure achievable with the current Raman shifter design). On lowering the pressure to 608 kPa the output energy dropped to 10 mJ.

To determine whether the infrared pulse induced a temperature-jump in water, Raman spectra of water were obtained at various time delays after the 1.9 μm pump. The 220 nm Raman probe wavelength was produced using a frequency doubled excimer (Lumonics *Pulsemaster PM-800*) pumped dye laser (Lambda Physik *FL3002*) containing Coumarin 120 and was focused to ca. 500 μm at the sample. After delivery to the triple stage Raman spectrometer (Spex *Triplemate 1877 Series*) the energy of the 1.9 μm beam was reduced to 2.5 mJ, made coaxial with the probe beam and focused to the same point.

All samples were HPLC grade water (Aldrich), contained in quartz tubes (2mm ID). All spectra were recorded in 90º geometry.

Results

Figure 2 shows four water spectra, one with probe only and three with pump and probe at different time delays. Figure 3 shows the three pump/probe spectra illustrated in Figure 2 with the probe only spectrum subtracted. All three difference spectra clearly show a peak at ca. 3560 cm^{-1} attributed to the temperature-jump induced by the 1.9 μm beam.

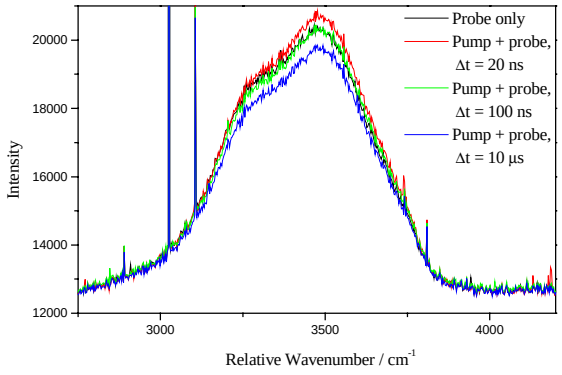

Figure 2. Raman spectra water, probe wavelength is 220 nm, 0.25 mJ, pump wavelength is 1.9 μm, 2.5 mJ. Acquisition time for all spectra is 200 s.

From Figure 3 it can clearly be seen that the changes in the 3500 cm^{-1} water created upon heating persist for more than 10 μs and there is little difference between short and long time delay. In fact the peak observed in the difference spectra is present out into the millisecond time delays.

Thus at present the combination of the YAG fundamental and the H_2 filled Raman shifter can be used as a 1.9 μm source to induce a rapid temperature-jump in solvents with an absorption band coincident with the pump. By recording steady state Raman spectra of the solvent at various elevated temperatures it will be possible to produce a calibration plot to enable the

temperature-jump to be calculated providing an "internal thermometer".

Drs Searle and George from the University of Nottingham have successfully used the Raman shifter in combination with Dr George's time-resolved infrared set-up to study the protein folding of bovine ubiquitin (a small protein of 76 residues). This work has recently been accepted for publication in Chemical Communications and is described in an article by Colley et al. within this annual report [11)].

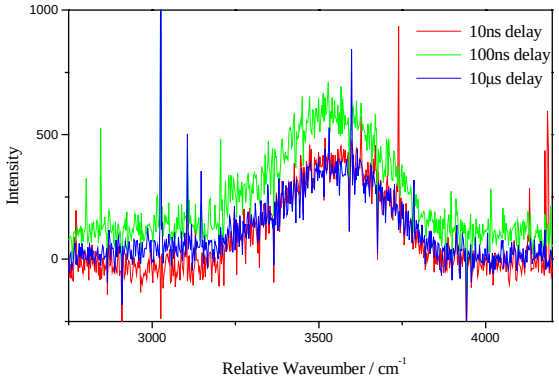

Figure 3. Pump/probe spectra illustrated in Figure 2 with the background (probe only) subtracted. All three spectra clearly show a peak attributed to the temperature produced by the 1.9 µm pump.

References

1. H Bryngelson, S G Sligar and P G Wolnes
Proc. Natl. Acad. Sci. USA 84, 7524 (1987).

2. P Jennings and P E Wright
Science, 262, 892 (1993).

3. L L P Hosszu, C J Craven, M J Parker, M Lorch, J Spencer, A R Clarke and J P Waltho
Nat. Struct. Biol. 4, 801 (1997).

4. M Gruebele, J Sabelko, R Ballew and J Ervin
Acc. Chem. Res. 31, 699 (1998).

5. W Eaton, V Munoz, P A Thompson, E R Henry and J Hofrichter, Acc. Chem. Res. 31, 745 (1998).

6. I K Lednev, A S Karnoup, M C Sparrow and S A Asher
J. Am. Chem. Soc. 121, 4076 (1999).

7. I K Lednev, A S Karnoup, M C Sparrow and S A Asher
J. Am. Chem. Soc. 121, 8074 (1999).

8. C Guntermann, V Schulz-von der Gathen and H F Döbele
Appl. Opt. 28, 135 (1989).

9. I Fischer and T Schultz
Appl. Phys. B. 64, 15 (1997).

10. D A Haner and I Stuart McDermid
IEEE J. Quantum Electron. 26, 1292 (1990).

11. C S Colley, S R Griffiths-Jones, M W George, M S Searle and I P Clark, A S Wilkinson, Central Laser Facility Annual Report 1999/2000, pg 120.

Ultrafast Optical Triggering for X-ray and Optical Femtosecond Streak Cameras

R J Clarke, R M Allott, S Bremner, J L Collier, S Hawkes, C Hernandez-Gomez, D Neely, R Wyatt

Central Laser Facility, CLRC Rutherford Appleton Laboratory, Chilton, Didcot, Oxon, OX11 OQX, UK.

Main contact email address: *R.J.Clarke@rl.ac.uk*

Introduction

The technique of Chirped Pulse Amplification (CPA) is now in common use on many laser systems and has resulted in the dramatic reduction of pulse lengths in order to increase intensities delivered to target. With this technique being adopted worldwide, streak cameras have had to follow and now units are produced with very high temporal resolution, some of which push the picosecond barrier. With such high resolution, the overall 'time window' for these cameras has had to be reduced, making triggering stability a more complicated task.

Streak Camera Triggering

With a completely electrical trigger derived from the Vulcan Nd:glass laser system, trigger jitter of up to 200 ps can be observed, restricting streak camera time windows to 500 ps. This means that the use of both x-ray and optical femtosecond streak cameras with electrical triggering is not feasible as time windows for the x-ray streak camera (80 ps) and optical streak camera (200, 100, 50 & 20 ps) are too small.

Optical triggering using a beam leakage has also been attempted using photodiodes. Unfortunately, trigger stability showed no improvement due to restrictions in signal level. To produce the trigger pulse early enough for streak camera triggering, the photodiodes have to be used with a stretched pulse part way through the amplifier chain. This produces further jitter problems due to the relatively long rise time of the optical pulse. The streak camera trigger level is also reached at a different time due to the diode rise time changing as energy changes were made.

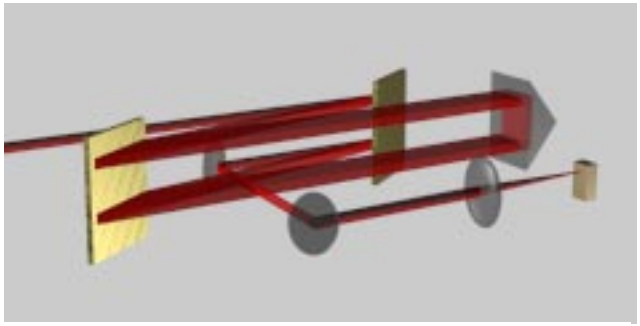

Figure 1. Schematic of the optical compressor.

In order to overcome these problems, a system was designed to take a Fresnel reflection from the end of the Vulcan 9 mm rod amplifier chain where energy variations between shot types is negligible. The reflected beam is image relayed to the target area where it is re-compressed to a short pulse, overcoming the problems encountered using the stretched pulse. The compressor consists of a double-pass grating system with a rooftop prism to shift the beam height before the second pass. The output from the compressor is then sent through a focussing lens onto the detector. A representation of the compressor is shown in Figure 1.

Detector

In order to take advantage of the compressed pulse, a 20 GHz photodiode capable of < 12 ps rise time (supplied by Advanced Photonic Systems) is used for the optical streak camera.

For use with an x-ray streak camera, the diode has to be replaced with an Austin switch in order to obtain the high output voltages required. The Austin switch is simply a small piece of silicon with a high voltage (~80 V) connected across it. When the laser light hits the detector, the semiconductor becomes conductive and both a fast rise time and high output voltage can be obtained. The Austin switch has a relatively slow fall-off time (around 60 ns) which is ideal for streak camera trigger units, operating on a charge basis rather than a standard voltage trigger. Due to the lower sensitivity of the Austin switch, an extra 9 mm rod amplifier is added to the laser system to increase the energy level onto the detector. Both detectors, along with a sample output trace from the Austin switch can be seen in Figure 2.

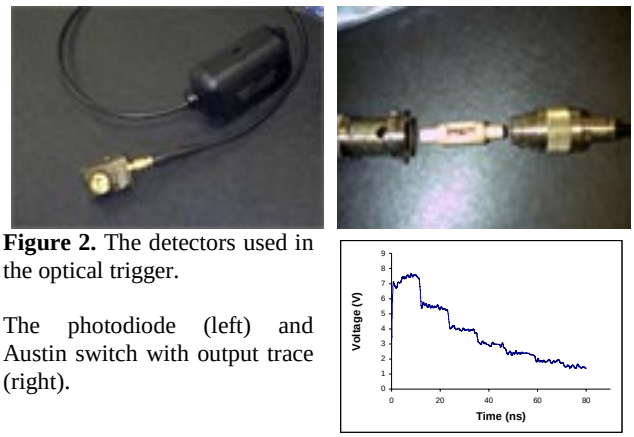

Figure 2. The detectors used in the optical trigger.

The photodiode (left) and Austin switch with output trace (right).

Operation

The optical trigger, using an Austin switch as the driving device, was used in a European experiment[1)] in Target Area West of the Vulcan Laser Facility. The fast optical triggering of a femtosecond x-ray streak camera led to the observation of a 3 ps x-ray laser pulse at 139.9 nm, shown in Figure 3. Measurements performed during the experiment showed trigger jitter of less than 30 ps.

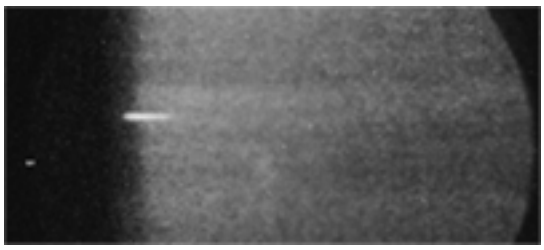

Figure 3. The 3ps x-ray laser observed using the femtosecond x-ray streak camera.

References

1. A.Klisnick et al, Central Laser Facility Annual Report 1999/2000, pg 50.

Manganese adhesion vacuum deposition trials

L J Coffey, D Neely, M Harman, R Allott, N Prior, D Shepherd, M Waite

Central Laser Facility, CLRC Rutherford Appleton Laboratory, Chilton, Didcot, Oxon, OX11 OQX, UK

J S Wark, D Chambers, J Hawreliak

Department of Physics, Clarendon Laboratory, University of Oxford, Oxford. OX1 3PU, UK

Main contact email address: *L.J.Coffey@rl.ac.uk*

Introduction

A radiation transport experiment to be carried out in the CLF Vulcan Target Area required a 1 µm thick flat, large surface area manganese film. Manganese is a hard, brittle metallic element and only commercially available supplied with a permanent backing support, which is too thick to assemble within the set-up. Removal of the foil causes irreversible destruction.

Development trials were undertaken to investigate the adhesion and surface roughness characteristics of manganese film deposition upon a variety of five metallic foil substrates and a plastic foil substrate. Durability of a film is largely dependent upon adhesion between the film and substrate.

During thin film processing substrates are subjected to mechanical and thermal stress. Heating coupled with expansion can lead to mechanical strain within the deposition layer, which may result in structural damage. The coefficient of linear expansion (thermal property responsible for determination of dimensional changes) for manganese is 23.0 x 10^{-6} K^{-1}. The selected foils were chosen with thermal properties greater and less than this value (as detailed to follow).

Method

Manganese, which has melting and boiling points of 1244˚C and 1962˚C is ideally suited to vacuum deposition using thermal evaporation.

The foils were mounted in an aluminium frame for simultaneous coating, to reduce any differences that may have otherwise occurred. The distance between the aluminium frame and the molybdenum boat source in which manganese powder was placed was approximately 20 cm. The area of each foil exposed to the manganese was 1.8 cm^2.

As a result of film deposition, each substrate becomes entirely heated and ultimately cooled. The additional thermal energy experienced by the substrate atoms leads to increased amplitudes of vibration and thereby average atomic separation and hence substrate expansion.

Foil material	Linear expansion coefficient (x10^{-6} K^{-1})
Iron	12.1
Stainless Steel	16.0
Copper	17.0
Manganese	**23.0**
Tin	23.5
Aluminium	23.5
PET (Polyethylene Terephthalate)	30.0 – 65.0

Table 1. Thermal properties of selected substrates and film.

The coefficient of linear expansion explains these structural changes. Mismatch between substrate and film coefficients results in adhesion differences.

Results

Each deposition was examined with a microscope and images captured via a CCD camera to illustrate the surface characteristics observed. Figures 1 to 6 depict the manganese deposition images, which identify tin as the ideal substrate with the smoothest deposition. The area of the images is approximately 0.6 cm^2.

Figure 1. Aluminium substrate with Manganese deposition.

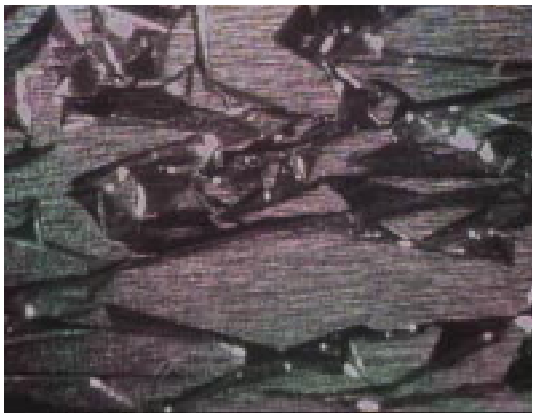

Figure 2. Iron substrate with Manganese deposition.

Figure 3. Copper substrate with Manganese deposition.

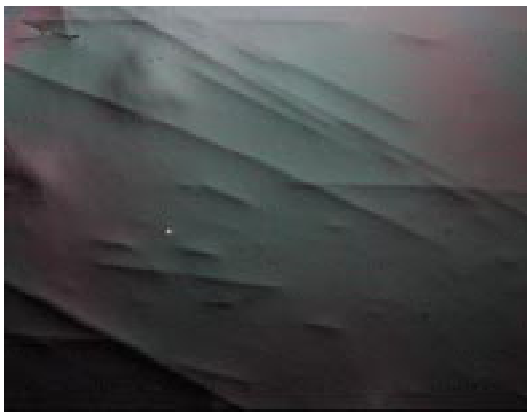

Figure 4. PET substrate with Manganese deposition.

Figure 5. Stainless steel substrate with Manganese deposition.

Figure 6. Tin substrate with Manganese deposition.

Foil material	Observations
Iron	Random jagged effect with smooth surrounding area, about 50% jagged
Stainless Steel	Mainly smooth with islands forming around the circumference
Copper	Variable striations over entire surface
Tin	Smooth over entire surface
Aluminium	Rough surface over entire coated area
PET	Smooth with minority area random lines

Table 2. Surface characteristic observations

The aluminium frame in which the foils were placed was observed to affect the manganese in the same way as the aluminium substrate. Observations recorded about the manganese deposition per material are detailed in Table 2.

After the coatings were examined under the microscope, each was tested for durability (adhesion) by the squashing and bending of the coated substrates. The unacceptable surfaces observed on the remaining substrates were indicative of mechanical failure with minimal handling, with the manganese parting easily as a result of poor adhesion.

Most films produced by thermal evaporation experience internal stress, which in extreme cases causes films to buckle and break up. The images of surface roughness illustrate the film in different stages of stress, demonstrating obvious differences between the substrates selected.

In Figures 1, 3 and 5 the film is observed to curl up upon separation from the substrate. This is indicative of non-uniform stress within the film. Breaking of the adhesive bond between the substrate and film allows the manganese to part from the substrate.

The coefficient of linear expansion has proved to play an important role in the determination of the correct substrate-film collaboration. The features observed in Figures 1 to 6 are associated with the variations of linear expansion coefficients. When there is a difference, heating and cooling produces additional stress (thermal stress) at the interface. The magnitude and type of stress induced is dependent upon the coefficient difference.

Conclusion

Tin was found to be the most resilient substrate and PET the second most resilient.

These trials readily demonstrate the adhesion limitations induced as a result of film-substrate coefficient variation.

After completion of these trials a 1 µm coating of manganese was deposited onto a 25 µm tin foil substrate for use during a Target Area East experiment on the Vulcan laser. The users were happy with the target, which, without such trials, would not have been available.

References

1. L. Maissel and R. Glang
Handbook of Thin Film Technology
M^{c}Graw Hill Book Company (1970)

An Investigation Into the Characterisation of Thin Films

T Stinson, R M Allott, R J Clarke, L J Coffey, D L Shepherd, M Waite

Central Laser Facility, CLRC Rutherford Appleton Laboratory, Chilton, Didcot, Oxon, OX11 0QX, UK

Main contact email address: *L.J.Coffey@rl.ac.uk*

Introduction

The target preparation laboratory within the Central Laser Facility is responsible for the production of interaction targets used during Vulcan experiments. The targets used in these experiments can be extremely complex in both design and construction and must meet the exact requirements calculated for the experiment. When it comes to quality controlling the experimental targets many different methods can be used to determine particular characteristics of each individual target. Thin film thickness characterisation can be very difficult to achieve. The aim of this investigation is to test the eligibility of the film spectrum program as a quality control method.

Experimental Schemes

Thin film targets can be deposited by physical or chemical methods. In the target preparation facility the physical deposition processes of evaporation and sputtering deposition are used. The pictures (shown below) are of typical thin film targets used in the target preparation laboratory. These targets are CH (plastic) film mounted onto an Aluminium holder and a Titanium film sputtered onto a glass microscope slide.

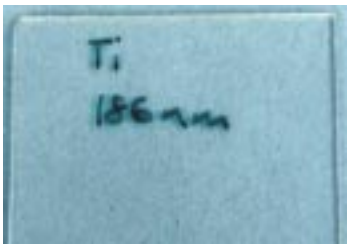

The previous method of thin film thickness characterisation involved using an interference microscope to measure the interference fringes between the film and the substrate material. This method has its limitations as damage to the target is often sustained while measuring. This new method of characterisation uses the extinction co-efficient, the index of refraction and the materials spectral properties at certain wavelengths of a thin film to calculate the thickness (d) of the film. The spectral properties of the film are measured using a spectrophotometer to determine the percentage transmission or reflection properties of the film. This data is then imported into the film spectrum program.

The Film Spectrum is a user-friendly software tool for the analysis and acquisition of spectroscopic and ellipsometric data. In particular, Film Spectrum: Simultaneously solves for refractive index n, extinction coefficient k and thickness of multi-layer and monolayer film structures of metals, dielectric, amorphous, and crystalline semiconductor materials for multiple wavelengths and angles of incidence.

Results

Using the spectral information the film spectrum program constructs a graph of the measured spectral properties. It then uses the model properties (entered into the computers model builder) to simulate a second plot (see Figure 1). The program then uses the generalised dispersion formula to fit the simulated plot onto the measured data (as shown in Figure 2).

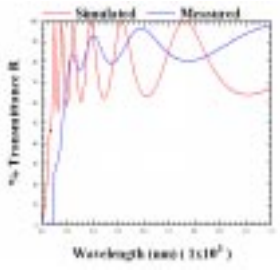

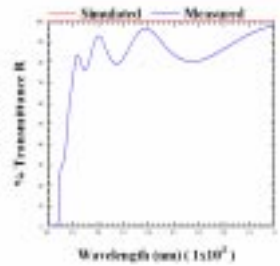

Figures 1 and 2. Initial and completed optimisations for a CH (plastic) film using the Film Spectrum program.

The simulated curve uses the wavelength and transmission (or reflectance) data, the Extinction co-efficient (k) and the index of refraction (n) of the material to calculate the thickness of the film, using a general dispersion formula similar to the Schult and Tangherlini equation for the determination of the thickness of the thin film.

For the initial investigation several CH and metal films of known thickness from outside manufacturers were processed to see if the program would calculate the thickness correctly. All the results were successful and the thickness of the processed films could be determined to within that stated by the manufacturer. This gave the program an overall uncertainty (incorporating both the manufacturer's error and the optimisation error) of ± 7.5 nm. Then the thicknesses of various deposited films of the following materials: Al (Aluminium), Ag (Silver), Au (Gold), CH (plastic) Ge (Germanium), Mn (Manganese), Mo (Molybdenum), Ni (Nickel), Sn (Tin), Ti (Titanium), V (Vanadium), and Zn (Zinc) were tested as well as multi-layered and semiconductor films.

Conclusions

It has been recommended that this method of quality control be used in future for the characterisation of all thin film targets within the limits of 10 nm and 1000 nm.

Calibration of a charge coupled device (CCD) using single photon counting

S J Pestehe, G J Tallents, Y Abou Ali

Department of Physics, University of York, Heslington, York, YO10 5DD, UK

E Turcu, M Powers

JMAR Research Inc., 3956 Sorrento , Valley Blvd., San Diego, CA 92121,USA

W Shaikh

Central Laser Facility, CLRC Rutherford Appleton Laboratory, Chilton, Didcot, Oxon, OX11 OQX, UK

Main contact email address: *sjp24@york.ac.uk*

Introduction

CCDs have found a wide range of applications as imaging sensors in the wavelength range from IR to hard x-ray[1)]. They are used in the spectroscopy of laser-produced plasmas [2,3,4)], x-ray laser studies[5,6)], and astrophysics[7,8)]. With this large range of applications, a reliable knowledge of their spectral response is important. The CCD's spectral response is usually calibrated using standard sources such as synchrotron radiation or gas discharges [9,10,11)]. There are also self-calibration methods, which have been employed[4,12)].

In this work we have calibrated an open electrode, front illuminated Andor CCD camera by a single photon counting technique using characteristic lines of different targets emitted from a laser produced plasma.

Experimental set-up

The experiment has been carried out at the Central Laser Facility (CLF) at the Rutherford Appleton Laboratory (RAL), under a contract between RAL and JMAR Research Incorporation. The laser system used in this experiment comprised two commercial KrF excimer lasers (Questek 2440), with a quenched dye laser oscillator[13,14)]. The laser system was operated with two different pulse configurations. First a train of pulses of ~20 ns duration containing 8 individual 5 ps pulses spaced by 2 ns with repetition rates of 12.5 and 50 Hz was focused to a spot size of approximately 70 μm^2. The maximum irradiance was 5×10^{15} Wcm^{-2}. In the second pulse configuration, the laser was operated with a single pulse of 2 ps duration with a repetition rate of 12.5 Hz and focused to a spot size of about 90 μm^2 giving a maximum irradiance of 5×10^{16} Wcm^{-2}. The schematic diagram of the experimental set-up is shown in Figure 1.

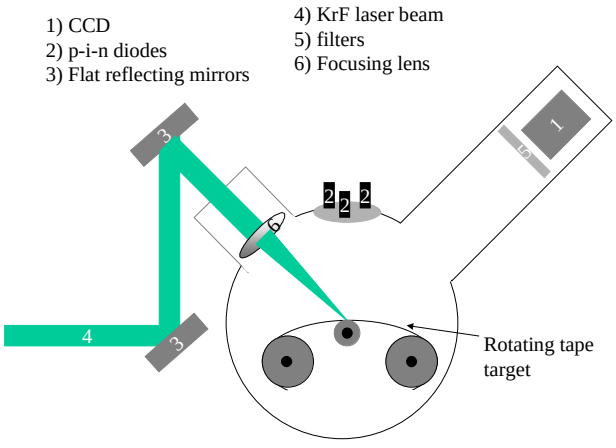

Figure 1. Schematic diagram showing the experimental set-up.

We have used an Andor technology front illuminated open electrode CCD and placed it a distance of 95 cm from the target. The CCD has been made light tight using a 25 µm Beryllium filter. Focusing the 248 nm KrF laser pulse on Al, Cl (PVC), Ti, Ag, and Fe thin tape moving targets generated the desired laser plasma x-ray sources. The target chamber was filled with helium gas at atmospheric pressure to stop debris particles[15)]. In addition the target was oriented such that the normal to the target plane makes an angle of 45° to the focusing lens. This reduces the amount of the debris ejected from the target towards the laser beam[13)].

Data acquisition and analyses

To get a set of suitable data for analyses with a single photon counting technique, without using any dispersing element, the number of incident photons on the CCD should be kept low, for example, less than one tenth of the total number of pixels. This ensures that the probability of finding two or more photons incident on one pixel is negligible. To do this the CCD has been placed far away from the source (95 cm), and different filter thicknesses placed in front of the camera have been adjusted so that only ~ 10% of the pixels are exposed in the image. Figure 2 shows a typical image, which has been taken from a Ti plasma.

Figure 2. A typical image from the Ti target taken with the Andor technology CCD camera filtered with 25 µm Be, 23 µm Mylar, 25µm Teflon, 10 µm Cu, and 10µm Ti. The probability of finding two or more photons in one pixel is low.

The detection of incident photons directly is complicated by event-splitting or charge migration[16)]. Charge migration between adjacent pixels is caused by (a) photon absorption in the distance between two pixels, (b) absorption of the charge in the field free region just below the depletion layer followed by charge diffusion into the depletion region, and (c) fast photoelectrons traveling large distances before exciting electrons from the valence to conduction bands. The incident photon polarisation gives a preferred velocity direction to the generated photoelectrons and hence a preferred direction to the charge migration[17)]. In data analysis, it is necessary to correct for the charge migration effect.

The charge collected in each pixel is quantified by the CCD system and we produce a spectrum by processing the images. A histogram of the pixel charge (proportional to photon energy) versus the number of pixels exposed in a charge range is produced. As the Andor software corrects the images for their background, in the histogram of the number of events versus the pixel counts, one obtains a high peak placed symmetrically around the zero count position, which is not a real signal. This peak arises because, by subtracting the background data from the real image data, one will get a statistically equal number of negative and positive counts in the histogram due to noise from both the exposed and background images. In a normal

histogram, without any photon reconstruction procedure, charge migration broadens this background correction peak asymmetrically on the positive side. Our photon reconstruction procedure counts the change in the neighboring pixels around a photon arrival by checking if the pixels have an exposure above a threshold level. This level is defined by assuming that the noise level should be at the same level as the negative end point of the background peak centred at zero. If the exposure is above the threshold, the count is included in the pulse height of the peak-exposed pixel. Both the normal histogram and the histogram corrected for charge migration of a typical image from Ti target filtered with 25 µm Be, 23 µm Mylar, 25 µm Teflon, 10 µm Cu, and 10µm Ti are shown in Figure 3.

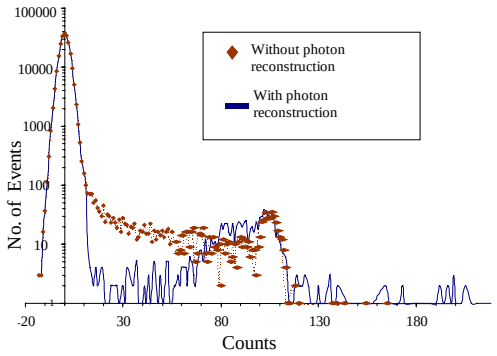

Figure 3. A histogram showing a high peak around the zero counts position typical of background corrected images.

Using this technique Silver Ne-like lines Titanium K_α, Flourine, Chlorine, and Aluminum hydrogen- and helium-like emission, and Cu L_α, lines have been detected. Figure. 4 shows some typical spectra from Ag, Ti, Cl, and Al targets.

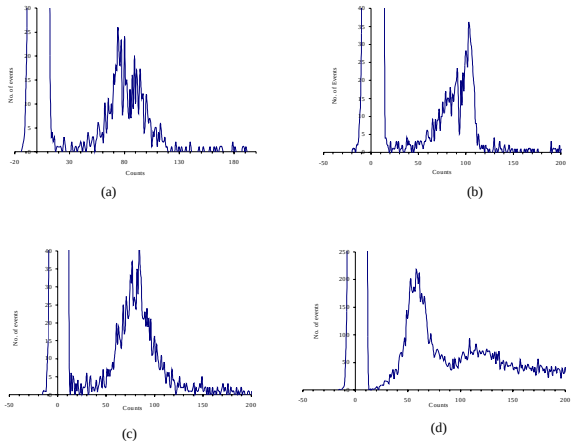

Figure 4. Corrected spectra showing (a) Ne-like Silver lines filtered with 25 µm Be, 23 µm Mylar, 25µm Teflon, 10 µm Cu, and 10µm Ti (b) Ti K_α filtered with 25 µm Be, 23 µm Mylar, 25µm Teflon, 10 µm Cu, and 10µm Ti (c) Cl filtered with 25 µm Be, 23 µm Mylar, 25µm Teflon, and 10 µm Cu, and (d) Al H-like and He-like lines filtered with 25 µm Be, 25µm Teflon, and 10µm Ti.

Using the above identified lines, the open-electrode Andor technology x-ray CCD camera has been calibrated for response as a function of photon energy, Figure 5. There is an offset of ~12 counts in the calibration curve, but the CCD response is otherwise linear with photon energy.

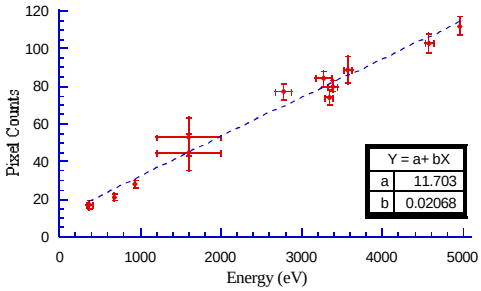

Figure 5. The calibration of the CCD. A fitted line is also shown on the graph.

References

1. J. R. Janesick, Opt. Eng. 26, 692-715 (1987).
2. P. Salieres, et al., in 'X-ray lasers 1992', edited by E. Fill (IOP, Bristol, 1992) p 367.
3. R. Smith et al, Laser and Particle Beams 17, 477-485 (1999.
4. S.J. Pestehe and G.J. Tallents CLF Annual Report 1998/99, p197-8.
5. J. Nilsen, et al, Phys. Rev. Lett. 70, 3713 (1993).
6. J Lin et al, J. Appl. Phys. 85, 672-675, (1999).
7. A.D. Holand, et al, Proc. SPIE 1159, 113 (1989).
8. Deacon, et al, Rev. Sci. Instr. 66, 1287 (1995).
9. D. Moses et al, Proc. SPIE 1656, 526 (1992).
10. R.A. Stern et al, Opt. Eng. 26, 875 (1987).
11. J.C. Lochner and E A Boldt, Nuc. Inst. And Meth. A.242, 382 (1986).
12. Y Li, G DTsakiris, and R Sigel, Rev. Sci. Instrum. 66, 80-86, (1995).
13. I.C.E. Turcu et al., J. Appl. Phys. 73, 12, (1993).
14. I.C.E. Turcu, I N. Ross, and G.J. Tallents, Appl. Phys. Lett. 63, 22, (1993).
15. I.C.E. Turcu et al, SPIE 1503, 391 (1991).
16. K. Hashimotani et al, Rev. Sci. Instruments 96, 3746 (1998)

A large aperture Interferometer for optical Quality Assurance

T B Winstone, K I Hughes, A J Frackiewicz, S J Hawkes, I N Ross, C B Edwards, C J Reason, C N Danson

Central Laser Facility, CLRC Rutherford Appleton Laboratory, Chilton, Didcot, Oxon, OX11 0QX, UK

Main contact email address: *T.B.Winstone@rl.ac.uk*

The measurement of optics, in particular the flatness and transmission characteristics, has always been an important part of the quality assurance for the Central Laser Facility.

Our existing MkII Fizeau Interferometer from Zygo is still working reliably using static analysis but optics on Vulcan in particular had for some time exceeded the aperture of the system. With the Vulcan Petawatt Upgrade the need for a larger aperture system became critical. Several options were considered and the most cost effective option which fulfilled most of our requirements would be to upgrade the MkII Zygo from 150 mm to 300 mm aperture[1].

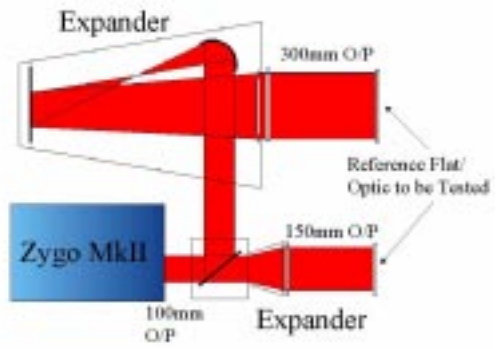

Figure 1. Schematic of the interferometer arrangement showing the ability to have the two permanently set up beams of 150 mm and 300 mm diameter respectively.

The output of the Zygo MkII can be directed into two possible arms. One arm contains the original 150 mm diameter optics whilst the reflected beam is put through a beam expander to increase the diameter to 300 mm. The layout of the system can be seen in Figure 1. This provides a facility to test both 150 mm and 300 mm diameter option permanently set up side by side.

The tightest specification of standard optics on Vulcan is for the transmission quality of the second harmonic optics which have to be better than λ/10 peak to valley at 527 nm. This corresponds to λ/12 at 632 nm and therefore this was chosen as the measurement specification. The commissioning phase of the interferometer was carried out by the manufacturer producing the results[2] as shown in Figure 3. This result of 0.080λ at 632.8 nm is marginally better than the target of λ/12.

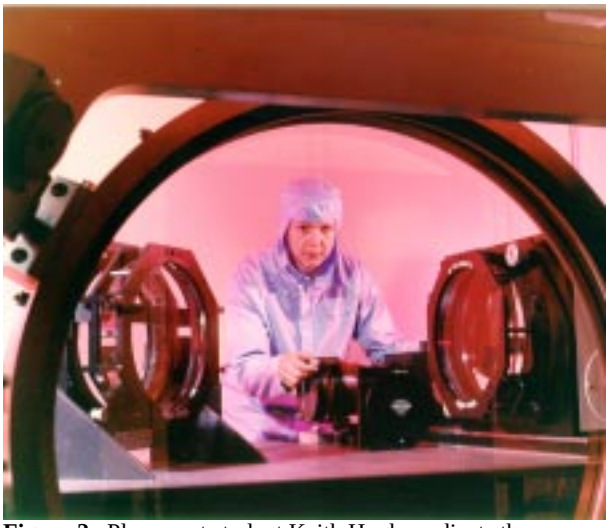

Figure 2. Placement student Keith Hughes adjusts the interferometer arrangement, with a 940 mm diameter mirror from the Vulcan Petawatt Upgrade in the foreground.

Conclusion

The improvements in the quality assurance capabilities of the Central Laser Facility have been significantly upgraded using a very cost effective solution which also brings with it a large amount of versatility. This enhancement has greatly assisted the assessment of medium to large aperture optics both for the Vulcan system and for the Petawatt upgrade.

References

1. Zygo Corporation, Middlefield, Connecticut, 06455, USA
2. OFA Fringe Master, Oxford Framestore Applications, Wantage, Oxfordshire, UK

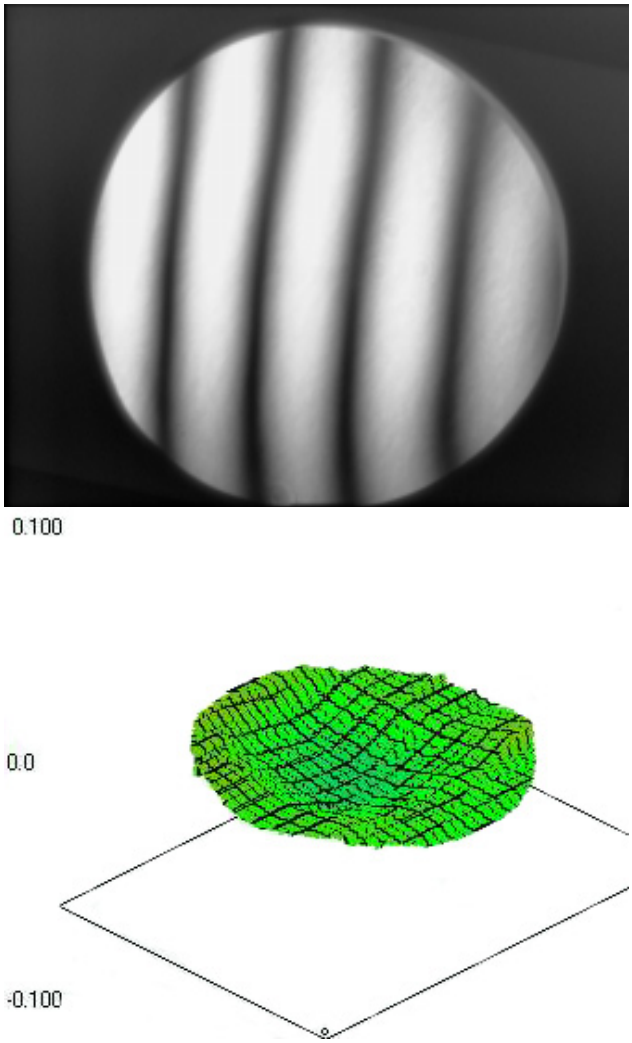

Figure 3. a) Fringes produced by the 300 mm diameter static Fizeau Interferometer testing the large aperture reference flat. b) 3 dimensional OPD analysis of the fringes in a).

A Spectral Phase Measurement Diagnostic for Vulcan

C Hernandez-Gomez, J Collier, F Budd

Central Laser Facility, CLRC Rutherford Appleton Laboratory, Chilton, Didcot, Oxon, OX11 0QX, UK.

Main contact address: *C.Hernandez-gomez@rl.ac.uk*

Introduction

A new single shot diagnostic has been developed for use on the Vulcan laser system based on the Spectral Phase Interferometry for Direct Electric Field Reconstruction (SPIDER) technique[1]. This diagnostic enables the measurement of the spectral phase of pulses with pulse lengths from 300 fs up to 2 ps at a centre wavelength of 1053 nm with bandwidths of 2 – 6 nm. This information will be used to optimize the setting of the CPA Stretcher/Compressor systems.

Description

The SPIDER apparatus is shown in Figure 1. It has been designed to fit on a 90 cm x 60 cm breadboard. It consists of four main parts: a pulse stretcher, a pulse replicator, a frequency mixing crystal and a high resolution spectrometer.

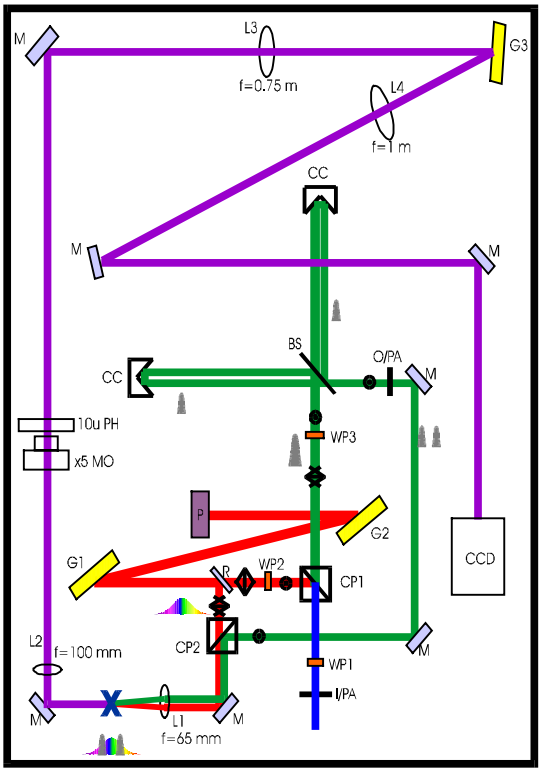

Figure 1. Schematic layout of the SPIDER apparatus.

The input pulse is split into two by the combination of a waveplate and cube polariser CP1. One pulse is injected into the stretcher where it is stretched in time and the second pulse is injected into the pulse replicator to create a pair of identical pulses separated in time by an amount τ. The stretched pulse and the two identical pulses are recombined by a cube polariser CP2 and directed to the frequency mixing crystal.

The double pass pulse stretcher is formed by two parallel 1660 lines/mm gratings 292 mm apart, operated at 55° incidence angle. It produces a group velocity dispersion of 39.6 ps/nm. The pulse replicator has the structure of a Michelson interferometer. A beam splitter generates the two identical pulses. Each pulse travels along an arm length of 220 mm. The path-length of one arm can be altered such that the delay τ between the two pulses can be adjusted. This pair of pulses overlap spatially in the near and far field upon recombination at the beam splitter. The distances of the two arms are chosen such that the two identical pulses will overlap in time with the stretched pulse at the recombination point CP2. The beam from the stretcher and the beam from the pulse replicator are set to overlap in the far field but are slightly spatially displaced in the near field at CP2. These orthogonally polarized beams are directed to the non linear frequency mixing crystal. The non linear crystal used is KTP. The identical pair are thus frequency mixed with the stretched pulse. Because of the chirp of the stretched pulse and the separation in time imposed in the pulse replicator, the replicated pair of pulses are up-converted with different frequencies of the stretched pulse thus generating two frequency sheared pulses at close to the second harmonic. These frequency sheared up-converted pulses are then directed to the spectrometer.

The spectrometer was designed and tested to have a resolution of 50,000. A x5 microscope objective focuses the beam through a 10 µm pinhole. The beam is then collimated by a 750 mm focal length lens. The beam is now 50 mm in diameter and is diffracted off a 1660 l/mm grating operated at 6.5° incidence angle and focussed by a 1000 mm focal length lens into a CCD camera.

Because these two pulses are separated in time by τ they will interfere spectrally. A typical image from the CCD camera showing the spectral interference between the two pulses is shown in Figure 2 for τ = 16.6 ps.

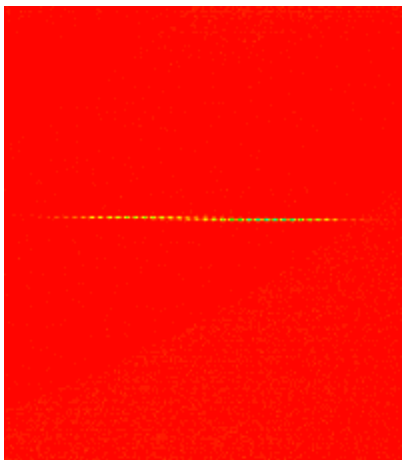

Figure 2. CCD image of the spectral interference between the two up-converted pulses.

Spectral Phase Retrieval

The recorded CCD image (Figure 2) of the spectral interference between the two pulses is vertically integrated to generate a 1D interferogram $D(\omega_c)$. The spectrally calibrated interferogram $D(\omega_c)$ obtained from Figure 2 is shown in Figure 3. $D(\omega_c)$ is a shearing interferogram of the form:

$$D(\omega_c) = \left|\tilde{E}(\omega_c - \Omega)\right|^2 + \left|\tilde{E}(\omega_c)\right|^2$$
$$+ 2\left|\tilde{E}(\omega_c - \Omega)\tilde{E}(\omega_c)\right| \cos\left[\phi_\omega(\omega_c - \Omega) - \phi_\omega(\omega_c) - \tau\omega_c\right]$$

where ω_c is the centre frequency of the spectrometer, $\phi(\omega)$ is the spectral phase of the input pulse at ω, Ω is the frequency

shear, $\left|\tilde{E}\left(\omega_C-\Omega\right)\right|^2$ and $\left|\tilde{E}\left(\omega_C\right)\right|^2$ are the second harmonic spectra for each of the sheared pulses and $\left|\tilde{E}\left(\omega_C-\Omega\right)\tilde{E}\left(\omega_C\right)\right|$ is the spectral amplitude of the envelope of $D(\omega_c)$.

The first two terms in $D(\omega_c)$ are eliminated from the interferogram by setting the stretched pulse and the pair of replicated pulses spatially separated in the nearfield. Use of an aperture prevents the injection of these second harmonic signals in to the spectrometer and thus only the frequency mixed pulses are injected (third term of $D(\omega_c)$) . Additionally, the crystal is phase matched to maximize the frequency mixed signals and minimize the second harmonic ones.

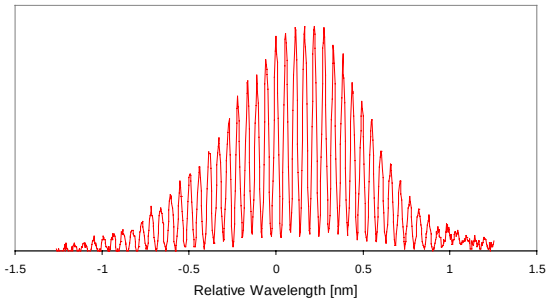

Figure 3. SPIDER Interferogram obtained from Figure 2.

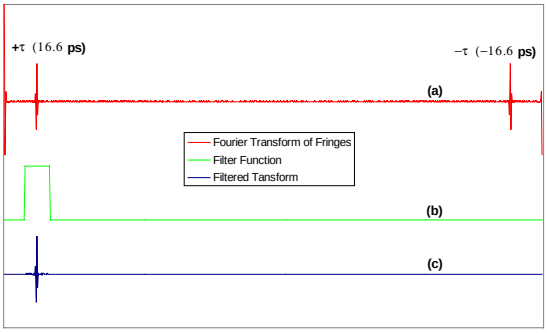

Figure 4. The filtering process of the Fourier transform of Figure 3 isolates positive temporal components only.

Spectral phase retrieval is accomplished following a procedure proposed by Takeda[2]. The interferogram is Fourier transformed with respect to the spectrometer frequency (Figure 4a). The components of the Fourier transform centered around $t=+\tau$ are filtered using a filter function (Figure 4b), removing the term centered at $t=0$ and the negative components centered around $t=-\tau$. The filtered components (Figure 4c) are inverse Fourier transformed and the phase of this inverse transform is subsequently extracted. This extracted phase is then the argument of the cosine term of $D(\omega_c)$ ie $\phi_\omega(\omega_c-\Omega)-\phi_\omega(\omega_c)-\tau\omega_c$

The next step is to remove the term $\tau\omega_c$. This term is obtained by recording the interferogram between two up-converted pulses that have not been frequency sheared ($\Omega=0$). This is achieved by blocking the stretched pulse, adjusting the KTP crystal such that the second harmonic signals are now maximized and opening the aperture at the input of the spectrometer to allow the second harmonic signals into the spectrometer. This calibration interferogram is treated in the same way as explained above. It is Fourier transformed, filtered and the filtered components inverse Fourier transformed to give the phase term $\tau\omega_c$ only. In this case the frequency spacing of the fringes is exactly $1/\tau$. This calibration phase is then simply subtracted from the transform phase retrieved from a normal SPIDER interferogram to yield $\phi_\omega(\omega_c-\Omega)-\phi_\omega(\omega_c)$.

The final step is to reconstruct the spectral phase from the spectral phase difference $\phi_\omega(\omega_c-\Omega)-\phi_\omega(\omega_c)$. This term manifests itself on the interferogram as modulations of the nominal fringe spacing $1/\tau$. If the frequency shear Ω is small, this phase difference is approximately the first derivative of the spectral phase. Therefore the spectral phase $\phi(\omega_c)$ can be obtained by integration:

$$\phi\left(\omega_C\right)=\frac{1}{\Omega}\int\left(\phi_\omega\left(\omega_C-\Omega\right)-\phi_\omega\left(\omega_C\right)\right)d\omega_C$$

The phase normalization to the frequency shear Ω is calculated from the stretcher dispersion and pulse separation.

Testing the SPIDER

To test the SPIDER apparatus pulses from one of the Vulcan Front End oscillators (SAM) were stretched using a double pass stretcher formed by two 300 l/mm gratings set at 200 mm and 400 mm apart. The bandwidth of the pulses from the oscillator is 4.0 nm and the stretcher applies a quadratic spectral phase profile (linear frequency chirp in time).

Table 1. Test Pulse Lengths

	Measured	**Calculated**
Transformed limited	-	285 fs
Directly from Oscillator	350 fs	350 fs
Stretched in 400 mm stretcher	600 fs	720 fs
Stretched in 800 mm stretcher	1.2 ps	1.26 ps

Table 1 shows the measured and calculated pulse lengths for the 4.0 nm bandwidth pulse. The pulse lengths were measured using a scanning autocorrelator. The different phase relationships obtained with the Spider are shown in Figure 5.

The transform limited pulse length for a 4 nm bandwidth sech^2 pulse at 1053 nm is 285 fs. However the pulse length measured directly from the oscillator was 350 fs. This increase can be explained by a small positive dispersion which will manifest itself as a residual quadratic phase as detected by the SPIDER shown in Figure 5.

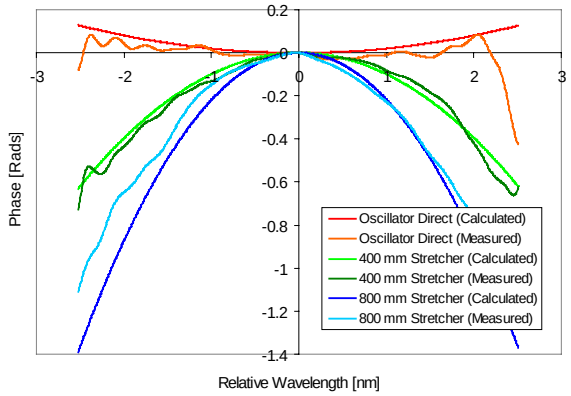

Figure 5. Results obtained using the SPIDER when known phase profiles are applied to a Vulcan Front End oscillator.

Also shown are the calculated and SPIDER measured phase imposed by stretching the pulses. It can be seen that there is a good agreement between the calculated and measured data giving us confidence that the SPIDER will prove an invaluable diagnostic for the Vulcan CPA system.

References

1. C. Iaconis, I A Walmsley,, IEEE J. Quantum Electronic., vol. 35, No4, pp. 501-509,(1999)

2. M Takeda, H Ina, and S Kobayashi, J. Opt. Soc. Amer., vol. 72,p. 156,1982.

A Grating Interferometer for the Recording of Large High Quality Gratings

I N Ross, C J Hooker

Central Laser Facility,CLRC Rutherford Appleton Laboratory, Chilton, Didcot, Oxon, OX11 0QX, UK

P Dombi

Department of Optical An Quantum Electronics, JATE University, Szeged,, Hungary

Main contact email address: *I.N.Ross@rl.ac.uk*

Introduction

Chirped pulse amplification laser systems require large gratings (up to 1 m) with very high quality (better than tenth wave). We report on a new cost-effective technique for generating these large high quality gratings.

The 'grating interferometer'

The assumption of all previous holographic techniques for generating diffraction gratings has been that: a) they require perfect quality optics of a size larger than the grating being made (see Figure 1) and b) the coherence length of the laser used to record the grating has to be greater than the number of lines on the grating times the recording wavelength. The coherence length requirement generally leads to greatly reduced output of the laser and hence to much longer recording exposure times. Stability then becomes a major issue leading to increased cost and a grating size limit.

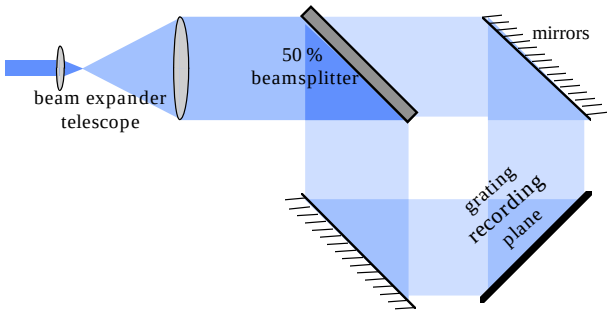

Figure 1. A typical interferometer for recording large gratings.

This assumption was proved incorrect by Hershey and Leith[1)], who proposed a new type of holographic interferometer which did not have these limitations.

The optical arrangement in its simplest form is shown in Figure 2. The interferometer is made up of three gratings. G1 acts as a beamsplitter of the diverging input beam. G2A and G2B are identical gratings having a groove density exactly twice that of G1. As a result of the Littrow operation of G2s the rays from the arms of the interferometer recombine at the recording plane producing a fringe pattern (G3) with a spatial frequency the same as that of the G2s. A simple formula can be derived from geometric considerations which states that the number of perfect, uniform and equally spaced fringes that can be written by recording this fringe pattern is $2(N_{G1}+N_{G2A})$, provided that the distances L are equal. (Here N_x designates the number of lines on the original gratings.) This means that the maximum linear magnification of this technique (size of G3)/(size of larger of G1 and G2)=3 and this occurs when (size of G1)=(size of G2A).

This interferometer has other beneficial properties. It has been proved theoretically that there is no requirement for source coherence, which means that the fringe spacing and the spatial phase of the fringes are independent of the wavelength. Consequently grating recording is possible even using a white light source! In practice we can use non-stabilised broad-bandwidth lasers for recording unlike previous techniques. It is also convenient to utilise a rotating diffuser in the input beam to increase the spatial uniformity of the beams. According to the zero-coherence-property this can be done without affecting the recorded grating.

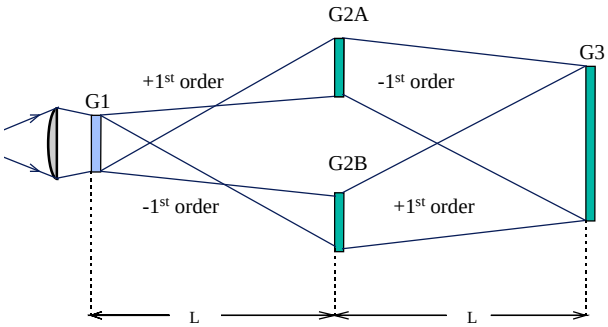

Figure 2. The grating interferometer.

A feature of the scheme is that it can be used in successive steps with a further factor of between two and three increase in size at each step. This is done by making an identical pair of gratings (G3) with the interferometer. Then we replace the original G2A and G2B gratings with these and, with a suitable increase in the beam expansion, we can make further gratings at least twice as large as G3. This process can be repeated so long as the reducing beam intensity with grating size does not lead to too long exposure times or until the increasingly tight mechanical tolerances cannot be met.

During the practical realisation of the interferometer we used the reflective grating equivalent of the setup in Figure 2. This can be seen on Figure 3. It can be seen that there is only one significant difference between the two. The reflective version involves an *H* elevation of the input beam through the interferometer. Our experience was that this did not affect the diffracted wavefront quality of the recorded gratings.

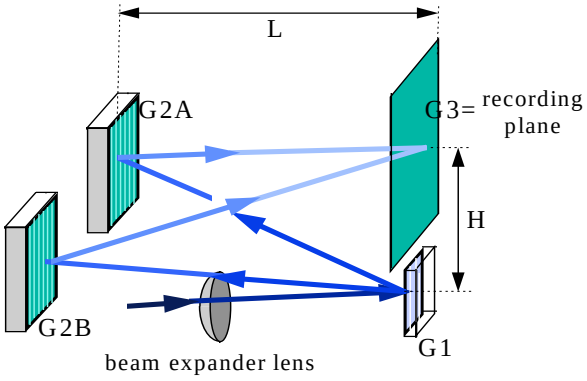

Figure 3. The grating interferometer using reflection gratings.

Experimental tests

The main aim of the experimental work was to demonstrate that the theoretical predictions about the advantages of this interferometer are valid. For this purpose we designed a compact interferometer, where L=1.4 m d_{G1}= 600 l/mm, $d_{G2}=d_{G3}$=1200 l/mm, λ=458 nm (one of the lines of a commercial argon-ion laser) and the magnification was 2.1 times. Alignment techniques were devised to ensure that all the elements of the system (G1, G2A, G2B, G3) whose position

and orientation determine the quality of the fringe pattern on G3 are all perfectly aligned. We also used a rotating diffuser in the 458 nm input beam to increase the spatial intensity uniformity of the beam. The initial gratings were commercially available gratings (G1: 30 x 30 mm, G2s: 60 x 60 mm). The conventional lithographic recording process was used with an aluminium coating applied after development.

In the first step we produced so-called "first-generation" gratings on circular substrates with a diameter of 120 mm. At this stage we demonstrated that with this magnification technique the diffracted wavefront quality of the gratings can be preserved. From interferograms of the wavefront we used two parameters to characterise the diffracted wavefront quality: the peak-to-valley (PV) and the root-mean-square (RMS) deviation values. We measured these values over 80% of the total area of our gratings and at a wavelength of λ = 633 nm. In Figure 4. the diffracted wavefront interferograms and the diffracted wavefront topographies can be seen of the initial and the resulting gratings. It can be seen that we could achieve a x2 grating magnification in the interferometer (G2s→G3) without a significant degradation of the diffracted wavefront quality (PV=0.07λ, RMS=0.012λ for G2s → PV=0.115λ RMS=0.021λ for G3). The small increase in aberration was due to flatness errors on the G3 substrate.

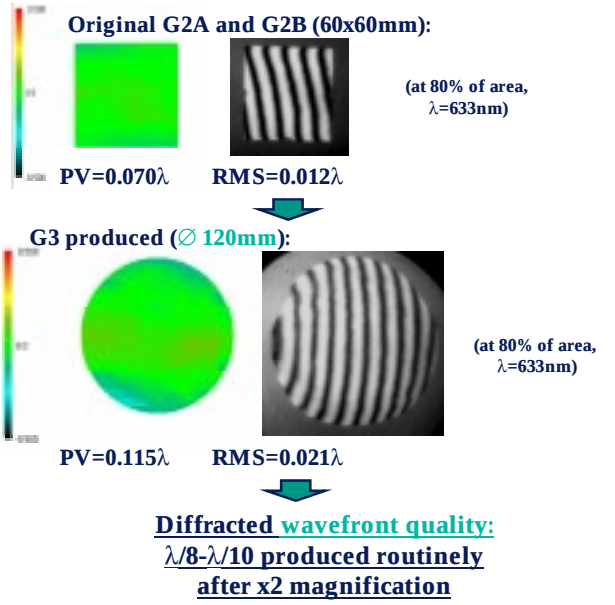

Figure 4. The diffracted wavefronts of small, commercial gratings (top) and large gratings (bottom) produced in the interferometer (x2.1 magnification).

The next step was to show that we can produce even larger "second generation" gratings by replacing the small 60 mm gratings (G2) with two identical 120 mm gratings (G3) recorded as first generation gratings in the above set-up. This enabled the recording of a larger grating of 200 mm, the results for which are shown in Figure 5. The diffracted wavefront has still to be improved (PV=0.337λ, RMS=0.083λ), since at these sizes the perfect alignment of the interferometer gets more critical. However, with appropriate refinements to the alignment procedure we expect to reproduce the initial diffracted wavefront quality or better at the ∅200 mm aperture sizes.

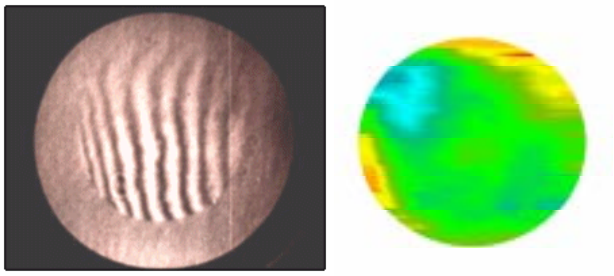

Figure 5. The diffracted wavefront quality of second generation ∅200 mm gratings.

One advantage of the second generation recording is the potential for complete cancellation of errors on the first generation G2 gratings since they are identical. To demonstrate this a deliberate error was introduced at the first generation stage. Two identical 120 mm gratings were recorded and used in a second generation 200 mm recording. Results are shown in Figure 6 where we see that the final grating has substantially less aberration than the two gratings used to record it.

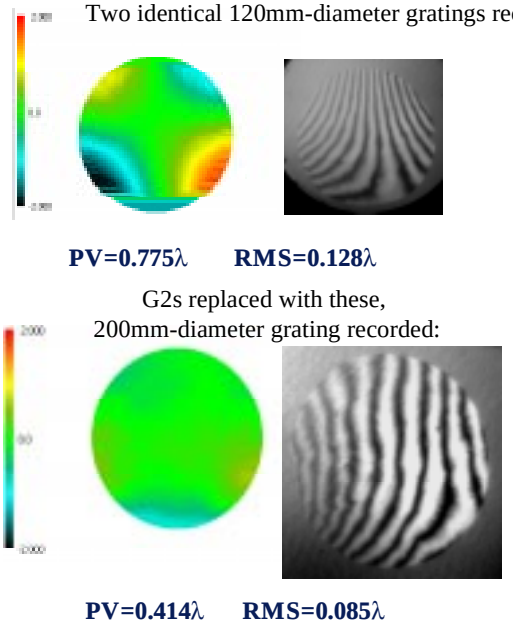

Figure 6. Cancellation of first generation errors during second generation.

Conclusion

In conclusion we have experimentally demonstrated all of the beneficial properties of this new cost-effective type of interferometer for the production of large holographic gratings. This new method does not need large, aberration-free optics, or expensive, frequency-stabilised laser sources as required by conventional techniques. By the actual production of "generations" of gratings we proved the feasibility of the successive use of the interferometer for bigger and better grating production.

Future developments will include the refinement of the alignment techniques to enable us to produce ∅200 mm gratings with a P/V better than λ/5 diffracted wavefront quality.

References

1. R.R.Herchey, E.N.Leith, Applied Optics, 29, 937 (1990)

Improved Contrast and Power from a Chirped Pulse Amplification Laser System

I N Ross, J L Collier

Central Laser Facility, CLRC Rutherford Appleton Laboratory, Chilton, Didcot, Oxon, OX11 0QX, UK

Main contact email address: *I.N.Ross@rl.ac.uk*

Introduction

The principal requirement for a chirped pulse amplification (CPA) laser system is the achievement of the maximum focused intensity and pulse contrast ratio in the recompressed pulse on target. Many of the factors affecting the performance have been noted and analysed in the literature[1-6] and the operation of CPA systems for best performance is largely well understood. However there are further improvements to be made and this note presents two new ideas arising from a detailed analysis of the CPA system. These improvements are universally applicable in CPA systems and lead to an increase in the contrast ratio and peak power of the recompressed pulse.

In most systems of practical interest the fundamental limit of performance is the Fourier transform (FT) of the laser output spectral intensity combined with diffraction limited (DL) beam focusing.

Power profile, P(t) = $\left[\int g(\nu)\exp(-2\pi\nu t)d\nu\right]^2$ (1)

where spectral profile = $[g(\nu)]^2$

For a uniform beam, focal intensity = $\frac{\pi P}{4\lambda^2 F^2} \times$ Airy profile:

where F = F-number (2)

In practice the intensity and contrast ratio are degraded by spectral and spatial amplitude and phase aberrations arising from for example spectral clipping, misalignment in the stretcher and compressor, and nonlinear refractive index giving rise to nonlinear phase errors (B-integral). In order to optimise the performance it is useful to look again at the underlying causes for the reduction in peak intensity and contrast ratio.

A fundamental property of the FT of pulses is important to this discussion of CPA. The intensity at a point in the FT well out in the wings of the distribution (where the contrast is generally measured) is related to the high frequency content in the spectrum while it is the low frequency content which largely determines the pulse profile and hence the peak power. For example it is well known that the sharp spectral cut-off in the stretcher contributes strongly to the eventual pulse contrast. Figure 1 plots for a sech^2 spectrum the contrast against the cut-off width, showing for example that the stretcher bandwidth must be at least 4.5 x spectral FWHM to achieve a contrast 10^{-5}. The peak intensity is also plotted showing little reduction for cut-off points beyond 3 x FWHM.

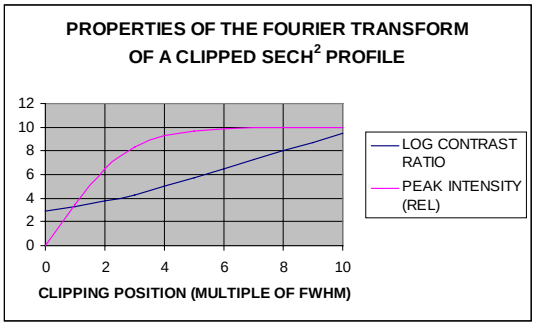

Figure 1.

An example of a low frequency aberration in the spectrum is that due to B-integral and the effect is illustrated in Figure 2 for a B-integral of 2. The peak intensity is substantially reduced while there is little effect on the pulse contrast.

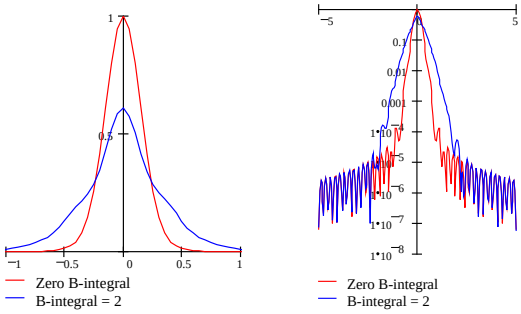

Figure 2. Effect of B-integral on the recompressed pulse.

Modelling

An estimation of the focused intensity and contrast ratio requires a determination of the pulse profile at focus from both the spectral and spatial distribution at the output of the compressor and the way this distribution propagates to the focus. Detailed calculations for the Vulcan laser have been described for the case of a square beam and rectangular gratings[7]. For other shapes of beam (including circular) the calculation is more complex, but it is found that the following simplified model gives results sufficiently accurate for the system to be optimised.

The laser, stretcher and compressor are regarded as spectral filters and for each of these the spectral transmission is calculated. For the propagation to the focus we need to consider the two cases of DL (diffraction limit) and non-DL. For non-DL each spectral component is distributed equally in the focal plane. The resulting temporal profile, I(t), is independent of position in the focal plane and is given by the FT of the output spectral profile of the compressor.

$$I(t) \approx \left[\int \sqrt{G_{IN}(\nu)T_{LAS}(\nu)T_{STR}(\nu)T_{COMP}(\nu)}\exp(-2\pi\nu t+\phi(\nu))d\nu\right]^2 \quad (3)$$

where $G_{IN}(\nu)$ = laser input pulse spectral intensity

$T(\nu)$ = spectral transmission of laser/stretcher/compressor

$\varphi(\nu)$ = spectral phase

For the DL case the spatial profile in the focal plane is different for each wavelength since the compressor imposes a different spatial clip for each wavelength. The consequence of propagation to the focus is a wavelength dependent focal spot width. To a good approximation this is taken into account using an additional spectral intensity attenuation factor given by the width of the input near field for that wavelength and hence equal to the spectral attenuation factor of the compressor.

$$I(t) \approx \left[\int T_{COMP}(\nu)\sqrt{G_{IN}(\nu)T_{LAS}(\nu)T_{STR}(\nu)}\exp(-2\pi\nu t+\phi(\nu))d\nu\right]^2 \quad (4)$$

Equation 4 only estimates the on-axis focal intensity profile. Off-axis, the additional spectral attenuation factor changes in such a way that the integrated focal profile is as given for a non-DL beam. For the purposes of this analysis the results for the non-DL beam will be used.

Optimisation of pulse contrast

It is clear that the dominant process determining pulse contrast is the sharp spectral cut-off in the stretcher and it is scarcely affected by other amplitude and phase aberrations in the spectrum. The normal solution for maximising contrast is to increase the size of the stretcher gratings to reduce the magnitude of this cut-off. However this may not be feasible in practice since it requires very large gratings to reach contrasts typically required with CPA systems. An alternative solution is to reduce the sharpness of the spectral cut-off of the stretcher, and this may be achieved for example by increasing the beam size in the stretcher. We illustrate this using the parameters of the Vulcan Nd:glass laser. Both the stretcher and compressor have a small beam spectral cut-off at 4 x FWHM and the output spectrum of the laser is approximately sech^2 in profile.

Figure 3 shows the spectral transmission of the stretcher and compressor in the standard configuration using a pencil beam in the stretcher and a full beam in the compressor. In this case the pulse contrast is primarily determined by the stretcher while the compressor transmission only affects the peak intensity and pulse duration.

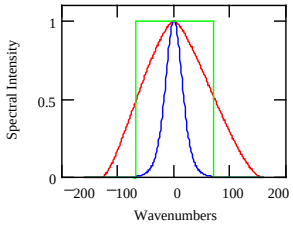

Figure 3. Spectral transmission of stretcher and compressor.

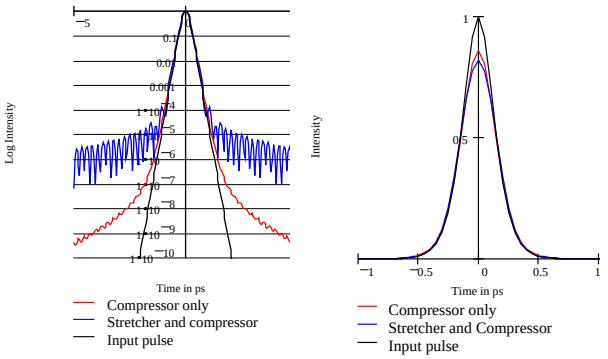

Figure 4. Recompressed pulse profiles.

Figure 4 shows the calculated pulse profile with and without the spectral cut-off due to the stretcher. Even with a cut-off width at 4 x FWHM the maximum achievable contrast is limited to $10^{-5.5}$ (defined at a point 10 x pulse duration from the pulse peak). The effect of the compressor is to reduce the maximum pulse intensity by 20%.

Figure 5 compares two ways of improving the contrast:

(i) by increasing the stretcher grating size by a factor 2 to completely eliminate the sharp spectral cut-off at the compressor output and so give the maximum contrast

(ii) by increasing the beam size in the stretcher to 30 mm.

It can be seen that the latter is a most effective technique and can normally be introduced without major modification to the laser system. A further advantage of minimising the total spectral width is to reduce the pulse degradation due to higher order spectral phase aberrations.

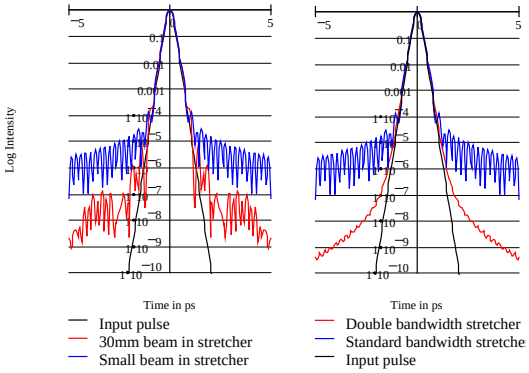

Figure 5. Two ways to improve the contrast ratio.

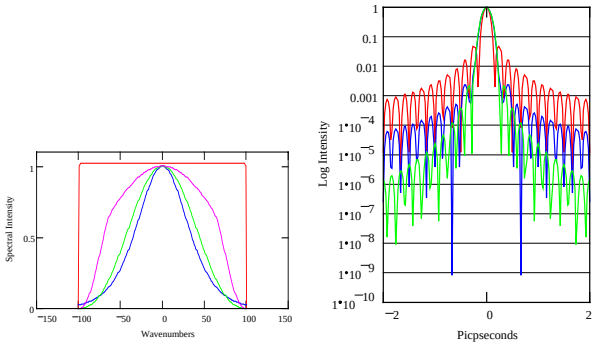

Figure 6. Effect of spectral shape on pulse contrast.

We can take this argument further and ask what is the optimum spectral profile within the cut-off width of stretcher/compressor. Some examples are illustrated in Figure 6 and demonstrate that it is important to eliminate discontinuities in both the profile and its slope and that if this is done it is possible to achieve high contrast with quite restricted cut-off widths. For example it can be seen from Figure 6 that a contrast of 10^6 can be achieved with a cut-off width of only 2.2 x spectral FWHM. This is less than half the cut-off width required for clipped sech^2 pulse.

Optimisation of focused intensity

Energy is usually lost in a compressor, and the eventual peak intensity reduced, since some spectral components miss the second grating.

This energy need not be lost if it is possible to appropriately tailor the spectral/spatial beam distribution early in the system and supplement the system gain to make up the deficit before recompression. There is a simple way to do this. An aperture equal to the input beam size, placed within the stretcher, can be positioned at a distance from the grating such that it exactly matches the clipping effect of the compressor.

Figure 7 illustrates this geometry for the case when the compressor input beam fills the first grating. Using the parameters of the Vulcan glass laser the recoverable energy loss is calculated to be 8%.

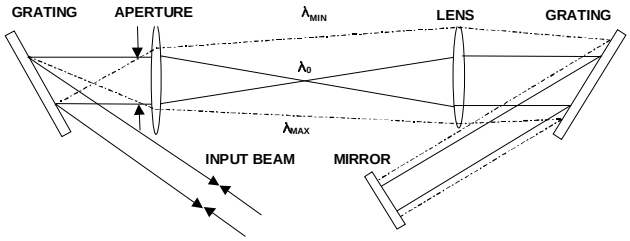

Figure 7. Apertured stretcher for higher efficiency compressor.

References

1. I.N.Ross et al. App. Opt. 36, 9348 (1997)
2. C.Fiorini et al. IEEE JQE 30, 1662 (1994)
3. M.D.Perry et al. Opt. Lett. 19, 2149 (1994)
4. R.L.Fork et al. Opt. Lett. 12, 483 (1987)
5. J.Squier et al. App. Opt. 37, 1638 (1998)
6. C.M.G.Inchauspe, O.E.Martinez, Opt. Lett, 22, 1186 (1997)
7. M.Trentelman et al. App. Opt. 36, 8567 (1997)

OPERATIONAL STATISTICS

1) **Vulcan**
2) **Astra**
3) **Lasers *for* Science Facility**

Vulcan Operational Statistics

A Kidd, K Hughes, D Pepler, C Danson

Central Laser Facility, CLRC Rutherford Appleton Laboratory, Chilton, Didcot, Oxon. OX11 0QX

Main contact email address *A.K.Kidd@rl.ac.uk*

Vulcan has completed an active experimental year, with 12 full experiments taking place in the two main target areas, East (TAE) and West (TAW).

Table 1 below indicates the operational schedule for the year in these two areas, and illustrates the shot rate statistics for each experiment. Numbers in parentheses indicate the total number of full energy laser shots delivered to target, followed by the number of these that failed.

PERIOD	TAE	TAW
12 Apr – 23 May	GR/L11964 – *C Lewis* Nonlinear X-ray Laser (192, 12)	GR/L12608 – *J Wark* OFI X-ray Laser (115, 1)
7 Jun – 18 Jul	GR/K95543 – *D Riley* X-ray Scattering (93, 2)	GR/L79151 – *AE Dangor* Wake Field (91, 2)
2 Aug – 19 Sep	GR/L11809 – *G Tallents* Nonlinear X-ray Laser (106, 9)	GR/K93815 – *P Norreys* Solid Target CPA (59, 6)
27 Sep – 8 Nov	GR/L72718 – *J Wark* Radiative Transfer (193, 3)	GR/K92815 – *P Norreys* Solid Target Interactions (89, 3)
15 Nov – 23 Dec		GR/L04436 – *O Willi* CPA Gas Interactions (126, 9)
10 Jan – 20 Feb	Training Weeks (31 Jan – 13 Feb)	GR/L04436 – *O Willi* CPA Gas Interactions (164, 3)
28 Feb – 9 Apr	Direct Access – *N Woolsey* Supernova Simulations (84, 10)	TMR (E34) - *A Klisnick* Transient X-ray laser (101, 2)

Table 1. Experimental schedule for the period April 1999 – March 2000.

For EPSRC experiments, the total number of full disc amplifier shots that have been fired this year is 1,312 with only 60 of these failing to meet user requirements. This gives an overall system reliability figure of 95.4%. The Service Level Agreement (SLA) requires Vulcan to be at least 90% reliable.

The SLA also requires that the laser system be available, during the four week periods of experimental data collection, from 09:00 to 17:00 hours, Monday to Thursday, and from 09:00 to 16:00 hours on Fridays (a total of 156 hours). The laser has not always met the startup target of 9:00 am but it has been common practice to operate the laser well beyond the standard contracted finish time on several days during the week and to operate during some weekends. On average, Vulcan has been available for each experiment for approximately 72.6 % of contracted hours (compared to 90 % required in the SLA). The shortfall in operational hours is more than made up by the out-of-hours operations, bringing the average total availability figure to 119.2 %.

The Vulcan laser remains very reliable; the overall shot failure rate to target for the year is 4.6%. This compares with 5.4% during 1998-99. Analysis of the reasons for failure of the individual shots enables a breakdown of these causes into specific categories. Figure 1 shows the identified failure modes and their individual failure rates.

This information enables servicing and equipment refurbishment to be focused on the most serious sources of system downtime. As indicated, the most serious causes of failed shots are shown to be the rod amplifier chain (19%), the alignment of the beam through the system (17%) and the oscillators (14%).

These issues are being addressed individually. Improvements to the alignment procedure include the use of CCD cameras to monitor the near field images at the output of the rod amplifier chain. Additional changes have been made to the system in order to make the oscillators more reliable and it is proposed to replace the existing pre-amplifiers (multiple double-passed 9 mm diameter rod amplifiers) with an OPCPA (optical parametric chirped pulse amplification) system. The computer control system also now includes predicted shot energies to indicate to the operator that the selected amplifier configuration is consistent.

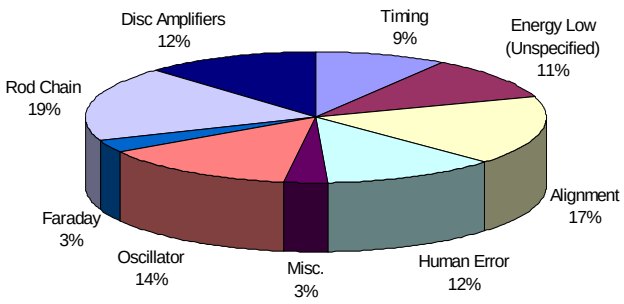

Figure 1. Analysis of Vulcan failure modes.

Astra Operational Statistics

A J Langley

Central Laser Facility, CLRC Rutherford Appleton Laboratory, Chilton, Didcot, Oxon. OX11 0QX

Main contact email address: *A.J.Langley@rl.ac.uk*

A total of 43 scheduled experiment weeks were carried out with the Astra laser during the reporting period April 1999 to April 2000. (See schedule below.) The majority of these were sponsored by the EPSRC. 90% of the experiment weeks were in the field of physics and the remaining 10% were concerned with chemistry related studies.

The Astra laser was available for experiments for 87% of the time in normal hours during scheduled experiments. The 13% downtime experienced during normal hours was fully recovered with additional time being provided outside the scheduled operating hours. Reliability defined as the time the laser was available as a percentage of the total time provided to scheduled user experiments was 90%.

The Astra laser was upgraded to multiterawatt performance during September 1999 to February 2000. This included commissioning an additional high-power TiS amplifier, new stretcher and two compressors, compressor and target chambers. More details are contained in an article entitled *The Development of a Multi-Terawatt femtosecond Laser facility – Astra* published elsewhere in this year's Annual Report (pg 196).

Astra experiment schedule 1999/2000

Date	Target Area 1	Target Area 2
22-Mar 29-Mar	**Newell/Williams** (QUB/UCL)	**Frasinski** (Reading)
5-Apr 12-Apr 19-Apr 26-Apr	Short pulse laser interactions with positive ions and molecules	Manipulating the dissociation dynamics of simple molecules in intense laser fields
3-May	**Pre- installation of 5 J YAG Laser**	
10-May 17-May	**Newell/Williams** (QUB/UCL)	**Frasinski** (Reading)
24-May	**Installation of 5 J YAG Laser**	
31-May 7-Jun 14-Jun	Short pulse laser interactions with positive ions and molecules	
21-Jun 28-Jun 5-Jul 12-Jul 19-Jul 26-Jul 2-Aug 9-Aug		**Frasinski** (Reading)
16-Aug 23-Aug 30-Aug 6-Sep	**Ledingham** (Glasgow) The potential of femtosecond laser mass spectrometry to chemical analysis	
13-Sep to 19-Dec	**ASTRA LASER DEVELOPMENT**	
20-Dec 27-Dec	**CHRISTMAS /NEW YEAR**	
3-Jan		
10-Jan	Target area preparation	
17-Jan	**Ross** (RAL) Gratings tests	
24-Jan	Target area preparation	
31-Jan 7-Feb 14-Feb 21-Feb	**Newell/Williams** (QUB/UCL) Short pulse laser interactions with positive ions and molecules	
28-Feb		Target area preparation
6-Mar 13-Mar 20-Mar 27-Mar	**Ledingham** (Glasgow) The potential of femtosecond laser mass spectrometry to chemical analysis	**Ledingham** (Glasgow) Proton generation with an intense femtosecond laser

Lasers *for* Science Facility Operational Statistics

S M Tavender, M Towrie, A W Parker

Central Laser Facility, CLRC Rutherford Appleton Laboratory, Chilton, Didcot, Oxon. OX11 0QX

Main contact email address *S.M.Tavender@rl.ac.uk*

RAL-based experiments

In the reporting period (April 1999 to March 2000), 25 different User groups performed a total of 52 experiments in the LSF laboratories at RAL. A total of 3861 hours laser time was scheduled throughout the year and 4811 hours delivered with only 113 hours downtime giving a reliability of 96.6%. Across the funding Councils the weeks scheduled were 69 to EPSRC, 6 to the MRC, 7 to BBSRC, 3 to Commercial Users, 15 to European Users, and 2 to Internal R&D giving 102 weeks delivered to the User community overall. Once again, a wide spread of disciplines was covered and a breakdown is shown in Figure 1 with the RAL-Based schedule Table 1. There were a total of 28 publications and 19 conference proceedings published during the reporting year.

Loan Pool

The Loan Pool delivered 318 weeks of laser time in the reporting period. Downtime was 26 weeks and was mainly due to new User groups who experienced teething problems as they became used to running unfamiliar equipment in their own laboratories. In the 26 laser loans there were 7 groups new to the Loan Pool with an increase in allocations to physics (up 11%) and engineering (up 5%). The chemistry community was once again the biggest user as shown in Figure 2. The Loan pool schedule is shown in Table 2. There were a total of 16 publications, 3 conference proceedings and 1 PhD in the reporting year.

Figure 1. Breakdown by discipline, RAL-Based experiments

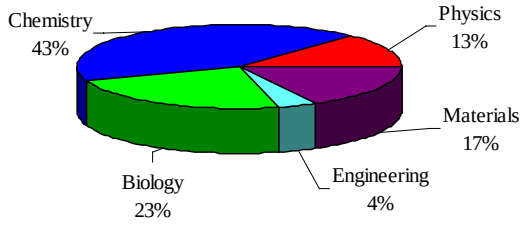

Figure 2. Breakdown by discipline, Loan Pool experiments

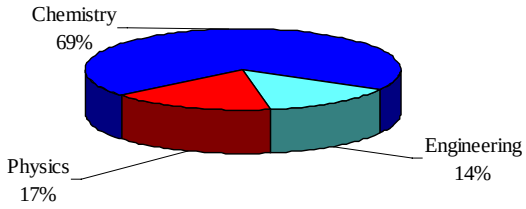

Table 1. RAL-BASED SCHEDULE April 1999 to March 2000.

Date	Laser Microscope Laboratory	Nanosecond Science Laboratory	Ultrafast Spectroscopy Laboratory	X-Ray Laboratory
05-Apr-99	**A J MACROBERT** (UCL) Confocal fluorescence			
12-Apr-99	lifetime imaging microscopy C1/C&M07157 CM1B1/99		**A C BENNISTON** (Glasgow) TR3 of Ru(bipy)2dppz US3C1/99	**J CAIRNS** (Dundee)
19-Apr-99		**W MILNE** (Cambridge)	**P MATOUSEK** (RAL)	High resolution X-ray masks GR/M41223 XU6P1/99
26-Apr-99		Preparation and Characterization of Carbon Nitride	Development of Kerr Gated TR3 and TR3 Study of DMABN	MAINTENANCE
03-May-99		NL2C199	GR/L83943 USC1C/99	**C THOMAS** TFEL Devices GR/K04330 XU5M1/99
10-May-99			DEVELOPMENT OF A	**P O'NEILL (MRC)** Nucleic acid modification XU2B1/99
17-May-99	**O SAPORA (ITALY)** Multiphoton Confocal lipid		DIODE ARRAY SYSTEM	**D GOODHEAD** (MRC) DNA Radiobiol & biochem XU4B1/99
24-May-99	peroxidation/ OH radical		MAINTENANCE	
31-May-99	generation CME39B199			**J COSTELLO** (Dublin)
07-Jun-99		**P SCULLY** (Liverpool John Moore)	**D.PHILLIPS** (Imperial College)	VUV photoabsorption imaging
14-Jun-99		Plastic Optical Fibre Sensors and Devices using Photo-Induced	Reorganisation Dynamics of	of laser-produced plasmas
21-Jun-99		Refractive Index Changes and Tapers NL3P199	Charge Transfer Reactions	XUE46P199
28-Jun-99			GR/L84001 USC2C1/99	
05-Jul-99	**LABORATORY**			**C THOMAS** TFEL Devices GR/K04330 XU5M1/99
12-Jul-99	**UPGRADE AND**		**PIRATE**	**H REEHAL** Photovoltaics GR/L63044 XU1P1/99
19-Jul-99	**REORGANISATION**		**INSTALLATION**	**G FRASER** (Leicester)
26-Jul-99				X-ray MCP optics XU3P199DA

Date	Laser Microscope Laboratory	Nanosecond Science Laboratory	Ultrafast Spectroscopy Laboratory	X-Ray Laboratory
02-Aug-99	**LABORATORY**		**PIRATE**	
09-Aug-99	**UPGRADE AND**		**INSTALLATION**	**J CAIRNS** (Dundee)
16-Aug-99	**REORGANISATION**	**P O'NEILL (**MRC) Dynamics of DNA by TR^3 NL3B2/99	**ULTRAFAST**	High resolution x-ray masks GR/M41223 XU8P2/99
23-Aug-99	**A J MACROBERT** (UCL) Confocal fluorescence	MAINTENANCE	**LABORATORY**	
30-Aug-99	Lifetime imaging microscopy CMB2/99 BBSRC	**D PHILLIPS** (IC) NL6C2/99 GR/L84001	**UPGRADE**	
06-Sep-99				**A MICHETTE** (KCL) Electromagnetic noise
13-Sep-99			**D PHILLIPS** (Imperial College)	reduction tests for x-ray microscopy XU11P2/99 DA
20-Sep-99	MAINTENANCE		Reorganisation Dynamics of Charge Transfer Reactions	**H REEHAL** (SBU)Photovoltaics GR/L63044 XU7E2/99
27-Sep-99			GR/L84001 US6C2/99	
04-Oct-99		**J CAIRNS** D'dence of masks on W'length GR/M41223 NL5P2/99	**P MATOUSEK** (RAL/IC)	MAINTENANCE
11-Oct-99		**M BRYCE** (Durham)	Kerr Gated TR^3 Study of DMABN	
18-Oct-99		ns-TR^3 study of photo-induced electron transfer reaction of	GR/L83943 US4C2/99	
25-Oct-99	**D DRYDEN (**Edinburgh)	TTF-anthraquinone hybrids NL4C2/99	**E TUITE** (Chalmers Sweden)	**C THOMAS** TFEL Devices GR/K90074 XU10E2/99
01-Nov-99	Time-resolved fluorescence spectroscopy of 2-aminopurine		Photophysics of monomeric	**D GOODHEAD** (MRC) DNA Radiobiol &biochem XU12B2/99
08-Nov-99	in a protein DNA complex CM3B2/99 DA		and dimeric Ru Enantomers with DNA	
15-Nov-99			EU USE48B1/99	**G HIRST** (RAL) Development of a high brightness
22-Nov-99			**J McGARVEY** (QUB) DNA Interactions at	X-ray microtomography system XU9P2/99 CEO
29-Nov-99			colloidal surfaces and with metal complexes	
06-Dec-99			GR/M45696 US5C2/99	
13-Dec-99		**P O'NEILL (**MRC) Dynamics of DNA by TR^3 NL3B2/99	**M GEORGE (**Nottingham)	**J CAIRNS** Production of X-ray masks XU14E3/99 GR/M41223
20-Dec-99			P.I.R.A.T.E.	
27-Dec-99	**X-MAS/NEW YEAR**			
03-Jan-00				
10-Jan-00		COMMERCIAL	P.I.R.A.T.E.	
17-Jan-00		**M SEARLE** Nottingham Fast time-resolved resonance	US7C2/99 GR/M40486	
24-Jan-00		Raman (TR^3) analysis of beta-sheet peptide folding in aqueous	**P MATOUSEK** (RAL/IC)	**J CAIRNS** Production of X-ray masks XU14E3/99 GR/M41223
31-Jan-00		solutions NL5C2/99	Kerr Gated TR^3 Study of DMABN	
07-Feb-00			GR/L83943 US9C3/99	
14-Feb-00		**D PHILLIPS** (IC) NL6C2/99 GR/L84001	**SCHNEIDER** Photophysical processes in bridged	
21-Feb-00		**J BUTLER (**Salford)	organic electron donor-acceptor systems USE42C1/99	**H REEHAL** (SBU) Silicon solar cells XU15M3/99 GR/L63044
28-Feb-00		A ns-TR^3 study of thiyl peroxyl radical structure by time-resolved	**D PHILLIPS** (Imperial College)	**C THOMAS** TFEL Devices GR/K90074 XU17E3/99
06-Mar-00	**BRINDLE** (Cambridge)	resonance Raman spectroscopy N11C3/99	Reorganisation Dynamics of Charge Transfer Reactions	
13-Mar-00	Novel fluorescence technique for studying proteins in vivo	**M BRYCE** (Durham)	GR/L84001 US8C3/99	
20-Mar-00	CM4B3/99 BBRSC	ns-TR3 study of photo-induced electron transfer reactions of	**SCHNEIDER (**Erlangen, Germany)	**H REEHAL** (SBU) Silicon solar cells XU15M3/99 GR/L63044
27-Mar-00		TTF-anthraquinone hybrids NL10C3/99	Relaxation kinetics of surface plasmons USE43C1/99	**M HILL** (MRC) Cellular radiobiology XU13B3/99

Table 2. LOAN POOL SCHEDULE April 1999 to March 2000.

Date	NSL1 YAG/Dye	NSL2 YAG/Dye	NSL3 YAG/Dye	NSL4 YAG/Dye	NSL5 Fluoride excimer	NSL6 YAG/Dye	CWL1 Argon Ion	CWL2 Ti:S	CWL3 FreD Ar Ion
Apr 5	**WAYNE**	**HINDS**	**GEORGE**	**SIMONS**	MAINTENANCE	**SIMS**	**DEVONSHIRE**	**TAYLOR**	
12	**Oxford**	**Sussex**	NsTRIR-using	Structures in	AT RAL	**Birmingham**	**Sheffield**	**Imperial**	
19	Reactions		a commercial	hydrogen		Reactive		In situ	
26	of Halogen	The electron	Step-scan	bonded		processes in	LP14/98	optical	
May 3	radicals	Dipole moment	interferometer	clusters	**LANGRIDGE-**	the gas phase		SHG	
10		edm:		LP10/98	**SMITH**	at Ultra-low		of	
17		finding the			**Edinburgh**	Temperatures	**SHIONO**	Semiconductor	
24	**WAYNE**	Rydberg states	**STACE**				**Loughborough**	Growth	
31	**Oxford**	YbF	**Sussex**	**SIMONS**		LP17C3/98	An	LP12/98	
Jun 7				**Oxford**	Characterisation		investigation		
14					of polycyclic		of secondary		
21					aromatic	**SMITH**	Currents in	**KUCERNAK**	
28			Spectroscopic	Ion dip	hydrocarbons	**Birmingham**	a two-layer	**Imperial**	
Jul 5	Investigation		studies of	spectroscopy	on size-		Density		
12	of	**HINDS**	doubly charged	of molecular	segregated	Vibrational	Stratified		
19	the kinetics of	**Sussex**	Transition	neurotransmitters	aerosols	energy	Shear	In situ optical	
26	reactions of		metal	and their	using two-	Transfer in	Flow	second	
Aug 2	Halogen		complexes	hydrated	step laser mass	Polyatomic		Harmonic	
9	radicals	The electron	in the gas	clusters	spectrometry	Molecules:		generation	
16		dipole	phase			collision-		Studies of	
23		moment				induced	LP6P1/99	Semiconductor	
30	LP3C1/99	edm:				Dissociation in		Growth	
Sep 6		finding the		LP4C1/99		highly excited			
13		Rydberg states				NCNO			
20	**WAYNE**	YbF			LP15/99				
27	**Oxford**					LP2C1/99		LP7C1/99	
Oct 4									
11	Laboratory								
18	investigation of	LP1C1/99		**UNALLOCATED**		**SCULLY**	**UNALLOCATED**	**KENT**	
25	the kinetics				MAINTENANCE	**Liverpool**		**Nottingham**	
Nov 1	of specific		LP10C1/99		RAL				
8	reactions of IO	**HINDS**						Coherent	
15	and OIO of	**Sussex**						acoustic	
22	relevance to		**COATS**					phonon	**CWL3 FreD Ar Ion**
29	the atmosphere	The electron	**Leicester**				**PEDERSON**	emission	
Dec 6		Dipole moment				Plastic optical	**Birmingham**	from	COMISSIONING
13		edm:		**SIMS**	**SIMS**	fibre sensors		impulsively	AND
20		finding the		**Birmingham**	**Birmingham**	and devices	Optical	stimulated	TESTS
27	LP18C2/99	Rydberg				using	properties	superlattices	
2000 Jan 3		states of	Acoustic			photoinduced	of nanoscale		
10		YbF	instability	Interstellar	Interstellar	refractive	silicon		
17			of fully	Chemistry:	Chemistry:	index changes	materials	LP13P2/99	
24			premixed	Synthesis of	Synthesis of	and tapers	fabricated		**SHIELDS**
31			Flames	Carbon-	Carbon-	LP21E2/99	by size-		**Oxford**
Feb 7				Containing	Containing		selected		UV- excited
14		LP24C2/99		Radicals at	Radicals at		cluster beams	**TAYLOR**	far- IR
21				Extremely Low	Extremely Low			**Imperial**	modulated
28	**UNALLOCATED**			Temperatures	Temperatures			Non- linear	photo-
Mar 6		**JONES**					LP32P3/99	investigation	luminescence
13		**Edinburgh**		LP23C2/99	LP23C2/99			of Si/SiGe	in Ga Nitride
20						**SIMONS**		epitaxy	semiconductors
27		LP28C3/99	LP15E2/99			LP26C3/99		LP27C3/99	LP31P3/99

PUBLICATIONS

1) **Science - High Power Laser Programme**
2) **Science - Astra Laser Programme**
3) **Science - Lasers *for* Science Facility Programme**
4) **Facility Developments**

Science – High Power Lasers

JOURNAL PUBLICATIONS, BOOKS AND PUBLISHED PROCEEDINGS

K M Aggarwal, P H Norrington, K L Bell, F P Keenan, G J Pert, S J Rose
Electron impact excitation of Ni-like gadolinium
J Phys B-Atomic Molecular and Optical Physics **32** (21) 5067-5082 (1999)

K M Aggarwal, P H Norrington, K L Bell, F P Keenan, G J Pert, S J Rose
Radiative rates for allowed transitions in Ni-like Nd, Sm, Eu, Ta and W
Atomic Data and Nuclear Data Tables **74** (2) 157-255 (2000)

R Azambuja, M Eloy, G Figueira, D Neely
Three-dimensional characterization of high-density non-cylindrical pulsed gas jets
J Phys D-Applied Physics **32** (8) L35-43 (1999)

D Batani, F Pisani, E Martinolli, A Bernardinello, A Antonicci, J R Davies, M Koening, F Amiranoff, L Gremillet, H Bandulet, C Rosseaux, T Hall, P A Norreys, A E Dangor
Fast electron propogation experiments for fast ignition: evidence for electric field effects
IFSA conference proceedings **1** 433-438 (1999)

A Bernardinello, D Batani, V Masella, T A Hall, S Ellwi, M Koenig, A Benuzzi, J Krishnan, F Pisani, A Djaoui, P Norreys, D Neely, S Rose, M H Key, P Fews
Fast electron propagation and energy deposition in laser shock compressed plasmas
Laser and Particle Beams **17** (3) 519-528 (1999)

M Borghesi, R Gaillard, A J Mackinnon, O Willi, D Riley
Absorption of subpicosecond UV laser pulses during interaction with solid targets
Phys Rev E **60** (6) 7374-7381 (1999)

M Borghesi, A J Mackinnon, A R Bell, G Malka, C Vickers, O Willi, J R Davies, A Pukhov, J Meyer-ter-Vehn
Observations of collimated ionization channels in aluminum-coated glass targets irradiated by ultraintense laser pulses
Phys Rev Letts **83** (21) 4309-4312 (1999)

M Borghesi, A J Mackinnon, N Blanchot, B Canaud, J R Davies, R Gaillard, E Lefebvre, G Malka, J Meyer-ter-Vehn, J L Miquel, A A Offenberger, A Pukhov, C Vickers, O Willi
Guiding of short, intense laser pulses through solid guides and preformed plasma channels
IFSA conference proceedings **1** 974-977 (1999)

R E Burge, X C Yuan, G E Slark, T Browne, P Charalambous, C L S Lewis, G F Cairns, A G MacPhee, D Neely
Optical source models for the 23.2-23.6 nm radiation from the germanium soft X-ray laser
Opt Comm **169** (1-6) 123-133 (1999)

A C Cefalas, P Argitis, Z Kollia, E Sarantopoulou, T W Ford, A D Stead, A Marranca, C N Danson, J Knott, D Neely
Laser plasma x-ray contact microscopy of living specimens
Tenth international school on quantum electronics, Eds P A Atanasov, D V Stoyanov, SPIE **3571** 388-391 (1999)

P Chessa, M Galimberti, A Barbini, C N Danson, A Giulietti, D Giulietti, L Gizzi
Phase measurements without interferometry: 2D transverse phase detection by numerical beam intensity analysis
Laser and Particle Beams **17** (4) 681-692 (1999)

E L Clark, K Krushelnick, J R Davies, M Zepf, M Tatarakis, F N Beg, A Machacek, P A Norreys, M I K Santala, I Watts, A E Dangor
Measurements of energetic proton transport through magnetized plasma from intense laser interactions with solids
Phys Rev Letts **84** (4) 670-673 (2000)

E L Clark, K Krushelnick, J R Davies, M Zepf, M Tatarakis, F N Beg, A C Machecek, P A Norreys, M I K Santala, I Watts, A E Dangor
Measurements of energetic proton generation from intense laser interactons with solids
IFSA conference proceedings **1** 961-965 (1999)

A Djaoui
Time-dependent hydrogenic ionization model for non-LTE mixtures
J Quant Spectr & Rad Trans **62** (3) 303-320 (1999)

L Gremillet, F Amiranoff, S D Baton, J-C Gauthier, M Koenig, E Martinolli, F Pisani, G Bonnaud, C Leborg, C Rousseaux, C Toupin, A Antonicci, D Batani, A Bernardinello, T Hall, D Scott, P Norreys, H Bandulet, H Pepin
Time-resolved observation of ultrahigh intensity laser produced electron jets propagating through transparent solid targets
Phys Rev Letts **83** (24) 5015-5018 (1999)

L Gremillet, F Amiranoff, M Koenig, F Pisani, G Bonnaud, C Lebourg, C Rousseaux, C Toupin, A Antonicci, D Batani, E Martinolli, T Hall, P A Norreys, H Bandulet, H Pepin
Experimental evidence of a fast electron jet travelling through solid targets irradiated at relativistic intensities
IFSA conference proceedings **1** 451-456 (1999)

D Hoarty, L Barringer, C Vickers, O Willi, W Nazarov
Observation of transonic ionization fronts in low density foam targets
Phys Rev Letts **82** (15) 3070-3073 (1999)

D Hoarty, O Willi, L Barringer, C Vickers, R Watt, W Nazarov
Observation of ionization fronts in low density foam targets
Physics of Plasmas **6** (5pt2) 2171-2176 (1999)

D Hoarty, O Willi, R Watt, P Gobby
Time dependent energy transport in laser heated targets
IFSA conference proceedings **1** 269-274 (1999)

K A Janulewicz, S B Healy, M P Kalachnikov, P J Warwick, P V Nickles, W Sandner, G J Pert
Influence of pump pulse parameters on the collisionally pumped germanium X-ray laser in the transient gain regime
Opt Comm **168** (1-4) 183-193 (1999)

F P Keenan, M E Phillips, S J Rose, D D Burgess
The search for extraterrestrial intelligence (SETI)
The Irish Astronomical Journal **26** (2) 87-90 (1999)

K Krushelnick, E L Clark, Z Najmudin, M Salvati, M I K Santala, M Tatarakis, A E Dangor, V Malka, D Neely, R Allott, C Danson
Multi-MeV ion production from high intensity laser interactions with underdense plasmas
Phys Rev Letts **83** (4) 737–740 (1999)

K W D Ledingham, I Spencer, T McCanny, R P Singhal, M I K Santala, E Clark, I Watts, F N Beg, M Zepf, K Krushelnick, M Tatarakis, A E Dangor, P A Norreys, R Allott, D Neely, R J Clarke, A C Machacek, J S Wark, A J Cresswell, D C W Sanderson, J Magill
Photonuclear physics when a multiterawatt laser pulse interacts with solid targets
Phys Rev Letts **84** (5) 899-902 (2000)

C L Lewis, R Keenan, A G MacPhee, B Moore, R M N O'Rourke, G J Tallents, S Dobosz, S J Pestehe, F Strati, J S Wark, E Wolfrum, G J Pert, S P McCabe, P A Simms, R M Allott, J L Collier, C N Danson, A Djaoui, D Neely
Progress with saturated soft X-ray lasers pumped by the Vulacn laser
Soft X-ray lasers and applications III, Eds J J Rocca, L B Da Silva, SPIE **3776** 292-301 (1999)

J Y Lin, G J Tallents, A G MacPhee, A Demir, C L S Lewis, R M N O'Rourke, G J Pert, D Ros, P H Zeitoun
Travelling wave chirped pulse amplified transient pumping for collisional excitation lasers
Opt Comm **166** (1-6) 211-218 (1999)

A J Mackinnon, M Borghesi, R Gaillard, G Malka, O Willi, A A Offenberger, A Pukhov, J Meyer-ter-Vehn, B Canaud, J L Miquel, N Blanchot
Intense laser pulse propagation and channel formation through plasmas relevant for the fast ignitor scheme
Physics of Plasmas **6** (5pt2) 2185-2190 (1999)

G Malka, C Courtois, B Cros, G Mattieussent, N Blanchot, G Bonnaud, M Busquet, B Canaud, D Desenne, L Disdier, J P Garconnet, M Louis-Jacquet, E Lefebvre, L Lours, A Mens, J L Miquel, O Peyrusse, C Rousseaux, M Borghesi, R Gaillard, A J Mackinnon, O Willi, C N Danson, D Neely, D Altenberndt, T Feurer, P Gibbon, R Sauerbrey, U Teubner, W Theobald, I Uschmann, F Amiranoff, S Baton, L Gremillet, J Fuchs, J R Marques, P Gallant, J C Kieffer, H Pepin, J C Adam, A Heron, G Laval, P Mora
High intensity subpicosecond laser pulse propagation in a 1 cm capillary tube and fast ignitor experiments
IFSA conference proceedings **1** 982-985 (1999)

S McCabe, G J Pert
Computational investigation of the Ni-like Gd collisionally pumped X-ray laser – art no 033804
Phys Rev A **61** 033804 (2000)

Z Najmudin, K Krushelnick, E L Clark, M Salvati, M I K Santala, M Tatarakis, A E Dangor, V Malka, C N Danson, R M Allott, D Neely
Hosing,sausaging,filamentation and sidescatter of a high-intensity short-pulse laser in an under-dense plasma
IFSA conference proceedings **1** 409-414 (1999)

D Neely, R M Allott, F Amiranoff, E L Clark, R J Clarke, J L Collier, A E Dangor, C N Danson, C B Edwards, D Gordon, C Hernandez-Gomez, M H R Hutchinson, K Krushelnick, G Malka, V Malka, A Modena, Z Najmudin, M Notley, D A Pepler, M Randelson, J Springall, M Salvati, M I K Santala, M Stubbs M Tatarakis
Gas jet electron acceleration using a 527nm frequency doubled CPA laser pulse
IFSA conference proceedings **1** 1163-1170 (1999)

P A Norreys, R M Allott, R J Clarke, D Neely, S J Rose, F N Beg, E L Clark, M I K Santala, M Tatarakis, I Watts, M Zepf, K Krushelnick, A E Dangor, T McCanny, I Spencer, R P Singhal, K W D Ledingham, A C Machacek, S C Wilks, J S Wark
Relativistic laser plasmas and guided conical compression experiments relevant to the fast ignitor scheme for ICF
ISFA conference proceedings **1** 427-432 (1999)

P A Norreys, M Santala, E Clark, M Zepf, I Watts, F N Beg, K Krushelnick, M Tatarakis, A E Dangor, X Fang, P Graham, T McCanny, R P Singhal, K W D Ledingham, A Creswell, D C W Sanderson, J Magill, A Machacek, J S Wark, R Allott, B Kennedy, D Neely
Observation of a highly directional γ-ray beam from ultrashort, ultraintense laser pulse interactions with solids
Physics of Plasmas **6** (5 Pt 2) 2150-2156 (1999)

D A Pepler, R M Allott, A Boba, R J Clarke, W Cranton, C N Danson, G Hirst, D Koutsogeorgis, M Mastio, D Neely, M Notley, M Payne, T B Winstone
Materials processing with high power lasers
Diffractive Optics 1999 (Jena, Germany) European Optical Society Topical Meetings Digest Series **22** 66-67 (1999)

D Riley, N C Woolsey, D McSherry, I Weaver, A Djaoui, E Nardi
X-ray diffraction from a dense plasma
Phys Rev Letts **84** (8) 1704-1707 (2000)

S J Rose
Calculations of Compton scattering of line radiation.
IFSA conference proceedings **1** 1073-1077 (1999)

S J Rose, R Bingham
New frontiers in astrophysics
The Observatory **120** 124 (2000)

P Salvatore, B Meyer, A Richard, M Valadon, J P Jadaud, P Munsch, P Troussel, B Viliette, C Reverdin, J P Thébault, O Willi, J Pasley
Short wavelength Rayleigh-Taylor instability at the ablation front with soft X-ray drive
Proceedings of the 7th international workshop on the physics of compressible and turbulent mixing (1999)

M I K Santala, E L Clark, I Watts, M Tatarakis, M Zepf, K Krushelnick, A E Dangor, T McCanny, I Spencer, K W D Ledingham, A C Machecek, J S Wark, R M Allott, R J Clarke, P A Norreys
Fast ion induced nuclear reactions in the plasma blow-off in intense laser-solid interactions
IFSA conference proceedings **1** 1016-1019 (1999)

M I K Santala, M Zepf, I Watts, F N Beg, E Clark, M Tatarakis, K Krushelnick, A E Dangor, T McCanny, I Spencer, R P Singhal, K W D Ledingham, S C Wilks, A C Machacek, J S Wark, R Allott, R J Clarke, P A Norreys
Effect of the plasma density scale length on the direction of fast electrons in relativistic laser-solid interactions
Phys Rev Letts **84** (7) 1459-1462 (2000)

A Schiavi, M Borghesi, J Pasley, O Willi, D Neely, M Notley, W Nazarov
Shock wave collisions in low density foams
IFSA conference proceedings **1** 1187-1190 (1999)

R Smith, G J Tallents, S J Pestehe, G Hirst, J Lin, S Rose, M Tagviashvili
A spectroscopic analysis of near solid density plasmas
Laser and Particle Beams **17** (3) 477-485 (1999)

G J Tallents, G Eker, F Strati, S J Pestehe, J Lin, R Smith, S Dobosz, A G MacPhee, C L Lewis, R M N O'Rourke, R Keenen, G J Pert, S P McCabe, D Neely, R M Allott
Saturated X-ray lasers
Soft X-ray lasers and applications III, Eds J J Rocca, L B Da Silva, SPIE **3776** 292-301 (1999)

O Willi, L Barringer, A Bell, M Borghesi, J Davies, R Gaillard, A Iwase, A Mackinnon, G Malka, C Meyer, S Nuruzzaman, R Taylor, C Vickers, D Hoarty, P Gobby, R Johnson, R G Watt, N Blanchot, B Canaud, H Croso, B Meyer, J L Miquel, C Reverdin, A Pukhov, J Meyer-ter-Vehn
Inertial confinement fusion and fast ignitor studies
Nuclear Fusion **40** (3Y S13) 537-545 (2000)

O Willi, J Pasley, A Iwase, W Nazarov, B Meyer, A Richard, P Salvatore, C Reverdin
Increase of the drive pressure in a soft X-ray irradiated foam foil package
IFSA conference proceedings **1** 1187-1190 (1999)

O Willi, J Pasley, A Iwase, S J Rose, Z Nazarov, B Meyer, A Richard, P Salvatore, J P Jadaud, P Munsch, C Reverdin
Measurements of the growth rate of the short wavelength Rayleigh-Taylor instability of foam foil packages driven by a soft X-ray pulse
IFSA conference proceedings **1** 224-227 (1999)

Y Xu, S J Rose
Designing cylindrical targets to measure the radiative properties of high density and temperature plasmas.
IFSA conference proceedings **1** 1073-1077 (1999)

PUBLISHED DURING 1998/1999

G J Pert
Electron distributions generated by tunnelling ionization during gas breakdown by high intensity laser radiation
J Phys B-Atomic Molecular and Optical Physics **32** (1) 27-52 (1999)

IN PRESS AT END OF 1999/2000

M E Beer, P K Patel, S J Rose, J S Wark
Calculations of the modal photon densities and gain in a K/Cl resonantly photopumped X-ray laser
J Quant Spectr & Rad Trans **65** (1-3) 71-81 (2000)

M Borghesi, A J Mackinnon, R Gaillard, G Malka, C Vickers, O Willi, J L Miquel, N Blanchot, B Canaud, J R Davies, A A Offenberger, A Pukhov, J Meyer-ter-Vehn
Short pulse interaction experiments for fast ignitor applications
Laser and Particle Beams (accepted for publication)

E L Clark, K Krushelnick, M Zepf, F N Beg, A Machacek, P A Norreys, M I K Santala, M Tatarakis, I Watts, A E Dangor
Energetic heavy ion and proton generation from ultra intense laser-plasma interactions with solids
Phys Rev Letts (submitted)

C E Clayton, D Gordan, K A Marsh, C Joshi, V Malka, Z Najmudin, A Modena, A E Dangor, D Neely, C N Danson
Observation of self-channelling of relativistically-intense laser light in a very underdense plasma
Phys Rev Letts (submitted)

S J Davidson, K Nazir, S J Rose, R Smith, G J Tallents
Short-pulse laser opacity measurements
J Quant Spectr & Rad Trans **65** (1-3) 151-160 (2000)

K Krushelnick, E L Clark, R M Allott, F N Beg, C N Danson, A Machacek, V Malka, Z Najmudin, D Neely, P A Norreys, M Salvati, M I K Santala, M Tatarakis, I Watts, M Zepf, A E Dangor
Ultra high intensity laser produced plasmas as a compact heavy ion injection source
IEEE Trans Plasma Science (accepted for publication)

K Krushelnick, E L Clark, Z Najmudin, M Salvati, M Tatarakis, A E Dangor, V Malka, D Neely, R M Allott, C N Danson
Diagnosis of peak laser intensity from high energy ion measurements during intense laser interactions with underdense plasma
Laser and Particle Beams (accepted for publication)

K Krushelnick, E L Clark, M Zepf, J R Davies, F N Beg, A Machacek, M I K Santala, M Tatarakis, I Watts, P A Norreys, A E Dangor
Energetic proton production from relativistic laser interaction with high density plasmas
Physics of Plasmas **7** (5) 2055-2061 (2000)

Z Najmudin, R M Allott, F Amiranoff, E L Clark, C N Danson, D Gordon, K Krushelnick, G Malka, V Malka, D Neely, M Salvati, M I K Santala, M Tatarakis, A E Dangor
Measurements of forward Raman scattering and electron acceleration from high intensity plasma interactions at 527nm
IEEE Trans Plasma Science (accepted for publication)

D Neely, R M Allott, F Amiranoff, E L Clark, R J Clarke, J L Collier, A E Dangor, C N Danson, C B Edwards, D Gordan, C Hernandez-Gomez, M H R Hutchinson, K Krushelnick, G Malka, A Modena, Z Najmudin, M Notley, D A Pepler, M Randelson, J Springall, M Salvati, M I K Santala, M Stubbs, M Tatarakis, T B Winstone
Gas jet electron acceleration using a 527nm frequency doubled CPA laser pulse and its optimisation
J Mod Opt (accepted for publication)

P A Norreys, R M Allott, R J Clarke, D Neely, S J Rose, M Zepf, M I K Santala, A R Bell, K Krushelnick, A E Dangor, N C Woolsey, R G Evans, H Habara, R Kodama
Guided conical compression experiments relevant to the fast ignitor scheme
Physics of Plasmas (submitted)

P K Patel, E Wolfrum, O Renner, A Loveridge, R Allott, D Neely, S J Rose, J S Wark
X-ray line reabsorption in a rapidly expanding plasma
J Quant Spectr & Rad Trans **65** (1-3) 429-439 (2000)

D Riley, N C Woolsey, D McSherry, E Nardi
X-ray scattering from a radiatively heated plasma
J Quant Spectr & Rad Trans **65** (1-3) 463-470 (2000)

S J Rose
The inclusion of Compton scattering in line radiation escape factors
J Quant Spectr & Rad Trans **65** (1-3) 471-475 (2000)

N C Woolsey, C A Back, R W Lee, A Calisti, C Mosse, R Stamm, B Talin, A Asfaw, L S Klein
Experimental results on line shifts from dense plasmas
J Quant Spectr & Rad Trans **65** (1-3) 573-578 (2000)

CONFERENCE PRESENTATIONS

International workshop on fast ignition, Palaiseau, France (April 2000)

O Willi
Propagation issues and particle beam characterisation

Ultra intense laser interactions and applications - 1, Elounda, Greece (May 1999)

M Borghesi, A J Mackinnon, R Gaillard, G Malka, C Vickers, O Willi, J L Miquel, N Blanchot, B Canaud, J R Davies, A A Offenberger, A Pukhov, J Meyer-ter-Vehn
Short pulse interaction experiments for fast ignitor applications

K Krushelnick, E L Clark, Z Najmudin, M Salvati, M I K Santala, M Tatarakis, A E Dangor, V Malka, D Neely, R M Allott, C N Danson
Multi-MeV ion production from high intensity laser interactions with underdense plasmas

A C Machacek, D M Chambers, J S Wark, I Watts, M Zepf, A E Dangor, E L Clark, K Krushelnick, M I K Santala, M Tatarakis, P A Norreys, R M Allott, C N Danson, D Neely, R S Marjoribanks
Observation and disscussion of optical scatter in ultra high intensity laser solid interactions

Z Najmudin, E L Clark, A E Dangor, C N Danson, K Krushelnick, V Malka, D Neely, M Salvati, M Tatarakis
Inverse Faraday effect and propagation instabilities in the interaction of highly underdense plasmas

D Neely, R M Allott, R J Clarke, J L Collier, C N Danson, C B Edwards, C Hernandez-Gomez, M H R Hutchinson, M Notley, D Pepler, M Randelson, I N Ross, J Springall, M Stubbs, T B Winstone, A E Dangor
Characterisation and application of second harmonic picosecond pulses generated for plasma interactions

International conference on plasma accelerators, Crete, Greece (May 1999)

K Krushelnick, E L Clark, R M Allott, F N Beg, C N Danson, A Machacek, V Malka, Z Najmudin, D Neely, P A Norreys, M Salvati, M I K Santala, M Tatarakis, I Watts, M Zepf, A E Dangor
Ultra high intensity laser produced plasmas as a compact heavy ion injection source

Z Najmudin, R M Allott, F Amiranoff, E L Clark, C N Danson, D Gordon, K Krushelnick, G Malka, V Malka, D Neely, M Salvati, M I K Santala, M Tatarakis, A E Dangor
Measurements of forward Raman scattering and electron acceleration from high intensity plasma interactions at 527nm

D Neely, R M Allott, F Amiranoff, E L Clark, R J Clarke, J L Collier, A E Dangor, C B Edwards, P S Flintoff, P Hatton, Z Najmudin, K Krushelnick, D A Pepler
Simultaneous dual wavelength high energy picosecond pulses for novel particle acceleration experiments

29th anomalous absorption conference, Monterey, USA (June 1999)

A R Bell
Short pulse laser solid interactions

E L Clark, K Krushelnick, M I K Santala, M Tatarakis, I Watts, M Zepf, A E Dangor, P A Norreys, J R Davies, A C Machecek, J S Wark, K W D Ledingham, T McCanny, I Spencer
Multi-megagauss magnetic field generation and ion transport inside solids from ultra-intense laser solid interactions

C N Danson, R M Allott, J L Collier, R J Clarke, C B Edwards, S Hancock, P Hatton, M H R Hutchinson, C Hernandez-Gomez, A Kidd, W Lester, D Neely, M Notley, D A Pepler, M Pitts, C J Reason, D A Rodkiss, T B Winstone, R W W Wyatt, B Wyborn
Achieving relativistic interaction intensities on Vulcan

A C Machecek, D M Chambers, J S Wark, I Watts, M Zepf, A E Dangor, E L Clark, K Krushelnick, M I K Santala, M Tatarakis, P A Norreys, R M Allott, C N Danson, D Neely, R J Majoribanks.
Observations and discussion of optical (3/2) scatter in ultra-high intensity laser-solid interactions

P A Norreys, R M Allott, F N Beg, E L Clark, R J Clarke, A E Dangor, K Krushelnick, K W D Ledingham, A C Machecek, T McCanny, D Neely, M I K Santala, R P Singhal, I Spencer, M Tatarakis, J S Wark, I Watts, S C Wilks, M Zepf
The dependence of the density scale-length of the directionality of the electron beam and the generation of ultra-large magnetic fields in relativistic laser plasmas

7th international workshop on the physics of compressible and turbulent mixing, Saint Petersberg, Russia (July 1999)

P Salvatore, B Meyer, A Richard, M Valadon, J P Jadaud, P Munsch, P Troussel, B Viliette, C Reverdin, J P Thébault, O Willi, J Pasley
Short wavelength Rayleigh-Taylor instability at the ablation front with soft X-ray drive

ICF computing and fast ignitor physics with femtosecond lasers, Garching, Germany (July 1999)

M Borghesi
Short laser pulse experiment for fast ignitor applications: channelling, guiding and fast electron propagation

Diffractive Optics 1999, Jena, Germany (August 1999)

D A Pepler, R M Allott, A Boba, R J Clarke, W Cranton, C N Danson, G Hirst, D Koutsogeorgis, M Mastio, D Neely, M Notley, M Payne, T B Winstone
Materials processing with high power lasers

1st international conference on inertial fusion sciences and applications, Bordeaux, France (September 1999)

D Batani, F Pisani, E Martinolli, A Bernardinello, A Antonicci, J R Davies, M Koening, F Amiranoff, L Gremillet, H Bandulet, C Rosseaux, T Hall, P A Norreys, A E Dangor
Fast electron propagation experiments for fast ignition: evidence for electric field effects

M Borghesi, A J Mackinnon, N Blanchot, B Canaud, J R Davies, R Gaillard, E Lefebvre, G Malka, J Meyer-ter-Vehn, J L Miquel, A A Offenberger, A Pukhov, C Vickers, O Willi
Guiding of short, intense laser pulses through solid guides and preformed plasma channels

E L Clark, K Krushelnick, J R Davies, M Zepf, M Tatarakis, F N Beg, A C Machacek, P A Norreys, M I K Santala, I Watts, A E Dangor
Measurements of energetic proton generation from intense laser interactons with solids

L Gremillet, F Amiranoff, M Koenig, F Pisani, G Bonnaud, C Lebourg, C Rousseaux, C Toupin, A Antonicci, D Batani, E Martinolli, T Hall, P A Norreys, H Bandulet, H Pepin
Experimental evidence of a fast electron jet travelling through solid targets irradiated at relativistic intensities

D Hoarty, O Willi, R Watt, P Gobby
Time dependent energy transport in laser heated targets

G Malka, C Courtois, B Cros, G Mattieussent, N Blanchot, G Bonnaud, M Busquet, B Canaud, D Desenne, L Disdier, J P Garconnet, M Louis-Jacquet, E Lefebvre, L Lours, A Mens, J L Miquel, O Peyrusse, C Rousseaux, M Borghesi, R Gaillard, A J Mackinnon, O Willi, C N Danson, D Neely, D Altenbernd, T Feurer, P Gibbon, R Sauerbrey, U Teubner, W Theobald, I Uschmann, F Amiranoff, S Baton, L Gremillet, J Fuchs, J R Marques, P Gallant, J C Kieffer, H Pepin, J C Adam, A Heron, G Laval, P Mora
High intensity subpicosecond laser pulse propagation in a 1cm capillary tube and fast ignitor experiments

Z Najmudin, E L Clark, A E Dangor, C N Danson, K Krushelnick, V Malka, D Neely, M Salvati, M Tatarakis
Propagation instabilities in the interaction of highly underdense plasmas

Z Najmudin, K Krushelnick, E L Clark, M Salvati, M I K Santala, M Tatarakis, A E Dangor, V Malka, C N Danson, R M Allott, D Neely
Hosing, sausaging, filamentation and sidescatter of a high-intensity short-pulse laser in an under-dense plasma

D Neely, R M Allott, F Amiranoff, E L Clark, R J Clarke, J L Collier, A E Dangor, C N Danson, C B Edwards, D Gordon, C Hernandez-Gomez, M H R Hutchinson, K Krushelnick, G Malka, V Malka, A Modena, Z Najmudin, M Notley, D A Pepler, M Randelson, J Springall, M Salvati, M I K Santala, M Stubbs, M Tatarakis
Gas jet electron acceleration using a 527nm frequency doubled CPA laser pulse

P A Norreys, R M Allott, R J Clarke, D Neely, S J Rose, F N Beg, E L Clark, M I K Santala, M Tatarakis, I Watts, M Zepf, K Krushelnick, A E Dangor, T McCanny, I Spencer, R P Singhal, K W D Ledingham, A C Machacek, S C Wilks, J S Wark
Relativistic laser plasmas and guided conical compression experiments relevant to the fast ignitor scheme for ICF

J Pasley, O Willi, M Borghesi, A Iwase, C E Vickers, A Schiavi, D Hoarty D Neely, M Notley
Experimental observations of coalescent and colliding shock waves in low density foam targets

D Riley, D McSherry
A new diagnostic of dense plasmas

S J Rose
Calculations on Compton scattering of line radiation

M I K Santala, E L Clark, I Watts, M Tatarakis, M Zepf, K Krushelnick, A E Dangor, T McCanny, I Spencer, K W D Ledingham, A C Machacek, J S Wark, R M Allott, R J Clarke, P A Norreys
Fast ion induced nuclear reactions in the plasma blow-off in intense laser-solid interactions

A Schiavi, M Borghesi, J Pasley, O Willi, D Neely, M Notley, W Nazarov
S*hock wave collisions in low density foams*

M Tatarakis, F Beg, E L Clark, K Krushelnick, A C Machecek, V Malka, Z Najmudin, D Neely, P A Norreys, M Salvati, M I K Santala, I Watts, M Zepf, B Wyborn
Magnetic fields generated during high intensity laser plasma interaction

O Willi, J Pasley, A Iwase, S J Rose, Z Nazarov, B Meyer, A Richard, P Salatore, J P Jadaud, P Munsch, C Reverdin
Measurments of the growth rate of the short wavelength Rayleigh-Taylor instability of foam foil packages driven by a soft X-ray pulse

O Willi, J Pasley, A Iwase, W Nazarov, B Meyer, A Richard, P Salvatore, C Reverdin
Increase of the drive pressure in a soft X-ray irradiated foam foil package

Y Xu, S J Rose
Designing cylindrical targets to measure the radiative properties of high density and temperature plasmas

41st meeting of the American physical society division of plasma physics, Seattle, USA (November 1999)

K Krushelnick
Magnetic fields generated during high intensity laser plasma interactions

Lasers 1999, Quebec, Canada (December 1999)

R M Allott, C B Edwards, J L Collier, C N Danson, M H R Hutchinson, D Neely, B Wyborn
Vulcan; a petawatt user facility for 10^{21} W cm^{-2} experiments

20th workshop on physics of high energy density in matter, Hirschegg, Austria (January 2000)

O Willi
Inertial fusion physics and ultrashort laser-pulse interaction

IOP optical group meeting on laser materials processsing, London, UK (March 2000)

R Allott, D Pepler, R Clarke, M Notley, A G MacPhee, R Steel, D Neely, C N Danson, T Winstone, G Hirst, I Ross
The development of a high energy density UV beamline for materials processing

27th IOP plasma physics conference, Brighton, UK (March 2000)

C B Edwards, C Aldis, R M Allott, R Clark, J Collier, C N Danson, B Eltham, A Frackiewicz, S Hancock, P Hatton, S Hawkes, C Hernandez-Gomez, P Holligan, C J Hooker, M H R Hutchinson, A Jackson, A Kidd, T Knott, W Lester, A MacPhee, D Neely, M M Notley, D A Pepler, M Pitts, C J Reason, K Rodgers, D A Rodkiss, I N Ross, N Symcox, R Wellstood, G Wiggins, T B Winstone, R W W Wyatt, B Wyborn
Vulcan; a petawatt user facility for 10^{21} W cm^{-2} experiments

O Willi
Inertial fusion and ultrashort laser-pulse interaction

O Willi
Recent progress in inertial confinement fusion

K Krushelnick, E L Clark, M Zepf, F N Beg, M I K Santala, M Tatarakis, I Watts, A E Dangor, P A Norreys, J R Davies, A Machacek,
Energetic ions and electrons from high intensity laser produced plasmas

N C Woolsey, R A D Grundy, R O Dendy, P A Norreys, S J Rose, J G Kirk
Supernova remnant simulation experiments using the Vulcan laser

THESES

S Nuruzzaman
Studies of parametric and hydrodynamic instabilities in laser produced plasmas
PhD, University of London, (1999)

Science – Astra

JOURNAL PUBLICATIONS, BOOKS AND PUBLISHED PROCEEDINGS

W A Bryan, J H Sanderson, A El-Zein, W R Newell, P F Taday, A J Langley
Laser-induced Coulomb explosion, geometry modification and reorientation of carbon dioxide
J Phys B-Atomic Molecular and Optical Physics **33** (4) 745-766 (2000)

X Fang, K W D Ledingham, P Graham, D J Smith, T McCanny, R P Singhal, A J Langley, P F Taday
Uniform molecular analysis using femtosecond laser mass spectrometry
Rap Comm Mass Spectrometry **13** (14) 1390-1397 (1999)

L J Frasinski, J H Posthumus, J Plumridge, K Codling, P F Taday, A J Langley
Manipulation of bond hardening in H_2^+ by chirping of intense femtosecond laser pulses
Phys Rev Letts **83** (18) 3625-3628 (1999)

P Graham, K W D Ledingham, R P Singhal, T McCanny, S M Hankin, X Fang, D J Smith, C Kosmidis, P Tzallas, A J Langley, P F Taday
An investigation of the angular distributions of fragment ions arising from the linear CS_2 and CO_2 molecules
J Phys B-Atomic Molecular and Optical Physics **32** (23) 5557-5574 (1999)

C Kosmidis, P Tzallas, K W D Ledingham, T McCanny, R P Singhal, P F Taday, A J Langley
Multiply charged intact ions of polyatomic cyclic molecules generated by a strong laser field
J Phys Chem A **103** (35) 6950-6955 (1999)

K W D Ledingham, D J Smith, R P Singhal, T McCanny, P Graham, H S Kilic, W X Peng, A J Langley, P F Taday, C Kosmidis
Multiply charged ions from aromatic molecules following irradiation in intense laser fields
J Phys Chem A **103** (16) 2952-2963 (1999)

J F McCann, J H Posthumus
Molecular dynamics in intense laser fields
Phil Trans R Soc Lond **A357** (1755) 1309-1329 (1999)

J H Sanderson, A El-Zein, W A Bryan, W R Newell, A J Langley, P F Taday
Geometry modifications and alignment of H_2O in an intense femtosecond laser pulse
Phys Rev A **59** (4) R2567-R2570 (1999)

D J Smith, K W D Ledingham, R P Singhal, T McCanny, P Graham, H S Kilic, P Tzallas, C Kosmidis, A J Langley, P F Taday
The onset of Coulomb explosions in polyatomic molecules
Rap Comm Mass Spectrometry **13** (14) 1366-1373 (1999)

I D Williams, W R Newell
Electron and laser interactions with positive ions
Phil Trans R Soc Lond **A357** (1755) 1297-1308 (1999)

I D Williams, B Srigengan, P McKenna, W R Newell, J H Sanderson, W A Bryan, A El-Zein, P F Taday, A J Langley
Short pulse laser interaction with positive ions
Physica Scripta **T80B** 534-535 (1999)

IN PRESS AT END OF 1999/2000

P Graham, X Fang, K W D Ledingham, R P Singhal, T McCanny, D J Smith, C Kosmidis, P Tzallas, A J Langley, P F Taday
Unusual fragmentation patterns from dissociation of some small molecules
Laser and Particle Beams (accepted for publication)

P Graham, K W D Ledingham, R P Singhal, T McCanny, S M Hankin, X Fang, P Tzallas, C Kosmidis, P F Taday, A J Langley
The angular distributions of fragment ions from labelled and unlabelled N_2O in intense laser fields
J Phys B-Atomic Molecular and Optical Physics (submitted)

N Hay, M Castillejo, R de Nalda, E Springate, K J Mendham, J P Marangos
High-order harmonic generation in cyclic organic molecules
Phys Rev A **61** 053810 (2000)

J H Posthumus, J Plumridge, L J Frasinski, K Codling, P F Taday, E J Divall, A J Langley
Zero-photon dissociation of H_2^+ in intense laser fields
J Phys B-Atomic Molecular and Optical Physics (submitted)

P Tzallas, C Kosmidis, K W D Ledingham, R P Singhal, T McCanny, S M Hankin, P F Taday, A J Langley
On the multielectron dissociation of some cyclic aromatic molecules induced by strong laser fields
J Phys Chem (submitted)

CONFERENCE PRESENTATIONS

25th national conference on atomic, molecular and optical physics, Manchester, UK (March-April 1999)

W A Bryan, A El-Zein, J H Sanderson, W R Newell, A J Langley, P F Taday
Triatomic molecular structure studied by ion-momentum imaging and Monte Carlo simulation

Ultraintense laser interactions and applications - 1, Elounda, Greece (May 1999)

P Tzalas, C Kosmidis, K W D Ledingham, T McCanny, R P Singhal, D J Smith, P F Taday, A J Langley
Dissociation phenomena following multicharged polyatomic ion formation in intense laser fields

W A Bryan, A El-Zein, J H Sanderson, W R Newell, A J Langley, P F Taday
Momentum imaging of carbon dioxide using 55 fs pulses

N Hay, E Springate, K J Mendham, J P Marangos, M Castillejo, R de Nalda
High harmonic generation in organic molecules

XXIst international conference on the physics of electronic and atomic collisions, Sendai, Japan (July 1999)

K Codling
Manipulating molecules with intense laser fields

P McKenna, A El-Zein, W A Bryan, B Srigengan, J H Sanderson, I D Williams, W R Newell, P F Taday, A J Langley
Beams of molecular ions in intense laser fields

J H Sanderson, W A Bryan, A El-Zein, W R Newell, I D Williams, P McKenna, P F Taday, A J Langley
Momentum imaging of ground state and vibrationally excited H_2 using a femtosecond laser pulse of intensity 10^{17} W cm^{-2}

W A Bryan, A El-Zein, J H Sanderson, W R Newell, A J Langley, P F Taday
Triatomic molecular structure studied by ion-momentum imaging and Monte Carlo simulation

8th international conference on multiphoton processes, Monterey, USA (October 1999)

L J Frasinski
Bond hardening and zero-photon dissociation in H_2^+

Invited talk at Queen's University, Belfast, UK (October 1999)

L J Frasinski
Bond hardening and zero-photon dissociation in H_2^+

High power laser users meeting, Abingdon, UK (December 1999)

L J Frasinski
Bond hardening and zero-photon dissociation in H_2^+

J H Sanderson
CO_2 and H_2O in intense femtosecond laser pulses

I D Williams
H_2^+ ion beams in intense laser fields

The Royal Society meeting on astronomy, physics and chemistry of H_3^+, London, UK (February 2000)

I D Williams, B Srigengan, P McKenna, W R Newell, J H Sanderson, W A Bryan, A El-Zein, P F Taday, A J Langley
H_2^+ ion beams in intense laser fields

THESES

R V Thomas
Short pulse high intensity laser interactions with molecules
PhD, University of London, 1999

N Hay
The interaction of organic molecules and atomic clusters with ultrashort high intensity laser pulses
PhD, University of London, 1999

Science - Lasers for Science Facility

JOURNAL PUBLICATIONS, BOOKS AND PUBLISHED PROCEEDINGS

P W Barnes, P Sharkey, I R Sims, I W M Smith
Rate coefficients for the reaction and relaxation of H_2O in specific vibrational states with H atoms and H_2O
Farad Discuss **113** 167-180 (1999)

J A Dickinson, M R Hockridge, E G Robertson, J P Simons
Molecular and supramolecular structures of N-phenyl formamide and its hydrated clusters
J Phys Chem A **103** (35) 6938-6949 (1999)

I Farrell, P Matousek, A Vlcek
Femtosecond spectroscopic study of MLCT excited-state dynamics of Cr(CO)4(bpy):excitation-energy-dependent branching between CO dissociation and relaxation
J Am Chem Soc **121** (22) 5296-5301 (1999)

R J Graham, R T Kroemer, M Mons, E G Robertson, L C Snoek, J P Simons
Infrared ion dip spectroscopy of a noradrenaline analogue: hydrogen bonding in 2-amino-1-phenylethanol and its singly hydrated complex
J Phys Chem A **103** (48) 9706-9711 (1999)

S Hess, R A Taylor, K Kyhm, J F Ryan, B Beaumont, P Gibart
Femtosecond exciton dynamics and the Mott transition in GaN under resonant excitation
Physica Status Solidi B **216** (1) 57-62 (1999)

S Hess, R A Taylor, E D O'Sullivan, J F Ryan, N J Cain, V Roberts, J S Roberts
Hot carrier relaxation by extreme electron-LO phonon scattering in GaN
Physica Status Solidi B **216** (1) 51-55 (1999)

R J Hicken, J Wu
Observation of ferromagnetic resonance in the time domain
J Appl Phys **85** (8) 4580-4582 (1999)

M R Hockridge, E G Robertson
Hydrated clusters of 2-phenylethyl alcohol and 2-phenylethylamine: structure, bonding and rotation of the $S_1 \leftarrow S_0$ electronic transition moment
J Phys Chem A **103** (19) 3618-3628 (1999)

M R Hockridge, S M Knight, E G Robertson, J P Simons, J McCombie, M Walker
Conformational landscapes in flexible organic molecules: 4-hydroxy phenyl ethanol (p-tyrosol) and its singly hydrated complex
Phys Chem Chem Phys **1** (3) 407-413 (1999)

S M Howdle, M Poliakoff, M W George
Infrared and Raman spectroscopy in supercritical fluids
Chapter 3 pp 147-209 in "Chemical Synthesis using supercritical fluids" eds W Leitner, P G Jessop, publ Wiley-VCH (1999)

T J Hughes, M R Levy
State-specific production of MnCl('IR', 'red') in the reaction Mn(a ^6S, a ^6D_J)+Cl_2*
Phys Chem Chem Phys **2** (4) 651-659 (2000)

P Jennings, A C Jones, A R Mount
In situ spectroelectrochemical studies of the fluorescence of 5-substituted indole trimer films
Phys Chem Chem Phys **2** (6) 1241-1248 (2000)

D J Liard, A Vlcek
Picosecond dynamics of photoinduced interligand electron transfer in [Re(MQ+)(CO)$_3$(dmb)]$^{2+}$(dmb=4,4'-Dimethyl-2,2'-bipyridine,MQ$^+$=N-Methyl-4,4'-bipyridinium)
Inorg Chem **39** (3) 485-490 (2000)

E A Mastio, M R Craven, W M Cranton, C B Thomas, M Robino, E Fogarassy
The effects of KrF pulsed laser and thermal annealing on the crystallinity and surface morphology of radiofrequency magnetron sputtered ZnS:Mn thin films deposited on Si
J Appl Phys **86** (5) 2562 2570 (1999)

P Matousek, M Towrie, A Stanley, A W Parker
Efficient rejection of fluorescence from Raman spectra using picosecond Kerr gating
Appl Spectr **53** (12) 1485-1489 (1999)

O Meighan, C Danson, L Dardis, C L S Lewis, A MacPhee, C McGuinness, R O'Rourke, W Shaikh, I C E Turcu, J T Costello
Application of a picosecond laser plasma continuum light source to a dual-laser plasma photoabsorption experiment
J Phys B-Atomic Molecular and Optical Physics **33** (6) 1159-1168 (2000)

V Meyer, S N Bagayev, P E G Baird, P Bakule, M G Boshier, A Breitrück, S L Cornish, S Dychkov, G H Eaton, A Grossmann, D Hübl, V W Hughes, K Jungmann, I C Lane, Y-W Liu, D Lucas, Y Matyugin, J Merkel, G zu Putlitz, I Reinhard, P G H Sandars, R Santra, P V Schmidt, C A Scott, W T Toner, M Towrie, K Träger, L Willmann, V Yakhontov
Measurement of the 1s-2s energy interval in muonium
Phys Rev Letts **84** (6) 1136-1139 (2000)

M Mons, E G Robertson, J P Simons
Intra- and intermolecular π-type hydrogen bonding in aryl alcohols: UV and IR-UV ion dip spectroscopy
J Phys Chem A **104** (7) 1430-1437 (2000)

M Mons, E G Robertson, L C Snoek, J P Simons
Conformations of 2-phenylethanol and its singly hydrated complexes: UV-UV and IR-UV ion-dip spectroscopy
Chem Phys Letts **310** (5-6) 423-432 (1999)

E D O'Sullivan, S Hess, R A Taylor, N J Cain, V Roberts, J S Roberts, J F Ryan
Hot carrier relaxation in GaN: LO phonon scattering and excitonic effects
Physica B **272** (1-4) 402-405 (1999)

F L Plows, A C Jones
Laser-desorption supersonic jet spectroscopy of phthalocyanines
J Mol Spec **194** (2) 163-170 (1999)

R J Potton
Adaptive spatial filtering using photochromic glass
Meas Sci Tech **10** (12) 1315-1318 (1999)

K L Reid, T A Field, M Towrie, P Matousek
Photoelectron angular distributions as a probe of alignment evolution in a polyatomic molecule: picosecond time- and angle-resolved photoelectron spectroscopy of S_1 para-difluorobenzene
J Chem Phys **111** (4) 1438-1445 (1999)

G D Scholes, T Fournier, A W Parker, D Phillips
Solvation and intramolecular reorganisation in 9,9'- bianthryl: analysis of resonance Raman excitation profiles and ab initio molecular orbital calculations
J Chem Phys **111** (13) 5999-6010 (1999)

R A Taylor, S Hess, K Kyhm, J Smith, J F Ryan, G P Yablonskii, E V Lutsenko, V N Pavlovskii, M Heuken
Stimulated emission and excitonic bleaching in GaN epilayers under high-density excitation
Physica Status Solidi B **216** (1) 465-470 (1999)

J R G Thorne, M Jones, C S McCaw, K M Murdoch, R G Denning, N M Khaidukov
Two photon spectroscopy of europium(III) elpasolites
J Phys C-Condensed Matter **11** (40) 7851-7866 (1999)

J R G Thorne, A Karunathilake, H Choi, R G Denning, T Luxbacher
Two photon spectroscopy of samarium(III) in the elpasolite CS_2NaYC1_6:Sm^{3+}
J Phys C-Condensed Matter **11** (40) 7867-7879 (1999)

E S Tok, R W Price, A G Taylor, J Zhang
Oscillatory optical second-harmonic generation from Si(001) surface during thin-film epitaxy
Appl Phys Letts **76** (7) 933-935 (2000)

E S Tok, N J Woods, R W Price, A G Taylor, J Zhang
Optical second harmonic generation studies of epitaxial growth of Si and SiGe
J Crystal Growth **209** (2-3) 297-301 (2000)

PUBLISHED DURING 1998/1999

A P Martin, A N Brunton, G W Fraser, A D Holland, A Keay, J Hill, N Nelms, I C E Turcu, R Allott, N Lisi, N Spencer
Imaging X-ray fluorescence spectroscopy using microchannel plate relay optics
X-ray Spectrometry **28** (1) 64-70 (1999)

S F Parker, S M Tavender, N M Dixon, H Herman, K J P Williams, W F Maddams
Raman spectrum of β-carotene using laser lines from green (514.5nm) to near-infrared (1064nm): implications for the characterization of conjugated polyenes
Appl Spectr **53** (1) 86-91 (1999)

IN PRESS AT END OF 1999/2000

W M Kwok, C Ma, P Matousek, A W Parker, D Phillips, W T Toner, M Towrie
Time-resolved resonance Raman spectra of the intramolecular charge transfer state of DMABN
Chem Phys Letts **322** (5) 395-400 (2000)

W M Kwok, C Ma, D Phillips, P Matousek, A W Parker, M Towrie
Picosecond time-resolved study of 4-dimethylaminobenzonitrile in polar and non-polar solvents
J Phys Chem A **104** (18) 4188-4197 (2000)

L C Snoek, E G Robertson, R T Kroemer, J P Simons
Conformational landscapes in amino acids: infrared and ultraviolet ion-dip spectroscopy of phenylalanine in the gas phase
Chem Phys Letts **321** (1-2) 49-56 (2000)

S Ameer-Beg, R G Brown, P Matousek, M Towrie, E Nibbering
Ultrafast studies of ESIPT in room temperature solutions of 3-hydroxyflavone
Chem Phys Letts (in press)

A C Benniston, P Matousek, A W Parker
Kerr-gated picosecond time-resolved resonance Raman spectroscopic probing of the excited states in lambda-[Ru(bipy)$_2$dppz](BF$_4$)$_2$
J Raman Spec (in press)

G J Berry, J A Cairns, M R Davidson, Y C Fan, A G Fitzgerald, J Thomson, W Shaikh
Analysis of metal features produced by UV irradiation of organometallic films
Appl Surf Sci (accepted for publication)

R H Bisby, S A Johnson, A W Parker
Radicals from one-electron oxidation of 4-aminoresorcinol: models for the active site radical intermediate in copper amine oxidases
J Phys Chem (in press)

E G Robertson
IR--UV ion-dip spectroscopy of N-phenyl formamide and its hydrated clusters
Chem Phys Letts (in press)

S Summers, H S Reehal, G J Hirst
KrF excimer laser crystallisation of silicon thin films
J Mat Sci (accepted for publication)

X-Z Sun, S M Nikiforov, M W George
Fast time-resolved step scan FTIR spectroscopy in supercritical fluids
Proceedings of the 12th international conference on Fourier transform spectroscopy (in press)

I G Childs, J Dyer, D C Grills, X-Z Sun, M W George
Investigation into the reactivity of (h5-C$_5$R$_5$)M(CO)$_2$(alkane) (M = Mn or Re; R = H or Ph; alkane = heptane or cyclopentane) and (h5-C$_5$H$_5$)Re(CO)$_2$(Xe) in solution at cryogenic and room temperature
J Chem Soc Dalton (submitted)

A Beeby, S W Botchway, I M Clarkson, S Faulkner, A W Parker, D Parker, J A G Williams
Luminescence imaging microscopy and lifetime mapping using kinetically stable lanthanide (III) complexes
Photochem. Photobiol (submitted)

C C Colley, S R Griffiths-Jones, I P Clark, M W George, M S Searle
Infrared spectroscopy of the native and unfolded states of bovine ubiquitin: proteins stability and fast time-resolved IR kinetic measurements of protein folding at low pH
Chem Comm (submitted)

CONFERENCE PRESENTATIONS

Bragg gratings and special filters, London, UK (May 1999)

R J Potton
Spectral and time response of photochromic glasses and their application to adaptive filtering

9th international conference on time-resolved vibrational spectroscopy, Tucson, USA (May 1999)

A W Parker
Early relaxation processes of photoexcited states

L C Abbott, P Foggi, R E Hester, I K Lednev, P Matousek, J N Moore, F V R Neuwahl, M Towrie, S Umapathy, T-Q Ye
Azobenzene photoisomerization pathways

A W Parker, P Matousek, M Towrie, W T Toner, A C Benniston, D Phillips
Early relaxation processes of photoexcited states

P Matousek, M Towrie, A Stanley, A W Parker
Novel method for efficient rejection of fluorescence from Raman spectra

M Towrie, M W George, D C Grills, P Matousek, A W Parker
Development of a new IR picosecond time resolved facility

5th international conference on atomically controlled surfaces, interfaces and nanostructures, Aix-en-Provence, France (July 1999)

G J Berry, J A Cairns, M R Davidson, Y C Fan, A G Fitzgerald, J Thomson, W Shaikh
Analysis of metal features produced by UV irradiation of organometallic films

Annual conference of the British association for crystal growth, Cambridge, UK (September 1999)

S Summers, H S Reehal, G J Hirst
Excimer laser crystallisation of silicon thin films

6th international conference on methods and applications of fluorescence spectroscopy, Paris France (September 1999)

J P Connelly, S W Botchway, L Kunz, A W Parker, A J MacRobert
Fluorescence lifetime imaging of photosensitizer distributions in mammalian cells using a picosecond gated laser line scanning confocal microscope

Lasers for science user meeting, Abingdon, UK (October 1999)

R Devonshire
New high resolution OPA and its application in photodissociation dynamics

Prof Oelkrug
Ultrafast photoprocesses in phenylenevinylene vapour deposited films

A Beeby
Luminescence microscopy using lanthanide chelates

J Simons
Model biomolecular clusters: A scorpion's tale

K Reid
Picosecond time and angle resolved photoelectron spectroscopy of pDFB

D Phillips
A ps Raman and Fluorescence study of dimethylaminobenzonitrile in polar and non-polar solvents

I W M Smith
State-to-state studies of inelastic and reactive collisions

A Benniston
Ps TR^3 studies into photoelectron transfer processes in metallo-based cyclophanes, catenanes and ruthenium intercalates

M George
Nanosecond step-scan time-resolved infrared spectroscopy in conventional and supercritical fluids

P O'Neill
Radiation induced charge migration in DNA initiated by 193 nm light

M Folkard
Targeting of individual cells using focused X-rays

K Brindle
A novel fluorescence technique for studying proteins in vivo

M Hill
Ultrasoft X-rays for cellular radiobiology and DNA biochemistry

J Cairns
The production of high resolution X-ray masks

R Hicken
Observation of ultrafast demagnetisation in a nickel foil

H Reehal
Excimer laser crystallisation of silicon thin films

R Taylor
Plasma and exciton dynamics in GaN

G Adomopoulos
Determination of bonding type in carbon films from Raman spectra

J Costello
Resonant photoionisation imaging of a calcium laser plasma plume

A Michette
Scanning X-ray microscope

P Matousek, M Towrie, A Stanley, A W Parker
Rejection of fluorescence from Raman spectra

C E Canosa-Mas, N J Hendy, D Shah, A Vipond, R P Wayne
Discharge flow studies of the kinetics of reactions of Br, Cl, BrO and ClO with CH_3O using LIF detection

T Dines
The assignment of vibrational spectra from ab initio calculations

C G Coates, P Callaghan, J J McGarvey
Time-resolved spectroscopy of the interaction of metal complexes with single and double stranded DNA

R H Bisby, C Mead, C G Morgan
Photosensitive liposomes as 'cages' for laser induced solute delivery

D Laird, A Vlcek
Picosecond dynamics of photo-induced interligand electron transfer in $[Re(MQ^+)(CO)_3(dmb)]^{2+}$

N Khan, G Hirst, W Shaikh
The CLF X--ray and UV laboratory

J Daub, R Engl, J Kurzawa, S Schneider, A Stockmann
Electrochemical properties of phenothiazine/pyrene-based dyes

C S Colley
Probing photopolymerisation and protein folding by time-resolved vibrational spectroscopy

P Baranyai, S Gangl, G Grabner, G Koehler, M Knapp, T Vidoczy
Use of triplet probes to study membrane fluidity

I Clark, S Wilkinson
CCLRC nanosecond science laboratory

D Chastaing, D Sebastien, D Le Picard, I R Sims, I W M Smith
Chemical synthesis in interstellar space

D Nees
Laser tweezers for colloidal science

C S Ma, W M Kwok, P Matousek, M Towrie, A W Parker, D Phillips
Time resolved studies on DMABN in polar and non-polar solvents

D C Smith, C J Stevens, P Gay, C Chen, J F Ryan
Ultrafast condensate dynamics of BSCCO-2212

S Botchway, A J MacRobert, J P Connelly, L Kunz, A W Parker
Confocal laser-line scanning fluorescence lifetime imaging of mammalian cells to study the distribution of photodynamic drugs using a subnanosecond time resolution

P Scully, R Bartlett, P Eldridge, S Caulder, R Chandy
Photo-induced refractive index changes in plastic optical fibres

W T Toner
Relaxation of photoexcited molecules in solution.

J S Hirsch, O Meighan, J-P Mosnier, P van Kampen, J T Costello, C L S Lewis, A G MacPhee, G J Hirst, J Westhall, W Shaikh
Vacuum-UV resonant photoabsorption imaging of laser produced plasmas – the experiment

I Farrell, A Vlcek
Ultrafast dynamics of $Cr(CO)_4(bpy)$

M Towrie, R Devonshire
Tunable, high resolution (0.012 cm^{-1}) optical parametric amplifier

M Towrie, M W George, D C Grills, P Matousek, A W Parker
Development of a new IR picosecond time resolved facility

S Tavender, M Towrie, A W Parker
The EPSRC laser loan pool

M-H Teiten
Meta-tetrahydroxyphenyl chlorin (mTHPC) subcellular localization, transport and photodynamic effects on sensitive and multidrug-resistant (MDR) human breast cancer cells

MRS fall meeting - optical microstructural characterization of semiconductors, Boston, USA (November 1999)

S J Webb, L Wang, S Summers, H S Reehal
Characterisation of plasma-assisted CVD grown polycrystalline Si on glass substrates

11th AINSE conference on nuclear techniques of analysis and 6th vacuum society of Australia congress, Lucas Heights, Australia, (November 1999)

N Barradas, S Summers, H S Reehal, E Wendler, C Jeynes
Characterisation of a-Si and c-Si alloys by RBS/ERD with self-consistent data analysis using simulated annealing

Infrared and Raman discussion group - 161st meeting, London, UK (December 1999)

A W Parker
Kerr-gated time-resolved Raman spectroscopy

Trombay symposium on radiation and photochemistry, Mumbia, India, (January 2000)

A W Parker
Intramolecular charge transfer investigated using Kerr gated time-resolved Raman and fluorescence spectroscopies

European conference on molecular clusters, Munich, Germany (1999)

M Mons
Ultraviolet and infrared ion dip spectroscopy of molecular conformers and their hydrated clusters

American geophysical union spring meeting, Boston, USA (June 1999)

D Shah, C E Canosa-Mas, N Hendy, A Vipond, R P Wayne
Discharge-flow studies of the reactions of Br, BrO, Cl and ClO with CH_3O

IOP optical group meeting on laser materials processsing, London, UK (March 2000)

P J Scully, R Bartlett, S Caulder, P Eldridge, R Chandy, J McTavish, I Clark, M Towrie, A W Parker
UV laser photo-induced refractive index changes in PMMA measured on-line using Fabry-Perot interferometry

European workshop on biological molecules in the gas phase, Les Houches, France (2000)

E G Robertson, L C Snoek
Structural studies of phenylalanine and of model peptides and their hydrates in a jet

Gas kinetics discussion group winter meeting, Reading, UK (March 2000)

C E Canosa-Mas, N Hendy, J Maclennan, D Shah, A Vipond, R P Wayne
Discharge-flow studies of some reactions of Br, BrO, Cl and ClO with CH_3O

COBRA workshop 2000, Oxford, UK (2000)

C E Canosa-Mas, N Hendy, J Maclennan, D Shah, A Vipond, R P Wayne
Discharge-flow studies of some reactions of Br, BrO, Cl and ClO with CH_3O

CONFERENCE PRESENTATIONS 1998/1999

CLEO/Europe-EQEC'98, Glasgow, UK (September 1998)

O Meighan, L Dardis, C Moloney, C McGuinness, J T Costello, C L S Lewis, R O'Rourke, A MacPhee, I C E Turcu, C Danson, S Huntingdon, N Takeyasu,W Shaikh
Characteristics of an extreme-UV continuum light source based on a laser plasma driven by a 7psec 248 nm pulse

O Meighan, L Dardis, C Moloney, C McGuinness, J T Costello, C L S Lewis, R O'Rourke, A MacPhee, I C E Turcu, C Danson, S Huntingdon, N Takeyasu,W Shaikh
Table top picosecond dual laser plasma photoabsorption experiment

2nd DTI/EPSRC conference on progress in photovoltaics, Manchester, UK (February 1999)

L Wang, S Summers, H S Reehal, D B Holt, E Napchan, G J Hirst
Growth and characterisation of thin film crystalline silicon for solar cells

ECAMP, Sienna, Italy, (July 1998)

O Meighan, L Dardis, C Moloney, C McGuinness, J T Costello, C L S Lewis, R O'Rourke, A MacPhee, I C E Turcu, C Danson, S Huntingdon, N Takeyasu,W Shaikh
Controlled collapse of the 5f wavefunction of thorium along its isonuclear sequence: first observation dual laser plasma photoabsorption experiments

O Meighan, L Dardis, C Moloney, C McGuinness, J T Costello, C L S Lewis, R O'Rourke, A MacPhee, I C E Turcu, C Danson, S Huntingdon, N Takeyasu,W Shaikh
A table top dual laser plasma based XUV photoabsorption experiment with 150 psec time resolution; performance characteristics and results

SEMINARS

Indian Institute of Science, Bangalore, India (January 2000)

A W Parker
Intramolecular charge transfer - TR^3 against fluorescence background

Departments of Inorganic and Physical Chemistry Seminar, Nottingham University, UK (February 2000)

A W Parker
Investigating reaction intermediates and dynamics using time-resolved resonance Raman spectroscopy

Department of Physical Chemistry, Queens University Belfast, UK (February 2000)

A W Parker
Advances in time resolved resonance Raman spectroscopy – picosecond reaction dynamics

CLF Seminar

M Towrie
Ultrafast lasers in chemistry

Invited lectures at University College Berkeley and University of Southern California, USA

J P Simons
Getting into shape: conformational landscapes and supramolecular structures in simple biomolecules

Invited lectures at Complutense University and CSIC, Madrid, Spain

J P Simons
Laser spectroscopy of small biomolecules and their hydrated clusters

European Gordon Conference, 'Molecular and Ionic Clusters 2000', Toulouse, France (April 2000)

J P Simons
Ion dip spectroscopy of conformers, tautomers and hydrated clusters

THESES

M R Hockridge
Laser spectroscopy of biologically-related molecules and their hydrated clusters
DPhil, University of Oxford, 1999

X Z Sun
Fast infrared spectroscopy in supercritical fluids
PhD, University of Nottingham, 2000

Facility Development

JOURNAL PUBLICATIONS, BOOKS AND PUBLISHED PROCEEDINGS

J L Collier, C Hernandez-Gomez, I N Ross, P Matousek, C N Danson, J Walczak
Evaluation of an ultrabroadband high-gain amplification technique for chirped pulse amplification facilities
Appl Opt **38** (36) 7486-7493 (1999)

C N Danson, R M Allott, S Angood, G Booth, J L Collier, A R Damerell, C B Edwards, P S Flintoff, J Govans, S Hancock, P Hatton, S J Hawkes, M H R Hutchinson, M H Key, C Hernandez-Gomez, J Leach, W Lester, D Neely, P A Norreys, M Notley, D A Pepler, C J Reason, D A Rodkiss, I N Ross, W T Toner, M Trentelman, J A Walczak, R A Wellstood, T B Winstone, R W Wyatt, B Wyborn
Focused intensities of 10^{20} W cm^{-2} with the upgraded Vulcan CPA interaction facility
Third international conference on solid state lasers for application to inertial confinement fusion, Ed W H Lowdermilk, SPIE **3492** 82-93 (1999)

C N Danson, R Allott, G Booth, J Collier, C B Edwards, P S Flintoff, S J Hawkes, M H R Hutchinson, C Hernandez-Gomez, J Leach, D Neely, P Norreys, M Notley, D A Pepler, I N Ross, J A Walczak, T B Winstone
Generation of focused intensities of 5×10^{19} W cm^{-2}
Laser and Particle Beams **17** (2) 341-347 (1999)

C N Danson, R M Allott, J L Collier, R J Clarke, C B Edwards, S Hancock, P Hatton, M H R Hutchinson, C Hernandez-Gomez, A Kidd, W Lester, D Neely, P A Norreys, M Notley, D A Pepler, M Pitts, C Reason, D Rodkiss, T B Winstone, R W W Wyatt, B Wyborn
Achieving relativistic interaction intensities on Vulcan
IFSA conference proceedings **1** 681-686 (1999)

V V Datsyuk, C J Hooker, E J Divall, G J Hirst, I N Ross, J M D Lister, K Osvay
On the origin of the dip in the KrF laser gain spectrum. II. The short pulse gain saturation experiment
J Chem Phys **112** (8) 3766-3771 (2000)

C Hooker, E Divall, T Kaneko, C Reason, I Ross, M Shaw, N Tucker
Low cost adaptive optical system for laser wavefront correction
Proceedings of the second international workshop on adaptive optics for industry and medicine (Durham, UK), Ed G D Love, publ World Scientific Publishing, pp 3-7 (1999)

C L S Lewis, I Weaver, L A Doyle, G W Martin, T Morrow, D A Pepler, C N Danson, I N Ross
Use of a random phase plate as a KrF laser beam homogenizer for thin film deposition applications
Rev Sci Instr **70** (4) 2116-2121 (1999)

P Matousek, B Rus, I N Ross
Design of a multi-petawatt optical parametric chirped pulse amplifier for the iodine laser ASTERIX IV
IEEE JQE **36** (2) 158-163 (2000)

D Neely, C N Danson, R M Allott, F Amiranoff, E L Clark, C E Clayton, J L Collier, A E Dangor, A Djaoui, C B Edwards, P S Flintoff, D Gordon, P Hatton, M Harman, M H R Hutchinson, K Krushelnick, G Malka, V Malka, A Modena, Z Najmudin, D A Pepler, I N Ross, M Salvati, M Santala, M Tatarakis, M Trentelman, T B Winstone
Multi-terawatt frequency doubling of picosecond pulses for plasma interactions
Third international conference on solid state lasers for application to inertial confinement fusion, Ed W H Lowdermilk, SPIE **3492** 414-423 (1999)

D Neely, C N Danson, R Allott, F Amiranoff, J L Collier, A E Dangor, C B Edwards, P Flintoff, P Hatton, M Harman, M H R Hutchinson, Z Najmudin, D A Pepler, I N Ross, M Salvati, T Winstone
Frequency doubling of multi-terawatt picosecond pulses
Laser and Particle Beams **17** (2) 281-286 (1999)

K Osvay, I N Ross
Efficient tuneable bandwidth frequency mixing using chirped pulses
Opt Comm **166** (1-6) 113-119 (1999)

K Osvay, I N Ross, J M D Lister, C J Hooker
High dynamic range measurement of temporal shape and contrast of ultrashort UV pulses
Appl Phys B **69** (1) 19-23 (1999)

I N Ross, P Matousek, M Towrie, A J Langley, J L Collier, C N Danson, C Hernandez-Gomez, D Neely, K Osvay
Prospects for a multi-PW source using optical parametric chirped pulse amplifiers
Laser and Particle Beams **17** (2) 331-340 (1999)

W Shaikh, G Hirst, R M Allott, I C E Turcu, M Folkard, K Ledingham, R Donovan, N Khan
A plasma light source for the VUV spectral region
X-ray lasers 1998, Eds Y Kato, H Takuma, H Daido, IEEE J Select Topics in Quant Electr **5** (6) 1522-1525 (1999)

IN PRESS AT END OF 1999/2000

C N Danson, R M Allott, J L Collier, R J Clarke, C B Edwards, S Hancock, P Hatton, S Hawkes, M H R Hutchinson, C Hernandez-Gomez, A Kidd, W Lester, D Neely, P A Norreys, M Notley, D Pepler, M Pitts, C J Reason, D A Rodkiss, T B Winstone, R W W Wyatt, B Wyborn
Achieving relativistic interaction intensities on Vulcan
J Mod Opt (accepted for publication)

C Hernandez-Gomez, J L Collier, S J Hawkes, C N Danson, C B Edwards, D A Pepler, I N Ross, T B Winstone
Wave-front control of a large-aperture laser system by use of a static phase corrector
Appl Opt **39** (12) 1954-1961 (2000)

D Neely, R M Allott, F Amiranoff, E L Clark, R J Clarke, J L Collier, A E Dangor, C B Edwards, P S Flintoff, P Hatton, Z Najmudin, K Krushelnick, D A Pepler
Simultaneous dual wavelength high energy, picosecond pulses for novel particle acceleration experiments
IEEE Trans Plasma Science (accepted for publication)

I N Ross, J L Collier, P Matousek, C N Danson, D Neely, R M Allott, D A Pepler, K Osvay
Generation of terawatt pulses by use of optical parametric chirped pulse amplification
Appl Opt **39** (15) 2422-2427 (2000)

CONFERENCE PRESENTATIONS

Ultra intense laser interactions and applications - 1, Elounda, Greece (May 1999)

C N Danson, R M Allott, J L Collier, R J Clarke, C B Edwards, S Hancock, P Hatton, S Hawkes, M H R Hutchinson, C Hernandez-Gomez, A Kidd, W Lester, D Neely, P A Norreys, M Notley, D Pepler, M Pitts, C J Reason, D A Rodkiss, T B Winstone, R W W Wyatt, B Wyborn
Developments on the Vulcan CPA interaction facility to achieve focused intensities of up to 10^{20} W cm^{-2}

I N Ross, J L Collier, P Matousek, C N Danson, D Neely, R M Allott, D A Pepler
Experimental investigation of a terawatt optical parametric chirped pulse amplification system

I N Ross, C Hernandez-Gomez, J L Collier, P Matousek, C N Danson, M Parkinson
A novel ultra short pulse preamplifier for large scale CPA facilities

C N Danson, J L Collier, C Hernandez-Gomez, R M Allott
A single shot order autocorrelator for pulse contrast and pulse shape measurements

P Chessa, M Galimbeti, C N Danson, A Giulietti, L A Gizzi
S*ingle shot non-interferometric beam phase retrieval by numerical anaylsis of intensity distributions*

International workshop on adaptive optics, Durham, UK (July 1999)

J L Collier
The measurement, analysis and improvement of the wavefront quality of the Vulcan laser system

C Hooker, E Divall, T Kaneko, C Reason, I Ross, M Shaw, N Tucker
Low cost adaptive optical system for laser wavefront correction

14th UK national quantum electronics and photonics conference, Manchester, UK (September 1999)

R Allott, R J Clarke, D Neely, J L Collier, C N Danson, C B Edwards, C Hernandez-Gomez, M H R Hutchinson, M Notley, D A Pepler, M Randerson, I N Ross, J Springall, M Stubbs, T Winstone
Frequency doubling for ultra-high intensity high contrast ratio plasma interactions

R Allott, D Pepler, M Notley, D Neely, C N Danson, T Winstone, M Payne, A Boba, G Hirst, I Ross
High energy density UV beamline for materials processing

J Collier, C Hernandez-Gomez, R Allott, C N Danson
A single shot 3rd order cross correlator for pulse contrast and pulse shape measurements

J Collier, C Hernandez-Gomez, I N Ross, P Matousek, C N Danson, M Parkinson
A novel ultra-short pulse pre-amplifier for large scale CPA facilities

C N Danson, R Allott, J Collier, R Clark, C B Edwards, S Hancock, P Hatton, M H R Hutchinson, C Hernandez-Gomez, A Kidd, W Lester, D Neely, P Norreys, M Notley, D Pepler, M Pitts, C Reason, D A Rodkiss, T B Winstone, R W W Wyatt, B Wyborn
Developments on the Vulcan CPA interaction facility to achieve focused intensities of up to 10^{20} W cm^{-2}

P Dombi, Z Bakonyi, C J Hooker, I N Ross
Large holographic grating production using a grating interferometer

C Hernandez-Gomez, J Collier, S Hawkes, D A Pepler, C N Danson, I N Ross, C B Edwards, T B Winstone
The measurement, analysis and improvement of the wavefront quality of the VULCAN laser system

1st international conference on inertial fusion sciences and applications, Bordeaux, France (September 1999)

C N Danson, R M Allott, J L Collier, R J Clarke, C B Edwards, S Hancock, P Hatton, M H R Hutchinson, C Hernandez-Gomez, A Kidd, W Lester, D Neely, P A Norreys, M Notley, D A Pepler, M Pitts, C Reason, D Rodkiss, T B Winstone, R W W Wyatt, B Wyborn
Achieving relativistic interaction intensities on Vulcan

PANEL MEMBERSHIP AND CLF STRUCTURE

PANEL MEMBERSHIP

HIGH POWER LASER DIRECT ACCESS PANEL 1999/00

Professor G J Pert (Chairman)
Department of Physics
University of York

Professor W Graham
Plasma & Laser Interaction Physics
Queens University, Belfast

Dr J-C J Gauthier
LULI
Paris, France

Secretary: Dr A MacPhee
Rutherford Appleton Laboratory

Mr P C Thompson
AWE
Aldermaston

Professor S Rose
Clarendon Laboratory
University of Oxford

Professor M G Haines
Plasma Physics Group
Imperial College

Mrs C Exton
Cross Programmes Group
EPSRC

LASERS *for* SCIENCE FACILITY PANEL 1999/00

Dr R Bisby (Chairman)
Department of Biological Sciences
University of Salford

Professor J A Cairns
Department of Electronic Engineering & Physics
University of Dundee

Dr R Devonshire
Department of Chemistry
Sheffield University

Secretary: Dr I P Clark
Rutherford Appleton Laboratory

Dr K G McKendrick
Department of Chemistry
Herriot-Watt University

Dr W R Newell
Department of Physics & Astronomy
University College London

Dr A Bramley
Chemistry
EPSRC

Mrs P Backway, Mrs C Exton
Cross Programmes Group
EPSRC

CLF EURO EXPERIMENTS PANEL 1999/00

Professor C L S Lewis (Chairman)
Department of Pure and Applied Physics
Queen's University of Belfast

Professor C Fotakis
Institute of Electronic Structure and Laser
FORTH, Greece

Professor D Phillips
Department of Chemistry
Imperial College

Dr E Rachlew-Kallne (1999)
Department of Physics
Royal Institute of Technology, Sweden

Secretary: Dr RM Allott
Rutherford Appleton Laboratory

Dr G Matthieussent
Laboratoire Physique Gaz et Plasmas, Universite Paris XI - CNRS, France

Dr R Sigel (1999)
Max-Planck-Institut für Quantenoptik
Garching, Germany

Professor J Meyer-ter-Vehn (2000)
Max-Planck-Institut für Quantenoptik
Garching, Germany

Dr Karel Rohlena (2000)
Institut of Physics
Prague

Professor J Kossanyi (2000)
CNRS – Laboratoire des Materiaux Moléculaires
Thiais, France

CENTRAL LASER FACILITY STRUCTURE